



JOHANNES GUTENBERG
UNIVERSITÄT MAINZ

Structure–Property Relationships of Responsive and Reversible Gels

**Chemical Design of Covalent and Supramolecular
Polymer Networks**

Dissertation

zur Erlangung des Grades „Doktor der Naturwissenschaften“

im Promotionsfach Chemie

am Fachbereich Chemie, Pharmazie, Geografie und Geowissenschaften

der Johannes Gutenberg-Universität Mainz

Katharina Breul

geboren in Burghaun

Mainz, 2021

Die vorliegende Arbeit wurde im Zeitraum von März 2018 bis Dezember 2021 im Arbeitskreis von [REDACTED] am Department für Chemie der Johannes Gutenberg-Universität Mainz angefertigt.

Dekanin:

1. Berichterstatter:

2. Berichterstatter:

Sondergutachterin:

Prüfungsvorsitz:

[REDACTED]

[REDACTED]

[REDACTED]

[REDACTED]

[REDACTED]

Datum der mündlichen Prüfung:

02.02.2022

EIGENSTÄNDIGKEITSERKLÄRUNG

Ich, Katharina Breul, versichere, dass ich die vorliegende Arbeit selbstständig verfasst und keine anderen als die angegebenen schriftlichen und elektronischen Quellen sowie andere Hilfsmittel benutzt habe. Alle Ausführungen, die anderen Schriften wörtlich oder sinngemäß entnommen wurden, habe ich kenntlich gemacht.

Mainz, 07.12.2021

(Ort, Datum)



(Unterschrift)

DANKSAGUNG

An dieser Stelle möchte ich mich zunächst bei [REDACTED] für die Übertragung des abwechslungsreichen Forschungsthemas, das Vertrauen und die Freiheiten bei der Ausgestaltung meiner Projekte sowie seine Unterstützung bei der fachlichen und persönlichen Weiterentwicklung bedanken.

Bei [REDACTED] möchte ich mich nicht nur für die Übernahme des Zweitgutachtens, sondern auch für die stete Ansprechbarkeit und Beratung während der Promotionszeit sowie die gute Zusammenarbeit bei der Praktikums-Betreuung herzlich bedanken.

[REDACTED] danke ich für die Übernahme des Prüfungsvorsitzes sowie die jederzeit unkomplizierte Zusammenarbeit mit seinem Arbeitskreis. Dabei gilt mein Dank im Besonderen [REDACTED] für die Durchführung einer Vielzahl an MALDI-ToF MS Messungen, [REDACTED] für all ihre Mühen mit meinen DSC Proben, [REDACTED] für die zuverlässige Hilfe bei GPC Messungen sowie [REDACTED] für die kompetente Beratung bei synthetischen und analytischen Herausforderungen.

Ich danke außerdem [REDACTED] und allen Mitgliedern seiner Arbeitsgruppe für die produktive Zusammenarbeit. Dies gilt im Besonderen für [REDACTED] die mich nicht nur bei allen Fragen zu Festphasensynthesen und HPLC-Analytik unterstützt haben, sondern deren Expertise und Zuverlässigkeit auch unsere spannenden und erfolgreichen Kooperationen ermöglicht haben.

Besonderer Dank gilt außerdem [REDACTED] und der gesamten Analytik-Abteilung des Departements für die kompetente Beratung bei Fragen und Schwierigkeiten. Auch den glas- und feinmechanischen Werkstätten möchte ich für die schnelle Hilfe und die Umsetzung aller Sonderwünsche danken. Hervorzuheben ist außerdem die Hilfsbereitschaft und Unterstützung des Chemikalienlager-Teams, das selbst unter schwierigsten äußeren Bedingungen immer eine Grundversorgung gewährleistet hat.

Darüber hinaus danke ich der Deutschen Forschungsgemeinschaft für die finanzielle Unterstützung. In diesem Zusammenhang möchte ich auch der „Materials Science in Mainz“ Graduiertenschule sowie dem „Max Planck Graduate Center“ für die finanzielle und organisatorische Unterstützung bei der Teilnahme an Kursen, Konferenzen und Summer Schools danken.

Ein unersetzlicher Baustein für das Gelingen dieser Arbeit war auch die Unterstützung durch die Mitarbeiter [REDACTED]. Hierbei möchte ich zunächst [REDACTED] für seinen unerschöpflichen Rat bei wissenschaftlichen Herausforderungen jeder Art danken.

[REDACTED] bin ich nicht nur für ihre Hilfe bei allen Geräte-, IT- und GPC-spezifischen Problemen, sondern auch für das offene Ohr bei Sorgen aller Art und die vielen schönen Gespräche dankbar. Auch [REDACTED] möchte ich für seine engagierte und motivierte Unterstützung bei der Untersuchung meiner verwirrenden Proben danken.

Für all ihre Mühen, die unerschöpfliche Energie und die kompetente Beratung bei bürokratischen Anliegen jeder Art sowie die stets aufmunternden Worte danke ich außerdem [REDACTED]

Ein großes Dankeschön gilt außerdem allen weiteren aktuellen und ehemaligen Mitgliedern der Arbeitsgruppe. Die hilfsbereite, freundliche und humorvolle Atmosphäre hat den Laboralltag sehr bereichert. Auch an die gemeinschaftliche Beratschlagung bei wissenschaftlichen und nicht-wissenschaftlichen Problemen sowie unsere gemeinsamen Ausflüge, Feiern und Reisen werde ich mich immer gerne zurückerinnern. Besondere Dankbarkeit empfinde ich auch für das Glück, diesen Weg von Anfang bis Ende mit [REDACTED] gemeinsam bestritten zu haben. Ein großer Dank gilt auch [REDACTED] für Ihre Unterstützung beim Korrekturlesen.

Ich danke außerdem meinen engagierten Praktikanten, Modulaten, Bachelor- und Masterstudenten [REDACTED] für ihren motivierten Einsatz und die unbezahlbare Unterstützung. Es war mir eine große Freude mit Euch zusammenzuarbeiten.

Ich danke außerdem allen anderen Wegbegleitern durch Studium, Auslandssemester und Promotion, ohne die nichts von alledem das Gleiche gewesen wäre. [REDACTED] danke ich für seine Beratung zu allen Fragen der organischen Chemie, dem Korrekturlesen dieser Arbeit sowie der immerwährenden Unterstützung. Zuletzt möchte ich mich bei meinen wundervollen Eltern [REDACTED] sowie meinen großartigen Schwestern [REDACTED] für ihren Rückhalt während des gesamten Studiums bedanken.

ZUSAMMENFASSUNG

Die makroskopischen mechanischen und funktionellen Eigenschaften responsiver und reversibler, weicher Materialien werden durch die chemische und topologische Struktur sowie die Dynamik der zugrundeliegenden (makro)molekularen Bausteine bestimmt. In dieser Arbeit werden Möglichkeiten untersucht, durch das gezielte chemische Design dieser Bausteine die viskoelastischen und responsiven Eigenschaften supramolekular vernetzter Polymergele, supramolekularer Gele und kovalent vernetzter Polymergele zu kontrollieren.

Der erste Teil der Arbeit widmet sich dabei dem Einfluss der räumlichen Verteilung der reversiblen Verknüpfungs-Motive (Sticker) in metallo-supramolekularen Polymergele. Zunächst wird eine Synthesemethode für alternierend oder zufällig sequenzierte lineare Multiblock-Polyurethane (PU) entwickelt, in denen Terpyridin (Tpy) Seitenketten-Sticker durch Polyethylenglykol (PEG) Fragmente mit variabler molarer Masse separiert werden. Rheologische Untersuchungen zeigen eine signifikante Verlangsamung der terminalen Netzwerk-Relaxationszeit sowie eine deutliche Abnahme des Skalierungsexponenten im terminalen Flussregime der zufällig sequenzierten gegenüber den alternierenden PU-Gelen. Da die tatsächliche Stickerverteilung in den zufälligen Polymeren jedoch unbekannt bleibt, ist die Zuordnung der Effekte zu einer bestimmten Stickersequenz nicht eindeutig.

Daher wird in einer zweiten Studie ein iterativer Syntheseansatz untersucht. Auf Grundlage der Amid-Kupplungsstrategie der Merrifield-Peptidsynthese werden PEG- und Tpy-Aminosäure Analoga an einer Festphase gekuppelt, um supramolekular assoziierende Polymere mit definierter Primärstruktur zu erhalten. Obwohl die grundsätzliche Realisierbarkeit und die Vorteile der Modularität dieses Ansatzes gezeigt werden können, stellt die limitierte Skalierbarkeit der Synthese ein grundsätzliches Hindernis für das Studium von makroskopischen Struktur-Eigenschaft Beziehungen dar.

Stattdessen werden in einer dritten Studie daher die Effekte einer unmittelbaren Nachbarschaft zweier metallo-supramolekularer Sticker als Grenzfall einer inhomogenen Sticker-Verteilung untersucht. Die viskoelastischen Eigenschaften reversibler Gele auf Basis eines telechelen, vier-Arm PEG- und eines linearen PU-Modellsystems (Studie 1) zeigen, dass ditopische Sticker zu einer Erhöhung der Netzwerk-Festigkeit sowie zu einer deutlichen Verlangsamung der terminalen Relaxationszeit gegenüber Netzwerken mit monotopischen Stickern führen.

In einer vierten Studie wird die reversible Terpyridin-Komplexierung mit der Selbst-Assemblierung C_3 -symmetrischer Peptid-Amphiphile verknüpft. Durch die supramolekulare Copolymerisation eines strukturgebenden und eines funktionellen Monomers werden in wässriger Lösung eindimensionale Nanostäbchen gebildet, die in Anwesenheit eines telechelen PEG Linkers durch die Zugabe verschiedener Übergangsmetalle zu weichen, reversiblen Hydrogelen verknüpft werden können.

Zuletzt wird der amphiphile Charakter der PEG-basierten Polyurethane aus Studie 1 genutzt, um lineare, UV-vernetzbare Polymere zu synthetisieren, deren untere kritische Lösungstemperatur in Wasser von der hydrophil/hydrophoben Balance des molaren Comonomer-Verhältnisses bestimmt wird. Mit diesem modularen Ansatz können somit kovalent vernetzte Hydrogele mit einstellbaren mechanischen und thermoresponsiven Eigenschaften dargestellt werden. Durch den Einbau von Catechol-Gruppen in die nicht-toxischen, hydrolytisch abbaubaren Netzwerke kann zudem die Zell-Adhäsion an der Geloberfläche deutlich verbessert werden.

ABSTRACT

The macroscopic mechanical properties and functions of responsive and reversible, soft materials depend on the chemical and topological structure, and the dynamics of their (macro)molecular building blocks. This thesis describes different possibilities to control the viscoelasticity and responsivity of supramolecular cross-linked polymer gels, supramolecular gels, and covalent cross-linked polymer gels through the rational, chemical design of these building blocks.

The first part focuses on the spatial distribution of the reversible cross-linking junctions in metallo-supramolecular polymer gels. Initially, a straightforward synthesis for alternating and random multiblock polyurethanes (PU) with associating terpyridine (tpy) side-groups, and polyethylene glycol (pEG) spacers of variable length is presented. Rheological measurements reveal a significant prolongation of the terminal relaxation times, and an exacerbated shallowing of the power-law scaling in the terminal flow regime in case of the random PU gels.

Since the actual sticker distribution in the random PU chains remains however unknown, the observed effects cannot be clearly attributed to a certain sticker sequence. Thus, an alternative, iterative growth approach is investigated in a second study. Applying the amide coupling strategy known from the Merrifield-peptide synthesis, pEG- and tpy-amino acid analogues are coupled on a solid support to create associating polymers with a completely controlled primary structure. Although the general realizability of this approach and the advantages of its modularity could be shown, the limited scalability as well as the financial and time expenditures make it unsuited for macroscopic structure-property relationship studies which commonly require macroscopic experiments.

Instead, a third study directly addresses the effects of ditopic stickers with two immediately neighboring tpy ligands as one extreme case of an inhomogeneous sticker distribution. The concentration and complexation strength dependent viscoelastic properties of a telechelic, four-arm pEG and a linear pEG-PU model system (study 1) demonstrate an enforcement of the networks and a severe prolongation of the terminal relaxation times through the reversible cross-linking with ditopic instead of monotopic stickers.

Further on, the metallo-supramolecular cross-linking is combined with the β -sheet driven self-assembly of C_3 -symmetric peptide amphiphiles. The supramolecular copolymerization of structural and functional comonomers leads to the formation of anisotropic nanorods with a tpy-decorated corona. In the presence of a flexible, bifunctional linker, these rigid, one-dimensional structures can be cross-linked by different transition metal ions to yield soft and reversible hydrogels.

Finally, the amphiphilic character of the pEG-based PUs developed in the first study, is used to create linear, UV cross-linkable PUs whose lower critical solution temperature in water linearly depends on the hydrophilic/hydrophobic balance of the molar comonomer ratio. The modular synthesis approach allows the formation of covalently cross-linked hydrogels with readily tunable mechanical and thermoresponsive properties. The incorporation of catechol groups into these nontoxic, hydrolytically degradable networks further enables a severe improvement of the cell-adhesiveness of the gel surfaces.

GENERAL REMARKS

After a general theoretical introduction and the definition of the scientific goals of this thesis, the results of five different projects are presented and discussed in independent chapters with individual bibliographies, and consecutively numbered molecule structures, figures, tables, and schemes. Each chapter is introduced by a brief summary which relates the respective project with the overarching scientific goals and clarifies the author contributions.

As listed below, the content of some chapters has been previously published in peer-reviewed journals. In these cases, the content is adapted with the permission of the co-authors and publishers. The publications are referenced in the beginning of each chapter and can also be found as first reference in the respective bibliographies. The graphical design, numbering, formatting etc. of the original publications has been adjusted for the present work. For an easy accessibility, the contents from the “Supporting Information” documents are shown in the experimental sections of each chapter. NMR spectra are provided in the appendix which is organized in analogous chapters.

For the adaptation or reproduction of other previously published graphics, the permission of the publishers has been granted. If no reference is mentioned in the figure caption, the respective graphic was originally created with PowerPoint. Graphical data analysis, plotting and fitting was performed with OriginPro 2019. NMR and mass spectra were analyzed with MestreNova v12.04-22023 while chemical structures and schemes were prepared with ChemDraw 20.1.1.

Chapter 3:

K. Breul, [REDACTED] Amphiphilic Poly(ether urethanes) carrying Associative Terpyridine Side Groups with Controlled Spacing. *Polymer Chemistry* **2021**, 12, 2305–2316.

Chapter 5:

K. Breul, [REDACTED] Sticker Multivalency in Metallo–supramolecular Polymer Networks. *Macromolecules* **2021**, 54, 8407–8422.

Chapter 6:

[REDACTED] K. Breul, [REDACTED] Bridging Rigidity and Flexibility: Modulation of Supramolecular Hydrogels by Metal Complexation. *Macromolecular rapid communications* **2021**, e2100473.

Chapter 7:

K. Breul, [REDACTED]
[REDACTED] Cell Adhesion on UV-Cross-Linked Polyurethane Gels with Adjustable Mechanical Strength and Thermoresponsiveness. *Macromolecular rapid communications* **2021**, e2100505.

LIST OF CONTENTS

Zusammenfassung	IX
Abstract	XI
General Remarks	XIII
Chapter 1: Theoretical Background	1
1.1 Sequence-Controlled, Synthetic Polymers	1
1.2 The Gel State	10
1.3 Supramolecular Polymer Gels	12
1.4 Mechanical Properties of Gel Systems	24
1.5 Thermoresponsivity of Polymer Gels	28
1.6 Polymer Gels for Biomedical Applications	31
1.7 References	33
Chapter 2: Motivation & Scientific Goals	49
Chapter 3: Sticker Distribution in Metallo–Supramolecular Cross-Linked Polymer Gels ..	53
3.1 Introduction	55
3.2 Results & Discussion	57
3.3 Conclusions	70
3.4 Experimental Section	71
3.5 References	83
Chapter 4: Solid Phase Synthesis of Metallo–Supramolecular Associating Polymers	87
4.1 Introduction	88
4.2 Results & Discussion	90
4.3 Conclusions	98
4.4 Experimental Section	99
4.5 References	116
Chapter 5: Multivalency Effects in Metallo–Supramolecular Cross-Linked Polymer Gels	119
5.1 Introduction	121
5.2 Results & Discussion	124
5.3 Conclusions	140

5.4	Experimental Section	141
5.5	References	157
Chapter 6: Hierarchically Self-Assembling, Multi-Stimuli Responsive Hydrogels		163
6.1	Introduction.....	165
6.2	Results & Discussion	166
6.3	Conclusions.....	172
6.4	Experimental Section	173
6.5	References.....	186
Chapter 7: Thermoresponsive Polyurethane Gels for Biological Applications.....		191
7.1	Introduction.....	193
7.2	Results & Discussion	194
7.3	Conclusions.....	202
7.4	Experimental Section	203
7.5	References.....	223
Chapter 8: Conclusions & Outlook		227
List of Abbreviations		231
List of Symbols		232
Appendix.....		233
A.3	Supplementary Information Chapter 3.....	233
A.4	Supplementary Information Chapter 4.....	239
A.5	Supplementary Information Chapter 5.....	258
A.6	Supplementary Information Chapter 6.....	268
A.7	Supplementary Information Chapter 7	276

Chapter 1: THEORETICAL BACKGROUND

1.1 Sequence-Controlled, Synthetic Polymers

The ability to produce macromolecules with a fully controlled, uniform monomer sequence (primary structure) is a central concept in biological systems. Crucial tasks, ranging from the storage and transfer of genetic information by poly(nucleotides)¹ to the versatile cell functions performed by poly(peptides) are enabled by the precise control of intra- and interchain interactions. On the level of single chains, the sequence-dependent monomer–monomer interactions determine the chain shape and chain folding. In bulk and concentrated solutions, interchain interactions and the uniformity of the whole ensemble become additional factors that control the association and self-assembling behavior.²

Especially on a macroscopic level, there are various examples in nature, in which the primary sequence greatly influences specific properties, but is not necessarily defined with absolute precision. One exemplary case are the alginates found in different seaweeds. Those carbohydrates mainly consist of mannuronate and guluronate units, which are arranged in separate and alternating blocks. The size and order of these blocks depends on the origin and age of the seaweed and leads to different mechanical properties.³ While investigations on the single–chain level, such as the folding of peptide mimetics, certainly require a completely defined primary structure, examples like these seaweeds gave rise to the question, what level of control is actually necessary to implement a certain macroscopic property. To systematically investigate this aspect, the synthesis of sequence-controlled macromolecules represents a heavily researched “grand challenge” for polymer and material scientists. At this, the term “sequence-control” refers to all polymers, in which the monomer sequence is somehow controlled, while the molar mass dispersity D is > 1 . By contrast, “sequence-defined” polymers are characterized by a completely controlled, uniform primary structures and a dispersity of $D = 1$.

In the case of synthetic (homo)polymers, the ensemble dispersity starts with the molar mass distribution of the individual chains as schematically depicted in **Figure 1.1**. If the polymers consist of different comonomers, the variation of their amount (average volume fractions) and distribution between, and inside individual chains adds two further levels of irregularity, referred to as compositional and sequence dispersity.² Especially with respect to the monomer sequence, modern variations of controlled polymerization techniques already enable a lot more than statistical comonomer distributions. Biased copolymers with different gradients^{4,5} or well-separated blocky structures⁶ are readily realized e.g., by making use of different reaction kinetics, consecutive monomer additions or other more specific approaches.

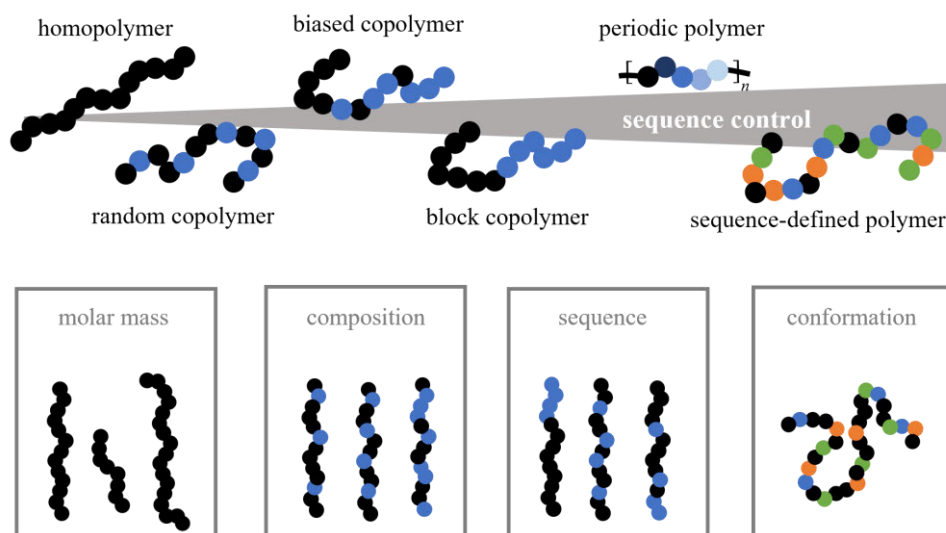


Figure 1.1. Increasing levels of sequence-control ranging from the molar mass distribution of homopolymers, over the compositional and sequence dispersity of random, biased and block-copolymers to polydisperse periodic and fully sequence-defined polymers.²

Actual sequence-controlled polymers can be divided into two categories (**Figure 1.3**):

- (1) Periodic copolymers based on well-defined monomer-sequences and compositions which however show a molar mass dispersity $D > 1$, and
- (2) Sequence-defined polymers in which molar mass, sequence and composition are completely uniform.

The only remaining level of dispersity is then usually the chain conformation which however controls the chain shape (persistence length, radius of gyration) and thus specific functionalities.² In this sense, sequence-controlled, synthetic polymers bridge the gap between completely uniform biopolymers and purely statistical synthetic polymers. Since the statistical nature and dispersity of synthetic polymers also represent valuable parameters to engineer important material properties like the viscosity^{7,8} or self-assembling behaviour of block-copolymers^{9,10}, it is an open question which synergetic advances can be generated through the combination of precision and statistics. The research potential reaches from the investigation of fundamental structure–property relationships with unprecedented accuracy, to the refinement and implementation of (new) material properties.² The scope of future applications reaches from long-term chemical data storage,¹¹ over the development of bioactive functional units e.g., containing pathogen recognition sites¹², to the mimicking of anti-microbial peptides¹³, biocatalysts¹⁴ or the inspiration of new (nano)medical applications.^{15,16}

Focusing on material science aspects, rather classical features of polymeric materials such as their degradability, permeability, thermal and mechanical behavior as well as the optical and electronic properties must be considered with respect to their sequence-dependency.²

In this regard, Li, Stayshich and Meyer investigated the hydrolysis behaviour of random and alternating poly(lactic-co-glycolic acid) (PLGA) copolymers and observed that alternating chains degrade slower and more linearly. As depicted in **Figure 1.2 A**, this finding is attributed to the considerable higher hydrolysis rate of the glycolic compared to the lactic units, which causes a faster degradation into however larger subunits within the random copolymers.¹⁷

Another property predestined for a distinct sequence-dependency, are the opto-electronic properties of π -conjugated, donor/acceptor materials e.g., applied in organic solar cells. In 2013, Meyer and co-workers systematically varied the sequences of unsubstituted *p*-phenylene-vinylenes (electron poor) and dialkoxy-substituted *p*-phenylene-vinylenes (electron rich) in di- to hexamers and found, that the most commonly applied alternating structures lead neither to the largest nor the smallest HOMO-LUMO gaps.²⁰ Following a similar permutation-strategy, Schroeder *et al.* developed an iterative technique to synthesize conjugated, sequence-defined di- to pentamers. Unexpectedly, four specific sequences showed a 10-fold enhanced molecular conductance due to an additional charge transport pathway as depicted on the right side of **Figure 1.2 B**.¹⁸ Both examples demonstrate the great potential of the monomer sequence as additional parameter to tune the properties of conjugated polymers.

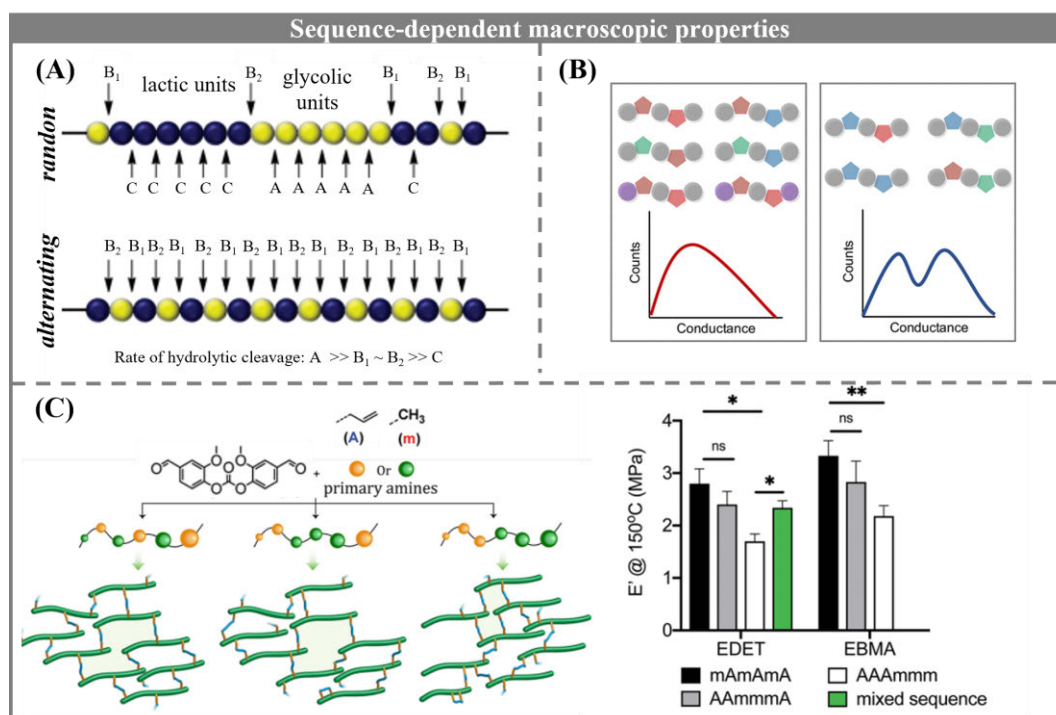


Figure 1.2. (A) Schematic representation of the hydrolytic cleavage sites in random and alternating PGLA copolymers whose differing hydrolysis rates cause a faster molar mass decrease in case of the random ones (Reproduced with permission.¹⁷ © 2011 American Chemical Society (ACS)). (B) Schematic summary of single molecule conductance measurements on sequenced-controlled, oligomers containing three different heterocycles; Occurrence of an additional conductance pathway for four specific sequences (right) (Reproduced with permission.¹⁸ © 2020 ACS). (C) Network topologies of polyurethane networks derived from vanillin-based macromers cross-linked by 2,2'-(ethylenedioxy)diethanethiol (EDET) and ethane-1,2-diyl bis(2-mercaptoacetate) (EBMA) (left) and their average storage moduli determined by dynamic mechanical analysis performed at 150 °C (Reproduced with permission.¹⁹ © 2020 ACS).

A third, specifically sequence-dependent feature are the mechanical properties of polymer networks and gels. One important parameter is their cross-linking density, which is however commonly not homogeneous, but shows spatial inhomogeneities as further detailed in **Chapter 1.2**. At this, the concentration of network defects strongly depends on the cross-linking reaction and thus the geometry and reaction kinetics of multifunctional monomers (cross-linking polymerization) or the position of cross-linkable groups inside a precursor chain (consecutive cross-linking).²¹ In the latter case, it is thus the primary sequence of the precursor chain, or more precisely, the arrangement and spacing of the cross-linkable groups, which determines the network homogeneity.

It should be noted, that several alternative approaches to control or mimic the (in)homogeneity of polymer networks have been implemented.^{22–25} Among these, the most successful pathway to produce homogeneous networks is the use of telechelic, tetra-functional macromers with defined polymerization degrees, which are cross-linked by A–B type click reactions around or above the coil overlap concentration.^{26,27} Despite their pioneering contributions in the understanding of fundamental structure–property relationships, the accessible chemical composition, and multi-arm structure inherently limits the possibilities to challenge and generalize established findings based on this model system. These limitations are also problematic, if the scope is extended from permanent to reversible networks, for which most theoretical descriptions rely on long linear chains with multiple cross-linkable side-groups as further explained in **Chapter 1.3.1**.

Sequence-defined, cross-linkable precursor polymers can thus create new opportunities to switch between homogeneous and precisely engineered heterogeneous structures on different length scales.² In a forward-looking study, Alabi and co-workers recently demonstrated an iterative, but scalable synthesis approach for vanillin-based polyurethane macromers with cross-linkable allyl-groups in defined positions as depicted in **Figure 1.2 C**. In the finally obtained thermosets, the storage moduli decreased significantly when the sequence was altered from alternating to blocky, which was explained by the higher number of topological network defects in form of elastically inactive loops.¹⁹

To extrapolate such interdependencies, the best suited synthesis approach towards the required model system depends on the required level of precision. As depicted in **Figure 1.3**, periodic copolymers can be synthesized *via* common chain-growth techniques, while sequence-defined structures usually require the application of iterative methods. Since these two fundamental synthesis principles represent to most versatile approaches, their scope and limitations are further specified in the following chapters.

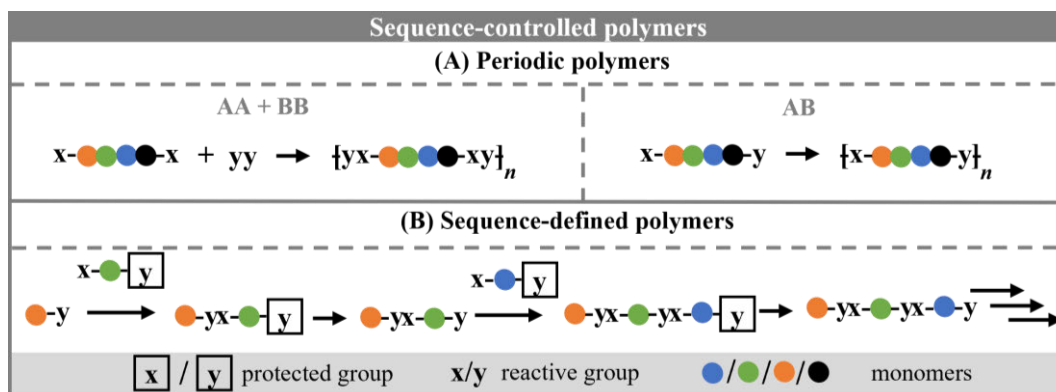


Figure 1.3. Generalized synthesis approaches for periodic and sequence-defined polymers. (A) Step-growth polymerization of AA (+ BB) or AB (macro)monomers with defined sequence leads to periodic polymers with a non-controlled molar mass distribution. (B) Iterative techniques based on orthogonal (protecting group) chemistry.¹

1.1.1 Periodic Copolymers

Polymers with periodic structures but non or partially controlled molar mass distributions are easily accessible *via* step-growth polymerizations as schematized in **Figure 1.3 A**. By using bifunctional, (a)symmetric or cyclic oligomers with built-in sequences, this approach represents a scalable synthesis option. Besides the classical polyaddition and -condensation reactions known from commercial polymers, any efficient reaction with negligible side-products can be applied.²⁸ At this, periodic polymers with carbon backbones have been prepared by acyclic²⁹ and macrocyclic ring-opening³⁰ diene metathesis polymerizations (**Figure 1.4 A**). Following this approach, Winey and co-workers exemplarily demonstrated that linear polyethylene chains with regularly-spaced instead of randomly distributed acid groups form more uniform ionic aggregates, which leads to an enhanced proton conductivity.³¹

The synthesis of hetero-chain polymers with periodic sequences reaches further back and includes polyesters, -amides, -urethanes and carbonates (**Figure 1.4 B**).²⁸ More recently, alternative click reactions such as Cu(I)-catalyzed azide–alkyne cycloadditions,³² or amine–thiol–ene conjugations³³ have also been applied to synthesize periodic polymers with complex repeating units.

The incorporated groups and structures denoted as R, R¹ and R² in **Figure 1.4 A** and **B**, reach from equally spaced side-groups to backbone incorporated monomer sequences such as elastin–mimetic pentapeptides³² or simple block structures.³⁴ Typical pendant group motives are either reactive groups for post-functionalizations or cross-linking reactions (carboxylic acid^{29,31,35}, allyl³³ etc.), reversibly associating groups (carboxylic acid, 2-ureido-4[1H]-pyrimidinone³⁶) or building blocks, which influence the solubility or self-assembling behavior (oligo(ethylene glycols), hydrocarbons)³³.

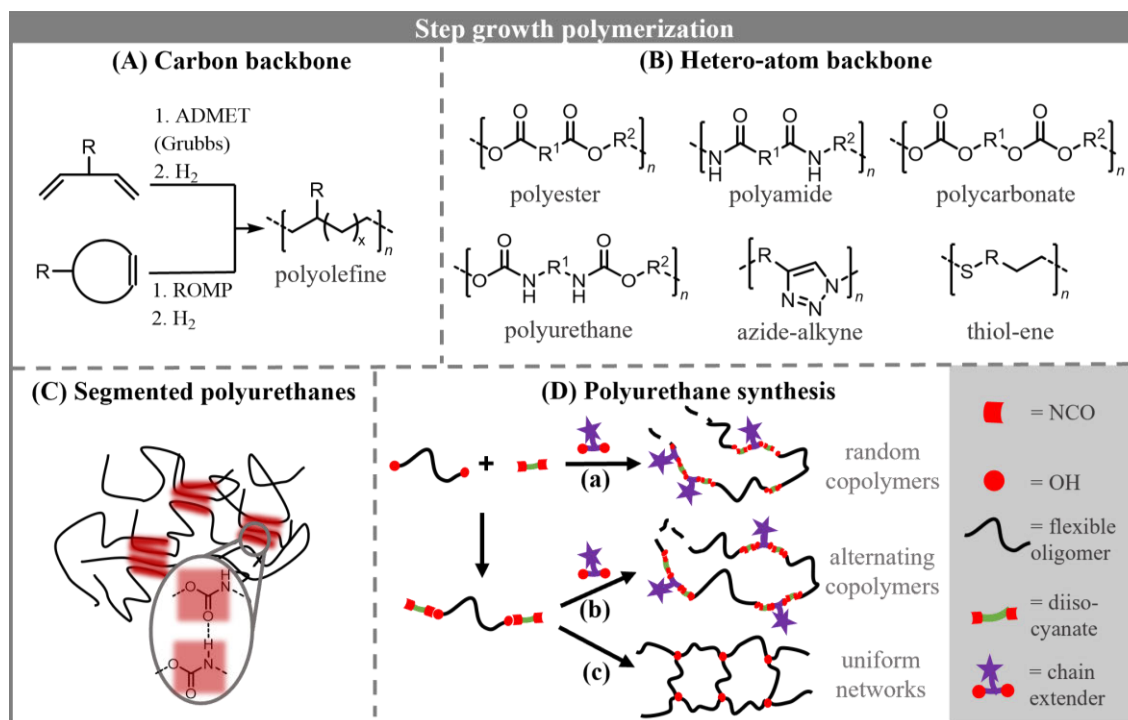


Figure 1.4. (A) Synthesis scheme for periodic polyolefins with equally spaced pendant groups by acyclic diene metathesis (ADMET) or ring-opening metathesis polymerization (ROMP). (B) Chemical structure of periodic copolymers obtained by common step-growth polymerizations. (C) Microscopic structure of segmented polyurethanes with microphase-separated hard domains. (D) Synthesis of segmented polyurethanes *via* (a) a one-shot polymerization resulting in linear, random copolymer structures, or *via* an isolated, diisocyanate end-capped pre-polymer which can be either (b) chain elongated with a (functional) chain extender to yield a linear copolymer with strictly alternating sequence or (c) reacted to a chemically cross-linked network through the trimerization of the telechelic isocyanate groups.⁵¹

Periodic Polyurethanes

Focusing on amphiphilic multiblock polyurethanes (PU, **Figure 1.4**), their tendency to microphase-separate in bulk and self-assemble into micelles or vesicles in aqueous solution, created a long-standing research interest, as well as numerous commercial applications.³⁷ Both properties result from the combination of flexible, polymeric soft segments (diol component, often polyesters or polyethers) and rigid hard segments (diisocyanates, chain extenders), which are often thermodynamically incompatible and aggregate into microphase-separated domains. The hydrogen bonding ability of the urethane linkages additionally stabilizes this morphology (**Figure 1.4 C**). If the hard domains form (semi)crystalline structures, those act as physical cross-linking points inside the flexible polymer matrix, which leads to thermoplastic properties.³⁷ Besides the chemical and physical properties of the soft segment and the diisocyanate (hydrogen bonding, glass transition and melt temperature, polarity differences, etc.), the dispersity of their block lengths is a key parameter to control the extent of phase separation and crystallinity of the hard domains. This long known dependency between the block structure and the thermal, solution and mechanical properties created a strong interest in well-defined PU model systems.^{34,38–40}

As illustrated in **Figure 1.4 D**, the dispersity of the hard segments results from the commonly necessary use of so-called chain extenders, which are usually low molecular weight diols. The chain extenders are applied to reach higher polymerization degrees but can also be used to incorporate functional pendant groups. If polymeric diol, diisocyanate and chain extender are polymerized in a one-pot reaction, the kinetically favored reaction between the latter two creates extended hard segments with differing polymerization degrees. This is usually avoided by applying a pre-polymer procedure, in which the polymeric diol and diisocyanate are first reacted with each other. The isocyanate endcapped pre-polymer is then elongated by applying the chain extender. During this, it is however inevitable that the polymeric diol partially reacts to di- or trimers which in turn leads to a broadening of the soft segment distribution.

To overcome this shortcoming, various strategies to create uniform, isocyanate endcapped pre-polymers have been developed.⁴¹ Since isocyanates are highly reactive and sensitive towards humidity, the purification of the isocyanate pre-polymers is technically challenging. Therefore, isocyanate-free approaches represent a popular alternative.⁴² Exemplarily, in 1992, Kohn and co-workers reported the synthesis of poly(ethylene glycol) (pEG)-based, strictly alternating multiblock polyurethanes with pendant carboxylic acid functionalities. For this purpose, pEG chains of differing molar mass (1000–8000 g·mol⁻¹) were converted into the corresponding bis(succinimidyl) carbonates after phosgene activation, and subsequently chain elongated with the α - and ϵ -amino groups of a methyl-ester protected lysine. Multiple derivatization reactions of the equally spaced, carboxylic acid groups allowed the preparation of stable and hydrolysable networks whose exceptional strength the authors explained with the regular distribution of the network junctions.³⁵

Another option is the use of a large excess of the diisocyanate component, which efficiently suppresses the dimerization reaction of the soft segment.⁴³ This can be further promoted by using asymmetric diisocyanates with different NCO-reactivities such as isophorone diisocyanate (IPDI).^{44–46} The excess reagent must then however be removed, before the chain elongation step can be conducted. Depending on polymer and diisocyanate, this can be accomplished by repeated solvent extractions⁴⁷, precipitations⁴³ or (thin layer) distillation.^{48–50}

These endcapped intermediates can also be used to directly create chemical networks. As shown by Driest *et al.*, the trimerization of isocyanate groups can be efficiently promoted under organotin catalysis and leads to very uniform network structures (**Figure 1.4 D.c**).⁵¹

Regarding the challenges imparted by the synthesis of (hetero-)telechelic macromers with complex, internal sequences, iterative polymerization techniques represent a viable option and are therefore introduced in the following chapter.

1.1.2 Sequence-Defined Copolymers

In contrast to statistically proceeding chain- or step-growth polymerizations, the iterative growth approach relies on the consecutive coupling of individual building blocks using orthogonal chemistry (**Figure 1.3 B**). To date, this represents the only chemical pathway to completely uniform, synthetic polymers. Again inspired by a natural material, Merrifield pioneered this field by the iterative build-up of oligo-peptides from orthogonally protected amino acids, which were coupled on a solid support (solid phase peptide synthesis).⁵² In 1984, he received the Nobel prize in chemistry for introducing this ground-breaking methodology.⁵³

The immobilization of the growing chains on a solid phase support enables to remove excess reagents and by-products by simple washing steps. The most common solid phase materials are loosely cross-linked polystyrene (PS) beads with diameters between 100–300 μm . The first monomer is attached to these beads through demand-specific, cleavable linkers. Since the only requirements for the subsequent coupling reactions are near quantitative yields, soluble by-products and reaction conditions, that are compatible with the solid support linker, the solid phase concept has been expanded to sequence-defined oligopeptoids⁵⁴, -nucleotides⁵⁵, -triazines⁵⁶, -thiolactones^{57,58} and even polyethers.⁵⁹ Inherent disadvantages of the method result from the limited surface area of the solid support which limits the synthesis of large or bulky structures, and the scale-up possibilities. Furthermore, huge amounts of the protected monomers, coupling reagents, solid phase materials and organic solvents are required, which makes the method uneconomical or sometimes impractical. Finally, the cleaved products usually require further purification by preparative, reversed phase high performance liquid chromatography (prep-RP-HPLC).

Nonetheless, impressive examples demonstrated the great variability of the backbone chemistry and the potential to realize long and complicated sequences with up to 100 repeating units.^{60–62} One example for the solid phase synthesis of polymers is presented in a study by Yang, Jiang and co-workers. They demonstrated the synthesis of amide-bond containing, monodisperse pEGs with molar masses up to 10 $\text{kg}\cdot\text{mol}^{-1}$ through the iterative coupling of hetero-telechelic, fluorenyl methoxycarbonyl (Fmoc) protected α -amino- ω -carboxylic acid ethylene glycol blocks on a solid support as shown in **Figure 1.5 A**.

Moreover, liquid support or support-free techniques have been invented to overcome the scale-up limitations and improve the economy of iterative syntheses.¹ Liquid supports are usually linear or branched, high molar mass polymers, which can be easily separated from a liquid supernatant by precipitation or nanofiltration.⁶³ Besides a simpler scale-up, this offers the advantage of faster kinetics and an easier monitoring of the reaction progress. However, both techniques are commonly accompanied by high purification losses and require excessive chromatography.⁶⁴

In an innovative study, Livingston and co-workers reported the stepwise synthesis of sequence-defined pEG chains through a Williamson etherification of tetra(ethylene glycol) blocks functionalized with four different pendant groups (azide, benzyl, *p*-methoxybenzyl, and *n*-heptyl). As depicted in **Figure 1.5 B**, one hydroxyl chain end of these building blocks is protected as tetrahydropyran-1-yl while the other one is activated by tosylation. The remarkable innovation is the use of three-armed star polymers as liquid support, which can be separated from the excess reagents by nanofiltration. By this method, molecular weights up to $8 \text{ kg} \cdot \text{mol}^{-1}$ were achieved.⁶³

Support-free techniques offer the same advantages as liquid support approaches but suffer from the need for purification steps after each coupling, which makes quantitative conversion even more important. They further allow the use of both chain ends for coupling reactions, which led to the development of iterative exponential growth (IEG) techniques. Here, orthogonally protected monomers are split, deprotected and activated separately in a divergent step and then reacted with each other in a convergent step. This procedure allows a duplication of the polymerization degree in each coupling step.⁶⁵ Johnson, Jamison and colleagues demonstrated an efficient combination of IEG and microflow-technology, which allowed the automated and scalable synthesis of unimolecular polymers with molar masses $> 6 \text{ kg} \cdot \text{mol}^{-1}$ (**Figure 1.5 C**).^{66,67}

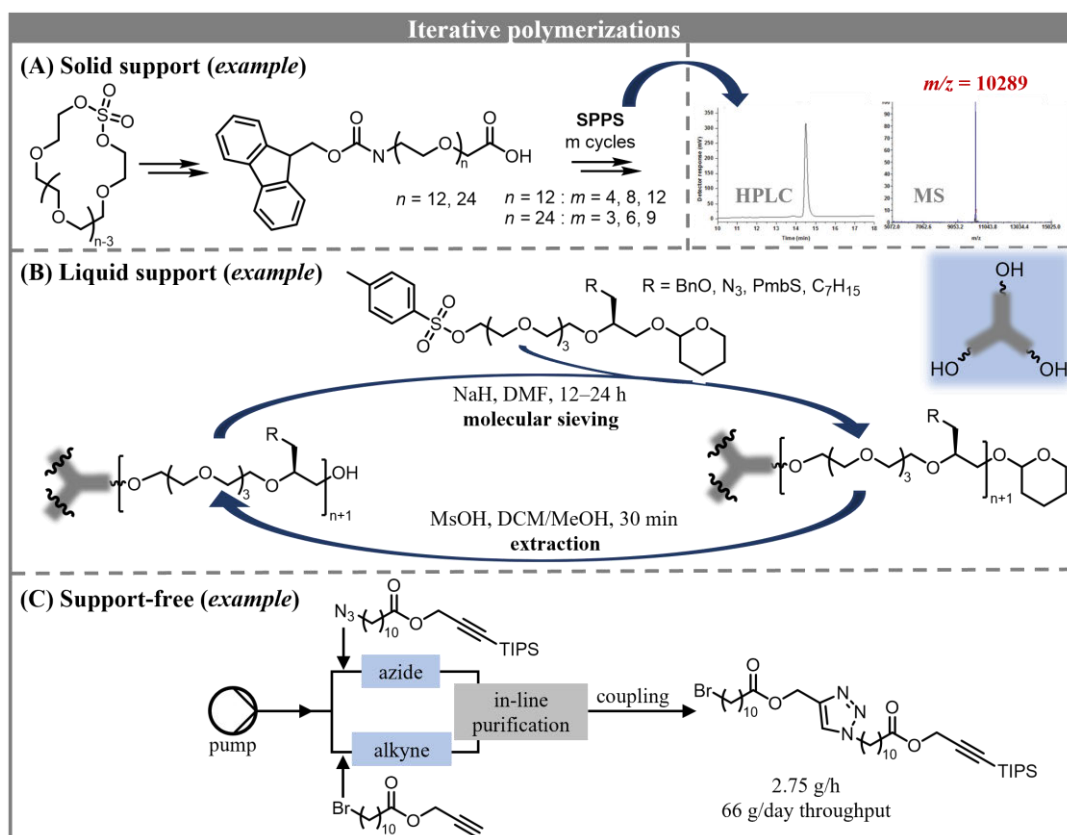


Figure 1.5. (A) Solid phase synthesis of amide bond containing monodisperse pEGs HPLC- and mass-spectrum of final coupling product (Adapted with permission.⁶⁸ © 2016, Royal Chemical Society). (B) Liquid phase synthesis of sequence-defined pEGs with different pendant groups (BnO, N₃, PmbS, C₇H₁₅) through the etherification of pentagol building blocks.⁶³ (C) Schematic setup of a Flow-IEG system in which deprotection, coupling and purification by a membrane separator are combined.⁶⁶

1.2 The Gel State

The introduction of interchain connections between dissolved but overlapping polymer chains leads to the formation of a percolated network, referred to as gel. The IUPAC definition (International Union of Pure and Applied Chemistry) of the term “gel” is however not restricted to polymeric systems, but references a „*non-fluid colloidal network or polymer network that is expanded throughout its whole volume by a fluid*“.⁶⁹ Besides the necessity to contain a fluid phase, the most fundamental prerequisite for a material to classify as a gel, is a measurable yield stress. Regarding this, Kramer and co-workers suggest a phenomenological definition according to the dynamic mechanical properties: In gels, the storage modulus $G'(\omega)$ is considerably larger than the loss modulus $G''(\omega)$ and exhibits a plateau value, extending to times in the order of seconds.⁷⁰ Regarding the solid components that build up the network, and the nature of the cross-linking points, the IUPAC divides gels into the following five categories:^{69,71}

- (1) Covalently cross-linked polymer networks.
- (2) Physically cross-linked polymer networks, in which the network junctions are comprised by physical aggregates based on hydrogen bonding, metal–ligand complexation, crystallization, or other specific interactions.
- (3) Polymer networks, in which glassy domains act as cross-linking points (e.g., block copolymers).
- (4) Gels, based on well-ordered lamellar structures (mesophases) such as soap gels and phospholipids.
- (5) Gels, based on disordered structures such as globular or fibrillar proteins (e.g., actin or collagen)⁷², or geometrically anisotropic (inorganic) particles (e.g., V_2O_5).⁷³

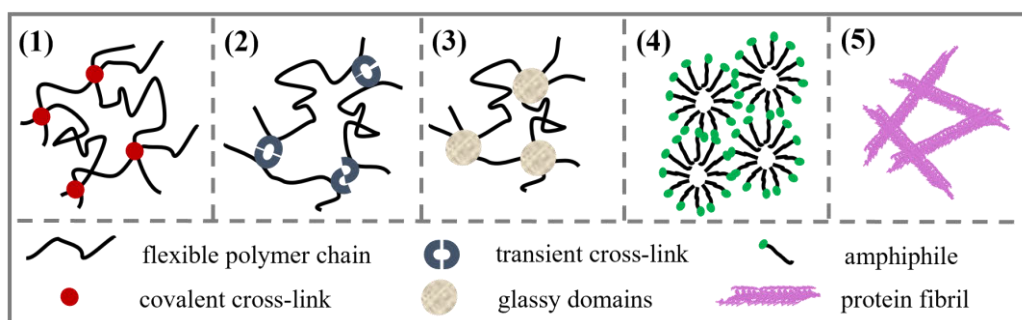


Figure 1.6. Schematic representation of the five gel categories defined by the IUPAC.⁶⁹

Another common definition distinguishes simply between “chemical” and “physical” networks. While chemical networks are represented by permanently cross-linked polymer gels, physical networks include all systems based on reversible interactions, which also covers covalent adaptable networks (vitrimers).⁷⁴ In the case of strong and kinetically stable physical bonds, the cross-links are only activated through severe changes in the physical environment, which makes those gels act like their chemical counterparts at non-triggering conditions.⁷⁵

It is further useful to differentiate between supramolecular gels, which are entirely based on non-permanently connected, low molecular weight gelators (**Chapter 1.3.3**) and supramolecular polymer gels, also referred to as supramacromolecular gels. In the latter case, the reversibly associating groups (stickers) are combined with covalent polymer segments (**Chapter 1.3.1**).⁷⁶

To engineer gels with demand-specific properties, a profound understanding of the interdependencies between the (macro)molecular network structure, the hierarchical dynamics and the mechanical properties is indispensable. Therefore, the following chapters focus on established structure–property relationships and yet open questions. For all these considerations, the network topology plays a fundamental role and is thus generally introduced at this point.⁷⁷

As shortly mentioned in **Chapter 1.1**, the topology of amorphous polymeric networks is commonly characterized by length-scale specific irregularities (**Figure 1.7**). At the molecular level of single network branches, it is the maximum number of network strands connected at one junction (branch functionality f , blue) that imposes the most important topological feature. Beyond that, on a macromolecular scale (10–100 nm, red), network defects can result from unreacted dangling chain ends or elastically inactive loops, which may consist of one (primary) or more (secondary, ternary) individual strands. The average mesh size is further affected by chain entanglements between the cross-linking points (red). Finally, the microscopic distribution of network junctions is also often irregular, which creates further inhomogeneities on a larger length scale of 10–100 nm (green).⁷⁷

The prevention, targeted incorporation and characterization of the different defect types and their influence on the macroscopic properties has been investigated intensely over the past decade.^{21,78} However, due to the large variety of defects and gel types, there are still many open questions.

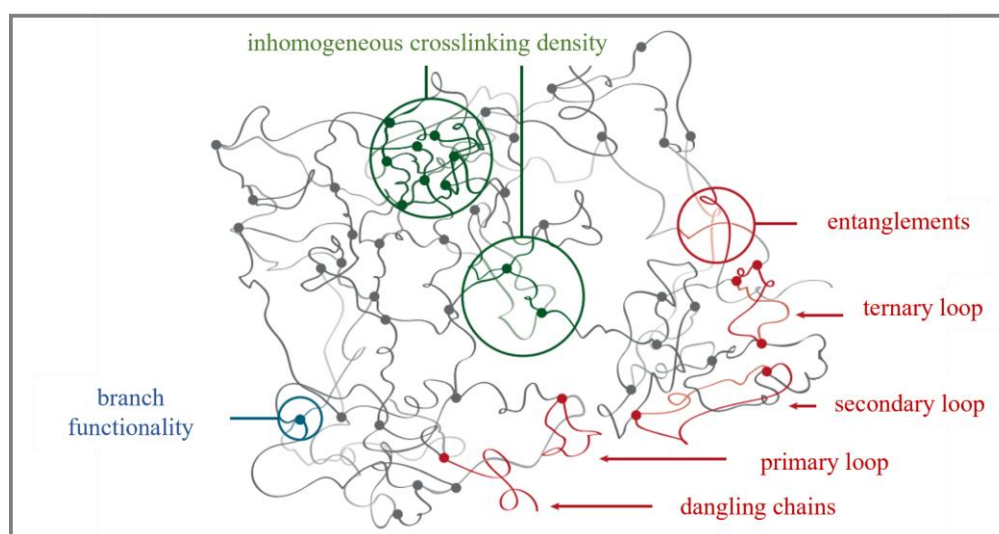


Figure 1.7. Length-scale specific, topological features typically occurring in amorphous (supra)macromolecular networks (Adapted from permission.⁷⁷ © 2019 Elsevier).

1.3 Supramolecular Polymer Gels

In covalently cross-linked polymer gels, the macroscopic mechanics are determined by the density and functionality of the cross-linking points and the volume fraction, architecture, molar mass, and number of entanglements of the polymer backbone. An increase of the gel strength can generally be achieved by a higher cross-linking density or polymer volume fraction, which is however accompanied by a trade-off relationship between toughness and tensile strength. This limitation can be overcome by introducing dynamic instead of permanent interchain associations.

The dynamics of chemical bonds generally depend on their activation energy in comparison to the thermal energy at room temperature (r.t.) ($k_B T \approx 2.5 \text{ kJ} \cdot \text{mol}^{-1}$). The energy of covalent bonds exceeds this value by a factor around 100 which makes them appear permanent and irreversible at ambient temperatures and pressures. Physical bonds are instead characterized by a lower activation barrier and thus break and reform with a higher frequency. Under stress, the reversibility of the cross-linking bonds offers an additional mechanism to dissipate energy which leads to an increased yield strength.⁷⁹ Since the lifetime of reversible bonds is often strongly affected by external parameters such as temperature, pH, solvent polarity or competing ligands, it is further possible to implement self-healing, stimuli-responsive, or shape-memory properties.^{80–82}

Consequently, the mechanical strength and dynamics of supramolecular polymer gels depend not only on the backbone-related parameters, but also on the strength and stability of the reversible interchain associations. As summarized in **Figure 1.8 A**, the binding energies of applicable physical interactions cover a very broad range. They reach from weak, non-specific van der Waals forces, to highly directional hydrogen bonds, long-ranging electrostatic interactions, and specific host–guest or metal–ligand bonds with defined stoichiometries.⁷⁹

To obtain three-dimensional networks, it is further necessary to either incorporate multiple associating groups along a linear chain or functionalize the chain ends of branched polymers (**Figure 1.8 B**). Reversible networks can also be obtained from linear, telechelic building blocks, if (i) the associating groups form network branches with functionalities $f > 2$, (ii) the associating groups phase-separate into lateral stacks or clusters, or (iii) the linear chains are entangled.^{78,83}

Despite the variety of design parameters, it is not sufficient to characterize backbone and association motif separately and combine them like a modular toolkit to engineer macroscopic properties. Instead, the dynamics and mechanics of the polymer backbone and the physical associating bonds affect each other in a number of ways and must be considered simultaneously (**Figure 1.8 B**). To identify general design principles, it is therefore necessary to study well-defined model systems, in which the backbone- and sticker-related parameters can be varied independently. Due to the unparalleled spectrum of possible binding energies, networks based on metal–ligand complexations are especially suitable for this purpose.

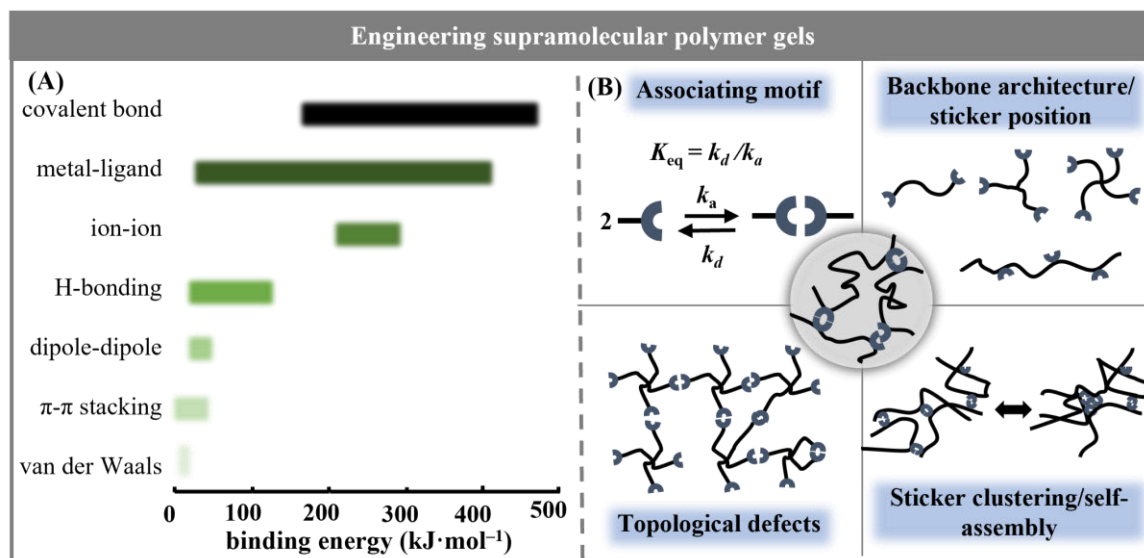


Figure 1.8. (A) Binding energies of commonly applied supramolecular interactions in comparison to that of covalent bonds.⁸³ (B) Chemical and structural parameters that influence the dynamics and mechanical properties of reversible polymer networks.

1.3.1 Metallo–Supramolecular Polymer Gels

To illustrate the potential of metallo–supramolecular polymer gels and additionally highlight the possibilities, offered by the combination of reversible cross-linking and sequence–regulated macromolecules, the byssus of marine mussels is a prime example. Marine mussels have the unique ability to stick to hard surfaces such as rocks by secreting byssal threads. These threads fulfill two crucial tasks:

- (1) They strongly adhere to stony and metallic surfaces in aqueous environments, and
- (2) damp the mechanical mismatch between the soft mussel tissue and the hard rock surface under mechanical stress e.g., resulting from the impact of ocean waves.⁸⁴

This is achieved through the strategic combination of mechanically different regions, whose properties are mainly controlled by metal–ligand complexations: The surface adhesiveness of the plaques at the end of the byssus threads results from an extensible cuticle, which is able to form very stable L-4-dihydroxy-phenylalanine (DOPA)– Fe^{3+} complexes.⁸⁵ By contrast, the core of the threads consists of partially crystalline, collagenous proteins with histidine-rich domains, which are cross-linked by histidine– Zn^{2+} complexes. These cross-links are kinetically less stable and thus more dynamic than the DOPA complexes in the cuticle. The density of the histidine cross-links and thus the stiffness of the byssal threads further decreases from the terminal plaques to the mussel core. This cross-link density distribution leads to a stiffness gradient in the threads, which effectively mediates the mechanical mismatch between the hard rock and the soft mussel.

In short, it is the combination of reversible cross-links with differing strength and kinetics and their lateral organization within a hierarchical protein structure that yield this extraordinarily adhesive, and yet extensible functional unit.

As illustrated in this example and further specified in **Figure 1.9**, one central advantage of metallo-supramolecular cross-links is the rich variety of natural and synthetic ligands whose chemical structure determines the strength, preferred geometry, and coordination number of the derived complexes. These parameters control the fraction of active cross-links and the branch functionality and thus the strength of the derived networks. Besides that, the kinetic stability and exchange mechanism (dissociative or associative) of the complexes strongly affect the relaxation dynamics in the networks. Although thermodynamic and kinetic stability are closely related, it is possible to variate both parameters independently e.g., by imparting steric hindrances through bulky ligands, which is an interesting feature for fundamental research and practical applications.^{86,87}

In contrast to other transient cross-linking motifs, all these parameters are however not solely decided by the ligand but also depend on the central metal ion.⁸⁴ Accordingly, the electronic configuration and size of the metal cation offer additional possibilities to control the transient cross-linking. The stability of the complexes further depends on the association tendency of the counterions and solvent molecules towards the respective central metal.⁸⁴

Regarding the stimuli-responsiveness of metallo-supramolecular cross-links, the binding affinity and preferred coordination number can be altered through the oxidation state of the central metal and the pH value of the liquid phase, which determines the protonation state of the ligand.⁸⁸ At this, it is advantageous that the metal ions are small, freely diffusing species which can e.g., be removed by complexation with small molecule chelators.

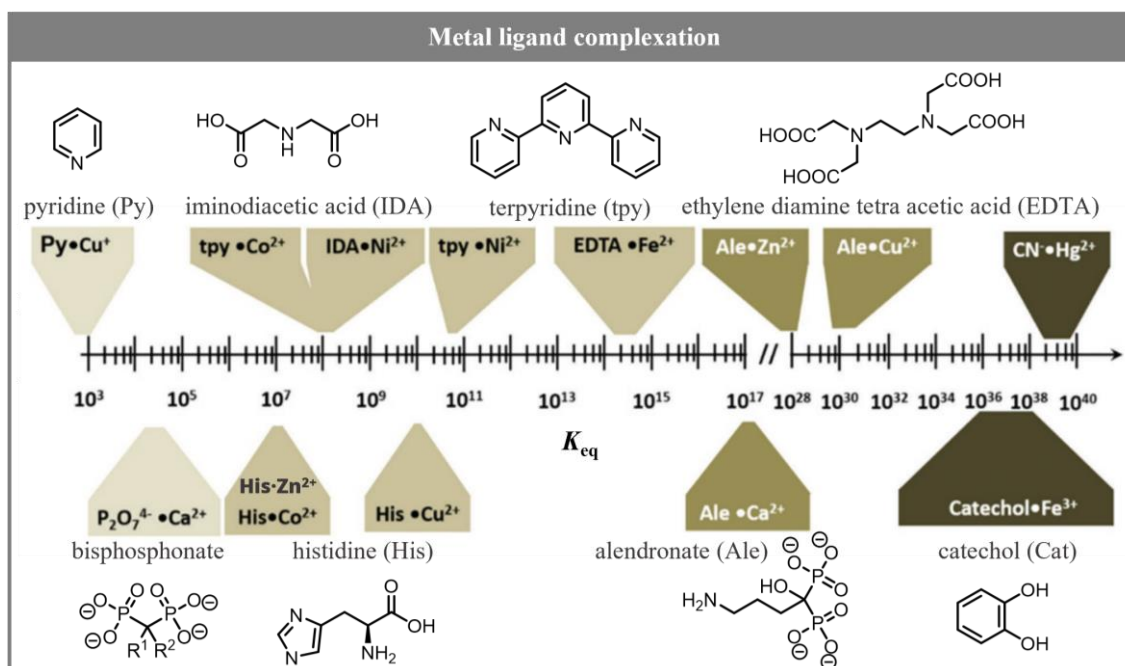


Figure 1.9. Chemical structure and association strength of a selection of natural and synthetic ligands (Adapted with permission.⁸⁹ © 2019 The Authors, Published by WILEY-VCH Verlag GmbH & Co. KGaA, Weinheim).

In this framework, one multifaceted example is the terpyridine (tpy) ligand. The currently most popular 2,2':6',2''-isomer was first described in 1932 by Morgan and Burstall who isolated it from a complex product mixture obtained by heating pyridine in the presence of FeCl_3 in an autoclave for 36 h.⁹⁰ Since then, a multitude of synthesis procedures for substituted, multitopic and chiral derivatives has been reported.⁹¹ In general, tpy derivatives are either synthesized by assembling the central ring, e.g., through a Kröhnke condensation (**Figure 1.10 A**), or by Pd-catalyzed cross-coupling reactions.⁹¹

The introduction of hetero-atom substituents in the 4'-position, represents the most common functionalization approach. 4'-haloterypyridines readily react with primary alcohols in a nucleophilic aromatic substitution, while $\text{S}_{\text{N}}2$ -type nucleophilic substitutions and Mitsunobu reactions are possible with 4'-hydroxyterpyridines (**Figure 1.10 A**).^{91,92} Carboxylic acid functionalities represent a third versatile possibility to attach tpy ligands by amidation reactions. The tpy-4'-carboxylic acid can be synthesized in an one-pot Hantzsch dihydropyridine reaction from furfural, 2-acetylpyridine and ammonia. After spontaneous oxidation to the corresponding pyridine with atmospheric oxygen, the furyl group is converted into the carboxylic acid by oxidative cleavage with potassium permanganate (**Figure 1.10 B**).⁹³ These three functionalization patterns further allow to introduce azide-, primary amine- or thiol-linkers which offer access to alternative click reactions.^{91,94-99}

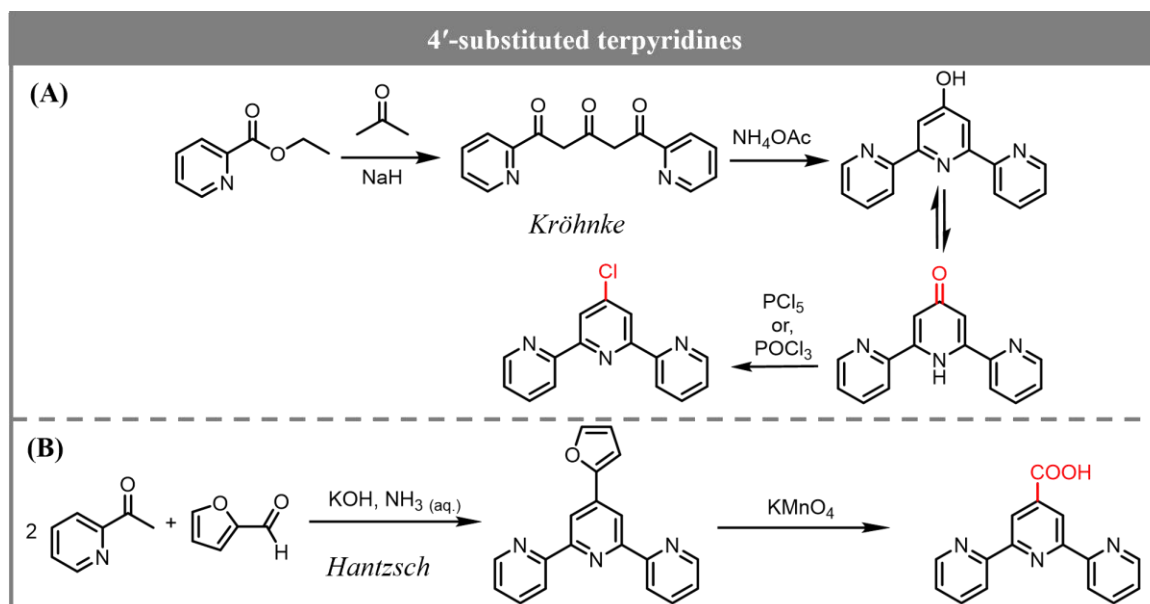


Figure 1.10. Ring assembly of (A) 2,6-dipyridin-2-yl-1*H*-pyridin-4-one and 4'-chloro-tpy in a Kröhnke-reaction and (B) tpy-4'-carboxylic acid by a Hantzsch dihydropyridine synthesis and subsequent oxidation.^{91,92}

Concerning the complexation behavior, the *N,N,N*-tridentate tpy ligand is well-known for its ability to form mono-tpy Pincer-type complexes as well as achiral, (pseudo)octahedral *bis*-tpy complexes with a multitude of transition metal ions. The generally high binding affinity results

from the chelate effect of the three pre-organized pyridine ligands, the strong σ -donor ability of the nitrogen atoms and the possibility of an effective metal-to-ligand back donation ($d-\pi^*$) resulting from the electron-deficiency of the pyridine ligands.⁹¹ Accordingly, the tpy complexes are characterized by a bathochromic shift of the ligand-centered (LC) absorption bands. In case of the brightly colored Fe^{2+} and Ru^{2+} complexes, additional bands in the visible region occur due to a metal-to-ligand charge transfer mechanism.⁹¹

The tpy complexation reaction proceeds stepwise with an equilibrium association constant K_1 for the rate-determining *mono*-complex formation, and a constant K_2 for the subsequent second step. The product of both steps corresponds to the overall complex formation constant $\beta = K_1 \cdot K_2$. As summarized in **Table 1.1**, the equilibrium constants of many tpy complexes have been reported in literature and cover a range from $\beta \approx 10^7 \text{ L}^2 \cdot \text{mol}^{-2}$ (Mn^{2+}) up to $\beta \approx 6 \cdot 10^{21} \text{ L}^2 \cdot \text{mol}^{-2}$ (Ni^{2+}).^{100,101} The preference for a *mono*- or *bis*-complexation depends on the electronic structure of the central metal cation and can in some cases be switched through the oxidation state (e.g. $\text{Ru}^{2+}/\text{Ru}^{3+}$).⁹¹

Table 1.1. Thermodynamic and kinetic stability of selected tpy complexes in aqueous and organic solvents.

metal ion	$\log(K_1[\text{L} \cdot \text{mol}^{-1}])$ (H_2O)	$\log(\beta[\text{L}^2 \cdot \text{mol}^{-2}])$ (H_2O)	$\log(\beta[\text{L}^2 \cdot \text{mol}^{-2}])$ ($\text{CHCl}_3/\text{MeOH}$)	method	$\log(k_a[\text{s}^{-1}])$ (H_2O)
Cd^{2+}	5.1	–	–	UV-Vis titration ¹⁰¹	1.4* (25 °C) ¹⁰¹
Mn^{2+}	4.4	–	–	UV-Vis titration ¹⁰¹	0.6* (25 °C) ¹⁰¹
	–	7.1	9.5	ITC ⁹⁶	
Zn^{2+}	6.7	11.9	–	UV-Vis titration ¹⁰¹	0.08* (25 °C) ¹⁰¹
	–	12.3	12.1	ITC ⁹⁶	
Co^{2+}	8.4	18.3	–	UV-Vis titration ¹⁰¹	–3.4 (11 °C) ¹⁰⁵
		10.9	10.3	ITC ⁹⁶	–3.0 (r.t.) ¹⁰³
Fe^{2+}	7.1	20.9	–	UV-Vis titration ¹⁰¹	–6.7 (r.t.) ¹⁰³
					–5.4 (46 °C) ¹⁰⁵
Ni^{2+}	10.7	21.8	–	UV-Vis titration ¹⁰¹	–7.5 (25 °C) ¹⁰¹
					–4.9 (45 °C) ¹⁰⁵

**mono*-tpy complex

As mentioned before, the kinetic lability of the complexes is also of great interest for the design of metallo-supramolecular networks. This property is quantified by the dissociation rate k_a , which is the inverse of the complex lifetime τ_d . Since the UV-Vis and fluorescence spectra of the free ligand and its metal complexes show characteristic differences, the kinetic complex stability is commonly determined by monitoring metal exchange experiments with a suitable spectroscopic method.^{101,102} As summarized in **Table 1.1**, the trends of thermodynamic and kinetic stability coincide for most metal cations. Exceptions can however be observed for Cd^{2+} and Zn^{2+} which are kinetically less, but thermodynamically more stable than the corresponding Mn^{2+} and Co^{2+} complexes. Kinetic studies by Henderson *et al.* further revealed that the complex stabilities are also influenced by the solvent polarity and the tpy substituents. In the case of electron withdrawing ether linkages in the 4'-position, the dissociation rate constants of Fe^{2+} and Co^{2+} *bis*-

tpy complexes are one to six orders of magnitude larger than that of their unsubstituted counterparts.¹⁰³ Regarding the solvent influence, the authors also compared the decay rates of both complexes in water and polar organic solvent such as ethanol, DMSO and DMF. A clear correlation between the tpy solubility and complex lifetime suggests that attractive solvent–ligand interactions stabilize transitional states and lower the activation barrier of the iron complex dissociation.¹⁰⁴ This dependency is however less clear for the Co²⁺ complexes.

In the design of self-assembling, supramolecular structures, terpyridines are often used as directional 180° linkers.¹⁰⁰ The general concept of coordination polymers based on ditopic tpy ligands with short and rigid linkers was introduced in 1992 by Constable *et al.*^{106–108} Since then, the great research interest in tpy-based metal organic frameworks generated a variety of approaches towards chains, macrocycles¹⁰⁹ or more complex structures such as self-assembled helices.¹¹⁰ In parallel to these research activities, the combination of tpy ligands with more flexible macromolecular linkers gained increasing interest. Regarding the huge number of reported approaches, it is useful to firstly differentiate between chains with tpy side-groups^{111–120} and telechelics with tpy end-groups.^{121,122} As schematically illustrated in **Figure 1.11 A**, both types are accessible by the polymerization of tpy-containing comonomers or initiators, and by post-functionalization methods. An overview of selected literature examples is given in **Table 1.2**. Since the polarity, crystallinity, melt- and glass transition-temperatures of the backbone strongly affect the final networks, the established synthesis library is an important prerequisite to select the best suited option for the respective research question or application.

For studies with a focus on structure–property relationships, the synthetically readily accessible pEG telechelics became most relevant. Narrow disperse pEGs with different architectures, molar masses and end-group functionalities are commercially available and soluble in organic and aqueous media. Taking advantage of these characteristics, Schmolke *et al.* investigated the interplay between backbone physics and supramolecular associations by measuring and modelling the rheological properties of linear pEG–tpy conjugates in the semi-dilute regime. In contrast to previous reports, it was shown that the attached pEG-chains can also lead to an acceleration of the dissociation kinetics of different tpy complexes.⁹⁴ It has further been shown that tpy-functionalized tetra-arm pEGs form quasi-ideal networks with highly regular network structures.⁹⁶ To refine the picture, a recent study by Koziol *et al.* focused on the gelation mechanism of these hydrogels. By using a combination of dynamic and static light scattering (DLS/SLS) and retarding the complex formation, it could be observed that the tpy stickers initially form micellar aggregates (**Figure 1.11 B**). Upon complexation, the hydrophobicity of the stickers vanishes and a network with equally distributed cross-links is formed. The initial non-uniform distribution can however lead to frozen inhomogeneities in the case of a rapidly proceeding gelation.^{123,124}

Focusing on future applications and combining the advantages of hydrophilic ethylene glycol units and low T_g -polymers, the Walther group developed a synthesis for tetra-arm poly(triethylene glycol methyl ether acrylates) with tpy endgroups. By using a fluorescent initiator, it was possible to obtain brightly colored, self-healing hydrogels processable by thermal 3D printing (**Figure 1.11 C**).¹²⁵ Tpy ligands have furthermore been applied in dual networks with chemical and physical cross-links to combine high mechanical strength and extensibility.^{126,127} As shown in a study by Ahmadi *et al.*, the dynamics of the reversible bonds and the structure of the dual networks mutually affect each other. The authors investigated the model network depicted in **Figure 1.11 D** by a combination of DLS/SLS and Double-Quantum-NMR. A clear correlation between an increasing complex strength and the concentration of nanoscopic clusters and topological defects (loops) could be extrapolated.¹²⁸ Recently, it has further been shown that it is possible to create reversible gels on the basis of heteroleptic complexes of tpy and phenanthroline, which opens yet unexplored possibilities to implement hierarchic relaxation processes.¹²⁹

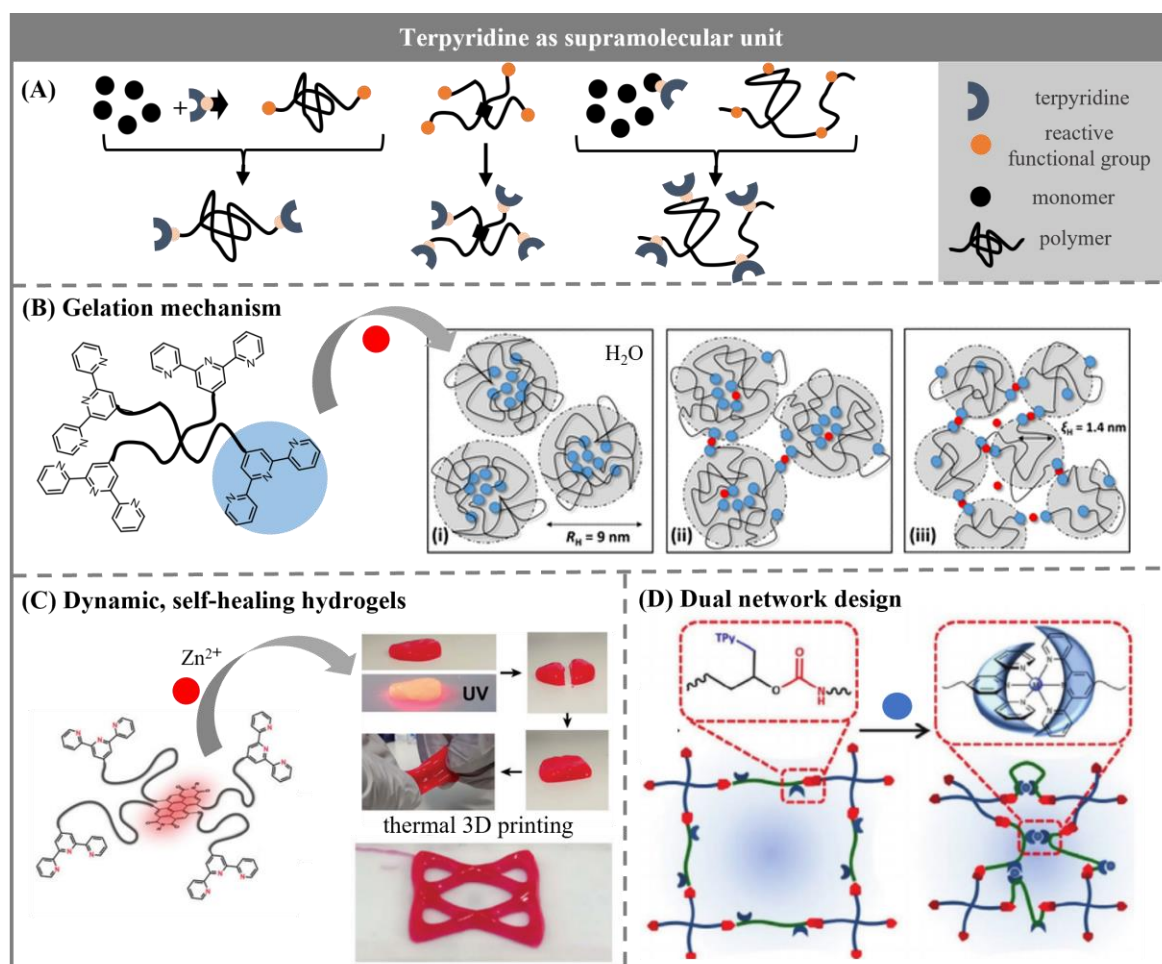


Figure 1.12. (A) Synthesis of telechelic and side-chain functionalized polymer-tpy conjugates. (B) Gelation mechanism of tetra-arm pEG-tpy hydrogels (Adapted with permission.¹²³ © 2021 ACS). (C) Supramolecular hydrogels from four-arm p(mTEGA)-tpy conjugates with self-healing and 3D printable properties. (Reprinted with permission.¹²⁵ © 2019 Royal Society of Chemistry). (D) Composition of dual networks with chemical and transient cross-links (Reprinted with permission.¹²⁸ © 2019 The Authors, Published by WILEY-VCH Verlag GmbH & Co. KGaA, Weinheim.).

Finally, it should be noted that the catalytic,¹⁰⁰ electro-optical^{130,131} and bio-active¹³² properties of the Fe²⁺, Zn²⁺ and Ru²⁺-tpy complexes usually remain intact upon the embedment into a larger structure.⁸⁹ This could facilitate the development of self-healing gels, which additionally possess complex-inherent functionalities.

Table 1.2. Synthesis of terpyridine functionalized polymers.

reference	backbone architecture	backbone chemistry	tpy-linkage	comments
PENDANT FUNCTIONALIZATION				
Potts, 1988 ¹¹²	linear	PE/PS	4'-vinyl-tpy	free radical polymerization, tpy-comonomer
Hanabusa, 1992 ¹¹⁶	linear	PS	4'-styrene-tpy	free radical polymerization, tpy-comonomer
Schubert, 1999 ¹¹⁵	linear	(tpy-IPDI-poly(propylene glycol-IPDI) _n)	5,5-bis(hydroxy-methyl)-tpy	PU, tpy in backbone
Calzia, 2002 ¹¹⁷	linear	PMA	tpy-Cl + R-OH	free radical polymerization with tpy-comonomer
Schubert, 2002 ¹¹⁸	linear	PMMA	tpy-Cl + R-OH	free radical polymerization with tpy-comonomer
Bode, 2013 ¹³³	linear	poly(methyl/butyl /lauryl-methacrylate)	tpy-Cl + R-OH	RAFT, tpy-comonomer
Rossow, 2013 ¹¹⁹	linear	pNiPAm	tpy-NH ₂ + succinimidyl ester	RAFT, tpy post-functionalization
Xu, 2019 ¹³⁴	linear	piPOx	tpy-COOH + piPOx	anionic polymerization + post-functionalization
Meurer, 2021 ¹²⁰	linear	poly(butyl methacrylate)	tpy-Cl + R-OH	RAFT, tpy-comonomer
TELECHELIC FUNCTIONALIZATION				
Schubert, 2000 ¹²¹	linear, mono ¹³⁵ - and bifunctional	pEG, PTMO	tpy-Cl + R-OH	concept extended to linear PS, and poly(ethylene-co-butylene), ¹³⁵ 4-arm ¹²³ and 8-arm pEG ¹³⁶
Heller, 2001 ¹³⁷	linear, monofunctional	poly(L-lactide)	tpy-CH ₂ -OH initiator	coordinative ring-opening polymerization
Rossow, 2014 ⁹⁶	4-arm	pEG	tpy-alkyne + R-N ₃	alternative: tpy-NH ₂ + <i>p</i> -nitrophenyl carbonate linkages ⁹⁵ ; option to introduce additional free hydroxyl group ¹³⁸
Czarnecki, 2016 ¹²⁷	linear, bifunctional	pEG	tpy-alkyne + R-N ₃	option to introduce an additional free azide group
Zhuge, 2017 ¹³⁹	linear/4-arm	poly(butyl acrylate)	tpy-COOH + R-NH ₂	tpy-functionalized RAFT agent
Creusen 2019 ¹²⁵	linear/4-arm	p(mTEGA)	tpy-NH ₂ + R-Br	fluorescent initiator

PE: polyethylene; PS: polystyrene; IPDI: isophorone diisocyanate; PMA: poly(methacrylate); PMMA poly(methyl methacrylate); pNiPAm: poly(*N*-isopropyl acrylamide); piPOx: poly(2-isopropenyl-2-oxazoline); PTMO: poly(tetramethylene oxide); p(mTEGA): poly(triethylene glycol methyl ether acrylate).

1.3.2 Multivalency and Cooperativity

In the context of reversible associations characterized by low activation energy barriers, special attention must be paid to the mutual interactions between adjacent binding sites. In contrast to covalent connections whose properties are minorly affected by neighboring bonds, the strength of non-covalent interactions often depends strongly on their microenvironment. If the dependency between overall binding strength and the number of individual binding sites is non-additive, this process is considered to be cooperative.¹⁴⁰ In a generalized, thermodynamic definition, this means interactions or binding events with multiple subsequent steps are non-cooperative, if the free energy change of each binding step is equal. By contrast, a system shows positive cooperativity, if the free-energy changes decrease while an increase occurs in negative or anti-cooperative systems.¹⁴¹ Since the living world is based on dynamic processes, the synergetic interplay of multiple binding sites and interactions is a key concept in biological systems and enables for instance the rapid folding of proteins or the formation of stable DNA double helices.^{140,141} Inspired by nature, cooperativity also developed into an indispensable tool for the chemical engineering of functional molecules and materials, and facilitated major breakthroughs in the fields of supramolecular self-assembly and catalysis.¹⁴⁰

Cooperativity effects can be categorized with respect to their origins. Considering the clustering of small molecules, a first reason for cooperativity are non-additive, many-body interactions. One example are induction effects imposed by the electric fields of neighboring molecules which e.g., promotes the alignment of charge dipoles.^{140,142} Furthermore, strong synergy can arise from secondary interactions. An illustrative and historically important example is the development of hydrogen bonding arrays such as the 2-ureido-4[1*H*]-pyrimidinone (UPy) group introduced by Sijbesma and Meijer.¹⁴³ As rationalized by Jorgensen and co-workers, the extraordinary strength of such arrays depends on the attractiveness of secondary electrostatic interactions of diagonal neighboring donor (D)-acceptor (A)-pairs (**Figure 1.12 B**).^{144,145} Cooperativity is however not necessarily enthalpy driven. Since binding generally decreases translational and conformational levels of freedom, subsequent binding steps are usually accompanied by smaller entropic penalties. If this majorly concerns the translational entropy, the phenomenon is referenced as chelate effect, well-known from metal chelates like the terpyridine ligand (**Figure 1.12 C**). If the first binding event does however initiate conformational changes which influence the subsequent steps, the systems shows allosteric cooperativity, most famously known from the oxygen binding of hemoglobin (**Figure 1.12 D**).¹⁴⁰

This classification highlights that most forms of cooperativity depend on the connection and spatial organization of individual binding sites within rigid arrays or through defined linkers. The rational design of multitopic or multivalent ligands is therefore the most central task in the creation of cooperative systems.¹⁴¹

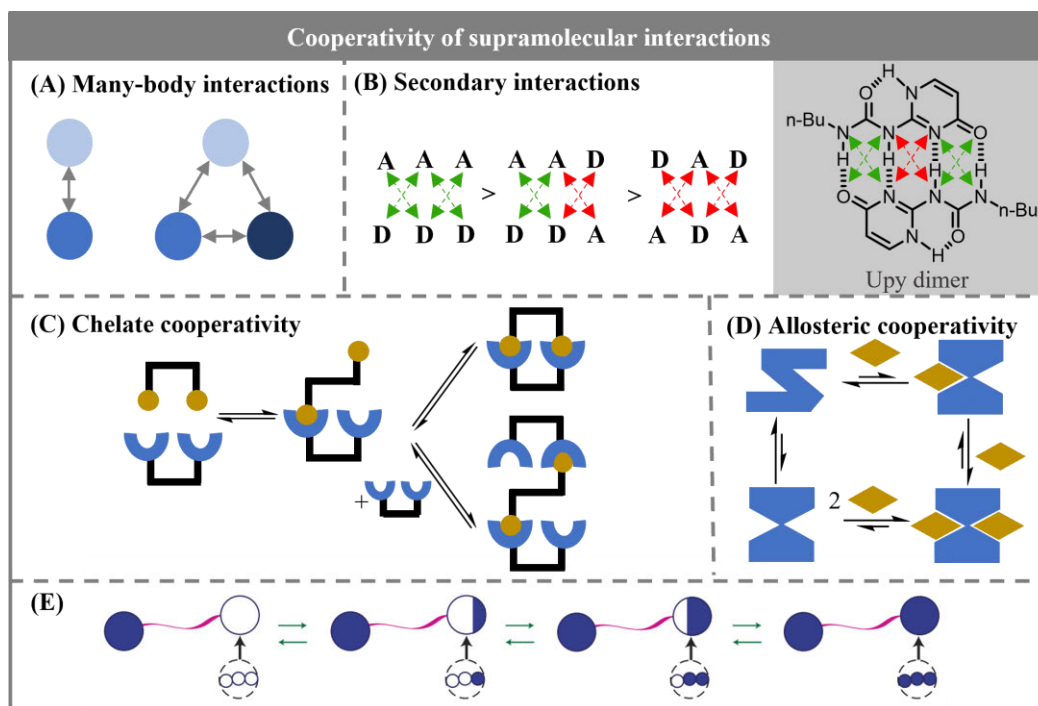


Figure 1.12. Schematic representations of **(A)** two- and three-body interactions, **(B)** secondary electrostatic interactions in H-bonding arrays and the UPy dimer. **(C)** Intermolecular chelate cooperativity.¹⁴¹ **(D)** Binding induced conformational changes in allosteric systems.¹⁴⁶ **(E)** Telechelic polymers containing sticky endgroups with one to three binding sites (Reproduced with permission.¹⁴⁷ © 2017 AIP Publishing).

A second challenge is represented by the quantification of cooperativity effects, which requires detailed knowledge about the equilibrium constants or free energy changes of the individual binding steps. Experimentally, these are accessible by titration experiments based on NMR, UV-Vis-, circular dichroism (CD) or fluorescence spectroscopy, or by isothermal titration calorimetry (ITC). The evaluation of these titration curves does however require the application of simplifying binding models.¹⁴¹ To test and refine such models, and furthermore determine relevant design parameters, computational quantum chemical methods are of great importance.^{141,148–150} To describe the avidity enhancement of multivalent ligands mathematically, it was found useful to focus on the dynamic nature of the bonds. This can e.g., be done by modeling the influences of a locally increased ligand concentration after the formation of the first bond.¹⁵¹ Following a similar approach, the re-binding model by Haag *et al.* considers the fully bound state and argues with its kinetic entrapment. The complex dissociation requires the simultaneous opening of all contributing binding sites which has a strongly reduced probability. The model e.g., elucidated the importance of the spacer length between the binding sites.¹⁵²

To extent such theoretical knowledge to supramolecular polymer systems, Sing *et al.* investigated how the mechanical response of telechelic chains is influenced by one-, two- or three-part stickers with identical overall association constant (**Figure 1.12 E**). While shear stress and extensional viscosity increased with the number of the binding sites, the influence on the terminal relaxation time is non-monotonic and activation energy-dependent.¹⁴⁷

1.3.3 Hierarchical Self-Assembly

As highlighted in the previous chapters, the combination, and defined spatial arrangement of (different) supramolecular binding motives can be very beneficial.⁷⁸ One earlier mentioned example is the formation of viscoelastic networks from linear, associating polymer chains, in which secondary forces cause an aggregation of the sticky groups into lateral stacks or clusters. The formation of defined and stable supramolecular nanostructures by self-assembling mechanisms is not restricted to polymeric systems but represents an important interdisciplinary research field of its own. Since pioneered by Jean-Marie Lehn and co-workers about 30 years ago, the rational design of supramolecular self-assembling monomers nowadays enables for instance the formation of non-covalently connected, 1D nanorods.¹⁵³ These linear structures can be considered as the reversible counterpart of covalently jointed polymer chains. By entanglement, branching or bundling of the linear rods, it is further possible to induce a physical gelation.¹⁵⁴

To obtain anisotropic structures, the highly directional nature of hydrogen bonds makes them ideally suited candidates. In biologically relevant, aqueous environments, water, however, acts as competing ligand with hydrogen bond donating and accepting properties. It is therefore commonly required to use multivalent binding arrays, shield the hydrogen bonds in hydrophobic pockets and/or support the derived assemblies by additional non-covalent interactions to obtain stable supramolecular assemblies.¹⁵⁴ These requirements can e.g., be fulfilled by the formerly mentioned, self-complementary UPy group with its extraordinary binding affinity or C_3 -symmetric monomers with an aromatic benzene-1,3,5-tricarboxamide (BTA) core. Both motives have therefore been established as important supramolecular platforms.^{155,156} The hydrogen bonding groups are then often combined with additional hydrophobic and hydrophilic blocks to provide sufficient solubility and secondary stabilization mechanisms. Accordingly, the hydrophobic/hydrophilic ratio is another crucial design parameter to promote an efficient supramolecular polymerization. Switching this ratio through external stimuli like temperature, pH, light exposure, or redox potential allows to induce and interrupt self-assembly processes and thus leads to stimuli-responsive properties.¹⁵⁴

In this regard, short oligo-peptide sequences became a further lead-structure in the field. Owing to the rich monomer toolbox, the ease and precision of their synthesis and the inherent biocompatibility, molecular peptide-amphiphiles have been used for 1D supramolecular polymerizations, as low molecular weight gelators and for the formation of other nanostructures like micelles or ribbons (**Figure 1.13 A**).^{154,157} The peptide sequences often encode β -sheet structures which are additionally stabilized by the π - π -stacking of aromatic amino acids such as phenylalanine (F) or complementary charged units.¹⁵⁴ The peptide-part is then often flanked by a hydrophobic moiety at the *N*-terminus, while charged or hydrophilic groups at the *C*-terminus ensure the sufficient solubility.¹⁵⁷

The Besenius group attached such peptide-amphiphiles to 1,3,5-substituted BTA cores, yielding C_3 -symmetric monomers with a hydrophobic core, surrounded by hydrogen bonding peptide sequences which are shielded by oligo(ethylene glycol) (oEG), Newkome-type dendrons and assemble into stable nanorods (**Figure 1.13 B**).¹⁵⁴ It was further shown that the temperature-driven collapse of the EG dendron can lead to a thermoresponsive hydrogelation (**Chapter 1.6**).¹⁵⁸

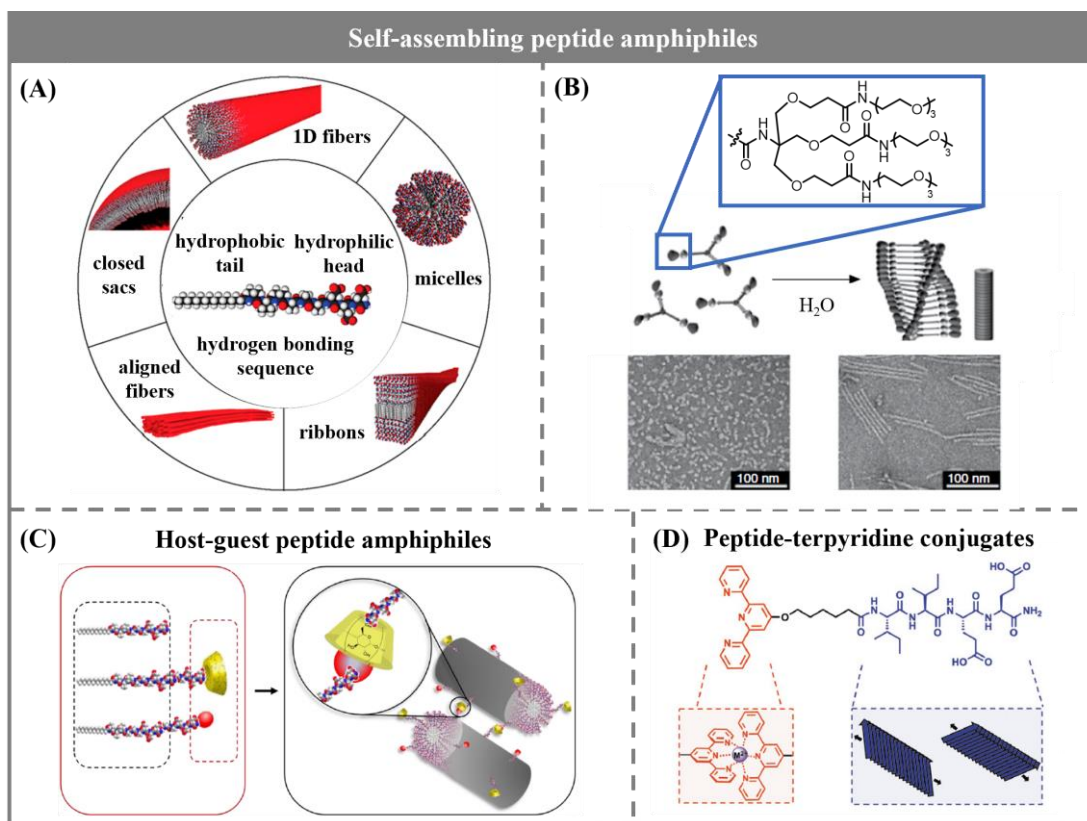


Figure 1.13. (A) Design of peptide amphiphiles for supramolecular self-assembly (Adapted with permission.¹⁵⁷ © 2017 ACS). (B) Nanorod formation of C_3 -symmetric peptide amphiphiles as investigated by TEM (Adapted with permission.¹⁶⁴ © 2018 ACS). (C) Cross-linking of nanorods through host-guest complexation (Adapted with permission.¹⁶² © 2019 ACS). (D) Amphiphilic peptide-terpyridine conjugates (Reprinted with permission.¹⁶³ © 2019 WILEY-VCH Verlag GmbH & Co. KGaA, Weinheim)

As mentioned, the gelation of supramolecular nanorods often relies on the condensation or aggregation of fibers.^{159–161} The applicable gelation switches have recently been broadened through the incorporation of additional associating motives into the nanorod corona. As depicted in **Figure 1.13 C**, Redondo-Gómez *et al.* demonstrated the cross-linking of peptide amphiphilic fibers through reversible adamantane and β -cyclodextrin complexes.¹⁶² Using a similar design approach but applying metal-ligand instead of host-guest complexations, Sahoo *et al.* presented an amphiphilic peptide-tpy conjugate (**Figure 1.13 D**). The addition of transition metal ions to the initially formed 1D nanorods induced a slow transformation into other nanostructures.¹⁶³

Both examples demonstrate that the development of supramolecular jointed polymers with a second, orthogonal gelation switch, represents a modern contribution to the library of molecular hydrogelators with multi-stimuli responsive properties.

1.4 Mechanical Properties of Gel Systems

1.4.1 Mechanical Testing and Phenomenological Models

As pointed out before, one of the most intriguing features of polymer gels is their tunable viscoelasticity comprised by viscous and elastic contributions (**Figure 1.14 A**). A versatile method to quantify the mechanical properties of soft materials is oscillatory shear rheology which can be used to perform stress relaxation, creep, and dynamic experiments. For dynamic experiments, the sample is placed between two flat- or cone-flat plates and a sinusoidal stress $\sigma = \sigma_0 \cdot \exp(i\omega t)$, (t : time, ω : angular frequency) is applied while the time-dependent strain γ is measured. The time scale of the deformation in dynamic experiments ranges typically from ≈ 100 ms up to several minutes. The complex modulus G^* which relates shear stress and strain can be separated into a storage (G') and loss modulus (G'') which allows to quantify the extent of stored and dissipated energy.¹⁶⁵ For this purpose, rheological measurements are conducted within the linear viscoelastic regime, in which the relaxation moduli are strain independent and Boltzmann superposition is possible.¹⁶⁶

$$G^* = \frac{\sigma}{\gamma} = G' + iG'' \quad (1.1)$$

Simple mathematical models to describe viscoelastic mechanics can be constructed through the combination of an ideal elastic spring with modulus G_1 following Hooke's law ($\sigma = G_1 \cdot \gamma$) and a dashpot with viscosity η following Newton's law ($\sigma = \eta \cdot (d\gamma/dt)$, $d\gamma/dt$: shear rate). These components can be either placed in series (Maxwell model, **Figure 1.14 B**) to describe viscoelastic fluids or in parallel (Kelvin-Voigt model) to capture the behavior of viscoelastic solids. Applied to oscillatory shear experiments, the Maxwell model yields the following expressions for the angular frequency-dependent storage $G'(\omega)$ and loss moduli $G''(\omega)$.

$$G' = G_N \frac{\omega^2 \cdot \tau_1^2}{1 + \omega^2 \cdot \tau_1^2} \quad (1.2)$$

$$G'' = G_N \frac{\omega \cdot \tau_1}{1 + \omega^2 \cdot \tau_1^2} \quad (1.3)$$

At this, the terminal relaxation time τ_1 represents the characteristic time scale for macromolecular rearrangements and connects viscosity and elastic modulus ($\eta = \tau \cdot G$).¹⁶⁵ On short time scales, the system has no time to rearrange, the elastic properties dominate and thus, the storage modulus shows a plateau value denoted as G_N (**Figure 1.14 A**). On times scales longer than τ_1 , the deformation energy is dissipated, and the system behaves like a fluid. For this terminal flow regime, the Maxwell model predicts a characteristic power-law scaling of $G' \propto \omega^{-2}$ and $G'' \propto \omega^{-1}$.

It should be noted, that the so far presented description captures only one singular relaxation mode. Polydisperse polymer systems can however be characterized by a multitude of relaxation modes and mechanisms on different time and length scales. Their respective influence depends on the concentration regime (melt, concentrated, semi-dilute), the presence and nature of cross-links, and/or chain entanglements.¹⁶⁶

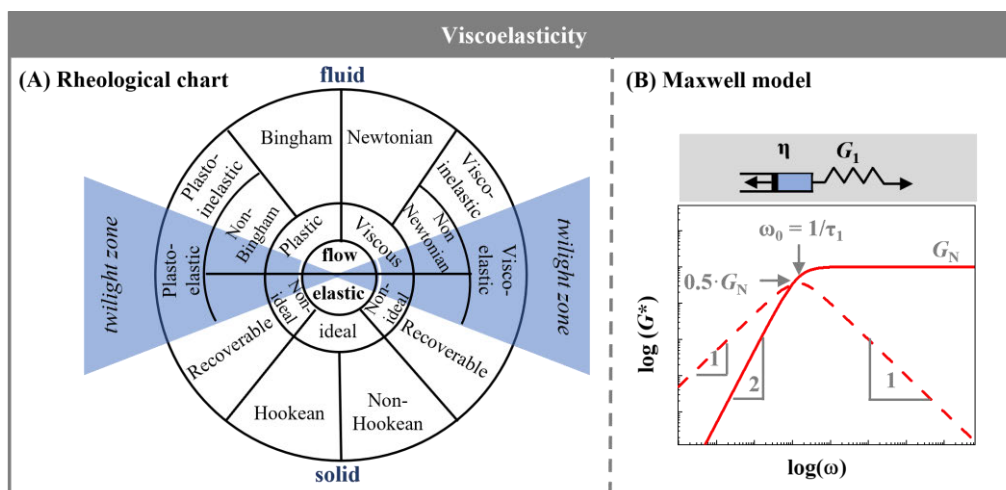


Figure 1.14. (A) Rheological chart presented by Bilmes¹⁶⁷ © 1942 Springer Nature) (B) Maxwell model to describe a single relaxation mode of a viscoelastic material constructed by the combination of a spring with modulus G_1 and a dashpot of viscosity η . Shear rheological spectrum of a viscoelastic material with single-mode Maxwell behavior characterized by a plateau modulus G_N at high frequencies, a $G' = G''$ crossover at the terminal relaxation time τ_1 , and a terminal flow regime.¹⁶⁵.

1.4.2 Linear Viscoelasticity of Supramolecular Polymer Gels

The following discussion focuses on supramolecular cross-linked polymer gels in the semi-dilute, non-entangled regime. The rheological spectra of such systems have been studied intensively because their relaxation times and terminal flow regime often fall into an experimentally easily observable frequency range and are not complicated by additional relaxation modes resulting from chain entanglements.^{87,96,97,168–172} Besides the position and density of cross-linkable stickers, the central parameter to control the viscoelasticity of reversible gels is the thermal activation energy E_A of the transient bonds. There is a broad consensus that this activation barrier determines the average time τ_b during which the stickers remain in a bound state.⁷⁹

$$\tau_b = \tau_0 \exp\left(\frac{E_A}{k_B T}\right) \quad (1.4)$$

This activation energy represents the enthalpic attraction that counteracts the thermal energy $k_B T$. At this, the pre-factor τ_0 represents the segmental relaxation time in the absence of any attractive forces and can be considered as an attempt time. It has been proven useful to differentiate between strong, medium, and weak sticker binding regimes to describe the chain dynamics. In the case of strong sticker interactions ($E_A > \ln(N_x) \cdot k_B T$, N_x : number of non-associating monomers between two associating ones) like the tpy metal complexation, the lifetime of the stickers is much longer than the Rouse relaxation time of the attached chain and thus, the terminal network relaxation is controlled by the sticker lifetime.¹⁷³

The in-gel lifetime of the bound state τ_b is neither necessarily equivalent to the often-shorter dissociation lifetime of the isolated stickers τ_d in dilute solutions nor to the terminal relaxation time τ_{ex} , observed in rheological experiments. In seminal studies, Yount, Loveless, and Craig, cross-linked poly(4-vinyl pyridine) chains with platinum or palladium pincer complexes. Through

the insertion of steric hindrances, it was possible to tune the dissociation kinetics of these complexes without significantly affecting the equilibrium constants. For these model systems, they observed a quantitative correlation between the dilute kinetics and the macroscopic relaxation time ($\tau_d = \tau_{ex}$) and demonstrated the clear correlation of both parameters^{86,87} However in many studies, the network relaxation times were shown to be 10–100 times longer than the intrinsic sticker lifetime τ_d .

Experimental methods to determine the actual in-gel sticker lifetime τ_b are either based on dielectric spectroscopy^{174,175} or “sticker diffusion and dissociation spectroscopy”.¹⁷² The latter has been applied in a study by Tang and Olsen, which revealed that the in-gel dissociation time τ_b is a concentration independent physical constant while the terminal relaxation time τ_{ex} of the corresponding gels increases with the polymer- and thus sticker concentration.¹⁷² This is reasonable since the relaxation of the complete chain requires the opening of not only one but multiple stickers along that chain. The only situation in which the opening of one sticker relaxes the whole chain is at the gel point, where according to definition, each chain contains only two elastically active stickers.⁷⁹

The prolongation of the macroscopically observable relaxation time is theoretically explained by a renormalization of the sticker lifetime introduced in the framework of the sticky Rouse model. This theory represents an adaptation of the Rouse model to describe the dynamics of non-entangled, linear polymer chains with equally distributed pendant stickers which form binary associations. Among other things, it predicts scaling-law relationships between the relaxation time and the sticker spacing or polymer concentration within different concentration regimes.^{176–178} At this, the renormalization of the intrinsic sticker lifetime is used to account for the fact that the network relaxation not only requires the dissociation of a sticker pair, but also a successful separation and re-association with a new partner.¹⁷³ During the opening time τ_{open} , the stickers can move by sub-diffusive Rouse motions. The renormalized lifetime τ_b^* thus also depends on the number of returns to the initial binding partner $J(\tau_{open})$ before a successful partner exchange takes place.¹⁷³ The number of attempts mainly depends on the concentration of open stickers and their explorable volume.

$$\tau_b^* = J(\tau_{open})\tau_b + \tau_{open} \quad (1.5)$$

In summary, the macroscopic relaxation time τ_{ex} corresponds to the renormalized sticker lifetime τ_b^* times the square of the number of interchain associations per chain.¹⁷⁹

It should be noted, that an alternative hopping exchange mechanism has been proposed for networks with clustering stickers.¹⁸⁰

The sticky Rouse model can also be applied to describe the time-dependent, complex moduli $G^*(t)$. As such, it represents a generalized form of the Maxwell model with two parallel series of

Maxwell elements, one accounting for the Rouse relaxation modes and the other for the sticker related terminal relaxation.¹⁷¹ As such, the original model or adaptations of it have been successfully applied to capture the rheological behavior of reversible melt- and gel-systems based on electrostatic interactions¹⁸¹, hydrogen bonding¹⁸² and metal ligand complexations.¹⁷¹ Parallel series of Maxwell elements can generally be applied to capture non-singular relaxation time spectra. A multi-modal relaxation time spectrum can be generated intentionally but often occurs unexpected.^{182–184} A multi-modal terminal relaxation is also indicated by a shallower scaling in the flow regime than predicted by the single-mode Maxwell model. In the past, the frequent observation of this effect has been attributed to the molar mass dispersity of the polymers chains, an irregular sticker distribution and/or the presence of sticker clusters.^{182,184}

Besides the dynamic properties, the elastic plateau modulus G_N at short time scales, on which the reversible cross-links are active, is an important parameter to evaluate the mechanical strength of the percolated network. In contrast to the dynamic properties, this property is mainly controlled by the spatial network parameters (chain architecture, sticker position and topological irregularities). The affine¹⁸⁵ and phantom¹⁸⁶ network model correlate this plateau value with the microscopic number of network strands per unit volume.⁷⁵ The affine model assumes that the displacement of each network strand ending is identical with the macroscopic deformation. Accordingly, the number density of elastically active strands ν_{eff} and the molar mass of the networks strand between two active cross-links M_x can be calculated from the plateau modulus (ρ : network mass density).

$$G_N = \nu_{\text{eff}} \cdot k_B T = \frac{\rho \cdot R T}{M_x} \quad (1.6)$$

By contrast, the phantom model takes a fluctuation of the network junctions into account which hinders the affine network deformation in dependence of the functionality f of the cross-linking points. In tetra-arm networks, the phantom network model thus predicts a bisection of the plateau modulus of the affine model. The predictions from the affine and phantom network model converge for high branch functionalities which do not fluctuate much.⁷⁵

$$G_N = \left(1 - \frac{2}{f}\right) \nu_{\text{eff}} \cdot k_B T \quad (1.7)$$

Although most applied, these two classical theories often fail to quantitatively predict the experimental plateau modulus of gels with known strand concentration. This is easily understandable, since both models ignore the presence of elastically inactive junctions resulting from loop formations and unreacted chain ends as well as microstructural network density heterogeneities (**Chapter 1.2**).⁷⁵

1.5 Thermoresponsivity of Polymer Gels

The adaptivity of responsive gels is not limited to the reversibility of transient cross-linking points. The interactions between the macromolecular backbone and the surrounding solvent molecules can also lead to a temperature-dependence of the swelling degree which then affects the average mesh sizes and mechanical stiffness of the corresponding gel.

The miscibility of polymer–solvent and polymer–polymer mixtures can be approximated by the Flory–Huggins mean field theory which delivers an expression for the Gibbs free energy of mixing ΔG_{mix} . It depends on the volume fractions of both components ϕ_i , their polymerization degrees N_i and the dimensionless Flory–Huggins interaction parameter χ , which describes the energy difference before and after mixing (k_B : Boltzmann constant, T = absolute temperature).

$$\Delta G_{\text{mix}} = k_B T \left(\frac{\phi_A}{N_A} \cdot \ln(\phi_A) + \frac{\phi_B}{N_B} \cdot \ln(\phi_B) + \chi \phi_A \phi_B \right) \quad (1.8)$$

At this, the Flory–Huggins parameter also accounts for the deviations between the simplifying theory and real systems and can be expressed as the sum of an enthalpic and an entropic part $\chi = \chi_S + \chi_H T^{-1}$. While the entropic term χ_S reflects longer ranging, entropic contributions, which cannot be captured by the combinatorial treatment of the theory, the enthalpic part χ_H describes whether the mixing is ex- or endothermic. In polar polymer–solvent mixtures with specific interactions between both components (e.g., hydrogen bonds), the mixing is often exothermic ($\chi_H < 0$). The enthalpic term χ_H then promotes the mixing, but its influence on the χ -parameter itself diminishes with increasing temperature.¹⁶⁵ On a molecular level, this means, the number of hydrogen bonds decreases when the thermal energy of the system rises. This is largely promoted by the entropy gain resulting from the release of polar solvent molecules from highly ordered hydration layers.¹⁸⁸ In this case, the temperature-dependent balance between the entropic and enthalpic forces can lead to miscibility gaps. Above a lower critical solution temperature (LCST), the polymer coils repel the solvent molecules, contract and precipitate from the solution.¹⁶⁵

If the corresponding polymer is cross-linked and forms a percolated network, the chain contraction leads to a temperature-induced deswelling, referred to as volume phase transition (VPT, **Figure 1.15 C**). The equilibrium swelling of polymeric gels is described by the Flory–Rehner theory which balances the elastic and thermodynamic contributions that determine the osmotic pressure Π of a gel in a defined solvent.

The prime example for thermoresponsive polymer–solvent mixtures are aqueous poly(*N*-isopropyl acrylamide) (pNiPAm) solutions, in which hydrogen bonding interactions between the amide-groups and water molecules promote the mixing whereas the non-polar polyvinyl backbone and isopropyl side-groups act as hydrophobic counterparts. The LCST transition occurs around 32 °C, when the entropic penalty for the hydrophobic hydration of the unpolar polymer

parts can no longer be compensated.¹⁸⁸ It is thus the given molar balance between hydrophilic and hydrophobic groups which determines the transition temperature. It is however possible to vary the LCST temperature through the incorporation of comonomers with differing polarity.^{189,190}

This general design principle has also been expanded to other polymer backbones, which offer more attractive properties than pNiPAm e.g., regarding the applicability in biological contexts, the mechanical strength of the derived gels or the backbone degradability.^{191,192}

Due to its excellent biocompatibility, the development of thermo-responsive pEG-based copolymers received much interest in this context. Exemplarily, Wurm, Frey and co-workers presented a modular toolbox consisting of ethylene oxide and different, functional oxiranes whose comonomer ratio allowed a precise LCST variation between 9°C and 82 °C.¹⁹³ Another popular approach is the use of oligo(ethylene glycol) side chains. As demonstrated by Lutz *et al.* the LCST of methacrylate-based EG-comb copolymers can be finely tuned through the molar composition and shows a high resilience towards changes in the physical environment including pH, salinity etc..¹⁹⁴

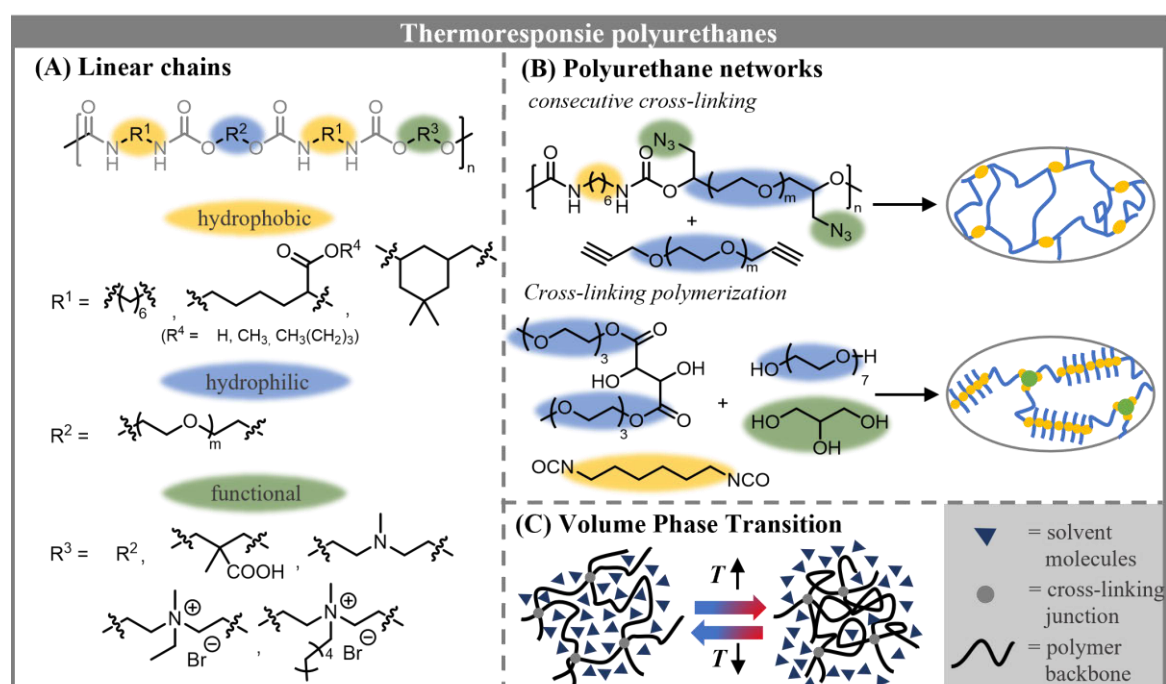


Figure 1.15. (A) Generalized molecular structure of linear, thermo-responsive polyethylene-glycol based PUs described in literature.^{192,195,196,198} (B) Thermo-sensitive pEG-based PU networks obtained from linear precursor chains through an azide-alkyne click reaction²⁰⁰ as well as the cross-linking polymerization of glycerol, pEG, hexamethylene diisocyanate and triethylene glycol tartrate ester.²⁰² (C) Volume phase transition of polymer gels derived from LCST polymers.

Despite the inherent advantages, the pEG backbone leaks hydrolysable linkages which limits its applicability. Therefore, the development of thermo-responsive and degradable polyesters, polyurethanes and polycarbonates represented another useful addition. Combining the attractive properties of pEG-based polymers with the mechanical strength and degradability of PUs, a large

variety of thermoresponsive systems has been described in the past years. Some representative examples are depicted in **Figure 1.15** and include linear PU chains^{192,195–198} and cross-linked networks derived by consecutive cross-linking reactions^{192,199} or by cross-linking polymerization.^{200–202}

In all these cases, the respective LCST or VPT temperatures depends on the molar ratio of hydrophilic and hydrophobic groups in the polymer chains. Accordingly, the transition temperature can be varied through the molar mass of the applied polyether or the incorporation of additional ionic or functional diols.¹⁹⁵ Charged side-groups generally lead to sharper LCST transitions but also cause a pronounced sensitivity towards pH and salinity changes, which is disadvantageous for applications in biological systems.¹⁹² Another possibility to obtain a sharper and more pronounced volume phase transition is the incorporation of oligo(ethylene glycol) side chains. As demonstrated by Aoki and Ajiro, this strategy increases the swelling degree changes of chemically cross-linked PU hydrogels between 5 °C and 40 °C from around 200% in conventional pEG-PU systems to 500–600%.^{201,202}

If the on-going efforts to optimize the temperature-induced swelling degree changes, the hydrolytic degradability, the processability, and the compatibility with biological systems are further continued, PU-based hydrogels have the potential to become valuable alternatives for biomedical and biotechnological applications.^{203–206}

1.6 Polymer Gels for Biomedical Applications

The potential of polymer gels for biomedical applications has now been mentioned several times in the previous chapters. To specify this aspect, especially with respect to the results presented in **Chapter 7**, the following section shortly summarizes the inherent advantages and specific requirements of hydrogels applied in this research area.

In native tissue, cells are embedded within an extracellular matrix (ECM) which acts as mechanical support but also creates a signaling microenvironment. As such, the ECM transmits biomechanical and -chemical cues which induce the maintenance or differentiation of cell-phenotypes and -functions (**Figure 1.16 A+B**).²⁰⁷ Adequate mimicking of certain ECM functions is therefore an important factor in the development of tissue-contacting devices such as medical implants, biosensors or drug-delivery systems. It is further a fundamental prerequisite to study and create cellular systems in the context of advanced 3D cell culturing²⁰⁸, tissue engineering and regenerative medicine.²⁰⁹ Hydrogels have been extensively explored for applications in these research areas since their permeable and tunable network structure is prone to provide tissue-like mechanics, and allows for an efficient nutrient and oxygen-transfer while the high-water content resembles that of native tissue. Accordingly, the macro- and mesoscopic key parameters in the design of hydrogel matrices are the material stiffness, swelling degree, mesh size and permeability, while the incorporation of cell-adhesive ligands and cleavable sites need to be considered on a molecular scale.^{210,211}

The native ECM is a complex multicomponent system usually consisting of a combination of collagen (up to 90%, type 1) which provides the structural integrity, different glycosaminoglycans such as heparin or hyaluronic acid to promote the water retention and adhesive molecules like fibronectins which reinforce the network.²⁰⁹ Many of these adhesive molecules also contain the protein domains which control the attachment of cells. These domains are often comprised by short amino acid sequences such as Arg-Gly-Asp (RGD) or Arg-Glu-Asp-Val (REDV).²⁰⁹

In artificial hydrogel matrices, all ECM functions relevant for the intended application must be fulfilled by correspondingly equipped macromolecule networks of natural or synthetic origin. Natural hydrogels such as collagen or fibrin offer an excellent biocompatibility, an ECM-like, fibrillar microstructure and inherently contain cell-mediated degradation sites. The adjustment of their chemical and mechanical properties to specific demands is however complicated, and their biological origin can cause batch-to-batch inconsistencies.²⁰⁸ Hydrogels, derived from nontoxic, synthetic polymers like poly(acrylamide) or pEG, complement these properties by providing straightforward handles to control the chemical and mechanical properties and provide a high synthetic consistency. They may however show pro-inflammatory effects and provide an insufficient cell-adhesiveness. Finally, polypeptide-based materials can be considered as hybrid form between natural and synthetic polymers which partially bridge the gap between them.²⁰⁸

Considering synthetic hydrogels, the classical parameters of polymer concentration, cross-linking density and branch functionality are applied to vary mechanical strength, swelling degree and mesh size. The design challenges are thus rather related with the incorporation of cell-adhesive ligands or proteins, and the necessity to implement enzymatic or hydrolytic cleavable sites.²¹⁰ Both features are necessary to obtain a sufficient cell-matrix adhesion and provide enough space for the cells to proliferate, differentiate and migrate later-on.

The interactions of cells are primarily controlled by integrins, which represent an important class of transmembrane proteins. As mentioned above, short sub-units of various ECM proteins such as the RGD sequence have been identified as efficient integrin-binding ligands.²¹¹ This is very advantageous since the scalable production of short peptides and their attachment to synthetic scaffolds provides a simple tool to achieve a direct cell-adhesion (**Figure 1.16 C**, top).²¹² Besides the development of peptide sequences with higher association constants, another viable alternative is the adsorption of proteins with integrin binding ligands onto the hydrogel surface which leads to an indirect cell adhesion (**Figure 1.16 C**, bottom). Coating with such mediators is usually achieved through physical interactions such as electrostatic attractions, hydrogen bonding or metal ligand complexations.²⁰⁷ One versatile motive in this regard is the catechol-group and there-upon poly(dopamine) which adhere to many ligand-rich proteins and synthetic polymers.^{213–215} Applying such nature-inspired strategies, considerable progress has been achieved with respect to ECM-mimicking hydrogels and lead to various commercial applications.²⁰⁸

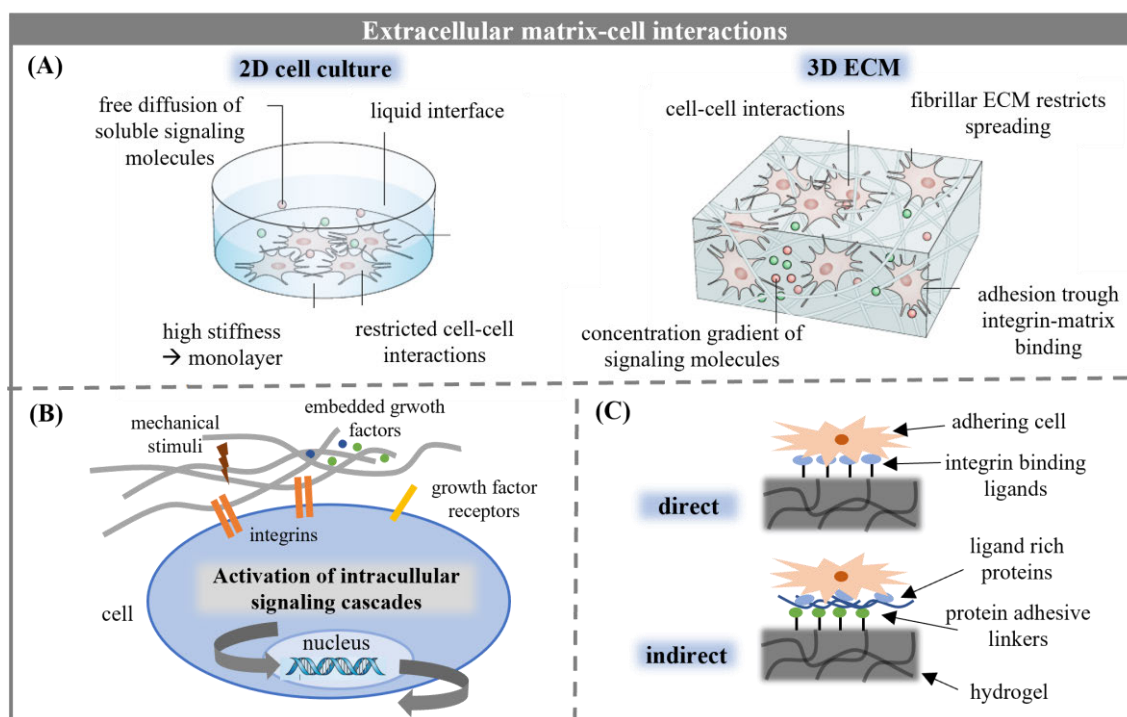


Figure 1.16. (A) Differences between cell culturing in 2D plastic substrates and in 3D extracellular matrix (ECM) environments (Adapted with permission.²⁰⁹ © 2018 Springer Nature). (B) Biochemical and -mechanical interactions between cells and ECM.²⁰⁹ (C) Direct and indirect mediation of cell adhesion on hydrogel surfaces through integrin binding ligands.

1.7 References

- (1) Yang, C.; Wu, K. B.; Deng, Y.; Yuan, J.; Niu, J. Geared Toward Applications: A Perspective on Functional Sequence-Controlled Polymers. *ACS Macro Lett.* **2021**, *10*, 243–257.
- (2) DeStefano, A. J.; Segalman, R. A.; Davidson, E. C. Where Biology and Traditional Polymers Meet: The Potential of Associating Sequence-Defined Polymers for Materials Science. *JACS Au.* **2021**, *1* (10), 1556–1671
- (3) Haug, A.; Larsen, B.; Smidsrød, O. Uronic acid sequence in alginate from different sources. *Carbohydrate Research* **1974**, *32*, 217–225.
- (4) Wahlen, C.; Blankenburg, J.; Tiedemann, P. von; Ewald, J.; Sajkiewicz, P.; Müller, A. H. E.; Floudas, G.; Frey, H. Tapered Multiblock Copolymers Based on Farnesene and Styrene: Impact of Biobased Polydiene Architectures on Material Properties. *Macromolecules* **2020**, *53*, 10397–10408.
- (5) Roy, R.; Park, J. K.; Young, W.-S.; Mastroianni, S. E.; Tureau, M. S.; Epps, T. H. Double-Gyroid Network Morphology in Tapered Diblock Copolymers. *Macromolecules* **2011**, *44*, 3910–3915.
- (6) Bates, F. S.; Fredrickson, G. H. Block Copolymers—Designer Soft Materials. *Physics Today* **1999**, *52*, 32–38.
- (7) Sifri, R. J.; Padilla-Vélez, O.; Coates, G. W.; Fors, B. P. Controlling the Shape of Molecular Weight Distributions in Coordination Polymerization and Its Impact on Physical Properties. *J. Am. Chem. Soc.* **2020**, *142*, 1443–1448.
- (8) Gentekos, D. T.; Sifri, R. J.; Fors, B. P. Controlling polymer properties through the shape of the molecular-weight distribution. *Nat Rev Mater* **2019**, *4*, 761–774.
- (9) Widin, J. M.; Schmitt, A. K.; Schmitt, A. L.; Im, K.; Mahanthappa, M. K. Unexpected consequences of block polydispersity on the self-assembly of ABA triblock copolymers. *J. Am. Chem. Soc.* **2012**, *134*, 3834–3844.
- (10) Oschmann, B.; Lawrence, J.; Schulze, M. W.; Ren, J. M.; Anastasaki, A.; Luo, Y.; Nothling, M. D.; Pester, C. W.; Delaney, K. T.; Connal, L. A.; *et al.* Effects of Tailored Dispersity on the Self-Assembly of Dimethylsiloxane–Methyl Methacrylate Block Co-Oligomers. *ACS Macro Lett.* **2017**, *6*, 668–673.
- (11) Martens, S.; Landuyt, A.; Espeel, P.; Devreese, B.; Dawyndt, P.; Du Prez, F. Multifunctional sequence-defined macromolecules for chemical data storage. *Nat Commun* **2018**, *9*, 4451.
- (12) Ponader, D.; Maffre, P.; Aretz, J.; Pussak, D.; Ninnemann, N. M.; Schmidt, S.; Seeberger, P. H.; Rademacher, C.; Nienhaus, G. U.; Hartmann, L. Carbohydrate-lectin recognition of sequence-defined heteromultivalent glycooligomers. *J. Am. Chem. Soc.* **2014**, *136*, 2008–2016.
- (13) Kuroki, A.; Sangwan, P.; Qu, Y.; Peltier, R.; Sanchez-Cano, C.; Moat, J.; Dowson, C. G.; Williams, E. G. L.; Locock, K. E. S.; Hartlieb, M.; *et al.* Sequence Control as a Powerful Tool for

Improving the Selectivity of Antimicrobial Polymers. *ACS applied materials & interfaces* **2017**, *9*, 40117–40126.

(14) Taylor, A. I.; Pinheiro, V. B.; Smola, M. J.; Morgunov, A. S.; Peak-Chew, S.; Cozens, C.; Weeks, K. M.; Herdewijn, P.; Holliger, P. Catalysts from synthetic genetic polymers. *Nature* **2015**, *518*, 427–430.

(15) Hartmann, L. Polymers for Control Freaks: Sequence-Defined Poly(amidoamine)s and Their Biomedical Applications. *Macromol. Chem. Phys.* **2011**, *212*, 8–13.

(16) Hartmann, L.; Börner, H. G. Precision polymers: monodisperse, monomer-sequence-defined segments to target future demands of polymers in medicine. *Adv. Mater.* **2009**, *21*, 3425–3431.

(17) Li, J.; Stayshich, R. M.; Meyer, T. Y. Exploiting sequence to control the hydrolysis behavior of biodegradable PLGA copolymers. *J. Am. Chem. Soc.* **2011**, *133*, 6910–6913.

(18) Yu, H.; Li, S.; Schwieter, K. E.; Liu, Y.; Sun, B.; Moore, J. S.; Schroeder, C. M. Charge Transport in Sequence-Defined Conjugated Oligomers. *J. Am. Chem. Soc.* **2020**, *142*, 4852–4861.

(19) Hoff, E. A.; Hoe, G. X. de; Mulvaney, C. M.; Hillmyer, M. A.; Alabi, C. A. Thiol-Ene Networks from Sequence-Defined Polyurethane Macromers. *J. Am. Chem. Soc.* **2020**, *142*, 6729–6736.

(20) Norris, B. N.; Zhang, S.; Campbell, C. M.; Auletta, J. T.; Calvo-Marzal, P.; Hutchison, G. R.; Meyer, T. Y. Sequence Matters: Modulating Electronic and Optical Properties of Conjugated Oligomers via Tailored Sequence. *Macromolecules* **2013**, *46*, 1384–1392.

(21) Seiffert, S. Origin of nanostructural inhomogeneity in polymer-network gels. *Polym. Chem.* **2017**, *8*, 4472–4487.

(22) Di Lorenzo, F.; Hellwig, J.; Klitzing, R. von; Seiffert, S. Macroscopic and Microscopic Elasticity of Heterogeneous Polymer Gels. *ACS Macro Lett.* **2015**, *4*, 698–703.

(23) Di Lorenzo, F.; Seiffert, S. Particulate and continuum mechanics of microgel pastes: effect and non-effect of compositional heterogeneity. *Colloid Polym. Sci.* **2013**, *291*, 2927–2933.

(24) Gao, H.; Matyjaszewski, K. Synthesis of functional polymers with controlled architecture by CRP of monomers in the presence of cross-linkers: From stars to gels. *Progress in Polymer Science* **2009**, *34*, 317–350.

(25) Mark, J. E.; Sullivan, J. L. Model networks of end-linked polydimethylsiloxane chains. I. Comparisons between experimental and theoretical values of the elastic modulus and the equilibrium degree of swelling. *The Journal of chemical physics* **1977**, *66*, 1006–1011.

(26) Sakai, T.; Matsunaga, T.; Yamamoto, Y.; Ito, C.; Yoshida, R.; Suzuki, S.; Sasaki, N.; Shibayama, M.; Chung, U.-I. Design and Fabrication of a High-Strength Hydrogel with Ideally Homogeneous Network Structure from Tetrahedron-like Macromonomers. *Macromolecules* **2008**, *41*, 5379–5384.

(27) Li, X. A benchmark for gel structures: bond percolation enables the fabrication of extremely homogeneous gels. *Polym. J.* **2021**, *53*, 765–777.

- (28) Lutz, J.-F., Ed. *Sequence-controlled polymers*; Wiley-VCH: Weinheim, Germany, 2018.
- (29) Baughman, T. W.; Chan, C. D.; Winey, K. I.; Wagener, K. B. Synthesis and Morphology of Well-Defined Poly(ethylene- co -acrylic acid) Copolymers. *Macromolecules* **2007**, *40*, 6564–6571.
- (30) Gutekunst, W. R.; Hawker, C. J. A General Approach to Sequence-Controlled Polymers Using Macrocyclic Ring Opening Metathesis Polymerization. *J. Am. Chem. Soc.* **2015**, *137*, 8038–8041.
- (31) Trigg, E. B.; Gaines, T. W.; Maréchal, M.; Moed, D. E.; Rannou, P.; Wagener, K. B.; Stevens, M. J.; Winey, K. I. Self-assembled highly ordered acid layers in precisely sulfonated polyethylene produce efficient proton transport. *Nature materials* **2018**, *17*, 725–731.
- (32) Chen, Y.; Guan, Z. Bioinspired modular synthesis of elastin-mimic polymers to probe the mechanism of elastin elasticity. *J. Am. Chem. Soc.* **2010**, *132*, 4577–4579.
- (33) Driessen, F.; Du Prez, F. E.; Espeel, P. Precision Multisegmented Macromolecular Lineups: A Display of Unique Control over Backbone Structure and Functionality. *ACS Macro Lett.* **2015**, *4*, 616–619.
- (34) Korley, L. T. J.; Pate, B. D.; Thomas, E. L.; Hammond, P. T. Effect of the degree of soft and hard segment ordering on the morphology and mechanical behavior of semicrystalline segmented polyurethanes. *Polymer* **2006**, *47*, 3073–3082.
- (35) Nathan, A.; Bolikal, D.; Vyavahare, N.; Zalipsky, S.; Kohn, J. Hydrogels based on water-soluble poly(ether urethanes) derived from L-lysine and poly(ethylene glycol). *Macromolecules* **1992**, *25*, 4476–4484.
- (36) Guo, M.; Pitet, L. M.; Wyss, H. M.; Vos, M.; Dankers, P. Y. W.; Meijer, E. W. Tough stimuli-responsive supramolecular hydrogels with hydrogen-bonding network junctions. *J. Am. Chem. Soc.* **2014**, *136*, 6969–6977.
- (37) Szycher, M. *Szycher's handbook of polyurethanes*, 2. ed.; CRC Press / Taylor & Francis: Boca Raton, Fla., 2013.
- (38) Versteegen, R. M.; Kleppinger, R.; Sijbesma, R. P.; Meijer, E. W. Properties and Morphology of Segmented Copoly(ether urea)s with Uniform Hard Segments. *Macromolecules* **2006**, *39*, 772–783.
- (39) Mondal, T.; Dan, K.; Deb, J.; Jana, S. S.; Ghosh, S. Hydrogen-bonding-induced chain folding and vesicular assembly of an amphiphilic polyurethane. *Langmuir* **2013**, *29*, 6746–6753.
- (40) Miller, J. A.; Lin, S. B.; Hwang, K. K. S.; Wu, K. S.; Gibson, P. E.; Cooper, S. L. Properties of polyether-polyurethane block copolymers: effects of hard segment length distribution. *Macromolecules* **1985**, *18*, 32–44.
- (41) Lal, J.; Mark, J. E., Eds. *Advances in Elastomers and Rubber Elasticity*; Springer US: Boston, MA, s.l., 1986.

- (42) Maisonneuve, L.; Lamarzelle, O.; Rix, E.; Grau, E.; Cramail, H. Isocyanate-Free Routes to Polyurethanes and Poly(hydroxy Urethane)s. *Chem. Rev.* **2015**, *115*, 12407–12439.
- (43) Lee, I.; Bates, F. S. Synthesis, Structure, and Properties of Alternating and Random Poly(styrene-*b*-butadiene) Multiblock Copolymers. *Macromolecules* **2013**, *46*, 4529–4539.
- (44) Bialas, N.; Höcker, H.; Marschner, M.; Ritter, W. *Makromol. Chem.* **1990**, *191*, 1843–1852.
- (45) Karpov, S. V.; Lodygina, V. P.; Komratova, V. V.; Dzhalumukhanova, A. S.; Malkov, G. V.; Badamshina, E. R. Kinetics of urethane formation from isophorone diisocyanate: The catalyst and solvent effects. *Kinet. Catal.* **2016**, *57*, 422–428.
- (46) Ono, H.-K.; Jones, F. N.; Pappas, S. P. Relative reactivity of isocyanate groups of isophorone diisocyanate. Unexpected high reactivity of the secondary isocyanate group. *J. Polym. Sci. B Polym. Lett. Ed.* **1985**, *23*, 509–515.
- (47) Eisenbach, C. D.; Baumgartner, M.; Günter, C. Polyurethane Elastomers with Monodisperse Segments and their Model Precursors: Synthesis and Properties. In *Advances in Elastomers and Rubber Elasticity*; Lal, J., Mark, J. E., Eds.; Springer US: Boston, MA, s.l., 1986; pp 51–87.
- (48) Schnabel WJ, O. J. M. US Patent 4,385,171, 1983.
- (49) Murrar I, L. T. DE Patent 102004038784, 2006.
- (50) Hachenberger A, J. K. WO Patent 09719123, 2004.
- (51) Driest, P. J.; Dijkstra, D. J.; Stamatialis, D.; Grijpma, D. W. The Trimerization of Isocyanate-Functionalized Prepolymers: An Effective Method for Synthesizing Well-Defined Polymer Networks. *Macromolecular rapid communications* **2019**, *40*, e1800867.
- (52) Merrifield, R. B. Solid Phase Peptide Synthesis. I. The Synthesis of a Tetrapeptide. *J. Am. Chem. Soc.* **1963**, *85*, 2149–2154.
- (53) NobelPrize.org. The Nobel Prize in Chemistry 1984. <https://www.nobelprize.org/prizes/chemistry/1984/summary>.
- (54) Knight, A. S.; Zhou, E. Y.; Francis, M. B.; Zuckermann, R. N. Sequence Programmable Peptoid Polymers for Diverse Materials Applications. *Adv. Mater.* **2015**, *27*, 5665–5691.
- (55) Edwardson, T. G. W.; Carneiro, K. M. M.; Serpell, C. J.; Sleiman, H. F. An efficient and modular route to sequence-defined polymers appended to DNA. *Angew. Chem. Int. Ed.* **2014**, *53*, 4567–4571.
- (56) Grate, J. W.; Mo, K.-F.; Daily, M. D. Triazine-Based Sequence-Defined Polymers with Side-Chain Diversity and Backbone-Backbone Interaction Motifs. *Angew. Chem. Int. Ed.* **2016**, *55*, 3925–3930.
- (57) Espeel, P.; Carrette, L. L. G.; Bury, K.; Capenberghs, S.; Martins, J. C.; Du Prez, F. E.; Madder, A. Multifunctionalized sequence-defined oligomers from a single building block. *Angew. Chem. Int. Ed.* **2013**, *52*, 13261–13264.

- (58) Martens, S.; van den Begin, J.; Madder, A.; Du Prez, F. E.; Espeel, P. Automated Synthesis of Monodisperse Oligomers, Featuring Sequence Control and Tailored Functionalization. *J. Am. Chem. Soc.* **2016**, *138*, 14182–14185.
- (59) Khanal, A.; Fang, S. Solid Phase Stepwise Synthesis of Polyethylene Glycols. *Chemistry* **2017**, *23*, 15133–15142.
- (60) Al Ouahabi, A.; Charles, L.; Lutz, J.-F. Synthesis of non-natural sequence-encoded polymers using phosphoramidite chemistry. *J. Am. Chem. Soc.* **2015**, *137*, 5629–5635.
- (61) Gunay, U. S.; Petit, B. E.; Karamessini, D.; Al Ouahabi, A.; Amalian, J.-A.; Chendo, C.; Bouquey, M.; Gigmes, D.; Charles, L.; Lutz, J.-F. Chemoselective Synthesis of Uniform Sequence-Coded Polyurethanes and Their Use as Molecular Tags. *Chem.* **2016**, *1*, 114–126.
- (62) Roy, R. K.; Laure, C.; Fischer-Krauser, D.; Charles, L.; Lutz, J.-F. Convergent synthesis of digitally-encoded poly(alkoxyamine amide)s. *Chem. Commun.* **2015**, *51*, 15677–15680.
- (63) Dong, R.; Liu, R.; Gaffney, P. R. J.; Schaeperstoens, M.; Marchetti, P.; Williams, C. M.; Chen, R.; Livingston, A. G. Sequence-defined multifunctional polyethers via liquid-phase synthesis with molecular sieving. *Nature chemistry* **2019**, *11*, 136–145.
- (64) Genabeek, B.; Lamers, B. A. G.; Hawker, C. J.; Meijer, E. W.; Gutekunst, W. R.; Schmidt, B. V. K. J. Properties and applications of precision oligomer materials; where organic and polymer chemistry join forces. *Journal of Polymer Science* **2021**, *59*, 373–403.
- (65) Solleder, S. C.; Schneider, R. V.; Wetzels, K. S.; Boukis, A. C.; Meier, M. A. R. Recent Progress in the Design of Monodisperse, Sequence-Defined Macromolecules. *Macromolecular rapid communications* **2017**, *38*.
- (66) Leibfarth, F. A.; Johnson, J. A.; Jamison, T. F. Scalable synthesis of sequence-defined, unimolecular macromolecules by Flow-IEG. *Proc Natl Acad Sci USA* **2015**, *112*, 10617–10622.
- (67) Barnes, J. C.; Ehrlich, D. J. C.; Gao, A. X.; Leibfarth, F. A.; Jiang, Y.; Zhou, E.; Jamison, T. F.; Johnson, J. A. Iterative exponential growth of stereo- and sequence-controlled polymers. *Nature chemistry* **2015**, *7*, 810–815.
- (68) Wan, Z.; Li, Y.; Bo, S.; Gao, M.; Wang, X.; Zeng, K.; Tao, X.; Li, X.; Yang, Z.; Jiang, Z.-X. Amide bond-containing monodisperse polyethylene glycols beyond 10 000 Da. *Organic & biomolecular chemistry* **2016**, *14*, 7912–7919.
- (69) Gold, V., Ed. *The IUPAC Compendium of Chemical Terminology*; International Union of Pure and Applied Chemistry (IUPAC): Research Triangle Park, NC, 2019.
- (70) Almdal, K.; Dyre, J.; Hvidt, S.; Kramer, O. Towards a phenomenological definition of the term ‘gel’. *Polymer Gels and Networks* **1993**, *1*, 5–17.
- (71) Flory, P. J. Introductory lecture. *Faraday Discuss. Chem. Soc.* **1974**, *57*, 7.
- (72) Jung, J. P.; Gasiorowski, J. Z.; Collier, J. H. Fibrillar peptide gels in biotechnology and biomedicine. *Biopolymers* **2010**, *94*, 49–59.
- (73) Livage, J. Vanadium pentoxide gels. *Chem. Mater.* **1991**, *3*, 578–593.

- (74) Jourdain, A.; Asbai, R.; Anaya, O.; Chehimi, M. M.; Drockenmuller, E.; Montarnal, D. Rheological Properties of Covalent Adaptable Networks with 1,2,3-Triazolium Cross-Links: The Missing Link between Vitrimers and Dissociative Networks. *Macromolecules* **2020**, *53*, 1884–1900.
- (75) Rubinstein, M.; Colby, R. H. *Polymer physics*; Oxford Univ. Press: Oxford, **2003**.
- (76) Seiffert, S.; Sprakel, J. Physical chemistry of supramolecular polymer networks. *Chemical Society reviews* **2012**, *41*, 909–930.
- (77) Gu, Y.; Zhao, J.; Johnson, J. A. A (Macro)Molecular-Level Understanding of Polymer Network Topology. *Trends in Chemistry* **2019**, *1*, 318–334.
- (78) Jangizehi, A.; Ahmadi, M.; Seiffert, S. Emergence, evidence, and effect of junction clustering in supramolecular polymer materials. *Mater. Adv.* **2021**, *13*, 2661.
- (79) Zhang, Z.; Chen, Q.; Colby, R. H. Dynamics of associative polymers. *Soft Matter* **2018**, *14*, 2961–2977.
- (80) Appel, E. A.; del Barrio, J.; Loh, X. J.; Scherman, O. A. Supramolecular polymeric hydrogels. *Chemical Society reviews* **2012**, *41*, 6195–6214.
- (81) Campanella, A.; Döhler, D.; Binder, W. H. Self-Healing in Supramolecular Polymers. *Macromolecular rapid communications* **2018**, *39* (17), 1700739
- (82) Voorhaar, L.; Hoogenboom, R. Supramolecular polymer networks: hydrogels and bulk materials. *Chemical Society reviews* **2016**, *45*, 4013–4031.
- (83) Rossow, T.; Seiffert, S. Supramolecular Polymer Networks: Preparation, Properties, and Potential. In *Supramolecular polymer networks and gels*; Seiffert, S., Anthamatten, M., Eds.; Advances in Polymer Science 268; Springer: Cham, 2015; pp 1–46.
- (84) Khare, E.; Holtén-Andersen, N.; Buehler, M. J. Transition-metal coordinate bonds for bioinspired macromolecules with tunable mechanical properties. *Nat Rev Mater* **2021**, *6*, 421–436.
- (85) Saiz-Poseu, J.; Mancebo-Aracil, J.; Nador, F.; Busqué, F.; Ruiz-Molina, D. The Chemistry behind Catechol-Based Adhesion. *Angew. Chem. Int. Ed.* **2019**, *58*, 696–714.
- (86) Yount, W. C.; Loveless, D. M.; Craig, S. L. Small-molecule dynamics and mechanisms underlying the macroscopic mechanical properties of coordinatively cross-linked polymer networks. *J. Am. Chem. Soc.* **2005**, *127*, 14488–14496.
- (87) Xu, D.; Craig, S. L. Scaling Laws in Supramolecular Polymer Networks. *Macromolecules* **2011**, *44*, 5465–5472.
- (88) Buck, C. C.; Dennis, P. B.; Gupta, M. K.; Grant, M. T.; Crosby, M. G.; Slocik, J. M.; Mirau, P. A.; Becknell, K. A.; Comfort, K. K.; Naik, R. R. Anion-Mediated Effects on the Size and Mechanical Properties of Enzymatically Crosslinked Suckerin Hydrogels. *Macromol. Biosci.* **2019**, *19*, e1800238.

- (89) Shi, L.; Ding, P.; Wang, Y.; Zhang, Y.; Ossipov, D.; Hilborn, J. Self-Healing Polymeric Hydrogel Formed by Metal-Ligand Coordination Assembly: Design, Fabrication, and Biomedical Applications. *Macromolecular rapid communications* **2019**, *40*, e1800837.
- (90) Morgan, G. T.; Burstall, F. H. 3. Dehydrogenation of pyridine by anhydrous ferric chloride. *J. Chem. Soc.* **1932**, 20.
- (91) Schubert, U. *Modern terpyridine chemistry*; Wiley-VCH: Weinheim, 2006.
- (92) Fallahpour, R.-A. Synthesis of 4'-Substituted-2,2':6',2''-Terpyridines. *Synthesis* **2003**, 155–184.
- (93) Husson, J.; Dehaut, J.; Guyard, L. Preparation of carboxylate derivatives of terpyridine via the furan pathway. *Nature protocols* **2014**, *9*, 21–26.
- (94) Schmolke, W.; Ahmadi, M.; Seiffert, S. Enhancement of metallo-supramolecular dissociation kinetics in telechelic terpyridine-capped poly(ethylene glycol) assemblies in the semi-dilute regime. *Physical chemistry chemical physics : PCCP* **2019**, *21*, 19623–19638.
- (95) Schubert, U. S.; Eschbaumer, C.; Hien, O.; Andres, P. R. 4'-Functionalized 2,2':6',2''-terpyridines as building blocks for supramolecular chemistry and nanoscience. *Tetrahedron Letters* **2001**, *42*, 4705–4707.
- (96) Rossow, T.; Seiffert, S. Supramolecular polymer gels with potential model-network structure. *Polym. Chem.* **2014**, *5*, 3018.
- (97) Rossow, T.; Habicht, A.; Seiffert, S. Relaxation and Dynamics in Transient Polymer Model Networks. *Macromolecules* **2014**, *47*, 6473–6482.
- (98) Constable, E. C.; Housecroft, C. E.; Johnston, L. A.; Armspach, D.; Neuburger, M.; Zehnder, M. Dicobalt cluster functionalized 2,2':6',2''-terpyridine ligands and their ruthenium(II) complexes. *Polyhedron* **2001**, *20*, 483–492.
- (99) Andres, P. R.; Hofmeier, H.; Lohmeijer, B. G.; Schubert, U. S. Synthesis of 4'-Functionalized 2,2':6',2''-Terpyridines via the Pyridone Route: Symmetric and Asymmetric Bis-Complex Formation. *Synthesis* **2003**, 2865–2871.
- (100) Wei, C.; He, Y.; Shi, X.; Song, Z. Terpyridine-metal complexes: Applications in catalysis and supramolecular chemistry. *Coordination chemistry reviews* **2019**, *385*, 1–19.
- (101) Holyer, R. H.; Hubbard, C. D.; Kettle, S. F. A.; Wilkins, R. G. The Kinetics of Replacement Reactions of Complexes of the Transition Metals with 2,2',2''-Terpyridine. *Inorg. Chem.* **1966**, *5*, 622–625.
- (102) Munzert, S. M.; Schwarz, G.; Kurth, D. G. Kinetic Studies of the Coordination of Mono- and Ditopic Ligands with First Row Transition Metal Ions. *Inorg. Chem.* **2016**, *55*, 2565–2573.
- (103) Henderson, I. M.; Hayward, R. C. Substituent effects on the stabilities of polymeric and small molecule bis-terpyridine complexes. *Polym. Chem.* **2012**, *3*, 1221.
- (104) Henderson, I. M.; Hayward, R. C. Kinetic stabilities of bis-terpyridine complexes with iron(ii) and cobalt(ii) in organic solvent environments. *J. Mater. Chem.* **2012**, *22*, 21366.

- (105) Hogg, R.; Wilkins, R. G. 57. Exchange studies of certain chelate compounds of the transitional metals. Part VIII. 2,2',2''-terpyridine complexes. *J. Chem. Soc.* **1962**, 0, 341–350.
- (106) Dobrawa, R.; Würthner, F. Metallocsupramolecular approach toward functional coordination polymers. *J. Polym. Sci. Part A: Polym. Chem.* **2005**, 43, 4981–4995.
- (107) Constable, E. C.; Thompson, A. M. W. C. Multinucleating 2,2' : 6',2''-terpyridine ligands as building blocks for the assembly of co-ordination polymers and oligomers. *J. Chem. Soc., Dalton Trans.* **1992**, 3467–3475.
- (108) Constable, E. C.; Thompson, A. M. C.; Tocher, D. A. Metal-directed assembly of coordination oligomers. *Macromol. Symp.* **1994**, 77, 219–228.
- (109) Constable, E. C.; Housecroft, C. E.; Smith, C. B. Self-assembly of two discrete polynuclear iron(II) metallomacrocycles from a ligand containing two 2,2':6',2''-terpyridine binding domains. *Inorganic Chemistry Communications* **2003**, 6, 1011–1013.
- (110) Kimura, M.; Sano, M.; Muto, T.; Hanabusa, K.; Shirai, H.; Kobayashi, N. Self-Assembly of Twisted Bridging Ligands to Helical Coordination Polymers. *Macromolecules* **1999**, 32, 7951–7953.
- (111) Xu, X.; Jerca, F. A.; Jerca, V. V.; Hoogenboom, R. Self-Healing and Moldable Poly(2-isopropenyl-2-oxazoline) Supramolecular Hydrogels Based on a Transient Metal Coordination Network. *Macromolecules* **2020**, 53, 6566–6575.
- (112) Potts, K. T.; Usifer, D. A. Polymers and polymer-metal complexes containing pendent 2,2':6',2''-terpyridinyl ligands. *Macromolecules* **1988**, 21, 1985–1991.
- (113) Bernhard, S.; Takada, K.; Díaz, D. J.; Abruña, H. D.; Mürner, H. Enantiomerically pure chiral coordination polymers: synthesis, spectroscopy, and electrochemistry in solution and on surfaces. *J. Am. Chem. Soc.* **2001**, 123, 10265–10271.
- (114) Hjelm, J.; Constable, E. C.; Figgemeier, E.; Hagfeldt, A.; Handel, R.; Housecroft, C. E.; Mukhtar, E.; Schofield, E. A rod-like polymer containing (Ru(terpy)₂) units prepared by electrochemical coupling of pendant thienyl moieties. *Chem. Commun.* **2002**, 284–285.
- (115) Schubert, U. S.; Eschbaumer, C.; Weidl, C. H. Design of supramolecular metal complexing polymers: synthesis, complexation, and polymerization of 5,5''-bisfunctionalized terpyridine building blocks. *Designed Monomers and Polymers* **1999**, 2, 185–198.
- (116) Hanabusa, K.; Nakamura, A.; Koyama, T.; Shirai, H. *Makromol. Chem.* **1992**, 193, 1309–1319.
- (117) Calzia, K. J.; Tew, G. N. Methacrylate Polymers Containing Metal Binding Ligands for Use in Supramolecular Materials: Random Copolymers Containing Terpyridines. *Macromolecules* **2002**, 35, 6090–6093.
- (118) Schubert, U. S.; Hofmeier, H. Metallo-Supramolecular Graft Copolymers: A Novel Approach Toward Polymer-Analogous Reactions. *Macromol. Rapid Commun.* **2002**, 23, 561.

- (119) Rossow, T.; Hackelbusch, S.; van Assenbergh, P.; Seiffert, S. A modular construction kit for supramolecular polymer gels. *Polym. Chem.* **2013**, *4*, 2515.
- (120) Meurer, J.; Hniopek, J.; Bätz, T.; Zechel, S.; Enke, M.; Vitz, J.; Schmitt, M.; Popp, J.; Hager, M. D.; Schubert, U. S. Shape-Memory Metallopolymers Based on Two Orthogonal Metal-Ligand Interactions. *Adv. Mater.* **2021**, *33*, e2006655.
- (121) Schubert, U. S.; Hien, O.; Eschbaumer, C. Functionalized polymers with metal complexing segments: a simple and high-yield entry towards 2,2':6',2"-terpyridine-based oligomers. *Macromol. Rapid Commun.* **2000**, *21*, 1156–1161.
- (122) Zhang, L.; Zhang, Y.; Chen, Y. Synthesis of bis(2,2':6',2"-terpyridine)-terminated telechelic polymers by RAFT polymerization and ruthenium–polymer complexation thereof. *European Polymer Journal* **2006**, *42*, 2398–2406.
- (123) Koziol, M. F.; Fischer, K.; Seiffert, S. Structural and Gelation Characteristics of Metallo–Supramolecular Polymer Model-Network Hydrogels Probed by Static and Dynamic Light Scattering. *Macromolecules* **2021**, *54*, 4375–4386.
- (124) Tang, S.; Habicht, A.; Li, S.; Seiffert, S.; Olsen, B. D. Self-Diffusion of Associating Star-Shaped Polymers. *Macromolecules* **2016**, *49*, 5599–5608.
- (125) Creusen, G.; Roshanasan, A.; Garcia Lopez, J.; Peneva, K.; Walther, A. Bottom-up design of model network elastomers and hydrogels from precise star polymers. *Polym. Chem.* **2019**, *10*, 3740–3750.
- (126) Ahmadi, M.; Seiffert, S. Dynamic Model Metallo-Supramolecular Dual-Network Hydrogels with Independently Tunable Network Cross-links. *Journal of Polymer Science* **2020**, *58*, 330–342.
- (127) Czarnecki, S.; Rossow, T.; Seiffert, S. Hybrid Polymer-Network Hydrogels with Tunable Mechanical Response. *Polymers* **2016**, *8*, 82.
- (128) Ahmadi, M.; Löser, L.; Fischer, K.; Saalwächter, K.; Seiffert, S. Connectivity Defects and Collective Assemblies in Model Metallo-Supramolecular Dual-Network Hydrogels. *Macromol. Chem. Phys.* **2020**, *221*, 1900400.
- (129) Ahmadi, M.; Seiffert, S. Direct Evidence of Heteroleptic Complexation in the Macroscopic Dynamics of Metallo–supramolecular Polymer Networks. *Macromolecules* **2021**, *54*, 7113–7124.
- (130) Winter, A.; Friebe, C.; Chiper, M.; Hager, M. D.; Schubert, U. S. Self-assembly of π -conjugated bis(terpyridine) ligands with zinc(II) ions: New metallosupramolecular materials for optoelectronic applications. *J. Polym. Sci. Part A: Polym. Chem.* **2009**, *47*, 4083–4098.
- (131) Marin, V.; Holder, E.; Hoogenboom, R.; Schubert, U. S. Functional ruthenium(II)- and iridium(III)-containing polymers for potential electro-optical applications. *Chemical Society reviews* **2007**, *36*, 618–635.

- (132) Hsu, T.-W.; Hsu, H.-C.; Chan, H.-Y.; Fang, J.-M. A Terpyridine Zinc Complex for Selective Detection of Lipid Pyrophosphates: A Model System for Monitoring Bacterial O- and N-Transglycosylations. *The Journal of organic chemistry* **2020**, *85*, 12747–12753.
- (133) Bode, S.; Zedler, L.; Schacher, F. H.; Dietzek, B.; Schmitt, M.; Popp, J.; Hager, M. D.; Schubert, U. S. Self-healing polymer coatings based on crosslinked metallosupramolecular copolymers. *Advanced materials (Deerfield Beach, Fla.)* **2013**, *25*, 1634–1638.
- (134) Xu, X.; Jerca, F. A.; Jerca, V. V.; Hoogenboom, R. Covalent Poly(2-Isopropenyl-2-Oxazoline) Hydrogels with Ultrahigh Mechanical Strength and Toughness through Secondary Terpyridine Metal-Coordination Cross-links. *Adv. Funct. Mater.* **2019**, *29*, 1904886.
- (135) Lohmeijer, B. G. G.; Schubert, U. S. Supramolecular Engineering with Macromolecules: An Alternative Concept for Block Copolymers. *Angew. Chem. Int. Ed.* **2002**, *41*, 3825–3829.
- (136) Wang, R.; Geven, M.; Dijkstra, P. J.; Martens, P.; Karperien, M. Hydrogels by supramolecular crosslinking of terpyridine end group functionalized 8-arm poly(ethylene glycol). *Soft Matter* **2014**, *10*, 7328–7336.
- (137) Heller, M.; Schubert, U. S. Optically Active Supramolecular Poly(L-lactide)s End-Capped with Terpyridine. *Macromol. Rapid Commun.* **2001**, *22*, 1358–1363.
- (138) Habicht, A.; Czarnecki, S.; Rossow, T.; Seiffert, S. Connectivity defects enhance chain dynamics in supramolecular polymer model-network gels. *J. Polym. Sci. Part B: Polym. Phys.* **2017**, *55*, 19–29.
- (139) Zhuge, F.; Brassinne, J.; Fustin, C.-A.; van Ruymbeke, E.; Gohy, J.-F. Synthesis and Rheology of Bulk Metallo-Supramolecular Polymers from Telechelic Entangled Precursors. *Macromolecules* **2017**, *50*, 5165–5175.
- (140) Mahadevi, A. S.; Sastry, G. N. Cooperativity in Noncovalent Interactions. *Chem. Rev.* **2016**, *116*, 2775–2825.
- (141) Krbek, L. K. S. von; Schalley, C. A.; Thordarson, P. Assessing cooperativity in supramolecular systems. *Chemical Society reviews* **2017**, *46*, 2622–2637.
- (142) Ouyang, J. F.; Bettens, R. P. A. When are Many-Body Effects Significant? *Journal of chemical theory and computation* **2016**, *12*, 5860–5867.
- (143) Sijbesma, R. P.; Beijer, F. H.; Brunsveld, L.; Folmer, B. J.; Hirschberg, J. H.; Lange, R. F.; Lowe, J. K.; Meijer, E. W. Reversible polymers formed from self-complementary monomers using quadruple hydrogen bonding. *Science (New York, N.Y.)* **1997**, *278*, 1601–1604.
- (144) Karas, L. J.; Wu, C.-H.; Das, R.; Wu, J. I.-C. Hydrogen bond design principles. *Wiley interdisciplinary reviews. Computational molecular science* **2020**, *10*.
- (145) Pranata, J.; Wierschke, S. G.; Jorgensen, W. L. OPLS potential functions for nucleotide bases. Relative association constants of hydrogen-bonded base pairs in chloroform. *J. Am. Chem. Soc.* **1991**, *113*, 2810–2819.

- (146) Whitty, A. Cooperativity and biological complexity. *Nature chemical biology* **2008**, *4*, 435–439.
- (147) Sing, M. K.; Ramírez, J.; Olsen, B. D. Mechanical response of transient telechelic networks with many-part stickers. *The Journal of chemical physics* **2017**, *147*, 194902.
- (148) Errington, W. J.; Bruncsics, B.; Sarkar, C. A. Mechanisms of noncanonical binding dynamics in multivalent protein-protein interactions. *Proceedings of the National Academy of Sciences of the United States of America* **2019**, *116*, 25659–25667.
- (149) Iqbal, M.; Huskens, J.; Sypula, M.; Modolo, G.; Verboom, W. Synthesis and evaluation of novel water-soluble ligands for the complexation of metals during the partitioning of actinides. *New J. Chem.* **2011**, *35*, 2591.
- (150) Ruiz-Herrero, T.; Estrada, J.; Guantes, R.; Miguez, D. G. A tunable coarse-grained model for ligand-receptor interaction. *PLoS computational biology* **2013**, *9*, e1003274.
- (151) Diestler, D. J.; Knapp, E. W. Statistical Mechanics of the Stability of Multivalent Ligand–Receptor Complexes. *J. Phys. Chem. C.* **2010**, *114*, 5287–5304.
- (152) Weber, M.; Bujotzek, A.; Haag, R. Quantifying the rebinding effect in multivalent chemical ligand-receptor systems. *The Journal of chemical physics* **2012**, *137*, 54111.
- (153) Fouquey, C.; Lehn, J.-M.; Levelut, A.-M. Molecular recognition directed self-assembly of supramolecular liquid crystalline polymers from complementary chiral components. *Adv. Mater.* **1990**, *2*, 254–257.
- (154) Kubik, S. *Supramolecular Chemistry in Water*; Wiley, 2019.
- (155) Cantekin, S.; Greef, T. F. A. de; Palmans, A. R. A. Benzene-1,3,5-tricarboxamide: a versatile ordering moiety for supramolecular chemistry. *Chemical Society reviews* **2012**, *41*, 6125–6137.
- (156) Garzoni, M.; Baker, M. B.; Leenders, C. M. A.; Voets, I. K.; Albertazzi, L.; Palmans, A. R. A.; Meijer, E. W.; Pavan, G. M. Effect of H-Bonding on Order Amplification in the Growth of a Supramolecular Polymer in Water. *J. Am. Chem. Soc.* **2016**, *138*, 13985–13995.
- (157) Hendricks, M. P.; Sato, K.; Palmer, L. C.; Stupp, S. I. Supramolecular Assembly of Peptide Amphiphiles. *Accounts of chemical research* **2017**, *50*, 2440–2448.
- (158) Spitzer, D.; Rodrigues, L. L.; Straßburger, D.; Mezger, M.; Besenius, P. Tuneable Transient Thermogels Mediated by a pH- and Redox-Regulated Supramolecular Polymerization. *Angew. Chem. Int. Ed.* **2017**, *56*, 15461–15465.
- (159) Tang, J. D.; Mura, C.; Lampe, K. J. Stimuli-Responsive, Pentapeptide, Nanofiber Hydrogel for Tissue Engineering. *J. Am. Chem. Soc.* **2019**, *141*, 4886–4899.
- (160) Huang, Z.; Lee, H.; Lee, E.; Kang, S.-K.; Nam, J.-M.; Lee, M. Responsive nematic gels from the self-assembly of aqueous nanofibres. *Nat Commun* **2011**, *2*, 459.
- (161) Moon, K.-S.; Kim, H.-J.; Lee, E.; Lee, M. Self-assembly of T-shaped aromatic amphiphiles into stimulus-responsive nanofibers. *Angew. Chem. Int. Ed.* **2007**, *46*, 6807–6810.

- (162) Redondo-Gómez, C.; Abdouni, Y.; Becer, C. R.; Mata, A. Self-Assembling Hydrogels Based on a Complementary Host-Guest Peptide Amphiphile Pair. *Biomacromolecules* **2019**, *20*, 2276–2285.
- (163) Sahoo, J. K.; VandenBerg, M. A.; Webber, M. J. Kinetic Evolution in Metal-Dependent Self-Assembly of Peptide-Terpyridine Conjugates. *Macromolecular rapid communications* **2019**, e1900565.
- (164) Kemper, B.; Zengerling, L.; Spitzer, D.; Otter, R.; Bauer, T.; Besenius, P. Kinetically Controlled Stepwise Self-Assembly of AuI-Metallopeptides in Water. *J. Am. Chem. Soc.* **2018**, *140*, 534–537.
- (165) Sebastian Seiffert. *Physical Chemistry of Polymers: A Conceptual Introduction*; De Gruyter, **2020**.
- (166) Danielsen, S. P. O.; Beech, H. K.; Wang, S.; El-Zaatari, B. M.; Wang, X.; Sapir, L.; Ouchi, T.; Wang, Z.; Johnson, P. N.; Hu, Y.; *et al.* Molecular Characterization of Polymer Networks. *Chem. Rev.* **2021**, *121*, 5042–5092.
- (167) BILMES, L. A Rheological Chart. *Nature* **1942**, *150*, 432–433.
- (168) Fumagalli, M.; Belal, K.; Guo, H.; Stoffelbach, F.; Cooke, G.; Marcellan, A.; Woisel, P.; Hourdet, D. Supramolecular polymer hydrogels induced by host-guest interactions with di-cyclobis(paraquat-p-phenylene) cross-linkers: from molecular complexation to viscoelastic properties. *Soft Matter* **2017**, *13*, 5269–5282.
- (169) Holten-Andersen, N.; Harrington, M. J.; Birkedal, H.; Lee, B. P.; Messersmith, P. B.; Lee, K. Y. C.; Waite, J. H. pH-induced metal-ligand cross-links inspired by mussel yield self-healing polymer networks with near-covalent elastic moduli. *Proceedings of the National Academy of Sciences of the United States of America* **2011**, *108*, 2651–2655.
- (170) Parada, G. A.; Zhao, X. Ideal reversible polymer networks. *Soft Matter* **2018**, *14*, 5186–5196.
- (171) Zhang, X.; Vidavsky, Y.; Aharonovich, S.; Yang, S. J.; Buche, M. R.; Diesendruck, C. E.; Silberstein, M. N. Bridging experiments and theory: isolating the effects of metal-ligand interactions on viscoelasticity of reversible polymer networks. *Soft Matter* **2020**, *16*, 8591–8601.
- (172) Tang, S.; Olsen, B. D. Relaxation Processes in Supramolecular Metallogels Based on Histidine–Nickel Coordination Bonds. *Macromolecules* **2016**, *49*, 9163–9175.
- (173) Stukalin, E. B.; Cai, L.-H.; Kumar, N. A.; Leibler, L.; Rubinstein, M. Self-Healing of Unentangled Polymer Networks with Reversible Bonds. *Macromolecules* **2013**, *46*.
- (174) Gold, B. J.; Hövelmann, C. H.; Lühmann, N.; Pyckhout-Hintzen, W.; Wischniewski, A.; Richter, D. The microscopic origin of the rheology in supramolecular entangled polymer networks. *Journal of Rheology* **2017**, *61*, 1211–1226.

- (175) Gold, B. J.; Hövelmann, C. H.; Lühmann, N.; Székely, N. K.; Pyckhout-Hintzen, W.; Wischniewski, A.; Richter, D. Importance of Compact Random Walks for the Rheology of Transient Networks. *ACS Macro Lett.* **2017**, *6*, 73–77.
- (176) Rubinstein, M.; Semenov, A. N. Thermoreversible Gelation in Solutions of Associating Polymers. 2. Linear Dynamics. *Macromolecules* **1998**, *31*, 1386–1397.
- (177) Leibler, L.; Rubinstein, M.; Colby, R. H. Dynamics of reversible networks. *Macromolecules* **1991**, *24*, 4701–4707.
- (178) Hackelbusch, S.; Rossow, T.; van Assenbergh, P.; Seiffert, S. Chain Dynamics in Supramolecular Polymer Networks. *Macromolecules* **2013**, *46*, 6273–6286.
- (179) Brassinne, J.; Cadix, A.; Wilson, J.; van Ruymbeke, E. Dissociating sticker dynamics from chain relaxation in supramolecular polymer networks—The importance of free partner! *Journal of Rheology* **2017**, *61*, 1123–1134.
- (180) Semenov, A. N.; Rubinstein, M. Dynamics of Entangled Associating Polymers with Large Aggregates. *Macromolecules* **2002**, *35*, 4821–4837.
- (181) Chen, Q.; Tudryn, G. J.; Colby, R. H. Ionomer dynamics and the sticky Rouse model. *Journal of Rheology* **2013**, *57*, 1441–1462.
- (182) Tang, S.; Wang, M.; Olsen, B. D. Anomalous self-diffusion and sticky Rouse dynamics in associative protein hydrogels. *J. Am. Chem. Soc.* **2015**, *137*, 3946–3957.
- (183) Grindy, S. C.; Learsch, R.; Mozhdzhi, D.; Cheng, J.; Barrett, D. G.; Guan, Z.; Messersmith, P. B.; Holten-Andersen, N. Control of hierarchical polymer mechanics with bioinspired metal-coordination dynamics. *Nature materials* **2015**, *14*, 1210–1216.
- (184) Seiffert, S. Effect of Supramolecular Interchain Sticking on the Low-Frequency Relaxation of Transient Polymer Networks. *Macromol. rapid commun.* **2016**, *37*, 257–264.
- (185) Flory, P. J. *Principles of polymer chemistry*, 19. print; Cornell Univ. Press: Ithaca, NY, ca. 2006.
- (186) James, H. M.; Guth, E. Statistical Thermodynamics of Rubber Elasticity. *The Journal of chemical physics* **1953**, *21*, 1039–1049.
- (187) Zhong, M.; Wang, R.; Kawamoto, K.; Olsen, B. D.; Johnson, J. A. Quantifying the impact of molecular defects on polymer network elasticity. *Science (New York, N.Y.)* **2016**, *353*, 1264–1268.
- (188) Lyon, L. A.; Meng, Z.; Singh, N.; Sorrell, C. D.; St John, A. Thermoresponsive microgel-based materials. *Chemical Society reviews* **2009**, *38*, 865–874.
- (189) Ohnsorg, M. L.; Ting, J. M.; Jones, S. D.; Jung, S.; Bates, F. S.; Reineke, T. M. Tuning PNIPAm self-assembly and thermoresponse: roles of hydrophobic end-groups and hydrophilic comonomer. *Polym. Chem.* **2019**, *10*, 3469–3479.

- (190) Valencia, L.; Enríquez, F. J.; Valencia, M.; Díaz, R. Tuning the LCST of PNIPAM via Random Oxidation-Sensitive Thioether Functionalities. *Macromol. Chem. Phys.* **2017**, *218*, 1600556.
- (191) Hoogenboom, R. Tunable Thermoresponsive Polymers by Molecular Design. In *Complex macromolecular architectures: Synthesis, characterization, and self-assembly*; Hadjichristidis, N., Ed.; Wiley Interscience: Hoboken, NJ, 2011; pp 685–715.
- (192) Ronco, L. I.; Basterretxea, A.; Mantione, D.; Aguirresarobe, R. H.; Minari, R. J.; Gugliotta, L. M.; Mecerreyes, D.; Sardon, H. Temperature responsive PEG-based polyurethanes “à la carte”. *Polymer* **2017**, *122*, 117–124.
- (193) Mangold, C.; Obermeier, B.; Wurm, F.; Frey, H. From an epoxide monomer toolkit to functional PEG copolymers with adjustable LCST behavior. *Macromolecular rapid communications* **2011**, *32*, 1930–1934.
- (194) Lutz, J.-F.; Akdemir, O.; Hoth, A. Point by point comparison of two thermosensitive polymers exhibiting a similar LCST: is the age of poly(NIPAM) over? *J. Am. Chem. Soc.* **2006**, *128*, 13046–13047.
- (195) Fu, H.; Gao, H.; Wu, G.; Wang, Y.; Fan, Y.; Ma, J. Preparation and tunable temperature sensitivity of biodegradable polyurethane nanoassemblies from diisocyanate and poly(ethylene glycol). *Soft Matter* **2011**, *7*, 3546.
- (196) Sardon, H.; Tan, J. P. K.; Chan, J. M. W.; Mantione, D.; Mecerreyes, D.; Hedrick, J. L.; Yang, Y. Y. Thermoresponsive Random Poly(ether urethanes) with Tailorable LCSTs for Anticancer Drug Delivery. *Macromolecular rapid communications* **2015**, *36*, 1761–1767.
- (197) Huynh, C. T.; Nguyen, Q. V.; Kang, S. W.; Lee, D. S. Synthesis and characterization of poly(amino urea urethane)-based block copolymer and its potential application as injectable pH/temperature-sensitive hydrogel for protein carrier. *Polymer* **2012**, *53*, 4069–4075.
- (198) Sun, X.; Gao, H.; Wu, G.; Wang, Y.; Fan, Y.; Ma, J. Biodegradable and temperature-responsive polyurethanes for adriamycin delivery. *International journal of pharmaceutics* **2011**, *412*, 52–58.
- (199) Li, K.; Zhou, C.; Liu, S.; Yao, F.; Fu, G.; Xu, L. Preparation of mechanically-tough and thermo-responsive polyurethane-poly(ethylene glycol) hydrogels. *Reactive and Functional Polymers* **2017**, *117*, 81–88.
- (200) Frydrych, M.; Román, S.; Green, N. H.; MacNeil, S.; Chen, B. Thermoresponsive, stretchable, biodegradable and biocompatible poly(glycerol sebacate)-based polyurethane hydrogels. *Polym. Chem.* **2015**, *6*, 7974–7987.
- (201) Aoki, D.; Ajiro, H. Thermoresponsive Polyurethane Bearing Oligo(Ethylene Glycol) as Side Chain Without Polyol at Polymer Backbone Achieved Excellent Hydrophilic and Hydrophobic Switching. *Macromolecular rapid communications* **2018**, *39*, e1800239.

- (202) Aoki, D.; Ajiro, H. One-Shot Preparation of Thermoresponsive Comb Polyurethane Hydrogel for Both Excellent Toughness and Large Volume Switching. *Macromolecular rapid communications* **2021**, e2100128.
- (203) Fortman, D. J.; Sheppard, D. T.; Dichtel, W. R. Reprocessing Cross-Linked Polyurethanes by Catalyzing Carbamate Exchange. *Macromolecules* **2019**, *52*, 6330–6335.
- (204) Mura, S.; Nicolas, J.; Couvreur, P. Stimuli-responsive nanocarriers for drug delivery. *Nature materials* **2013**, *12*, 991–1003.
- (205) Klouda, L. Thermoresponsive hydrogels in biomedical applications: A seven-year update. *European journal of pharmaceutics and biopharmaceutics : official journal of Arbeitsgemeinschaft fur Pharmazeutische Verfahrenstechnik e.V* **2015**, *97*, 338–349.
- (206) Meng, F.; Zhong, Z.; Feijen, J. Stimuli-responsive polymersomes for programmed drug delivery. *Biomacromolecules* **2009**, *10*, 197–209.
- (207) Seliktar, D. Designing cell-compatible hydrogels for biomedical applications. *Science (New York, N.Y.)* **2012**, *336*, 1124–1128.
- (208) Caliri, S. R.; Burdick, J. A. A practical guide to hydrogels for cell culture. *Nature methods* **2016**, *13*, 405–414.
- (209) Hussey, G. S.; Dziki, J. L.; Badylak, S. F. Extracellular matrix-based materials for regenerative medicine. *Nat. Rev. Mater.* **2018**, *3*, 159–173.
- (210) Thiele, J.; Ma, Y.; Bruekers, S. M. C.; Ma, S.; Huck, W. T. S. 25th anniversary article: Designer hydrogels for cell cultures: a materials selection guide. *Adv. Mater.* **2014**, *26*, 125–147.
- (211) Rice, J. J.; Martino, M. M.; Laporte, L. de; Tortelli, F.; Briquez, P. S.; Hubbell, J. A. Engineering the regenerative microenvironment with biomaterials. *Advanced healthcare materials* **2013**, *2*, 57–71.
- (212) Hersel, U.; Dahmen, C.; Kessler, H. RGD modified polymers: biomaterials for stimulated cell adhesion and beyond. *Biomaterials* **2003**, *24*, 4385–4415.
- (213) Stengelin, E.; Nzigou Mombo, B.; Mondeshki, M.; Beltramo, G. L.; Lange, M. A.; Schmidt, P.; Frerichs, H.; Wegner, S. V.; Seiffert, S. Rational Design of Thermoresponsive Microgel Templates with Polydopamine Surface Coating for Microtissue Applications. *Macromol. Biosci.* **2021**, e2100209.
- (214) Wei, K.; Chen, X.; Zhao, P.; Feng, Q.; Yang, B.; Li, R.; Zhang, Z.-Y.; Bian, L. Stretchable and Bioadhesive Supramolecular Hydrogels Activated by a One-Stone-Two-Bird Postgelation Functionalization Method. *ACS applied materials & interfaces* **2019**, *11*, 16328–16335.
- (215) Brubaker, C. E.; Kissler, H.; Wang, L.-J.; Kaufman, D. B.; Messersmith, P. B. Biological performance of mussel-inspired adhesive in extrahepatic islet transplantation. *Biomaterials* **2010**, *31*, 420–427.

CHAPTER 2: MOTIVATION & SCIENTIFIC GOALS

The capability to reversibly alter the chemical and/or physical properties in response to external stimuli is intrinsic to many biological materials. The urge to implement this ability into synthetic soft matter promoted the development of a variety of stimuli-responsive materials, sensitive towards changes of the temperature, pH value, or light exposure, the application of mechanical, electrical, and magnetic forces, or the presence of small molecules and biological messengers.

For polymer and material scientists, one special focus in this area is the targeted engineering of the macroscopic mechanical properties of responsive gels. In this regard, stimuli-responsivity includes shear-thinning properties, the reversible transition from low-viscous solutions to viscoelastic solids, or a significant temporal alteration of the mechanical strength in general.

These responsive properties originate from different mechanisms, which are closely related to the nature of the building blocks that form the respective networks. **Figure 2.1** summarizes the three responsive gel classes, which are investigated within this thesis. Firstly, responsive properties can be implemented into *covalently cross-linked polymer gels* consisting of a permanent, percolated network. Besides these permanent networks, *supramolecular gels* based on hierarchically self-assembled structures stabilized by physical interactions, represent a second responsive material class. Due to the reversibility of the non-covalent linkages, these networks can fully disassemble, but often lack the mechanical strength of covalent networks. Consequently, a third class of responsive materials has emerged. In *supramolecular polymer networks*, covalent polymer chains are cross-linked by supramolecular interchain associations combining the advantages of both approaches.

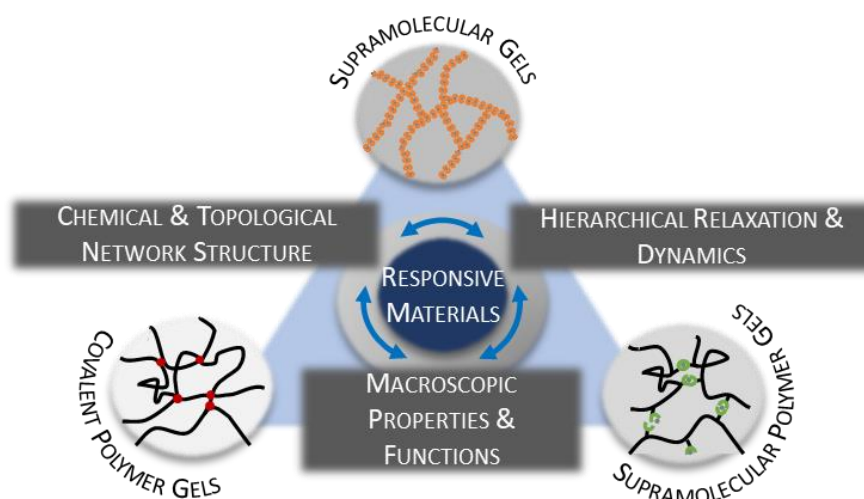


Figure 2.1. Schematic overview of the structure–dynamics–property relationships of responsive materials based on covalent polymer gels, supramolecular cross-linked polymer gels and supramolecular, self-assembling gels.

In all three types of responsive gels, the macroscopic properties are determined by the chemical and topological network structure and the dynamics of the (macro)molecular building blocks. Since these parameters show mutual interdependencies, the comprehensive understanding of the structure–(dynamics–)property relationships is a crucial prerequisite for the rational design of functional responsive and/or reversible materials and the main focus of this thesis.

In the first three chapters, different methods to control the distribution of reversible cross-linking junctions and the effects of this spatial arrangement on the mechanical properties of supramolecular polymer gels are investigated. Afterwards, important design parameters, namely the reversible cross-linking motive and the polymerization approach, are transferred to the development of a self-assembling, supramolecular hydrogel and a bio-adhesive, covalent polymer gel, which both show stimuli-responsive properties.

Regarding the structure-dependent viscoelasticity of supramolecular polymer gels, much knowledge has been gained over the past ten years by using (1) metallo–supramolecular cross-linking motives which offer the ability to alter the cross-linking strength and/or dynamics without exchanging the precursor polymer and (2) applying well-defined model systems either based on telechelic multi-arm polymers or linear side-functionalized chains. While the telechelic systems offer an unparalleled control of the sticker and thus latter mesh size distribution, their architecture limits the possible number of stickers per chain and imparts a major deviation from most theoretical models. The side-sticker model systems are however commonly obtained by controlled radical polymerizations, which yields narrow molar mass dispersities but leads to random sticker– and thus mesh size–distribution.

To bridge this gap, the first goal of this thesis is the development of a complementary side-sticker model system, in which the spacing of the stickers can be altered from random to uniform. At this, the metal coordinating terpyridine (tpy) ligand is chosen as supramolecular sticker and incorporated into amphiphilic poly(ethylene glycol) (pEG) based polyurethane (PU) multiblocks with equal sticker–, but broad molar mass–distributions. The behavior of the precursor polymers in bulk and solution, as well as the mechanical properties of the cross-linked gels are then analyzed, to study the influence of an alternating compared to a random sticker arrangement.

Since this step-growth approach only allows to switch between alternating and random sequences, the actual sticker distribution in the random PUs remains unknown. Therefore, an alternative, iterative growth approach is explored in a second study. Applying the solid support strategy known from the Merrifield peptide synthesis, uniform, amide-bond containing pEGs with tpy side-stickers are synthesized. The modularity of this approach allows for an easy variation of the sticker spacing, the linker that connects backbone and sticker and the total number of stickers per chain. It is also possible to introduce defined multiplets of neighboring supramolecular stickers, which perspectively opens the opportunity to study cooperativity effects between them.

Further focusing on synergetic effects between spatially close stickers, a third study aims to elucidate the differences between supramolecular model gels either cross-linked by isolated, monotopic tpy-stickers or adjacent, ditopic tpy-sticker pairs. Since macroscopic rheological experiments require rather large product amounts, the solid phase approach is unsuited for this purpose. Instead, the PU synthesis strategy from project 1 is applied to create linear PUs with equally spaced mono- and ditopic tpy-stickers. To complement this polydisperse side-sticker system, an established telechelic four-arm pEG model is chosen and accordingly equipped with either one or two tpy groups per chain end. The effects of the multivalent chain-sticking are then investigated by concentration- and cross-linking strength dependent rheological experiments.

In a fourth, collaborative project, the metallo-supramolecular cross-linking *via* tpy complexes is combined with the self-assembly of C_3 -symmetric peptide amphiphiles to create a multi-stimuli responsive hydrogelator. In dilute, aqueous solutions, the synergetic hydrogen bonding and hydrophobic forces of certain peptide-amphiphiles lead to the formation of anisotropic nanorod structures. It has been shown that the incorporation of a temperature-sensitive ethylene glycol dendron into the hydrophilic corona of these nanorods further enables a reversible thermogelation. This gelation switch is however limited to nanorods derived from oppositely charged peptide-amphiphiles, which are additionally stabilized by electrostatic forces. Neutral peptide-nanorods, which offer the advantage of being less affected by the pH or salinity of the surrounding liquid, did not show a similar temperature-induced gelation. To overcome this limitation, the combination of neutral peptide-amphiphiles and the coordinative metal tpy cross-linking is explored in this study.

In the last part, the amphiphilic properties of the pEG-based PUs from project 1, are used to create a permanently cross-linked, thermosensitive hydrogel as potential material platform for bio(medical) applications. The temperature-dependent swelling properties of covalent gels based on polymer-solvent mixtures with miscibility gaps, offer unique possibilities for (micro)tissue engineering or drug encapsulating applications. In this context, the mechanical strength, degradability, and biocompatibility of the hydrogel matrix are of great importance. PU gels intrinsically provide hydrolytically cleavable sites in their backbone and offer an excellent mechanical performance, but generally lack bio-adhesive properties. To extent their potential in this regard, the incorporation of cell-adhesive bio-linkers into UV cross-linked PU gels with tunable thermoresponsivity and mechanical strength is investigated.

CHAPTER 3: STICKER DISTRIBUTION IN METALLO–SUPRAMOLECULAR CROSS-LINKED POLYMER GELS

Publication:

Amphiphilic Poly(ether urethanes) Carrying Associative Terpyridine Side Groups with Controlled Spacing

K. Breul, XXXXXXXXXX *Polymer Chemistry* **2021**, *12*, 2305–2316 (doi.org/10.1039/D1PY00121C).

The results presented in the following chapter (p. 55–86) were first published on March 23, 2021 and are adapted with permission.¹

Further supporting information can be found in appendix, **Chapter A.3**.

Copyright © 2021 Royal Society of Chemistry.

Summary

The rational design of reversible polymer gels requires a comprehensive understanding of the relationships between the network structure, and the macroscopic mechanical response. In this context, the influence of the spacing between the associating motives (stickers) and thus the supramolecular cross-linking density is not yet fully understood. While it has been clearly established that the average cross-linking density is an important determinant for the mechanical stiffness, the effects of an inhomogeneous density distribution remain partially inconclusive. One example is the frequently observed shallowing of the power-law scaling in the terminal flow regime of reversible gels in comparison to the predictions of the Maxwell model. It has been hypothesized that this characteristic rheological feature results either primarily from the dispersity of the overall molar mass of the polymers, the irregularity of the sticker spacing, or from the combination of both. To investigate this and related question, complementary model systems in which these parameters can be varied independently, still represent a crucial prerequisite.

In this study, we therefore present a straightforward synthesis method for linear associating polymers, which allows to switch between uniform and irregular sticker distributions. For this purpose, multiblock polyurethanes (PUs) are synthesized from isophorone diisocyanate (IPDI), a terpyridine (tpy) functionalized diol and poly(ethylene glycol) (pEG) diols with differing molar masses. Applying either a modified pre-polymer approach or a facile one-shot polymerization, multiblocks with strictly alternating or random pEG–tpy sequences and a broad overall molar mass dispersity ($\mathcal{D} \approx 2$) are prepared. The sticker spacing in the alternating multiblocks is then exclusively determined by the pEG segments ($\mathcal{D} < 1.05$).

Although differential scanning calorimetry and infrared spectroscopy experiments indicate a low degree of phase-separation between the polyether matrix and the IPDI–tpy domains, the strong hydrogen bonding between the urethane groups nonetheless affects the solution behavior of the copolymers. Concentration-dependent dynamic light scattering measurements in methanol demonstrate the presence of a small fraction of diffusive aggregates besides the molecularly dissolved polymer chains in solutions of both PU types. In water, the alternating PUs dissolve in the form of micellar aggregates whose size strongly depends on temperature and polymer volume fraction, while the random PUs remain insoluble. The aqueous solutions of the alternating PUs show a lower critical solution temperature, which depends on the amphiphilic balance of hydrophilic and hydrophobic units in the PU backbone.




Finally, shear rheological investigations of the Mn^{2+} cross-linked gels reveal systematical deviations between the viscoelastic properties of the random and alternating PU gels. At equal sticker concentrations, the plateau moduli of the random PUs are slightly upshifted, while the relaxation times are significantly prolonged and the power-law scaling in the terminal flow regime is shallower than that of the alternating PU gels. These effects and the water insolubility of the random PUs are explained by synergetic effects between $(\text{–IPDI-tpy–})_n$ multiplets which are only possible in the random PUs.

Author Contributions:

Katharina Breul: Concept development, monomer and polymer synthesis and characterizations, rheological measurements, manuscript preparation.

 Concept development, scientific supervision, and manuscript correction.

Acknowledgements:

We thank  and  for their kind help with DSC and HPLC-CC measurements, as well as  for the inspiring discussions. Funding by the German Research Foundation under grant number SE 1888/7-1 (Project No. 376900084) is gratefully acknowledged.

3.1 Introduction

Supramolecular associating polymers contain functional units, commonly referred to as stickers, that can bind to one another *via* non-covalent interactions such as hydrogen bonding, host–guest, or metal–ligand complexations.² Above a critical concentration of the precursor polymers in aqueous or organic solutions, a percolated, transient network is formed upon sticker association.³ Such supramolecular gels are characterized by their intrinsic self-healing ability⁴, processability, and tunable viscoelasticity ranging from liquid to rubbery elastic, mainly determined by the concentration, position, and association strength and kinetics of the non-covalent cross-links.⁵ This combination of tunable responsivity and mechanical strength makes supramolecular polymer gels a promising material platform⁶ especially for biomedical applications with a scope ranging from injectable drug carriers,⁷ to wound healing scaffolds,⁸ tissue adhesives,⁹ and smart sensors¹⁰ or actuators.¹¹ However, a rational molecule–to–material design for such high-tech applications requires a comprehensive understanding of the relations between the network (nano)structure, sticker dynamics, and macroscopic relaxation and strength. Over the last decade, numerous experimental and theoretical studies on well-defined model systems created a widely accepted picture about basic structure–property relationships.¹² In an unentangled, homogeneous single-phase network with only binary associations, the concentration and binding constant of the stickers determine the average fraction of closed stickers and thus the mechanical strength of the transient network. Furthermore, the in–gel dissociation kinetics of the stickers control the terminal network relaxation time.¹³

Nonetheless, the idealized view of the network topology as a regular array is an oversimplification in most cases, and it still remains difficult to clearly allocate deviations from theoretical predictions and simulations to the molecular network structure.¹⁴ An intensively studied example for such a complication is the multitude of hierarchical self-assembly processes resulting from a (micro)phase-separation of the associating units and their subsequent aggregation into sticker clusters.¹⁵ The resulting structural inhomogeneities are comparable to those of thermoplastic elastomers and lead to pronounced alterations of the dynamic and mechanical properties which remain difficult to predict.

Another often observed phenomenon without a clear rationale is the shallowing of the power-law scaling in the terminal flow regime of the frequency-dependent storage G' and loss moduli G'' of transient networks and gels.¹⁶ It is a well-known rheological feature that an increasing dispersity of the molar mass broadens the relaxation time distribution in the terminal flow regime of macromolecules, resulting in such shallower scalings.¹⁷ Based on this fundamental relation, it has been speculated that the here-observed behavior of transient polymer networks is mainly caused by either the molar mass dispersity, an irregular sticker distribution, or a combination of both.¹⁴

However, other studies relate the shallowing rather to the presence of phase-separated sticker clusters and transient branching.¹⁸ To address these and further uncertainties about fundamental structure–property relationships, associating model polymers with a controlled and regular spacing of the stickers along the backbone are required.

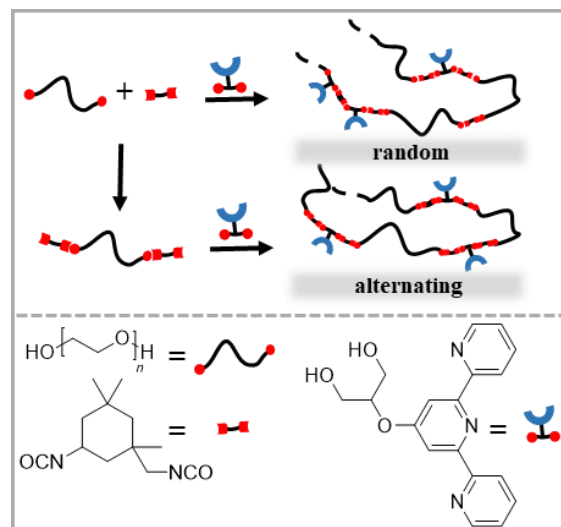
In this regard, supramolecular gels derived from narrowly disperse star-shaped poly(ethylene glycols) (pEGs) with telechelic associating groups can be considered as an almost ideal model system with a highly regular mesh size structure. Consequently, the rheological properties of these gels largely coincide with the single-mode Maxwell model predictions.¹² Despite the valuable insights obtained with these model systems, however, there remains a lack of comparability and generalizability regarding the influence of the polymer architecture, the average number of stickers per chain, and the backbone chemistry in comparison to the more abundant side-sticker polymer gels.¹⁹

Such side-sticker polymers are most often synthesized using (controlled) radical copolymerization techniques and thus commonly show statistic sticker distributions.²⁰ Implementing a regular spacing in side-sticker polymers requires some level of control over the monomer sequence. The synthesis of sequence-controlled macromolecules is however not straightforward and represents a challenging research field of its own. Although multiple advanced methods have been developed over the past years,²¹ the gram-scale sample amounts and rather high molar masses required for macroscopic measurements make the most versatile, iterative techniques unsuitable.²² However, by keeping the molecular design as simple as possible, a regular sticker spacing in a periodic copolymer can already be achieved through a facile step-growth polymerization,²³ even though that approach yields a Schulz–Flory distribution regarding the overall molar mass. The resulting combination of a narrow sticker and broad molar mass distribution is interesting, since it complements most of the so-far investigated supramolecular associating polymers.²⁴

One highly efficient, and scalable step-growth polymerization is the polyaddition of diisocyanates of type AA and diols of type BB, yielding segmented polyurethanes (PU) of type (AB)_n.² We follow this synthesis strategy and use it with one of the two reaction partners being a supramolecular associating motif. The modular nature of this approach allows for an easy variation of the associating motive, the backbone chemistry, and the molar mass of a spacing unit. 2,2':6',2''-Terpyridine (tpy) is chosen as the supramolecular unit because the complexation with transition metal ions leads to highly directional, reversible cross-links with well-defined stoichiometry and tunable kinetic and thermodynamic stability, usable in organic and aqueous media.²⁶ To obtain strictly alternating sequences, poly(ethylene glycol) (pEG) diols are firstly end-capped with isophorone diisocyanate (IPDI) and isolated prior to the chain elongation with the tpy diol. PUs with similar chemical composition but random sequences are obtained in a common one-shot polymerization as schematically depicted in **Figure 3.1**.

Three different molar masses of the pEG diol (2k, 4k, 6k) are used to implement different sticker spacings. The structural properties of the amphiphilic PUs in bulk are compared by Fourier-transformed infrared (FT-IR) and differential scanning calorimetry (DSC). Further on, the molecular solubility and thermo-responsiveness of the PUs in methanol and water is studied by concentration-dependent dynamic light scattering (DLS), before the rheological properties of the Mn^{2+} cross-linked gels are finally compared by linear shear rheology.

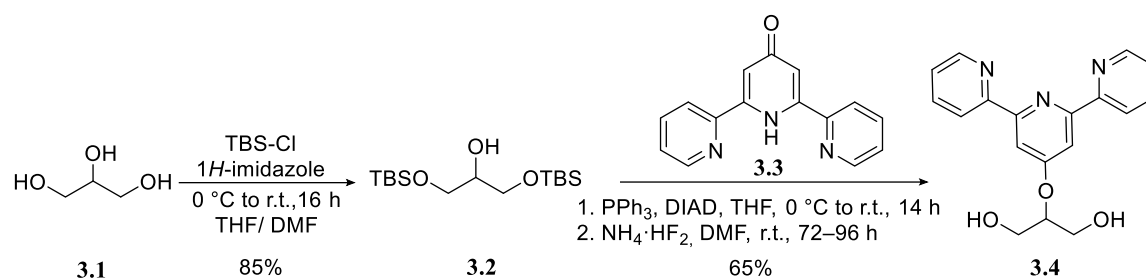
Figure 3.1. Synthesis concept for pEG-based PUs carrying pendant tpy groups with random and alternating spacing.



3.2 Results & Discussion

Synthesis

A tpy-functionalized glycerol derivate is synthesized as supramolecular cross-linkable diol. After the selective protection of the terminal hydroxy groups of glycerol **3.1** as *tert*-butyldimethylsilyl ether, the secondary hydroxy group is reacted with 2,6-bis(2-pyridyl)-4(1*H*)-pyridone **3.3** in a Mitsunobu reaction.²⁷ Deprotection of the primary alcohols using NH_4HF_2 as mild and selective fluoride source at almost neutral pH, yields the required tpy diol **3.4** in a yield of 55% over three steps (Scheme 3.1).



Scheme 3.1. Synthesis of terpyridine diol **3.4** from glycerol **3.1**.

To create strictly alternating PUs, pEGs with different molar masses (**3.5a** pEG-2k: $1.95 \text{ kg}\cdot\text{mol}^{-1}$, **3.5b**: pEG-4k: $4.2 \text{ kg}\cdot\text{mol}^{-1}$, **3.5c**: pEG-6k: $6.27 \text{ kg}\cdot\text{mol}^{-1}$) are end-capped with isophorone diisocyanate **3.6** (*Z/E* mixture $\approx 4:1$, Figure 3.2 A). In the past, the asymmetric IPDI has been found to be particularly suitable for polymer end-capping reactions, because the reactivities of the aliphatic and the cycloaliphatic NCO groups differ from each other depending on catalyst, solvent, and reaction temperature.²⁸ Since the relative reactivity of the secondary NCO group was shown to be most considerably increased in the presence of organotin compounds²⁹, the end-

capping reactions in this work are conducted under di-*n*-butyltin dilaurate (DBTDL) catalysis. To completely avoid the chain elongation of the pre-polymer, the dilute pEG diol solutions are added to an excess of the diisocyanate.³⁰ However, the GPC traces of the pEG-2k pre-polymers **3.7a** show a shoulder at shorter retention times corresponding to the dimerized pre-polymer when 5.0 and 10.0 eq. IPDI are applied (**Figure 3.2 B**). The use of 15.0 eq. IPDI is found to be sufficient to fully suppress the dimerization reaction, which is a considerably lower excess than the previously reported need for 100 eq. IPDI.²⁸

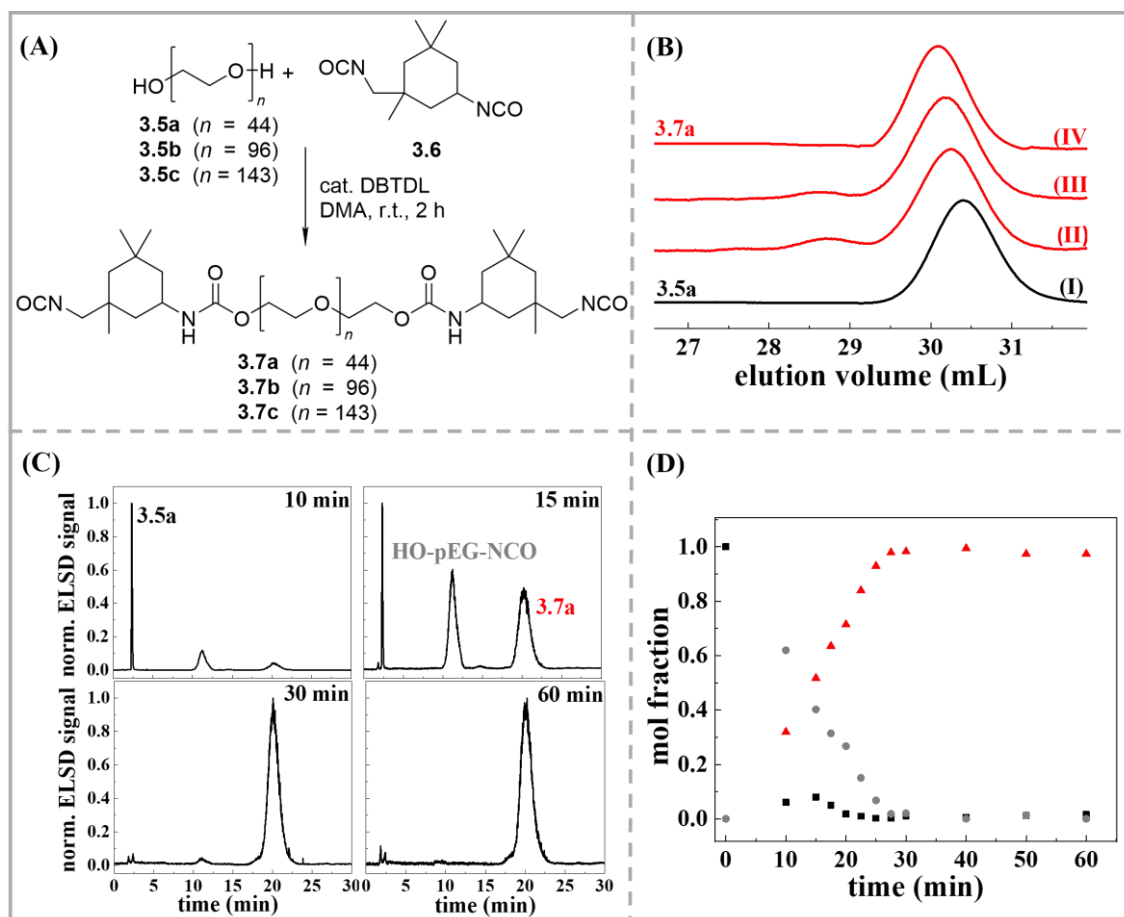


Figure 3.2. (A) Synthesis of α,ω -diisocyanato-pEGs **3.7a**, **3.7b** and **3.7c** with average polymerization degrees n . (B) GPC traces of (I) **3.5a** and the IPDI end-capped pre-polymer **3.7a** applying an excess of (II) 5.0 eq. (6% dimer), (III) 10.0 eq. (5% dimer) and (IV) 15.0 eq. IPDI (0% dimer) (aliquots quenched with MeOH). (C) Representative HPLC-CC elugrams of benzyl-terminated aliquots from the end-capping of the pEG-2k diol taken from the reaction mixture after 10, 15, 30 and 60 min. (D) Conversion of pEG-2k diol **3.5a** (■) to NCO-pEG-OH (●) and NCO-pEG-NCO **3.7a** (▲) as analyzed by peak integration in the respective HPLC-CC elugrams.

The time required to achieve a complete hydroxyl-group conversion is investigated by high performance liquid chromatography at critical conditions (HPLC-CC). The critical conditions correspond to a certain solvent composition for a given stationary phase, at which the macromolecular backbone becomes chromatographically invisible, and the end-group polarity determines the retention time.³¹ Aliquots are withdrawn from the reaction mixture after completed

pEG addition, quenched with benzyl alcohol to reduce the end-group polarity, precipitated into diethyl ether, and analyzed by HPLC-CC. The critical conditions allow a direct peak allocation according to the end-group polarity. As shown in the elugrams in **Figure 3.2 C**, the hydroxyl functionalized educt **3.5a** is converted into two less polar species (mono- and diisocyanato-pEG derivates). The reaction is finished after 30 min at r.t., which is considerably faster than reported for comparable polymer end-capping procedures with IPDI.²⁸ The peak assignment and the desired pre-polymer structure are confirmed by ¹H-NMR and electron spray mass spectrometry investigations of the final pre-polymer (**Chapter 3.4: Figure 3.11, Figure 3.12**).

Prior to the subsequent chain elongation reaction, the excess IPDI is removed by precipitation of the pre-polymer into anhydrous diethyl ether under inert conditions. The content of free IPDI in the pre-polymers before and after consecutive precipitation steps is analyzed by GPC. As shown in **Figure 3.3 A**, the remaining IPDI fraction after two precipitations is reproducibly below 3–7% for all three molar masses. This is considered sufficient since every purification step also contributes to a degradation of the reactive NCO end-groups.

To ensure equimolarity in the chain elongation step, the purified pre-polymers are freeze-dried from benzene and weighed under inert atmosphere. The relative NCO content of the pre-polymers after precipitation and freeze-drying is investigated by FT-IR spectroscopy. Spectra of the drop-cast films are recorded under nitrogen atmosphere and normalized to the C-O-C stretching vibration at 1100 cm⁻¹. After IPDI end-capping, the isocyanate (N=C=O), carbonyl (C=O) and N-H bands of the urethane group appear at 2260, 1716 and 3327 cm⁻¹ as shown in **Figure 3.3 B**. According to the relative peak area of the normalized bands, the NCO content decreases around 7% over the purification steps.

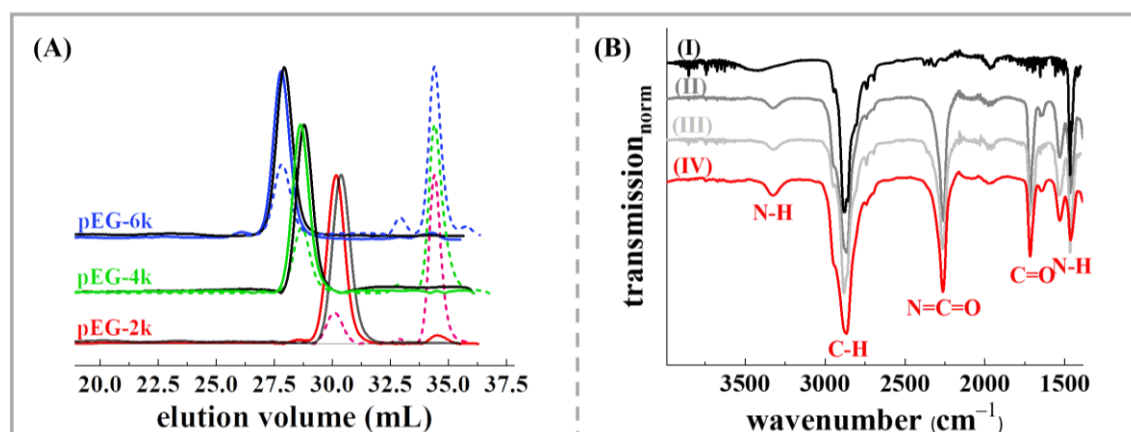


Figure 3.3. (A) GPC traces of the crude (dotted lines) and purified α,ω -diisocyanato pre-polymers (pEG-2k: —, pEG-4k: —, pEG-6k: —) and pEG diols (black; 2k: bottom, 4k: middle, 6k: top). (B) Normalized FT-IR spectra of (I) the pEG-2k diol, and of the α,ω -diisocyanato pre-polymers after (II) one and (III) two precipitation steps and (IV) after freeze-drying (drop-cast films, r.t., N₂).

Further on, the efficiency of the subsequent chain elongation reaction is considerably increased by taking uncertainties regarding the exact NCO content of the purified pre-polymers into account. By initially adding a sub-stoichiometric amount of the tpy diol (0.8 eq.) and increasing it in 0.2 eq. steps after 12 h and 24 h, the average molar mass of the PUs increases while the amount of unreacted pre-polymer drops (**Figure 3.13**).

In addition to the alternating PUs, three random copolymers with similar chemical composition are prepared in a common one-shot procedure as depicted in **Figure 3.4 B**. The reaction progress is monitored by FT-IR spectroscopy until full conversion is ensured by the complete disappearance of the NCO band at 2257 cm^{-1} (**Figure 3.14**). GPC analysis of the purified PUs reveals that the chain elongation efficiency in terms of the average number of repeating blocks per chain $\langle x \rangle$ is in all cases higher for the randomly polymerized PUs (**Table 3.1**, **Figure 3.4 C**). This is likely caused by the fewer possible side reactions and higher stoichiometric accuracy feasible in the one-shot polymerization. Except for PU_4k-alt, the elongation efficiency also decreases with the molar mass of the pre-polymer, most likely due to the reduced chain-end accessibility.

Table 3.1. Molecular properties of pEG–tpy polyurethanes with random and alternating sequences.

#	$M_n^a)$ ($\text{kg}\cdot\text{mol}^{-1}$)	$M_w^a)$ ($\text{kg}\cdot\text{mol}^{-1}$)	$D^a)$	$\langle x \rangle^b)$	$f_{\text{tpy}}^c)$ ($\mu\text{mol}\cdot\text{g}^{-1}$)	$\alpha^d)$ (%)	N_R
PU_2k-alt	14.2	27.0	2.0	5.6	270	76	4.3
PU_2k-ran	22.2	45.9	2.1	8.8	320	90	7.9
PU_4k-alt	31.8	61.8	1.9	6.7	147	75	5.0
PU_4k-ran	33.8	64.8	1.9	7.1	171	88	6.2
PU_6k-alt	33.2	63.7	1.9	4.8	110	80	3.9
PU_6k-ran	43.0	77.9	1.8	6.2	122	89	5.6

^{a)} Determined by GPC (DMF, pEG calibration). ^{b)} Average number of blocks $\langle x \rangle = M_{n,\text{PU}}/M_{n,\text{repeating unit}}$ ($M_{n,\text{repeating unit}} = 2.50, 4.69$ and $6.90\text{ kg}\cdot\text{mol}^{-1}$). ^{c)} Terpyridine content $f_{\text{tpy}} = n_{\text{tpy}}/m_{\text{PU}}$ as determined with the Lambert-Beer law from the absorbance at $\lambda = 278\text{ nm}$ (tpy diol: $\epsilon = (22.6 \pm 1) \cdot 10^2\text{ L}\cdot\text{mol}^{-1}\cdot\text{cm}^{-1}$). ^{d)} Tpy functionalities in comparison to the targeted contents of 354, 195 and $187\text{ }\mu\text{mol}\cdot\text{g}^{-1}$ calculated under the assumption that every repeating unit contains one tpy ligand $n_{\text{tpy}}^{\text{theo}} = n_{\text{PU}} \langle x \rangle = m_{\text{PU}}/M_{\text{repeating unit}}$.

Further on, the chemical structure of the copolymers is analyzed by $^1\text{H-NMR}$ based on the peak assignment illustrated in **Figure 3.4 A**.³² The spectra of the random PUs and their alternating counterparts largely coincide with respect to the peak shapes and positions, as well as the molar comonomer ratios as shown for PU_4k-alt/ran in **Figure 3.4 A**. This analogy further confirms the intended structural similarity of both PU types. The integrals of the low-field signals at 7.49, 7.99, 8.61, and 8.71 ppm (**h**, **i**, **j**, **k** and **l**), which are assigned to the tpy group, however, are strongly dependent on the first-order phase correction of the spectra and thus subject to a large systematic error. Therefore, the molar tpy content per gram polymer $f_{\text{tpy}} = n_{\text{tpy}}/m_{\text{PU}}$ is instead *via* UV-Vis spectroscopy. To ensure that the determination is not distorted by an absorbance of the PU backbone, a spectrometric titration with CuBr_2 is conducted for PU_6k-alt. Since the results of

both methods are in excellent agreement, the PU absorbance is considered to be negligible at the tpy absorbance maximum at 278 nm (**Figure 3.15**).

The consistently lower tpy functionalization degrees α of the alternating ($\alpha = 75\text{--}80\%$) compared to the random PUs ($\alpha = 88\text{--}90\%$) are attributed to the not fully suppressible side-reactions of the isocyanates during the pre-polymer purification. It is suspected that water traces lead to amine terminated pre-polymer fragments, which then form urea linkages with isocyanate endcapped pre-polymers. This causes a duplication of the tpy spacing and leads to a lower functionalization degree and broadened sticker distribution. Additionally, the stepwise tpy diol addition in the chain elongation step increases the possibility for a high fraction of pEG-terminated PU chains.

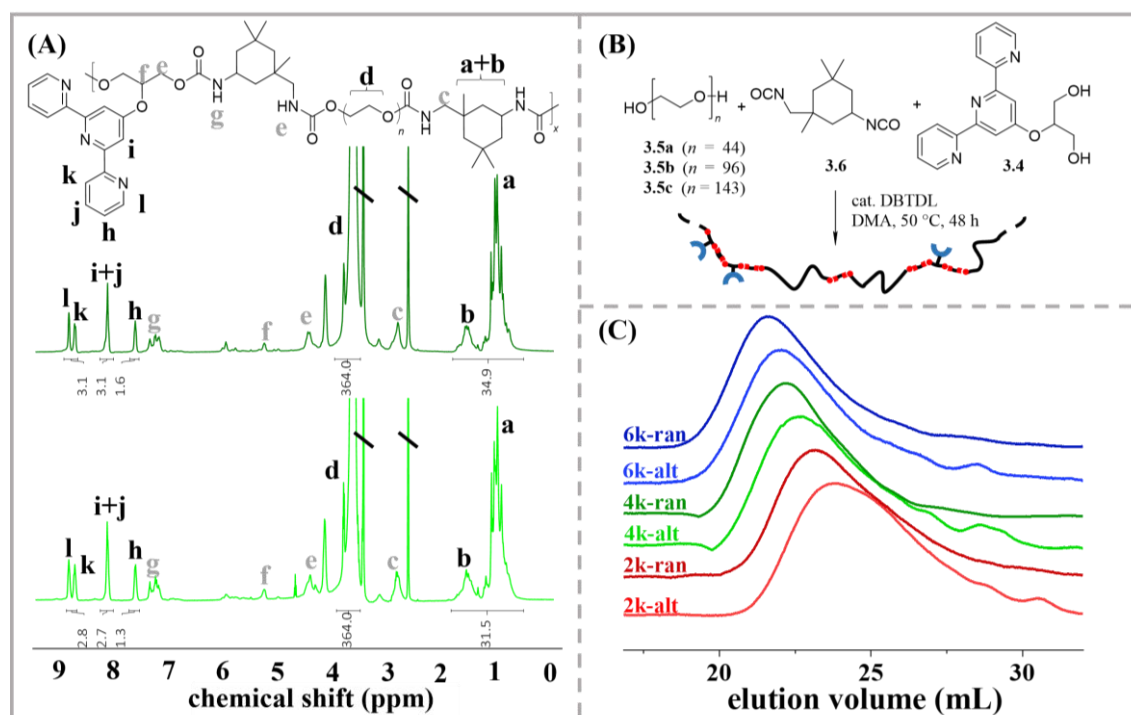


Figure 3.4. (A) $^1\text{H-NMR}$ of PU_4k-alt (bottom) and PU_4k-ran (top) in $\text{DMSO-}d_6$. (B) Synthesis scheme for the randomly sequenced pEG-IPDI-tpy polyurethanes. (C) GPC elugrams of the alternating and random PUs in DMF.

Bulk Properties

Next, FT-IR spectroscopy is used to compare the hydrogen bonding properties of the random and alternating polyurethanes by analyzing the location, intensity, and shape of the N-H and C=O stretching vibrations. In general, bands of H-bonded carbonyls are broader and located at lower frequencies than those of free C=O groups with frequency shifts between $20\text{--}30\text{ cm}^{-1}$. Since hydrogen bonding is a cooperative phenomenon, the energy of H-bonded carbonyl bands additionally depends on the number of interacting groups and their order (amorphous or crystalline) as it determines the hydrogen-bond length and thus the bonding energy. However, the exact location of these bands depends on the chemical composition of the respective polymer.³³

In the herein synthesized PUs, H-bonding is possible between the hydrogen-donating urethane N-H and hydrogen-bond receiving ether and urethane carbonyl groups. The content of H-bonded carbonyls is therefore a measure of urethane–urethane interactions and thus indicative for the degree of phase mixing.³⁴ To analyze this property, the FT-IR spectra of the drop-cast PU films are normalized to the C-O-C stretching vibration at 1100 cm^{-1} (**Figure 3.5 A**). Comparing the random and alternating PUs, the intensity of the broad N-H stretching vibration at 3330 cm^{-1} and the width of the carbonyl band between 1750 and 1620 cm^{-1} are increased for all random PUs.

For a quantitative analysis, a peak deconvolution of the carbonyl region is conducted with Gaussian fit functions (insert **Figure 3.5 A**, **Figure 3.17**).³⁵

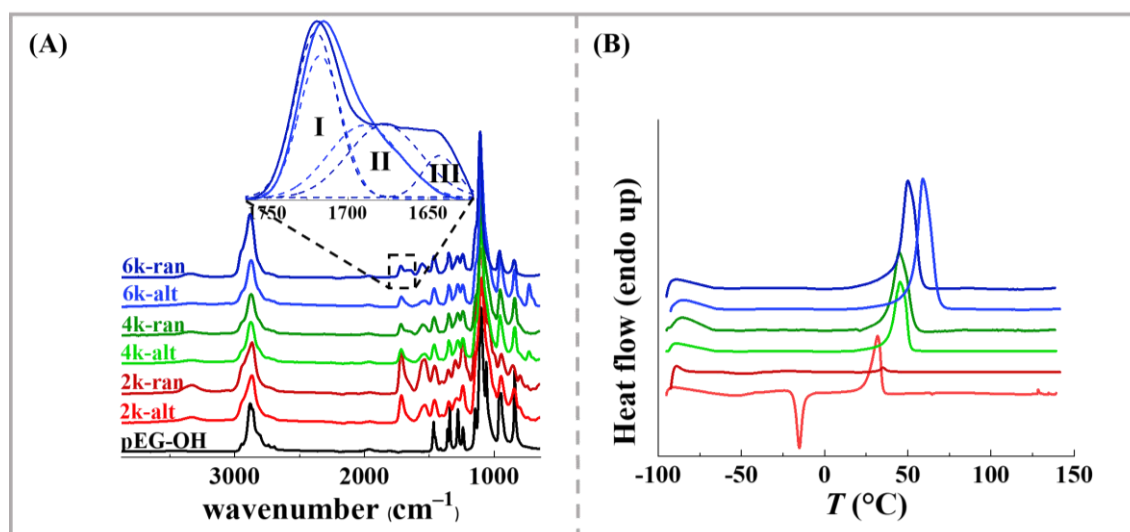


Figure 3.5. (A) FT-IR spectra of pEG diols and random and alternating PUs at r.t. normalized to the C-O-C stretching vibration at 1100 cm^{-1} ; Insert: Deconvolution of the carbonyl region of PU_6k-alt (light blue) and PU_6k-ran (dark blue). (B) DSC thermograms of the 2nd heating run (rate: $10.0\text{ °C}\cdot\text{min}^{-1}$) of the random and alternating PUs (baseline corrected).

While the carbonyl stretching region of the three alternating PUs can be best fit under the assumption of two distinct bands at (I) $1717\text{--}1720\text{ cm}^{-1}$ and (II) $1686\text{--}1689\text{ cm}^{-1}$, the fitting of the random PU bands requires the assumption of a third band (III) to take the emerging low frequency shoulder with a maximum located between $1643\text{--}1657\text{ cm}^{-1}$ into account. In agreement with previous studies on polyether-based polyurethanes, band (I) is assigned to the free carbonyl groups.³⁶ The relative intensity of these bands is $> 50\%$ in all cases, which indicates that a large fraction of urethane groups is distributed within the semi-crystalline polyether matrix (**Table 3.2**). It is further observed that the fraction of H-bonded urethane groups slightly increases with the molar mass of the polyether, which is reasonable since an increasing length and flexibility of the soft segment facilitate the phase separation. Furthermore, the relative amount of free carbonyl groups is found to be similar for the random and alternating PUs. It must however be noticed that a pronounced low frequency shoulder (III) emerges in the spectra of all random PUs.

Table 3.2. Position and relative intensity of the FT-IR bands in the carbonyl region determined by peak-deconvolution, as well as the thermal properties measured by DSC, and the cloud point temperatures of aqueous solutions of the alternating and random PUs and of their pEG precursors.

sample	I (cm^{-1})	II (cm^{-1})	III (cm^{-1})	T_g ($^{\circ}\text{C}$)	T_m ($^{\circ}\text{C}$)	ΔH ($\text{J}\cdot\text{g}^{-1}$)	$T_c^{\text{H}_2\text{O}}$ ($^{\circ}\text{C}$)
pEG-2k 3.5a	–	–	–	–	62.1	159.2	–
pEG-2k pre-polymer 3.7a	x	x	x	–42.6*	47.0*	71.9*	–*
PU_2k-alt	1716 (59%)	1686 (41%)	x	–47.0	31.9	51.0	17.5
PU_2k-ran	1719 (53%)	1694 (35%)	1657 (12%)	–39.7	35.6	1.66	–
pEG-4k 3.5b	–	–	–	–	66.0	155.0	–
pEG-4k pre-polymer 3.7b	x	x	x	–*	58.1*	95.3*	–*
PU_4k-alt	1717 (58%)	1687 (42%)	–	–	45.4	63.5	55.0
PU_4k-ran	1718 (56%)	1686 (36%)	1647 (9%)	–	43.3	61.8	–
pEG-6k 3.5c	–	–	–	–	68.4	151.3	–
pEG-6k pre-polymer 3.7c	x	x	x	–*	58.2*	104.5*	–*
PU_6k-alt	1717 (52%)	1689 (47%)	–	–	55.1	83.0	74.8
PU_6k-ran	1720 (51%)	1677 (39%)	1643 (10%)	–	48.6	80.7	–

– : property does not occur, x: not investigated, * MeOH quenched aliquots.

Neglecting phase separation effects, the main difference between the alternating and random PUs is the probability of directly neighboring $(-\text{IPDI-tpy-})_n$ sequences in the latter ones. It is thus reasonable that the emergence of this additional shoulder is caused by a synergetic H-bonding between the urethane groups of such multiplets.³⁴

Further on, the thermal properties of the three IPDI endcapped pEG pre-polymers and the alternating and random PUs are analyzed by differential scanning calorimetry. The thermograms of all samples (2nd heating run) show an endothermic peak attributed to the melting of crystalline pEG domains (**Figure 3.5 B**). As expected, the melting temperatures and enthalpies of the IPDI endcapped pre-polymers are reduced in comparison to the pEG diols of the same molar mass (**Table 3.2**). The relative crystallinity of the pre-polymers in comparison to the corresponding pEG diols increases with the molar mass of the polyether from 45% (2k) to 69% (6k) which is attributed to the decreasing volume fraction of end-groups and the higher flexibility of longer pEG chains, which facilitates the packing into lamellae and ordered arrangements.³⁶ Accordingly, the melting temperatures and enthalpies of the multiblock PUs are further reduced in comparison to the respective pre-polymers whereat a crystallinity reduction around 15% is observed for all

three molar masses. While the melting enthalpies of the alternating and random PUs largely coincide for PU_4k-alt/rand and PU_6k-alt/ran, the enthalpy of PU_2k-alt exceeds the one of PU_2k-ran by a factor > 30 . We suspected that the structural regularity of the alternating PU generally facilitates the packing into crystalline lamellae. This is however most relevant for the PU with the shortest pEG segment, in which the chain mobility is the most restricted.³⁷ A glass transition exotherm is also only detectable for the pEG-2k pre-polymer and PUs. As expected, the glass transition temperatures are increased in comparison to pure pEG and the respective pre-polymer because the chain flexibility is reduced inside the multiblock copolymers.

Solution Properties

With respect to the intended application of the associating PUs as precursor polymers for metallo–supramolecular gels, their solution properties are of great interest. All synthesized PUs are fully soluble in (non)protic polar organic solvents such as dimethylacetamide (DMA), dimethylformamide (DMF), acetonitrile (ACN), methanol (MeOH), or dichloromethane (DCM). In water however, the randomly polymerized PUs swell but do not dissolve. This is in accordance with former reports describing that additional ionizable groups are required as ionic emulsifiers to obtain fully water-soluble IPDI-based pEG polyurethanes.³⁸ Nonetheless, the alternating PUs form transparent solutions showing a pEG segment length dependent lower critical solution temperature (LCST). The cloud point temperatures of these solutions are determined by turbidity measurements at a concentration of $5 \text{ g} \cdot \text{L}^{-1}$ (**Figure 3.6 A** and **Table 3.2**). As similarly reported in a study by Ronco *et al.* in which pEG–IPDI-based PUs with carboxylic acid side-groups were investigated, the cloud point temperatures increase with the weight content of the hydrophilic polyether soft segment (18–75 °C, 72–89 wt%).³² As expected, the hydrogen-bond receiving ether groups thus prove to be the main source of attractive polymer–solvent interactions that balance the hydrophobicity of the tpy and IPDI groups as well as the attractive polymer–polymer interactions resulting from the H-bonding urethane linkages. It remains however unclear, what causes the fundamental solubility difference between the alternating and random PUs. Therefore, the solution behavior of PU_6k-alt and -ran as representative examples without the complication of a LCST below r.t. is investigated in further detail.

The water solubility of amphiphilic PUs generally results from their ability to form aggregates in which the hydrophobic hard segments are shielded by a hydrophilic corona. Thus, the micellar nature of aqueous PU_6k-alt solutions is firstly tested by a fluorometric determination of the critical aggregation concentration (*cac*) using pyrene as hydrophobic fluorescence probe.³⁹ The intensity ratio between the first I_1 ($\lambda = 372 \text{ nm}$) and third vibronic band I_3 ($\lambda = 384 \text{ nm}$) in the emission spectrum of pyrene indicates the polarity of its microenvironment. For the *cac* determination, the emission spectra of PU–pyrene solutions with different polymer concentrations are compared as depicted in **Figure 3.6 B** ($c_{\text{pyrene}} = 2 \text{ } \mu\text{M}$).⁴⁰

Due to an auto-fluorescence of the polymers, all PU–pyrene spectra are corrected with a pure PU spectrum, measured at the same polymer concentration. The insert in **Figure 3.6 B** shows the intensity ratio I_1/I_3 as a function of the logarithmic polymer concentration. The *cac* is determined from the abrupt decrease of I_1/I_3 as $cac(\text{PU_6k-alt}) = 1.1 \text{ g}\cdot\text{L}^{-1}$ which is well within the range of comparable amphiphilic polymers.⁴¹

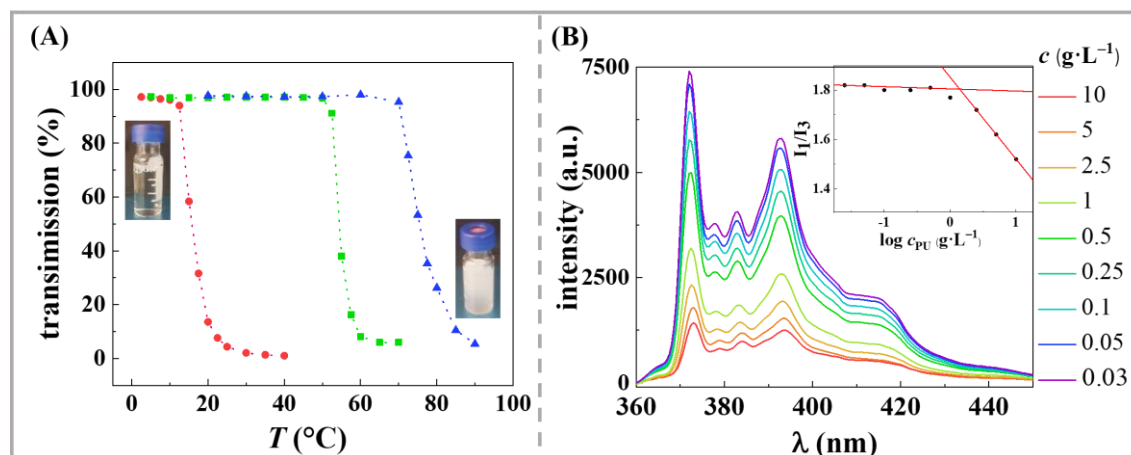


Figure 3.6. (A) Turbidity measurements of aqueous solutions of PU_2k-alt (●), 4k-alt (■), and 6k-alt (▲) at $c = 5 \text{ g}\cdot\text{L}^{-1}$ by UV-Vis transmission at 500 nm. (B) Fluorescence emission spectra of aqueous solutions of PU_6k-alt in the presence of pyrene ($c_{\text{pyrene}} = 2 \mu\text{M}$, $\lambda_{\text{ex}} = 334 \text{ nm}$, corrected with the PU emission spectra) at different PU concentrations. Insert: $I_1(\lambda = 372 \text{ nm})/I_3(\lambda = 384 \text{ nm})$ ratio as a function of the logarithmic PU concentration.

The aggregation in water is further investigated by multi-angle dynamic light scattering. The experimental autocorrelation data $g^{(1)}(\tau)$ are fitted with a biexponential function to take the polymer dispersity into account (**Figure 3.7 A**)

$$g^{(1)}(\tau) = a + b \exp\left(-\frac{\tau}{\tau_1}\right) + c \exp\left(-\frac{\tau}{\tau_2}\right) \quad (3.1)$$

At this, the inverse relaxation time corresponds to the product of the square of the scattering vector q and the diffusion coefficient D_i of the respective mode: $\tau_i^{-1} = q^2 \cdot D_i$. Since the averaged, apparent self-diffusion coefficients $\langle D_{\text{app}} \rangle$ do not show an angular dependency (insert **Figure 3.7 A**), the hydrodynamic radii R_h of an equivalent sphere can be calculated *via* the Stokes–Einstein equation $D = k_B T \cdot (6\pi\eta \cdot R_h)^{-1}$ with the Boltzmann constant k_B and the solvent viscosity η . The hydrodynamic radius R_h of the narrowly disperse PU aggregates decrease linearly with the concentration as shown in **Figure 3.7 B**. Upon further dilution, the scattering intensity is too low for additional measurements, revealing that the trend of the decreasing aggregate size likely continues.

In summary, turbidimetry, *cac* determination, and DLS measurements reveal that the alternating PUs form dispersible aggregates in water whose size depends strongly on the polymer concentration and the temperature.

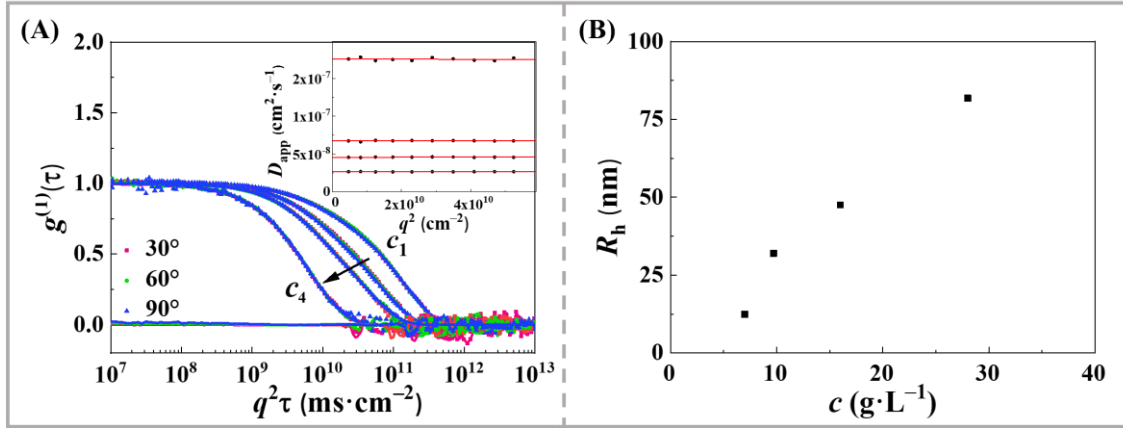


Figure 3.7. (A) Normalized DLS autocorrelation function $g^{(1)}(\tau)$ of an aqueous solution of PU_6k-alt ($c_1 = 28 \text{ g}\cdot\text{L}^{-1}$, $c_2 = 16 \text{ g}\cdot\text{L}^{-1}$, $c_3 = 9.7 \text{ g}\cdot\text{L}^{-1}$ and $c_4 = 7.1 \text{ g}\cdot\text{L}^{-1}$) at scattering angles of 30° (■), 60° (●), and 90° (▲) measured at 20 °C, along with fits and corresponding residuals to a biexponential fit function. Inset: Angular dependency of the apparent diffusion coefficients. (B) Hydrodynamic radii $R_h = (81.8 \pm 0.4)$, (47.5 ± 0.3) , (32.3 ± 0.2) and (12.4 ± 0.1) nm of PU_6k-alt as a function of the polymer concentration.

For a direct comparison of the alternating and random PUs, further concentration dependent DLS measurements are conducted in MeOH. The autocorrelation functions, exemplary shown for the 30° measurements in **Figure 3.8 A** and **Figure 3.18 A**, display two well-separated relaxation modes. The initial decay (fast mode) is fitted with a single exponential while a stretched exponential of Kohlrausch-Williams-Watts type is applied to the second one (slow mode).⁴²

$$g^{(1)}(\tau) = a + b \exp\left(-\frac{\tau}{\tau_1}\right) + c \exp\left(-\left(\frac{\tau}{\tau_2}\right)^d\right) \quad (3.2)$$

The first relaxation time directly corresponds to the fast mode $\tau_{\text{fast}} = \tau_1$, whereas the relaxation time of the slow mode is obtained as $\tau_{\text{slow}} = \tau_2 \cdot d^{-1} \cdot \Gamma(d^{-1})$ with the Gamma function Γ . The inverse relaxation times of both modes show a linear dependence on the square of the scattering vector q^2 and pass through the origin, as expected for translational diffusion processes. From the slopes of these lines, two diffusion coefficients are obtained which differ by two orders of magnitude. In **Figure 3.8 B**, the derived diffusion coefficients are plotted as a function of the polymer concentration. The correlation length corresponding to the diffusion coefficient of the fast process (4.9–3.5 nm) decreases slightly with concentration and coincides for the alternating and random PU. Therefore, this mode is attributed to the movement of the molecularly dissolved PU chains. The slight decrease is explainable with a concentration-induced coil contraction.⁴³ The slow diffusion coefficient is associated with the translational motion of polydisperse PU aggregates, which show a more pronounced concentration-dependence and have comparable dimensions in the alternating and random PU solutions (alt: 43–1030 nm, ran: 94–1590 nm). The stretching exponent d in the fit function (3.2) is a measure for the dispersity of the diffusive species. The obtained d values are similar for both PUs and decrease with the concentration from ≈ 0.8 (c_1) to ≈ 0.6 (c_5).

Regarding the relative contributions of the fast and the slow mode, we observed that the normalized amplitude of the slow relaxation process increases with the polymer concentration for both PU types but is consistently larger in case of the random one (**Figure 3.18 B**).

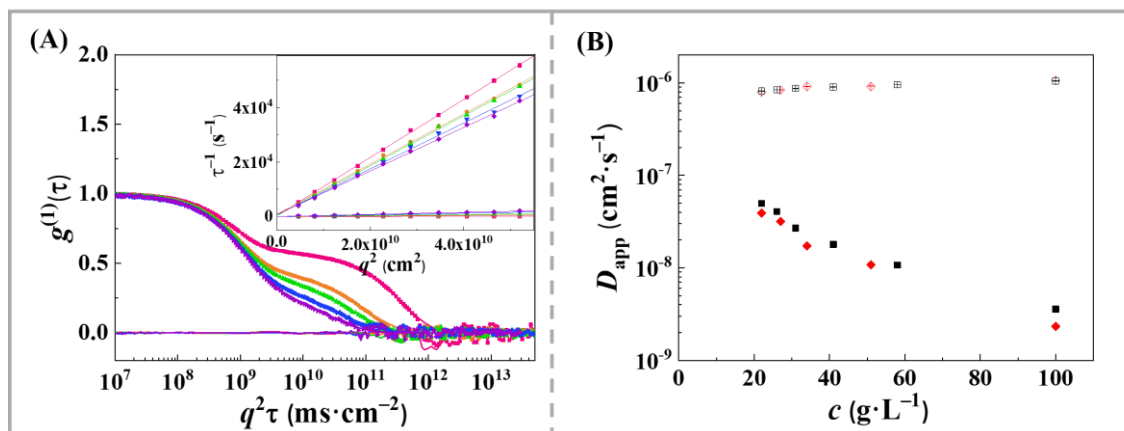


Figure 3.8. (A) Normalized DLS autocorrelation function $g^{(1)}(\tau)$ of PU_6k-ran in MeOH (\bullet : $c_1 = 100 \text{ g}\cdot\text{L}^{-1}$, \circ : $c_2 = 51 \text{ g}\cdot\text{L}^{-1}$, $\color{green}\bullet$: $c_3 = 34 \text{ g}\cdot\text{L}^{-1}$, $\color{blue}\bullet$: $c_4 = 27 \text{ g}\cdot\text{L}^{-1}$ and $\color{purple}\bullet$: $c_5 = 22 \text{ g}\cdot\text{L}^{-1}$) along with biexponential fits according to equation (3.2) and corresponding residuals (30° , 20° C). Insert: Inverse relaxation times τ^{-1} as a function of q^2 with linear fits (color code as before). (B) Concentration-dependence of the fast (open symbols) and slow (closed symbols) diffusion coefficients of PU_6k-alt (\blacksquare/\square) and PU_6k-ran (\blacklozenge/\lozenge).

The incomplete molecular dissolution of both PU types in MeOH indicates the presence of a driving force that exceeds the pure hydrophobic association observed in water. Since MeOH is a good solvent for all individual PU components, the hydrogen-bonding urethane groups are the most likely source of this strong polymer–polymer attraction. Due to the synergetic nature of hydrogen bonds, their distribution along a polymer chain has been shown to be an important factor in the coil-to-globule⁴⁴ and thermoresponsive phase-transitions⁴⁵ of amphiphilic block-copolymers. In view of these findings and the bulk properties of the synthesized PUs, we suspect that the cooperativity of the interchain H-bonding of neighboring $(\text{-IPDI-tpy-})_n$ multiplets by far exceeds that of isolated ones and thus prevents the dispersion of the random PUs in water.

Mechanical Properties of Transient Gels

Finally, the mechanical properties of supramolecular cross-linked gels derived from the precursor polymers in MeOH are investigated by frequency-dependent shear rheology. Manganese triflate is chosen as cross-linking agent because the relaxation time of gels based on the kinetically labile *bis*(terpyridine)- Mn^{2+} complex enables the determination of the plateau modulus G_N at high frequencies, the sticker exchange time τ_{ex} from the $G'-G''$ crossover frequency, and the frequency-dependent power-law scaling in the terminal flow regime in a single measurement. Instead of the polymer, the tpy concentration is kept constant to compare the different gels, since it is theoretically only the crosslinking density which determines the network strength below the entanglement concentration. A concentration of $c_{\text{tpy}} = 20 \text{ mM}$ is found suitable to obtain stable gels from all PU precursors.

The dynamic nature of the tpy cross-links is firstly verified by investigating PU-4k-alt gels, prepared with different metal–terpyridine ratios. As shown in **Figure 3.10 A**, the longest relaxation time and highest plateau modulus is obtained at a stoichiometrically balanced, 2:1 tpy to Mn^{2+} ratio. In accordance with previous studies, both parameters decrease monotonously, if a sub-stoichiometric amount of the metal is applied.⁴⁶

The frequency sweeps and network parameters of the PU gels prepared with a stoichiometric metal–ligand ratio are summarized in **Figure 3.9** and **Table 3.3**. The plateau moduli G_N increase linearly with the average tpy spacing $\langle M_x \rangle$ determined by the molar mass of the applied pEG spacer as shown in **Figure 3.10 B**. This trend is most probably an artifact of the increasing polymer concentrations. Within the semi-dilute, nonentangled regime, higher polymer concentrations commonly lead to a preference of inter- over intramolecular binding and thus a higher number of elastically active cross-links.²⁰ Comparing the alternating and random PU gels with similar sticker spacing (**Figure 3.9**) shows that the plateau moduli of the ran-PU gels slightly exceed those of the alt-PU gels. Since the tpy functionalities of the ran-PU are throughout higher, this small deviation can be explained by a reduced number of dangling ends and network defects.

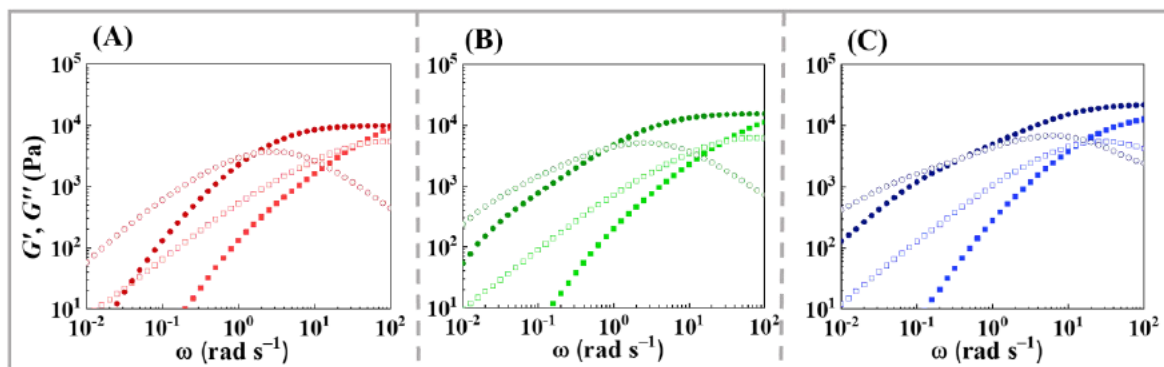


Figure 3.9. Frequency sweeps of (A) PU_2k-alt (■), PU_2k-ran (●), (B) PU_4k-alt (■), PU_4k-ran (●), (C) PU_6k-alt (■) and PU_6k-ran (●) in MeOH at $c_{\text{tpy}} = 20 \text{ mmol}\cdot\text{L}^{-1}$ cross-linked by Mn^{2+} triflate (tpy: $\text{Mn}^{2+} = 2:1$) ($T = 20 \text{ }^\circ\text{C}$, G' : filled symbols, G'' : open symbols).

Table 3.3. Network parameters of the random and alternating PU gels in MeOH ($c_{\text{tpy}} = 20 \text{ mmol}\cdot\text{L}^{-1}$, cross-linked by Mn^{2+} -triflate (tpy: $\text{Mn}^{2+} = 2:1$), $T = 20 \text{ }^\circ\text{C}$).

sample	c_{PU} (wt%)	G_N (kPa)	τ_{ex} (s)	scaling G'	scaling G''
PU_2k-alt	7.4	8.98	0.17	1.61	0.93
PU_2k-ran	6.3	9.85	3.86	1.62	1.05
PU_4k-alt	13.6	11.24	0.22	1.67	0.97
PU_4k-ran	11.7	15.50	7.31	0.92*	0.70
PU_6k-alt	18.2	12.73	0.44	1.64	0.98
PU_6k-ran	16.4	21.94	15.22	0.62*	0.43

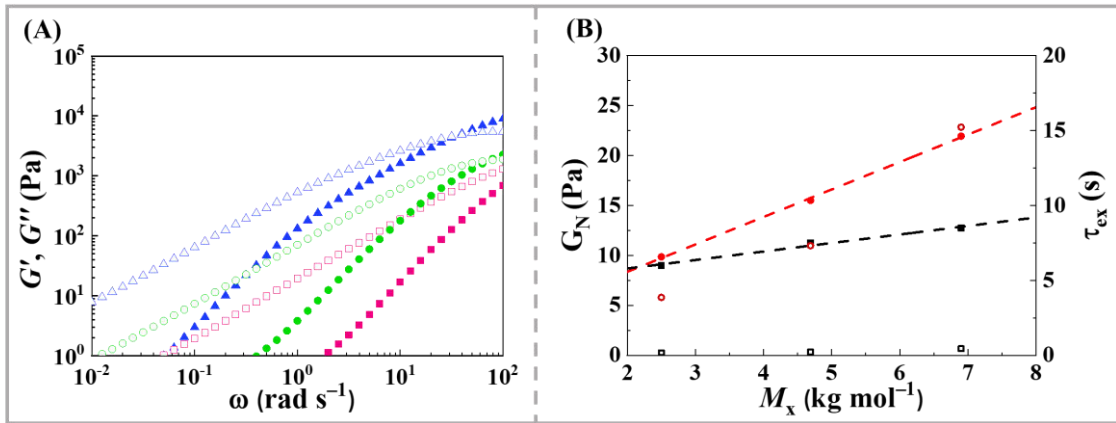


Figure 3.10. (A) Frequency sweeps of PU_4k-alt gels cross-linked with 0.125 (■), 0.25 (●) and 0.5 eq. (▲) of Mn^{2+} triflate (MeOH, $c_{\text{tpy}} = 20 \text{ mmol}\cdot\text{L}^{-1}$, $T = 20 \text{ }^\circ\text{C}$; G' : filled symbols, G'' : open symbols). (B) Plateau moduli G_N (closed symbols) and sticker exchange time τ_{ex} (open symbols) as a function of the average sticker spacing M_x for the alternating (■) and random (●) PUs with linear fits.

The terminal network relaxation (average sticker exchange times τ_{ex}) also increase monotonously with the sticker spacing in the random and alternating PU series (**Figure 3.10 B**). This can be explained with the bond lifetime renormalization concept which considers the number of opening attempts of supramolecular stickers before an actual partner exchange and thus network relaxation takes place.⁴⁷ At lower sticker densities, the probability of finding a new partner gets reduced and thus the number of reassociations with the old binding partner increases.⁴⁸ This concentration-related effect is however by far exceeded by the prolongation of the network relaxation times of the random compared to the alternating PU gels with similar, average sticker spacings (**Figure 3.10 B**). The DLS measurements in MeOH revealed that the PU precursor solutions contain a considerable fraction of aggregated chains. Upon gelation, these aggregates likely become frozen clusters with a high local density of stickers, which are known to slow down the exchange dynamics of reversible networks. However, since the concentration of these clusters appeared to be similar in both PU types, their presence cannot explain the differences observed in the rheological measurements. The longer relaxation times of the ran-PU gels are therefore considered as further proof for the presence of multiplets with neighboring tpy ligands within the random PUs. Adjacent stickers are phenomenologically comparable to clustered stickers and contribute to a pronounced lifetime renormalization. For a partner exchange, all individual stickers within the multiplet need to open at the same, which increases the attempt number.¹⁵

Finally, it can be observed that the scaling exponents of the frequency-dependent storage and loss moduli in the terminal flow regime of the random and alternating PU gels show systematic deviations. The scaling exponents are overall smaller than the Maxwell model prediction ($G' \propto \omega^2$ and $G'' \propto \omega^1$), which is expected for a polydisperse polymer gel. The shallowing is however significantly enhanced for the random compared to the alternating PU_4k and _6k gels.

This observation supports the initially mentioned hypothesis that the power-law shallowing is considerable exacerbated by a polydisperse sticker distribution. An in-depth analysis of the differences in the relaxation time spectra is beyond the scope of the present work but will be beneficial for further insights.

3.3 Conclusions

We developed a straightforward synthesis strategy for amphiphilic pEG-based PUs bearing metallo–supramolecular cross-linkable tpy side-stickers with irregular or controlled sticker spacings. Due to the modular nature of the approach, the average spacing between the tpy–stickers can be easily varied by applying pEG diols with different molar masses. To obtain polymers with a strictly alternating pEG–tpy sequence, the polyethers are endcapped with IPDI and isolated prior to the chain elongation step. In comparison to randomly polymerized PUs with a similar chemical composition, the alternating polymers show slightly smaller polymerization degrees and functionalization degrees. In the melt state, all PUs are semi-crystalline solids and DSC and FT-IR analysis indicate a high level of phase mixing between the hard IPDI–tpy and soft polyether segments. The carbonyl-bands in the FT-IR spectra of the random PUs do however show an additional low energy shoulder, which is attributed to the cooperative H-bonding of $(-IPDI-tpy-)_n$ multiplets. The strength of the interchain H-bonding further affects the solution behavior of the polymers. Although the PUs are soluble in MeOH, DLS measurements show a small fraction of diffusive aggregates (< 1000 nm) that are of comparable size for the alternating and random polymers. However, only the alternating PUs are soluble in water and show a pEG length dependent LCST behavior. Finally, shear rheological measurements reveal how the mechanical properties of the Mn^{2+} cross-linked PU gels in MeOH are influenced by the different sticker distributions. At similar tpy concentrations, the plateau moduli of the random PU gels are slightly upshifted while the relaxation times are more considerably prolonged and the shallowing of the power-law scaling in the terminal flow regime is exacerbated in comparison to their alternating counterparts. These effects can again be explained by the presence of $(-IPDI-tpy-)_n$ multiplets. To specifically study synergetic effects of $(-IPDI-Tpy-)_n$ multiplets on the gel properties, the presented monomer platform and polyaddition approach can also be applied to create terpyridine oligomers with adjustable polymerization degree n .

In summary, it can be stated that the presented synthesis platform complements existing model systems with narrow molar mass– but statistical sticker distributions and is thus useful to study effects of sticker density and distribution in hierarchically assembling polymer networks. In a specific example, the derived gels can and will be further used for a comprehensive study about the effects of a polydisperse sticker distribution on the relaxation time and terminal flow scaling of transient networks in the view of commonly observed deviations between experimental results and theoretical models.

3.4 Experimental Section

Materials

tert-Butyl-dimethylsilyl chloride (TBDMS-Cl, 98%, Acros Organics), 1*H*-imidazole (99%, Acros Organics), triphenyl phosphine (PPh₃, > 99%, Alfa Aesar), diisopropyl azodicarboxylate (DIAD, 98% Sigma Aldrich), 2,6-bis(2-pyridyl)-4(1*H*)-pyridone (tpy-OH, > 98%, TCI), ammonium hydrogen difluoride (NH₄HF₂, > 94%, Acros Organics), methanolic HCl (1.25M, Acros Organics), di-*n*-butyltin dilaurate (DBTDL, 98%, Alfa Aesar), copper(II)bromide (CuBr₂, 99%, Sigma Aldrich) and manganese(II)*bis*(trifluoromethanesulfonate) (MnOTf₂, Sigma Aldrich) are purchased from commercial resources and used without further purification. Isophorone diisocyanate (IPDI, mixture of *cis/trans* isomers (72:28), 98%, Acros Organics) is freshly vacuum distilled. Glycerol (Sigma Aldrich, > 99.5) is stirred over CaH₂ and vacuum distilled prior to use. The linear poly(ethylene glycol)s (Sigma Aldrich) are first purified by precipitation into diethyl ether, freeze dried from benzene containing 5vol% 1.25M methanolic HCl and further dried in high vacuum prior to polymerization. Cyclohexan (^CHex), ethylacetate (EA), dichloromethane (DCM) and methanol (MeOH) are used as received. Anhydrous THF, DMF, DMSO, benzene, 1,4-dioxane and *N,N*-dimethylacetamide (DMA) are purchased from Acros Organics and used as received. Diethyl ether (Et₂O) is dried over sodium and freshly distilled under nitrogen atmosphere. Uvasol[®] grade solvents (Sigma Aldrich) and Milli Q water are used for Light Scattering, UV-Vis and fluorescence spectroscopy.

Chromatography

Thin-layer chromatography is performed on F₂₅₄ silica gel 60 (Merck), silica gel 60 RP-18 (Merck) or aluminum oxide 60 (Merck) coated plates. Spots are detected with UV-light ($\lambda = 254$ nm) and immersion in KMnO₄ or iron(II)chloride solutions. Flash chromatography is performed on silica gel 60 (40–63 μ m, Merck Millipore), LiChroPrep[®] RP-18 (40–63 μ m, Merck Millipore) or aluminum oxide (neutral, Brockmann I, 500–200 μ m, Acros Organics). Analytical High Performance Liquid Chromatography at Critical Conditions (HPLC-CC) is performed with an Agilent Technologies 1260 Infinity system (1260 Quat pump, Softa 1300 evaporative light scattering detector). A Reprosil 100 (C₁₈, 5 μ m particle size, 4.6 \times 250 mm i.d.) column from Maisch GmbH is used. All data are analyzed with the PSS WinSEC Unity v7 software provided by Polymer Standards Service GmbH (PSS). The mobile phase consists of acetonitrile and water (*v/v* = 44:56). Samples (1 g·L⁻¹) are filtered through a Chromafil PET-45/15 MS syringe filter prior to injection. Size exclusion chromatography (SEC) measurements are performed at 60 °C in DMF (1 g·L⁻¹ LiCl) using a 1260 Infinity GPC/SEC-system from Agilent (PSS SECcurity pump, VWR Elite Chrom RI detector) equipped with a PSS GRAM guard column, two PSS GRAM 1000Å and one PSS GRAM 100 Å columns at a flow rate of 1 mL min⁻¹. All data are analyzed with the software PSS WinSEC provided by PSS.

The number- and weight average molecular weight (M_n , M_w) and dispersity (\mathcal{D}) are calculated with a pEG calibration (calibration standards provided by PSS). Samples ($2 \text{ g}\cdot\text{L}^{-1}$) are filtered through a Chromafil PET-45/15 MS syringe filter prior to injection.

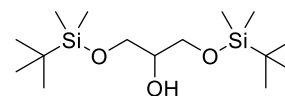
Instrumentation

NMR spectra are recorded on a Bruker Avance-III HD 300 or a Bruker Avance-II HD 400 instrument at 20 °C. The chemical shift δ is given in ppm by using tetramethylsilane as internal standard ($\delta = 0$ ppm) and deuterated solvents (CDCl_3 , $\text{DMSO-}d_6$, CD_3CN) as internal reference. The reported signal splittings are abbreviated as follows: s = singlet, d = doublet, t = triplet, p = quintet. Coupling constants J are reported in Hz. High resolution electron spray mass spectra (HR-ESI MS) are measured with an Agilent 6545 QTOF-instrument. UV-Vis spectroscopy measurements are performed on a Jasco V-760-ST UV/Vis Spectrophotometer equipped with a magnetic stirrer and an external thermostat at 20 °C. Fourier transform infrared spectra (FT-IR) are measured on a JASCO FT/IR-4700 FT-IR instrument equipped with Attenuated Total Reflection (ATR) diamond. Fluorescence spectroscopy is performed on a spectrofluorometer FP-8200 by Jasco at room temperature. Dynamic light scattering measurements are performed using a ALV/SP-125 compact goniometer system equipped with a Uniphase He/Ne Laser ($\lambda = 632.8 \text{ nm}$, 22 mW), ALV/High QE APD-Avalanche photo-diode (Excelitas Technologies SPCM CD3296H) and a ALV/LSE-5004 multiple-tau digital correlator (all components: ALV-Laser Vertriebsgesellschaft mbH, Langen, Germany). A constant temperature of 20 °C for all measurements is assured with an external thermostat (Lauda RC-6 CS). Thermal properties of polymers are studied by differential scanning calorimetry with a Mettler Toledo DSC 823. Linear shear rheology is performed on a stress-controlled modular compact rheometer of the type MCR 302 (Anton Paar, Graz, Austria) equipped with a stainless-steel cone–plate geometry (cone angle: 1°, cone diameter: 25 mm) and a solvent trap. The temperature is controlled by a Peltier plate. Motor adjustment and inertial calibration are performed before each measurement.

Synthesis

Compound 3.2

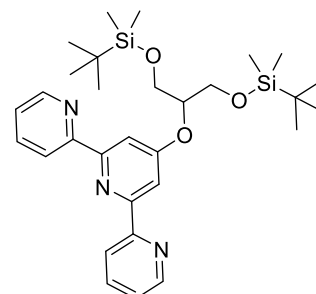
According to a modified procedure by Bunnelle *et al.*⁴⁹ Freshly distilled glycerol **3.1** (12.3 g, 134 mmol, 1.0 eq.) and 1*H*-imidazole (20.0 g, 294 mmol, 2.2 eq.) are dissolved in a mixture of anhydrous



THF (60 mL) and DMF (40 mL) under inert atmosphere and cooled to 0 °C in an ice-bath. A solution of *tert*-butyl-dimethyl chlorosilane (27.8 g, 140 mmol, 4.9M, 1.05 eq.) in anhydrous THF (60 mL) is added dropwise under vigorous stirring. After complete addition, the ice-bath is removed and the white suspension is stirred for 16 h at r.t., poured into water (600 mL) and extracted with Et₂O (5 x 150 mL). The combined extracts are washed with brine (100 mL), dried over Na₂SO₄, and concentrated under reduced pressure. The alcohol **3.2** is purified *via* flash chromatography on silica gel (°Hex:EA = 4:1). **Yield:** 36.4 g (114 mmol, 85%), colorless oil. **Molecular formula:** C₁₅H₃₆O₃Si₂. **TLC:** R_f = 0.70 (°Hex:EA = 4:1, SiO₂). **ESI-HRMS** (*m/z*): Calculated for [M+Na]⁺: 343.2095, found: 343.2099. **¹H-NMR, COSY** (300 MHz, DMSO-*d*₆): δ = 4.60 (d, ³J = 4.7 Hz, 1H, OH), 3.54–3.47(m, 5H, OCH(CH₂O)₂), 0.86 (s, 18H, SiCCH₃), 0.03 (s, 12H, Si(CH₃)₂) ppm. **¹³C-NMR, HMBC, HSQC** (75 MHz, DMSO-*d*₆): δ = 71.76 (OCH), 63.96 (OCH₂), 25.84 (SiC), 18.05 (SiCCH₃), 5.29 (SiCH₃), -5.33 (SiCH₃) ppm. The spectroscopic data is consistent with literature.⁴⁹

Compound 3.2a

According to a modified procedure by Hovinen.²⁷ Compound **3.2** (2.00 g, 6.24 mmol, 1.0 eq.) and 2,6-bis(2-pyridyl)-4(1*H*)-pyridone **3.3** (1.87 g, 7.49 mmol, 1.2 eq.) are dissolved in anhydrous THF (20 mL) under inert atmosphere and cooled to 0 °C. After addition and complete dissolution of triphenyl phosphine (3.60 g, 13.7 mmol, 2.2 eq.), a solution of diisopropyl azodicarboxylate (2.7 mL, 13.7 mmol, 2.2 eq.) in anhydrous THF (25 mL) is added dropwise. After complete

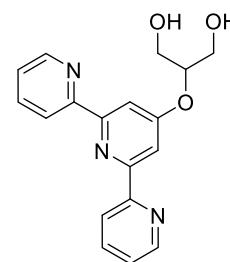


addition, the ice-bath is removed, and the yellow solution is stirred for 14 h at r.t. The reaction mixture is diluted with saturated NaHCO₃ solution (50 mL) and air is bubbled through the solution for 1 h to oxidize the excess of triphenyl phosphine. The solution is extracted with DCM (3 x 100 mL) and the combined organic phases are washed with brine (50 mL), dried over Na₂SO₄, and concentrated under reduced pressure. The residue suspended in ACN, heated to reflux for 15 min, cooled to 0 °C and insoluble triphenyl phosphine oxide is filtered off. This step is repeated twice. The product is then purified *via* flash chromatography on neutral Alox (°Hex:EA = 30:1). **Yield:** 2.86 g (5.18 mmol, 83%), colorless solid. **Molecular formula:** C₃₀H₄₅N₃O₃Si₂. **TLC:** R_f = 0.18 (ACN/H₂O = 50:1, RP₁₈ silica gel); R_f = 0.20 (°Hex:EA = 30:1, Alox neutral). **ESI-HRMS** (*m/z*): Calculated for [M+H]⁺: 552.3072, found: 552.3081. **¹H-NMR,**

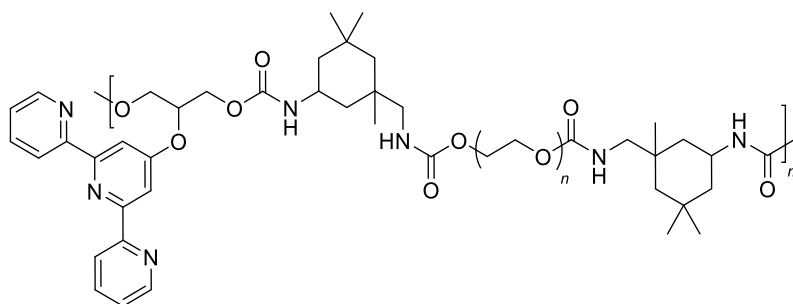
COSY (300 MHz, CDCl₃): δ = 8.68 (ddd, 3J = 4.8 Hz, 4J = 1.7 Hz, 5J = 0.9 Hz, 2H, tpy: C_{6/6'}-H), 8.60 (ddd, 3J = 7.8 Hz, 4J = 1.1 Hz, 5J = 0.9 Hz, 2H, tpy: C_{3/3'}-H), 8.08 (s, 2H, tpy: C_{3'/5'}-H), 7.83 (atd, 3J = 7.8 Hz, 4J = 1.7 Hz, 2H, tpy: C_{4/4'}-H), 7.31 (ddd, 3J = 7.8 Hz, 3J = 4.8 Hz, 4J = 1.1 Hz, 2H, tpy: C_{5/5'}-H), 4.78 (p, 3J = 5.0 Hz, 1H, tpy–OCH), 3.97–3.85 (m, 4H, OCH₂CH), 0.87 (s, 18H, SiCCH₃), 0.07 (s, 6H, SiCH₃), 0.04 (s, 6H, SiCH₃) ppm. **¹³C-NMR, HMBC, HSQC** (75 MHz, CDCl₃): δ = 167.07 (tpy: C_{4'}), 157.22 (tpy: C_{2/2''}), 156.30 (tpy: C_{2'/6'}), 149.14 (tpy: C_{6/6''}), 136.83 (tpy: C_{4/4''}), 123.84 (tpy: C_{5/5''}), 121.39 (tpy: C_{3/3''}), 108.50 (tpy: C_{3'/5'}), 79.06 (tpy–OCH), 62.14 (OCH₂), 25.99 (SiC), 18.43 (SiCH₃), –5.22 (SiCH₃) ppm.

Terpyridine diol 3.4

According to a modified procedure by Seki *et al.*⁵⁰ Compound **3.2a** (2.74 g, 4.96 mmol, 1.0 eq.) is dissolved in anhydrous DMF (10 mL) in a Teflon flask and ammonium hydrogen fluoride (4.53 g, 80 mmol, 16 eq.) is added. After stirring for 72 h at r.t. (complete conversion indicated by TLC), the reaction mixture is neutralized with saturated NaHCO₃ solution, and the solvents are removed under reduced pressure. The residue is suspended in



water (30 mL) and extracted with DCM (3 x 50 mL). The combined organic phases are washed with brine (30 mL), dried over Na₂SO₄, and concentrated under reduced pressure. A white solid is precipitated through the addition of Et₂O and isolated by filtration. **Yield:** 1.28 g (3.97 mmol, 80%), colorless crystals. **Molecular formula:** C₁₈H₁₇N₃O₃. **TLC:** R_f = 0.14 (ACN/H₂O = 20:1, RP₁₈ silica gel) **ESI-HRMS** (*m/z*): Calculated for [M+H]⁺: 324.1343, found: 324.1347. **¹H-NMR, COSY** (300 MHz, DMSO-*d*₆): δ = 8.72 (dd, 3J = 4.8 Hz, 4J = 1.2 Hz, 2H, tpy: C_{6/6''}), 8.61 (dd, 3J = 7.8 Hz, 4J = 1.1 Hz, 2H, tpy: C_{3/3''}), 8.04 (s, 2H, tpy: C_{3'/5'}), 8.00 (atd, 3J = 7.8 Hz, 4J = 1.2 Hz, 2H, tpy: C_{4/4''}), 7.49 (ddd, 3J = 7.8 Hz, 3J = 4.8 Hz, 4J = 1.1 Hz, 2H, tpy: C_{5/5''}), 4.97 (t, 3J = 5.7 Hz, OH) 4.65 (p, 3J = 5.3 Hz, 1H, tpyOCH), 3.75–3.36 (m, 4H, OCH₂CH) ppm. **¹³C-NMR, HMBC, HSQC** (75 MHz, CDCl₃): δ = 166.98 (tpy: C_{4'}), 156.59 (tpy: C_{2/2''}), 154.93 (tpy: C_{2'/6'}), 149.23 (tpy: C_{6/6''}), 137.39 (tpy: C_{4/4''}), 124.47 (tpy: C_{5/5''}), 120.91 (tpy: C_{3/3''}), 107.78 (tpy: C_{3'/5'}), 80.32 (tpyOCH), 60.28 (OCH₂) ppm.

Alternating (pEG-alt-tpy)_n Multiblock Copolymers

Alternating multiblock copolymers are synthesized in a two-step procedure according to the following Standard Procedures (SOP). Firstly, pEG diols with differing molar masses ($M_n = 1.95$ (2k, $n = 45$), 4.22 (4k, $n = 96$) and $6.27 \text{ kg}\cdot\text{mol}^{-1}$ (6k, $n = 143$)) are endcapped with isophorone diisocyanate, isolated and dried (SOP I.). Secondly, linear multiblock-polyurethanes with m blocks are obtained *via* chain extension with terpyridine diol **3.4** (SOP II).

SOP I: α,ω -Diisocyanato Poly(ethylene glycol):

All steps are carried out under argon atmosphere. IPDI **3.6** (30 eq.) is dissolved in anhydrous DMA ($2.0 \text{ g}\cdot\text{L}^{-1}$) in a flame-dried three-neck round bottom flask equipped with a dripping funnel. Freshly dried pEG (1.0 g, 1.0 eq.) is dissolved in anhydrous DMA ($0.2 \text{ g}\cdot\text{L}^{-1}$) at 40°C in a Schlenk-flask and transferred to the dripping funnel with a syringe. After addition of DBTDL (2 drops) to the IPDI mixture, the pEG solution is added dropwise under vigorous stirring over 10–30 min. Next, the clear solution is stirred for 2 h at r.t. and precipitated into anhydrous Et_2O (4 x 45 mL centrifuge tubes equipped with septum and argon balloon). After cooling the tubes to 0°C for 30 min, the precipitate is centrifuged for 5 min at 10000 rpm. The ether is decanted in an argon counter flow and the polymer is re-precipitated analogously from benzene (2 mL/tube). After the second decanting, the polymer is dissolved in benzene, transferred to a flame-dried Schlenk-flask, freeze-dried and weighed.

SOP II: Chain extension of α,ω -Diisocyanato Poly(ethylene glycol) with Terpyridine Diol:

The pre-polymer (1.0 eq.) is dissolved in anhydrous DMA ($0.5 \text{ g}\cdot\text{L}^{-1}$) and heated to 50°C under argon atmosphere. Then, DBTDL (2 drops) and the tpy diol **3.4** (0.8 eq., 0.2 mol L^{-1} solution in DMA) are added. Further equivalents of the tpy diol are added after 12 and 24 h (0.2 eq. respectively, $0.2 \text{ mol}\cdot\text{L}^{-1}$ solution in DMA). After 48 h, the reaction mixture is cooled to r.t., diluted with MeOH (2–5 mL) before the PU is precipitated into ice-cold Et_2O . After a further re-precipitation into Et_2O , the polymer is obtained as colorless solid by lyophilization.

Reaction Control

NCO End-capping: Liquid Chromatography at Critical Conditions

To follow the hydroxyl group conversion by LC-CC, α,ω -diisocyanato poly(ethylene glycol)-2k is prepared according to SOP I. The addition of the pEG solution is finished after 10 min. Aliquots are taken from the reaction mixture after 10, 12.5, 15, 17.5, 20, 22.5, 25, 27.5, 30, 40, 50, 60 min (with respect to the beginning of the pEG addition) and quenched with a 100-fold excess of benzyl alcohol under inert atmosphere. The aliquots are precipitated into Et₂O, centrifuged, and dried in vacuo prior to LC-CC analysis. The aliquot taken after 60 min is further analyzed by ESI-MS (Figure 3.11) and ¹H-NMR (Figure 3.12) to confirm the molecular structure of the product.

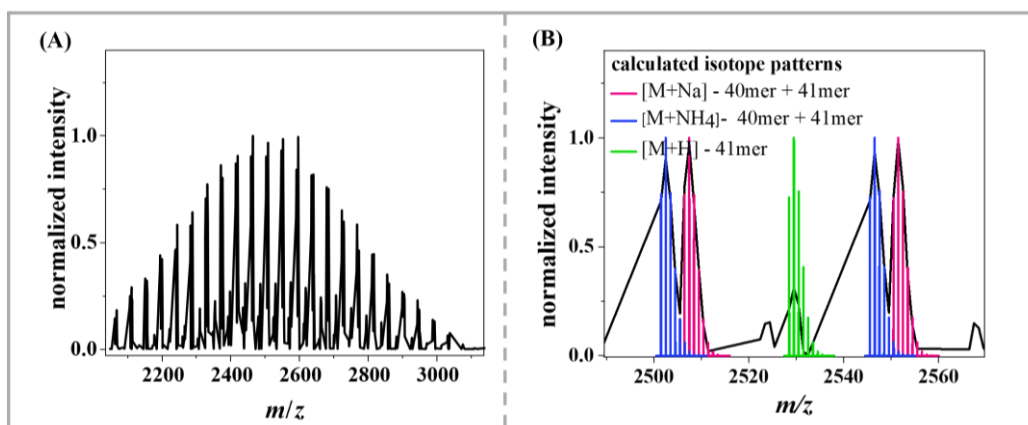


Figure 3.11. (A) ESI-MS spectrum of the benzyl alcohol quenched aliquots from the isophorone diisocyanate end-capping of pEG-2k **3.7a** and (B) overlay of experimental spectrum and calculated isotope pattern for the pEG 40- and 41-mer provided by <https://www.envipat.eawag.ch/index.php>.

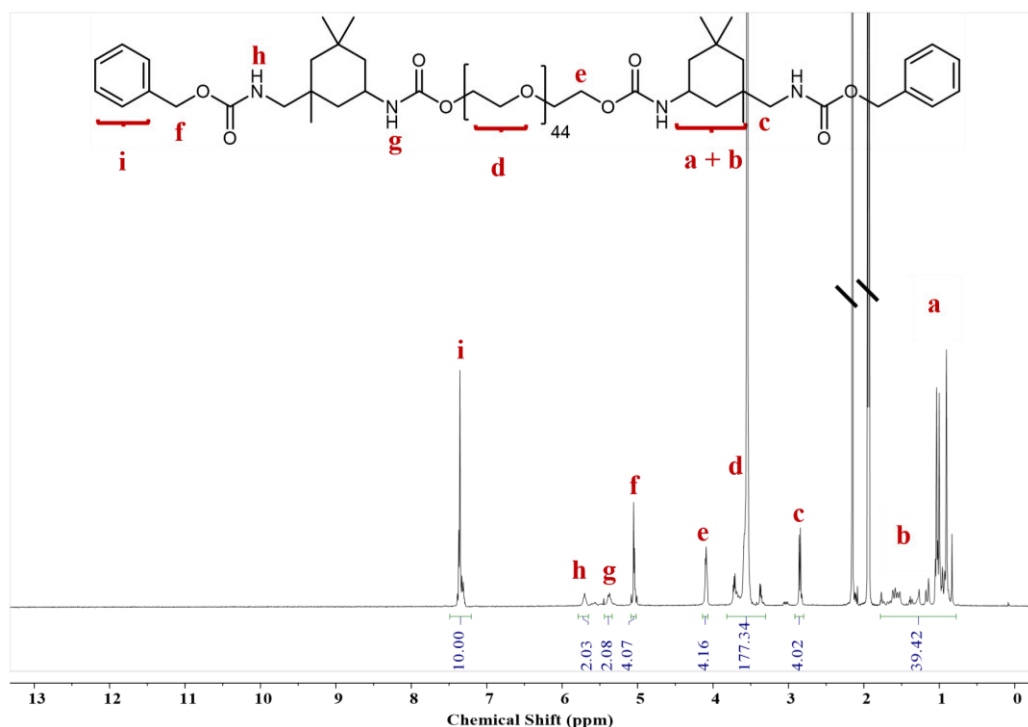


Figure 3.12. ¹H-NMR (CD₃CN) of the benzyl alcohol quenched aliquot of isophorone diisocyanate endcapped pEG-2k **3.7a**.

Chain Elongation

Due to the high dependency on the stoichiometry accuracy, the chain elongation step is carried out with different amounts of initially added tpy diol **3.4**. The reactions are performed according to SOP II with an initial addition of 1, 0.9 and 0.8 eq. of the tpy diol **3.4**, followed by further tpy additions in 0.2 eq. portions until 1.2 eq. have been added in each case. The molar mass distribution of the finally obtained PUs are analyzed by GPC as summarized in **Figure 3.13**.

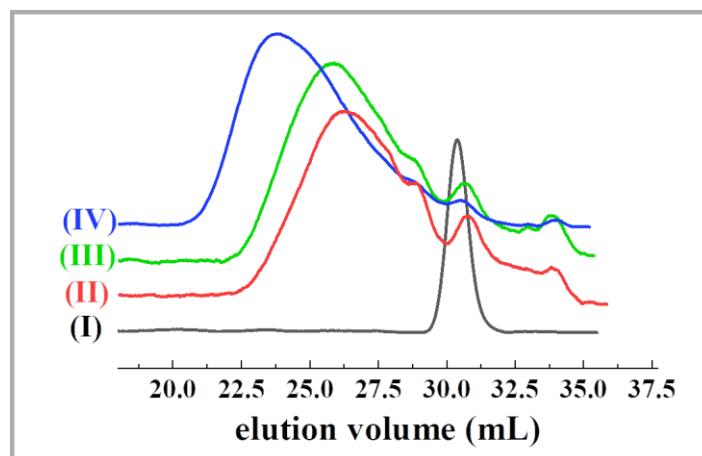


Figure 3.13. GPC traces of (I) pEG-2k **3.5a** (black) and PU_2k-alt with an initial addition of (II) 1.0 eq., (III) 0.9 eq. and (IV) 0.8 eq. of tpy diol **3.4**.

Polymer Characterization

PU_2k-alt

Yield: 0.72 g (71%). **GPC:** $M_n = 14.2 \text{ kg}\cdot\text{mol}^{-1}$, $M_w = 27.0 \text{ kg}\cdot\text{mol}^{-1}$, $D = 2.0$. **$^1\text{H-NMR}$** (400 MHz, DMSO- d_6): $\delta = 8.69$ (m, 1.3H, tpy: C_{6/6'}), 8.65 (m, 1.3H, tpy: C_{3/3'}), 8.05 (m, 2.6H, tpy: C_{3'/5'}, C_{4/4'}), 7.49 (m, 1.3H, tpy: C_{5/5'}), 7.25–7.03 (m, 2.6H, NH), 5.61–5.92 (m, 1.7H, NH), 5.27 (s, 0.7H, tpyOCH), 4.1–4.39 (m, 2.8H, tpyOCHCH₂), 4.06 (m, 4H, NHC(=O)OCH₂CH₂O), 3.88–3.45 (m, 180H, (CH₂CH₂O)_n), 2.86 (m, 4.1H, IPDI: OC(=O)NHCH₂), 1.36–0.68 (m, 32H, IPDI) ppm. Peak assignment according to literature reports.⁵¹

PU_4k-alt

Yield: 0.41 g (65%). **GPC:** $M_n = 31.8 \text{ kg}\cdot\text{mol}^{-1}$, $M_w = 61.8 \text{ kg}\cdot\text{mol}^{-1}$, $D = 1.9$. **$^1\text{H-NMR}$** (400 MHz, DMSO- d_6): $\delta = 8.75$ (m, 1.4H, tpy: C_{6/6'}), 8.68 (m, 1.4H, tpy: C_{3/3'}), 8.12 (m, 2.7H, tpy: C_{3'/5'}, C_{4/4'}), 7.53 (m, 1.3H, tpy: C_{5/5'}), 7.26–6.96 (m, 2.7H, NH), 5.91–5.66 (m, 1.9H, NH), 5.37 (s, 0.7H, tpyOCH), 4.25 (m, 2.3H, tpyOCHCH₂), 4.05 (m, 4H, NHC(=O)OCH₂CH₂O), 3.91–3.43 (m, 364H, (CH₂CH₂O)_n), 2.91 (m, 4.4H, IPDI: OC(=O)NHCH₂), 1.76–0.67 (m, 32H, IPDI) ppm.

PU_6k-alt

Yield: 0.54 g (64%). **GPC:** $M_n = 33.2 \text{ kg}\cdot\text{mol}^{-1}$, $M_w = 63.7 \text{ kg}\cdot\text{mol}^{-1}$, $D = 1.9$. **$^1\text{H-NMR}$** (400 MHz, $\text{DMSO-}d_6$): $\delta = 8.71$ (m, 1.3H, tpy: $\text{C}_{6/6''}$), 8.61 (m, 1.3H, tpy: $\text{C}_{3/3''}$), 8.01 (m, 2.6H, tpy: $\text{C}_{3/5'}$, $\text{C}_{4/4''}$), 7.50 (m, 1.3H, tpy: $\text{C}_{5/5''}$), 7.22–7.01 (m, 2.3H, NH), 5.92–5.62 (m, 1.6H, NH), 5.13 (s, 0.6H, tpyOCH), 4.37–4.19 (m, 2.2H, tpyOCHCH₂), 4.05 (m, 4.6H, NHC(=O)OCH₂CH₂O), 3.67–3.39 (m, 528H, $(\text{CH}_2\text{CH}_2\text{O})_n$), 2.68 (m, 4H, IPDI: OC(=O)NHCH₂), 1.59–0.63 (m, 35H, IPDI) ppm.

Random pEG-Polyurethanes**SOP III**

Freshly dried pEG (1.0 eq.) is dissolved in anhydrous DMA ($0.5 \text{ g}\cdot\text{L}^{-1}$) in a 50 mL Schlenk flask and heated to 50 °C under argon atmosphere. After the addition of tpy diol **3.4** (1.0 eq.), IPDI (2.0 eq.) and DBTDL (2 drops) the reaction mixture is stirred 50 °C until complete conversion of the isocyanate band is indicated by the disappearance of the NCO band in the FT-IR spectrum (**Figure 3.14**). The reaction times vary between 48h and 72 h.

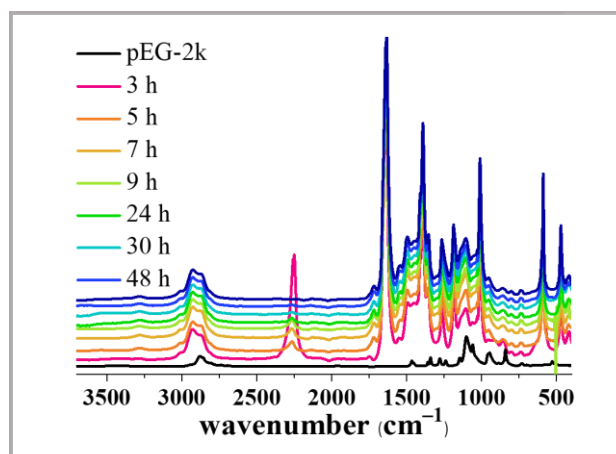


Figure 3.14. FT-IR spectra of films drop-cast onto the ATR crystal from the reaction mixture of PU_2k-ran under nitrogen atmosphere after different reaction times.

Polymer Characterization**PU_2k-ran**

Yield: 0.48 g (90%). **GPC:** $M_n = 22.2 \text{ kg}\cdot\text{mol}^{-1}$, $M_w = 45.9 \text{ kg}\cdot\text{mol}^{-1}$, $D = 2.1$. **$^1\text{H-NMR}$** (400 MHz, $\text{DMSO-}d_6$): $\delta = 8.71$ (m, 1.7H, tpy: $\text{C}_{6/6''}$), 8.63 (m, 1.7H, tpy: $\text{C}_{3/3''}$), 7.98 (m, 3.4H, tpy: $\text{C}_{3/5'}$, $\text{C}_{4/4''}$), 7.49 (m, 1.6H, tpy: $\text{C}_{5/5''}$), 7.32–6.95 (m, 2.6H, NH), 5.92–5.41 (m, 2.7H, NH), 5.18 (s, 0.8H, tpyOCH), 4.45–4.13 (m, 3.3H, tpyOCHCH₂), 4.03 (m, 4.5H, NHC(=O)OCH₂CH₂O), 3.67–3.36 (m, 180H, $(\text{CH}_2\text{CH}_2\text{O})_n$), 2.71 (m, 4H, IPDI: OC(=O)NHCH₂), 1.61–0.73 (m, 40H, IPDI) ppm. Peak assignment according to literature reports.⁵¹

PU_4k-ran

Yield: 0.86 g (94%). **GPC:** $M_n = 33.8 \text{ kg}\cdot\text{mol}^{-1}$, $M_w = 64.8 \text{ kg}\cdot\text{mol}^{-1}$, $D = 1.9$. **$^1\text{H-NMR}$** (400 MHz, DMSO- d_6): $\delta = 8.71$ (m, 1.5H, tpy: $\text{C}_{6/6''}$), 8.62 (m, 1.6H, tpy: $\text{C}_{3/3''}$), 7.98 (m, 3H, tpy: $\text{C}_{3'/5'}$, $\text{C}_{4/4''}$), 7.49 (m, 1.5H, tpy: $\text{C}_{5/5''}$), 7.36–7.02 (m, 3.1H, NH), 6.03–5.52 (m, 3.0H, NH), 5.19 (s, 0.9H, tpyOCH), 4.48–4.23 (m, 2.5H, tpyOCHCH₂), 4.06 (m, 4H, NHC(=O)OCH₂CH₂O), 3.95–3.39 (m, 364H, (CH₂CH₂O)_n), 2.73 (m, 5H, IPDI: OC(=O)NHCH₂), 1.67–0.55 (m, 35H, IPDI) ppm.

PU_6k-ran

Yield: 0.89 g (89%). **GPC:** $M_n = 43.0 \text{ kg}\cdot\text{mol}^{-1}$, $M_w = 77.9 \text{ kg}\cdot\text{mol}^{-1}$, $D = 1.8$. **$^1\text{H-NMR}$** (400 MHz, DMSO- d_6): $\delta = 8.70$ (m, 1.5H, tpy: $\text{C}_{6/6''}$), 8.58 (m, 1.5H, tpy: $\text{C}_{3/3''}$), 7.99 (m, 3H, tpy: $\text{C}_{3'/5'}$, $\text{C}_{4/4''}$), 7.49 (m, 1.5H, tpy: $\text{C}_{5/5''}$), 7.20–7.03 (m, 2.8H, NH), 5.92–5.46 (m, 3H, NH), 5.15 (s, 0.9H, tpyOCH), 4.4–4.2 (m, 3H, tpyOCHCH₂), 4.03 (m, 3.9H, NHC(=O)OCH₂CH₂O), 3.67–3.36 (m, 528H, (CH₂CH₂O)_n), 2.71 (m, 4H, IPDI: OC(=O)NHCH₂), 1.64–0.67 (m, 40H, IPDI) ppm.

UV-Vis Measurements**Spectrometric Titration**

PU_6k-alt (19.5 mg) is dissolved MeOH in a volumetric flask (100 mL). After measuring an initial spectrum (260–450 nm), 25 μL of a CuBr₂ solution (2.1 mM in MeOH) are added and the mixture is stirred for 5 min before taking an aliquot and measuring another spectrum. Afterwards, the aliquot is transferred back to the volumetric flask before the titration is continued analogously with 5 μL portions of the CuBr₂ solution (**Figure 3.15 A**). The relative intensity increase at the absorption maximum of the CuTpy₂ complex at ($\lambda_{\text{max}} = 313.5 \text{ nm}$) shows two regimes which are separately fitted. The equivalence point is determined from the intersection point of these linear fits ($n_{\text{CuBr}_2} = 1.1 \mu\text{mol}$). A terpyridine content of $113 \mu\text{mol}\cdot\text{g}^{-1}$ is calculated under the assumption $n_{\text{Tpy}} = 2n_{\text{Cu(II),equivalence point}}$.

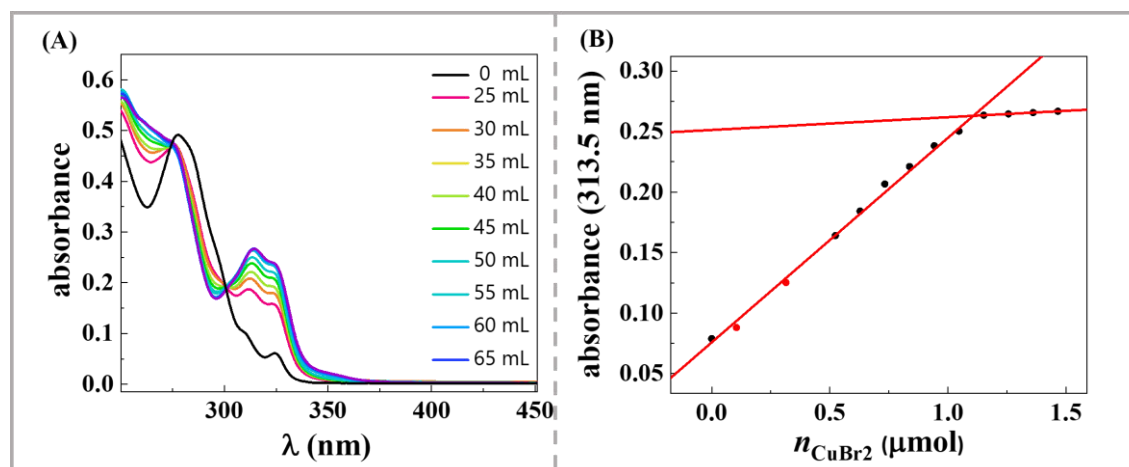


Figure 3.15. (A) UV-Vis spectra of PU_6k-alt in methanol upon the stepwise addition of CuBr₂ (2.1 mM solution). (B) Absorbance at the absorption maximum of the CuTpy₂ complex ($\lambda_{\text{max}} = 313.5 \text{ nm}$) as function of the amount of added CuBr₂ and determination of the equivalence point by linear fitting.

Molar Extinction Coefficient and Terpyridine Content

The molar decadic extinction coefficient of tpy diol **3.4** in MeOH is determined from the calibration shown in **Figure 3.16** as $\varepsilon = (22.6 \pm 1) \cdot 10^2 \text{ L} \cdot \text{mol}^{-1} \cdot \text{cm}^{-1}$. For the tpy content determination, the PUs (10–20 mg) are dissolved in MeOH in volumetric flasks (25 mL). These stock solutions are diluted with methanol ($v:v = 1:5$) prior to the UV-Vis measurements.

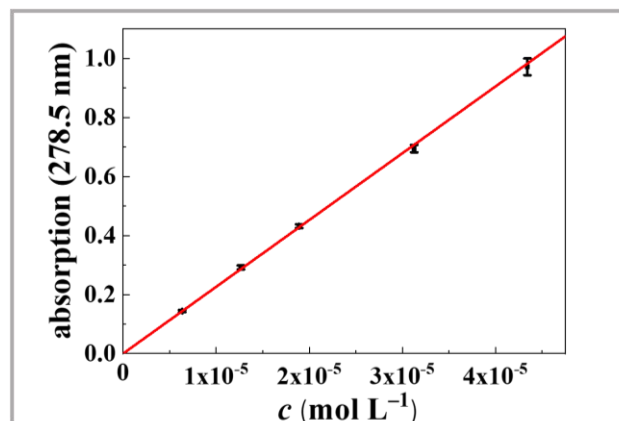


Figure 3.16. Absorption of tpy diol **3.4** in MeOH as a function of the molar concentration with linear fit.

Fluorescence Spectroscopy

The fluorometric determination of the critical aggregation concentration (cac) with pyrene as hydrophobic probe is conducted according to a standard procedure by Zhu and co-workers.⁵² A stock solution of pyrene (9.9 mg) in EtOH is prepared in a volumetric flask (100 mL, $c_{\text{pyrene,EtOH}} = 0.49 \text{ mM}$). The ethanolic pyrene solution is further diluted to a concentration of $c_{\text{pyrene,H}_2\text{O}} = 2 \mu\text{M}$ in Milli-Q water (100 mL volumetric flask). To prepare a polymer–pyrene stock solution, PU_6k-alt (50 mg), 20 μL of the ethanolic pyrene stock solution and Milli-Q water (around 3 mL) are added to a volumetric flask (5 mL) and gently shaken at 35 °C for 60 min before filling the flask to the mark with water. Next, the PU–pyrene stock solution is diluted to polymer concentrations of $c_{\text{PU}} = 10, 5, 2.5, 1, 0.5, 0.25, 0.1, 0.05, \text{ and } 0.025 \text{ g L}^{-1}$ (1 mL each) with the aqueous pyrene stock solution and shaken for 30 min. Finally, the emission spectra of all solutions are recorded (excitation wavelength $\lambda_{\text{ex}} = 334 \text{ nm}$). Additionally, a stock solution of PU_6k-alt is prepared in pure Milli-Q water and diluted analogously. The emission spectra of the pure PU solutions are recorded and subtracted from the PU–pyrene spectra before the I_1/I_3 intensity ration is analyzed to determine the cac .

FT-IR Spectroscopy

The PUs are dissolved in DCM, dropped onto the ATR crystal and left to dry under N_2 atmosphere. Afterwards, a spectrum is recorded and normalized to the C–O–C stretching vibration at 1100 cm^{-1} . The peak deconvolution of the carbonyl region is performed with the Software OriginPro 2019. The area between $1800\text{--}1620 \text{ cm}^{-1}$ is normalized and baseline-subtracted before a peak fitting is conducted. The spectra, and corresponding fits are summarized in **Figure 3.8**.

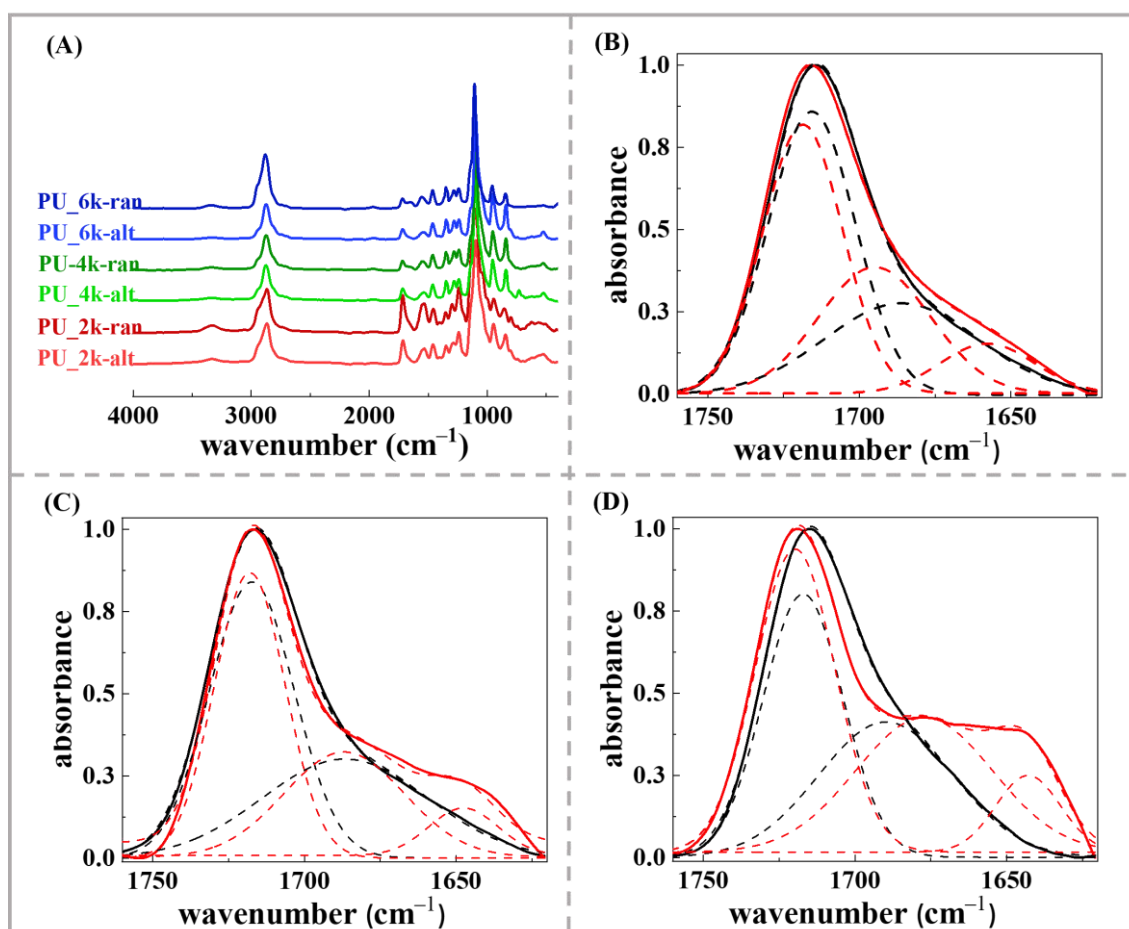


Figure 3.17. (A) Normalized FT-IR spectra of drop-cast PU films. Baseline subtracted, normalized carbonyl region of (B) PU_2k-alt (black)/-ran (red), (C) PU_4k-alt (black)/-ran (red) and (D) PU_6k-alt (black)/-ran (red) with Gaussian curve fitting (dashed lines in corresponding color) performed for peak deconvolution.

Dynamic Light Scattering Measurements

Prior to all DLS measurements, the polymer solutions are filtered through a combination of a Whatman Anotop filter (20 nm pore size) and a Millex-LG[®] filter (200 nm pore size) at a concentration of 1 g·L⁻¹ (MeOH) to remove impurities. After freeze drying, the PUs are dissolved in Milli-Q water or methanol to the required concentration. Dust particles are removed from the light scattering quartz cuvettes by rinsing them with hot acetone before the polymer solutions are filtered into the cuvettes (syringe filter: Millex-LG[®], 200 nm pore size) inside a dust-free laminar flow box. Angular-dependent DLS measurements are performed at 20 °C with a successively increasing scattering angle of 30 to 120° (10° steps). At each angle, ten runs with a correlation time of 60 s are recorded. For data evaluation, the experimental intensity autocorrelation functions $g^{(2)}(q, \tau) = \langle I(q, t) \cdot I(q, t + \tau) \rangle \cdot \langle I(q, t) \rangle^{-2}$ are converted to the amplitude autocorrelation function $g^{(1)}(q, \tau)$ by applying the Siegert relation. Herein, $I(q, \tau)$ denotes the angular- and time dependent intensity with the lag time τ and the scattering vector $q = 4\pi \cdot n_D \cdot \lambda^{-1} \cdot \sin(\theta/2)$ which depends on the scattering angle θ , the laser wavelength ($\lambda = 632.8$ nm), and the refractive index of

the solvent n_D ($n_D(\text{MeOH}) = 1.329$, $n_D(\text{H}_2\text{O}) = 1.333$). The amplitude auto-correlation functions $g^{(1)}(q, \tau)$ are fitted with a sum of (stretched) exponentials as detailed in **Chapter 3.2**. The normalized amplitude correlation functions measured at 30° , the fits and corresponding residuals of concentration-dependent measurements of PU_6k-alt and -ran in MeOH are shown in and **Figure 3.8** and **Figure 3.8 A**. In **Figure 3.18 B**, the normalized amplitudes of the fast and slow mode are shown as a function of the concentration.

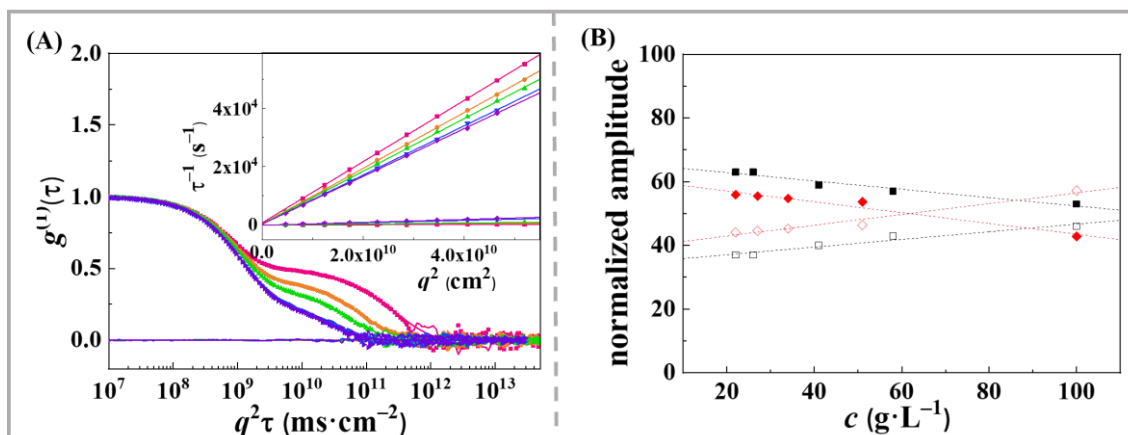


Figure 3.18. (A) Normalized DLS autocorrelation function $g^{(1)}(\tau)$ of PU_6k-alt in methanol (●: $c_1 = 100 \text{ g}\cdot\text{L}^{-1}$, ●: $c_2 = 58 \text{ g}\cdot\text{L}^{-1}$, ●: $c_3 = 41 \text{ g}\cdot\text{L}^{-1}$, ●: $c_4 = 26 \text{ g}\cdot\text{L}^{-1}$ and ●: $c_5 = 22 \text{ g}\cdot\text{L}^{-1}$) with fits to a double exponential decay and corresponding residuals measured at a scattering angle of 30° at $T = 20^\circ \text{C}$. Inset: Inverse relaxation times as a function of the square of the scattering vector q^2 (color code as before) with linear fits. (B) Concentration dependence of the relative amplitudes of the fast (open symbols) and slow mode (closed symbols) in the fit function (PU_6k-alt: ■/□ and PU_6k-ran: ◆/◇).

Gel Preparation and Rheological Measurements

All gels are prepared in a total volume of $250 \mu\text{L}$ and a terpyridine concentration of $20 \mu\text{M}$. The respective amount of the PU is dissolved in $150 \mu\text{L}$ MeOH before an appropriately concentrated manganese²⁺ triflate solution ($100 \mu\text{L}$, $n_{\text{Mn}^{2+}} = 0.5 \cdot n_{\text{tpy}}$) is added which is followed by immediate vortexing for 10–20 s. Afterwards, the samples are sealed and equilibrated for at least 24 h at 35°C . Before the measurement, all samples are centrifuged for 10 min to remove air bubbles. The gels are further equilibrated for 15 min after application onto the rheometer and between different experiments at a constant shear amplitude and frequency ($\gamma = 0.1\%$; $\omega = 1 \text{ rad}\cdot\text{s}^{-1}$). Frequency sweeps are measured between $\omega = 100\text{--}0.01 \text{ rad}\cdot\text{s}^{-1}$ with an increasing shear amplitude of $\gamma = 1\text{--}10\%$ (logarithmic ramp).

3.5 References

- (1) Breul, K. [REDACTED] Amphiphilic poly(ether urethanes) carrying associative terpyridine side groups with controlled spacing. *Polym. Chem.* **2021**, *12*, 2305–2316.
- (2) Voorhaar, L.; Hoogenboom, R. Supramolecular polymer networks: hydrogels and bulk materials. *Chemical Society reviews* **2016**, *45*, 4013–4031.
- (3) Semenov, A. N.; Rubinstein, M. Thermoreversible Gelation in Solutions of Associative Polymers. 1. Statics. *Macromolecules* **1998**, *31*, 1373–1385.
- (4) Guimard, N. K.; Oehlenschlaeger, K. K.; Zhou, J.; Hilf, S.; Schmidt, F. G.; Barner-Kowollik, C. Current Trends in the Field of Self-Healing Materials. *Macromol. Chem. Phys.* **2012**, *213*, 131–143.
- (5) Annable, T.; Buscall, R.; Ettelaie, R.; Whittlestone, D. The rheology of solutions of associating polymers: Comparison of experimental behavior with transient network theory. *Journal of Rheology* **1993**, *37*, 695–726.
- (6) Enke, M.; Döhler, D.; Bode, S.; Binder, W. H.; Hager, M. D.; Schubert, U. S. Intrinsic Self-Healing Polymers Based on Supramolecular Interactions: State of the Art and Future Directions. In *Self-healing Materials*; Hager, M. D., van der Zwaag, S., Schubert, U. S., Eds.; Advances in Polymer Science; Springer International Publishing: Cham, 2016; pp 59–112.
- (7) Yavvari, P. S.; Pal, S.; Kumar, S.; Kar, A.; Awasthi, A. K.; Naaz, A.; Srivastava, A.; Bajaj, A. Injectable, Self-Healing Chimeric Catechol-Fe(III) Hydrogel for Localized Combination Cancer Therapy. *ACS Biomater. Sci. Eng.* **2017**, *3*, 3404–3413.
- (8) Shi, L.; Zhao, Y.; Xie, Q.; Fan, C.; Hilborn, J.; Dai, J.; Ossipov, D. A. Moldable Hyaluronan Hydrogel Enabled by Dynamic Metal-Bisphosphonate Coordination Chemistry for Wound Healing. *Advanced healthcare materials* **2018**, *7*.
- (9) Liu, Y.; Meng, H.; Qian, Z.; Fan, N.; Choi, W.; Zhao, F.; Lee, B. P. A Moldable Nanocomposite Hydrogel Composed of a Mussel-Inspired Polymer and a Nanosilicate as a Fit-to-Shape Tissue Sealant. *Angew. Chem. Int. Ed.* **2017**, *56*, 4224–4228.
- (10) Liu, S.; Li, K.; Hussain, I.; Oderinde, O.; Yao, F.; Zhang, J.; Fu, G. A Conductive Self-Healing Double Network Hydrogel with Toughness and Force Sensitivity. *Chemistry (Weinheim an der Bergstrasse, Germany)* **2018**, *24*, 6632–6638.
- (11) Lee, B. P.; Konst, S. Novel hydrogel actuator inspired by reversible mussel adhesive protein chemistry. *Advanced materials (Deerfield Beach, Fla.)* **2014**, *26*, 3415–3419.
- (12) Grindy, S. C.; Learsch, R.; Mozhdehi, D.; Cheng, J.; Barrett, D. G.; Guan, Z.; Messersmith, P. B.; Holten-Andersen, N. Control of hierarchical polymer mechanics with bioinspired metal-coordination dynamics. *Nature materials* **2015**, *14*, 1210–1216.
- (13) Seiffert, S.; Sprakel, J. Physical chemistry of supramolecular polymer networks. *Chemical Society reviews* **2012**, *41*, 909–930.

- (14) Seiffert, S. Effect of Supramolecular Interchain Sticking on the Low-Frequency Relaxation of Transient Polymer Networks. *Macromol. rapid commun.* **2016**, *37*, 257–264.
- (15) Jangizehi, A.; Ahmadi, M.; Seiffert, S. Emergence, evidence, and effect of junction clustering in supramolecular polymer materials. *Mater. Adv.* **2021**, *13*, 2661.
- (16) Hackelbusch, S.; Rossow, T.; van Assenbergh, P.; Seiffert, S. Chain Dynamics in Supramolecular Polymer Networks. *Macromolecules* **2013**, *46*, 6273–6286.
- (17) Cassagnau, P.; Montfort, J. P.; Marin, G.; Monge, P. Rheology of polydisperse polymers: relationship between intermolecular interactions and molecular weight distribution. *Rheola Acta* **1993**, *32*, 156–167.
- (18) Golkaram, M.; Loos, K. A Critical Approach to Polymer Dynamics in Supramolecular Polymers. *Macromolecules* **2019**, *52*, 9427–9444.
- (19) Rossow, T.; Hackelbusch, S.; van Assenbergh, P.; Seiffert, S. A modular construction kit for supramolecular polymer gels. *Polym. Chem.* **2013**, *4*, 2515.
- (20) Tang, S.; Olsen, B. D. Relaxation Processes in Supramolecular Metallogels Based on Histidine–Nickel Coordination Bonds. *Macromolecules* **2016**, *49*, 9163–9175.
- (21) Lutz, J.-F.; Ouchi, M.; Liu, D. R.; Sawamoto, M. Sequence-controlled polymers. *Science (New York, N.Y.)* **2013**, *341*, 1238149.
- (22) Lutz, J.-F.; Lehn, J.-M.; Meijer, E. W.; Matyjaszewski, K. From precision polymers to complex materials and systems. *Nat Rev Mater* **2016**, *1*, 2836.
- (23) Lutz, J.-F., Ed. *Sequence-controlled polymers*; Wiley-VCH: Weinheim, Germany, 2018.
- (24) Guo, M.; Pitet, L. M.; Wyss, H. M.; Vos, M.; Dankers, P. Y. W.; Meijer, E. W. Tough stimuli-responsive supramolecular hydrogels with hydrogen-bonding network junctions. *J. Am. Chem. Soc.* **2014**, *136*, 6969–6977.
- (25) Gunay, U. S.; Petit, B. E.; Karamessini, D.; Al Ouahabi, A.; Amalian, J.-A.; Chendo, C.; Bouquey, M.; Gignes, D.; Charles, L.; Lutz, J.-F. Chemoselective Synthesis of Uniform Sequence-Coded Polyurethanes and Their Use as Molecular Tags. *Chem* **2016**, *1*, 114–126.
- (26) Uflyand, I. E.; Dzhardimalieva, G. I. Molecular design of supramolecular polymers with chelated units and their application as functional materials. *Journal of Coordination Chemistry* **2018**, *71*, 1272–1356.
- (27) Hovinen, J. Synthesis of 4'-substituted 2,2':6',2''-terpyridines via a Mitsunobu reaction. *Tetrahedron Letters* **2004**, *45*, 5707–5709.
- (28) Lee, I.; Bates, F. S. Synthesis, Structure, and Properties of Alternating and Random Poly(styrene-*b*-butadiene) Multiblock Copolymers. *Macromolecules* **2013**, *46*, 4529–4539.
- (29) Karpov, S. V.; Lodygina, V. P.; Komratova, V. V.; Dzhalukhanova, A. S.; Malkov, G. V.; Badamshina, E. R. Kinetics of urethane formation from isophorone diisocyanate: The catalyst and solvent effects. *Kinet Catal* **2016**, *57*, 422–428.

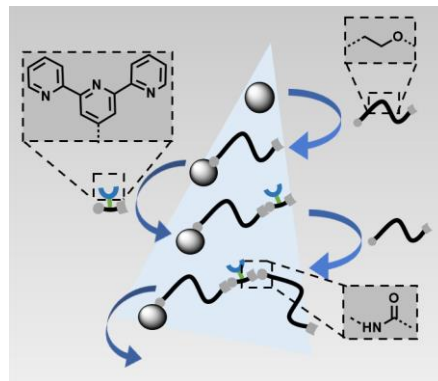
- (30) Korley, L. T. J.; Pate, B. D.; Thomas, E. L.; Hammond, P. T. Effect of the degree of soft and hard segment ordering on the morphology and mechanical behavior of semicrystalline segmented polyurethanes. *Polymer* **2006**, *47*, 3073–3082.
- (31) Skvortsov, A. M.; Gorbunov, A. A.; Berek, D.; Trathnigg, B. Liquid chromatography of macromolecules at the critical adsorption point: Behaviour of a polymer chain inside pores. *Polymer* **1998**, *39*, 423–429.
- (32) Ronco, L. I.; Basterretxea, A.; Mantione, D.; Aguirresarobe, R. H.; Minari, R. J.; Gugliotta, L. M.; Mecerreyes, D.; Sardon, H. Temperature responsive PEG-based polyurethanes “à la carte”. *Polymer* **2017**, *122*, 117–124.
- (33) Irusta, L.; Iruin, J. J.; Fernández-Berridi, M. J.; Sobkowiak, M.; Painter, P. C.; Coleman, M. M. Infrared spectroscopic studies of the self-association of ethyl urethane. *Vibrational Spectroscopy* **2000**, *23*, 187–197.
- (34) Miller, J. A.; Lin, S. B.; Hwang, K. K. S.; Wu, K. S.; Gibson, P. E.; Cooper, S. L. Properties of polyether-polyurethane block copolymers: effects of hard segment length distribution. *Macromolecules* **1985**, *18*, 32–44.
- (35) Mattia, J.; Painter, P. A Comparison of Hydrogen Bonding and Order in a Polyurethane and Poly(urethane-urea) and Their Blends with Poly(ethylene glycol). *Macromolecules* **2007**, *40*, 1546–1554.
- (36) Trinh, N. H.; Jaafar, M.; Xuan Viet, C.; Ahmad Zubir, S. Palm kernel oil polyol based shape memory polyurethane: effect of polycaprolactone and polyethylene glycol as soft segment. *Mater. Res. Express* **2020**, *7*, 25704.
- (37) Li, G.; Liu, Y.; Li, D.; Zhang, L.; Xu, K. A comparative study on structure-property elucidation of P3/4HB and PEG-based block polyurethanes. *Journal of biomedical materials research. Part A* **2012**, *100*, 2319–2329.
- (38) Szycher, M. *Szycher's handbook of polyurethanes*, 2. ed.; CRC Press / Taylor & Francis: Boca Raton, Fla., 2013.
- (39) Brassinne, J.; Bourgeois, J.-P.; Fustin, C.-A.; Gohy, J.-F. Thermo-responsive properties of metallo-supramolecular block copolymer micellar hydrogels. *Soft Matter* **2014**, *10*, 3086–3092.
- (40) Li, H.; Hu, D.; Liang, F.; Huang, X.; Zhu, Q. Influence factors on the critical micelle concentration determination using pyrene as a probe and a simple method of preparing samples. *Royal Society open science* **2020**, *7*, 192092.
- (41) Zheng, J.; Shen, T.; Ma, J.; Liang, L.; Lu, M. Physicochemical studies on micelle formation of amphiphilic polyurethane in aqueous solution. *Chemical Physics Letters* **2011**, *502*, 211–216.
- (42) Nystrom, B.; Walderhaug, H.; Hansen, F. K. Dynamic crossover effects observed in solutions of a hydrophobically associating water-soluble polymer. *J. Phys. Chem.* **1993**, *97*, 7743–7752.

- (43) Branca, C.; D'Angelo, G. Aggregation behavior of pluronic F127 solutions in presence of chitosan/clay nanocomposites examined by dynamic light scattering. *Journal of colloid and interface science* **2019**, *542*, 289–295.
- (44) Murnen, H. K.; Khokhlov, A. R.; Khalatur, P. G.; Segalman, R. A.; Zuckermann, R. N. Impact of Hydrophobic Sequence Patterning on the Coil-to-Globule Transition of Protein-like Polymers. *Macromolecules* **2012**, *45*, 5229–5236.
- (45) Hao, Z.; Li, G.; Yang, K.; Cai, Y. Thermoresponsive synergistic hydrogen bonding switched by several guest units in a water-soluble polymer. *Macromolecular rapid communications* **2013**, *34*, 411–416.
- (46) Rossow, T.; Habicht, A.; Seiffert, S. Relaxation and Dynamics in Transient Polymer Model Networks. *Macromolecules* **2014**, *47*, 6473–6482.
- (47) Rubinstein, M.; Semenov, A. N. Dynamics of Entangled Solutions of Associating Polymers. *Macromolecules* **2001**, *34*, 1058–1068.
- (48) Brassinne, J.; Cadix, A.; Wilson, J.; van Ruymbeke, E. Dissociating sticker dynamics from chain relaxation in supramolecular polymer networks—The importance of free partner! *Journal of Rheology* **2017**, *61*, 1123–1134.
- (49) Casida, J. E.; Gulevich, A. G.; Sarpong, R.; Bunnelle, E. M. S-Arachidonoyl-2-thioglycerol synthesis and use for fluorimetric and colorimetric assays of monoacylglycerol lipase. *Bioorganic & medicinal chemistry* **2010**, *18*, 1942–1947.
- (50) Seki, M.; Yamanaka, T.; Kondo, K. Practical synthesis of @-4-mercaptopyrrolidine-2-thione from L-aspartic acid. Preparation of a novel orally active 1-beta-methylcarbapenem, TA-949. *The Journal of organic chemistry* **2000**, *65*, 517–522.
- (51) Prabhakar, A.; Chattopadhyay, D. K.; Jagadeesh, B.; Raju, K. V. S. N. Structural investigations of polypropylene glycol (PPG) and isophorone diisocyanate (IPDI)-based polyurethane prepolymer by 1D and 2D NMR spectroscopy. *J. Polym. Sci. Part A: Polym. Chem.* **2005**, *43*, 1196–1209.
- (52) Li, H.; Hu, D.; Liang, F.; Huang, X.; Zhu, Q. Influence factors on the critical micelle concentration determination using pyrene as a probe and a simple method of preparing samples. *Royal Society open science* **2020**, *7*, 192092.

CHAPTER 4: SOLID PHASE SYNTHESIS OF METALLO–SUPRAMOLECULAR ASSOCIATING POLYMERS

Summary

The microscopic network structure of supramolecular polymer gels critically depends on the distribution and position of the reversible associating motives along the polymeric backbone. In the previous chapter, a polyaddition approach has been presented which allows the synthesis of metallo–supramolecular associating poly(ethylene glycol)–terpyridine (pEG–t₃p)_n multiblock polyurethanes with irregular or controlled sticker



distributions and a broad molar mass dispersity ($D \approx 2$). The mechanical properties of the reversible gels derived from these precursors showed a severe relaxation time prolongation in case of the irregular sequences. Since the actual structure of the random copolymers remains unknown, this rheological feature could not be clearly assigned to a certain sticker distribution.

Accordingly, alternative synthesis strategies, which provide a higher level of control over the primary sequence, are required to investigate this and other sequence-dependent structure–property relationships. To improve the sequence control and reduce the chain length dispersity, an alternative concept based on the iterative coupling of sticker– and polymer–fragments on a solid phase support is presented in the following chapter. For this purpose, pEG- and t₃p-amino acid analogues are conjugated by an established amide coupling strategy. The flexibility of this modular approach is emphasized by using three different t₃p amino acids with variable linker polarities. Besides the linkers, it is further possible to alter the spacing between the stickers on two different length scales: Firstly, the molar mass of the pEG spacer between two stickers can be altered ($M = 1000$ or $2000 \text{ g}\cdot\text{mol}^{-1}$) while it is further possible to position up to three t₃p amino acids directly besides each other.

Contributions:

Katharina Breul:	Synthesis conception, development and optimization of the synthesis routes, polymer characterization.
██████████	Reproduction of the t ₃ p amino acid synthesis.
██████████	Reproduction of the t ₃ p amino acid synthesis.
██████████████████	MALDI-Tof MS measurements.
██████████	Concept development and scientific supervision.

4.1 Introduction

In supramolecular polymer networks, macromolecular chains are cross-linked through reversibly associating motives, often called stickers. The physical and mechanical properties of such networks critically depend on the concentration, position, distribution as well as the strength and kinetics of these stickers. Among those variables, the precise control of the sticker distribution represents one of the most challenging parameters for synthetic polymer scientists.^{1–3} On a first level, this distribution is controlled by the primary sequence of the associating polymer chains or more precisely, the spacing of the stickers by non-associative monomers. In a statistical copolymerization of sticky- and non-sticky comonomers, the respective reactivity parameters control the sticker distribution, which is therefore commonly statistical. More homogeneous distributions can be achieved with telechelic systems, in which the molar mass dispersity controls the sticker dispersity. Beyond the sequence-related distribution, the thermodynamic incompatibility between stickers and polymer matrix often causes a (partial) aggregation of the associating groups into (ir)regular, microphase-separated domains, which affects the spatial sticker distribution on a secondary level.¹

The effects of heterogeneous sticker distributions strongly depend on the extent of this irregularity. In non-phase-separated networks with only binary sticker associations, statistical spacing variations mostly concern the later mesh size distribution. An irregular mesh size structure can firstly lead to increasing deviations from theoretical models. This complicates the mathematical description of the mechanical properties e.g., by the Maxwell-, or sticky-Rouse and reptation models, which is however crucial to establish quantitative structure–property relationships.⁴ Chemical side-sticker systems with a controllable spacing dispersity therefore represent an important asset to e.g., adjust and verify the mathematical implementation of polydispersity effects into theoretical models.⁵ Additionally, the proximity of individual stickers on a shorter, molecular length scale can lead to non-additive cooperativity effects between them. At this, the spatial proximity of individual stickers can either be implemented in the primary structure or result from the above-mentioned sticker clustering.

In summary, gaining control over the sticker distribution within supramolecular polymer networks requires to implement a homogeneous sticker spacing, and to control the clustering tendency of the associating motives. Until today, the only possibilities to produce synthetic macromolecules with a completely controlled primary structure rely on iterative growth techniques. For this purpose, orthogonally protected repeating units are successively reacted to the end of a growing chain. The perfection of the obtained chains critically depends on the completeness of each coupling step and the avoidance of side-reactions. This limits the applicable coupling chemistry to highly efficient click reactions.⁶ To avoid tedious work-up and purification procedures after each coupling and deprotection step, the covalent linkage of the growing chain to a solid-phase support

led to a technological breakthrough as pioneered by Merrifield for the synthesis of oligo(peptides) (SPS - solid phase synthesis).⁷ Applying this concept to polymers, the limited surface area inside the swollen solid phase–resin, the often-reduced reactivity of macromolecular chain-ends and the limited scale-up possibilities impart the most critical synthetic challenges. As exemplarily shown by Wan, Li *et al.*, it is nonetheless possible to create uniform, amide containing poly(ethylene glycols) (pEGs) with molecular weights up to $10 \text{ kg}\cdot\text{mol}^{-1}$ by reacting hetero-telechelic, fluorenyl methoxycarbonyl (Fmoc) protected α -amino- ω -carboxylic acid–ethylene glycol oligomers by established amide coupling protocols.⁸ The avoidance of amide bonds in the pEG backbone has also been proven to be possible in a study by Livingston, Gaffney and co-workers. Their soluble-substrate approach however requires special nano-sieving equipment.⁹

To our best knowledge, the application of pEG-based solid phase polymerization approaches has not yet been applied to create sequence-controlled polymers with reversibly associating side-stickers. To contribute a defined and tunable model system for fundamental structure–property relationship investigations, the present study aims to provide a versatile synthesis platform, which allows to precisely control and engineer the sticker spacing and sticker microenvironment. To avoid the need for specialist equipment, a classical, amide-coupling SPS with Fmoc–strategy is chosen. At this, the usage of flexible pEG chains not only offers the advantage of an excellent compatibility with many polar solvents and supramolecular stickers, but also allows to purchase hetero-telechelic building blocks from commercial sources. Regarding the sticky side-groups, the metal-coordinating terpyridine (tpy) ligand is chosen. Metallo-supramolecular cross-linking offers the possibility to create network junctions with variable strength and kinetics from one precursor by applying different metal ions for the cross-linking reaction.¹⁰ It is further advantageous that the inherent clustering tendency of coordinative ligands is generally less pronounced than that of hydrogen bonding motives or ionic groups whose polarity imposes an inherent driving force.^{1,11,12}

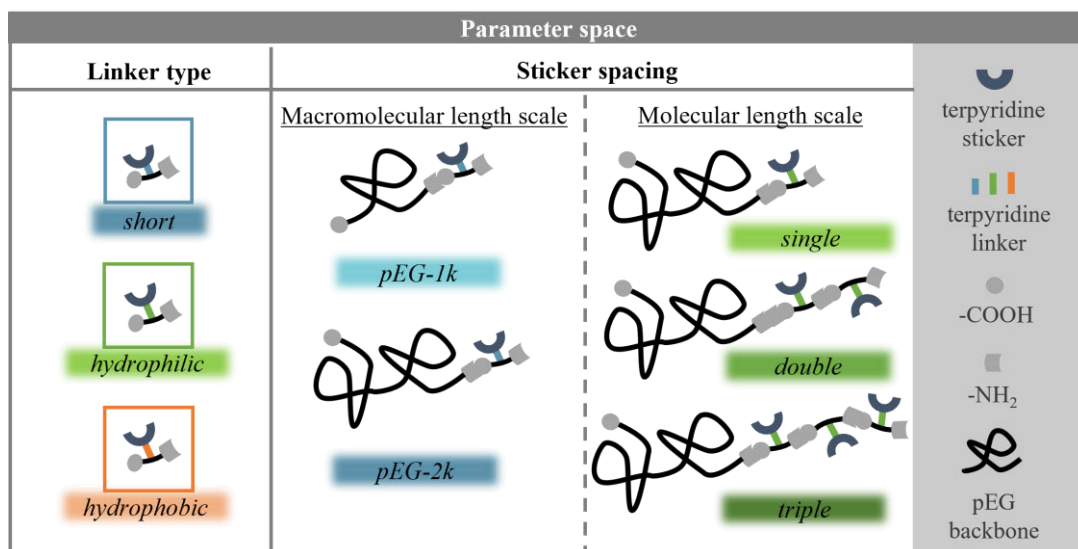


Figure 4.1. Overview of the independently variable chemical parameters in metallo–supramolecular associating polymers synthesized *via* solid phase synthesis.

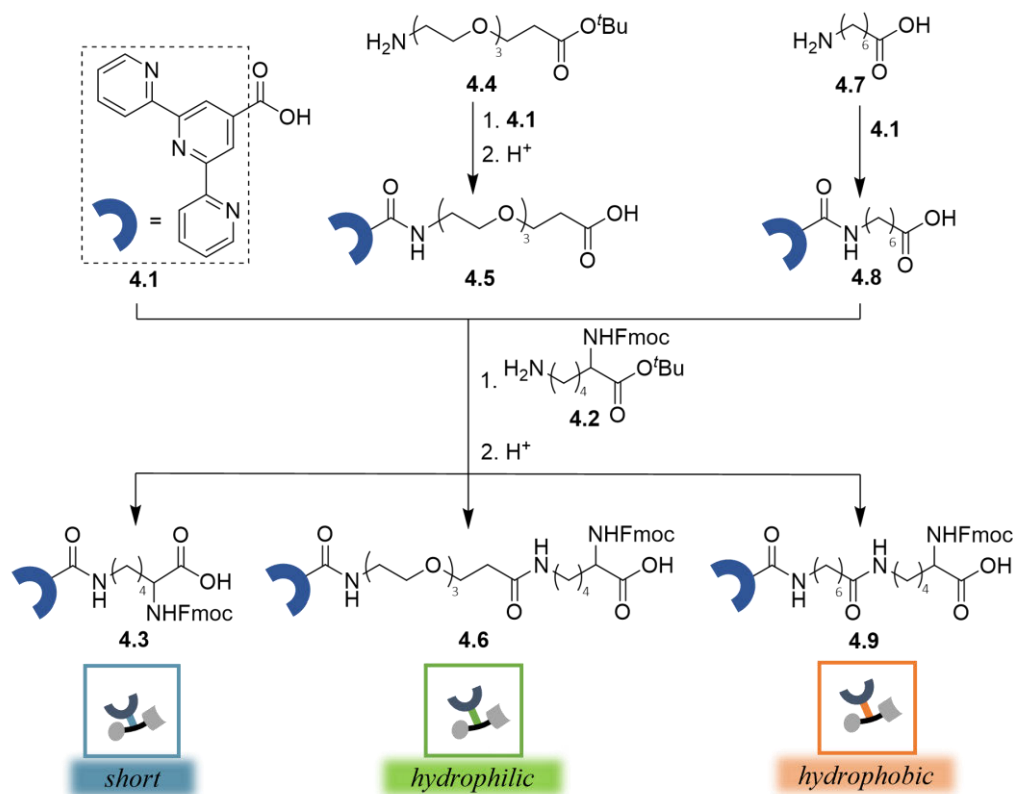
Therefore, we firstly present a synthesis strategy for Fmoc-protected, tpy-amino acids. At this, we do not rely on an earlier presented 5-step synthesis for terpyridyl-alanine which does not allow to influence the polarity of the sticker microenvironment.¹³ To include this possibility and ensure maximum compatibility with the established SPS protocols, the tpy ligand is attached to L-lysine by using linkers with differing length and polarity.

In summary, the modular SPS synthesis offers the possibility to vary: (1) The polarity of the linkers that connects sticker and polymer backbone, (2) the sticker spacing on a macromolecular length scale by using unimolecular or narrow disperse hetero-telechelic pEG building blocks with differing molar mass ($1 \text{ kg}\cdot\text{mol}^{-1} = 1\text{k}$, $2 \text{ kg}\cdot\text{mol}^{-1} = 2\text{k}$), and (3) the sticker spacing on a molecular scale by precisely controlling the primary sequence (**Figure 4.1**). The possibility to incorporate single, doubles and triples of directly neighbouring ligands is highly relevant to study cooperativity effects between adjacent supramolecular stickers.

4.2 Results & Discussion

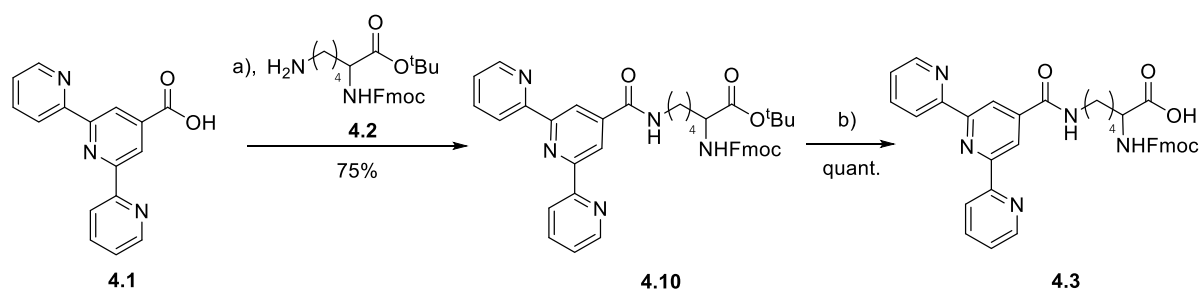
Monomer Design

The synthesis of the artificial tpy-amino acids is based on the amide coupling of different tpy-linkers with the free ϵ -amino group of *N*- α -Fmoc-L-lysine *tert*-butyl ester **4.2** and the subsequent deprotection of the OH-terminus by standard acidic cleavage as summarized in **Scheme 4.1**.



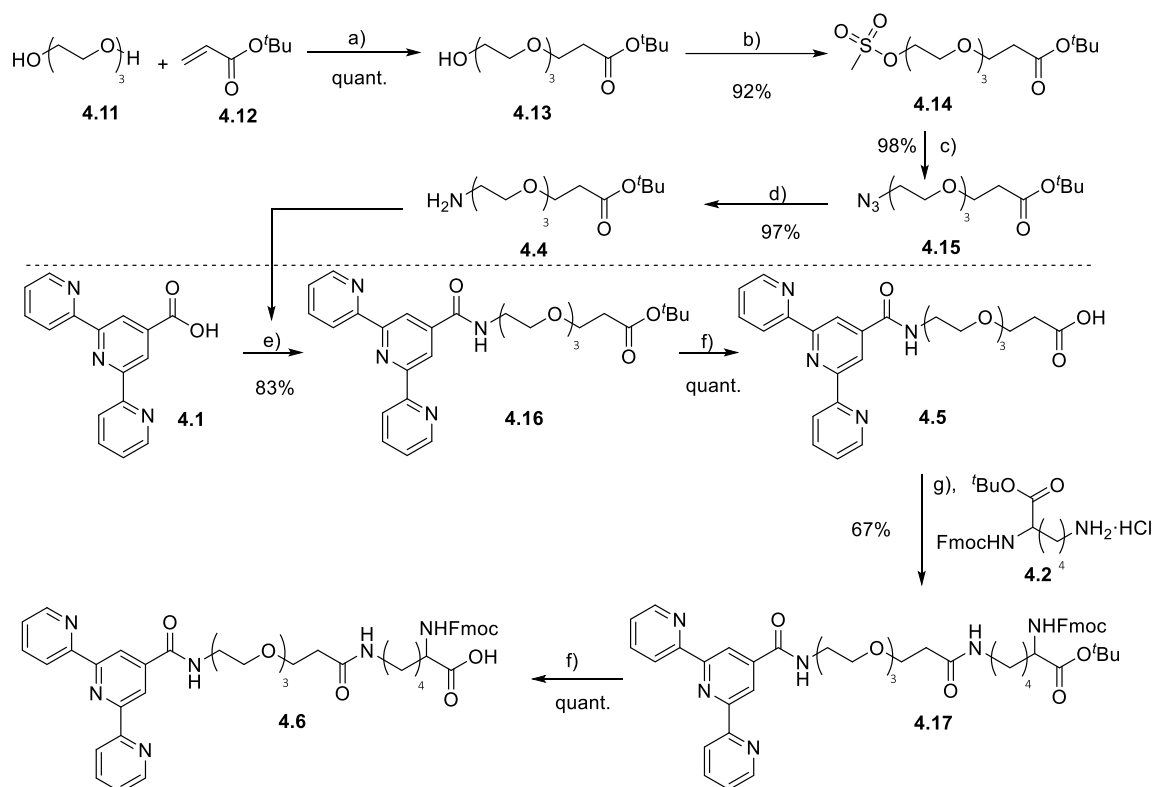
Scheme 4.1. Synthesis of lysine based tpy-amino acids **4.3**, **4.6** and **4.9** containing a short (blue), hydrophilic (green) and hydrophobic (orange) linker.

Accordingly, the first and simplest approach is the direct coupling of the protected lysine **4.2** and [2,2':6',2''-terpyridine]-4'-carboxylic acid (tpy-carboxylic acid) **4.1** which leads to a short spacing between ligand and reactive sites. As summarized in **Scheme 4.2**, the hexafluorophosphate azabenzotriazole tetramethyl uranium (HATU) mediated amidation and subsequent purification by recrystallization from an acetonitrile (ACN)/water mixture, yields the *tert*-butyl ester protected intermediate **4.10** in a yield of 75%. The final amino acid **4.3** is obtained after standard acidic cleavage of the *tert*-butyl group. The Fmoc-protected amino acid is only slightly soluble in water, dimethylformamide (DMF) and dimethyl sulfoxide (DMSO) under neutral conditions but fully dissolves upon deprotonation of the carboxylic acid moiety.



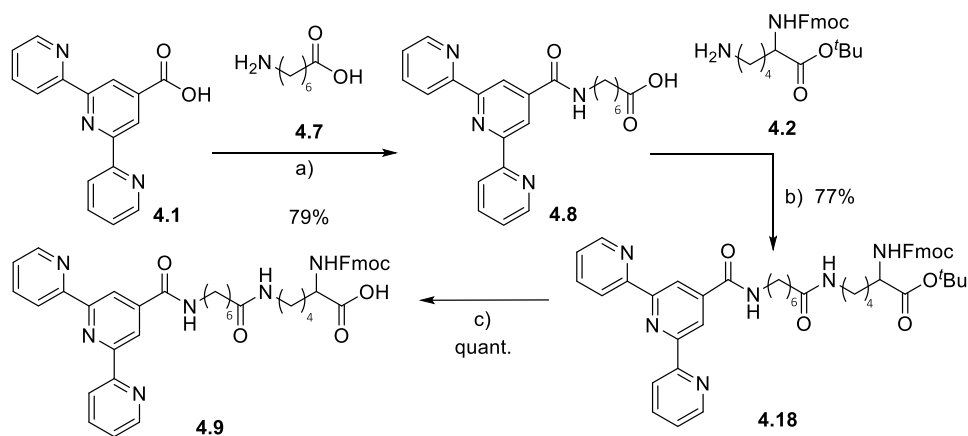
Scheme 4.2. Synthesis of compound **4.3**: a) **4.2**, HATU, DIPEA, DMF, 0 °C to r.t., 4 h; b) DCM:TFA:TES (2:1:0.02), 0 °C to r.t., 7 h.

To incorporate a flexible, polar spacer, which mimics the pEG backbone, triethylene glycol (tEG) is chosen. For this purpose, tEG **4.11** is firstly desymmetrized in a sodium-glycolate catalysed Michael addition with *tert*-butyl acrylate **4.12** (0.3 eq.) as shown in **Scheme 4.3**.¹⁴ The free hydroxyl group is then activated by mesylation before an azide group is introduced by nucleophilic substitution. Subsequent reduction to the primary amine is performed under Staudinger conditions. The α -amino- ω -*tert*-butyl carboxylate linker **4.4** is thus obtained over four steps in a total yield of 87%. For the following coupling, the tpy-carboxylic acid **4.1** is *in-situ* activated with thionyl chloride whose excess is afterwards removed by distillation. The obtained compound **4.16** is chromatographically purified on reversed phase silica gel (RP-SiO₂) before the *tert*-butyl group is removed by trifluoroacetic acid (TFA) treatment. At this, it is crucial to use freshly glass distilled TFA to avoid a contamination of **4.5** with iron traces, which leads to a violet coloration of the product resulting from the formation of the kinetically highly inert Fe(II)-*bis*(terpyridine) complex. Once formed, it is however possible to separate the complexed and non-complexed compounds *via* size exclusion chromatography on Sephadex[®] LH20. The subsequent coupling with the protected lysine **4.2** and the final deprotection proceed as described above. At this, a chromatographic purification of **4.17** is unavoidable since the excellent solubility in many organic solvents including ACN, dichloromethane (DCM), methanol (MeOH), DMF and DMSO prevents a recrystallization. The total yield over seven consecutive steps comprises 50%.



Scheme 4.3. Synthesis of compound **4.6**: a) Na, THF, r.t., 20 h; b) MsCl, NEt₃, DCM, 0 °C to r.t., 15 h; c) NaN₃, DMF, 60 °C, 15 h; d) 1. PPh₃, THF, 0 °C to r.t., 12 h, 2. H₂O, r.t., 12 h; e) 1. **4.1**, SOCl₂, 75 °C, 3 h, 2. **4.4**, DIPEA, DCM, r.t., 48 h; f) DCM:TFA:TES (2:1:0.02), 0 °C to r.t., 3 h.; g) **4.2**, HATU, DIPEA, DCM, 0 °C to r.t., 20 h.

Finally, a hydrophobic linker is synthesized as an opposite extreme (**Scheme 4.4**). For this purpose, the tpy-carboxylic acid **4.1** is *in-situ* activated as *p*-nitrophenyl carbonate before amino heptanoic acid **4.7** is added.¹⁵ The hydrophobic tpy-compound **4.8** is then purified by isoelectric precipitation from the aqueous reaction mixture and obtained in 79% yield. The following coupling and deprotection steps are performed as detailed before and yield the hydrophobic tpy-amino acid **4.9** in 61% yield. It shows similar solubility properties to amino acid **4.3**.

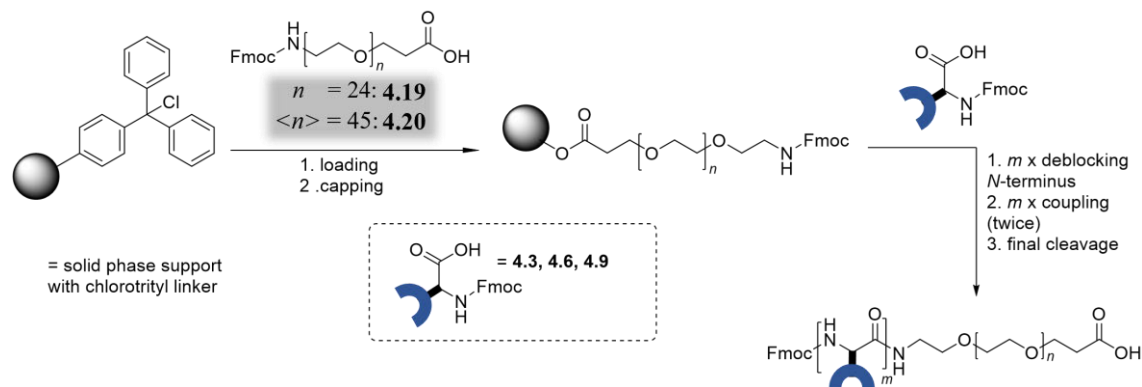


Scheme 4.4. Synthesis of compound **4.9**; a) 1. 4-nitrophenyl chloroformate, NEt₃, DMAP, ACN, r.t., 60 min; 2. **4.7**, NEt₃, H₂O, r.t., 12 h; b) **4.2**, HATU, DIPEA, DMF, 0 °C to r.t., 14 h; c) DCM:TFA:TES (2:1:0.02), 0 °C to r.t., 6 h.

The α -amino- ω -carboxylic acid pEGs **4.19/4.20** ($M = 1/2 \text{ kg}\cdot\text{mol}^{-1}$) are commercially available with and without Fmoc protecting groups. To protect the free amino end-group, the use of Fmoc-succinimide in the presence of sodium carbonate in a water/dioxane mixture proved as most efficient method to prevent a dimerization of the polymer, which is observed with the Fmoc-chloride. All experimental details are described in **Chapter 4.4**.

Solid Phase Coupling of Polyether- and Terpyridine Amino Acids

Further on, the attachment of pEG-2k amino acid **4.20** to a solid phase resin and the coupling with the different tpy-amino acids is investigated. Due to its supreme swelling capacities in DCM and DMF, a loosely cross-linked poly(styrene) (PS) resin with covalently attached pEG chains (TentaGel[®] XV) is chosen. This resin composition supposedly provides more space for the extended polymer structure than conventional PS resins. For the loading with the first pEG-2k amino acid, resins with a chlorotriptyl linker show significantly better results than OH-terminated ones e.g., equipped with a Wang-linker (**Scheme 4.5**). With the chlorotriptyl linker, the resin loadings vary between 0.04–0.08 mmol·g⁻¹ which corresponds to 18–36% of the manufacturer specification for standard amino acids. Increasing the pEG excess above 3.0 eq. or extending the reaction time to more than 24 h fails to improve the achievable loadings.



Scheme 4.5. Solid phase coupling of Fmoc-protected α -amino- ω -carboxylic acid pEG-1k **4.19** and -2k **4.20** with tpy-amino acids **4.3**, **4.6** and **4.9**.

After deprotecting the *N*-terminus with piperidine, one of the three tpy-amino acids **4.3**, **4.6** or **4.9** is coupled to the pEG chain in a benzotriazol-1-yloxy-tripyrrolidino phosphonium hexafluorophosphate (PyBOP) mediated amidation reaction. Full conversion of the chain ends is ensured by performing two consecutive couplings for 12–18 h with initially 3.0 eq. and secondly 1.0 eq. of the tpy-amino acid. An additional equivalent of the coupling reagent PyBOP is added in both couplings after ≈ 6 h reaction time. Finally, the coupling products are cleaved off from the solid support using a HFIP (hexafluoro-2-propanol)/DCM mixture ($v/v = 1:1$), isolated by precipitation in diethyl ether and further purified by size exclusion chromatography. The mild cleavage conditions of the trityl-linker are an additional advantage, since the use of corrosive organic acids frequently led to a contamination with iron traces.

The molecular structures of the coupling products obtained from the coupling of the tpy-amino acids **4.3**, **4.6** and **4.9** with the pEG-2k amino acid **4.20** are verified by $^1\text{H-NMR}$ (Figure S4.17–19) and MALDI-ToF mass spectrometry. As shown in Figure 4.2 E, the molar mass dispersity of the pEG building blocks is clearly reflected in the mass spectrum ($\Delta m/z = 44$ Da). Overlaying the experimental data with the expected mass of the molecular ions $[\text{M}+\text{H}]^+$ and $[\text{M}+\text{Na}]^+$ of the 45-mer of the compounds **4.21**, **4.23** and **4.26**, shows good agreement in all cases.

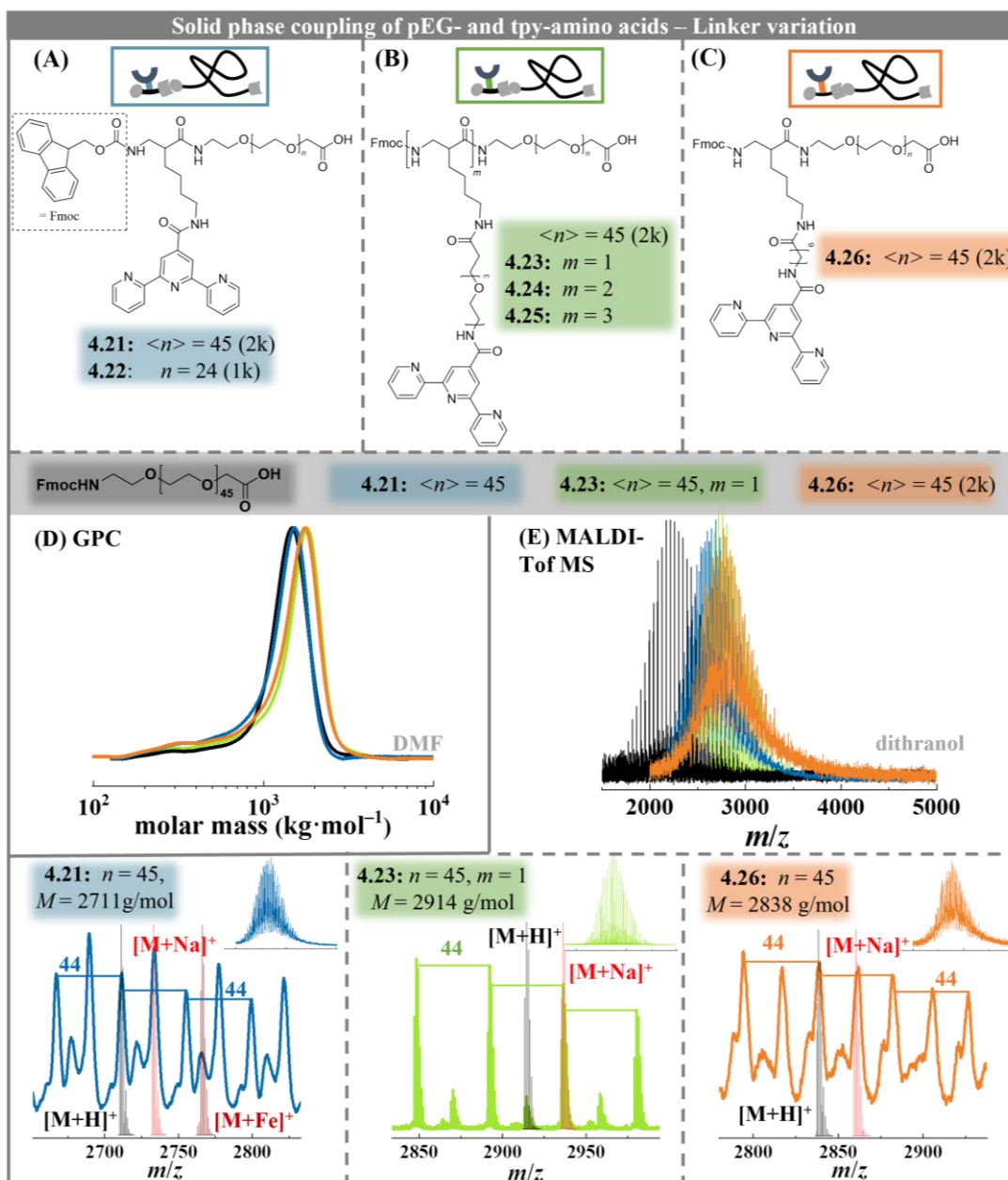


Figure 4.2. Chemical structure of Fmoc-protected tpy-pEG-amino acids obtained by SPS from the tpy-amino acids (A) **4.3** (blue), (B) **4.6** (green) and (C) **4.9** (orange) (D) Molar mass distributions (GPC, DMF, pEG calibration) and (E) mass spectra (MALDI-ToF-MS) of the coupling products **4.21**, **4.23** and **4.26** with enlarged extracts overlaid with the simulated isotope patterns of $[\text{M}+\text{H}]^+$, $[\text{M}+\text{Na}]^+$ (and $[\text{M}+\text{Fe}]^+$) of the respective $n = 45$ -multimers (color code as before).¹⁶

Next, the molar mass of the pEG fragment is reduced to $1.0 \text{ kg}\cdot\text{mol}^{-1}$. For this purpose, the tpy-amino acid with the short linker **4.3** is applied as representative example. It should further be noted that the shorter pEG amino acid is a unimolecular building block with a defined number of repeating blocks ($n = 24$). As shown in the mass spectrum and HPLC elugram depicted in **Figure 4.3 B + C** and the $^1\text{H-NMR}$ (**Figure S4.20**), the solid phase coupling yields the targeted, sequence-defined oligomer in high purity.

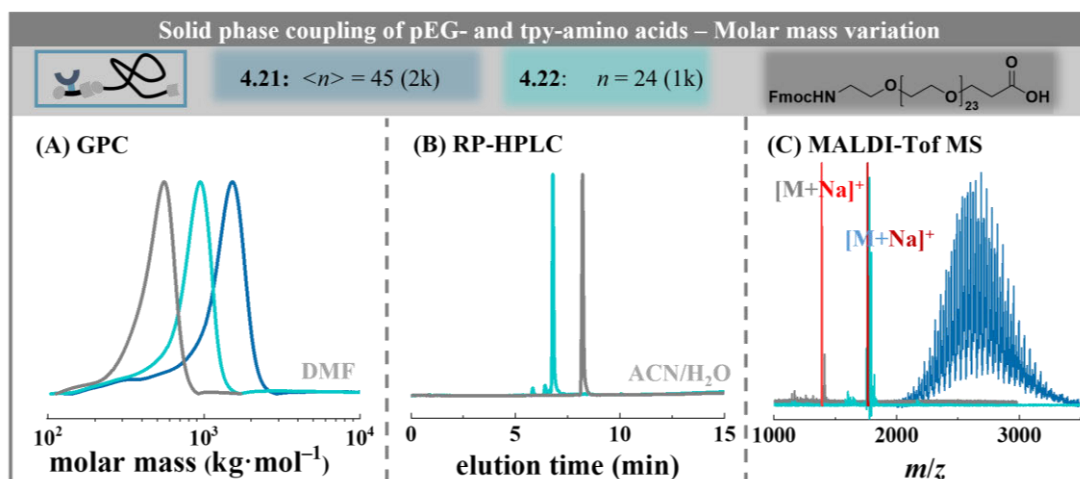


Figure 4.3. (A) Molar mass distributions (GPC, DMF, pEG calibration), (B) HPLC-chromatogram (gradient: 30 to 100% ACN over 12 min, 100% ACN for 3 min, 254 nm) and (C) mass spectra (MALDI-ToF-MS) of FmocNH-pEG-1k-COOH **4.19** (grey) and its coupling product **4.22** with tpy-amino acid **4.3** (light blue); The data for compound **4.21** with the same tpy-amino acid but the longer pEG fragment are included for comparison (dark blue). (C) Isotope patterns of $[M+H]^+$ and $[M+Na]^+$ are shown in red.¹⁶

Finally, the possibility to introduce multiple neighboring stickers is investigated under application of the hydrophilic tpy- and the pEG-2k-amino acids **4.6** and **4.20**. By consecutive amide couplings, one, two and three tpy stickers are attached to the chain-end. The expected increase of the molar mass is proven by GPC and mass spectrometry as shown in **Figure 4.4**. The $^1\text{H-NMR}$ spectra (**Figure S4.18/4.21/4.22**) further verify the increasing molar content of tpy groups in comparison to pEG backbone and the Fmoc protecting group. Considering the molar mass of the 45-mers, an overlay with the expected masses of the $[M+Na]^+$ adducts (red) proves the expected increase by the tpy-amino acid molar mass of $m/z = 591 \text{ Da}$ (**Figure 4.4 C**).

In summary, these experiments demonstrate that the solid phase coupling of oligo- or poly(ethylene glycol)- and tpy-amino acids is generally possible. After establishing these fundamental prerequisites, the following section focuses on the synthesis of multiblock polymers on the basis of the presented building blocks.

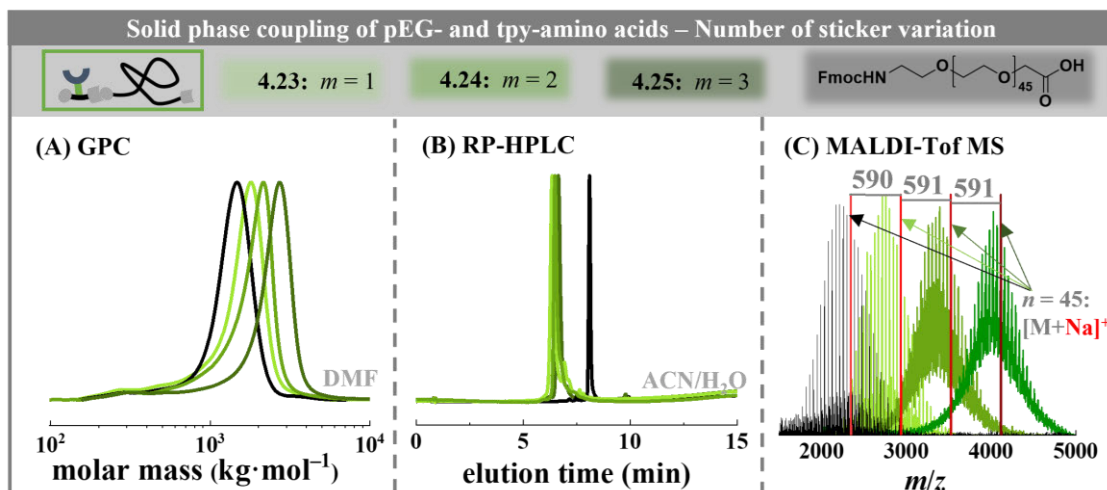


Figure 4.4 (A) Molar mass distributions (GPC, DMF, pEG calibration), (B) HPLC-chromatograms (gradient: 30 to 100% ACN over 12 min, 100% ACN for 3 min, 254 nm) and (C) mass spectra (MALDI-ToF-MS) of FmocNH-pEG-2k-COOH **4.20** (black) and its coupling product with one (light green), two (green) and three (dark green) hydrophilic tpy-amino acid blocks **4.6**. (C) Isotope patterns of $[M+Na]^+$ for the 45-mers of all compounds are shown in red.¹⁶

Towards Periodic Multiblock Polymers

To create linear chains with multiple, associating side-groups in defined positions, the number of coupling steps is increased. As depicted in **Figure 4.5 A**, this can be achieved by introducing each tpy- and pEG-amino acid separately in consecutive coupling steps (Method A). For multiblock structures, it is however also possible to firstly synthesize the complete repeating unit, cleave it off from the solid support and apply the pre-coupled fragment for a second SPS as schematized in **Figure 4.5 B** (Method B). Most importantly, the use of pre-coupled fragments reduces the number of solid phase coupling steps and thus the overall reaction time. This aspect is especially relevant due to the long reaction times which are required to achieve full conversions with the polymeric units (> 24 h per amino acid).

To compare both approaches, four pEG-2k- **4.20** and four hydrophilic tpy-amino acid blocks **4.6** are coupled in an alternating fashion by each method. Since the targeted molecule represents a multimer of the pEG-tpy conjugate **4.23**, it is referenced as $(4.23)_4$ (**Figure 4.5 C**). Besides the reaction time, the yield in comparison to the solid phase support and the applied amino acids are important parameters. Due to the low resin loadings, it requires $\approx 8x$ more solid phase material (3.1 g vs. 0.4 g) to synthesize a similar product amount (≈ 30 mg) by Method B compared to Method A. However, regarding the most expensive component, the pEG amino acid, an additional aspect must be considered. The excess of the polymeric amino acid analogues can be easily recovered and purified by precipitation and size exclusion chromatography. At this, 80% of the amino acid from the loading step can be recovered in high purity (**Figure 4.6, Chapter 4.4**). By contrast, the GPC curves of the excess regained after the amide couplings, show bimodal distributions. This dimerization is likely by the high concentrations of coupling agent and organic base used in the amide coupling, which leads to the partial deprotection of the *N*-terminus and

subsequent amidation reactions. Due to this aspect, twice as much as pEG amino acid is required in the consecutive coupling method. In summary, the use of pre-coupled fragments is chosen as more practical and economical method.

Further focusing on the coupling efficiency, the molar mass distributions of the tri- **(4.23)**₃ and tetra-block **(4.23)**₄ synthesized by Method B, show increasing low molar mass shoulders, which indicate incomplete conversions (**Figure 4.5 C**). Since a further increase of the reagent excess or an elongation of the reaction time are impractical, the final product is instead purified by preparative-HPLC. As shown in **Figure 4.5 D**, this yields a monomodal molar mass distribution. The remaining peak tailing in the GPC curve is commonly observed for tpy-functionalized polymers and can be attributed to specific interactions between ligand and column material.

Initial tests to synthesize multiblock structures from other the pre-coupled pEG–tpy amino acid blocks **(4.21)** and **(4.26)** have been performed on a small scale. The GPC and HPLC investigations summarized in **Figure 4.8 (Chapter 4.4)** indicate lower coupling efficiencies, which is however inconclusive due to practical handling difficulties on the scale of these tests (30 mg resin, 1–2 mg isolated yield). A reliable transfer of the multiblock synthesis to the other pEG–tpy amino acids and the incorporation of multiple directly neighbouring tpy–stickers thus requires further experimental work, which exceeds the scope of the present thesis.

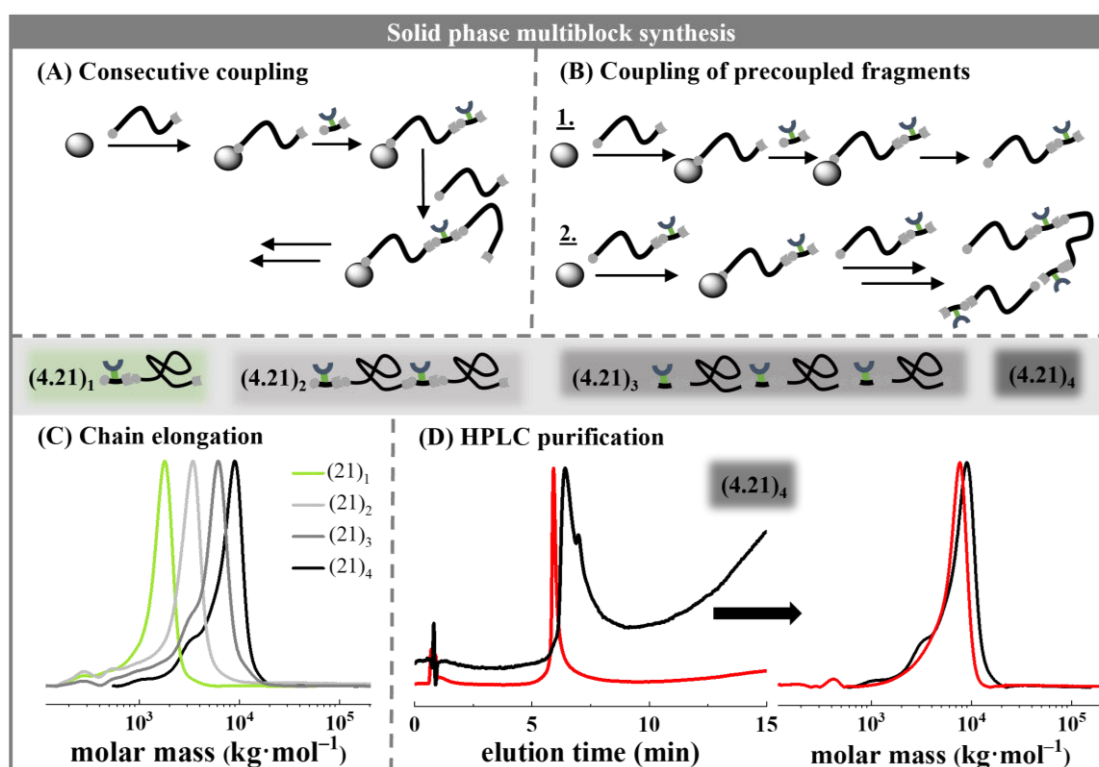


Figure 4.5. Alternative approaches for the synthesis of associating multiblock copolymers by solid phase synthesis: **(A)** Consecutive couplings of the amino acid building blocks or **(B)** use of pre-coupled fragments. **(C)** Chain elongation of the pEG–tpy fragment **4.23** as analyzed by GPC (DMF, pEG calibration). **(D)** HPLC-elugram and GPC molar mass distribution of coupling product **(4.23)**₄ before (black) and after (red) HPLC purification.

4.3 Conclusions

In this project, the solid phase synthesis of sequence-defined, amide bond-containing pEGs with associating terpyridine side-groups is investigated. To implement a synthetic handle that allows to alter the polarity of the sticker microenvironment, three tpy-amino acids with different linkers are synthesized from L-lysine. All tpy-amino acids are shown to be equally suitable for a solid phase amide coupling with pEG amino acid analogous. Besides the variation of the linker type, the sticker spacing can be altered on two different length scales, either by adjusting the molar mass of the pEG amino acid (1k/2k) or by increasing the number of directly neighbouring tpy ligands (1–3). Finally, the solid phase synthesis and chromatographical purification of a multiblock polymer derived from a pre-coupled pEG–tpy amino acid is demonstrated for one representative example.

In future investigations, the optimized synthesis protocol should be applied to the other pEG–tpy fragments to broaden the scope of accessible structures. It could also be an interesting opportunity, to incorporate fluorescent labels in defined positions to study the self-diffusion of the associating chains by microscopic techniques. To reduce inconsistencies regarding the reaction time or the dosage of chemicals, the complete solid phase synthesis should ideally be performed with an automated peptide synthesizer.

One inherent and unavoidable drawback of the presented approach is the limited scalability and low economic and atomic efficiency, which makes it a highly labour- and cost-intensive method. This is especially critical for the intended structure–property relationship studies, which commonly rely on macroscopic methods such as shear rheology. To circumvent the need for large product amounts, a combination with microscopic mechanical testing methods such as atomic force microscopy could be a viable option.¹⁷

Another possibility to increase the available product amount is the avoidance of the particularly low-yielding multiblock formation on the solid support. Instead, the solid phase synthesis could only be used to produce any desired pEG–tpy sequence, which could e.g., include multiple neighboring stickers or additional functional units such as fluorophores or other types of stickers. After deprotection of the *N*-terminus and cleavage from the solid support, the obtained AB-monomer could then be chain-elongated in a simple step-growth polycondensation. The resulting periodic polyamide would however show a broad molar mass distribution. For some research questions, the overall chain dispersity may however not be of great importance or can be easily captured by theoretical models while the incorporated sticker sequence is not accessible by other synthetic methods.

4.4 Experimental Section

4.4.1 General Remarks

Materials

2-Acetylpyridine (Aldrich, > 99%), aqueous ammonia solution (25%, VWR), 7-aminoheptanoic acid (TCI, 98%), *O*-(7-aza-1H-benzotriazol-1-yl)-*N,N,N',N'*-tetramethyluronium hexafluorophosphate (HATU, Alfa Aesar, 99%), benzotriazol-1-yloxy)tripyrrolidinophosphonium hexafluorophosphate (PyBOP, Acros Organics, 99%), *tert*-butyl acrylate (Fluka, 98%), celite (VWR), diisopropylethylamine (VWR, peptide grade), dimethyl aminopyridine (Alfa Aesar, 99%), *N*-(9-fluorenylmethoxycarbonyl)-L-lysine-*O*-*tert*-butyl ester hydrochloride (Fmoc-Lys-*O*-*tert*-Bu·HCl, Iris Biotech, 99.5%), *N*-(9H-fluoren-9-ylmethoxycarbonyloxy) succinimide (Alfa Aesar, 98%), 1,1,1,3,3,3-hexafluoro-2-propanol (HFIP, fluorochem), methanesulfonyl chloride (Acros Organics, 99.5%), 4-nitrophenyl chloroformate (Aldrich, 96%), potassium hydroxide (Aldrich, 85–100%), potassium permanganate (Merck, > 99%), triethylamine (NEt₃, Aldrich, > 99%), triethylene glycol (Sigma Aldrich, anhydrous, >99%), triphenylphosphine (PPh₃, Alfa Aesar, > 99%), triethylsilane (TES, Acros Organics, 99%), sodium (Aldrich, 99.9%) and sodium azide (Alfa Aesar, 99%), thionyl chloride (Acros Organics, 99.5+%) and TentaGel XV TRT-Cl (Rapp Polymere) are used as received. Heterobifunctional polyethylene glycols are purchased from JenKem Technology (Fmoc Amino pEG Carboxyl MW 2000 > 95%) and Iris Biotech (Amino pEG Carboxyl MW 1000, 98.9%) and used without further purification. Trifluoroacetic acid (TFA, VWR, peptide grade) and furfural aldehyde (Acros Organics, 99%) are distilled prior to use. Cyclohexane (Hex, 99.5%), ethyl acetate (EA, 99.8%), dichloromethane (DCM, > 99.5%), methanol (MeOH, HPLC grade), ethanol (EtOH, absolute) and acetonitrile (ACN, HPLC grade) are used as received. Anhydrous dimethylformamide (DMF), acetonitrile (ACN), chloroform (CHCl₃), dichloromethane and tetrahydrofuran (THF) is purchased from Acros Organics (AcroSeal™) and used as received.

Chromatography

Thin-layer chromatography is performed on F₂₅₄ silica gel 60 (Merck) or silica gel 60 RP-18 (Merck) coated plates. Spots are detected with UV-light ($\lambda = 254$ nm) and immersion in KMnO₄ or iron(II)chloride solutions. Flash chromatography is performed on silica gel 60 (40–63 μ m, Merck Millipore) or LiChroprep® RP-18 (40–63 μ m, Merck Millipore). Size exclusion chromatography (SEC) is performed in DMF (+ 1 g·L⁻¹ LiCl) at 60 °C with a 1260 Infinity GPC/SEC-system from Agilent (PSS SECcurity pump, VWR Elite Chrom RI detector) equipped with two PSS GRAM 1000Å and one PSS GRAM 100 Å columns at a flow rate of 1 mL min⁻¹. The data are analyzed with the software PSS WinSEC provided by PSS. The number- and weight average molecular weight (M_n , M_w) and dispersity (\mathcal{D}) are calculated under application of a pEG calibration (standards by PSS).

Analytical and semipreparative HPLC are performed on a JASCO (Tokyo, Japan) LC-4000 system equipped with a binary pump system, an in-line degasser, dynamic mixer, and a UV/VIS-detector. Signals are detected in a range at 210 and 256 nm. The system is operated with the software ChromNAV by JASCO (Version: 2.00.02). For analytical purpose, a reverse phase Luna C₁₈(2) (250 × 4.6 mm), 100 Å pore size, 10 µm particle size, by Phenomenex (Torrance, USA) is used as stationary phase (20 °C, flow rate: 1.5 mL·min⁻¹). Semipreparative HPLC is performed with a Luna C₁₈(2) (250 × 21.2 mm) column with 100 Å pore size, 10 µm particle size, provided by Phenomenex (Torrance, USA). The fractions are collected automatically by a CHF122SC fraction collector (Advantec MFC Inc., Dublin, USA). Acetonitrile (B) and ultrapure water (A), each with 0.1 vol% TFA, are used as eluents.

Characterization techniques

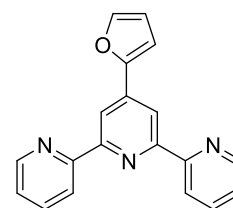
NMR spectra are recorded on a Bruker Avance-III HD 300 or a Bruker Avance-II HD 400 instrument at 20 °C. The chemical shift δ is given in ppm by using tetramethylsilane as internal standard ($\delta = 0$ ppm) and deuterated solvents (CDCl₃, DMSO-*d*₆) as internal reference. The reported signal splittings are abbreviated as follows: s = singlet, d = dublet, t = triplet (*a* = appearing). Coupling constants *J* are reported in Hz. High resolution electron spray mass spectra (HR ESI-MS) are measured with an Agilent 6545 QTOF instrument. Matrix Assisted Laser Desorption/Ionization Time of Flight (MALDI-ToF) measurements are performed on a Bruker autoflex maX MALDI-TOF/TOF instrument. Dithranol is applied as matrix in all cases while THF is used as solvent.

4.4.2 Synthesis of Terpyridine functionalized Amino Acids

[2,2':6',2''-Terpyridine]-4'-carboxylic acid 4.1

Compound 4.27

According to a procedure by Husson *et al.*¹⁸ Furfural is purified by vacuum distillation prior to reaction. 2-Acetylpyridine (20.0 g, 165 mmol, 2.0 eq.) is suspended in ethanol under vigorous stirring (380 mL) and furfural **4.11** (6.90 mL, 82.6 mmol, 1.0 eq.) is added. Shortly after, potassium hydroxide pellets (13.1 g, 227 mmol, 3.0 eq.) and 25% (wt/v) aqueous ammonia

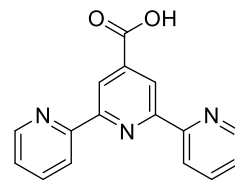


solution (250 mL) are added to the reaction mixture. A dark red solution is stirred at r.t. for 4 h. A colorless solid precipitates from the yellow mixture which is isolated and washed with an ice-cold 50 % (v/v) ethanol/water mixture (300 mL) until the washings are colorless. The solid is dried for 24 h under high vacuum at r.t. and compound **4.27** is obtained as colorless solid. **Yield:** 12.7 g, 43 mmol, 51%. **Molecular Formula:** C₁₉H₁₃N₃O (*M* = 299.3 g·mol⁻¹). **¹H-NMR** (300 MHz, CDCl₃): δ = 8.74 (ddd, ³*J* = 4.8 Hz, ⁴*J* = 1.8 Hz, ⁵*J* = 0.9 Hz, 2H, tpy: C_{6/6''}), 8.72 (s, 2H, tpy: C_{3/3'}), 8.65 (adt (ddd), ³*J* = 8.0 Hz, ⁴*J* = 1.2 Hz, ⁵*J* = 0.9 Hz, 2H, tpy: C_{3/3''}), 7.88 (atd, ³*J* = 7.7 Hz,

$^4J = 1.8$ Hz, 2H, tpy: C_{4/4''}), 7.59 (dd, $^3J = 1.7$ Hz, $^4J = 0.8$ Hz, 1H, OCH), 7.36 (ddd, $^3J = 7.5$ Hz, $^3J = 4.8$ Hz, $^4J = 1.2$ Hz, 2H, tpy: C_{5/5''}), 7.12 (dd, $^3J = 3.4$ Hz, $^4J = 0.8$ Hz, 1H, OCCH), 6.57 (dd, $^3J = 3.4$ Hz, $^3J = 1.7$ Hz, 1H, OCH=CH) ppm. The analytical data complies with literature.¹⁸

[2,2':6',2'']-Terpyridine]-4'-carboxylic acid **4.1**

According to a procedure by Husson *et al.*¹⁸ Compound **4.27** (12.7 g, 43.5 mmol, 1.0 eq.) is suspended in deionized water (710 mL). Potassium hydroxide pellets are added until the pH of the solution is ≈ 10 . Then, potassium permanganate (27.5 g, 173.8 mmol, 4.0 eq.) is

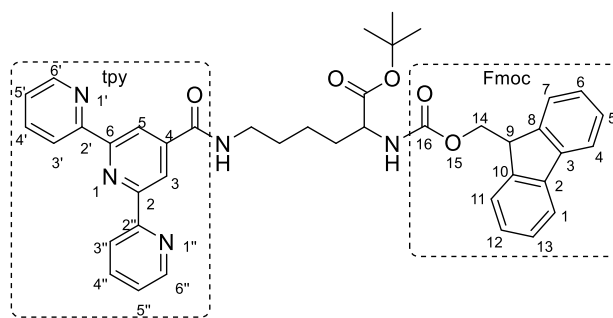


added and the violet mixture is stirred under reflux for 3 h. After cooling to r.t., the brown mixture is filtered through Celite and the Celite pad is washed with deionized water (3 x 60 mL). The pH of the filtrate is adjusted to 5 by dropwise addition of concentrated HCl_{aq} resulting in a colorless precipitate. Precipitation is completed for 12 h at 0 °C. The solid is isolated by filtration and washed thoroughly with demineralised water until the washings are neutral. The solid is dried under high vacuum for 24 h before compound **4.1** is obtained as a colorless solid. **Yield:** 9.75 g, 35.2 mmol, 81%. **Molecular Formula:** C₁₆H₁₁N₃O₂ ($M = 277.3$ g·mol⁻¹). **TLC:** $R_f = 0.36$ (ACN:H₂O = 20:1, SiO₂-RP18). **¹H-NMR, COSY** (300 MHz, DMSO-*d*₆): $\delta = 13.82$ (s, 1H, OH), 8.84 (s, 2H, tpy: C_{3/5'}), 8.75 (m, 2H, tpy: C_{6/6''}), 8.62 (d, $^3J_H = 7.9$ Hz, 2H, tpy: C_{3/3''}), 8.02 (atd, $^3J = 7.7$ Hz, $^4J = 1.8$ Hz, 2H, tpy: C_{4/4''}), 7.53 (m, 2H, tpy: C_{5/5''}) ppm. **¹³C-NMR, HSQC, HMBC** (75 MHz, DMSO-*d*₆): $\delta = 155.7$ (COOH), 154.8 (tpy: C_{2/2''}), 150.7 (tpy: C_{2'/6'}), 149.3 (tpy: C_{6/6''}), 145.1 (tpy: C_{4'}), 137.5 (tpy: C_{4/4''}), 124.6 (tpy: C_{5/5''}), 120.8 (tpy: C_{3/3''}), 114.1 (tpy: C_{3/5'}) ppm. The analytical data complies with literature.¹⁸

Terpyridine-Amino Acid Without an Additional Linker **4.3**

Compound **4.10**

[2,2':6',2'']-Terpyridine]-4'-carboxylic acid **4.1** (1.00 g, 3.58 mmol, 1.0 eq.) is dried under high vacuum for 12 h in a 50 mL Schlenk flask. Fmoc-Lys-O^{tert}Bu·HCl **4.2** (1.65 g, 3.58 mmol, 1.0 eq) is added and the white solids are suspended in anhydrous DMF (6 mL).

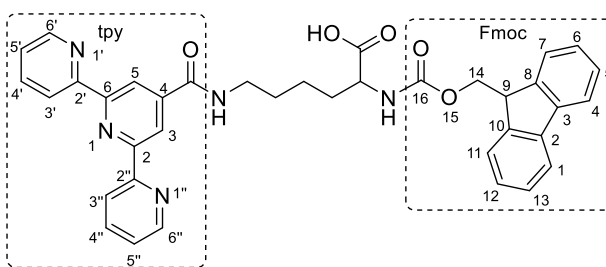


After addition of DIPEA (1.8 mL, 10.8 mmol, 3.0 eq.), the obtained solution is cooled to 0 °C in an ice-bath. HATU (1.50 g, 3.95 mmol, 1.1 eq.) is dissolved in anhydrous DMF (7 mL) and added to the reaction mixture over 30 min. After stirring for another 30 min at 0 °C and 3 h at r.t., EA (50 mL) is added to the clean brown solution. The mixture is washed with 0.1M HCl_{aq}, water and brine (25 mL each) and dried over Na₂SO₄ before the solvent is removed under reduced pressure. The obtained brown solid is recrystallized from a 1:1 mixture ACN and H₂O (30 mL), isolated by

filtration and washed with water (100 mL). Compound **4.10** is obtained as beige solid after drying in high vacuum for 24 h. **Yield:** 1.84 g, 2.69 mmol, 75%. **Molecular formula:** C₄₁H₄₁N₅O₅ ($M = 683.8 \text{ g}\cdot\text{mol}^{-1}$). **TLC:** $R_f = 0.36$ (ACN:H₂O = 4:1, SiO₂-RP18). **ESI-HRMS** (m/z): Calculated for [M+H]⁺: 684.3181, found: 684.3178. **¹H-NMR, COSY** (400 MHz, DMSO-*d*₆): $\delta = 9.10$ (t, ³ $J = 5.6$ Hz, 1H, TpyCONH), 8.84 (s, 2H, tpy: C_{3/5'}), 8.75 (d, ³ $J = 4.8$ Hz, 2H, tpy: C_{6/6''}), 8.64 (d, ³ $J = 7.9$ Hz, 2H, tpy: C_{3/3''}), 8.03 (m, 2H, tpy: C_{4/4''}), 7.86 (d, ³ $J = 7.4$ Hz, 2H, Fmoc: C_{1/4}), 7.68 (d, ³ $J = 7.4$ Hz, 2H, Fmoc: C_{7/11}), 7.53 (dd, ³ $J = 7.5$ Hz, ³ $J = 4.8$ Hz, 2H, tpy: C_{5/5''}), 7.38 (t, ³ $J = 7.4$ Hz, 2H, Fmoc: C_{5/13}), 7.28 (t, ³ $J = 7.4$ Hz, 2H, Fmoc: C_{6/12}), 4.40–4.13 (m, 3H, Fmoc: C₁₄, FmocNH), 4.15–4.05 (m, 1H, Fmoc: C₉), 3.95–3.83 (m, 1H, Lys: CH), 3.25–3.08 (m, 2H, TpyCONHCH₂), 1.84–1.36 (m, 6H, CH₂), 1.36 (s, 9H, CH₃) ppm. **¹³C-NMR, HSQC, HMBC** (101 MHz, DMSO-*d*₆): $\delta = 171.7$ (COO^{tert}Bu), 164.5 (TpyCONH), 156.1 (tpy: C_{2/2''}), 155.7 (tpy: C_{2/6'}), 154.6 (NHCOOFmoc), 149.4 (tpy: C_{6/6''}), 144.2 (tpy: C_{4'}), 143.8 (Fmoc: C_{2/3}), 140.7 (Fmoc: C_{8/10}), 137.5 (tpy: C_{4/4''}), 127.6 (Fmoc: C_{5/13}), 127.0 (Fmoc: C_{6/12}), 125.2 (Fmoc: C_{7/11}), 124.7 (tpy: C_{5/5''}), 121.0 (tpy: C_{3/3''}), 120.1 (Fmoc: C_{1/4}), 118.3 (tpy: C_{3/5'}), 80.4 (C(CH₃)₃), 65.6 (Fmoc: C₁₄), 54.5 (CH), 46.6 (Fmoc: C₉), 39.3 (TpyCONHCH₂), 30.5 (CH₂), 28.5 (CH₂), 27.6 (CH₃), 23.1 (CH₂) ppm.

Compound 4.3

Compound **4.10** (1.84 g, 2.69 mmol, 1.0 eq.) is dissolved in DCM (40 mL) under inert atmosphere before triethyl silane (0.4 mL) is added. Freshly distilled TFA (20 mL) is added dropwise, and the solution is stirred for 7 h at r.t. until full



conversion is indicated by TLC. TFA and DCM are removed under reduced pressure and the obtained yellow oil is freeze dried from a mixture of water and ACN (10:1, 5x) before compound **4.3** is obtained as slight yellow solid. **Yield:** 1.67 g, 2.69 mmol, quant. **Molecular formula:** C₃₇H₃₃N₅O₅ ($M = 627.7 \text{ g}\cdot\text{mol}^{-1}$). **ESI-HRMS** (m/z): Calculated for [M+Na]⁺: 650.2374, found: 650.2366. **¹H-NMR, COSY** (400 MHz, DMSO-*d*₆): $\delta = 9.12$ (t, ³ $J = 5.2$ Hz, 1H, TpyCONH), 8.85 (s, 2H, tpy: C_{3/5'}), 8.78 (m, 2H, tpy: C_{6/6''}), 8.69 (d, ³ $J = 7.9$ Hz, 2H, tpy: C_{3/3''}), 8.10 (m, 2H, tpy: C_{4/4''}), 7.85 (d, ³ $J = 7.4$ Hz, 2H, Fmoc: C_{1/4}), 7.69 (m, 2H, Fmoc: C_{7/11}), 7.57 (dd, ³ $J = 7.6$ Hz, ³ $J = 4.8$ Hz, 2H, tpy: C_{5/5''}), 7.37 (t, ³ $J = 7.4$ Hz, 2H, Fmoc: C_{5/13}), 7.28 (t, ³ $J = 7.4$ Hz, 2H, Fmoc: C_{6/12}), 4.29–4.16 (m, 3H, Fmoc: C₁₄, Fmoc: C₉), 3.95 (m, 1H, Lys: CH), 3.37–3.32 (m, 2H, TpyCONHCH₂), 1.81–1.44 (m, 6H, CH₂) ppm. **¹³C-NMR, HSQC, HMBC** (101 MHz, DMSO-*d*₆): $\delta = 174.0$ (COOH), 164.4 (TpyCONH), 156.2 (tpy: C_{2/2''}), 155.1 (tpy: C_{2/6'}), 154.0 (NHCOOFmoc), 148.9 (tpy: C_{6/6''}), 144.4 (tpy: C_{4'}), 143.8 (Fmoc: C_{2/3}), 140.7 (Fmoc: C_{8/10}), 138.3 (tpy: C_{4/4''}), 127.6 (Fmoc: C_{5/13}), 127.0 (Fmoc: C_{6/12}), 125.3 (Fmoc: C_{7/11}), 125.0 (tpy: C_{5/5''}),

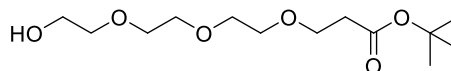
121.4 (tpy: C_{3/3'}), 120.1 (Fmoc: C_{1/4}), 118.7 (tpy: C_{3/5'}), 65.59 (Fmoc: C₁₄), 53.8 (CH), 46.7 (Fmoc: C₉), 39.5 (TpyCONHCH₂), 30.5 (CH₂), 28.5 (CH₂), 23.2 (CH₂) ppm.

Terpyridine-Amino Acid with Hydrophilic Linker 4.6

Compound 4.13

According to a procedure by Seitz and Kunz.¹⁴

Triethylene glycol **4.11** (1.79 mL, 13.3 mmol, 3.3 eq.) is

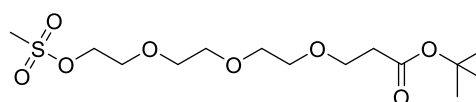


dried in vacuum and then dissolved in anhydrous THF (10 mL). Sodium (3.00 mg, 0.13 mmol, 3 mol%) is inserted into the murky solution before *tert*-butyl acrylate **4.12** (0.68 mL, 4.00 mmol, 1.0 eq.) is added dropwise. The reaction mixture is stirred for 20 h. After addition of 1M hydrochloric acid (0.50 mL), the solvent is removed in vacuum. The residue is dissolved in brine (20.0 mL) and the aqueous phase is extracted with EA (4 x 20.0 mL). The combined organic layers are dried over MgSO₄ and the solvent is removed under reduced pressure. The residue is dried in vacuum and compound **4.13** is obtained as colorless oil. **Yield:** 1.11 g (4.00 mmol, quant.). **Molecular Formula:** C₁₃H₂₆O₆ (*M* = 278.4 g·mol⁻¹). **TLC:** *R*_f = 0.48 (Hex:EA = 1:1, SiO₂). **¹H-NMR, COSY:** (300 MHz, CDCl₃): δ = 3.74–3.56 (m, 14H, CH₂O), 2.63 (s, 1H, OH), 2.49 (t, ³*J* = 6.6 Hz, 2H, CH₂COO^{tert}Bu), 1.42 (s, 9H, CH₃) ppm. **¹³C-NMR, HSQC, HMBC:** (75 MHz, CDCl₃): δ = 170.96 (COO^{tert}Bu), 80.57 (C(CH₃)₃), 77.16 (CH₂O), 72.60 (CH₂O), 70.60 (CH₂O), 70.46 (CH₂O), 70.32 (CH₂O), 66.88 (CH₂O), 61.66 (CH₂O), 36.20 (CH₂COO^{tert}Bu), 28.09 (CH₃) ppm.

Compound 4.14

According to a procedure by Maggi *et al.*¹⁹

Compound **4.13** (7.50 g, 27.0 mmol, 1.0 eq.) is dried in high vacuum and dissolved in anhydrous CHCl₃

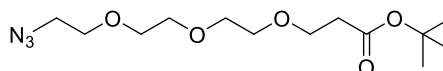


(20.0 mL) under inert atmosphere. Triethyl amine (7.48 mL, 54.0 mmol, 2.0 eq.) is added using a syringe. The mixture is cooled in an ice-bath and a solution of mesyl chloride (2.50 mL, 32.4 mmol, 1.2 eq.) in CHCl₃ (5.0 mL) is added dropwise. The reaction mixture is stirred under cooling for 30 min, before the ice is removed, and the solution is stirred for another 12 h at r.t. The mixture is diluted with CHCl₃ (25.0 mL) and washed with saturated NaHCO₃ solution, water and brine (50.0 mL each). The organic phase is dried over Na₂SO₄ before the solvent is removed under reduced pressure. The product **4.14** is obtained as light-yellow oil. **Yield:** 8.91 g (25.0 mmol, 92 %). **Molecular Formula:** C₁₄H₂₈O₈S (*M* = 356.4 g·mol⁻¹). **TLC:** *R*_f = 0.21 (Hex:EA = 2:1, SiO₂). **¹H-NMR:** (300 MHz, CDCl₃): δ = 4.30–4.25 (m, 2H, CH₂OS), 3.69–3.47 (m, 12H, CH₂O), 2.98 (s, 3H, SCH₃), 2.38 (t, ³*J* = 6.2 Hz, 2H, (CH₂COO^{tert}Bu), 1.34 (s, 9H, C(CH₃)₃) ppm.

Compound 4.15

According to a modified procedure by Tavernaro *et al.*²²

The mesylate **4.14** (8.91 g, 25.0 mmol, 1.0 eq.) is

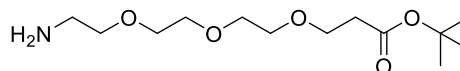


dissolved in anhydrous DMF (15.0 mL) under inert atmosphere. Sodium azide (9.60 g, 150 mmol, 6.0 eq.) is added and the orange reaction mixture is stirred at 60 °C for 15 h. The solvent is removed in vacuum by co-rotation with toluene (3 x 20.0 mL each). The residue is dissolved in brine (20.0 mL) and extracted with DCM (5 x 20.0 mL each). The combined organic phases are dried over Na₂SO₄ before the solvent is removed in vacuum and compound **4.15** is obtained as orange oil. **Yield:** 7.44 g (24.5 mmol, 98 %). **Molecular Formula:** C₁₃H₂₅N₃O₅ (*M* = 303.4 g·mol⁻¹). **TLC:** *R*_f = 0.25 (Hex:EA = 3:1, SiO₂). **¹H-NMR** (300 MHz, CDCl₃): δ = 3.77–3.53 (m, 12H, CH₂O), 3.39 (t, ³*J* = 5.1 Hz, 2H, CH₂N₃), 2.50 (t, ³*J* = 6.6 Hz, 2H, CH₂COO^{tert}Bu), 1.44 (s, 9H, CH₃) ppm. **¹³C-NMR, HSQC, HMBC:** (75 MHz, CDCl₃): δ = 170.4 (COO^{tert}Bu), 79.7 (C(CH₃)₃), 69.8 (CH₂O), 69.9 (CH₂O), 69.7 (CH₂O), 69.7 (CH₂O), 69.3 (CH₂O), 66.2 (CH₂O), 50.0 (CH₂N₃), 35.8 (CH₂COO^{tert}Bu), 27.7 (CH₃) ppm.

Compound 4.4

According to a modified procedure by Maduskuie *et*

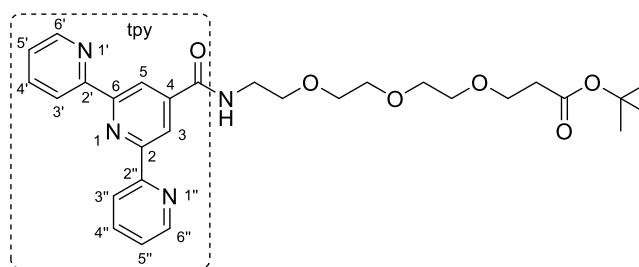
*al.*²⁰ Triphenylphosphine (7.05 g, 26.9 mmol, 1.1 eq) is



added to a stirred solution of compound **4.15** (7.40 g, 24.4 mmol, 1.0 eq) in THF (50.0 mL) at 0 °C under inert atmosphere. The yellow reaction mixture is allowed to warm up to r.t. and stirred for another 12 h. The solution is diluted with water (50.0 mL) and stirred for an additional 12 h before 1M hydrochloric acid is added until the pH is adjusted to 3. The reaction mixture is washed with toluene (3 x 20.0 mL) and the water is removed by lyophilisation. Compound **4.4** is obtained as light-yellow oil. **Yield:** 7.27 g (26.2 mmol, 97 %). **Molecular Formula:** C₁₃H₂₇NO₅ (*M* = 277.4 g·mol⁻¹). **TLC:** *R*_f = 0.15 (ACN:H₂O = 100:1, SiO₂-RP18), 0.88 (DCM:MeOH = 25:1, SiO₂). **¹H-NMR:** (300 MHz, DMSO-*d*₆): δ = 3.63–3.42 (m, 12H, CH₂O) 2.92 (t, ³*J* = 5.8 Hz, 2H, CH₂NH₂), 2.41 (t, ³*J* = 6.2 Hz, 2H, CH₂COO^{tert}Bu), 1.39 (s, 9H, CH₃) ppm. **¹³C NMR, HSQC, HMBC:** (75 MHz, DMSO-*d*₆): δ = 170.36 (COO^{tert}Bu), 79.7 (C(CH₃)₃), 69.8 (CH₂O), 69.7 (CH₂O), 69.7 (CH₂O), 69.3 (CH₂O), 66.3 (CH₂O), 38.4 (CH₂NH₂), 35.9 (CH₂COO^{tert}Bu), 27.8 (CH₃) ppm.

Compound 4.16

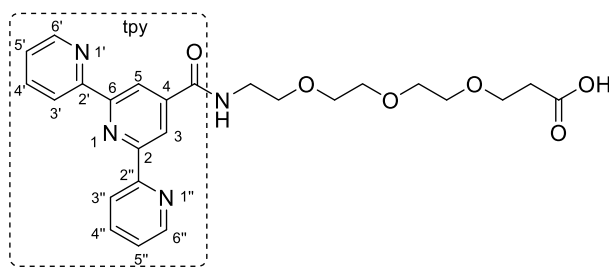
Terpyridine carboxylic acid **4.1** (4.00 g, 14.4 mmol, 1.0 eq.) is heated under reflux in thionyl chloride (31.4 mL, 433 mmol, 30.0 eq.) for 3 h under inert atmosphere. The excess thionyl chloride



is removed by distillation before the light brown acid chloride is dried in high vacuum for 1 h and dissolved in anhydrous DCM (30.0 mL). Freshly dried amine **4.4** (5.19 g, 18.8 mmol, 1.3 eq.) and DIPEA (4.17 mL, 24.5 mmol, 1.7 eq.) are separately dissolved in anhydrous DCM (30.0 mL each). The resulting solutions of DIPEA and amine **4.4** are consecutively added to the acid chloride under ice cooling. The resulting orange solution is stirred at r.t. for 48 h. The reaction mixture is quenched with a saturated NaHCO₃ solution (15.0 mL). The aqueous layer is extracted with DCM (3 x 50.0 mL). The combined organic layers are washed with brine (15.0 mL) and dried over Na₂SO₄ before the solvent is removed under reduced pressure. The raw product (8.49 g) is purified by column chromatography (ACN:H₂O = 3:2; SiO₂-RP18). Product **4.16** is obtained as light-yellow oil after lyophilization. **Yield:** 6.38 g (11.9 mmol, 83 %). **Molecular Formula:** C₂₉H₃₆N₄O₆ (*M* = 536.6 g·mol⁻¹). **TLC:** *R*_f = 0.50 (ACN:H₂O = 3:2, SiO₂-RP18), 0.38 (DCM:MeOH = 25:1, SiO₂). **ESI-HRMS** (*m/z*): Calculated for [M+H]⁺: 537.2713, found: 537.2706. **¹H-NMR:** (300 MHz, DMSO-*d*₆): δ = 8.81 (s, 2H, tpy: C_{3/5'}), 8.72 (m, tpy: C_{6/6''}), 8.63–8.60 (m, 2H, tpy: C_{3/3''}), 7.88 (*atd*, ³*J* = 7.6 Hz, ³*J* = 1.8 Hz, 2H, tpy: C_{4/4''}), 7.36 (ddd, ³*J* = 7.6 Hz, ³*J* = 4.8 Hz, ⁴*J* = 1.2 Hz, 2H, tpy: C_{5/5''}), 3.80–3.53 (m, 14H, CH₂O), 2.43 (t, ³*J* = 6.6 Hz, 2H, CH₂COO^{*tert*}Bu), 1.40 (s, 9H, CH₃) ppm. **¹³C-NMR, HSQC, HMBC:** (75 MHz, DMSO-*d*₆): δ = 170.4 (COO^{*tert*}Bu), 164.8 (TpyCONH), 155.7 (tpy: C_{2/6'}), 154.6 (NHCOOFmoc), 149.4 (tpy: C_{6/6''}), 144.0 (tpy: C_{4'}), 137.5 (tpy: C_{4/4''}), 124.7 (tpy: C_{5/5''}), 121.0 (tpy: C_{3/3''}), 118.3 (tpy: C_{3/5'}), 79.7 (C(CH₃)₃), 69.7 (CH₂O), 69.6 (CH₂O), 68.7(CH₂O), 66.2 (CH₂O), 35.8 (CH₂COO^{*t*}Bu), 27.7 (CH₃) ppm.

Compound 4.5

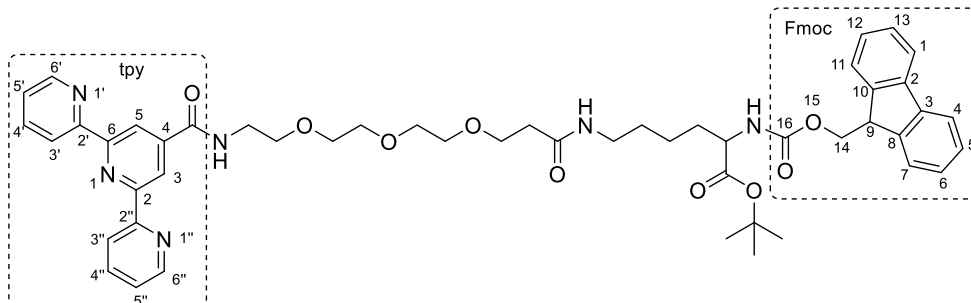
Compound **4.16** (6.10 g, 11.4 mmol, 1.0 eq.) is dissolved in DCM (50.0 mL, *c* = 0.22M) under inert atmosphere and cooled in an ice-bath to 0 °C before TES (1.0 mL, 6.4 mmol, 0.6 eq.) and TFA (25.4 mL, 332 mmol, 29 eq.) are added. The reaction mixture is



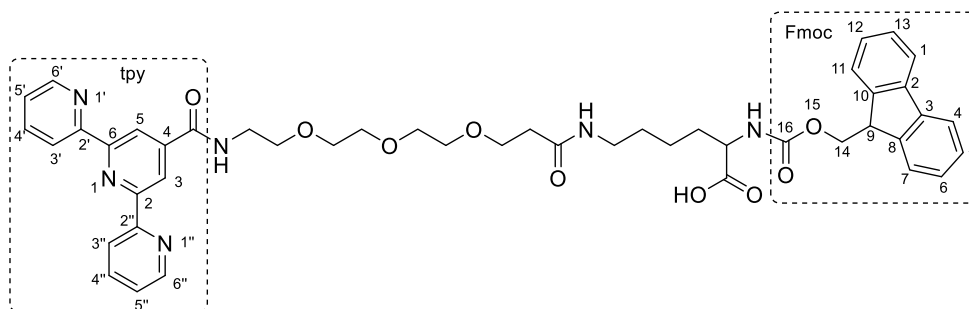
allowed to warm to r.t. and stirred for 3 h until full conversion is indicated by TLC. Afterwards, TFA and DCM are removed under reduced pressure. The residue is dissolved in an ACN/H₂O mixture (1:2) and lyophilized (5 x) to remove TFA traces. Compound **4.5** is obtained as a yellow oil. **Yield:** 5.47 g (11.4 mmol, quant.). **Molecular Formula:** C₂₅H₂₈N₄O₆ (*M* = 480.2 g·mol⁻¹). **TLC:** *R*_f = 0.52 (ACN:H₂O = 4:1., SiO₂-RP18). **ESI-HRMS** (*m/z*): Calculated for [M+H]⁺: 481.2087, found: 481.2089. **¹H-NMR, COSY** (400 MHz, DMSO-*d*₆): δ = 11.2 (s, 2H, COOH), 9.18 (t, ³*J* = 5.5 Hz, CONH), 8.86 (s, 2H, tpy: C_{3/5'}), 8.81 (m, 2H, tpy: C_{6/6''}), 8.73 (d, ³*J*_H = 7.8 Hz, 2H, tpy: C_{3/3''}), 8.14 (*atd*, ³*J* = 7.8 Hz, ⁴*J* = 1.8 Hz, 2H, tpy: C_{4/4''}), 7.62 (m, 2H, tpy: C_{5/5''}), 3.63–3.44 (m, 14H, CH₂O), 2.40 (t, ³*J* = 6.3 Hz, 2H, CH₂COOH) ppm. **¹³C-NMR, HSQC,**

HMBC (101 MHz, DMSO-*d*₆): δ = 173.1 (COOH), 165.0 (CONH), 155.3 (tpy: C_{2/2''}), 154.0 (tpy: C_{2'/6'}), 149.1 (tpy: C_{6/6''}), 144.7 (tpy: C_{4'}), 139.2 (tpy: C_{4/4''}), 125.6 (tpy: C_{5/5''}), 122.0 (tpy: C_{3/3''}), 119.4 (tpy: C_{3'/5'}), 70.2 (CH₂O), 70.1 (CH₂O), 69.1 (CH₂O), 66.7 (CH₂O), 35.2 (CH₂COOH) ppm.

Compound 4.17



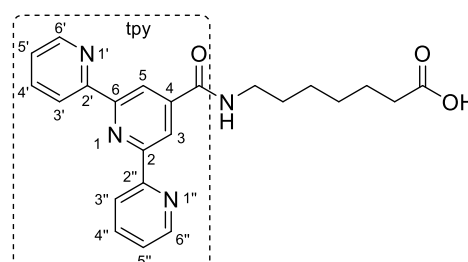
Compound **4.5** (2.83 g, 5.88 mmol, 1.0 eq.) is dissolved in anhydrous DCM (150.0 mL) under inert atmosphere in a flame-dried 500 mL Schlenk flask and cooled to 0 °C in an ice-bath. HATU (2.46 g, 6.46 mmol, 1.1 eq.) and DIPEA (4.09 mL, 23.5 mmol, 4.0 eq.) are added and the yellow solution is stirred for 15 min, before a solution of Fmoc-Lys-*O*^{tert}Bu·HCl **4.2** (2.71 g, 5.88 mmol, 1.0 eq) in DCM (50 mL) is added dropwise over a dripping funnel. After stirring for 18 h at r.t., the solvent is removed and the crude product is purified by column chromatography (ACN:H₂O = 4:1; SiO₂-RP18). Compound **4.17** is isolated as white solid by lyophilization. **Yield:** 3.49 g (3.93 mmol, 67%). **Molecular Formula:** C₅₀H₅₈N₆O₉ (*M* = 887.1 g·mol⁻¹). **TLC:** *R*_f = 0.25 (ACN:H₂O = 4:1., SiO₂-RP18). **ESI-HRMS** (*m/z*): Calculated for [M+Na]⁺: 909.4162, found: 909.4147. **¹H-NMR, COSY** (400 MHz, DMSO-*d*₆): δ = 9.16 (t, ³*J* = 5.5 Hz, TpyCONH), 8.83 (s, 2H, tpy: C_{3'/5'}), 8.76 (³*J* = 4.8 Hz, ⁴*J* = 1.8 Hz, ⁵*J* = 0.9 Hz, 2H, tpy: C_{6/6''}), 8.65 (adt, ³*J* = 8.0 Hz, *J* = 1.1 Hz, 2H, tpy: C_{3/3''}), 8.04 (atd, ³*J* = 7.7 Hz, ⁴*J* = 1.8 Hz, 2H, tpy: C_{4/4''}), 7.88 (d, ³*J* = 7.5 Hz, 2H, Fmoc: C_{1/4}), 7.79 (t, ³*J* = 5.7 Hz, 1H, CONH), 7.72 (d, ³*J* = 7.4 Hz, 2H, Fmoc: C_{7/11}), 7.62 (d, ³*J* = 7.8 Hz, 1H, FmocNH), 7.54 (ddd, ³*J* = 7.5 Hz, ³*J* = 4.8 Hz, ⁴*J* = 1.1 Hz, 2H, tpy: C_{5/5''}), 7.40 (m, 2H, Fmoc: C_{5/13}), 7.33 (m, 2H, Fmoc: C_{6/12}), 4.34–4.18 (m, 3H, Fmoc: C_{9/14}), 3.81 (m, 1H, Lys: CH), 3.60–3.43 (m, 14H, CH₂O), 3.00 (m, 2H, CH₂NHCO), 2.25 (t, ³*J* = 5.5 Hz, 2H, CH₂NHCOTpy), 1.69–1.22 (m, 6H, CH₂), 1.36 (s, 9H, CH₃) ppm. **¹³C-NMR, HSQC, HMBC** (101 MHz, DMSO-*d*₆): δ = 175.1 (COO^{tert}Bu), 169.8 (TpyCONH), 164.8 (tpy: C_{2/2''}), 155.7 (tpy: C_{2'/6'}), 154.6 (NHCOFmoc), 149.4 (tpy: C_{6/6''}), 144.1 (tpy: C_{4'}), 142.6 (Fmoc: C_{2/3}), 139.4 (Fmoc: C_{8/10}), 137.6 (tpy: C_{4/4''}), 128.9 (Fmoc: C_{5/13}), 127.3 (Fmoc: C_{6/12}), 125.2 (Fmoc: C_{7/11}), 124.7 (tpy: C_{5/5''}), 121.4 (tpy: C_{3/3''}), 120.0 (Fmoc: C_{1/4}), 118.3 (tpy: C_{3/5'}), 80.4 (C(CH₃)₃), 69.7 (CH₂O), 69.5 (CH₂O), 68.7 (CH₂O), 66.9 (CH₂O), 65.6 (Fmoc: C₁₄), 54.5 (CH), 46.7 (Fmoc: C₉), 39.5 (CH₂O), 38.4 (CH₂O), 38.2 (CH₂O), 36.2 (CH₂CONH), 34.8 (CH₂), 29.1 (CH₂), 28.1, (CH₃), 23.0 (CH₂) ppm.

Compound 4.6

Compound **4.17** (1.70 g, 1.92 mmol, 1.0 eq.) is dissolved in DCM (17.0 mL, $c = 0.11\text{M}$) under inert atmosphere and cooled in an ice-bath to $0\text{ }^{\circ}\text{C}$ before TES (0.34 mL, 2.1 mmol, 1.1 eq.) and TFA (8.50 mL, 111 mmol, 58 eq.) are added. The reaction mixture is allowed to warm to r.t. and stirred for 2 h until full conversion is indicated by TLC. Afterwards, TFA and DCM are removed under reduced pressure. The residue is dissolved in an ACN/H₂O mixture (1:1) and lyophilized (5 x) to remove TFA traces. Compound **4.6** is finally obtained as a slight yellow solid. **Yield:** 1.59 g (1.9 mmol, quant.). **Molecular Formula:** C₄₆H₅₀N₆O₉ ($M = 830.9\text{ g}\cdot\text{mol}^{-1}$). **TLC:** $R_f = 0.61$ (ACN:H₂O = 4:1., SiO₂-RP18). **ESI-HRMS** (m/z): Calculated for $[\text{M}+\text{Na}]^+$: 853.3537, found: 853.3522. **¹H-NMR, COSY** (400 MHz, DMSO-*d*₆): $\delta = 9.19$ (t, $^3J = 5.5$ Hz, TpyCONH), 8.87 (s, 2H, tpy: C_{3'/5'}), 8.82 (m, 2H, tpy: C_{6/6''}), 8.76 (adt, $^3J = 8.0$ Hz, $J = 1.1$ Hz, 2H, tpy: C_{3/3''}), 8.18 (atd, $^3J = 7.8$ Hz, $^4J = 1.7$ Hz, 2H, tpy: C_{4/4''}), 7.86 (d, $^3J = 7.5$ Hz, 2H, Fmoc: C_{1/4}), 7.81 (m, 1H, CONH), 7.71 (m, 2H, Fmoc: C_{7/11}), 7.66 (m, 2H, tpy: C_{5/5''}), 7.61 (d, 1H, FmocNH), 7.39 (m, 2H, Fmoc: C_{5/13}), 7.31 (m, 2H, Fmoc: C_{6/12}), 4.27–4.20 (m, 3H, Fmoc: C_{9/14}), 3.90 (m, 1H, CH₂), 3.62–3.39 (m, 14H, CH₂O), 3.01 (m, 2H, CH₂NHCO), 2.26 (t, $^3J = 6.4$ Hz, 2H, CH₂NHCOTpy), 1.74–1.26 (m, 6H, CH₂) ppm. **¹³C-NMR, HSQC, HMBC** (101 MHz, DMSO-*d*₆): $\delta = 174.0$ (COOH), 169.8 (TpyCONH), 164.7 (tpy: C_{2/2''}), 156.2, 155.4 (tpy: C_{2'/6'}), 154.3 (NHCOOFmoc), 149.2 (tpy: C_{6/6''}), 144.1 (tpy: C_{4'}), 143.8 (Fmoc: C_{2/3}), 140.7 (Fmoc: C_{8/10}), 137.9 (tpy: C_{4/4''}), 127.6 (Fmoc: C_{5/13}), 127.1 (Fmoc: C_{6/12}), 125.3 (Fmoc: C_{7/11}), 124.9 (tpy: C_{5/5''}), 121.2 (tpy: C_{3/3''}), 120.1 (Fmoc: C_{1/4}), 118.5 (tpy: C_{3/5'}), 69.7 (CH₂O), 69.6 (CH₂O), 69.5 (CH₂O), 68.6 (CH₂O), 66.9 (CH₂O), 65.6 (Fmoc: C₁₄), 53.8 (CH), 46.7 (Fmoc: C₉), 39.5 (CH₂O), 38.2 (CH₂O), 36.2 (CH₂CONH), 30.4 (CH₂), 28.7 (CH₂), 23.1 (CH₂) ppm.

Terpyridine-Amino Acid with Hydrophobic Linker 4.9**Compound 4.8**

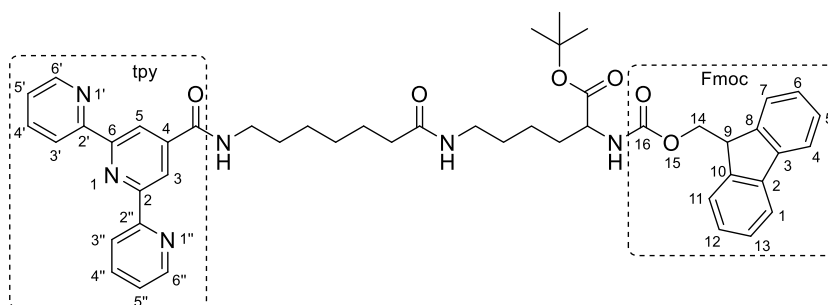
According to a modified procedure by Keillor *et al.*¹⁵ Terpyridine carboxylic acid **4.1** (2.00 g, 7.21 mmol, 1.0 eq.) is dried in vacuum for 12 h and then suspended in anhydrous ACN (200 mL) under inert atmosphere. After addition of DIPEA (1.35 mL,



7.93 mmol, 1.1 eq.), the obtained solution is cooled in an ice-bath and 4-nitrophenyl chloroformate (1.61 g, 7.93 mmol, 1.1 eq.) is added. Five minutes later, DMAP (0.090 mg, 0.72 mmol, 0.1 eq.) is inserted, before ice-bath is removed and the yellow solution is stirred for 50 min until TLC indicated complete conversion of **4.1**. Next, 7-amino heptanoic acid **4.7** is dissolved in water (200 mL) before DIPEA (2.8 mL, 16.6 mmol, 2.3 eq.) is added and the obtained solution is dropped into the chloroformate solution over 30 min. After stirring over night, the reaction mixture is filtered and the solvent is removed under reduced pressure. Then, water (100 mL) is added and the pH is adjusted to ≈ 5 with 6N HCl_{aq}. The precipitate is completed at 0 °C for 12 h before the solid is isolated by filtration and recrystallized from MeOH (30 mL). **Yield:** 2.31 g (5.71 mmol, 79%). **Molecular formula:** C₂₃H₂₄N₄O₃ ($M = 404.5 \text{ g}\cdot\text{mol}^{-1}$). **TLC:** $R_f = 0.40$ (ACN:H₂O = 4:1, SiO₂-RP8). **ESI-HRMS** (m/z): Calculated for [M+Na]⁺: 427.1740, found: 427.1731. **¹H-NMR, COSY** (300 MHz, DMSO-*d*₆): $\delta = 11.99$ (s, 1H, COOH), 9.08 (t, $^3J = 5.6$ Hz, 1H, TpyCONH), 8.82 (s, 2H, tpy: C_{3'/5'}), 8.77 (ddd, $^3J = 4.8$ Hz, $^4J = 1.8$ Hz, $^5J = 0.9$ Hz, 2H, tpy: C_{6/6''}), 8.65 (dt, $^3J = 7.9$ Hz, $^4J = 1.1$ Hz, 2H, tpy: C_{3/3''}), 8.04 (atd, 2H, $^3J = 7.7$ Hz, $^4J = 1.8$ Hz, tpy: C_{4/4''}), 7.53 (ddd, $^3J = 7.6$ Hz, $^3J = 4.8$ Hz, $^4J = 1.1$ Hz, 2H, tpy: C_{5/5''}), 3.31 (m, 2H, CH₂NH), 2.21 (t, $^3J = 7.3$ Hz, 2H, CH₂COOH), 1.55 (m, 4H, CH₂), 1.34 (m, 4H, CH₂) ppm. **¹³C-NMR, COSY** (300 MHz, DMSO-*d*₆): $\delta = 174.5$ (COOH), 164.6 (TpyCONH), 155.7 (tpy: C_{2'/6'}), 154.6 (NHCOOFmoc), 149.4 (tpy: C_{6/6''}), 144.3 (tpy: C_{4'}), 137.6 (tpy: C_{4/4''}), 124.7 (tpy: C_{5/5''}), 121.0 (tpy: C_{3/3''}), 118.3 (tpy: C_{3/5'}), 39.7 (CH₂NH), 33.7 (CH₂COOH), 28.8 (CH₂), 28.3 (CH₂), 26.3 (CH₂), 24.5 (CH₂) ppm.

Compound 4.18

Compound **4.8** (0.60 g, 1.48 mmol, 1.0 eq.) is dissolved in anhydrous DMF (5.0 mL) under inert atmosphere in a flame-dried 50 mL Schlenk flask and

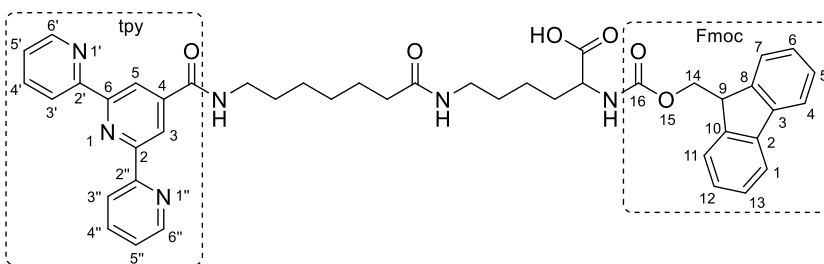


cooled to 0 °C in an ice-bath. DIPEA (1.0 mL, 5.93 mmol, 4.0 eq.) and a solution of HATU (0.62 g, 1.63 mmol, 1.1 eq.) in DMF (3 mL) are added and the brown solution is stirred for 30 min at 0 °C. Afterwards, a solution of Fmoc-Lys-O^{tert}Bu·HCl **4.2** (0.683 g, 1.48 mmol, 1.0 eq.) in DMF (5 mL) is added and the reaction mixture is stirred for 14 h at r.t. The orange solution is diluted with DCM (100 mL) and washed with water (50 mL) and brine (50 mL) before the organic phase is dried over Na₂SO₄ and the solvent is removed under reduced pressure. The crude product is recrystallized twice from a ACN/H₂O mixture (1:1) and finally dried under vacuum. **Yield:** 0.925 g (1.14 mmol, 77%). **Molecular Formula:** C₄₈H₅₄N₆O₆ ($M = 811.0 \text{ g}\cdot\text{mol}^{-1}$). **TLC:**

$R_f = 0.23$ (ACN:H₂O = 4:1., SiO₂-RP18). **ESI-HRMS** (m/z): Calculated for [M+Na]⁺: 833.4003, found: 833.3990. **¹H-NMR, COSY** (400 MHz, DMSO-*d*₆): $\delta = 9.07$ (t, ³ $J = 5.5$ Hz, 1H, TpyCONH), 8.82 (s, 2H, tpy: C_{3'/5'}), 8.76 (ddd, ³ $J = 4.8$ Hz, ⁴ $J = 1.8$ Hz, ⁵ $J = 0.9$ Hz, 2H, tpy: C_{6/6''}), 8.65 (adt, ² $J = 8.0$ Hz, $J = 1.1$ Hz, 2H, tpy: C_{3/3''}), 8.04 (atd, ³ $J = 7.7$ Hz, ⁴ $J = 1.8$ Hz, 2H, tpy: C_{4/4''}), 7.88 (d, ³ $J = 7.5$ Hz, 2H, Fmoc: C_{1/4}), 7.72 (m, 2H, Fmoc: C_{7/11}), 7.63 (d, ³ $J = 7.6$ Hz, 1H, FmocNH), 7.53 (ddd, ³ $J = 7.7$ Hz, ³ $J = 4.8$ Hz, ⁴ $J = 1.1$ Hz, 2H, tpy: C_{5/5''}), 7.40 (m, 2H, Fmoc: C_{5/13}), 7.31 (m, 2H, Fmoc: C_{6/12}), 4.30–4.20 (m, 3H, Fmoc: C_{9/14}), 3.83 (m, 1H, Lys: CH), 3.31 (m, 2H, CH₂NHCOTpy), 3.01 (m, 2H, CH₂NHCO), 2.05 (m, 2H, CH₂CONH), 1.58–1.50 (m, 6H, CH₂), 1.37 (s, 9H, CH₃), 1.36–1.18 (m, 8H, CH₂) ppm. **¹³C-NMR, HSQC, HMBC** (101 MHz, DMSO-*d*₆): $\delta = 171.9$ (COO^{tert}Bu), 164.5 (TpyCONH), 156.1 (tpy: C_{2/2''}), 155.7 (tpy: C_{2'/6'}), 154.6 (NHCOOFmoc), 149.4 (tpy: C_{6/6''}), 144.3 (tpy: C_{4'}), 143.8 (Fmoc: C_{2/3}), 140.7 (Fmoc: C_{8/10}), 137.6 (tpy: C_{4/4''}), 127.6 (Fmoc: C_{5/13}), 127.0 (Fmoc: C_{6/12}), 125.2 (Fmoc: C_{7/11}), 124.7 (tpy: C_{5/5''}), 121.0 (tpy: C_{3/3''}), 120.1 (Fmoc: C_{1/4}), 118.3 (tpy: C_{3/5'}), 80.4 (C(CH₃)₃), 65.6 (Fmoc: C₁₄), 54.5 (CH), 46.7 (Fmoc: C₉), 39.5 (TpyCONHCH₂), 38.1 (CH₂), 35.4 (CH₂), 30.5 (CH₂), 28.8 (CH₂), 28.5 (CH₂), 27.6 (CH₃), 26.3 (CH₂), 25.3 (CH₂), 23.0 (CH₂) ppm.

Compound 4.9

Compound **4.18**
(0.915 g, 1.13 mmol,
1.0 eq.) is dissolved in
DCM (20.0 mL,
 $c = 0.06$ M) under inert
atmosphere and cooled



in an ice-bath to 0 °C before TES (0.2 mL, 1.2 mmol, 1.0 eq.) and TFA (10 mL, 130 mmol, 115 eq.) are added. The reaction mixture is allowed to warm to r.t. and stirred for 6 h until full conversion is indicated by TLC. TFA and DCM are removed under reduced pressure. The residue is dissolved in H₂O and lyophilized (5 x) to remove TFA traces before compound **4.9** is finally obtained as a yellow powder. **Yield:** 0.85 g (1.1 mmol, quant.). **Molecular Formula:** C₄₄H₄₆N₆O₆ ($M = 754.9$ g·mol⁻¹). **TLC:** $R_f = 0.51$ (ACN:H₂O = 4:1., SiO₂-RP18). **ESI-HRMS** (m/z): Calculated for [M+Na]⁺: 777.3377, found: 777.3359. **¹H-NMR, COSY** (400 MHz, DMSO-*d*₆): $\delta = 9.33$ (t, ³ $J = 5.5$ Hz, 1H, TpyCONH), 9.03 (s, 2H, tpy: C_{3'/5'}), 8.99 (d, m, 2H, tpy: C_{6/6''}), 8.93 (m, 2H, tpy: C_{3/3''}), 8.04 (m, 2H, tpy: C_{4/4''}), 7.88–7.80 (m, 5H, Fmoc: C_{1/4/7/11}, FmocNH), 7.71 (m, 2H, tpy: C_{5/5''}), 7.40 (m, 2H, Fmoc: C_{5/13}), 7.31 (m, 2H, Fmoc: C_{6/12}), 4.29–4.17 (m, 3H, Fmoc: C_{9/14}), 3.92 (m, 1H, Lys: CH), 3.35 (m, 2H, CH₂NHCOTpy), 3.01 (m, 2H, CH₂NHCO), 2.05 (m, 2H, CH₂CONH), 1.59–1.19 (m, 16H, CH₂) ppm. **¹³C-NMR, HSQC, HMBC** (101 MHz, DMSO-*d*₆): $\delta = 172.0$ (COOH), 164.5 (TpyCONH), 156.2 (tpy: C_{2/2''}), 155.3 (tpy: C_{2'/6'}), 154.2 (NHCOOFmoc), 149.1 (tpy: C_{6/6''}), 144.4 (tpy: C_{4'}), 143.8 (Fmoc: C_{2/3}), 140.7 (Fmoc: C_{8/10}),

138.1 (tpy: C_{4/4'}), 127.6 (Fmoc: C_{5/13}), 127.1 (Fmoc: C_{6/12}), 125.3 (Fmoc: C_{7/11}), 124.9 (tpy: C_{5/5'}), 121.2 (tpy: C_{3/3'}), 120.1 (Fmoc: C_{1/4}), 118.3 (tpy: C_{3/5}), 65.6 (Fmoc: C₁₄), 54.5 (CH), 46.7 (Fmoc: C₉), 39.5 (TpyCONHCH₂), 38.2 (CH₂), 35.4 (CH₂), 30.4 (CH₂), 28.8 (CH₂), 28.5 (CH₂), 26.3 (CH₂), 25.3 (CH₂), 23.1 (CH₂) ppm.

4.4.3 Poly(ethylene glycol) Functionalization 4.19

α -Amino-pEG₂₄- ω -propionic acid (4.00 g, 3.49 mmol, 1.0 eq.) is dissolved in water (30 mL) before Na₂CO₃ (1.93 g, 14.0 mmol, 4.0 eq.) is added. The polymer solution is cooled in an ice-bath and a solution of *N*-(9H-fluoren-9-ylmethoxycarbonyloxy) succinimide (2.35 g, 6.98 mmol, 2 eq.) in 1,4-dioxan (30 mL) is added dropwise. The reaction mixture is stirred for 4 h at 0 °C and for 18 h at r.t., quenched with 1M HCl (20 mL) and extracted with DCM (5 x 100 mL). The combined organic phases are dried over Na₂SO₄, concentrated under reduced pressure, and precipitated into ice-cold Et₂O (2 L). The product **4.19** is isolated by filtration and lyophilized from water (3.82 g, 96%). **Molecular Formula:** C₆₆H₁₁₃N₆O₂₈ (*M* = 1368 g·mol⁻¹). **¹H NMR** (400 MHz, DMSO-*d*₆): δ = 7.89 (d, ³*J* = 7.6 Hz, 2H, Fmoc: C_{1/4}), 7.69 (d, 2H, Fmoc: C_{7/11}), 7.41 (m, 2H, Fmoc: C_{5/13}), 7.33 (m, 2H, Fmoc: C_{6/12}), 4.28 (m, 2H, Fmoc: C₁₄), 4.21 (m, 1H, Fmoc: C₉), 3.65–3.37 (m, 103H, CH₂O), 3.13 (m, 2H,), 2.36 (t, ³*J* = 6.6 Hz, 2H, CH₂COOH) ppm.

4.4.4 Solid Phase Coupling

Standard Operation Procedure

Loading to the resin: Chlorotriptyl-functionalized TentaGel[®] XV resin (loading capacity = 0.22 mmol·g⁻¹) is placed in a Merrifield flask. A solution of the first amino acid (3.0 eq.) in DCM (12 mL·g⁻¹ resin) and DIPEA (5.0 eq.) is added and the reaction mixture is agitated for 20 h at r.t. under inert atmosphere. The reactor is drained and the resin is washed with DCM (3x). *Capping:* MeOH (10 mL·g⁻¹ resin) is added to the resin and the vessel is agitated for 1 h. Afterwards, the resin is washed consecutively with DCM (3 x), DMF (3 x), DCM (3 x) and MeOH (3 x). *Deblocking N-terminus:* Next, the resin is twice treated with piperidine in DMF (20 vol%, 10 mL·g⁻¹ resin) for 45 min. After draining, the resin is washed with DMF (3 x), DCM (3 x) and a 1:1 mixture of DMF and DCM. *Amide Coupling:* Then, a solution of the next amino acid (3.0 eq.), PyBOP (4.0 eq.) and DIPEA (6.0 eq.) in an 8:2 mixture of DCM and DMF (12 mL·g⁻¹ resin) is added and the resin is agitated for 8–12 h at r.t. Next, another portion of PyBOP (1.0 eq.) is added and after 4–6 h reaction time. The reactor is drained, and the resin is washed with DCM (2 x) and DMF (2 x). The coupling step is repeated analogously with another portion of the same amino acid (amino acid: 1.0 eq., PyBOP: 1.5 eq., DIPEA: 3.0 eq.). Then, either the *N*-terminal Fmoc group is removed as described above and the next amino acid is coupled, or the complete coupling product is cleaved off from the resin. *Final Cleavage:* The final coupling product is cleaved by treating the resin twice with HFIP in DCM (20 vol%, 25 mL·g⁻¹

resin) for 1 h. The resin is washed with DCM (3 x). The combined cleavage cocktail and washing solutions are concentrated under reduced pressure, precipitated into Et₂O, kept at -20 °C for 24 h and isolated by centrifugation. Finally, the product is purified by size exclusion chromatography on Sephadex[®] LH20 in MeOH and lyophilized from water. Please note that the reported equivalents of the applied reagents refer to the manufacturer information about the loading capacity. The resin loading achieved with the polymeric amino acids is reproducibly around a fourth of this value.²¹

Spectrophotometric Loading Determination

After loading, capping, and washing: A small amount of the resin is dried under high vacuum for 3–5 h. Afterwards, three 5–10 mg portions of the loaded resin are weighed into 1.5 mL centrifuge vials and piperidine in DMF (20 vol%, 1 mL) is added. The mixture is agitated for 20 min at r.t., centrifuged, and 200 µL top liquid are diluted with 2 mL piperidine-DMF mix before an UV-Vis spectrum (280–350 nm, blank correction with piperidine-DMF mix, 20 vol%) is recorded. The Fmoc concentration and thus resin loading in relation to the dry mass (loading in mmol·g⁻¹) is determined applying the molar extinction coefficient of the generated dibenzofulvene–piperidine adduct at $\lambda = 301$ nm ($\epsilon = 8021$ M⁻¹·cm⁻¹).²²

Regaining excess reagents

The excess of the pEG-amino acid is recovered after the loading and amide coupling steps. For this purpose, the loading/coupling reaction mixtures are collected, and the resin is washed with DCM (3 x 10 mL). The volume of the obtained solution is reduced immediately, and the residue is precipitated into ice-cold Et₂O. After isolation, the residue is purified by size exclusion chromatography on Sephadex[®] LH20 in MeOH. After removal of the solvent, the final product is isolated by lyophilization from water and analyzed by GPC and RP-HPLC as depicted for two representative examples in **Figure 4.6**.

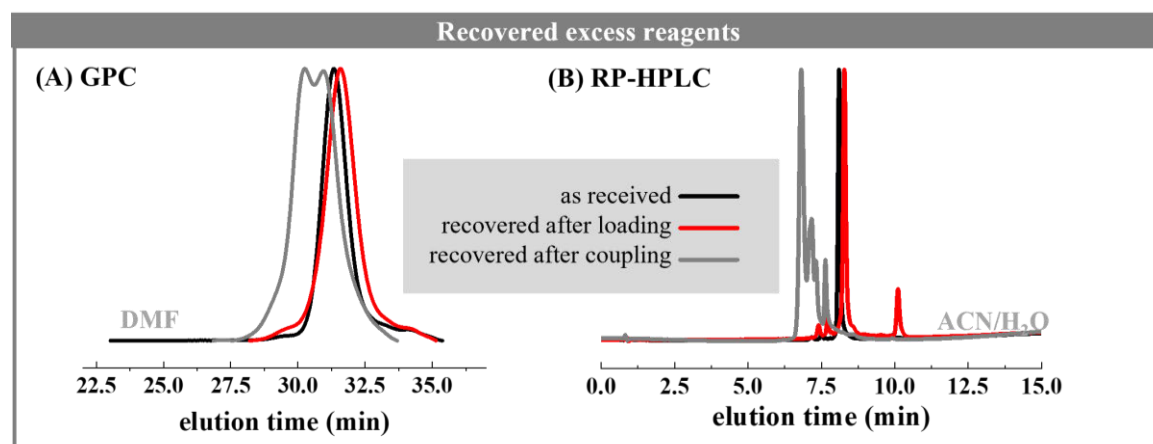


Figure 4.6. (A) GPC- (DMF, pEG calibration) and (B) HPLC-chromatogram (gradient: 30 to 100% ACN over 12 min, 100% ACN for 3 min, 254 nm) of α -Fmoc-amino- ω -carboxylic acid pEG-2k **4.20** as initially received (black) and after regaining the excess of the resin loading (red), or after an amide coupling (grey) by precipitation (2 x) in diethyl ether and size exclusion chromatography on Sephadex[®] LH20.

Compound 4.21

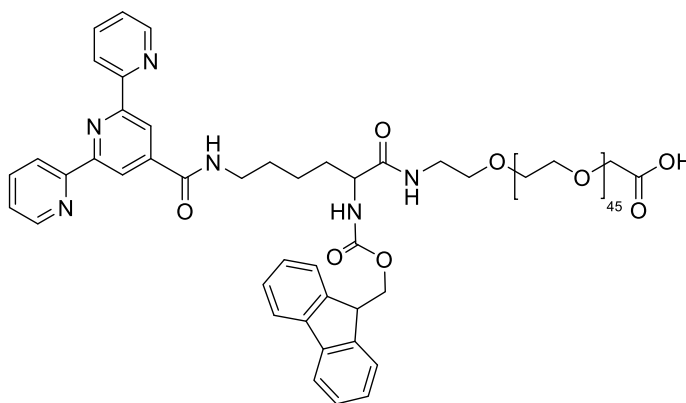
The synthesis is conducted according to SOP 1 with 2.00 g TentaGel resin.

Compound **4.21** is isolated as colorless solid by lyophilization (143 mg). **¹H-NMR** (400 MHz, DMSO-*d*₆):

$\delta = 12.56$ (s, 1H, COOH), 9.09, t, $^3J = 5.6$ Hz, 1H, tpy:

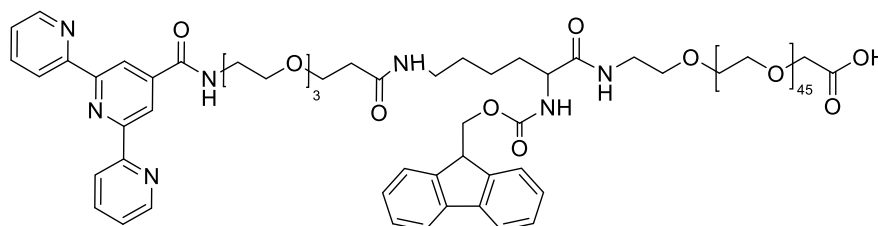
NH), 8.84 (s, 2H, tpy: C_{3/5}^{''}), 8.75 (m, 2H, tpy: C_{6/6}^{''}), 8.64 (m, 2H, tpy:

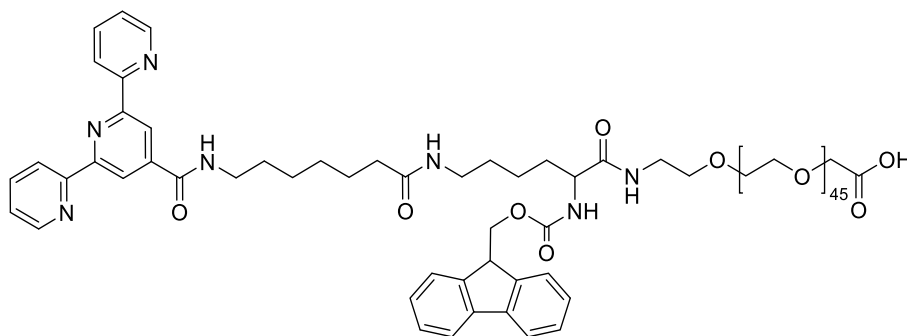
C_{3/3}^{''}), 8.03 (m, 2H, tpy: C_{4/4}^{''}), 7.93 (t, $^3J = 5.9$ Hz, 1H, Lys: NH), 7.86 (d, $^3J = 7.5$ Hz, 2H, Fmoc: C_{1/4}), 7.70 (m, 2H, Fmoc: C_{7/11}), 7.53 (m, 2H, tpy: C_{5/5}^{''}), 7.45 (d, 1H, Fmoc: NH), 7.38 (m, 2H, Fmoc: C_{5/13}), 7.28 (m, 2H, Fmoc: C_{6/12}), 4.36–4.14 (m, 3H, Fmoc: C₁₄, Lys: CH), 4.02 (s, 2H, CONHCH₂CH₂O), 3.97 (m, 1H, Fmoc: C₉), 3.72–3.36 (m, 212H, CH₂O), 1.57 (m, 6H, Lys: CH₂) ppm.

**Compound 4.23**

The synthesis is conducted according to SOP 1 with 5.00 g TentaGel resin. Compound **4.23** (480 mg) is

isolated as colorless solid by lyophilization. **¹H-NMR** (400 MHz, MeOH-*d*₄): $\delta = 8.80$ (s, 2H, tpy: C_{3/5}^{''}), 8.74 – 8.68 (m, 2H, tpy: C_{6/6}^{''}), 8.65 (d, $^3J = 7.8$ Hz, 2H, tpy: C_{3/3}^{''}), 8.00 (t, $^3J = 7.8$ Hz, 2H, tpy: C_{4/4}^{''}), 7.79 (d, $^3J = 7.5$ Hz, 2H, Fmoc: C_{1/4}), 7.65 (m, 2H, Fmoc: C_{7/11}), 7.65 (m, 2H, tpy: C_{5/5}^{''}), 7.38 (m, 2H, Fmoc: C_{5/13}), 7.30 (m, 2H, Fmoc: C_{6/12}), 4.37 (m, 2H, Fmoc: C₁₄), 4.19 (m, 1H, Lys: CH), 4.05 (m, 1H, Fmoc: C₉), 4.01 (s, 2H, CONHCH₂CH₂O), 3.87–3.35 (m, 217H, CH₂O), 3.15 (m, 2H, CH₂NHCOLys), 2.36 (t, $^3J = 6.1$ Hz, 2H, CH₂NHCOTpy), 1.86–1.15 (m, 6H, CH₂) ppm.

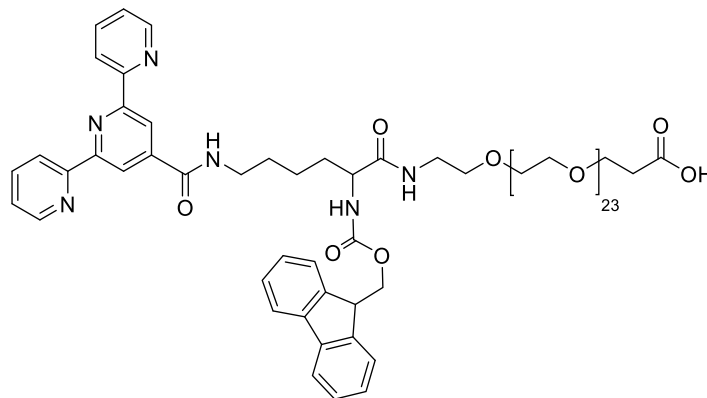


Compound 4.26

The synthesis is conducted according to SOP 1 with 2.00 g TentaGel resin. Compound **4.26** (170 mg) is isolated as colorless solid. $^1\text{H-NMR}$ (400 MHz, $\text{DMSO-}d_6$): δ = 12.55 (s, 1H, COOH), 9.07 (t, 3J = 5.6 Hz, 1H, tpy: NH), 8.82 (s, 2H, tpy: $\text{C}_{3/5}$), 8.76 (d, 3J = 4.7 Hz, 2H, tpy: $\text{C}_{6/6'}$), 8.65 (d, 3J = 7.9 Hz, 2H, tpy: $\text{C}_{3/3'}$), 8.04 (atd, 3J = 7.7 Hz, 4J = 1.8 Hz, 2H, tpy: $\text{C}_{4/4'}$), 7.93 – 7.83 (m, 2H, Fmoc: $\text{C}_{1/4}$), 7.72 (m, 3H, Fmoc: NH, $\text{C}_{7/11}$), 7.54 (m, 2H, tpy: $\text{C}_{5/5'}$), 7.41 (m, 2H, Fmoc: $\text{C}_{5/13}$), 7.31 (m, 2H, Fmoc: $\text{C}_{6/12}$), 4.31–4.15 (m, 3H, Fmoc: C_{14} , Lys: CH), 4.01 (s, 2H, $\text{CONHCH}_2\text{CH}_2\text{O}$), 3.93 (m, 1H, Fmoc: C_9), 3.78–3.38 (m, 25H, CH_2O), 2.99 (m, 2H, $\text{CH}_2\text{NHCOLys}$), 2.04 (t, 3J = 7.4 Hz, 2H, $\text{CH}_2\text{NHCOTpy}$), 1.69–1.19 (m, 15H, CH_2) ppm.

Compound 4.22

The synthesis is conducted according to SOP 1 with 2.00 g TentaGel resin. Compound **4.22** (350 mg) is isolated as slightly yellow solid. $^1\text{H NMR}$ (400 MHz, $\text{DMSO-}d_6$): δ = 9.10 (t, 3J = 5.6 Hz, 1H, TpyCONH), 8.83 (s, 2H, tpy: $\text{C}_{3/5}$), 8.75 (m, 2H, tpy: $\text{C}_{6/6'}$), 8.64 (m, 2H, tpy:



$\text{C}_{3/3'}$), 8.03 (atd, 3J = 7.7 Hz, 4J = 1.8 Hz, 2H, tpy: $\text{C}_{4/4'}$), 7.96 (t, 3J = 5.7 Hz, 1H), 7.85 (d, 3J = 7.5 Hz, 2H, Fmoc: $\text{C}_{1/4}$), 7.69 (m, 2H, Fmoc: $\text{C}_{7/11}$), 7.53 (ddd, 3J = 7.7 Hz, 4J = 4.7 Hz, 5J = 1.2 Hz, 2H, tpy: $\text{C}_{5/5'}$), 7.47 (d, 1H, Fmoc: NH), 7.38 (m, 2H, Fmoc: $\text{C}_{5/13}$), 7.28 (m, 2H, Fmoc: $\text{C}_{6/12}$), 4.29–4.15 (m, 3H, Fmoc: C_{14} , Lys: CH), 3.98 (m, 1H, Fmoc: C_9), 3.60–3.33 (m, 114H), 2.39 (t, 3J = 6.5 Hz, 2H, $\text{CH}_2\text{NHCOTpy}$), 1.77–1.15 (m, 6H, Lys: CH_2) ppm.

Compound 4.24

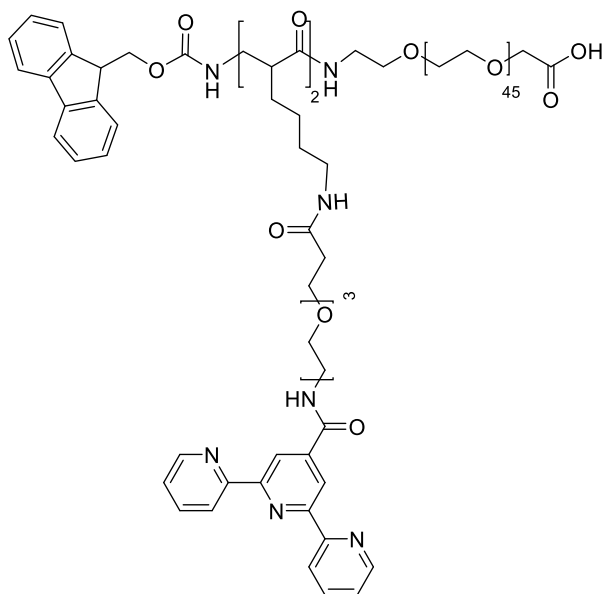
The synthesis is conducted according to SOP 1 with 2.00 g TentaGel resin.

Compound **4.24** is isolated as yellow solid (160 mg) ¹H-NMR (400 MHz, DMSO-*d*₆):

δ = 12.59 (s, 1H, COOH), 9.16 (t, ³*J* = 5.3 Hz, 2H, TpyCONH), 8.83 (s, 4H, tpy: C_{3/5'}), 8.76 (d, 4H, ³*J* = 4.9 Hz, tpy: C_{6/6''}), 8.65 (d, ³*J* = 7.9 Hz, 4H, tpy: C_{3/3''}),

8.04 (td, ³*J* = 7.7 Hz, ⁴*J* = 1.9 Hz, 4H, tpy: C_{4/4''}), 7.93 (t, ³*J* = 5.5 Hz, 1H, NH), 7.86 (d, ³*J* = 7.5 Hz, 2H, Fmoc: C_{1/4}), 7.78 (m, 1H, NH), 7.70 (m, 2H, Fmoc: C_{7/11}), 7.54 (m,

4H, tpy: C_{5/5''}), 7.39 (m, 2H, Fmoc: C_{5/13}), 7.30 (m, 2H, Fmoc: C_{6/12}), 4.21 (m, 4H, Fmoc: C₁₄, Lys: CH), 4.01 (s, 2H, CONHCH₂CH₂O), 3.96 (m, 1H, Fmoc: C₉), 3.73–2.86 (m, 260H, CH₂O), 2.25 (m, 4H, CH₂NHCOTpy), 1.68–0.96 (m, 12H, CH₂) ppm.

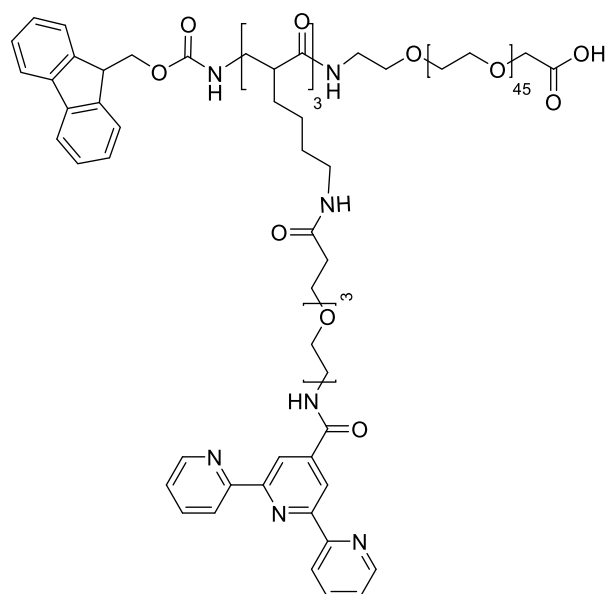
**Compound 4.25**

The synthesis is conducted according to SOP 1 with 1.80 g TentaGel resin.

Compound **4.25** is isolated as yellow solid (90 mg) ¹H-NMR (400 MHz, DMSO-*d*₆):

δ = 9.15 (t, ³*J* = 5.3 Hz, 3H, TpyCONH), 8.82 (s, 6H, tpy: C_{3/5'}), 8.75 (d, 6H, ³*J* = 4.7 Hz, tpy: C_{6/6''}), 8.64 (d, ³*J* = 7.9 Hz, 6H, tpy: C_{3/3''}), 8.02 (td, ³*J* = 7.7 Hz,

⁴*J* = 1.9 Hz, 6H, tpy: C_{4/4''}), 7.93 (m, 2H, NH), 7.84 (d, ³*J* = 7.6 Hz, 2H, Fmoc: C_{1/4}), 7.76 (m, 1H, NH), 7.69 (m, 2H, Fmoc: C_{7/11}), 7.52 (m, 6H, tpy: C_{5/5''}), 7.38 (m, 2H, Fmoc: C_{5/13}), 7.29 (m, 2H, Fmoc: C_{6/12}), 4.21 (m, 5H, Fmoc: C₁₄, Lys: CH), 3.98 (m, 1H, Fmoc: C₉), 3.93 (s, 2H, CONHCH₂CH₂O), 3.78–2.89 (m, 225H, CH₂O), 2.25 (³*J* = 6.6 Hz, 6H, CH₂NHCOTpy), 1.71–1.09 (m, 18H, CH₂) ppm.



Compound (4.23)_n

The synthesis is conducted according to SOP 1 with 150 mg TentaGel resin. Three coupling steps are performed and a test cleavage is done after each step (isolated yield: 2–3 mg). The isolated yield of compound (23)₃ comprises $m = 29$ mg. For comparison, the same molecular structure is also synthesized by consecutive couplings of pEG- and tpy-amino acids. The HPLC elugrams of these two approaches are compared in **Figure 4.7**.

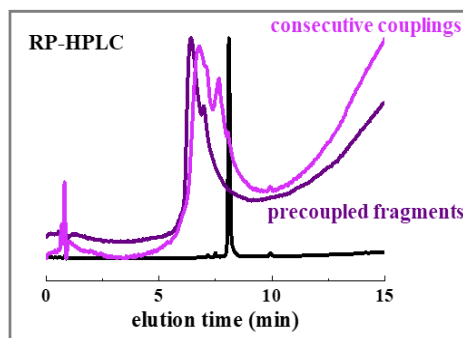


Figure 4.7. HPLC-chromatogram (gradient: 30 to 100% ACN over 12 min, 100% ACN for 3 min, 254 nm) of the solid phase coupling product (4.21)₄ obtained by coupling the hydrophilic tpy- 4.6 and pEG-2k 4.20 amino acids in seven consecutive coupling steps or by using the pre-coupled fragment 4.21 and performing three consecutive coupling steps.

Compound (4.21/4.26)_n

The synthesis is conducted according to SOP 1 with 30 mg TentaGel resin. One or two coupling steps are performed. The isolated yield of each step is below 1 mg. The analysis results by GPC and HPLC are summarized in **Figure 4.8**.

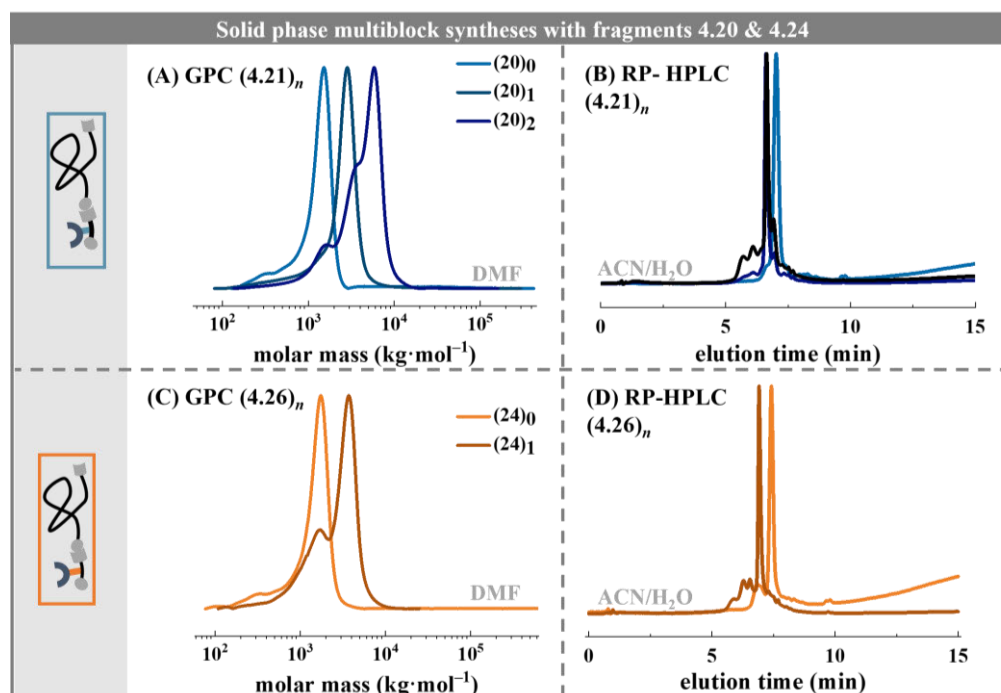


Figure 4.8. (A)/(C) GPC- (DMF, pEG calibration) and (B)/(D) HPLC-chromatogram (gradient: 30 to 100% ACN over 12 min, 100% ACN for 3 min, 254 nm) of the solid phase coupling products of the pEG-tpy repeating unit with short 4.21 and hydrophobic linker 4.26 respectively.

4.5 References

- (1) Jangizehi, A.; Ahmadi, M.; Seiffert, S. *Mater. Adv.* **2021**, *13*, 2661. DOI: 10.1039/D0MA00795A.
- (2) *Sequence-controlled polymers*; Lutz, J.-F., Ed.; Wiley-VCH: Weinheim, Germany, 2018.
- (3) Hartmann, L. *Macromol. Chem. Phys.* **2011**, *212* (1), 8–13. DOI: 10.1002/macp.201000479.
- (4) Seiffert, S. *Macromol. rapid commun.* **2016**, *37* (3), 257–264. DOI: 10.1002/marc.201500605.
- (5) Shabbir, A.; Javakhishvili, I.; Cerveny, S.; Hvilsted, S.; Skov, A. L.; Hassager, O.; Alvarez, N. J. *Macromolecules* **2016**, *49* (10), 3899–3910. DOI: 10.1021/acs.macromol.6b00122.
- (6) Yang, C.; Wu, K. B.; Deng, Y.; Yuan, J.; Niu, J. *ACS Macro Lett.* **2021**, *10* (2), 243–257. DOI: 10.1021/acsmacrolett.0c00855.
- (7) Merrifield, R. B. *J. Am. Chem. Soc.* **1963**, *85* (14), 2149–2154. DOI: 10.1021/ja00897a025.
- (8) Wan, Z.; Li, Y.; Bo, S.; Gao, M.; Wang, X.; Zeng, K.; Tao, X.; Li, X.; Yang, Z.; Jiang, Z.-X. *Organic & biomolecular chemistry* **2016**, *14* (33), 7912–7919. DOI: 10.1039/C6OB01286H.
- (9) Dong, R.; Liu, R.; Gaffney, P. R. J.; Schaeperstoens, M.; Marchetti, P.; Williams, C. M.; Chen, R.; Livingston, A. G. *Nature chemistry* **2019**, *11* (2), 136–145. DOI: 10.1038/s41557-018-0169-6.
- (10) Rossow, T.; Seiffert, S. *Polym. Chem.* **2014**, *5* (8), 3018. DOI: 10.1039/C3PY01692G.
- (11) Burnworth, M.; Tang, L.; Kumpfer, J. R.; Duncan, A. J.; Beyer, F. L.; Fiore, G. L.; Rowan, S. J.; Weder, C. *Nature* **2011**, *472* (7343), 334–337. DOI: 10.1038/nature09963.
- (12) Weng, W.; Beck, J. B.; Jamieson, A. M.; Rowan, S. J. *J. Am. Chem. Soc.* **2006**, *128* (35), 11663–11672. DOI: 10.1021/ja063408q.
- (13) Schneider, T.; Gavrilova, I.; Budisa, N. *Tetrahedron Letters* **2019**, *60* (13), 906–910. DOI: 10.1016/j.tetlet.2019.02.037.
- (14) Seitz, O.; Kunz, H. *Angew. Chem. Int. Ed.* **1995**, *34* (7), 803–805. DOI: 10.1002/anie.199508031.
- (15) Gagnon, P.; Huang, X.; Therrien, E.; Keillor, J. W. *Tetrahedron Letters* **2002**, *43* (43), 7717–7719. DOI: 10.1016/S0040-4039(02)01840-3.
- (16) Loos, M.; Gerber, C.; Corona, F.; Hollender, J.; Singer, H. *Analytical chemistry* **2015**, *87* (11), 5738–5744. DOI: 10.1021/acs.analchem.5b00941.
- (17) Di Lorenzo, F.; Hellwig, J.; Klitzing, R. von; Seiffert, S. *ACS Macro Lett.* **2015**, *4* (7), 698–703. DOI: 10.1021/acsmacrolett.5b00228.
- (18) Husson, J.; Dehaut, J.; Guyard, L. *Nature protocols* **2014**, *9* (1), 21–26. DOI: 10.1038/nprot.2013.162.
- (19) Maggi, V.; Bianchini, F.; Portioli, E.; Peppicelli, S.; Lulli, M.; Bani, D.; Del Sole, R.; Zanardi, F.; Sartori, A.; Fiammengo, R. *Chem. Eur. J.* **2018**, *24* (46), 12093–12100. DOI: 10.1002/chem.201801823.

- (20) Maduskuie, T. P.; Wilde, R. G.; Billheimer, J. T.; Cromley, D. A.; Germain, S.; Gillies, P. J.; Higley, C. A.; Johnson, A. L.; Pennev, P.; Shimshick, E. J. *Journal of medicinal chemistry* **1995**, *38* (7), 1067–1083. DOI: 10.1021/jm00007a004.
- (21) Gude, M.; Ryf, J.; White, P. D. *Lett Pept Sci* **2002**, *9* (4-5), 203–206. DOI: 10.1007/BF02538384.
- (22) Eissler, S.; Kley, M.; Bächle, D.; Loidl, G.; Meier, T.; Samson, D. *Journal of peptide science : an official publication of the European Peptide Society* **2017**, *23* (10), 757–762. DOI: 10.1002/psc.3021.

CHAPTER 5: MULTIVALENCY EFFECTS IN METALLO–SUPRAMOLECULAR CROSS-LINKED POLYMER GELS

Publication:

Sticker Multivalency in Metallo–Supramolecular Polymer Networks

K. Breul, [REDACTED] *Macromolecules* **2021**, *54*, 8407–8422
(doi.org/10.1021/acs.macromol.1c01201).

The results presented in the following chapter (p. 121–161) were first published on September 16, 2021 and are adapted with permission.¹

Further supporting information can be found in appendix, **Chapter A.5**.

Copyright © 2021 American Chemical Society.

Summary

The first two studies presented in this thesis, emphasized the general importance of a controlled sticker distribution for the understanding of fundamental structure–property relationships of reversible polymer gels. Besides the relevance for well-defined model systems, gaining control over the sticker distribution is also a valuable tool to identify yet new design parameters. Regarding the sticker arrangement under this aspect, the concept of multivalent binding is a promising approach. The strategic combination of different binding sites or motives allows for an additive and often synergetic enhancement of the individual association constants without the need to replace the associating group itself. Therefore, multivalency already represents a key concept in responsive biological and synthetic materials, which has however not yet been systematically used for the design of metallo–supramolecular polymer gels.

To overcome this shortcoming, the following study investigates the effects of multivalent binding on the mechanical properties of reversible gels with two complementary model systems. Firstly, the formerly described synthesis approach for poly(ethylene glycol) (pEG)-based multiblock polyurethanes (PU) with strictly alternating sequences is used to incorporate equally spaced, monotopic or ditopic terpyridine (tpy) ligands. To complement this polydisperse side-sticker system with a more established model network, telechelic four-arm pEG is chosen and accordingly functionalized with mono- and ditopic tpy–stickers. Star-pEG precursors are known to form very homogeneous networks which prevents an interference of multivalency– and heterogeneity–effects.

With these two model systems, the concentration- and association strength-dependent, linear viscoelasticity of the mono- and ditopic sticker gels is investigated within the semi-dilute, nonentangled regime. In case of the homogeneous star-pEG gels, the ditopic stickers increase the

network strength at identical tpy concentrations, most likely through the formation of cross-linking junctions with branch functionalities $f > 4$. The mechanical enforcement of the partially clustering PU gels is less pronounced but nonetheless evident, when the gels are compared with respect to the polymer overlap concentration.

The terminal relaxation times of both gel types are severely prolonged by the ditopic stickers. At this, the activation energies of the mono- and ditopic sticker gels remain similar, while the lifetime renormalization increases with the intrinsic lifetime of the basic metal tpy complex. On the basis of these observations, the deceleration of the network dynamics in the ditopic sticker networks is attributed to an increased number of opening attempts before a partner exchange and thus macroscopic relaxation take place.

Author Contributions:

Katharina Breul: Development and optimization of the synthesis routes, polymer characterizations, rheological measurements, manuscript preparation.
[REDACTED] Optimization of the ditopic tpy diol synthesis, polyurethane synthesis.
[REDACTED] Concept development, scientific supervision, manuscript correction.

Acknowledgments:

We thank [REDACTED] for the helpful and critical discussions. Funding by the German Research Foundation under grant number SE 1888/7-1 (Project No. 376900084) is gratefully acknowledged. We further thank the reviewers of this manuscript for their extremely helpful remarks and constructive criticism.

5.1 Introduction

The incorporation of reversible binding motifs into polymer matrixes opens unparalleled possibilities for the engineering of responsive networks and gels with tunable viscoelasticity. Furthermore, the dynamic nature of non-covalent or dynamic-covalent chain cross-linking enables the design of functional materials with autonomous self-healing ability, stimuli-responsiveness, or shape-memory switching.^{2,3} However, for these and other applications, the lack of stability and mechanical integrity that comes along with the non-permanent cross-linking often limits the utility of such supramolecular polymer networks and gels. Especially the fragility and brittleness of polymer gels in general is one of their inherent weaknesses, and so, the design of tough gels received much research interest. Strategies to overcome this limitation in the case of chemically cross-linked gels mostly focus on the introduction of additional energy dissipation mechanisms by designing multiple network-,⁴ nano-composite-,⁵ slide-ring-,⁶ or dually-cross-linked gels.⁷ Although these innovations greatly improved the mechanical performance of permanent gels, the application of these principles to their non-permanent counterparts is not straightforward and does not address the lacking stability of reversible gels in solution environments.

To provide strategies for an enhancement of reversible gels, the general interdependencies between the material properties and the constituent polymer backbone and stickers must be considered. This assessment has been done extensively in experimental and theoretical studies, investigating the mechanical response of a great variety of physical gels. Focusing on gels in the semi-dilute, nonentangled regime with sticker lifetimes that are sufficiently long in comparison to the chain relaxation of the polymer backbone, the sticker density and dissociation kinetics were shown to govern the rheological characteristics. Most prominently, these are the network strength in terms of the plateau modulus determined by the concentration of closed stickers on timescales shorter than the average sticker lifetime, and the terminal relaxation time defining the onset of network relaxation on timescales longer than that.^{8,9,10} While the qualitative influence of the sticker dissociation rate is generally very distinct, various studies on well-defined transient gels with a single relaxation time could not show a quantitative agreement between the intrinsic dissociation time of the stickers and the network relaxation time.¹¹⁻¹⁵ The commonly observed prolongation of the relaxation time is phenomenologically understood by considering that network relaxation requires not only a dissociation event but an exchange of binding partners. This necessity leads to a renormalization of the intrinsic sticker lifetime resulting from the need of multiple opening attempts before the attached polymer chain relaxes. Accordingly, the number of opening attempts depends on the diffusive mobility of the chains (Rouse or Reptation dynamics) and the concentration and distribution of open stickers, which makes it difficult to predict network relaxation times from the kinetics of the isolated stickers.^{16,17}

Considering the strong dependence of the gel- and sticker-dynamics, a straightforward approach to enhance the stability of reversible gels is the implementation of binding motifs with higher binding affinities and longer lifetimes. Despite the multitude of available cross-linking motifs, however, their synthesis and conjugation may require substantial synthetic effort. Furthermore, the arbitrary replacement of association groups is limited by their thermodynamic compatibility with polymer backbone and solvent. To avoid these complications, the sticker valency is another useful parameter to alter the gel dynamics based on the circumstance that multivalent or even cooperative interactions tend to be much stronger than the corresponding monovalent ones. As such, multivalency is a key principle in biological systems resulting from the easier variability of the number of interacting groups in comparison to a complete group exchange.¹⁸ Besides other factors such as preorganization and reduced entropic penalty, the binding avidity of multivalent ligands increases, because the permanent linkage of the individual binding sites restricts the movement of a dissociated one. This leads to a locally increased effective concentration and thus a higher rebinding rate in comparison to a monovalent ligand.^{19,20} Implementing this principle into reversible polymer gels, Tang *et al.* have recently shown how the introduction of multivalent binding between poly(histidine), Ni²⁺, and iminodiacetic acid ligands strongly improves the stability of these stimuli-responsive hydrogels. While hydrogels based on monovalent binding disassembled within hours at non-triggering neutral pH, the multivalent counterparts remained stable and only dissolved upon acidification.²¹ Figueiredo *et al.* showed a comparable dependence in transient hyaluronic acid (HA) gels based on different borate–carbohydrate complexes. Detailed mechanistic studies by NMR spectroscopy revealed that the network relaxation times of these gels not only depend on the pH value but also on the number of coordination sites in the predominant complex.²² A similar relaxation time prolongation has been reported by Zhang *et al.* in a metal–ligand cross-linked melt system where mono- and multi-ion associations are compared.²³ Another experimental study by Charlot *et al.* focused on reversible gels based on well-defined monomeric and dimeric β -cyclodextrin (CD) and adamantane (AD) inclusion complexes randomly distributed along a HA backbone. At identical sticker concentrations, the dynamics in the bivalent system are slowed down, whereas the plateau modulus is reduced. The authors attribute this to a smaller density of effective interchain junctions in the bivalent gel because the stickers are arranged in pairs. It is also suspected that the differences between the mono- and bivalent system are relatively small because steric constraints and hydrophobic AD/AD interactions cause a high energy penalty for the sticker association in the bivalent system.²⁴

Regarding the importance of the sticker distribution, another relevant aspect is the comparison of parallels and differences between sticker multivalency and clustering. In many supramolecular polymer gel systems, the spatial distribution of the cross-linking junctions is not that of

homogeneously arranged binary assemblies but complicated by the formation of larger sticker aggregates. The binding situation inside these clusters resembles that of a multivalent sticker with a large energy barrier for the dissociation of a single binding site. Accordingly, the network relaxation times in supramolecular gels comprised by sticker clusters are commonly prolonged.²⁵ Furthermore, the formation of multivalent super-nodes with high degrees of network connectivity have been applied to explain counterintuitive network enforcements reported in some studies. In an illustrative example, Weck *et al.* studied reversible networks cross-linked by hydrogen bond arrays with differing valency and observed that it is rather the sticker tendency to assemble into clusters than their intrinsic association constant which determines the network elasticity.²⁶ A similar observation was reported by Rossow *et al.* from the investigation of Zn^{2+} and Co^{2+} cross-linked gels based on terpyridine (tpy) end-capped star-shaped poly(ethylene glycols) (pEGs) by oscillatory shear rheology and static light scattering. It was found that an increase of the nano-structural heterogeneity observed in the Co^{2+} gels is accompanied by a plateau modulus exceeding the theoretical expectation of the affine network model theory.²⁷ Because the size and extent of clusters are commonly difficult to control and determine, a comparison with well-defined multivalent systems may contribute to a better understanding of these clustering effects.

To systematize and supplement the established, partially contradictory knowledge about the effects of multivalent sticker binding on the mechanics and dynamics of reversible polymer gels, we study the concentration-dependent linear viscoelasticity of two otherwise similar sets of associating polymers possessing either strictly isolated, monotopic stickers or well-defined ditopic sticker pairs. To provide a complementary picture, these mono- and bivalent stickers are incorporated into two model systems with different backbone architectures based on four-arm star-shaped pEGs with telechelic stickers and linear pEG-based polyurethanes (PU) with equidistant side-stickers as schematically illustrated in **Figure 5.1**. Using the differing binding constants of the *bis*(tpy) complexes of Mn^{2+} and Zn^{2+} ions, we further investigate how the multivalency effects are influenced by an increasing binding affinity.

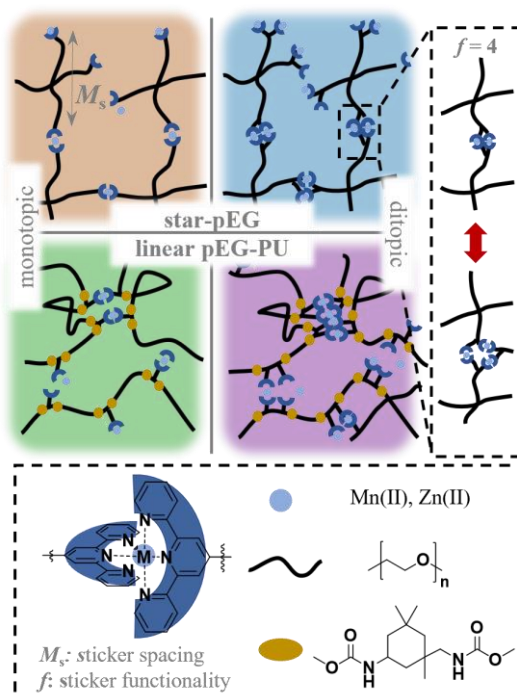
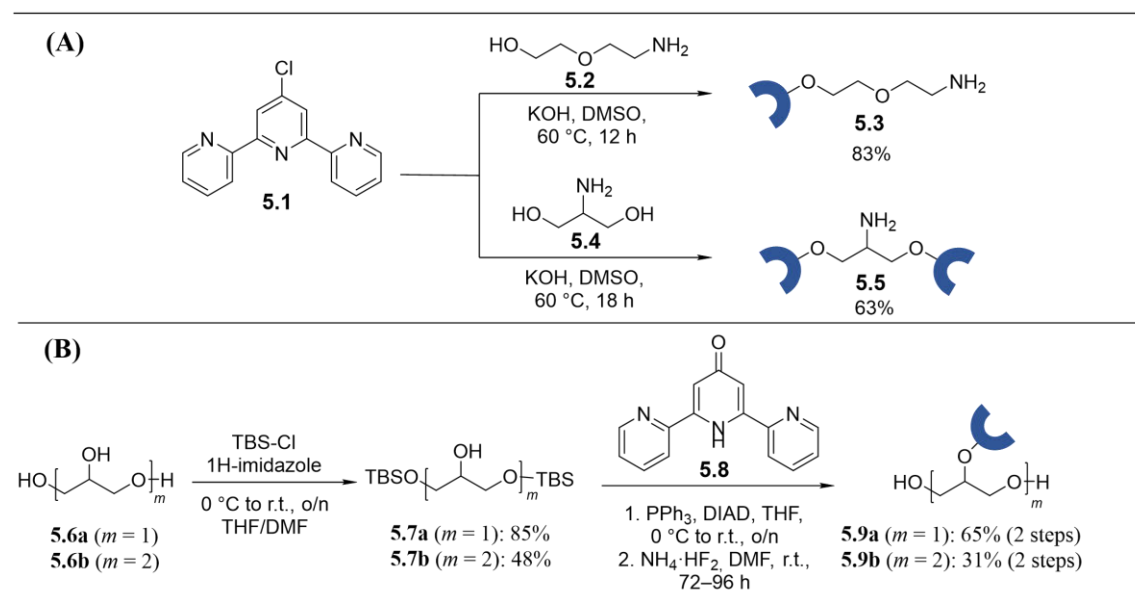


Figure 5.1. Schematic representation of the applied model systems based on telechelic star-pEG and linear pEG-based PUs with mono- and ditopic tpy-stickers (M_s : sticker spacing; f : branch functionality).

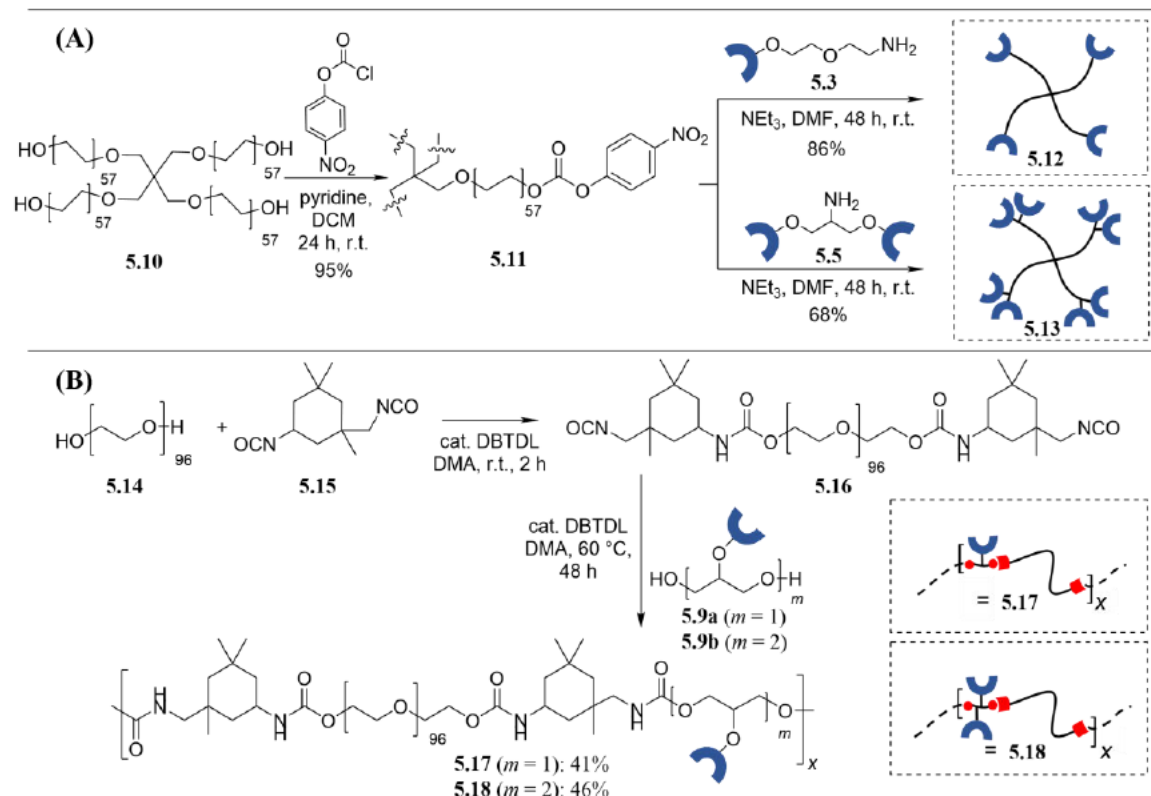
5.2 Results & Discussion

Material Basis

For the synthesis of the telechelic model system, hydroxy-terminated star-pEG ($M = 10 \text{ kg mol}^{-1}$) is first activated with 4-nitrophenyl chloroformate and then reacted with a mono- **5.3** or ditopic **5.5** terpyridine amine (**Scheme 5.1**) in a carbamate coupling which yields sufficient functionalization degrees of $\alpha = 98\%$ (**5.12**) and $\alpha = 86\%$ (**5.13**) (**Scheme 5.2**).¹² The functionalization degrees are determined by UV-Vis spectroscopy as detailed in **Chapter 5.4** (p. 149) and summarized in **Table 5.1**. In the star-pEG system, the spacing between the stickers and the molar mass of the complete chain are narrowly distributed and identical for both sticker types (**Table 5.1**). The side-sticker multiblock polyurethanes are obtained from narrow-disperse isophorone diisocyanate **5.15** (IPDI) end-capped pEG pre-polymers **5.16** which are chain-elongated with either a mono- **5.9a** or ditopic **5.9b** terpyridine diol.²⁸ As a result, strictly alternating sequences of pEG spacers and tpy-stickers are obtained, which leads to a narrow sticker but broad molar mass distribution. The functionalization degrees of 74% (**5.17**) and 72% (**5.18**) are significantly lower than those accessible for the star-pEGs. Even so, the average pEG molar mass M_s , between the stickers and sticker pairs (referred to as sticker spacing), is similar in both model systems, thereby ensuring their comparability with respect to the average mesh size in the later obtained networks. It must be noted, though, that the number of network defects due to dangling ends decreases with the functionalization degree and will thus be higher in case of the PU precursor polymers. Besides that, the mole fraction of stickers in the different model systems, which is denoted as sticker density $\langle s \rangle$, is another useful parameter to compare the precursor polymers (**Chapter 5.4**, p. 152, **Table 5.1**). At this, the relative sticker densities of the mono- compared to the ditopic tpy polymers corresponds to 57% (star-pEGs) and 47% (PUs), which is in both cases reasonably close to the targeted 50%.



Scheme 5.1. Synthesis of mono- and ditopic terpyridine (A) -amines **5.3/5.5** and (B) -diols **5.9a/5.9b**.



Scheme 5.2. Synthesis of **(A)** telechelic star-pEGs **5.12** and **5.13** and **(B)** linear pEG-polyurethanes **5.17** and **5.18** with mono- and ditopic tpy-stickers.

Table 5.1. Molecular properties of telechelic star-pEGs and linear pEG-polyurethanes with mono- and ditopic terpyridine stickers.

	M_w ^{a)} (kg mol ⁻¹)	\mathcal{D} ^{a)}	M_s ^{b)} (kg mol ⁻¹)	$\langle\beta^{\text{exp}}\rangle$ ^{c)} ($\mu\text{mol g}^{-1}$)	α ^{d)} (%)	$\langle s \rangle$ ^{e)}	c^* (g L ⁻¹)
4-pEG-10k-1 (5.12)	10.0	1.1	4.6	392 ± 3	98	0.015	46 [‡]
4-pEG-10k-2 (5.13)	10.0	1.1	4.6	690 ± 4	86	0.030	23 [‡]
4-pEG-5k-1 (5.20)	5.0	1.1	2.5	776 ± 2	97	0.035	106 [‡]
8-pEG-20k-1 (5.21)	20.0	1.2	4.2	372 ± 3	93	0.017	35 [‡]
PU-1 (5.17)	61.8	1.9	4.3	145 ± 1	74	0.009	27 [‡]
PU-2 (5.18)	29.0	1.6	4.3	270 ± 5	72	0.018	28 [‡]
PU-1 ^{2k} (5.19)	29.6	2.0	2.8	223 ± 1	63	0.018	x

^{a)} Determined by GPC (DMF, pEG calibration). ^{b)} Sticker spacing: number average molar mass of the pEG spacer between two stickers or sticker pairs. ^{c)} Experimental tpy content $\langle\beta^{\text{exp}}\rangle = n_{\text{tpy}}/m_{\text{polymer}}$ determined by UV-Vis spectroscopy (p. 149). ^{d)} Degree of functionalization $\alpha = \langle\beta^{\text{exp}}\rangle/\beta^{\text{theo}}$ (p. 149). ^{e)} Number density/mole fraction of stickers as determined by ¹H-NMR (p. 152). [‡] Geometrically estimated overlap concentrations (p. 155, Table 5.5). [‡] Overlap concentration of pEGs of corresponding molar mass and architecture determined by viscosimetry.

For the following investigations, methanol (MeOH) is chosen as polar organic solvent; we prefer that medium over the use of water due to the limited and strongly temperature-dependent solubility of the PUs in the latter.²⁸ As the properties of reversible gels strongly depend on the presence of network inhomogeneities, the molecular solubility of the precursor polymers in MeOH is firstly checked by concentration-dependent multi-angle dynamic light scattering (DLS). While the autocorrelation function of 4-pEG-10k-1 **5.12** (●) is monomodal (**Figure 5.2 A**) and the hydrodynamic radius derived for an equivalent sphere ($R_h \approx 3.4 \pm 0.2$ nm) is essentially concentration-independent (**Figure 5.2 B**), the autocorrelation functions of 4-pEG-10k-2 **5.13** (■), PU-1 **5.17** (▲) and PU-2 **5.18** (▼) show an additional slow mode. The presence of impurities causing this additional mode is excluded by thorough filtering through 20 nm pore-size filters at low polymer concentrations. From the angular dependency of the inverse relaxation times derived by fitting the autocorrelation data with a stretched biexponential function (**5.9**), two diffusion coefficients differing by two orders of magnitude are derived for the three polymer solutions as detailed in **Chapter 5.4** (p. 152–153). The fast relaxation process can be attributed to the motion of individual (dilute) or overlapping (semi-dilute) polymer chains, whereas the slow relaxation process most likely results from the translational movement of larger polymer aggregates ($R_h \geq 100$ nm). The respective concentration portions of these aggregates can be roughly estimated from the relative amplitudes A_i of the fast and slow process in the fit function under the assumption of monodisperse Gaussian coils (p. 153). In case of the 4-pEG-10k-2 **5.13** solutions, the hydrodynamic radii ($R_h \approx 100$ nm) and relative amplitudes ($A_{\text{slow}} \approx 10\%$) of the slow mode (□) are concentration-independent, as shown in **Figure 5.2 B** and **C**, and the approximated concentration portion of the aggregates corresponds to ≈ 2 wt% and is thus mostly negligible. For PU-1 **5.17** and PU-2 **5.18**, however, the size of the aggregates (▲, ▼) increases strongly with concentration and comprises relative amplitudes A_i up to 50%. The approximation of the corresponding aggregate concentrations yields similar weight portions between 6–11 wt% for both PUs. In general, the self-assembly of amphiphilic, (non-ionic) polyurethanes into micellar structures is most pronounced and thus commonly studied in aqueous environments^{29,30} but also known in polar organic solvents.³¹ In a former study, we correspondingly observed the aggregation of similar pEG-based PUs with terpyridine side groups in water while a mixture of aggregates and molecularly dissolved chains occurred in MeOH.²⁸ In the present investigation, the polarity differences between polymer backbone and stickers in combination with the polymer–polymer attractions resulting from the hydrogen bonding urethane groups, apparently cause the same aggregation tendency. Upon complexation of the tpy groups, these aggregates likely become locally frozen clusters and represent a deviation from the idealized picture of only binary associations and non-entangled chains, which must be taken into consideration throughout the following investigations. It should however be noted that the actual size and concentration of the aggregates in the gel state cannot be concluded from these solution experiments.

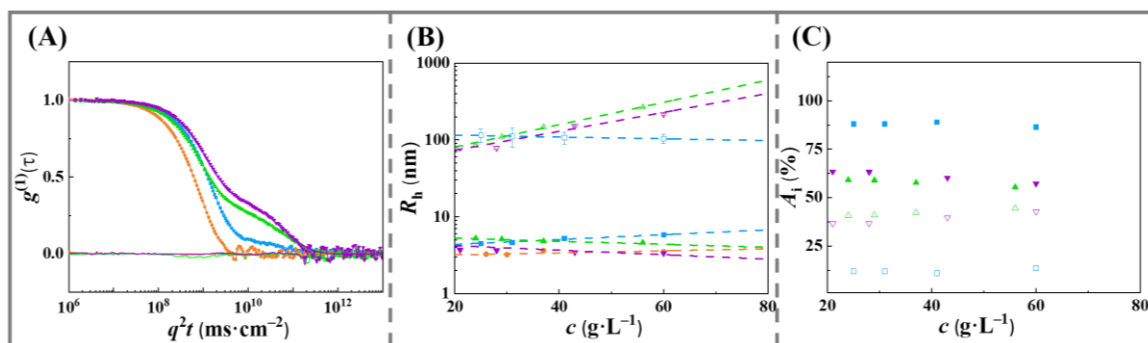


Figure 5.2. (A) Experimental DLS autocorrelation functions of 4-pEG-10k-1 **5.12** (●), 4-pEG-10k-2 **5.13** (■), PU-1 **5.17** (▲) and PU-2 **5.18** (▼) in MeOH ($c = 60 \text{ g}\cdot\text{L}^{-1}$) recorded at $20 \text{ }^\circ\text{C}$ at a scattering angle of 30° along with (stretched) biexponential fit functions and the corresponding residuals. (B) Hydrodynamic radii corresponding to the fast (full symbols) and slow (open symbols) relaxation times derived from the respective autocorrelation functions. (C) Relative amplitudes of the fast (full symbols) and slow (open symbols) relaxation processes as a function of the polymer concentration.

Sticker Association

Metal-Terpyridine Complexation

Further on, the metal complexation of the mono- **5.3** and ditopic **5.5** tpy-amines and corresponding star-polymers **5.12** and **5.13** are first compared in the dilute regime based on UV-Vis- and $^1\text{H-NMR}$ titration experiments. As shown in **Figure 5.3** and **Figure 5.11** (Chapter 5.4), the titration of the amines and star-polymers with ZnOTf_2 leads to the occurrence of two additional bands in the UV-Vis spectra of all compounds with maxima at 311 and 324 nm which are characteristic for the Zn^{2+} -tpy complexation (shift of the π - π^* transition).³² From the equivalence points upon which no further intensity changes of these bands are observed, a preferred L:M ratio of 2:1 can be concluded in all cases. This finding and the clear isosbestic points indicate that the formation of the *bis*(tpy)-complexes is generally not restricted with the ditopic stickers.

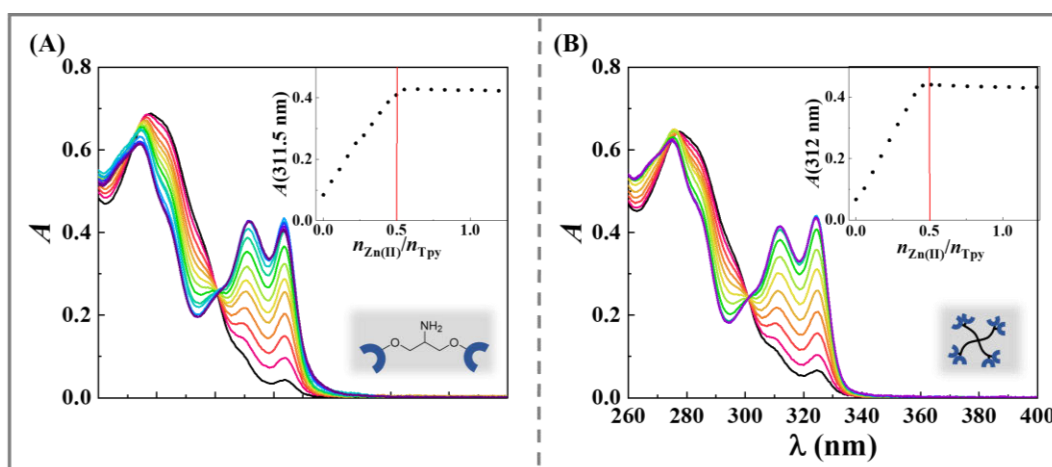


Figure 5.3. UV-Vis spectra of (A) ditopic tpy-amine **5.5** and (B) 4-pEG-10k-2 **5.13** in MeOH upon titration with ZnOTf_2 ; Inserts: Absorption at 311.5 nm/312 nm as a function of the molar M:L ratio.

To gain further insights about the complex formation, the $^1\text{H-NMR}$ spectra of the ligands **5.3** and **5.5** in the absence of metal ions and after addition of 0.5 eq. ZnOTf_2 are compared next. The aromatic signals of the free mono- and ditopic ligands differ slightly with respect to the chemical shift of the H-3'/5' protons but coincide otherwise. Upon complexation with ZnOTf_2 , characteristic shifts are observed for both ligands, which are in accordance with former reports and can thus be assigned as indicated in **Figure 5.4** (middle).^{32,33} The spectrum of the complexed, ditopic ligand does not indicate the formation of supramolecular open-chain polymers, which would be recognizable by their non-complexed end-groups.^{33,34} The possibility of intramolecular mono-cycles can be precluded based on the insights of former studies, which revealed the necessity of much longer spacers between two 4'-substituted tpy ligands.^{33,35} Thus, the most likely binding scenario is the formation of metallo-macrocycles of different sizes ([3+3], [4+4] etc.), which also explains the broadness of the aromatic signals.³⁵ Next, the spectra of the low molar mass complexes are compared to those of the corresponding star-pEGs. While the spectra of the complexed single tpy-amine **5.5** and -polymer **5.12** coincide perfectly, additional signals occur in case of the double tpy star-pEG. These additional signals can be assigned to the $\text{Zn}(\text{tpy})^{2+}$ mono-complex and indicate the presence of a mixture of mono- and *bis*(tpy)-complexes (**Figure S5.2, A.5**)³⁶. It is suspected that the limited ligand mobility prevents the formation of the thermodynamically favored *bis*-complexes at the chosen polymer concentration slightly below the gel point.

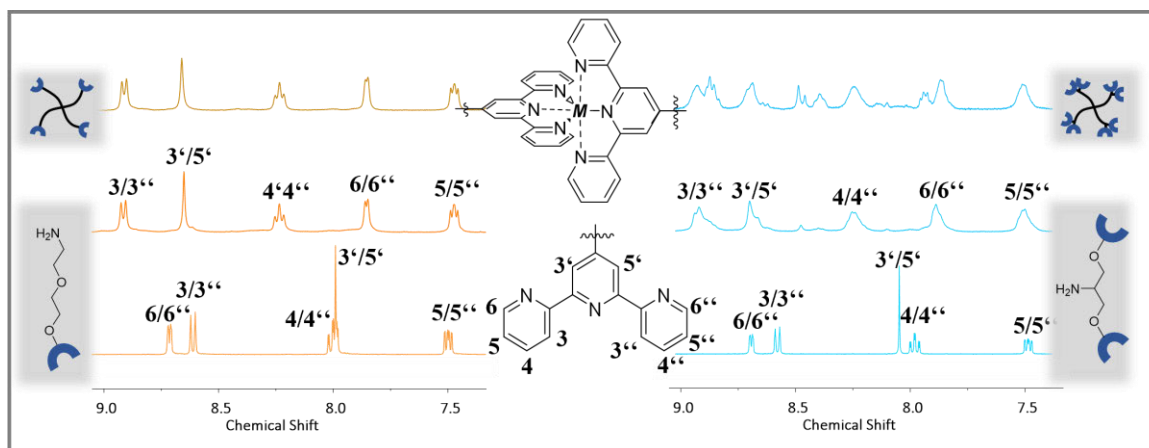


Figure 5.4. Extract from the $^1\text{H-NMR}$ spectra of the mono- **5.3** (left) and ditopic (right) tpy-amine **5.5** before (bottom) and after addition of 0.5 eq. ZnOTf_2 (middle) as well as those of 4-pEG-10k-1 **5.12** and 4-pEG-10k-2 **5.13** in the presence of 0.5 eq. ZnOTf_2 (top), all measured in $\text{DMSO-}d_6$.

Kinetic Complex Stabilities

For a latter correlation with the in-gel dynamics, the kinetic stabilities of the *bis*(tpy)-complexes of the low molar mass ligands **5.3** and **5.5** are measured in the dilute limit by metal exchange experiments. The dissociation constants k_d of the Zn^{2+} complexes can be determined by capturing dissociated tpy groups with an excess of the stronger binding Cu^{2+} according to a method reported by Holyer *et al.*³⁷ The formation of the $\text{Cu}(\text{tpy})^{2+}$ -complex can be quantified using the UV-Vis

absorbance of the emerging MLCT band at 335 nm, as further detailed in **Chapter 5.4**. The dissociation rates and corresponding complex lifetimes are then obtained through an exponential fitting of the absorbance profiles and summarized in **Table 5.2**. Additionally, the activation energies E_A are determined from temperature-dependent measurements, which reveal an Arrhenius-type activation of the dissociation process (**Figure 5.5**). The rate constants of the kinetically less stable Mn^{2+} complexes could not be determined by this method.

The dissociation time of the $Zn(tpy)_2^{2+}$ complex of single tpy-amine **5.3** is around a factor two smaller than that reported for the complex of the unsubstituted ligand in aqueous solutions by Holyer *et al.* ($\tau_{d,Zn(II),H_2O} = 1.7$ s, $T = 18$ °C).³⁷ This deviation can be explained by the findings of Henderson *et al.* who reported that the decay rates of the *bis*(tpy) complexes in water are several orders of magnitude larger than those measured in organic solvents due to the better ligand solubility.³⁸ Additionally, the same authors reported that an ethoxy substituent in the 4'-position further accelerates the dissociation.³⁹ Based on these findings, the determined values are considered as reliable and not remarkably influenced by the free amino group. In comparison to the monotopic ligand, the kinetic stability and activation energy of the ditopic ligand **5.5** are increased by a factor 1.7 and 1.2 respectively. The stabilization of the ditopic complex is thus of similar magnitude as a formerly described duplication of the association rate of mono- *versus* ditopic terpyridine ligands connected by a rigid spacer.⁴⁰

Table 5.2. Dissociation times and activation energies of $Zn(tpy)_2^{2+}$ complexes in MeOH.

sample	τ_d (20 °C) (s)	E_A (kJ/mol)
mono-tpy amine (5.3)	0.94 ± 0.04	25 ± 1
di-tpy amine (5.5)	1.5 ± 0.1	31 ± 1

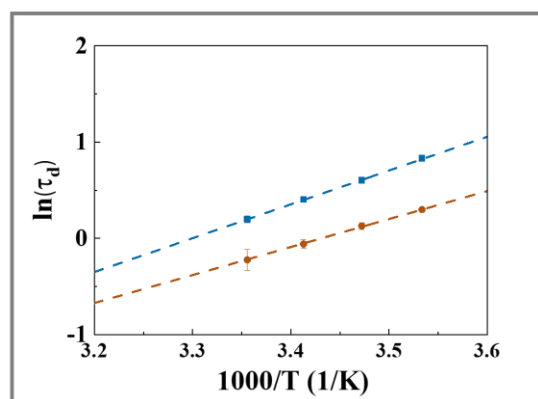


Figure 5.5. Arrhenius plot of the temperature-dependent dissociation times of the $Zn(tpy)_2^{2+}$ complexes of the mono- **5.3** (●) and ditopic ligand **5.5** (■) as determined by metal exchange experiments in MeOH with Arrhenius-type fits (dashed lines).

Linear-Viscoelastic Mechanics

Concentration, Metal Ion, and Polymer Backbone Dependency

After establishing the efficient binding of the ditopic ligands, we probe, how the multivalency of the stickers affects the properties of the corresponding supramolecular gels. For this purpose, the associating polymers are cross-linked with stoichiometric amounts of Mn^{2+} or Zn^{2+} ions (triflate salts) whose binding affinities in polar organic media differ by several orders of magnitude

($K_{\text{MeOH/CHCl}_3}^{\text{Mn(II)}} = 3.5 \cdot 10^9 \text{ L}^2 \text{ mol}^{-1}$, $K_{\text{MeOH/CHCl}_3}^{\text{Zn(II)}} = 1.3 \cdot 10^{12} \text{ L}^2 \text{ mol}^{-1}$).²⁷ The concentration- and frequency-dependent mechanical response of these gels is probed by linear oscillatory shear rheology. To ensure the greatest possible comparability of the different model systems, the concentration of tpy groups (referred to as sticker concentration), rather than the polymer concentration is considered as critical parameter, as it controls the densities of elastically active chains *v.* Nevertheless, the polymer chain conformation is also crucial, and we target to study gels within the semi-dilute nonentangled regime, which requires polymer concentrations above the overlap concentration c^* but well-below the entanglement threshold ($c_e = 5\text{--}10c^*$). The overlap concentrations c^* are thus geometrically approximated as $c^* = (3M)/(4\pi \cdot N_A \cdot R_G)$ with the Avogadro constant N_A and the radius of gyration R_G which is calculated from the hydrodynamic radii R_h applying the universal literature ratios $\rho_{\text{star}} = R_G/R_h = 1.58$ and $\rho_{\text{PU}} = 2.05$ as further detailed in the **Chapter 5.4** (p. 155) and summarized in **Table 5.1**.⁴¹ The results are applied as guideline for the choice of appropriate sticker concentrations for the respective model systems ($c_{\text{tpy}} = 8\text{--}64 \text{ mM}$, **Table 5.6**).

The mechanical spectra of the cross-linked star-pEGs **5.12/5.13** (**Figure 5.6**) and PUs **5.17/5.18** (**Figure 5.7**) show the typical features of physical networks with a plateau modulus on short time scales when the cross-links are active, a single relaxation time τ_{ex} defined by the G' – G'' crossover frequency, and a terminal flow regime at low frequencies. Apparently, the network strength in terms of the plateau modulus G_N is mostly independent of the applied metal ion at all concentrations. It can thus be concluded that the fraction of closed stickers is not affected by the variation of the sticker strength in this order of magnitude. By contrast, the terminal relaxation times τ_{ex} clearly reflect the longer average sticker lifetime of the kinetically more stable Zn^{2+} complexes and confirm that the sticker dissociation governs the macroscopic relaxation. Regarding the terminal flow regime, the Maxwell model fits included in **Figure 5.6** demonstrate that the mechanical spectra of the star-pEG gels show the predicted $G' \propto \omega^2$ and $G'' \propto \omega^1$ scaling which is in accordance with former studies.^{12,42} In case of the PU gels, the terminal flow scaling gets significantly shallower with increasing concentration as shown for the Mn^{2+} cross-linked gels in **Figure 5.7**. This is caused by the greater dispersity of the polymer backbones and additional relaxation modes resulting from the less homogeneous network structure.⁴³

In accordance with previous studies of reversible gels in the semi-dilute regime, the plateau moduli and network relaxation times increase with the sticker and thus polymer concentration. This results primarily from the increasing number of available cross-links and is exacerbated by the increasing probability of inter- compared to intra-chain sticking at higher polymer concentrations.^{11,27,44} Before a more quantitative discussion of these concentration dependencies follows, the influence of the polymer backbone is discussed at first.

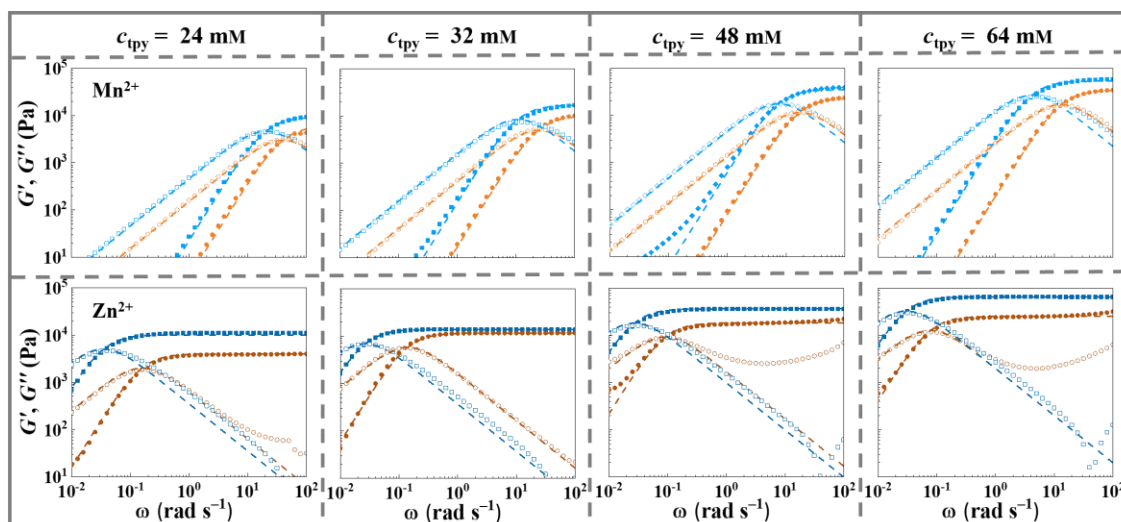


Figure 5.6. Frequency-sweeps of metallo-supramolecular polymer gels based on monotopic 4-pEG-10k-1 **5.12** (top – Mn^{2+} : ●, bottom – Zn^{2+} : ●) and ditopic 4-pEG-10k-2 **5.13** (top – Mn^{2+} : ■, bottom – Zn^{2+} : ■) at tpy concentrations of 24, 32, 48 and 64 mM with Maxwell model fits (dashed lines) (G' : full symbols, G'' : empty symbols, MeOH, 20 °C, polymer concentrations: **Table 5.6**).

For a meaningful comparison of the gels derived from the star-shaped and the linear model system, a sticker concentration of 24 mM is chosen to ensure that both polymers are roughly within the same concentration regime. Furthermore, it must be noted that the sticker density $\langle s \rangle$ of the side-sticker polymer comprises only around 50% of that in the star-pEG due to the lower functionalization degree while the average sticker spacing M_s is similar (**Table 5.1**). To compare a star-shaped and linear polymer with similar sticker density, a further side-sticker polymer denoted as PU-1^{2k} **5.19** with a shorter pEG spacing ($M_s = 2.8 \text{ kg} \cdot \text{mol}^{-1}$) is synthesized. Here, the sticker density is identical with that of 4-pEG-10k-1 **5.12**, while the spacing between the stickers is bisected (**Table 5.1**). A comparison of the mechanical spectra of the Zn^{2+} cross-linked gels shows that the different sticker spacings in the linear PUs **5.17** and **5.19** do not significantly affect the gel properties at identical sticker concentrations as shown in the third column of **Figure 5.7** (PU-1^{2k}: $c = 108 \text{ g} \cdot \text{L}^{-1}$). If the PU gels are compared at similar polymer concentration (PU-1^{2k}: 24 mM and PU-1^{4k}: 16 mM), the shorter spacing leads to an enhancement of the gel strength which is in accordance with former findings.^{45,46}

However, in comparison to the star-pEG gel, the plateau moduli of both PU gels are upshifted by a factor around six while the terminal relaxation time is prolonged by a factor around nine. Although the polymer concentrations and molar masses of the PUs are higher, it seems unlikely that this severe enhancement could already result from chain entanglements. Since the number of stickers per chain N_x (**Table 5.4**) is also similar in both model systems, the polymer architecture and backbone composition represent the most important differences. To firstly focus on the influence of the backbone architecture, we compare the results of related studies, in which linear and star-shaped precursors were applied.

Fullenkamp *et al.* and Tang and Olsen investigated supramolecular gels respectively obtained from telechelic star-pEG¹⁴ and linear poly(*N,N*-dimethyl acrylamide) chains¹¹ with histidine end- or side-groups cross-linked through the complexation of Ni²⁺ ions. Although the sticker density of the star system ($s = 0.018$) is only around a third of that in the linear one ($s = 0.053$), the star-pEG gels show higher plateau moduli and slower relaxation dynamics at comparable polymer concentrations. The authors explained this finding by a higher likelihood of loop formations along the linear chains.¹¹ A similar literature comparison can be made for star-pEG ($s = 0.018$)²⁷ and linear poly(*N*-isopropyl acrylamide) ($s = 0.046$)⁴⁷ gels cross-linked by *bis*(tpy)–Mn²⁺ complexes. Here, the plateau moduli of both systems are similar, while the linear system shows significantly prolonged terminal relaxation times at identical conditions. These opposing observations of these complementary studies elucidate that the backbone architecture can probably not explain the differing viscoelastic properties.

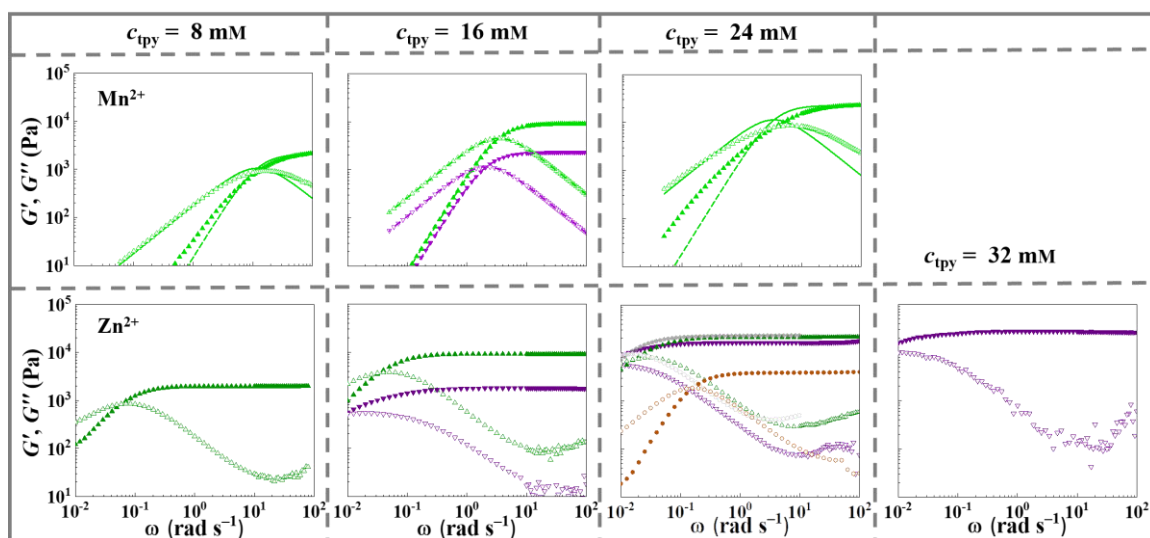


Figure 5.7. Frequency sweeps of metallo–supramolecular polymer gels based on monotopic PU-1 **5.17** (top – Mn²⁺: ▲, bottom – Zn²⁺: ▲) and ditopic PU-2 **5.18** (top – Mn²⁺: ▼, bottom – Zn²⁺: ▼) at tpy concentrations of 8, 16, 24 and 32 mM along with those of 4-pEG-10k-1 **5.12** (●) and PU-1^{2k} **5.19** (◆) measured at corresponding conditions (G' : full symbols, G'' : empty symbols, MeOH, 20 °C, polymer concentrations: **Table 5.6**).

Under the assumption that the different sticker densities and polymerization degrees cannot cause the observed deviations, it is thus necessary to further focus on the clustering tendency of the cross-linking motives and the polymer backbone chemistry. In our study this aspect is especially relevant due to the attractive interactions between the hydrogen bonding urethane groups in the immediate neighborhood of the initially hydrophobic stickers. To understand the possible impact of such an arrangement, a previous study by Guo and co-workers on reversible hydrogels based on amphiphilic pEG-PU polymers cross-linked by self-complementary 2-ureido-4[1H]-pyrimidinone (UPy) side stickers can be considered.⁴⁸ Here, cryo-transmission electron microscopy revealed that the UPy–UPy interactions are shielded from the aqueous surrounding in

phase-segregated pockets comprised by UPy aggregates. Such a sticker clustering of the supramolecular stickers is generally known to enforce networks, if it contributes to a higher coordination number, stabilizes weak supramolecular bonds or develops intra-chain connections to elastically active interchain junctions.²⁵ In view of these insights and the DLS measurements performed on the precursor polymer solutions, the most likely explanation for the enhancement of the here-in investigated PU gels is the formation of sticker aggregates. Based on the calculated mass fraction of the aggregates (≈ 10 wt%), we suspect the PU networks to be a mixture of binary sticker assemblies with randomly distributed clusters with higher functionalities ($f > 4$).²⁷ The exploration of size and concentration of the in-gel clusters requires further structural investigations, which are beyond the scope of the present study.

Influence of the Sticker Valency

It is now further evaluated how the neighboring stickers affect (1) the network structure, (2) the relaxation time, and (3) whether the observed differences may simply result from the higher sticker density of the precursor polymers with ditopic stickers. To compare the elastic properties of the different gels, we first consider the extent of cross-linking. With the network plateau moduli G_N , the apparent molar concentration of elastically active chains v_{exp} can be approximated as $v_{\text{exp}} = G_N/[RT(1-2/f)]$ according to the phantom network model with the functionality f , the gas constant R and the absolute temperature T (v_{exp} in $\text{mol}\cdot\text{L}^{-1}$). In contrast to the affine network model, which assumes permanent network connections and an affine deformation, the phantom model additionally considers a fluctuation of the cross-links and is thus more appropriate for reversible networks.⁹ It must however be noted that both models consider the network structure to be homogeneous with imparts a major deviation from the experimentally observed aggregation tendency of the PU precursors and limits the reliability of the derived values.^{8,9,49} The functionality f describes how many polymer strands are connected by one cross-link and is firstly assumed to be four in all cases (**Figure 5.1**). This initial assumption does purposely ignore the possibility that the ditopic stickers can form higher functional cross-links to set a reference value for latter comparisons. Because the plateau moduli of the Mn^{2+} and Zn^{2+} cross-linked gels are independent from the applied metal ion, averaged values are used for this calculation. Further on, the average number of elastically active stickers per chain $N_{x,a} = (v_{\text{exp}}/c_{n,p}) + 1$ can be calculated using the molar polymer concentration $c_{n,p} = m_p/M_{n,p}$. The fraction of elastically active stickers per chain $N_{x,a}$ can then be compared to the number of individual tpy groups per chain N_x , which allows us to estimate the fraction of interchain bonds $p_{\text{inter}} = N_{x,a}/N_x$.⁴⁴ The differing functionalization degrees α of the associating polymers are taken into account for the calculation of N_x as detailed in **Chapter 5.4** (p. 149).

Since the network strength depends on the number of elastically active chains, it naturally increases with the sticker concentration in all gels as depicted in **Figure 5.8 A**. According to the

Flory definition, the percolation threshold is attained if each polymer chain contributes at least one cross-link to the network ($N_{x,a} \geq 1$). Upon completed gelation, all chains are connected to the network, and the gel regime begins ($N_{x,a} \geq 2$).⁵⁰ The number of elastically active chains shown in **Figure 5.8 B** shows that except for 4-pEG-10k-2, the gels prepared at the lowest concentrations are above the gel point ($N_{x,a} \geq 1$) but still within the gelation regime ($N_{x,a} < 2$). As visible in **Figure 5.8 C**, this contributes to a fraction of interchain bonds $< 50\%$, and it can thus be assumed that the transition from intra-chain to inter-chain bonds is of major importance.

To add another point of view with respect to the concentration regime, the power law scaling of the experimental concentration-dependency can be compared to the theoretical predictions of the sticky Rouse model developed by Rubinstein and Semenov. It describes the linear dynamics of reversibly associating polymers in the semi-dilute, non-entangled regime and predicts various concentration dependent scaling relations.¹⁷ The model distinguishes between a regime near the gel point, in which the polymer strands between the stickers not yet overlap and the conversion of intra- to intermolecular bonds dominates ($G_N \propto \phi^{2.6}$, ϕ : polymer volume fraction), and a later gel regime characterized by mostly intermolecular associations ($G_N \propto \phi^1$).¹⁷ However, the linear chains in this model are assumed to contain a large number of stickers, which are arranged equidistantly along the backbone, separated by long, non-associating segments and only able to form binary assemblies.¹⁷ Since the experimental realization of these requirements is very challenging and also not met in the current study, the scaling predictions usually only allow qualitative classifications.^{9,15,27,44} Another limitation results from the narrow range of applicable concentrations (usually one order of magnitude), which impedes the accuracy of the derived scaling exponents. Nonetheless, assuming an equivalence of polymer volume fraction ϕ and sticker concentration, the comparison of the scaling exponents $G_N \propto c_{\text{tpy}}^q$ (**Table 5.3**) reveals intermediate exponents of $q = 1.8$ and 1.7 for the star-pEG gels, while the PU gels more clearly fall into the gelation regime ($q = 2.3$ and 2.8).

The discrepancy regarding the concentration regime of the PU gels indicated by the scaling exponent ($q \gg 1$) and the calculated number of elastically active chains ($N_{x,a} \geq 2$) can be explained by an overestimation of the latter due to the formerly discussed clustering tendency. By aggregation, stickers that prefer intra-chain associations at the given polymer concentration can be developed into elastically active inter-chain connections which is reflected in the numbers of $N_{x,a}$ and p_{inter} . With increasing concentration, the network strength still grows faster than expected within the gel regime due to the still dominant intra- to inter-chain transition not reflected in the numbers of $N_{x,a}$. Because of the limited applicability of the phantom network model to the PU system, the calculated values are generally less conclusive than for the star-pEG system and unsuited for quantitative comparisons.

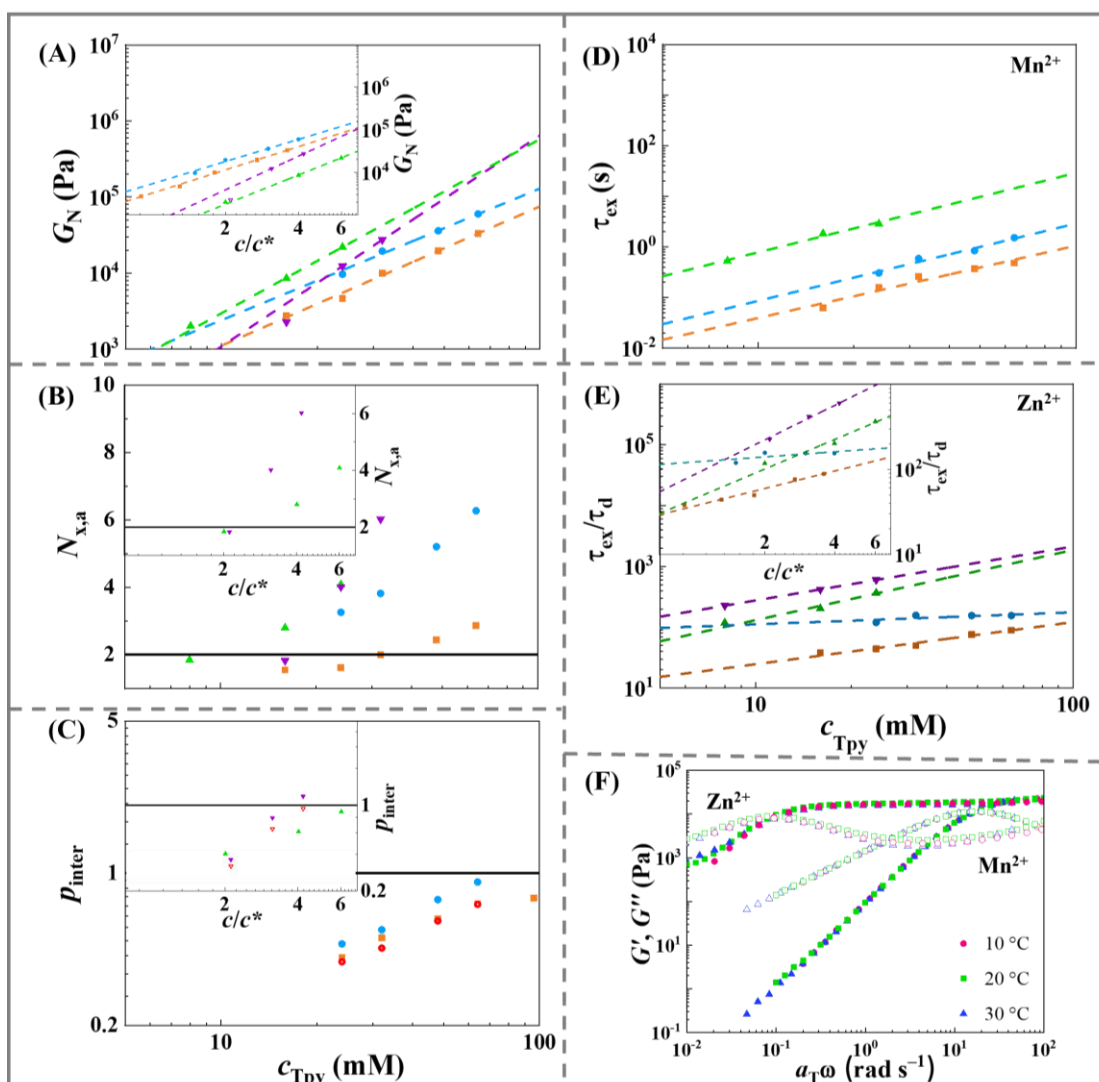


Figure 5.8. (A) Plateau modulus, (B) average number of elastically active stickers per chain $N_{x,a}$ and (C) fraction of interchain bonds p_{inter} of supramolecular gels based on 4-pEG-10k-1 **5.12** (■), 4-pEG-10k-2 **5.13** ($f=4$: ●, $f=6$: ●), PU-1 **5.17** (▲) and PU-2 **5.18** ($f=4$: ▼, $f=6$: ▼) as a function of the sticker, and normalized polymer concentration (inserts) along with allometric fits (dashed lines). (D)/(E) (Normalized) network relaxation times of supramolecular gels based on 4-pEG-10k-1 **5.12** (Mn^{2+} : ■, Zn^{2+} : ■), 4-pEG-10k-2 **5.13** (Mn^{2+} : ●, Zn^{2+} : ●), PU-1 **5.17** (Mn^{2+} : ▲, Zn^{2+} : ▲) and PU-2 **5.18** (Mn^{2+} : ▼, Zn^{2+} : ▼) cross-linked by (D) $MnOTf_2$ and (E) $ZnOTf_2$ as a function of the tpy concentration and/or normalized polymer concentration (insert) along with allometric fits (dashed lines). (F) Master curves from temperature-dependent frequency-sweeps of 4-pEG-10k-1 **5.12** cross-linked with $MnOTf_2$ (high frequency crossover) or $ZnOTf_2$ (low frequency crossover) (G' : full symbols, G'' : empty symbols, $c_{tpy} = 48$ mM, $c_{PU} = 122$ g·L⁻¹ MeOH, $T = 20$ °C).

To further focus on the differences between the mono- and ditopic sticker gels, **Figure 5.8 A** shows that the plateau moduli of the ditopic star-PEG gels exceed those of the monotopic ones at identical sticker concentrations while the opposite is the case for the PU gels. This can be explained by the larger deviations regarding the PU concentration regime in terms of c/c^* at identical sticker concentrations (16 mM: PU-1: $4.0c^*$, PU-2: $2.1c^*$). As shown in the insert in **Figure 5.8 A**, the plateau moduli of the ditopic PU gels actually exceed those of the monotopic

ones, if compared with respect to the normalized polymer concentration c/c^* . Since the normalized polymer concentrations of the star-pEG precursors at identical sticker concentrations are very similar (24 mM: 4-pEG-1: $1.3c^*$, 4-pEG-2: $1.5c^*$), these gels are rather compared with respect to the assumption-free, exactly known sticker concentration. It should also be noted that a comparison of the linear and star-pEG systems with respect to c/c^* is not reasonable. The molar masses applied to calculate the overlap concentrations are well-known for the star-pEG, but only approximated for the PUs (GPC, pEG calibration).

Using the respectively most appropriate representation, the comparison of the concentration dependence of $N_{x,a}$ and p_{inter} (**Figure 5.8 B + C**) reveals that the ditopic gels of both model systems show a significantly steeper increase than their monotopic counterparts. To explain this finding, we reconsider the initial assumption of $f=4$ for the calculation of v_{exp} in the ditopic sticker gels. This naive treatment ignored the possibility that the ditopic stickers may contribute to a higher functionality by connecting three (or four) different chains instead of forming double strand bridges (**Figure 5.1**). The NMR spectrum of the ditopic sticker indicated that double-strand bridges are actually a highly unlikely binding situation and larger metallo-cycles are probably preferred. If an average functionality of $f=6$ is assumed for the calculation of the elastically active chains in the ditopic star-pEG gel, the fraction of interchain bonds coincides quantitatively with that, calculated for the monotopic star-pEG gel as shown in **Figure 5.8 C**. From this observation, we conclude that the fraction of interchain bonds at a given concentration is not affected by the multivalency of the stickers. Instead, an increasing cross-linking functionality develops especially at higher polymer concentrations, which leads to an increased plateau modulus at identical sticker concentrations. Since the effects of aggregation and increased functionality cannot be clearly distinguished in case of the PU gels, a similar superposition under consideration of a higher functionality fails (Insert **Figure 5.8 C**). For an unperturbed, quantitative comparison molecularly identical precursors and more knowledge around the in-gel structure are required.

Further on, we compare the network dynamics in terms of the longest network relaxation time τ_{ex} derived from the $G'-G''$ crossover frequency (**Figure 5.8 D + E**). The network relaxation times can firstly be compared with the dissociation times τ_d of the isolated $Zn(tpy)_2^{2+}$ complexes. Here, it can firstly be noted that the lifetime of the monotopic Zn^{2+} complex in the dilute limit ($\tau_{d,Zn(II),MeOH} = 0.9$ s, $\tau_{d,Zn(II),H_2O} = 1.7$ s)³⁷ and inside the least concentrated 4-pEG-1 gel ($c_{tpy} = 16$ mM, $\tau_{ex} = 34$ s) already differ by a factor around 40. This reveals a considerable lifetime renormalization resulting from the need of multiple sticker-opening attempts before a partner exchange and thus network relaxation take place.^{11,51,52} The relaxation times of the corresponding Mn^{2+} cross-linked gels can in turn only be compared to a literature value measured in aqueous solution $\tau_{d,Mn(II),H_2O} = 0.4$ s ($T = 19$ °C).³⁷ Assuming that the exchange kinetics in MeOH are also

around a factor two faster than in water as observed for the Zn^{2+} complexes, this corresponds to an essentially non-renormalized exchange time inside the star-pEG gels ($\tau_{\text{ex},\text{Mn(II)},4\text{-pEG-1}} = 0.2\text{--}0.5$ s). The renormalization concept assumes that the number of returns is generally inversely proportional to the sticker dissociation rate.¹⁷ Apparently, the $\text{Mn}(\text{tpy})_2^{2+}$ complexes open and close with such a high frequency that the number of returns remains close to one. For the PU gels ($\tau_{\text{ex},\text{Mn(II)},\text{PU-1}} = 0.5\text{--}2.9$ s, $\tau_{\text{ex},\text{Zn(II)},\text{PU-1}} = 107\text{--}330$ s) the lifetime prolongation is generally more pronounced, which again indicates an additional influence; most likely caused by sticker aggregates with slower exchange kinetics. Analogously to the star-pEG gels, the renormalization increases tremendously with the intrinsic sticker lifetime.

The concentration-dependence of the (normalized) relaxation times can be adequately captured by allometric fits with similar scaling exponents of $p = 1.5 \pm 0.1$ ($\tau_{\text{ex}} \propto c_{\text{tpy}}^p$) for all Mn^{2+} cross-linked gels and stronger varying values in case of the Zn^{2+} cross-linked ones ($\tau_{\text{ex}}/\tau_{\text{d}} \propto c_{\text{tpy}}^p$, **Table 5.3**). For the Mn^{2+} cross-linked gels, the similarity of the scaling exponents again underlines that the fast sticker kinetics weaken network specific influences. The scaling exponents can also be compared to the predictions of the sticky-Rouse model before ($\tau_{\text{ex}} \propto \phi^p$, unrenormalized bond lifetime: $p = 3.2$, renormalized bond lifetime: $p = 5$)¹⁵ and after ($p = 0.2$) the network strands between the stickers start to overlap ($\phi > \phi_s$). If approximated as $\phi_s = (N/N_{x^*})^{1-3\nu}$, all gels with $c_{\text{tpy}} > 16$ mM fulfill this condition. However, as concluded before from the concentration-dependence of the plateau moduli, the derived exponents support the former finding that most systems are still transitioning from intra- to intermolecular binding.

Table 5.3. Activation energies determined from temperature-dependent rheology measurements and concentration-dependent scaling law relations of relaxation time and plateau modulus.

sample	cross-linking agent	E_A (kJ·mol ⁻¹)	$\tau_{\text{ex}}/\tau_{\text{d}} \propto c_{\text{tpy}}^p$	$G_N \propto c_{\text{tpy}}^q$
4-pEG-10k-1 (12)	–	10 ^{a)}	x	x
	Mn ²⁺	52 ± 2 ^{b)}	x	1.8 ± 0.1
	Zn ²⁺	55 ± 3 ^{b)}	1.2 ± 0.2	
4-pEG-10k-2 (13)	Mn ²⁺	52 ± 2 ^{b)}	x	1.7 ± 0.1
	Zn ²⁺	57 ± 1 ^{b)}	0.2 ± 0.1	
PU-1 (17)	–	18 ± 3 ^{c)}	x	x
	Mn ²⁺	68 ± 3 ^{c)}	x	2.3 ± 0.1
	Zn ²⁺	67 ± 1 ^{c)}	0.9 ± 0.1	
PU-2 (18)	Mn ²⁺	61 ± 3 ^{c)}	x	2.8 ± 0.1
	Zn ²⁺	x	0.7 ± 0.1	

^{a)} determined by viscosity measurements at $c_{\text{pEG}} = 200$ g·L⁻¹²⁷; ^{b)} determined at $c_{\text{tpy}} = 48$ mM; ^{c)} determined at $c_{\text{tpy}} = 16$ mM; x: quantity not determined.

Further focusing on the differences between the mono- and ditopic sticker gels, it can be noted that the relaxation times of the latter ones are significantly prolonged at identical sticker and normalized polymer concentrations. This prolongation is quantified in terms of the multiplication factor separating both values. For the Mn^{2+} cross-linked gels, averaged multiplication factors of 2.2 ± 0.2 (star-pEG, 24–48 mM) and 1.6 (PU, 16 mM) are obtained due to the similar scaling. By

contrast, the concentration dependencies of the Zn^{2+} cross-linked ditopic gels are considerably weaker than those of their monotopic counterparts, and thus decreasing factors between 4.5–2.9 (star-pEG) and 3.2–2.7 (PU) are found. Normalizing the in-gel lifetimes with the dilute kinetics fails to superimpose the exchange times of the mono- and ditopic systems and thus an additional stabilization mechanism must occur inside the gel (**Figure 5.8 E**). Applying the illustrative concept of the bond-lifetime renormalization and assuming a similar fraction of interchain bonds, the prolonged relaxation times can be explained by an increased number of opening attempts. The effective bond-lifetime of the ditopic stickers increases because all binding sites involved in one junction, need to open at the same time before the attached network strands can relax (re-binding effect). As pointed out before, it is also consistent that the attempt number in gels cross-linked by the kinetically less stable Mn^{2+} complexes is only doubled but further increased in the Zn^{2+} cross-linked gels. A quantitatively similar dependence between multivalency, lifetime prolongation and binding affinity was reported in a computational study on linear chains with telechelic many-part stickers.⁵³ Considering the smaller differences between the mono- and ditopic PU gels in comparison to the star-pEGs, the presence of long-living sticker clusters inside which valency and renormalization are of minor importance, is again a reasonable assumption. To further explain the diminishing difference between the relaxation times of the mono- and ditopic gels at high concentrations, it can be argued that the explored volume of an open sticker generally decreases with the polymer concentration, and thus the differences imparted by the multivalent stickers becomes less pronounced at higher concentrations. For the Mn^{2+} cross-linked gels, a comparable trend remains invisible due to the weaker influence of the multivalency on the gel dynamics.

Since the gel dynamics are governed by the in-gel lifetime of the stickers, temperature is another easily accessible parameter to tune the physical interactions. Temperature-dependent rheology measurements lead to a variation of the network relaxation times while the plateau moduli remain constant. Thus, master-curves can be obtained by applying horizontal shift factors as shown in **Figure 5.8 E** and **Figure 5.15**. The temperature dependence of the relaxation time shows an Arrhenius-type activation and allows to calculate the activation energies E_A . As summarized in **Table 5.3**, the activation energies of the tetra-pEG gels are neither affected by the metal ion nor significantly increased by the ditopic stickers. Analogously, the activation energies of the PU gels are mostly independent of metal ion and sticker type, but generally $\sim 15 \text{ kJ}\cdot\text{mol}^{-1}$ higher than those of the star-pEGs. This increase can be attributed to the backbone chemistries as also indicated by the higher activation energy of the non-cross-linked solutions.²⁷ This is likely caused by the interactions of the H-bonding urethane groups, which once again underlines the formerly discussed aggregation tendency.²⁸ The similar activation energies of the mono- and ditopic sticker gels show that the different relaxation dynamics must result from the pre-exponential factor in the Arrhenius equation.

It could still be argued that the observed enhancement of the mechanical properties mainly results from the higher sticker density imparted by the ditopic stickers. To address this uncertainty, we probe the mechanical properties of gels based on tpy-functionalized star-pEGs with (1) an identical number of arms, but a reduced sticker spacing (4-pEG-5k-1 **5.20**), or (2) a higher number of arms, but an identical sticker spacing (8-pEG-20k-1 **5.21**) (**Table 5.1**). As shown in **Figure 5.9 A + B**, gels derived from these precursors exhibit faster relaxation times and lower plateau moduli if compared to the monotopic 4-pEG-10k-1 **5.12** gel. We attribute the reduced network strength to an increasing probability of loop formations in case of the shorter or more densely packed arms, which reduces the number of elastically active network strands. At the same time, the higher sticker density increases the probability to find a new binding partner, which in turn reduces the lifetime renormalization.²³ This argument is applicable because the sticker mobility is not reduced through a higher polymer concentration, which often accompanies higher sticker concentrations.¹³ These findings demonstrate that the enforcement of physical networks through the sticker density is limited and can be easily overcompensated by opposing effects.

Finally, we probed whether the gel enhancement introduced by the ditopic stickers is gradual or abrupt by measuring the rheological properties of mixed **5.12/5.13** star-pEG gels. As shown in **Figure 5.9 C**, the relaxation times increase linearly with the mass fraction of the ditopic sticker polymer while the plateau modulus initially drops and only increases, if the ditopic stickers impart the majority. Both observations are in agreement with the so-far presented conceptual picture. While the stronger bond-lifetime renormalization caused by the ditopic sticker gels is a local phenomenon happening at individual network junctions, a higher number of connectivity defects weakens the mixed gels. It can thus be concluded that the introduction of multivalent stickers into metallo-supramolecular networks immediately leads to a kinetic stabilization whereas an enhancement of the mechanical strength requires a complete exchange of the stickers.

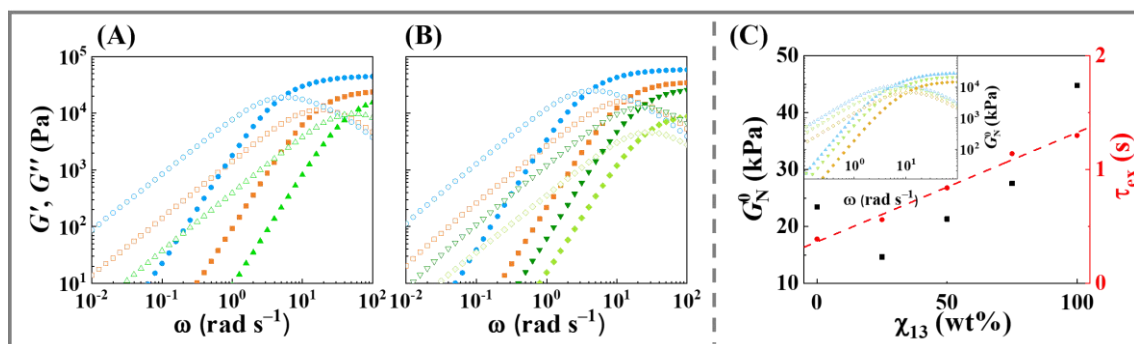


Figure 5.9. Frequency-sweeps of metallo-supramolecular polymer gels based on 4-pEG-10k-1 **5.12** (■), 4-pEG-10k-2 **5.13** (●) and (A) 8-pEG-20k-1 **5.21** (▲) at $c_{\text{tpy}} = 48$ mM or (B) 4-pEG-5k-1 **5.20** (◆: $c_{\text{tpy}} = 64$ mM, $0.9c^*$; ▼: $c_{\text{tpy}} = 96$ mM, $1.3c^*$). (C) Plateau moduli and network relaxation times of gels based on mixtures of **5.12** and **5.13** as function of the mass fraction χ_{13} of **5.13**. Insert: Frequency sweeps of gels containing 25 (◆), 50 (▼) and 75 wt% (▲) of **5.13** (G' : full symbols, G'' : empty symbols, cross-linked by MnOTf_2 , $c_{\text{tpy}} = 48$ mM if not stated otherwise, MeOH, 20 °C).

5.3 Conclusions

In this work, we explored how the immediate neighborhood of transient cross-linking motifs affects the macroscopic mechanical properties of metallo–supramolecular polymer gels. For this purpose, we designed two model systems based on star-shaped four-arm pEGs with telechelic stickers and linear pEG-based polyurethanes with equally spaced side-stickers comprised by either mono- or ditopic terpyridine ligands. Cross-linking these precursor polymers above their respective overlap concentrations with Mn^{2+} or Zn^{2+} yields viscoelastic gels with metal ion, polymer backbone, sticker concentration and -valency dependent properties. Comparing the concentration-dependent scaling relations of plateau moduli and relaxation times with the predictions from the sticky Rouse model indicates that the transformation from intra- to interchain binding is a major contribution for the concentration induced gel enhancement in the semi-dilute regime. In case of the star-pEG gels, the ditopic stickers appear to enable the development of multi-valent cross-linking junctions, which causes a duplication of the plateau moduli at similar sticker concentrations. Regarding the dynamics of these gels, the network relaxation times of the Mn^{2+} cross-linked ditopic gels are only doubled in comparison to their monotopic counterparts, but further prolonged in the Zn^{2+} cross-linked gels (x 3–5). Due to this increasing stabilization at higher binding affinities and a largely unaffected thermal activation energy, the enhanced lifetime renormalization in the ditopic sticker gels can be attributed to an increased number of opening attempts due to a higher re-binding rate. Comparing the star-shaped pEGs and linear PUs, DLS measurements of the precursor polymer solutions demonstrate the formation of PU aggregates, which are suspected to cause a partial sticker aggregation that leads to an increased mechanical strength and decelerates the relaxation dynamics of the corresponding gels. While the ditopic stickers prolong the relaxation times of the PU gels to a similar extent as within the star-pEG gels, the effect on the plateau modulus is less clear and further investigations concerning the in-gel homogeneity must be conducted. Nonetheless, our findings underline the great potential of multivalent ligands for the enhancement of supramolecular polymer networks and gels.

5.4 Experimental Section

Materials

Dimethyl carbonate (DMC, > 99%, Sigma Aldrich), *tert*-Butyl-dimethylsilyl chloride (TBDMS-Cl, 98%, Acros Organics), 1*H*-imidazole (99%, Acros Organics), triphenyl phosphine (PPh₃, > 99%, Alfa Aesar), diisopropyl azodicarboxylate (DIAD, 98%, Sigma Aldrich), 2,6-bis(2-pyridyl)-4(1*H*)-pyridone (tpy-OH, > 98%, TCI), ammonium hydrogen difluoride (NH₄HF₂, > 94%, Acros Organics), isophorone diisocyanate (IPDI, mixture of *cis/trans* isomers, 98%, Acros Organics), di-*n*-butyltin dilaurate (DBTDL, 98%, Alfa Aesar), 4'-chloro-2:2':6'.2"-terpyridine (tpy-Cl, > 99%, Sigma Aldrich), potassium hydroxide (KOH, Sigma Aldrich), triethylamine (NEt₃, 99%, Acros Organics), pyridine (99,8%, extra dry, Acros Organics), 4-nitrophenyl chloroformate (96%, Sigma-Aldrich), 4,7,13,16,21,24-hexaoxa-1,10-diazabicyclo[8.8.8]hexacosan (Kryptofix® 222, Sigma Aldrich), manganese(II)*bis*(trifluoromethane sulfonate) (Mn(OTf)₂, 97%, Sigma Aldrich) and zinc(II)*bis*(trifluoromethane sulfonate) (Zn(OTf)₂, > 98%, Strem Chemicals) are purchased from commercial resources and used without further purification. Glycerol (Sigma Aldrich, > 99.5%) is stirred over CaH₂ and vacuum distilled prior to use. Commercially available diglycerol (TCI, > 80%) is purified according to a literature procedure by derivatization as *bis*(2,3-dihydroxypropyl)ether decarbonate using DMC, recrystallization from ethyl acetate and subsequent deprotection.⁵⁴ Linear pEG-OH ($M_w = 4.3 \text{ kg mol}^{-1}$, $D = 1.03$) is purchased from Sigma Aldrich while the 4-arm pEG-OH ($M_w = 10 \text{ kg mol}^{-1}$, $D = 1.09$) and 8-arm pEG-OH ($M_w = 20 \text{ kg mol}^{-1}$, $D = 1.1$) are obtained from Creative PEG works. The polymers are purified by precipitation in diethyl ether, freeze dried from benzene and further dried under high vacuum at 60 °C for at least 4 h. Cyclohexane (^CHex), ethyl acetate (EA) dichloromethane (DCM) and methanol (MeOH) are used as received. Anhydrous tetrahydrofuran (THF), *N,N*-dimethyl formamide (DMF), dimethyl sulfoxide (DMSO), benzene and *N,N*-dimethyl acetamide (DMA) are purchased from Acros Organics (AcroSeal™) and used as received. Diethyl ether (Et₂O) is dried over sodium and freshly distilled under nitrogen atmosphere.

Chromatography

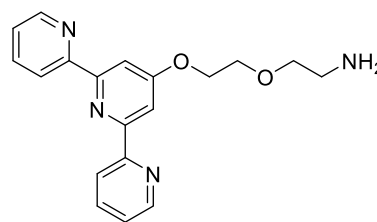
Thin-layer chromatography is performed on F₂₅₄ silica gel 60 (Merck), silica gel 60 RP-18 (Merck) or aluminum oxide 60 (Merck) coated plates. Spots are detected with UV-light ($\lambda = 254 \text{ nm}$) and immersion in KMnO₄ or iron(II)chloride solutions. Column chromatography is performed on silica gel 60 (40–63 μm , Merck Millipore), LiChroprep® RP-18 (40–63 μm , Merck Millipore), aluminum oxide (neutral, Brockmann I, 500–200 μm , Acros Organics) and Sephadex® LH-20. GPC measurements are performed at 60 °C in DMF (+ 1 g·L⁻¹ LiCl) using a 1260 Infinity GPC/SEC-system from Agilent (PSS SECurity pump, VWR Elite Chrom RI detector) equipped with a PSS GRAM guard column, two PSS GRAM 1000Å and one PSS GRAM 100 Å columns at a flow rate of 1 mL·min⁻¹. All data are analyzed with the software PSS WinSEC provided by

PSS. The number- and weight average molecular weight (M_n , M_w) and dispersity (\mathcal{D}) is calculated on the basis of a pEG calibration (calibration standards provided by PSS). NMR spectra are recorded on a Bruker Avance-III HD 300 or a Bruker Avance-II HD 400 instrument at 20 °C. The chemical shift δ is given in ppm by using tetramethylsilane as internal standard ($\delta = 0$ ppm) and deuterated solvents (CDCl_3 , MeOD, DMSO- d_6) as internal reference. The reported signal splittings are abbreviated as follows: s = singlet, d = doublet, t = triplet, a = appearing). Coupling constants J are reported in Hz. High resolution electron spray mass spectra (HR-ESI MS) are recorded on an Agilent 6545 QTOF-instrument. UV-Vis spectroscopy is performed on a Jasco V650 Spectrophotometer using a 1 cm quartz glass cuvette. Spectra are recorded in triplicate and corrected by dark and baseline measurements. Dynamic Light Scattering measurements are performed on an ALV/SP-125 compact goniometer system equipped with a Uniphase He/Ne Laser ($\lambda = 632.8$ nm, 22 mW), ALV/High QE APD-Avalanche photo-diode (Excelitas Technologies SPCM CD3296H) and a ALV/LSE-5004 multiple-tau digital correlator (all components: ALV-Laser Vertriebsgesellschaft mbH, Langen, Germany). A constant temperature of 20 °C is assured with an external thermostat (Lauda RC-6 CS). Shear rheological measurements are performed on a stress-controlled MCR 302 rheometer (Anton Paar) with a stainless-steel cone–plate geometry (cone angle: 1°, cone diameter: 25 mm) equipped with a solvent trap. The temperature is controlled by a Peltier plate. Motor adjustment and inertial calibration are performed before each measurement. Samples are equilibrated for 30 min after application and between different experiments at constant shear amplitude and frequency to ensure full equilibration. Amplitude sweeps are performed to determine the linear viscoelastic regime ($\gamma = 0.01$ –100 %, $\omega = 1/100$ rad·s⁻¹) before frequency sweeps are recorded between $\omega = 100$ –0.05/0.01 rad·s⁻¹ with a logarithmic increasing shear amplitude of $\gamma = 1$ –10 %.

Sticker Synthesis

Single terpyridine amine 5.3

Amine **5.3** is synthesized according to a modified procedure by Burazerovic *et al.*⁵⁵ Powdered KOH (1.160 g, 20.0 mmol, 5.4 eq.) is dried in a 50 mL Schlenk flask under high vacuum for 12 h. After addition of anhydrous DMSO (15 mL), the dispersion is heated to 60 °C and 2-(2-aminoethoxy) ethanol **5.2**

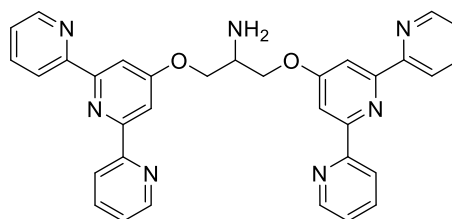


(0.390 g, 3.71 mmol, 1.0 eq.) is added under nitrogen atmosphere. After 30 min, 4'-chloro-2:2':6'.2"-terpyridine **5.1** (0.993 g, 3.71 mmol, 1.0 eq.) is added and the mixture is stirred for an additional 12 h. After cooling to r.t., the reaction mixture is poured into water (150 mL) and kept in a fridge for 2 h. The aqueous phase is filtered and extracted with DCM (3 x 100 mL). The combined organic phases are dried over Na_2SO_4 and the solvent is removed under reduced pressure. The product is obtained as slightly beige powder. **Yield:** 1.061 g, 83%. **TLC:** $R_f = 0.20$

(ACN:H₂O = 10:1, SiO₂-RP₁₈). **ESI-HRMS** (*m/z*): Calculated for [M+H]⁺: 337.1665, found: 337.1661. **¹H-NMR, COSY** (400 MHz, DMSO-*d*₆): δ = 8.71 (ddd, ³*J* = 4.8 Hz, ⁴*J* = 1.7 Hz, ⁵*J* = 0.9 Hz, 2H, tpy: C_{6/6''}), 8.61 (adt, ³*J* = 7.8 Hz, ^{4/5}*J* = 0.9 Hz, 2H, tpy: C_{3/3''}), 8.00 (atd, ³*J* = 7.8 Hz, ⁴*J* = 1.7 Hz, 2H, tpy: C_{4/4''}), 7.99 (s, 2H, tpy: C_{3'/5'}), 7.50 (ddd, ³*J* = 7.8 Hz, ⁴*J* = 4.8 Hz, ⁵*J* = 0.9 Hz, 2H, tpy: C_{5/5''}), 4.38 (m, 2H, tpyOCH₂), 3.81 (m, 2H, tpyOCH₂CH₂), 3.47 (t, ³*J* = 5.7 Hz, 2H, OCH₂CH₂NH₂), 2.68 (t, ³*J* = 5.7 Hz, 2H, CH₂NH₂) ppm. **¹³C-NMR, HMBC, HSQC** (100.1 MHz, DMSO-*d*₆): δ = 166.66 (tpy: C₄), 156.66 (tpy: C_{2/2''}), 154.82 (tpy: C_{2'/6'}), 149.21 (tpy: C_{6/6''}), 137.32 (tpy: C_{4/4''}), 124.47 (tpy: C_{5/5''}), 120.86 (tpy: C_{3/3''}), 106.80 (tpy: C_{3'/5'}), 73.11 (CH₂CH₂NH₂), 68.48 (tpyOCH₂CH₂), 67.69 (tpyOCH₂), 41.30 (CH₂NH₂) ppm.

Double terpyridine amine 5.5

Amine **5.5** is synthesized analogously with powdered KOH (1.540 g, 27.4 mmol, 10 eq.) and serinol **5.4** (0.250 g, 2.74 mmol, 1.0 eq.) in anhydrous DMSO (30 mL). After the addition of 4'-chloro-2':2':6'.2"-terpyridine **5.1** (1.469 g, 5.49 mmol, 2.0 eq.) the mixture

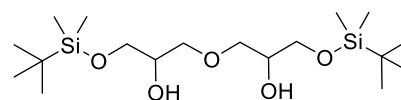


is stirred under heating for an additional 18 h. After cooling to r.t., the reaction mixture is poured into water (200 mL) and kept in a fridge for 2 h. The crude product is isolated by filtration and recrystallized from MeOH **Yield**: 0.955 g, 1.73 mmol, 63%. **TLC**: *R*_f = 0.10 (ACN:H₂O = 5:1, SiO₂-RP₁₈). **ESI-HRMS** (*m/z*): Calculated for [M+H]⁺: 554.2314, found: 554.2304. **¹H-NMR, COSY** (400 MHz, DMSO-*d*₆): δ = 8.71 (ddd, ³*J* = 4.8 Hz, ⁴*J* = 1.8 Hz, ⁵*J* = 1.0 Hz, 4H, tpy: C_{6/6''}), 8.60 (adt, ³*J* = 7.8 Hz, ^{4/5}*J* = 1.0 Hz, 4H, tpy: C_{3/3''}), 8.06 (s, 4H, tpy: C_{3'/5'}), 7.99 (atd, ³*J* = 7.8 Hz, ⁴*J* = 1.8 Hz, 4H, tpy: C_{4/4''}), 7.49 (ddd, ³*J* = 7.8 Hz, ⁴*J* = 4.8 Hz, ⁵*J* = 1.0 Hz, 4H, tpy: C_{5/5''}), 4.34 (m, 4H, tpyOCH₂), 3.57 (t, ³*J* = 5.6 Hz, 1H, tpyOCH₂CH), 1.98 (s, 2H, NH₂) ppm. **¹³C-NMR, HMBC, HSQC** (100.1 MHz, CDCl₃): δ = 166.6 (tpy: C₄), 157.37 (tpy: C_{2/2''}), 156.08 (tpy: C_{2'/6'}), 149.20 (tpy: C_{6/6''}), 136.91 (tpy: C_{4/4''}), 123.99 (tpy: C_{5/5''}), 121.44 (tpy: C_{3/3''}), 107.48 (tpy: C_{3'/5'}), 69.94 (tpyOCH₂), 50.34 (CHNH₂) ppm.

Single terpyridine diol **5.9a** is synthesized as described previously.²⁸

Compound 5.7b

Anhydrous diglycerol **5.6b** (5.0 g, 31 mmol, 1.0 eq.) and 1*H*-imidazole (6.3 g, 93 mmol, 3.0 eq.) are dissolved in a mixture of anhydrous THF (80 mL) and DMF (15 mL) under

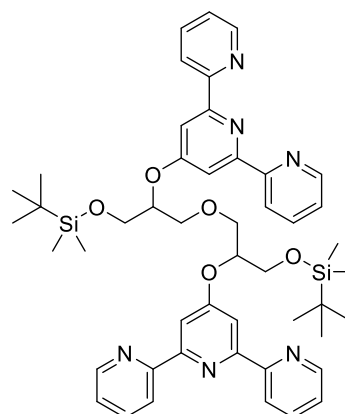


nitrogen atmosphere and cooled to 0 °C. A solution of *tert*-butyl-dimethyl chlorosilane (10.3 g, 68 mmol, 2.2 eq.) in anhydrous THF (40 mL) is added dropwise under vigorous stirring. After completed addition, the ice-bath is removed and the white suspension is stirred o/n at r.t. The reaction mixture is diluted with water (80 mL) and extracted with Et₂O (4 x 70 mL). The

combined extracts are washed with brine (50 mL), dried over Na_2SO_4 and concentrated under reduced pressure. The product is purified twice *via* flash chromatography on silica gel (DCM:MeOH = 20:1 to 100:1) and obtained a colorless oil. **Yield:** 6.0 g, 114 mmol, 48%. **TLC:** $R_f = 0.39$ (DCM/MeOH = 100:1, SiO_2). **ESI-HRMS** (m/z): Calculated for $[\text{M}+\text{Na}]^+$: 417.2463, found: 417.2465. **$^1\text{H-NMR}$, COSY** (400 MHz, $\text{DMSO-}d_6$): $\delta = 4.65$ (d, $^3J = 5.3$ Hz, 2H, OH), 3.60–3.28 (m, 10H, OCH/OCH₂), 0.85 (s, 18H, $\text{SiC}(\text{CH}_3)_3$), 0.02 (s, 12H, SiCH_3) ppm. **$^{13}\text{C-NMR}$, HMBC, HSQC** (100.6 MHz, $\text{DMSO-}d_6$): $\delta = 72.51$ (OCH), 70.11 (OCH), 64.45 (OCH₂), 25.83 (SiC), 18.02 (SiCCH_3), 5.31 (SiCH_3) ppm.

Compound 5.7.1b

Compound **5.7b** (2.09 g, 5.3 mmol, 1.0 eq.) and 2,6-bis(2-pyridyl)-4(1H)-pyridone **5.8** (2.77 g, 11.1 mmol, 2.1 eq.) are dissolved in anhydrous THF (20 mL) under nitrogen atmosphere and cooled to 0 °C. After addition and complete dissolution of triphenyl phosphine (5.83 g, 23.3 mmol, 4.2 eq.), a solution of diisopropyl azodicarboxylate (4.6 mL, 23.3 mmol, 4.4 eq.) in anhydrous THF (40 mL) is added dropwise before the ice-bath is removed and the solution is stirred o/n at r.t. Then, saturated NaHCO_3 solution (50 mL) is added to the reaction mixture and air

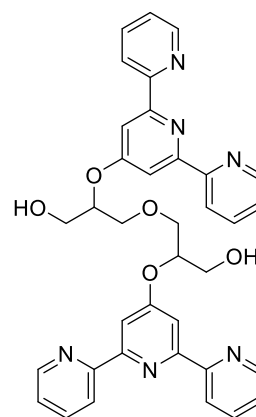


is bubbled through the solution for 1 h to oxidize the excess triphenyl phosphine. The reaction mixture is extracted with DCM (3 x 100 mL) and the combined organic phases are washed with brine (50 mL), dried over Na_2SO_4 and concentrated under reduced pressure. The residue is refluxed in ACN, cooled to 0 °C and the insoluble triphenyl phosphine oxide is filtered off (3x). The product is purified *via* flash chromatography on neutral Alox ($^c\text{Hex:EA} = 10:1$) and obtained as a colorless solid. **Yield:** 3.41 g, 4.54 mmol, 75%. **TLC:** $R_f = 0.23$ ($^c\text{Hex:EA} = 10:1$, Alox neutral). **ESI-HRMS** (m/z): Calculated for $[\text{M}+\text{H}]^+$: 857.4237, found: 857.4233. **$^1\text{H-NMR}$, COSY** (300 MHz, $\text{DMSO-}d_6$): $\delta = 8.68$ (d, $^3J = 4.7$ Hz, 4H, tpy: $\text{C}_{6/6''}$), 8.60 (d, $^3J = 7.8$ Hz, 4H, tpy: $\text{C}_{3/3''}$), 8.04/8.03 (s, 4H, tpy: $\text{C}_{3/5'}$), 7.79 (d, $^3J = 7.8$ Hz, 4H, tpy: $\text{C}_{4/4''}$), 7.27 (dd, 4H, $^3J = 7.8$ Hz, $^3J = 4.7$ Hz tpy: $\text{C}_{5/5''}$), 4.87 (p, $^3J = 5.0$ Hz, 2H, tpyOCH), 3.93–3.78 (m, 8H, OCH₂), 0.82 (s, 18H, $\text{SiC}(\text{CH}_3)_3$), 0.02 (s, 6H, SiCH_3), 0.01 (s, 6H, SiCH_3) ppm. **$^{13}\text{C-NMR}$, HMBC, HSQC** (75 MHz, $\text{DMSO-}d_6$): $\delta = 166.82$ (tpy: C_4'), 157.16 (tpy: $\text{C}_{2/2''}$), 156.20 (tpy: $\text{C}_{2/6'}$), 149.08 (tpy: $\text{C}_{6/6''}$), 136.74 (tpy: $\text{C}_{4/4''}$), 123.76 (tpy: $\text{C}_{5/5''}$), 121.34 (tpy: $\text{C}_{3/3''}$), 108.47 (tpy: $\text{C}_{3/5'}$), 77.73/70.82 (tpyOCH), 62.41z (OCH₂), 25.94 (SiC), 18.35 (SiCCH_3), -5.29 (SiCH_3) ppm.

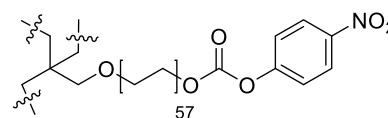
Double terpyridine diol 5.9b

Compound **5.7.1b** (3.20 g, 3.73 mmol, 1.0 eq.) is dissolved in anhydrous DMF (30 mL) in a Teflon flask and ammonium hydrogen fluoride (2.92 g, 51.2 mmol, 16 eq.) is added. After 96 h stirring at r.t. (complete conversion indicated by TLC), the reaction mixture is neutralized with saturated NaHCO₃ solution and the solvent is removed under reduced pressure at 60 °C. The residue is suspended in water (30 mL) and extracted with DCM (3 x 80 mL). The combined organic phases are dried over Na₂SO₄ and concentrated under reduced pressure. The white solid is purified *via* flash chromatography on RP₁₈ modified silica gel

(ACN:H₂O = 4:1) **Yield:** 1.24 g, 1.98 mmol, 54%. **TLC:** *R*_f = 0.22 (ACN/H₂O = 4:1, SiO₂-RP₁₈ silica gel) **ESI-HRMS** (*m/z*): Calculated for [M+H]⁺: 629.2507, found: 629.2504. **¹H-NMR, COSY** (400 MHz, DMSO-*d*₆): δ = 8.61 (m, 4H, tpy: C_{6/6''}), 8.46 (m, 4H, tpy: C_{3/3''}), 7.94 (s, 4H, tpy: C_{3/5'}), 7.91 (m, 4H, tpy: C_{4/4''}), 7.490 (m, 4H, tpy: C_{5/5''}), 5.02 (s, 2H, OH), 4.97 (t, ³*J* = 5.7 Hz, OH) 4.77 (m, 2H, tpyOCH), 3.90–3.65 (m, 8H, OCH₂CHCH₂O) ppm. **¹³C-NMR, HMBC, HSQC** (100.6 MHz, DMSO-*d*₆): δ = 166.48 (tpy: C_{4'}), 156.47 (tpy: C_{2/2''}), 154.84 (tpy: C_{2/6'}), 149.04 (tpy: C_{6/6''}), 137.13 (tpy: C_{4/4''}), 124.25 (tpy: C_{5/5''}), 120.77 (tpy: C_{3/3''}), 107.56 (tpy: C_{3/5'}), 78.25 (tpyOCH), 70.57 (HOCH₂), 60.04 (OCH₂) ppm.

**Polymer Synthesis****Compound 5.11**

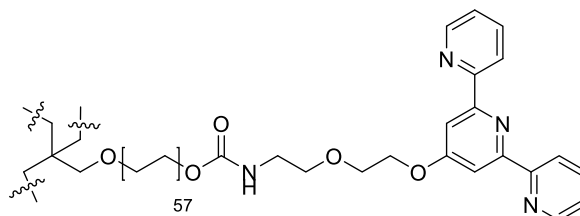
Compound **5.11** is synthesized according to a procedure by Rossow *et al.* starting from four-arm star-pEG (*M* = 10 kg·mol⁻¹, 2.996 g, 0.30 mmol, 1.0 eq.).¹² The product



is isolated by filtration as a slightly yellow powder and dried under high vacuum. **Yield:** 2.85 g, 95%. **¹H-NMR** (400 MHz, DMSO-*d*₆): δ = 8.32 (d, ³*J* = 9.2 Hz, 8H), 7.57 (d, ³*J* = 9.2 Hz, 8H), 4.37 (m, 8H, CH₂OC(=O)O), 3.51 (m, 1037H, (CH₂CH₂O)_{*n*}) ppm.

4-pEG-10k-1 5.12

The activated star-pEG **5.11** (1.009 g, 0.10 mmol, 1.0 eq.) is dissolved in anhydrous DMF (15 mL) before triethylamine (0.14 mL, 1.00 mmol, 10 eq.) and single terpyridine amine **5.3** (0.202 g, 0.60 mmol, 6.0 eq.) are



added. The reaction mixture is stirred for 48 h under nitrogen atmosphere at r.t., concentrated under reduced pressure at 60 °C, diluted with DCM (200 mL) and washed with saturated NaHCO₃ solution (3 x 50 mL). The organic phase is dried over Na₂SO₄ and the solvent is removed under reduced pressure. The product is purified by size-exclusion chromatography on Sephadex® LH-20

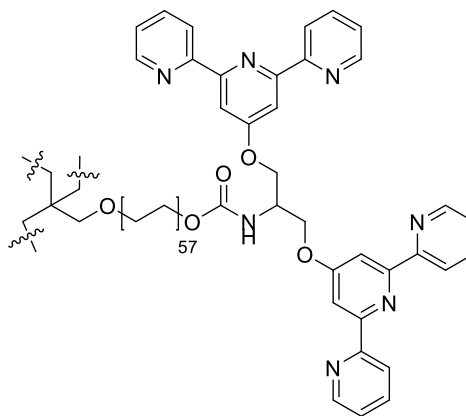
and isolated by lyophilization as colorless powder. **Yield:** 0.861 g, 86%. **¹H-NMR** (400 MHz, DMSO-*d*₆): δ = 8.72 (m, 8H, tpy: C_{6/6''}), 8.62 (d, ³*J* = 7.8 Hz, 8H, tpy: C_{3/3''}), 8.00 (atd, ³*J* = 7.8 Hz, ⁴*J* = 1.8 Hz, 8H, tpy: C_{4/4''}), 7.99 (s, 8H, tpy: C_{3'/5'}), 7.50 (ddd, ³*J* = 7.8 Hz, ⁴*J* = 4.8 Hz, ⁵*J* = 1.1 Hz, 8H, tpy: C_{5/5''}), 7.25 (t, ³*J* = 5.6 Hz, 4H, O(C=O)NH), 4.37 (m, 8H, CH₂OC(=O)N), 4.04 (m, 8H, tpyOCH₂), 3.82 (m, 8H, tpyOCH₂CH₂), 3.50 (m, 1094H, (CH₂CH₂O)_{*n*}) ppm.

4-pEG-10k-2 5.13

Analogously, the activated star-pEG **5.11** (1.002 g, 0.10 mmol, 1.0 eq.) is dissolved in anhydrous DMF (15 mL) before triethylamine (0.25 mL, 1.60 mmol, 16.0 eq.) and double terpyridine amine **5.5** (0.554 g, 1.00 mmol, 10.0 eq.) are added and stirred for 48 h.

Work-up and purification are carried out as described above. **Yield:** 0.681 g, 68%. **¹H-NMR** (400 MHz, DMSO-*d*₆): δ = 8.72 (m, 16H, tpy: C_{6/6''}), 8.61 (d,

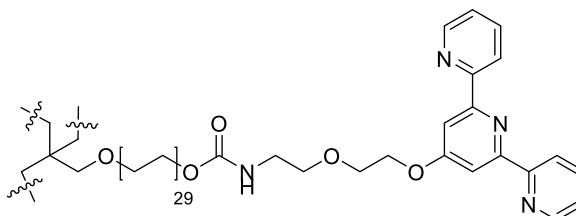
³*J* = 7.8, 16H, tpy: C_{3/3''}), 8.06 (s, 16H, tpy: C_{3'/5'}), 8.00 (atd, ³*J* = 7.8 Hz, ⁴*J* = 1.8 Hz, 16H, tpy: C_{4/4''}), 7.81 (d, ³*J* = 7.2 Hz, 4H, O(C=O)NH), 7.49 (ddd, ³*J* = 7.8 Hz, ⁴*J* = 4.8 Hz, ⁵*J* = 1.0 Hz, 16H, tpy: C_{5/5''}), 4.45 (m, 16H, CH₂CH₂OC(=O)N), 4.12 (m, 8H, tpyOCH₂), 3.49 (m, 1047H, (CH₂CH₂O)_{*n*}) ppm.



4-pEG-5k-1 5.20

Compound **5.20** is synthesized according to a modified procedure by Schlütter *et al.*⁵⁶ Powdered KOH (0.445 g, 8.0 mmol, 20.0 eq.) is dried in a 50 mL Schlenk flask

under high vacuum for 24 h at r.t. while 4-arm pEG (*M* = 5 kg mol⁻¹, 1.998 g, 0.40 mmol, 1.0 eq.) is dried in a separate 50 mL Schlenk flask under high vacuum for 24 h at 60 °C. Anhydrous DMSO (10 mL each) is added to both flasks and the KOH dispersion is heated to 60 °C under nitrogen atmosphere before [2.2.2]cryptand (0.150 g, 0.4 mmol, 1.0 eq.) and the pEG solution are added. After 30 min reaction time, 4'-chloro-2:2':6'.2"-tpy **5.1** (1.282 g, 4.8 mmol, 12.0 eq.) is added and the reaction mixture is stirred for 48 h at 60 °C. The mixture is cooled to r.t. and poured into water (150 mL). After filtration, the aqueous phase is extracted with CHCl₃ (3 x 100 mL). The combined organic phases are dried over Na₂SO₄, concentrated under reduced pressure, and precipitated into ice-cold Et₂O (1.0 L). The product is isolated as brownish powder. **Yield:** 1.779 g, 89%. **¹H-NMR** (400 MHz, DMSO-*d*₆): δ = 8.71 (m, 8H, tpy: C_{6/6''}), 8.61 (d,



$^3J = 7.8$ Hz, 8H, tpy: C_{3/3'}), 8.01 (m, 8H, tpy: C_{4/4'}), 7.98 (s, 8H, tpy: C_{3'/5'}), 7.50 (ddd, $^3J = 7.8$ Hz, $^4J = 4.7$ Hz, $^5J = 1.2$ Hz, 8H, tpy: C_{5/5'}), 4.37 (m, 8H, tpyOCH₂), 3.84 (m, 8H, tpyOCH₂CH₂), 3.18 (m, 446H, (CH₂CH₂O)_n) ppm.

4-pEG-20k-1 5.21

Compound **5.21** is synthesized according to a modified procedure by Wang *et al.*⁵⁷ Powdered KOH (0.147 g, 2.66 mmol, 63.0 eq.) is dried in a 50 mL Schlenk flask under high vacuum for 12 h at r.t. while 8-arm pEG ($M = 20$ kg mol⁻¹, 0.840 g, 0.04 mmol, 1.0 eq.) is dried in a separate 50 mL Schlenk flask under high vacuum for 12 h at 60 °C. Anhydrous DMSO (10 mL) is added to both flasks and the KOH dispersion is heated to 80 °C under nitrogen atmosphere before [2.2.2]cryptand (0.049 g, 0.13 mmol, 3.1 eq.) and the pEG solution are added. After 30 min reaction time, 4'-chloro-2':2':6'.2"-terpyridine **5.1** (0.269 g, 1.01 mmol, 24.0 eq.) is added and the reaction mixture is stirred for 5 days at 80 °C. The slightly brown mixture is cooled to r.t., poured into water (100 mL) under stirring and kept in a fridge for 2 h. After filtration, the aqueous phase is extracted with CHCl₃ (3 x 100 mL). The combined organic phases are dried over Na₂SO₄, concentrated under reduced pressure and precipitated into ice-cold Et₂O (1.5 L). The product is isolated as colorless powder by filtration and dried under high vacuum for 24 h. **Yield:** 0.335 g, 42%. **¹H-NMR** (400 MHz, DMSO-*d*₆): $\delta = 8.71$ (m, 16H, tpy: C_{6/6'}), 8.62 (adt, $^3J = 7.8$ Hz, $^4/5J = 1.1$ Hz, 16H, tpy: C_{3/3'}), 8.02 (atd, $^3J = 7.8$ Hz, $^4J = 1.9$ Hz, 16H, tpy: C_{4/4'}), 7.98 (s, 16H, tpy: C_{3'/5'}), 7.50 (ddd, $^3J = 7.8$ Hz, $^4J = 4.8$ Hz, $^5J = 1.1$ Hz, 16H, tpy: C_{5/5'}), 4.38 (m, 16H, tpyOCH₂), 3.84 (m, 16H, tpyOCH₂CH₂), 3.18 (m, 1853H, (CH₂CH₂O)_n) ppm.

The alternating PUs are synthesized according to a prior published procedure.²⁸

PU-1^{4k} 5.17

In short: IPDI (1.4 mL, 6.8 mmol, 30 eq.) is dissolved in anhydrous DMA (1.4 mL) in a flame-dried three-neck round bottom flask equipped with a dripping funnel. Freshly dried pEG-OH ($M_n = 4.2$ kg mol⁻¹, 1.00 g, 0.23 mmol, 1.0 eq.) is dissolved in anhydrous DMA (0.2 g·L⁻¹, 5.2 mL) at 40 °C and transferred into the dripping funnel. After addition of DBTDL (2 drops) to the IPDI mixture, the pEG solution is added dropwise and stirred for 2 h at r.t.. Next, the transparent solution is precipitated into anhydrous Et₂O (4 x 45 mL) under inert atmosphere. After cooling in an ice-bath for 30 min, the tubes are centrifuged, and the ether is decanted before the pre-polymer is re-precipitated analogously. Afterwards, the polymer is freeze-dried from benzene and weighed (0.886 mg, 0.18 mmol, 1.0 eq.) before it is re-dissolved in anhydrous DMA (1.0 mL) and heated to 50 °C. Next, DBTDL (2 drops) and a DMA solution of the single terpyridine diol **5.9a** (0.7 mL, 0.2 mol·L⁻¹, 0.8 eq.) are added. Further equivalents of the terpyridine diol are added after 12 and 24 h (0.18 mL, 0.2 eq. each) as 0.2M DMA solution. After 48 h at 50 °C, the reaction mixture is diluted with MeOH (5 mL) and precipitated into ice-cold Et₂O. After a further re-

precipitation, the polymer is obtained as white solid by lyophilization. **Yield:** 0.41 mg, 41%. **GPC** (DMF, pEG calibration): $M_n = 31.8 \text{ kg}\cdot\text{mol}^{-1}$, $M_w = 61.8 \text{ kg}\cdot\text{mol}^{-1}$, $D = 1.9$; $\langle x \rangle = 6.7$. **$^1\text{H-NMR}$** (400 MHz, MeOD): $\delta = 8.75$ (m, 1.6H, tpy: $\text{C}_{6/6''}$), 8.68 (m, 1.6H, tpy: $\text{C}_{3/3''}$), 8.12 (s, 1.6H, tpy: $\text{C}_{3/5''}$), 8.05 (m, 1.6H, tpy: $\text{C}_{4/4''}$), 7.53 (m, 1.6H, tpy: $\text{C}_{5/5''}$), 4.51 (m, 4H, tpyOCH), 4.19 (m, 4H, $\text{NHC(=O)OCH}_2\text{CH}_2\text{O}$), 3.91–3.43 (m, 384H, $(\text{CH}_2\text{CH}_2\text{O})_n$), 2.91 (m, 4H, IPDI: OC(=O)NHCH_2), 1.76–0.67 (m, 41H, IPDI) ppm.

PU-1^{2k} 5.19

The synthesis is carried out as described above with pEG-2k-OH ($M_n = 2.3 \text{ kg}\cdot\text{mol}^{-1}$, 0.998 g, 0.4 mmol, 1.0 eq.) and yielded the product as a white solid. **Yield:** 0.72 mg, 72%. **GPC** (DMF, pEG calibration): $M_n = 14.2 \text{ kg}\cdot\text{mol}^{-1}$, $M_w = 29.6 \text{ kg}\cdot\text{mol}^{-1}$, $D = 2.1$; $\langle x \rangle = 5.6$. **$^1\text{H-NMR}$** (600 MHz, MeOD): $\delta = 8.69$ (m, 1.5H, tpy: $\text{C}_{6/6''}$), 8.65 (m, 1.5H, tpy: $\text{C}_{3/3''}$), 8.05 (s, 1.5H, tpy: $\text{C}_{3/5''}$), 8.01 (m, 1.5H, tpy: $\text{C}_{4/4''}$), 7.49 (m, 1.5H, tpy: $\text{C}_{5/5''}$), 4.43 (m, 2H, tpyOCH), 4.14 (m, 4H, $\text{NHC(=O)OCH}_2\text{CH}_2\text{O}$), 3.88–3.45 (m, 180H, $(\text{CH}_2\text{CH}_2\text{O})_n$), 2.86 (m, 4H, IPDI: OC(=O)NHCH_2), 1.36–0.68 (m, 37H, IPDI) ppm.

PU-2^{4k} 5.18

The synthesis is conducted as described above with IPDI (1.4 mL, 6.75 mmol, 30 eq.), freshly dried pEG ($M_n = 4.2 \text{ kg}\cdot\text{mol}^{-1}$, 1.00 g, 0.23 mmol, 1.0 eq.) and a 0.2M solution of the double terpyridine diol **5.9b** (in total: 0.150 g, 0.24 mmol., 0.8 eq. + 0.2 eq. + 0.2 eq.) and yields the product as a white solid. **Yield:** 0.46 mg, 46%. **GPC** (DMF, pEG calibration): $M_n = 17.9 \text{ kg}\cdot\text{mol}^{-1}$, $M_w = 29.0 \text{ kg}\cdot\text{mol}^{-1}$, $D = 1.6$; $\langle x \rangle = 3.5$. **$^1\text{H-NMR}$** (400 MHz, MeOD): $\delta = 8.74$ –8.30 (m, 6.7H, tpy: $\text{C}_{6/6''}$, $\text{C}_{3/3''}$), 8.06–7.70 (s, 6.9H, tpy: $\text{C}_{3/5''}$, $\text{C}_{4/4''}$), 7.39 (m, 3.4H, tpy: $\text{C}_{5/5''}$), 4.35 (m, 2H), 4.17 (m, 4H, tpyOCH), 3.91–3.35 (m, 384H, $(\text{CH}_2\text{CH}_2\text{O})_n$), 2.89 (m, 4H, IPDI: OC(=O)NHCH_2), 1.75–0.58 (m, 38H, IPDI) ppm.

Molar Mass Distributions

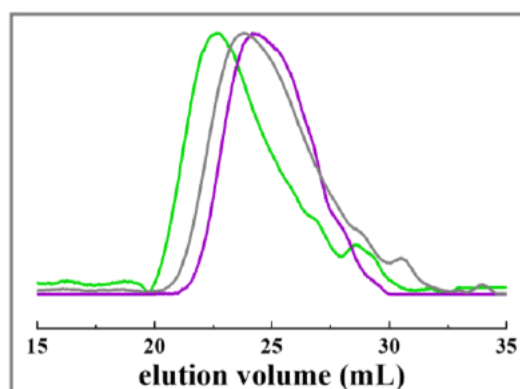


Figure 5.10. GPC elugrams of PU-1^{4k} **5.17** (—), PU-1^{2k} **5.19** (—) and PU-2^{4k} **5.18** (—) (DMF, RI signal, pEG calibration).

UV-Vis Spectroscopy

Polymer Functionalization

To determine the terpyridine content, the respective polymer (10–20 mg) is dissolved in methanol in a volumetric flask (25 mL). Three measurement solutions are prepared from this stock solution by dilution with methanol ($v/v = 1:5$). The molar decadic extinction coefficient of the single terpyridine amine **5.3** $\epsilon = (22.6 \pm 1) \cdot 10^2 \text{ L} \cdot \text{mol}^{-1} \cdot \text{cm}^{-1}$ ($\lambda_{\text{max}} = 278 \text{ nm}$) is applied to calculate the averaged terpyridine content $\langle \beta^{\text{exp}} \rangle$. The results are summarized in **Table 5.1** and **Table 5.4**. To obtain the corresponding functionalization degrees, theoretical values β^{theo} are calculated under the assumption that either every arm (star-pEGs) or repeating unit (PU: $\beta^{\text{theo}} = 1/M_{\text{n, repeating unit}}$, with $M_{\text{n, repeating unit}}(\text{PU-1}) = 5.12 \text{ kg} \cdot \text{mol}^{-1}$, $M_{\text{n, repeating unit}}(\text{PU-2}) = 5.42 \text{ kg} \cdot \text{mol}^{-1}$) contains one or two terpyridine molecules. The relative degree of functionalization α is then calculated by comparison of the experimental and theoretical values as $\alpha = 100\% \cdot \langle \beta^{\text{exp}} \rangle / \beta^{\text{theo}}$. The average number of individual terpyridine groups per chain is then estimated as $N_x = \alpha \cdot N_x^{\text{theo}}$ from the experimental functionalization degree α and the theoretically possible number of terpyridine groups per chain. Applying the assumptions from above, these are calculated as $N_x^{\text{theo}}(\text{5.12}) = 4$, $N_x^{\text{theo}}(\text{5.13}) = 8$, $N_x^{\text{theo}}(\text{5.17}) = 6.2$ and $N_x^{\text{theo}}(\text{5.18}) = 6.6$.

Table 5.4. Terpyridine functionalization of the star-pEGs **5.12** and **5.13** and linear pEG-polyurethanes **5.17** and **5.18**.

	β^{theo} ($\mu\text{mol g}^{-1}$)	$\langle \beta^{\text{exp}} \rangle$ ($\mu\text{mol g}^{-1}$)	α (%)	N_x^{theo}	N_x^{exp}
4-pEG-10k-1 (5.12)	400	392 ± 3	98	4	3.9
4-pEG-10k-2 (5.13)	800	690 ± 4	86	8	6.9
PU-1 (5.17)	213	145 ± 1	74	6.2	4.6
PU-2 (5.18)	394	270 ± 5	72	6.6	4.8

Terpyridine Titration

Solutions of the respective ligands (or polymers) ($c_{\text{tpy}} = 3 \mu\text{M}$) and Zn^{2+} salt (ZnOTf_2 , $c_{\text{Zn(II)}} = 2.8 \text{ mM}$) are prepared in methanol in a 50 mL volumetric flask. The metal salt solution is added in 30 μL portions to the ligand stock solution and stirred for 5 min at r.t., before an aliquot (2 mL) is taken and an UV-Vis spectrum is recorded. Afterwards, the aliquot is transferred back into the volumetric flask before the next Zn^{2+} portion is added, and the titration is continued analogously. The UV-Vis spectra and titration results are summarized in **Figure 5.3** and **Figure 5.11**.

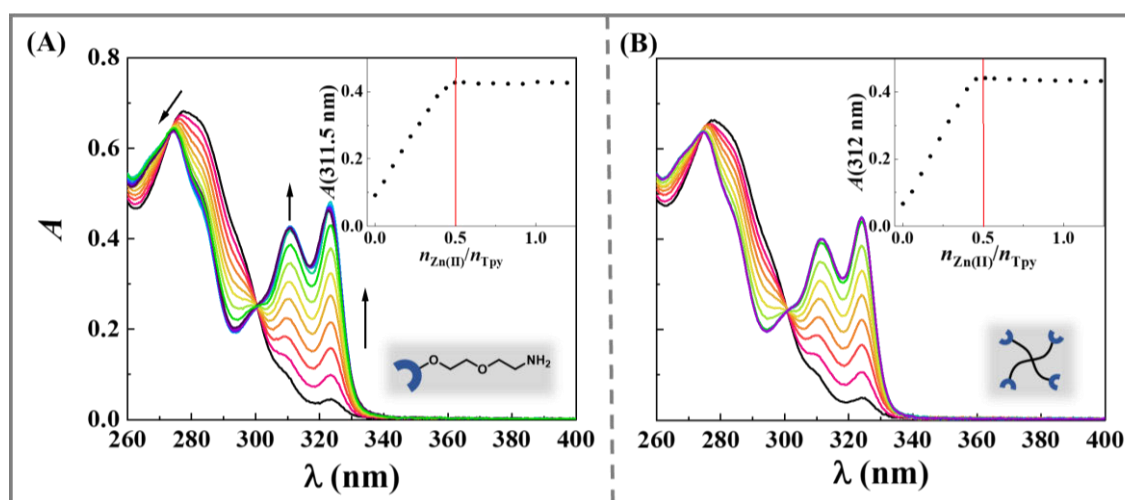


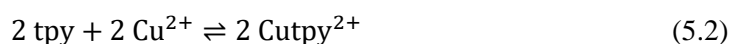
Figure 5.11. UV-Vis spectra of (A) monotopic tpy amine **5.3** and (B) 4-pEG-10k-1 **5.12** in MeOH upon titration with ZnOTf_2 ; Inserts: Absorption at 311.5 nm or 312 nm as a function of the molar $\text{M(II)}:\text{L}$ ratio.

Metal Exchange Kinetics

The dissociation rates of the $\text{Zn}(\text{tpy})_2^{2+}$ complexes of the mono- **5.3** and ditopic **5.5** tpy amines in MeOH are determined by time-dependent UV-Vis measurements according to a method reported by Holyer *et al.*³⁷ A solution of pre-mixed ligand and ZnOTf_2 ($V = 30 \mu\text{L}$, $c_{\text{tpy}} = 3 \text{ mM}$, $\text{L}:\text{M} = 2:1$, equilibrated for 24 h at 35 °C) is added to an excess of the stronger complexing CuBr_2 ($V = 2 \text{ mL}$, $c_{\text{Cu(II)}} = 0.5 \text{ mM}$, $\text{Cu}^{2+}/\text{Zn}^{2+} = 25:1$) leading to an exchange of the metal ion in the terpyridine complex. Since the UV-Vis band of the Cu^{2+} complex is shifted to higher wavelengths in comparison to the Zn^{2+} complex, a time-dependent measurement of the absorbance at 335 nm allows to follow the exchange reaction (**Figure 5.12 A**). Prior to each measurement, the CuBr_2 solution is equilibrated for 10 min at 10, 15, 20 and 25 °C in a quartz-glass cuvette inside the UV-Vis spectrometer and a baseline spectrum is measured. Then, the evenly tempered Zn^{2+} complex solution is added under vigorous stirring and the time-dependent absorbance measurement is simultaneously started (time interval: 0.05 s, 5 nm bandwidth). Each measurement is performed in triplicate.

The data evaluation is based on the following assumptions: It was shown that the $\text{Zn}(\text{tpy})_2^{2+}$ complex is the final product in the reaction with a stoichiometric amount of the ligand. The

formation of the mono-complex is the rate-determining step and takes place in the range of a few seconds while the second association happens within milliseconds. For the purpose of this study, the concentration of the mono-complex is thus considered to be negligible.⁵⁸ By contrast, it has been shown that the *bis*-complex of Cu²⁺ rearranges instantaneously to the mono-complex in non-aqueous media.⁵⁹ The formation of the Cu(tpy)²⁺ complex under the given experimental conditions is further supported by comparing the UV-Vis spectra taken at the end of the kinetic measurements to those of [Cutpy₂](PF₆) and [CutpyCl₂] reported by Merbach and co-workers. The shape of the complex-associated bands in the here-in recorded spectrum strongly resembles that of to the latter complex.⁵⁸ Based on these findings and neglecting the association of counter anions and solvent molecules, the following key reaction steps are suspected.



The dissociation rate of the Zn(tpy)₂²⁺ complex is given by

$$\frac{d[\text{Zntpy}_2^{2+}]}{dt} = -k_d[\text{Zntpy}_2^{2+}] \quad (5.3)$$

with the solution

$$[\text{Zntpy}_2^{2+}] = [\text{Zntpy}_2^{2+}]_0 \exp(-k_d t) \quad (5.4)$$

It can further be assumed that the concentration of free terpyridine in the presence of an excess of Zn²⁺ and Cu²⁺ is negligible. Applying the above-described simplifications, the mass balance of the terpyridine is approximated as

$$[\text{tpy}]_{\text{total}} = 2[\text{Zntpy}_2^{2+}]_0 = 2[\text{Zntpy}_2^{2+}] + [\text{Cutpy}^{2+}] \quad (5.5)$$

which leads to

$$[\text{Cutpy}^{2+}] = 2[\text{Zntpy}_2^{2+}]_0 (1 - \exp(-k_d t)) \quad (5.6)$$

Since the absorption at 335 nm is proportional to the concentration of Cu(tpy)²⁺, the dissociation constant k_d of interest is obtained from an exponential fit of the experimental data. The experimental data are normalized before the fitting.

$$A_{335\text{nm}}(t) = b_1 - b_2 \exp(-k_d t) \quad (5.7)$$

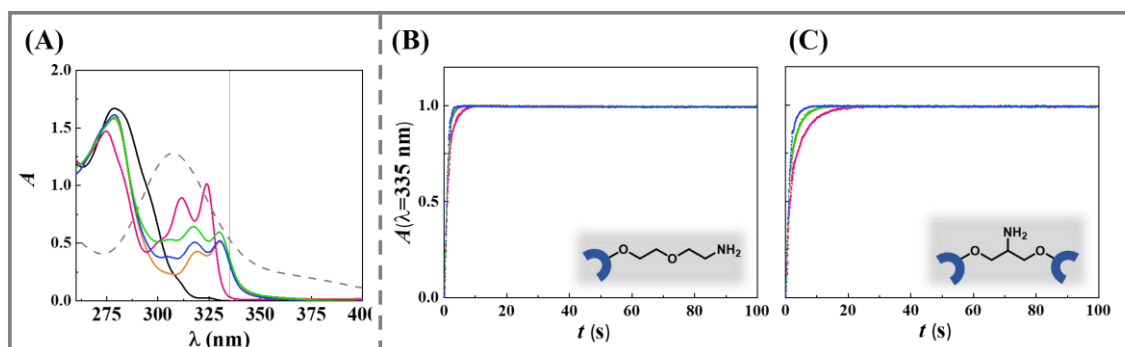


Figure 5.12. (A) UV-Vis spectra of the pure mono tpy-amine **5.3** (0.05 mM, \blacksquare), a 2:1 mixture of **5.3** and Zn^{2+} (\blacksquare), a 1:1 mixture of **5.3** and Cu^{2+} (\blacksquare), a 1:10 mixture of **5.3** and Cu^{2+} (\blacksquare), a 2:1:10 mixture of **5.3**, Zn^{2+} and Cu^{2+} (\blacksquare), and plain CuBr_2 (\blacksquare) all measured at a concentration of $c_{\text{tpy}} = 0.05$ mM in MeOH at 20 °C. Time-dependent absorbance profile at 335 nm at 10 (\blacksquare), 15 (\bullet), 20 (\blacktriangle) and 25 °C (\blacktriangledown) of (B) mono-**5.3** and (C) ditopic **5.5** $\text{Zn}(\text{tpy})_2^{2+}$ complexes.

Sticker Density

To compare the different model systems with respect to their relative sticker contents, the mole fraction of terpyridine groups in comparison to the pEG backbone is estimated from the $^1\text{H-NMR}$ spectra. For this purpose, the molar ratio between ethylene glycol (EG) and terpyridine (tpy) groups is firstly calculated by comparing the integrals of the EG backbone (3.88–2.53 ppm) and the terpyridine signal at 7.53 ppm.¹¹

$$\frac{n_{\text{EG}}}{n_{\text{tpy}}} = \frac{\frac{I_{3.6 \text{ ppm}}}{4}}{\frac{I_{7.5 \text{ ppm}}}{2}} \quad (5.8)$$

The molar terpyridine fraction is then calculated as $\langle s \rangle = \frac{n_{\text{tpy}}}{n_{\text{EG}} + n_{\text{tpy}}} = \frac{1}{1 + \frac{n_{\text{EG}}}{n_{\text{tpy}}}}$

Dynamic Light Scattering

Concentration Dependency

Prior to the light scattering measurements, dilute solutions of 4-pEG-10k-1 **5.12**, 4-pEG-10k-2 **5.13**, PU-1 **5.17** and PU-2 **5.18** in MeOH ($c \approx 1 \text{ g}\cdot\text{L}^{-1}$) are filtered using a combination of a Whatman Anotop filter (20 nm pore size) and a Millex-LG[®] filter (200 nm pore size). After freeze-drying these solutions, the polymers are dissolved in MeOH for 24 h to the initial measurement concentration. The light scattering cuvettes are rinsed with hot acetone before the polymer solutions are filtered into the cuvettes inside a dust-free laminar flow box (syringe filter: Millex-LG[®], 200 nm pore size). DLS measurements are performed at 20 °C at a successively increasing scattering angle between 30 and 120° (10° steps) recording ten runs with a correlation time of 60 s at each angle. The experimental intensity autocorrelation functions $g^{(2)}(q, \tau) = \langle I(q, t) \cdot I(q, t+\tau) \rangle \cdot \langle I(q, t) \rangle^{-2}$ are converted to the amplitude autocorrelation function $g^{(1)}(q, \tau)$ using the Siegert relation. $I(q, \tau)$ denotes the angular- and time-dependent intensity with the lag time τ and the scattering vector $q = 4\pi \cdot n_D \cdot \lambda^{-1} \cdot \sin(\theta/2)$ depending on the

refractive index of the solvent n_D ($n_D(\text{MeOH}) = 1.326$), the scattering angle θ and the laser wavelength $\lambda = 632.8$ nm.

In case of the 4-pEG-10k-1, the experimental amplitude auto-correlation function $g^{(1)}(q, \tau)$ shows a mono-exponential decay for all concentrations as exemplarily depicted in **Figure 5.13 A** for the 30° measurement. To take polydispersity effects into account, a biexponential function ($d = 1$) is applied to fit the experimental data. The obtained relaxation times τ_1 and τ_2 are within one order of magnitude and a weighted average applying the relative amplitudes $A_1 = a_2/(a_2+a_3)$ and $A_2 = a_3/(a_2+a_3)$ is used for the further data evaluation.

$$g^{(1)}(\tau) = a_1 + a_2 \cdot \exp\left(-\frac{\tau}{\tau_1}\right) + a_3 \cdot \exp\left(-\frac{\tau}{\tau_2}\right)^d \quad (5.9)$$

In contrast, the auto-correlation functions of 4-pEG-10k-2, PU-1 and PU-2 show a second, considerably slower relaxation process at all concentrations (**Figure 5.13 C, E, G**). The experimental data can be well-described by a stretched biexponential function of Kohlrausch-Williams-Watt's type ($0 < d < 1$) in case of the slow relaxation process which indicates a significantly broader distribution of this process. The first relaxation time corresponds directly to the fast mode $\tau_{\text{fast}} = \tau_1$, whereas the relaxation time of the slow mode is obtained applying the relation $\tau_{\text{slow}} = \tau_2 \cdot d^{-1} \cdot \Gamma(d^{-1})$ with the Gamma function Γ . Further on, the inverse relaxation times of both modes are plotted against the square of the scattering vector q^2 as shown in **Figure 5.13 D, F and H**. In all cases, linear dependencies are found, and the corresponding fits pass through the origin, as expected for translational diffusion processes. Therefore, the diffusion coefficients D_{fast} and D_{slow} are obtained directly from these slopes and the hydrodynamic radius R_h of an equivalent sphere can be calculated *via* the Stokes-Einstein equation $D = k_B T \cdot (6\pi\eta \cdot R_h)^{-1}$ with the Boltzmann constant k_B and the solvent viscosity η at 20°C ($\eta(\text{MeOH}) = 0.583$ mPa·s).

Additionally, the concentration portions χ_i of the species corresponding to the fast and slow relaxation processes are roughly estimated according to a former reported approach from the relative amplitudes A_i in the fit functions.⁶⁰ In short: The total scattering intensity $I_{\text{total}} = \sum I_i$ is the sum of the contributions from each scattering species I_i which is described by their respective normalized amplitude $I_i = \sum A_i \cdot I_{\text{total}}$. The relative amplitude A_i is however proportional to the concentration c_i and the molar mass M_i of species i $A_i \sim c_i M_i$. To estimate the molar mass of each species, the scaling of the radius of gyration R_G of a monodisperse Gaussian coil is applied $R_G \sim M^{0.6}$. The radius of gyration of each species is estimated from the experimentally obtained hydrodynamic radius R_h using the relation $\rho_{\text{star}} = R_G/R_h = 1.58$ for a monodisperse star and $\rho_{\text{PU}} = 2.05$ for a polydisperse random coil in a good solvent respectively.⁴¹ Finally, the concentrations of the slow and fast diffusing species along with their concentration portion χ_i are estimated as $c_i \sim \frac{A_i}{(\rho \cdot R_{h,i})^{1.6}}$ and $\chi_i \sim \frac{c_i}{\sum c_i}$.

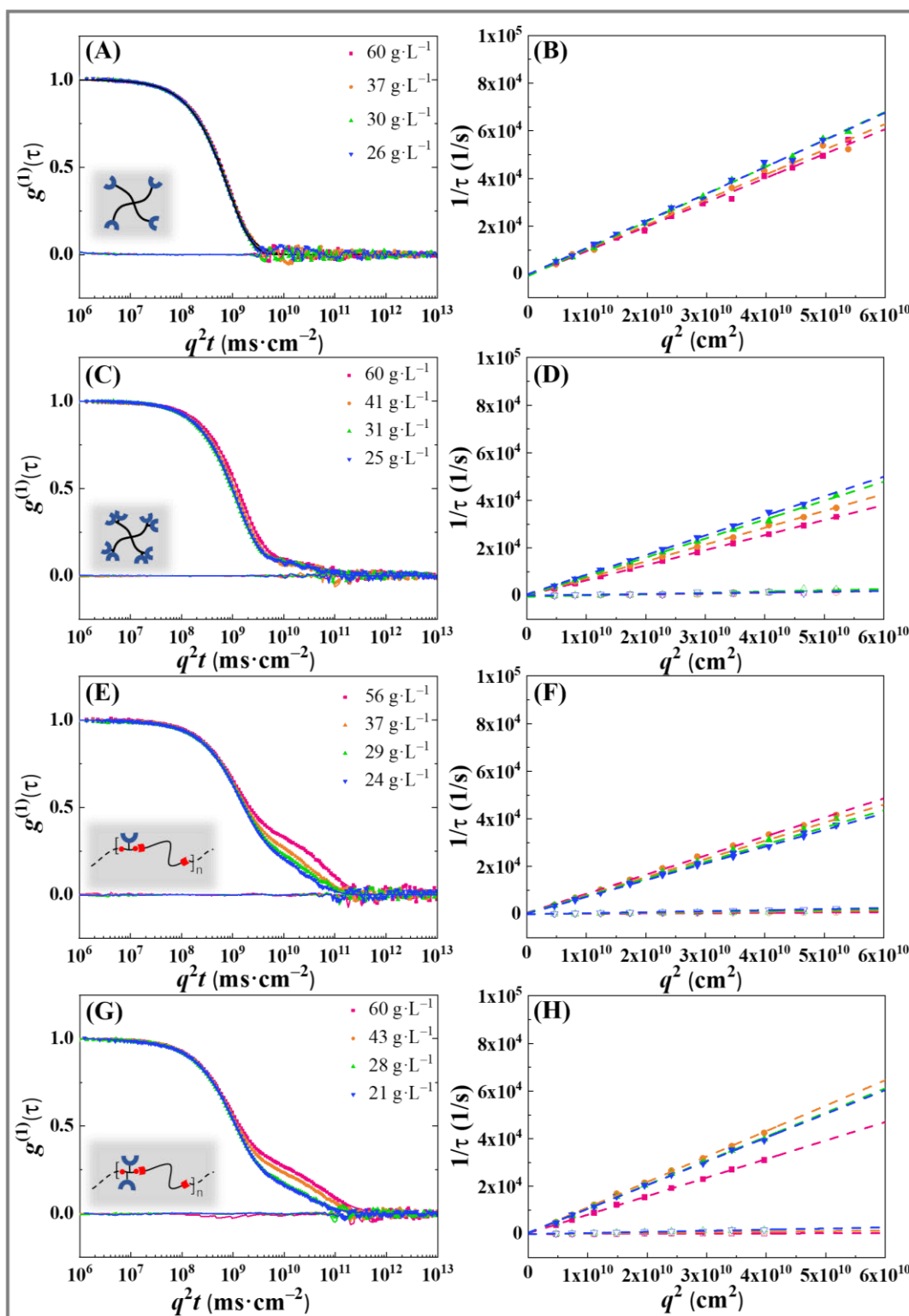


Figure 5.13. Normalized DLS autocorrelation functions of (A) 4-pEG-10k-1 **5.12**, (C) 4-pEG-10k-2 **5.13**, (E) PU-1 **5.17** and (G) PU-2 **5.18** at different concentrations in MeOH recorded at 20 °C at a scattering angle of 30° and the inverse relaxation times $1/\tau$ as a function q^2 with linear fits of (B) **5.12**, (D) **5.13**, (F) **5.17** and (H) **5.18** (same color code for the concentrations).

Overlap Concentration

Due to the presence of polyurethane aggregates in MeOH, the (self)-diffusion coefficient and thus the hydrodynamic radius of the individual polymer coils is instead determined from DLS measurements on dilute solutions in acetonitrile ($c = 10 \text{ g}\cdot\text{L}^{-1}$). Sample preparation and measurements are conducted as described previously between 30 and 150° in 15° steps. The experimental autocorrelation functions depicted in **Figure 5.14 A** and **B** are monomodal and fitted with a biexponential function as described above. The derived diffusion coefficients do not show an angular dependence as shown in **Figure 5.14 C** and thus the hydrodynamic radii R_h of an equivalent sphere are calculated from the averaged diffusion coefficients.

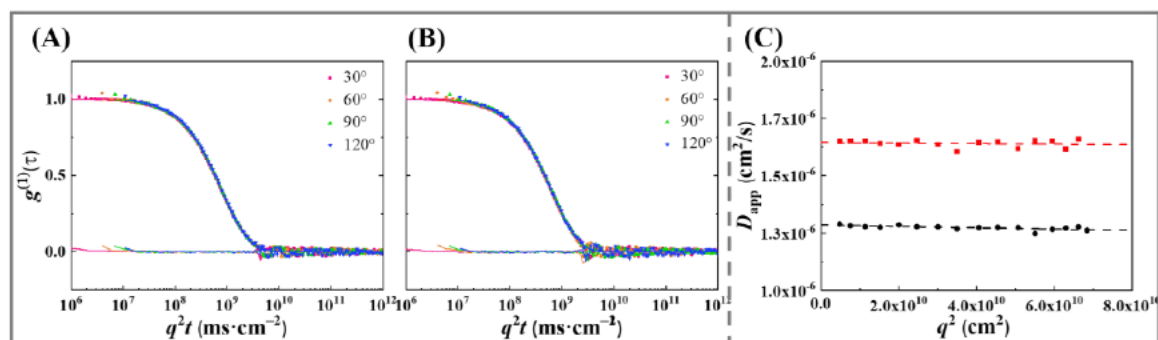


Figure 5.14. Normalized DLS autocorrelation functions of (A) PU-1 5.17 and (B) PU-2 5.18 in acetonitrile ($c = 10 \text{ g}\cdot\text{L}^{-1}$) recorded at 20 °C at 30, 60, 90 and 120°. (C) Angular dependency of the derived apparent diffusion coefficients with linear fits.

For the star-pEGs, the self-diffusion coefficient and thus sphere-equivalent hydrodynamic radius of an individual chain is extrapolated from the concentrations-dependent measurement in MeOH ($c \rightarrow 0$). Based on these results, the radii of gyration R_G are calculated applying the ratios $\rho_{\text{star}} = R_G/R_h = 1.58$ or $\rho_{\text{PU}} = 2.05$.⁴¹ The overlap concentrations are then approximated as $c^* = (3M_w)/(4\pi \cdot N_A \cdot R_G)$ with the weight average of the molar mass M_w and the Avogadro number N_A .

Table 5.5. Hydrodynamic radii of the tpy-functionalized polyurethanes in acetonitrile ($c = 10 \text{ g}\cdot\text{L}^{-1}$) and star-pEGs ins MeOH ($c \rightarrow 0$) as determined by DLS and geometrically estimated overlap concentrations.

sample	R_h (nm)	c^* (g L ⁻¹)
4-pEG-10k-1 (5.12)	2.8	46
4-pEG-10k-2 (5.13)	3.5	23
PU-1 (5.17)	4.7 ± 0.1	27
PU-2 (5.18)	3.6 ± 0.1	28

Gel Preparation

All gels are prepared in a total solvent volume of 250 μL . The respective polymer is first dissolved in 200 μL MeOH. A stock solution of the metal triflate is then diluted to the required concentration ($c_{\text{Me}^{2+}} = 0.5c_{\text{tpy}}$) and 50 μL are added to the polymer solution followed by immediate vortexing for 10–20 s and centrifugation for 10 min to remove air bubbles.

Afterwards, the samples are sealed and equilibrated for 24 h at 30 °C. The respective terpyridine and polymer concentrations are summarized in **Table 5.6**.

Table 5.6. Terpyridine- and polymer concentrations of the investigated metallo–supramolecular gels.

sample	c_{tpy} (mmol·L ⁻¹)	c_{polymer} (g·L ⁻¹)	c/c^*
4-pEG-10k-1 (5.12)	16	41	0.9
	24	61	1.3
	32	82	1.8
	48	122	2.7
	64	163	3.6
4-pEG-10k-2 (5.13)	24	35	1.5
	32	47	2.0
	48	70	3.0
	64	93	4.0
4-pEG-5k-1 (5.20)	64	88	0.9
	96	132	1.3
8-pEG-20k-1 (5.21)	48	130	3.7
PU-1 ^{4k} (5.17)	8	55	2.0
	16	110	4.0
	24	165	6.0
PU-2 (5.18)	16	60	2.1
	24	89	3.1
	32	119	4.2
PU-1 ^{2k} (5.19)	24	108	-

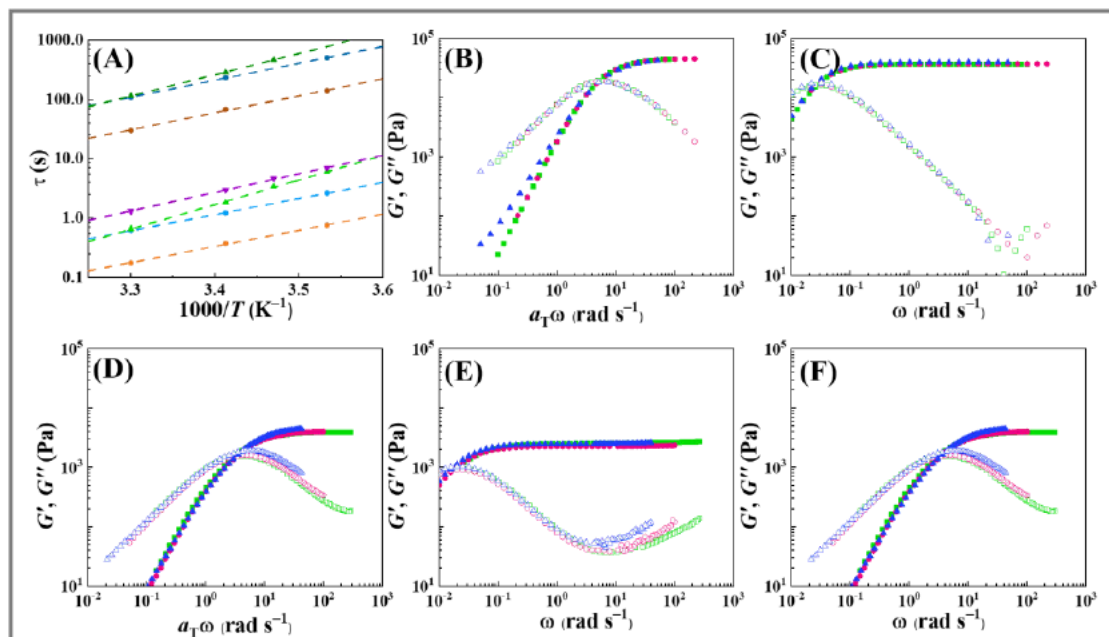


Figure 5.15. (A) Network relaxation times of supramolecular gels based on 4-pEG-10k-1 **5.12** (Mn²⁺: ●, Zn²⁺: ○), 4-pEG-10k-2 **5.13** (Mn²⁺: ■, Zn²⁺: □), PU-1 **5.17** (Mn²⁺: ▲, Zn²⁺: △) and PU-2 **5.18** (Mn²⁺: ▼) as a function of the temperature with Arrhenius-type fits (dashed lines). Master curves derived from frequency sweeps at 10 (●), 20 (■) and 30 °C (▲) of gels based on 4-pEG-10k-2 **5.13** cross-linked with (B) MnOTf₂ and (C) ZnOTf₂ at a concentration of $c_{\text{tpy}} = 48\text{mM}$, PU-1 **5.17** cross-linked with (D) MnOTf₂ and (E) ZnOTf₂ at a concentration of $c_{\text{tpy}} = 16\text{mM}$, and (F) PU-2 **5.18** cross-linked with MnOTf₂ at a concentration of $c_{\text{tpy}} = 16\text{mM}$ (G' : full symbols, G'' : empty symbols, all measured in MeOH).

5.5 References

- (1) Breul, [REDACTED] Sticker Multivalency in Metallo-supramolecular Polymer Networks. *Macromolecules* **2021**, *54*, 8407–8422.
- (2) Jourdain, A.; Asbai, R.; Anaya, O.; Chehimi, M. M.; Drockenmuller, E.; Montarnal, D. Rheological Properties of Covalent Adaptable Networks with 1,2,3-Triazolium Cross-Links: The Missing Link between Vitrimers and Dissociative Networks. *Macromolecules* **2020**, *53*, 1884–1900.
- (3) Voorhaar, L.; Hoogenboom, R. Supramolecular polymer networks: hydrogels and bulk materials. *Chemical Society reviews* **2016**, *45*, 4013–4031.
- (4) Ducrot, E.; Chen, Y.; Bulters, M.; Sijbesma, R. P.; Creton, C. Toughening elastomers with sacrificial bonds and watching them break. *Science (New York, N.Y.)* **2014**, *344*, 186–189.
- (5) Haraguchi, K.; Takehisa, T. Nanocomposite Hydrogels: A Unique Organic–Inorganic Network Structure with Extraordinary Mechanical, Optical, and Swelling/De-swelling Properties. *Adv. Mater.* **2002**, *14*, 1120.
- (6) Okumura, Y.; Ito, K. The Polyrotaxane Gel: A Topological Gel by Figure-of-Eight Cross-links. *Adv. Mater.* **2001**, *13*, 485–487.
- (7) Sun, J.-Y.; Zhao, X.; Illeperuma, W. R. K.; Chaudhuri, O.; Oh, K. H.; Mooney, D. J.; Vlassak, J. J.; Suo, Z. Highly stretchable and tough hydrogels. *Nature* **2012**, *489*, 133–136.
- (8) Seiffert, S.; Sprakel, J. Physical chemistry of supramolecular polymer networks. *Chemical Society reviews* **2012**, *41*, 909–930.
- (9) Xu, D.; Craig, S. L. Scaling Laws in Supramolecular Polymer Networks. *Macromolecules* **2011**, *44*, 5465–5472.
- (10) Yount, W. C.; Loveless, D. M.; Craig, S. L. Small-molecule dynamics and mechanisms underlying the macroscopic mechanical properties of coordinatively cross-linked polymer networks. *J. Am. Chem. Soc.* **2005**, *127*, 14488–14496.
- (11) Tang, S.; Olsen, B. D. Relaxation Processes in Supramolecular Metallogels Based on Histidine–Nickel Coordination Bonds. *Macromolecules* **2016**, *49*, 9163–9175.
- (12) Rossow, T.; Habicht, A.; Seiffert, S. Relaxation and Dynamics in Transient Polymer Model Networks. *Macromolecules* **2014**, *47*, 6473–6482.
- (13) Brassinne, J.; Cadix, A.; Wilson, J.; van Ruymbeke, E. Dissociating sticker dynamics from chain relaxation in supramolecular polymer networks—The importance of free partner! *Journal of Rheology* **2017**, *61*, 1123–1134.
- (14) Fullenkamp, D. E.; He, L.; Barrett, D. G.; Burghardt, W. R.; Messersmith, P. B. Mussel-inspired histidine-based transient network metal coordination hydrogels. *Macromolecules* **2013**, *46*, 1167–1174.

- (15) Hackelbusch, S.; Rossow, T.; van Assenbergh, P.; Seiffert, S. Chain Dynamics in Supramolecular Polymer Networks. *Macromolecules* **2013**, *46*, 6273–6286.
- (16) Ge, S.; Tress, M.; Xing, K.; Cao, P.-F.; Saito, T.; Sokolov, A. P. Viscoelasticity in associating oligomers and polymers: experimental test of the bond lifetime renormalization model. *Soft Matter* **2020**, *16*, 390–401.
- (17) Rubinstein, M.; Semenov, A. N. Thermoreversible Gelation in Solutions of Associating Polymers. 2. Linear Dynamics. *Macromolecules* **1998**, *31*, 1386–1397.
- (18) Badjić, J. D.; Nelson, A.; Cantrill, S. J.; Turnbull, W. B.; Stoddart, J. F. Multivalency and cooperativity in supramolecular chemistry. *Accounts of chemical research* **2005**, *38*, 723–732.
- (19) Errington, W. J.; Bruncsics, B.; Sarkar, C. A. Mechanisms of noncanonical binding dynamics in multivalent protein-protein interactions. *Proceedings of the National Academy of Sciences of the United States of America* **2019**, *116*, 25659–25667.
- (20) Weber, M.; Bujotzek, A.; Haag, R. Quantifying the rebinding effect in multivalent chemical ligand-receptor systems. *The Journal of chemical physics* **2012**, *137*, 54111.
- (21) Tang, Q.; Zhao, D.; Yang, H.; Wang, L.; Zhang, X. A pH-responsive self-healing hydrogel based on multivalent coordination of Ni²⁺ with polyhistidine-terminated PEG and IDA-modified oligochitosan. *J. Mater. Chem. B* **2019**, *7*, 30–42.
- (22) Figueiredo, T.; Cosenza, V.; Ogawa, Y.; Jeacomine, I.; Vallet, A.; Ortega, S.; Michel, R.; Olsson, J. D. M.; Gerfaud, T.; Boiteau, J.-G.; *et al.* Boronic acid and diol-containing polymers: how to choose the correct couple to form “strong” hydrogels at physiological pH. *Soft Matter* **2020**, *16*, 3628–3641.
- (23) Zhang, X.; Vidavsky, Y.; Aharonovich, S.; Yang, S. J.; Buche, M. R.; Diesendruck, C. E.; Silberstein, M. N. Bridging experiments and theory: isolating the effects of metal-ligand interactions on viscoelasticity of reversible polymer networks. *Soft Matter* **2020**, *16*, 8591–8601.
- (24) Charlot, A.; Auzély-Velty, R. Novel Hyaluronic Acid Based Supramolecular Assemblies Stabilized by Multivalent Specific Interactions: Rheological Behavior in Aqueous Solution. *Macromolecules* **2007**, *40*, 9555–9563.
- (25) Jangizehi, A.; Ahmadi, M.; Seiffert, S. Emergence, evidence, and effect of junction clustering in supramolecular polymer materials. *Mater. Adv.* **2021**, *13*, 2661.
- (26) Nair, K. P.; Breedveld, V.; Weck, M. Complementary Hydrogen-Bonded Thermoreversible Polymer Networks with Tunable Properties. *Macromolecules* **2008**, *41*, 3429–3438.
- (27) Rossow, T.; Seiffert, S. Supramolecular polymer gels with potential model-network structure. *Polym. Chem.* **2014**, *5*, 3018.
- (28) Breul, K.; Seiffert, S. Amphiphilic poly(ether urethanes) carrying associative terpyridine side groups with controlled spacing. *Polym. Chem.* **2021**, *12*, 2305–2316.

- (29) Zheng, J.; Lu, M. Monitoring Micelle Formation of Nonionic Polyurethane in Water by Fluorescence Spectrophotometry. *Journal of Macromolecular Science, Part B* **2014**, *53*, 1739–1749.
- (30) Mondal, T.; Dan, K.; Deb, J.; Jana, S. S.; Ghosh, S. Hydrogen-bonding-induced chain folding and vesicular assembly of an amphiphilic polyurethane. *Langmuir* **2013**, *29*, 6746–6753.
- (31) Paiva, G. M. S.; Duarte, L. G. T. A.; Faleiros, M. M.; Atvars, T. D. Z.; Felisberti, M. I. Z-E isomerization of azobenzene based amphiphilic poly(urethane-urea)s: Influence on the dynamic mechanical properties and the effect of the self-assembly in solution on the isomerization kinetics. *European Polymer Journal* **2020**, *127*, 109583.
- (32) Winter, A.; Friebe, C.; Chipper, M.; Hager, M. D.; Schubert, U. S. Self-assembly of π -conjugated bis(terpyridine) ligands with zinc(II) ions: New metallosupramolecular materials for optoelectronic applications. *J. Polym. Sci. Part A: Polym. Chem.* **2009**, *47*, 4083–4098.
- (33) Constable, E. C.; Housecroft, C. E.; Smith, C. B. Self-assembly of two discrete polynuclear iron(II) metallomacrocycles from a ligand containing two 2,2':6',2''-terpyridine binding domains. *Inorganic Chemistry Communications* **2003**, *6*, 1011–1013.
- (34) Beck, J. B.; Ineman, J. M.; Rowan, S. J. Metal/Ligand-Induced Formation of Metallo-Supramolecular Polymers. *Macromolecules* **2005**, *38*, 5060–5068.
- (35) Andres, P. R.; Schubert, U. S. Formation of Metallo-Polymers and -Macrocycles by Complexation of Alkyl-Linked Di-Terpyridines with Iron(II) Ions. *Synthesis* **2004**, *2004*, 1229–1238.
- (36) Dobrawa, R.; Lysetska, M.; Ballester, P.; Grüne, M.; Würthner, F. Fluorescent Supramolecular Polymers: Metal Directed Self-Assembly of Perylene Bisimide Building Blocks. *Macromolecules* **2005**, *38*, 1315–1325.
- (37) Holyer, R. H.; Hubbard, C. D.; Kettle, S. F. A.; Wilkins, R. G. The Kinetics of Replacement Reactions of Complexes of the Transition Metals with 2,2',2''-Terpyridine. *Inorg. Chem.* **1966**, *5*, 622–625.
- (38) Henderson, I. M.; Hayward, R. C. Kinetic stabilities of bis-terpyridine complexes with iron(ii) and cobalt(ii) in organic solvent environments. *J. Mater. Chem.* **2012**, *22*, 21366.
- (39) Henderson, I. M.; Hayward, R. C. Substituent effects on the stabilities of polymeric and small molecule bis-terpyridine complexes. *Polym. Chem.* **2012**, *3*, 1221.
- (40) Munzert, S. M.; Schwarz, G.; Kurth, D. G. Kinetic Studies of the Coordination of Mono- and Ditopic Ligands with First Row Transition Metal Ions. *Inorg. Chem.* **2016**, *55*, 2565–2573.
- (41) Burchard, W. Solution Properties of Branched Macromolecules. In *Branched Polymers II*; Roovers, J., Ed.; Advances in Polymer Science; Springer Berlin Heidelberg: Berlin, Heidelberg, 1999; pp 113–194.
- (42) Parada, G. A.; Zhao, X. Ideal reversible polymer networks. *Soft Matter* **2018**, *14*, 5186–5196.

- (43) Seiffert, S. Effect of Supramolecular Interchain Sticking on the Low-Frequency Relaxation of Transient Polymer Networks. *Macromol. rapid commun.* **2016**, *37*, 257–264.
- (44) Fumagalli, M.; Belal, K.; Guo, H.; Stoffelbach, F.; Cooke, G.; Marcellan, A.; Woisel, P.; Hourdet, D. Supramolecular polymer hydrogels induced by host-guest interactions with dicyclobis(paraquat-p-phenylene) cross-linkers: from molecular complexation to viscoelastic properties. *Soft Matter* **2017**, *13*, 5269–5282.
- (45) Grindy, S. C.; Lenz, M.; Holten-Andersen, N. Engineering Elasticity and Relaxation Time in Metal-Coordinate Cross-Linked Hydrogels. *Macromolecules* **2016**, *49*, 8306–8312.
- (46) Mahmad Rasid, I.; Holten-Andersen, N.; Olsen, B. D. Anomalous Diffusion in Associative Networks of High-Sticker-Density Polymers. *Macromolecules* **2021**, *54*, 1354–1365.
- (47) Rossow, T.; Hackelbusch, S.; van Assenbergh, P.; Seiffert, S. A modular construction kit for supramolecular polymer gels. *Polym. Chem.* **2013**, *4*, 2515.
- (48) Guo, M.; Pitet, L. M.; Wyss, H. M.; Vos, M.; Dankers, P. Y. W.; Meijer, E. W. Tough stimuli-responsive supramolecular hydrogels with hydrogen-bonding network junctions. *J. Am. Chem. Soc.* **2014**, *136*, 6969–6977.
- (49) Akagi, Y.; Gong, J. P.; Chung, U.-I.; Sakai, T. Transition between Phantom and Affine Network Model Observed in Polymer Gels with Controlled Network Structure. *Macromolecules* **2013**, *46*, 1035–1040.
- (50) Flory, P. J. *Principles of polymer chemistry*, 19. print; Cornell Univ. Press: Ithaca, NY, ca. 2006.
- (51) Cromwell, O. R.; Chung, J.; Guan, Z. Malleable and Self-Healing Covalent Polymer Networks through Tunable Dynamic Boronic Ester Bonds. *J. Am. Chem. Soc.* **2015**, *137*, 6492–6495.
- (52) McKinnon, D. D.; Domaille, D. W.; Cha, J. N.; Anseth, K. S. Bis-Aliphatic Hydrazone-Linked Hydrogels Form Most Rapidly at Physiological pH: Identifying the Origin of Hydrogel Properties with Small Molecule Kinetic Studies. *Chem. Mater.* **2014**, *26*, 2382–2387.
- (53) Sing, M. K.; Ramírez, J.; Olsen, B. D. Mechanical response of transient telechelic networks with many-part stickers. *The Journal of chemical physics* **2017**, *147*, 194902.
- (54) Tryznowski, M.; Świdarska, A.; Żółek-Tryznowska, Z.; Gołofit, T.; Parzuchowski, P. G. Facile route to multigram synthesis of environmentally friendly non-isocyanate polyurethanes. *Polymer* **2015**, *80*, 228–236.
- (55) Burazerovic, S.; Gradinaru, J.; Pierron, J.; Ward, T. R. Hierarchical self-assembly of one-dimensional streptavidin bundles as a collagen mimetic for the biomineralization of calcite. *Angewandte Chemie (International ed. in English)* **2007**, *46*, 5510–5514.
- (56) Schlütter, F.; Pavlov, G. M.; Gohy, J.-F.; Winter, A.; Wild, A.; Hager, M. D.; Hoepfner, S.; Schubert, U. S. Synthesis, characterization, and micellization studies of coil-rod-coil and ABA

ruthenium(II) terpyridine assemblies with π -conjugated electron acceptor systems. *J. Polym. Sci. Part A: Polym. Chem.* **2011**, *49*, 1396–1408.

(57) Wang, R.; Geven, M.; Dijkstra, P. J.; Martens, P.; Karperien, M. Hydrogels by supramolecular crosslinking of terpyridine end group functionalized 8-arm poly(ethylene glycol). *Soft Matter* **2014**, *10*, 7328–7336.

(58) Priimov, G. U.; Moore, P.; Helm, L.; Merbach, A. E. Kinetic and Mechanistic Studies of Substitution Reactions of Solvated Cobalt(II), Nickel(II), Copper(II) and Zinc(II) Ions with 2,2':6',2''-Terpyridine and Several 2,2':6',2''-Terpyridine Derivatives. Evidence for the Formation of Intermediates. *BioInorganic Reaction Mechanisms* **2001**, *3*, 1–24.

(59) Harris, C. M.; Lockyer, T. N. Nitrogenous chelate complexes of transition metals. VI. Complexes of copper(II) with 2,2',2''-terpyridine. *Aust. J. Chem.* **1970**, *23*, 673.

(60) Koziol, M.; Fischer, K.; Seiffert, S. Origin of the low-frequency plateau and the light-scattering slow mode in semidilute poly(ethylene glycol) solutions. *Soft Matter* **2019**, *15*, 2666–2676.

CHAPTER 6: HIERARCHICALLY SELF-ASSEMBLING, MULTI-STIMULI RESPONSIVE HYDROGELS

Publication:

Bridging Rigidity and Flexibility: Modulation of Supramolecular Hydrogels by Metal Complexation

██████████ K. Breul*, ██████████ *Macromolecular rapid communications* **2021**, e2100473 (doi.org/10.1002/marc.202100473).

*The authors contributed equally.

The results presented in the following chapter (p. 165–190) were first published on September 10, 2021 and are adapted with permission.¹

Further supporting information can be found in appendix, **Chapter A.6**.

Copyright © 2021 The Authors. *Macromolecular Rapid Communications* published by Wiley-VCH GmbH.

Summary

As demonstrated in **Chapter 5**, the combination of multiple binding sites represents an efficient method to increase the stability of supramolecular polymer gels. For self-assembling systems, the synergism of multivalent, reversible binding motives is even more essential to create reversible and yet stable, supramolecular structures. In the case of supramolecular hydrogels based on C_3 -symmetric peptide-amphiphiles, it is a combination of hydrogen bonding between β -sheet forming oligopeptides and hydrophobic interactions, which leads to the formation of anisotropic nanorod structures. These nanorods can be described as non-covalently jointed, linear chains whose aggregation induces the gelation of a formerly viscous solution. Such networks are especially useful for applications that require stimuli-responsive and reversible gelation switches e.g., for injectable thermogels.

In the following study, the self-assembly of peptide-amphiphiles is combined with a metal–ligand cross-linking approach to create a multi-stimuli responsive, reversible hydrogelator. For this purpose, two C_3 -symmetric monomers are synthesized, which are both equipped with β -sheet forming triphenyl alanine (FFF) tripeptides and contain either a Newkome-type, ethylene glycol dendron or a terpyridine (tpy) ligand. These monomers can be copolymerized with each other and form 1D nanorods as investigated by circular dichroism spectroscopy and transmission electron microscopy (TEM). The modular copolymerization approach allows to incorporate different molar ratios of the tpy monomer to evaluate its effect on the self-assembling process.

Further on, the metallo–supramolecular cross-linking of the self-assembled structures through the formation of *bis*-terpyridine complexes with different transition metal ions (Fe^{2+} , Zn^{2+} , Ni^{2+}) is investigated by linear shear rheology. These experiments reveal that a soft and reversible hydrogel can be formed from the nanorod solutions at a solids weight fraction of 1 wt%, if an additional, flexible pEG-linker with telechelic tpy groups is added. While the mechanical response of the Fe^{2+} and Zn^{2+} cross-linked systems largely coincide, weaker hydrogels are obtained in the presence of a stronger complexating Ni^{2+} salt. To explain this observation, the rheological investigations are complemented by TEM imaging. It is shown that the aspect ratios of the nanorod structures decreases drastically, when the kinetically very stable $\text{Ni}(\text{tpy})_2^{2+}$ -complex is formed. These findings demonstrate that it is not necessarily sufficient to increase the association strength of one binding motive in hierarchically assembling systems. Instead, it is essential to carefully adjust the strength and dynamics of the individual supramolecular binding motives.

Author Contributions:

■■■■■■■■■■ Synthesis of the C_3 -symmetric tpy-comonomer, CD measurements, gel preparation, manuscript preparation.

Katharina Breul: Concept and synthesis route development, synthesis of tpy-linkers, rheology measurements, manuscript preparation.

■■■■■■■■■■ Concept and synthesis route development, synthesis of the C_3 -symmetric structural comonomer, manuscript preparation.

■■■■■■■■■■ Synthesis of the C_3 -symmetric structural comonomer, TEM measurements.

■■■■■■■■■■ Manuscript correction.

■■■■■■■■■■ Scientific supervision, manuscript correction.

Acknowledgments:

The authors acknowledge funding through the Deutsche Forschungsgemeinschaft through GRK 2516 (Grant No. 405552959) and SE 1888/7-1 (Project No. 376900084). This work was further supported by the Max Planck Graduate Center with the Johannes Gutenberg–Universität Mainz. Open access funding is enabled and organized by Projekt DEAL.

6.1 Introduction

The interactions of proteins, enzymes, lipids and signaling cascades rely on synergistic supramolecular associations whose interplay has been optimized during millions of years of evolution. In natural systems, this commonly includes dissipative processes like the self-organization of microtubuli or actin filaments.²⁻⁴ These biological concepts inspired generations of material scientists to develop a multitude of responsive and adaptive materials based on self-assembling and self-organizing building blocks, which interact through non-covalent, reversible interactions.^{5,6} Especially the progress achieved in understanding the principles that control the hierarchic ordering and macroscopic functionality on a micro- and mesoscopic level, facilitated the rational design of supramolecular synthetic materials with adaptive features.⁷⁻¹¹ One prominent and widely applied approach uses monomeric or polymeric building blocks with hydrophobic and hydrophilic domains whose interplay induces a supramolecular polymerization in aqueous environments.¹²⁻¹⁴ The obtained aggregates are stabilized through cooperative, reversible interactions resulting from hydrogen bonding,¹⁵⁻¹⁹ electrostatic²⁰⁻²² or host-guest interactions,^{23,24} metal-ligand coordinations,²⁵⁻²⁷ hydrophobic effects or π - π stacks.²⁸⁻³² Note, that multiple hydrogen bonding as well as π - π stackings not only stabilize the supramolecular structures but also induce directed columnar stacks with high aspect ratios.^{29,33}

To create responsive materials that are functional in biologically relevant, aqueous environments, peptidic structures are especially suitable due to their well-established and tunable driving force in forming extended, regular superstructures in combination with an excellent biocompatibility e.g., required for medical applications.³⁴⁻³⁷ In this regard, our group previously reported the supramolecular self-assembly of C_3 -symmetric dendritic peptide amphiphiles in water, which can be controlled through different switches such as charge-screening, and redox-reactions.³⁸⁻⁴⁴ Moreover, we have been able to implement thermo-responsive dendritic units into the C_3 -symmetric monomers to enable a thermoresponsive hydrogelation.⁴⁵ Since the engineering of biomimetic materials generally requires the implementation of multi-stimuli responsive functionalities, such a combination of orthogonal gelation switches remains of great interest. To broaden the scope of multi-stimuli responsive hydrogels, this work combines the hydrophobic β -sheet driven self-assembly of uncharged peptide-amphiphiles and their reversible association using metal-ligand coordination chemistry. The tridentate terpyridine (tpy) ligand offers the advantage of forming highly directional *bis*-terpyridine complexes with controlled stoichiometry and easily variable complexation strength through the choice of the applied bivalent transition metal ion.⁴⁶ In previous studies, the supramolecular association of telechelic polyethylene glycol-tpy conjugates has been demonstrated on multiple occasions. However, due to the flexible polymer backbone, the formation of hydrogels generally required the use of branched telechelic precursors and high polymer contents around the coil overlap concentration.⁴⁷⁻⁴⁹ Previous reports

have shown, that the combination of such flexible linkers with rigid supramolecular structures decreases the critical solid weight content required to induce a hydrogelation.⁵⁰⁻⁵⁵ Following this approach, we designed a multicomponent system that combines the benefits of macromolecular and supramolecular polymers by interconnecting rigid, self-assembled peptide 1D nanostructures with flexible, telechelic polyethylene glycol (pEG) chains through the reversible complexation of tpy ligands with Zn^{2+} , Fe^{2+} and Ni^{2+} .⁵⁶ To incorporate tpy groups into 1D nanorods, a previously reported modular approach is applied, using the β -sheet encoded statistical supramolecular copolymerization of FFF-containing, structural monomers. Such a copolymerization strategy relies on the incorporation of functional comonomers and yields surface decorated anisotropic nanostructures, with a tunable density of cross-linkable ligands.⁵⁷

6.2 Results & Discussion

A terpyridine bearing C_3 -symmetric peptide monomer C_3^{tpy} **6.12** (Figure 6.1) was synthesized starting from *tert*-butyl[tri(ethylene glycol) propionate] **6.1** (Chapter 6.4, Scheme 6.1). After activation with methanesulfonyl chloride, nucleophilic substitution with sodium azide and a consecutive Staudinger reduction, [2,2':6',2''-terpyridine]-4'-carboxylic acid **6.6** was attached to this hydrophilic linker *via* an amide coupling. Standard acidic cleavage of the *tert*-butyl group yielded the tpy functionalized linker **6.7**. The structure defining oligo-peptide sequence N_3 -GFFF-OH **6.8** was synthesized by solid phase peptide synthesis and coupled with *N*-Boc-1,6-hexane amine hydrochloride **6.9** in a PyBOP-mediated amidation. The resulting peptide **6.10** was attached to 1,3,5-triethynylbenzene in a Cu^I -catalyzed azide-alkyne cycloaddition (CuAAC). The C_3 -symmetric scaffold **6.11** was obtained after removal of the *tert*-butyl group under acidic conditions and finally attached to the tpy linker **6.7** to give the tpy-functionalized monomer C_3^{tpy} **6.12**. To obtain a structural comonomer, a two-step synthesis was performed starting from the previously reported Newkome-type dendron **6.13** and the oligo peptide sequence N_3 -GFFF-OH **6.8**.⁴³ Attachment of the peptide amphiphile **6.14** to 1,3,5-triethynylbenzene yielded C_3^{EG} **6.15** (Figure 6.1, Scheme 6.2).

Due to the successful application in a previous study, it appeared promising to incorporate the tpy monomers through a statistical supramolecular copolymerization approach (Figure 6.1).⁵⁷ An initial indication for the successful copolymerization of both monomers was the observed transition from turbid suspensions of pure C_3^{tpy} in water to transparent solutions when mixed with C_3^{EG} . Further on, we used circular dichroism (CD) spectroscopy to investigate the supramolecular copolymerization of the monomers in water at ratios of $C_3^{EG}:C_3^{tpy} = 100:1$, $50:1$ and $10:1$ (Figure 6.2).

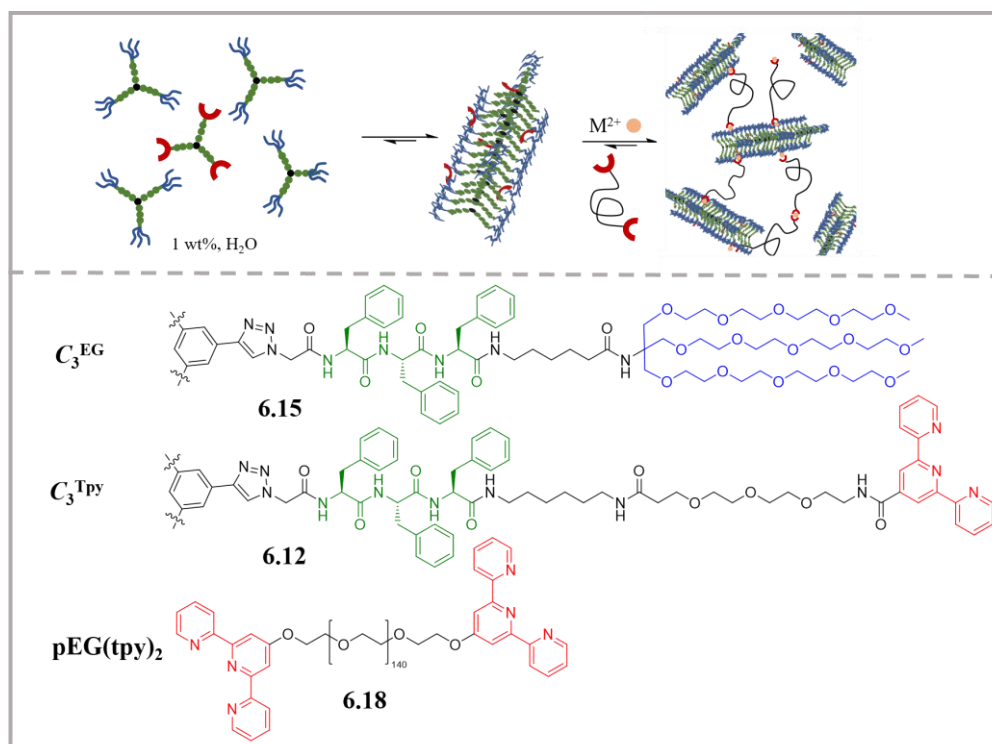


Figure 6.1. Schematic representation of the transition from the molecularly dissolved structural (C_3^{EG}) and functional (C_3^{tpy}) C_3 -symmetric comonomers into 1D nanorods in water and their interconnection with telechelic terpyridine functionalized pEG cross-linkers *via* metal ion complexation with the corresponding chemical structures of both monomers and the telechelic cross-linker.

The CD spectrum of pure C_3^{EG} in water serves as reference for all further comparisons and displays strong negative bands at $\lambda = 204$ nm and $\lambda = 211$ nm, which can be identified as characteristic signals for the formation of β -sheet secondary structures (**Figure 6.2**). In addition to the representative β -sheet indicating signals, weak positive bands at $\lambda = 265$ nm and $\lambda = 270$ nm appeared, which belong to the aromatic benzene tris(triazole) moiety from the hydrophobic monomer core.⁴³ While no shift of the signal was observed, the copolymers with ratios of 100:1 ($\Delta\epsilon = -204 \text{ L}\cdot\text{mol}^{-1}\cdot\text{cm}^{-1}$, green) and 50:1 ($\Delta\epsilon = -186 \text{ L}\cdot\text{mol}^{-1}\cdot\text{cm}^{-1}$, blue) revealed weaker intensities of the characteristic β -sheet bands at $\lambda = 204$ nm in comparison to the pure C_3^{EG} solution ($\Delta\epsilon = -241 \text{ L}\cdot\text{mol}^{-1}\cdot\text{cm}^{-1}$, black). When the amount of the tpy monomer is increased to 10%, an even more pronounced intensity decrease of the negative and positive bands is noticeable ($\Delta\epsilon = -140 \text{ L}\cdot\text{mol}^{-1}\cdot\text{cm}^{-1}$). These results are independent of the monomer concentration (**Figure 6.6 A–C**), which, together with the transition of turbid suspensions of C_3^{tpy} to clear solutions of both monomers, indicates the successful copolymerization of both monomers in water. The decreasing band intensity at higher tpy monomer ratios is indicative for competing interactions between the hydrophobic tpy moieties and the hydrophobic FFF tripeptide.

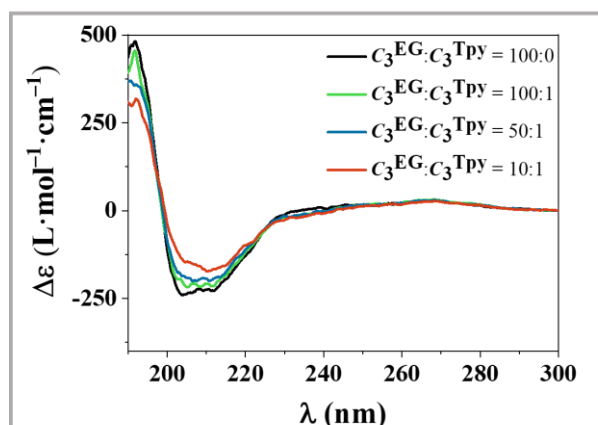


Figure 6.2. CD spectroscopic investigation of the self-assembly of C_3^{EG} and C_3^{tpy} : Pure C_3^{EG} (black) and of $C_3^{EG}:C_3^{tpy}$ in ratios of 100:1 (green), 50:1 (blue), and 10:1 (red) ($c = 50 \mu\text{M}$, water).

To probe this hypothesis, transmission electron microscopy (TEM) images were recorded to characterize the morphology of the supramolecular homo- and copolymers in water (**Figure 3A + B**). While anisotropic 1D nanorods are formed in both cases, the average length of the nanostructures formed in pure C_3^{EG} solutions ($L_n = 94 \pm 58 \text{ nm}$) is significantly larger than that of the $C_3^{EG}:C_3^{tpy} = 10:1$ copolymer ($L_n = 40 \pm 16 \text{ nm}$) which supports the assumption of competing interactions and an interference of the monomer stacking at higher tpy contents.

Once the supramolecular copolymerization of both monomers was confirmed, the anticipated metal-induced cross-linking of the described nanorods was investigated. To characterize the hydrogelation and viscoelastic properties of the resulting networks, shear rheological measurements were performed at a total monomer concentration of 1 wt% and a comonomer ratio of $C_3^{EG}:C_3^{tpy} = 10:1$. After sonication for five minutes and equilibration for 24 h, amplitude sweeps ($\gamma = 0.01\text{--}100\%$) were conducted at a constant frequency of $\omega = 1 \text{ rad}\cdot\text{s}^{-1}$ ($T = 20 \text{ }^\circ\text{C}$).

To firstly address the question, if and under which conditions a gelation is possible, Fe^{2+} was chosen as cross-linking metal ion as it rapidly forms thermodynamically and kinetically stable *bis*-terpyridine complexes in water ($\log(k_{\text{ass}}) = 4.9$, $\log(k_{\text{dis}}) = -2.2$, $\log K = 20.9$).⁵⁸ However, as shown in **Figure 6.4 A**, the addition of a stoichiometric amount of Fe^{2+} ($\text{Fe}^{2+}:\text{tpy} = 1:2$) to the pure comonomer mixture only leads to a slightly increased solution viscosity whereas no viscoelastic plateau emerges. Only after the further addition of the flexible, tpy-functionalized pEG cross-linker **6.18** ($n(\text{pEG}(\text{tpy})_2) = 3/2 n(C_3^{tpy})$), a weak hydrogel with a plateau modulus of $G_N = 16 \text{ Pa}$ and a considerable dissipation factor ($\tan\delta = G'/G''$) is formed within a linear viscoelastic (LVE) regime reaching from $\gamma = 0.01\%$ to 5%.

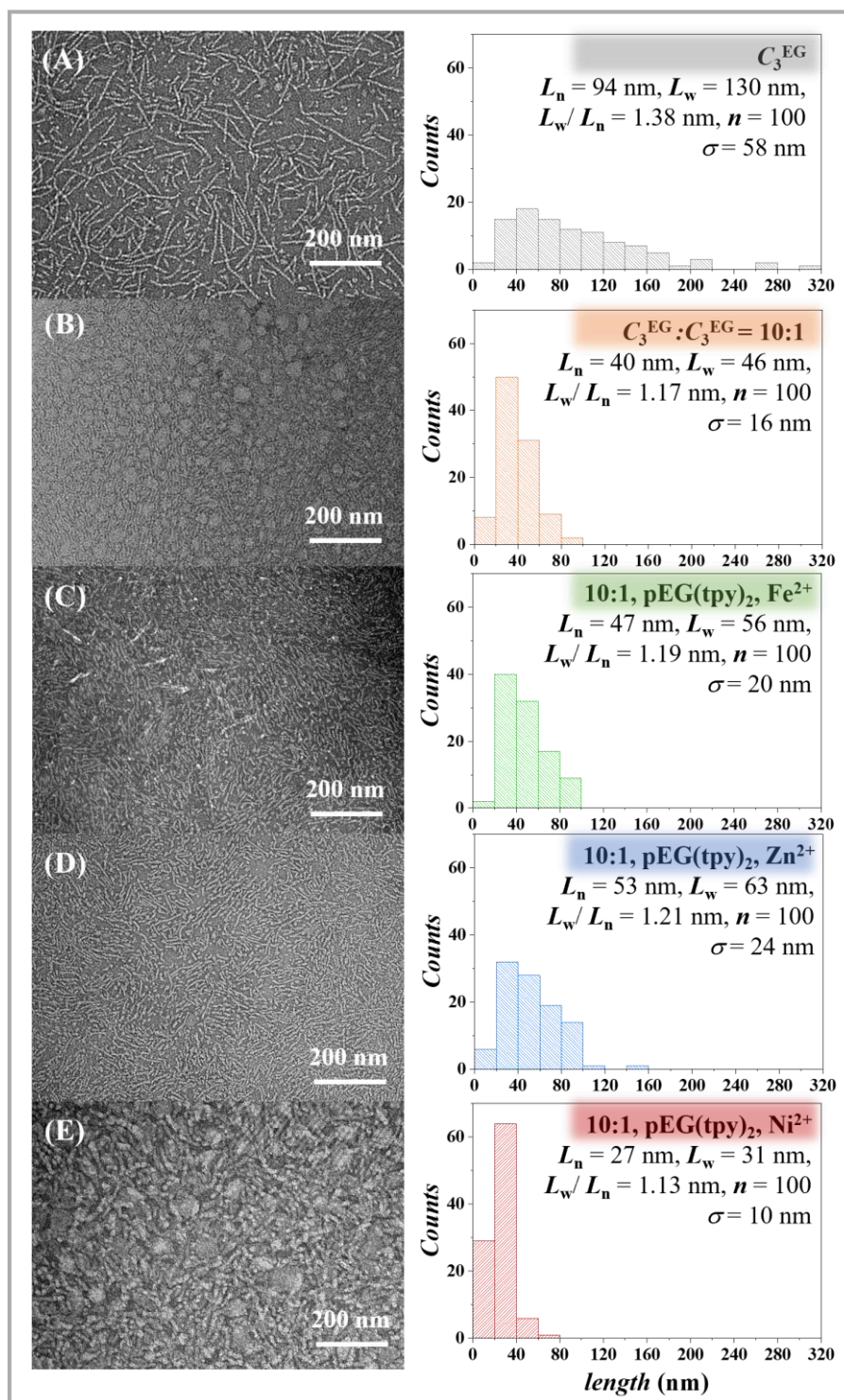


Figure 6.3. Negative stained TEM micrographs with the corresponding histograms of aqueous solutions of (A) C_3^{EG} , (B) $C_3^{EG}:C_3^{tpy}$ (10:1), (C) $C_3^{EG}:C_3^{tpy}$ (10:1), $pEG(tpy)_2$ and Fe^{2+} , (D) $C_3^{EG}:C_3^{tpy}$ (10:1), $pEG(tpy)_2$ and Zn^{2+} , and (E) $C_3^{EG}:C_3^{tpy}$ (10:1), $pEG(tpy)_2$ and Ni^{2+} ($c = 25 \mu M$, water, $20^\circ C$). Note, that all metal ions were added in form of their respective triflate salts.

To investigate how the gel properties depend on the tpy cross-linking reaction, the thermodynamic and kinetic stability of the complexation was next varied through the choice of the applied metal ion. In case of a kinetically and thermodynamic less stable $Zn(tpy)_2^{2+}$ complexation ($\log(k_{ass}) = 6.1$, $\log(k_{dis}) = -0.1$, $\log K = 6$)⁵⁸, a similar plateau modulus but a

smaller dissipation factor and lower flow point ($G' = G''$) are observed in comparison to the Fe^{2+} cross-linked hydrogel as shown in **Figure 6.4 B**. Apparently, the different association strengths and average lifetimes (Zn^{2+} : 1.3 s, Fe^{2+} : 160 s) of the *bis*-tpy complexes do not significantly affect the extent of cross-linking on the investigated time scale. This observation is consistent with the initially hypothesized metal-induced cross-linking of the pre-assembled 1D nanorods. Although the complexation seems to be the hydrogelation switch, the ultimate viscoelasticity is not limited by the tpy complexation and its binding kinetics or strength. The most likely limiting factor is thus rather the dynamic dis- and re-assembly of the nanorods themselves. To provide further proof for this binding scenario, we performed a control experiment with an over stoichiometric amount of Zn^{2+} (**Figure 6.4 B**). The equilibrium of the Zn^{2+} terpyridine complexation can be shifted towards the thermodynamically less stable mono-tpy complex if an excess of the metal ion is applied. This should impede the interconnection of the 1D nanorods.⁵⁹ As anticipated, the respective amplitude sweep (**Figure 6.4 B**, \blacklozenge) does not show any viscoelastic plateau but resembles that of the plain comonomer solution.

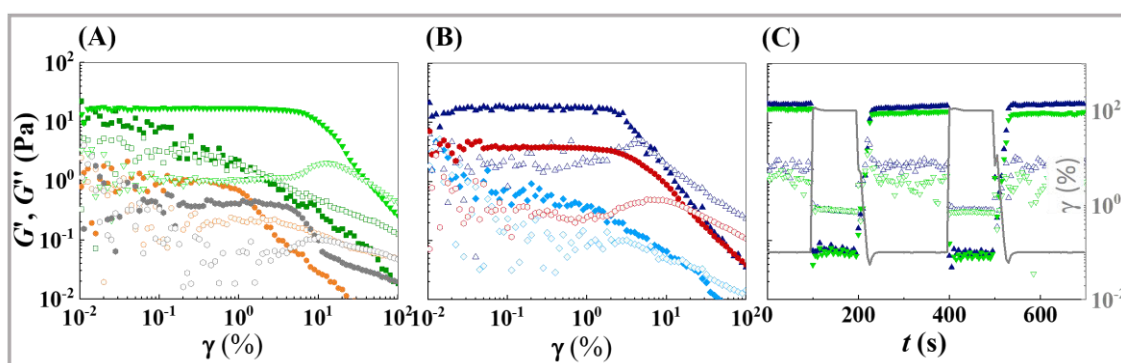


Figure 6.4. Amplitude-sweeps of aqueous solutions of $\text{C}_3^{\text{EG}}:\text{C}_3^{\text{tpy}} = 10:1$ mixtures (1 wt%) in the presence of (A) no further components (\bullet), $\text{pEG}(\text{tpy})_2$ (\blacksquare), only C_3^{EG} , Fe^{2+} (\blacksquare), Fe^{2+} and $\text{pEG}(\text{tpy})_2$ (\blacktriangledown) and (B) Zn^{2+} and $\text{pEG}(\text{tpy})_2$ (\blacktriangle), Ni^{2+} and $\text{pEG}(\text{tpy})_2$ (\bullet) and $\text{pEG}(\text{tpy})_2$ together with an over-stoichiometric amount of Zn^{2+} (\blacklozenge). (C) Step strain measurements (color code as before) ($\text{M}^{2+}:\text{tpy} = 1:2$ if not indicated otherwise, ($\omega = 1 \text{ rad s}^{-1}$), H_2O , $T = 20 \text{ }^\circ\text{C}$, G' : full symbols, G'' : empty symbols).

Further on, we investigated the hydrogel formation upon addition of Ni^{2+} ions (**Figure 6.4 B**, \bullet) which form the kinetically most inert complexes with average dissociation times in the range of hours ($\log(k_{\text{ass}}) = 3.1$, $\log(k_{\text{dis}}) = -7.6$, $\log K = 21.8$).⁵⁸ Due to the high association constant, reversible polymer networks cross-linked by $\text{Ni}(\text{tpy})_2^{2+}$ complexes actually show the purely elastic behavior of their covalent counterparts at ambient conditions.⁶⁰ Typical network relaxation times measurable by stress relaxation experiments at elevated temperatures ($70 \text{ }^\circ\text{C}$) comprise more than 15 h.⁶¹ However, in the present study, a lower plateau modulus but similar LVE regime was observed in comparison to the Fe^{2+} and Zn^{2+} cross-linked gels. The nanostructural investigation of the Ni^{2+} cross-linked nanorods *via* TEM revealed not only a decrease in the average length compared to the other metal ion treated samples (Fe^{2+} : $L_n = 47 \pm 20 \text{ nm}$; Zn^{2+} :

$L_n = 53 \pm 24$ nm; Ni^{2+} : $L_n = 27 \pm 10$ nm) but also a significantly increased number of clustering assemblies (**Figure 6.3 E**). This is indicative for the formation of nanorod bundles, which reduces the number of potentially elastically active components. It appears likely that the practically covalent binding of the tpy-functionalized comonomers to each other or the pEG linker prohibits the dynamic assembly of the anisotropic nanostructures. Note also, that we have already shown that telechelic pEG–tpy conjugates do not form hydrogels at such low concentrations of 1 wt%.⁴⁷ To probe the reversible nature of the non-covalent networks, step-strain tests were conducted (**Figure 6.4 C**). Under high strain conditions ($\gamma = 100\%$), the microstructure undergoes disruption, leading to a liquid-like state with $G' < G''$. After removal of the strain ($\gamma = 1\%$), an immediate transition to the initial status is observed as the microstructure regenerates. Such behavior was observed for at least two cycles of testing, demonstrating the rapid self-healing characteristics of these metallo–supramolecular hydrogels.

Finally, considering the formerly described thermoresponsive properties of related C_3 -symmetric monomers with dendritic oligo(ethylene glycol) moieties, temperature dependent CD measurements were performed using the 10:1 monomer mixture between 10 °C and 90 °C. As shown in **Figure 6.5 A**, the position, shape, and intensity of the characteristic CD bands does not alter significantly upon increasing the temperature. However, while still showing the presence of β -sheet structures, plotting the signal intensity at $\lambda = 210$ nm against the temperature shows a 10% decrease in the signal intensity from $\Delta\epsilon = -165 \text{ L}\cdot\text{mol}^{-1}\cdot\text{cm}^{-1}$ at 10 °C to $\Delta\epsilon = -148 \text{ L}\cdot\text{mol}^{-1}\cdot\text{cm}^{-1}$ at 90 °C (**Figure 6.7 A**). We also examined the influence of temperature on the viscoelastic properties. As shown in **Figure 6.5 B**, the plain comonomer mixture, as well as the Fe^{2+} and Zn^{2+} cross-linked samples, display a parallel increase of storage and loss modulus when the temperature is raised from 20 °C to 50 °C.

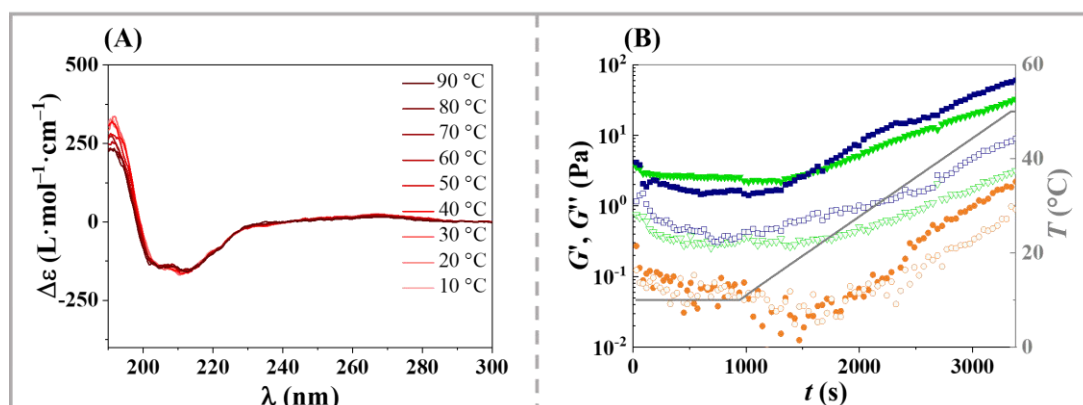


Figure 6.5. Temperature-dependent investigation of aqueous solutions of $C_3^{\text{EG}}:C_3^{\text{tpy}} = 10:1$ mixtures. **(A)** CD spectra with a stepwise temperature increase from 10 °C to 90 °C ($c = 50 \mu\text{M}$). **(B)** Temperature dependent time sweeps (1 wt%, $\gamma = 1\%$, $\omega = 1$ Hz, G' : full symbols, G'' : empty symbols) in the presence of no further components (\bullet), Fe^{2+} and **pEG(tpy)₂** (\blacktriangledown), Zn^{2+} and **pEG(tpy)₂** (\blacksquare).

In case of the plain comonomer solution, G' increases from ~ 0.1 Pa to 2 Pa, which can be explained by the decreasing hydrophilicity of the oligo-ethylene glycol corona at elevated temperatures. This effect is analogously observed in the Zn^{2+} and Fe^{2+} cross-linked samples, where the temperature rise leads to an increase of the storage moduli by more than an order of magnitude (**Figure 6.5 B**).

6.3 Conclusions

In summary, we have presented the synthesis and application of a terpyridine decorated supramolecular copolymer on the basis of C_3 -symmetric β -sheet driven self-assembling triphenyl alanine domains (FFF). The copolymerization of the structural C_3^{EG} and the functional C_3^{tpy} monomers was investigated by circular dichroism (CD) and transmission electron microscopy (TEM). The TEM imaging revealed that the aspect ratios of the self-assembled 1D nanorods got reduced by the incorporation of the tpy monomer. However, the tpy-decorated corona allowed to cross-link the 1D nanorods through a flexible, telechelic pEG-linker by metal-induced coordination. Interestingly, shear rheological investigations did not show significant differences between the viscoelastic properties of Fe^{2+} and Zn^{2+} cross-linked gels ($G' \sim 16$ Pa) while the cross-linking by the kinetically mostly inert Ni^{2+} complex led to significantly weaker hydrogels ($G' \sim 5$ Pa). Moreover, the reversible hydrogels showed a temperature-induced increase of the gel strength by one order of magnitude between 20 °C and 50 °C.

Within this work, we have tuned our C_3 -symmetric modular system to incorporate an insoluble, functional comonomer which could be used to cross-link the soluble supra-structures and yield soft and reversible hydrogels.

6.4 Experimental Section

Materials

Schlenk techniques were used at all reactions with air and moisture sensitive reagents or intermediates, performed under argon atmosphere with dry solvents. The used laboratory glassware was dried in an oven at 130 °C or at high vacuum with a hot air gun. In these instances, the solvents and reagents were added through septa *via* disposable syringes and cannulas whereas solids were added under continuous argon counterflow. In addition, solvents were degassed within three freeze-pump-thaw cycles if necessary.

Before usage, water was demineralized, using an Elga Purelab® *flex* 4 water purification system. All solvents and reagents were purchased from commercial sources at the highest purity available. The respective suppliers are Acros Organics (Thermo Scientific GmbH, Nidderau), Alfa Aesar (Alfa Aesar GmbH & Co. KG, Karlsruhe), Carbolution Chemicals (Carbolution Chemicals GmbH, Saarbrücken), IRIS Biotech (Iris Biotech GmbH, Markredwitz), Merck (Merck KGaA, Darmstadt), Sigma-Aldrich (Sigma-Aldrich Chemie GmbH, Taufkirchen), TCI (TCI Deutschland GmbH, Eschborn) and Umicore (Umicore AG & Co. KG, Hanau). All reagents were utilized without further purification unless stated otherwise. Solvents used for flash or thin layer chromatography were purchased in technical quality and applied without further purification.

Chromatography

Qualitative thin layer chromatography (TLC) was carried out using silica coated aluminum sheets (60 Å, F₂₅₄) or RP-18 modified silica coated aluminum sheets (60 Å, F₂₅₄), purchased from Merck. Detection of the analytes happened by UV light ($\lambda = 254$ nm and $\lambda = 366$ nm) and detection reagents of ninhydrin (0.1 g, 50.0 mL ethanol, 1.5 mL acetic acid), KMnO₄ (0.8 g, 200.0 mL water, 2.5 g NaHCO₃), FeCl₂ (2.0 g, 50.0 mL water) or iodine.

Purification *via* flash chromatography (FC) was performed either by using silica gel with an average grain size of 15–40 µm or Lichroprep® RP-18 with an average grain size of 40–63 µm, both purchased from MerckMillipore. The respective eluent was either chloroform (CHCl₃), cyclohexane (Hex), dichloromethane (DCM), ethyl acetate (EA) or methanol (MeOH) for using silica gel as the stationary phase and a mixture of acetonitrile (ACN) and water for purification *via* Lichroprep® RP-18. Purification by size-exclusion chromatography (SEC) was carried out using Sephadex® LH-20 medium with either MeOH, dimethylformamide (DMF) or a mixture of chloroform and MeOH (2:1) as the eluent. High performance liquid chromatography (HPLC) for analytical operations was performed on a Jasco LC-4000 system with UV/vis-detection in a range from 200–400 nm, using an endcapped reversed phase Chromolith® RP-C₁₈sec column with a pore size of 150 Å, purchased from Merck with a flow rate adjusted to 1.5 mL min⁻¹. The system operation was done *via* the software ChromNAV v2.00.02 by Jasco.

For semipreparative usage, samples were injected manually to a 1000 μL sample loop on a reversed phase XBridge™ Prep C₁₈ column by Waters™ with a particle size of 5 μm and a pore size of 130 Å at a constant flow rate of 18.9 $\text{mL}\cdot\text{min}^{-1}$. The fractions were collected *via* a CHF122SC fraction collector by AdvanTec MFC Inc. Acetonitrile (HPLC grade, VWR International) and ultrapure deionized water (deionized by Elga Purelab® *flex* 4 water purification system) were used as the eluent, each with the addition of 0.1% of trifluoroacetic acid. Medium pressure liquid chromatography (MPLC) was performed on a Büchi X50 system with UV/vis-detection in a range from 200–400 nm, using a modified silica reversed phase Chromabond® RP-C₁₈ column with a pore size of 60 Å at varying flow rates, purchased from Macherey-Nagel. Acetonitrile (HPLC grade, VWR International) and ultrapure deionized water (deionized by Elga Purelab® *flex* 4 water purification system) were used as the eluent, each with the addition of 0.1% of trifluoroacetic acid. The system operation was done using the software SepacoreControl v1.3.3000.4091 by Büchi.

Instrumentations

All NMR spectra were recorded on a Bruker *Avance* II 400 (¹H-NMR: 400 MHz) or a Bruker *Avance* II HD 300 (¹H-NMR: 300 MHz) spectrometer by Bruker using deuterated solvents (CDCl₃, DMSO-*d*₆). The chemical shifts (δ) are reported in part per million (ppm) relative to the chemical shifts of the residual protons of the deuterated solvents. The spin multiplicity of the signals is stated as s (singlet), d (doublet), t (triplet), q (quartet) and m (multiplet). The measured coupling constants (*J*) were calculated in Hertz (Hz). All received NMR spectra were analyzed using the NMR processing software MestReNova v14.0.1 by Mestrelab Research S.L. Mass spectra for characterization were recorded on an 6545QToF-MS spectrometer by Agilent, using electrospray ionization (ESI). Samples with high molecular weights were analyzed on an autoflex maX MALDI-ToF/ToF mass spectrometer system by Bruker and were ionized by matrix assisted laser desorption ionization (MALDI) and subjected to ToF-MS (*time of flight mass spectrometry*). The used samples were prepared at a concentration of 0.1 $\text{mg}\cdot\text{mL}^{-1}$ for ESI and 1.0 $\text{mg}\cdot\text{mL}^{-1}$ for MALDI-ToF in either MeOH, water, CHCl₃ or DMSO as the solvent. The used corresponding matrices are named in the synthetic procedures. CD spectroscopy was performed on a Jasco J-815 spectrometer with the software Spectra Manager v2.12.00. All samples were baseline corrected and measured, using a 110-QS Suprasil® quartz glass cuvettes with a path length of 2 mm at varying temperature, controlled by a Jasco PTC-423S/15 Peltier element. For prevention of noise increase, all concentrations were adjusted to keep the photomultipliers high voltage (HV) value below 600V at the respective wavelength area of interest ($\lambda > 190$ nm). Each sample was measured at least three times and averaged to minimize further errors. The data were processed by using the software Origin v9.0 by OriginLab Corporation.

Rheological studies were performed on a stress-controlled MCR 302 rheometer by Anton Paar equipped with a stainless-steel cone-plate geometry (cone angle: 1°; cone diameter: 25 mm) and a solvent trap. Inertial calibration was performed prior to each measurement. Samples were prepared from stock solutions of each monomer dissolved in DMSO, and stock solutions of telechelic cross-linker and the respective metal salts in water. After mixing, the monomers were lyophilized consecutively from DMSO and water. The lyophilizate was dissolved in water again, followed by the addition of the dissolved pEG(tpy)₂ and metal salt solutions. After addition of the metal salt, the samples were sonicated for 5 min and further equilibrated for 24 h at r.t. Afterwards, 80–100 µL of the solutions were placed on the lower rheometer plate using an Eppendorf pipette. Eventually occurring air bubbles are removed with the pipette tip. The upper geometry was lowered onto the sample and any excess amount of the sample was removed using a paper wipe. All samples underwent conditioning and were monitored for 30 min at a constant shearing amplitude and frequency ($\gamma = 0.01\%$; $\omega = 1 \text{ rad}\cdot\text{s}^{-1}$) to ensure sample equilibration. Following parameter were used for the respecting experiments. Amplitude sweeps: $\gamma = 0.01\text{--}100\%$ ($\omega = 1 \text{ rad}\cdot\text{s}^{-1}$, $T = 293 \text{ K}$). Stress-Strain experiments: 100 s: $\gamma = 0.1\%$; $\omega = 1 \text{ rad}\cdot\text{s}^{-1}$, 100 s: $\gamma = 100\%$; $\omega = 1 \text{ rad}\cdot\text{s}^{-1}$, 200 s: $\gamma = 0.1\%$; $\omega = 1 \text{ rad}\cdot\text{s}^{-1}$, 100 s: $\gamma = 100\%$; $\omega = 1 \text{ rad}\cdot\text{s}^{-1}$ etc. Temperature sweeps: Constant shearing amplitude and frequency ($\gamma = 1\%$; $\omega = 1 \text{ rad}\cdot\text{s}^{-1}$), 15 min equilibration at 283 K, linear temperature ramp from 283–313 K, 3 points per K, linear rate backwards to 283 K. Transmission electron microscopy (TEM) images were recorded on a *Tecnai* T12 system by Fei, equipped with a BioTWIN lens and a LaB₆ cathode, operating at 120 kV. The digital electron micrographs were recorded with a MegasSYS 1k x 1k CCD camera and the received imaged were analyzed with the processing application ImageJ. A glow-discharged CF300-CU copper grid by Electron Microscopy Sciences, coated with a 3–4 nm carbon layer, was used by adsorbing 5 µL of the sample for 2 min. Negative staining was performed by using 5 µL of a 2 wt% solution of uranyl acetate for 1 min. An excess of liquid was removed with Whatman® grade 4 filter papers by GE Healthcare Bio-Sciences. Length characterization of the rod-like nanostructures was performed by using the software ImageJ 1.53i (Wayne Rasband National Institutes of Health, USA). The corresponding histograms were prepared with Origin v9.0 by OriginLab Corporation. For the calculation of the number average (L_n) and the weighted average (L_w) following equations were used:

$$L_n = \frac{\sum_{i=1}^n n_i L_i}{\sum_{i=1}^n n_i} \quad (6.1)$$

$$L_w = \frac{\sum_{i=1}^n n_i L_i^2}{\sum_{i=1}^n n_i L_i} \quad (6.2)$$

$$PDI = \frac{L_w}{L_n} \quad (6.3)$$

L_n = number average of the rod length in nm, L_w = weighted average of the rod length in nm, n = sample size, PDI = polydispersity

Synthetic procedures

Standard Operating Procedure for the Preparation of Protected Peptides by SPPS (SOP 1)

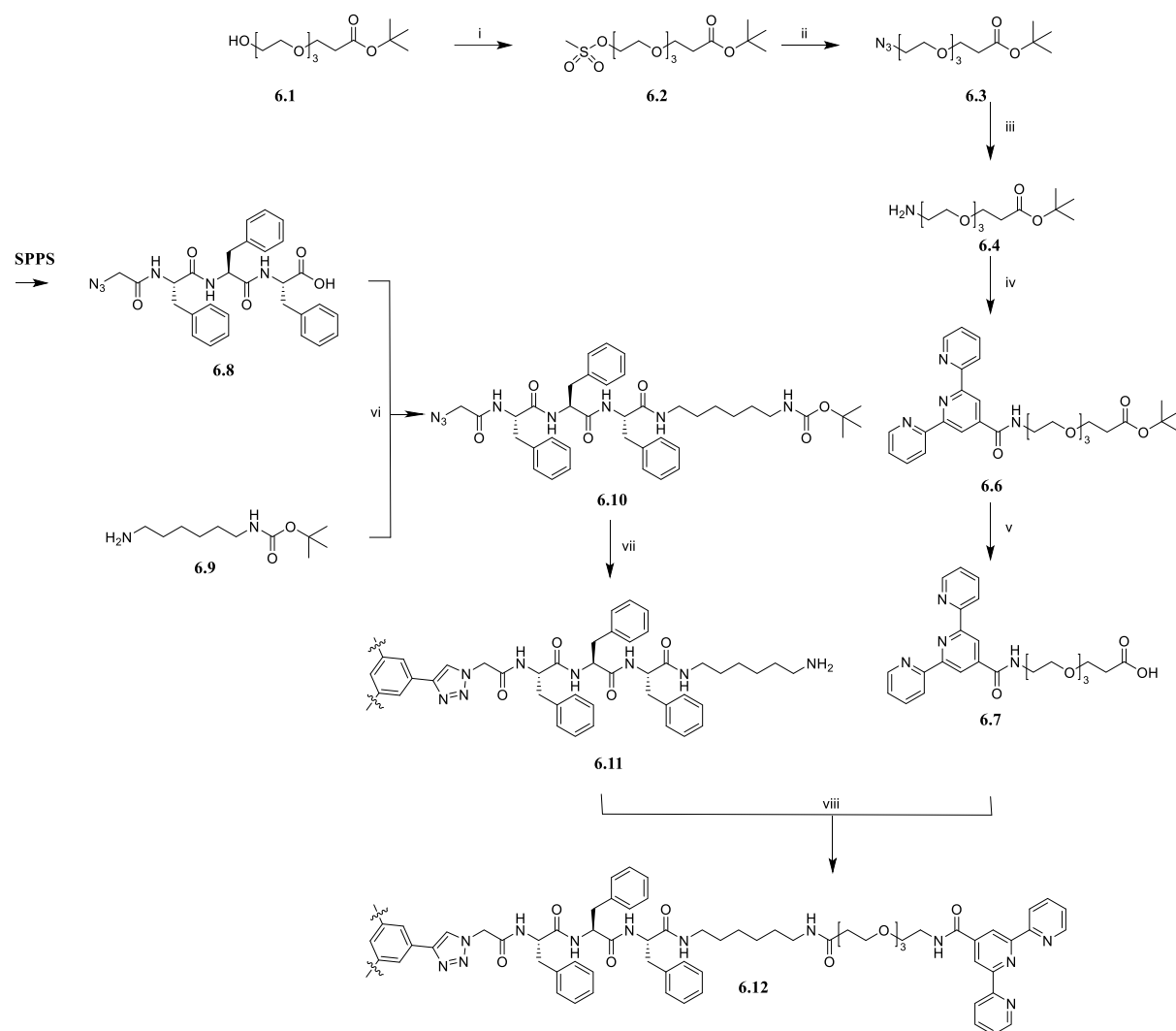
Loading of the used 2-chlorotriptyl chloride resin took place by dissolving the appropriate amount of the respective Fmoc-protected amino acid (2.0 eq. relative to the resin loading capacity) in DCM (10 mL·g⁻¹ resin) and a small amount of DMF for better solubility, followed by adding the solution to the vessel containing the resin within a nitrogen atmosphere. DIPEA (2.0 eq.) was added, and the mixture was shaken for five minutes, followed by the addition of DIPEA (3.0 eq.). The mixture was shaken for one hour at r.t. MeOH (1 mL mL·g⁻¹ resin) was added and the mixture was shaken again for 15 min before the vessel was drained and the resin was washed successively three times with each 10 mL DCM, DMF, DCM and MeOH.

The loaded resin was swollen up in DCM for 10 min while shaking, followed by the addition of piperidine (20 vol% in DMF (peptide grade)) and shaking for 20 min. After draining the vessel and washing the resin with DMF four times and with DCM twice, solutions of the respective Fmoc-protected amino acid (4.0 eq.), HBTU (4.0 eq.), HOBT (4.0 eq.) and DIPEA (6.0 eq.) in DMF were added and the mixture was shaken for one hour. The vessel was drained again, and the resin was washed with DMF five times. This routine was repeated for every following Fmoc-protected amino acid and the resulting beads were washed with DMC once. Finally, the resin was washed with DCM twice.

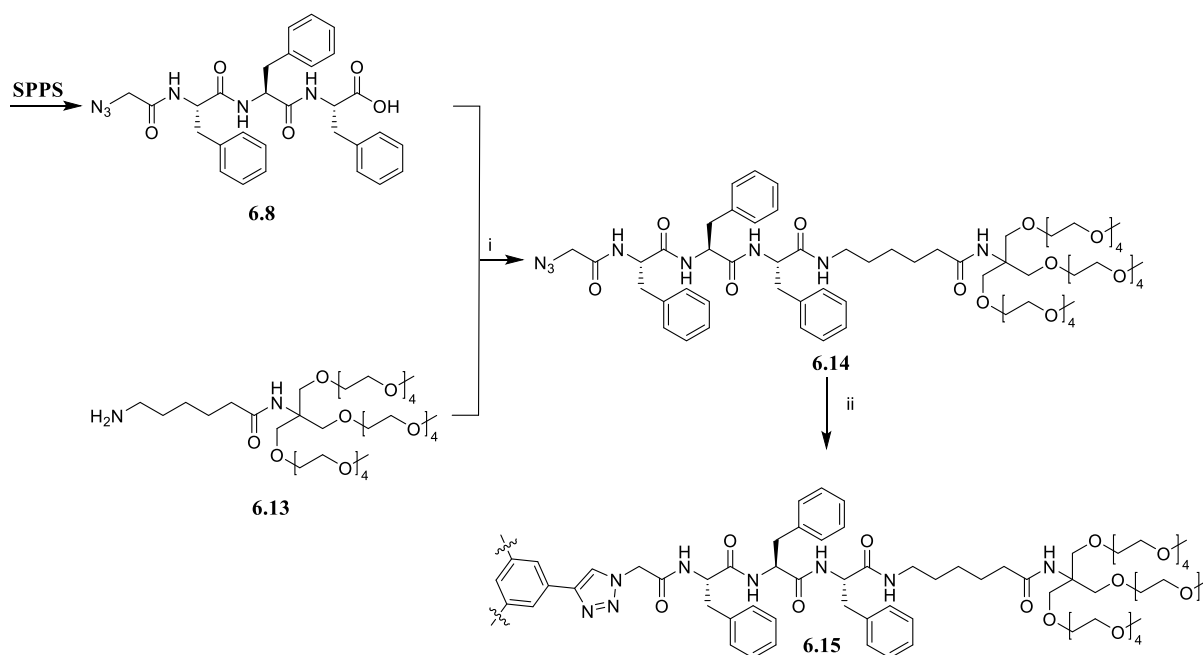
For the cleavage of the peptide from resin the beads were treated with TFA (50 vol% in DCM) by shaking for 40 min at r.t. The solution was drained into a flask and the resin was washed twice with DCM. The procedure was repeated three to five times. These combined solutions were concentrated in vacuo and the resulting residue was co-distilled with toluene and freeze-dried out of water to give the pure peptide.

Stepwise chain elongation was carried out by using the automated batch peptide synthesizer CS136XT by CS BIO CO. A 2-chlorotriptyl chloride resin (1.0–1.6 mmol·g⁻¹ loading capacity) was utilized together with peptide grade solvents for the loading of the respective Fmoc modified amino acids.

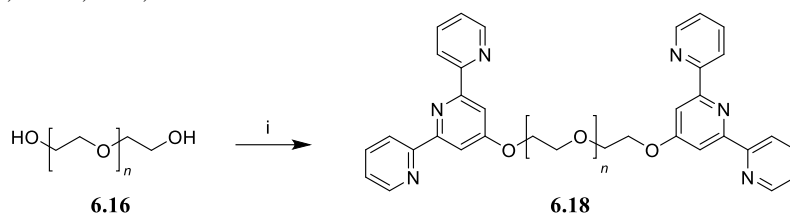
Synthesis Scheme



Scheme 6.1. Synthetic route for the preparation of the C_3 -symmetric monomer C_3^{tpy} (6.12): (i) **6.1** (1.0 eq.), methanesulfonyl chloride (1.2 eq.), NEt_3 (2.0 eq.), $CHCl_3$, 0 °C → r.t., 12 h, 98%; (ii) **6.2** (1.0 eq.), NaN_3 (6.0 eq.), DMF, 60 °C, 17 h, 98%; (iii) **6.3** (1.0 eq.), PPh_3 (1.0 eq.), THF, r.t., 12 h, 80%; (iv) **6.4** (1.1 eq.), 4'-carboxy-2,2':6,6',2''-terpyridine (**6.5**) (1.0 eq.), $SOCl_2$ (30.0 eq.), DIPEA (3.0 eq.), DCM, 70 °C, 48 h, 79%; (v) **6.6** (1.0 eq.), HCl (4 M), 1,4-dioxane, r.t., 3 h, 94%; (vi) **6.8** (1.0 eq.), **6.9** (1.2 eq.), PyBOP (1.3 eq.), HOBT (1.3 eq.), DIPEA (1.3 eq.), DCM/DMF (2:1), 0 °C → r.t., 12 h, 46%; (vii) 1. **6.10** (3.5 eq.), 1,3,5-triethynylbenzene (1.0 eq.), $CuSO_4 \cdot 5 H_2O$ (1.0 eq.), TBTA (0.7 eq.), sodium ascorbate (2.3 eq.), DMSO, r.t., 12 h; 2. TFA/DCM (1:1), 0 °C → r.t., 2 h, 31%; (viii) **6.11** (1.0 eq.), **6.7** (3.5 eq.), PyBOP (3.5 eq.), HOBT (3.5 eq.), DIPEA (5.0 eq.), DMSO, 0 °C → r.t., 24 h, 50%.



Scheme 6.2. Synthetic route for the C_3 -symmetric monomer C_3^{EG} (**6.15**): (i) **6.8** (1.3 eq.), **6.13** (1.0 eq.), PyBOP (1.3 eq.), HOBT (1.3 eq.), DIPEA (1.3 eq.), DCM/ DMF (4:1), 0 °C → r.t., 12 h, 46%; (ii) **6.14** (3.5 eq.), 1,3,5-triethynylbenzene (1.0 eq.), $CuSO_4 \cdot 5 H_2O$ (1.0 eq.), TBTA (0.7 eq.), sodium ascorbate (2.3 eq.), DMSO, 40 °C, 24 h, 40%.



Scheme 6.3. Synthetic route for the telechelic cross-linker tpy(pEG)₂ (**6.18**): (i) **6.16** (1.0 eq.), KOH (10.0 eq.), [2.2.2]Cryptand (0.5 eq.), 4'-chloro-2,2':6,6',2''-terpyridine (**6.17**) (6.0 eq.), DMSO, 70 °C, 72 h, 67%.

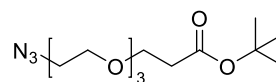
Synthesis

Compound 6.2

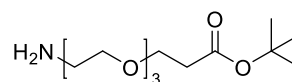
Compound **6.1** (6.9 g, 25.1 mmol, 1.0 eq.) was dissolved in dry $CHCl_3$ (25 mL), followed by the addition of NEt_3 (7.0 mL, 50.2 mmol, 2.0 eq.) and cooling of the resulting solution to 0 °C. With stirring, a solution of methanesulfonyl chloride (2.3 mL, 30.1 mmol, 1.2 eq.) in dry $CHCl_3$ (10 mL) was added dropwise with a nitrogen counterflow and the reaction mixture was warmed to r.t. After stirring overnight, the reaction mixture was diluted with $CHCl_3$ (35 mL) and then washed with a saturated solution of $NaHCO_3$ (25 mL), H_2O (25 mL) and brine (25 mL). The organic phase was dried over Na_2SO_4 and the solvent was removed under reduced pressure. **Yield:** 8.8 g (24.7 mmol, 98%), colorless oil. **Chemical formula:** $C_{14}H_{28}O_8S$. **ESI-HRMS** (MeOH) (*positive*) (m/z): 357.1512 ($[M+H]^+$, calc. 357.1505). **1H -NMR** (300 MHz, $CDCl_3$, 298 K): δ = 4.38 (m, 2H, $MsCH_2$), 3.78–3.57 (m, 12H, CH_2^{EG}), 3.07 (s, 3H, CH_3^{Ms}), 2.49 (t, 2H, $^3J = 6.5$ Hz, α - CH_2), 1.44 (s, 9H, $CH_3^{tert}Bu$) ppm.

Compound 6.3

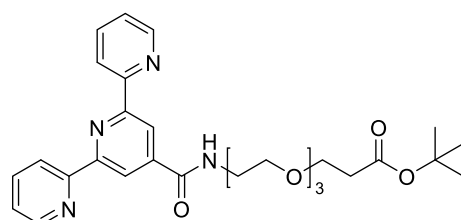
Compound **6.2** (8.8 g, 24.7 mmol, 1.0 eq.) was dissolved in dry DMF (10 mL) and NaN₃ (9.6 g, 148.1 mmol, 6.0 eq.) was added to the solution with a nitrogen counterflow. The reaction mixture was stirred for 17 h at 60 °C. After stirring, the solvent was removed under reduced pressure and the remaining residue was suspended with brine (30 mL). The suspension was washed with DCM (5 x 25 mL) and the resulting organic layer was dried over Na₂SO₄. Removal of the solvent *in vacuo* gave a yellow oil. **Yield:** 7.3 g (24.1 mmol, 98%), yellow oil. **Chemical formula:** C₁₃H₂₅N₃O₅. **ESI-HRMS** (MeOH) (*positive*) (*m/z*): 326.1688 ([M+Na]⁺, calc. 326.1686). **¹H-NMR** (400 MHz, CDCl₃, 298 K): δ = 3.70–3.57 (m, 12H, CH₂^{EG}), 3.36 (t, 2H, ³J = 10.2 Hz, N₃CH₂), 2.48 (t, 2H, ³J = 11.9 Hz, α-CH₂), 1.42 (s, 9H, CH₃^{tert}Bu) ppm.

**Compound 6.4**

Compound **6.3** (6.7 g, 22.1 mmol, 1.0 eq.) was dissolved in THF (100 mL) and cooled to 0 °C before Ph₃P (5.8 g, 22.1 mmol, 1.0 eq.) was added to the stirring solution. After stirring overnight at r.t., the reaction mixture was diluted with H₂O (50 mL) and acidified to pH 4 via dropwise addition of 1 M HCl. The suspension was washed with toluene (3 x 50 mL) and the aqueous layer was freeze-dried to give a yellow oil. **Yield:** 4.9 g (17.7 mmol, 80%), yellow oil. **Chemical formula:** C₁₃H₂₈NO₅. **ESI-HRMS** (MeOH) (*positive*) (*m/z*): 278.1965 ([M+H]⁺, calc. 278.1962). **¹H-NMR** (300 MHz, DMSO-*d*₆, 298 K): δ = 8.12 (s, 2H, NH₂), 3.63–3.36 (m, 12H, CH₂^{EG}), 2.94 (t, 2H, ³J = 6.0 Hz, CH₂), 2.42 (t, 2H, ³J = 6.0 Hz, α-CH₂), 1.40 (s, 9H, CH₃^{tert}Bu) ppm.

**Compound 6.6**

A mixture of 4'-carboxy-2,2':6,6',2''-terpyridine (**6.5**) (1.5 g, 5.4 mmol, 1.0 eq.) and thionyl chloride (11.8 mL, 162.3 mmol, 30.0 eq.) was refluxed for 1 h, followed by the removal of remaining SOCl₂ via distillation. The residue was suspended in DCM

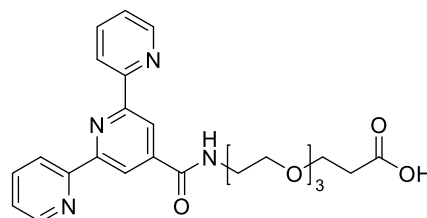


(15 mL) and cooled to 0 °C. Compound **6.4** (1.7 g, 5.9 mmol, 1.1 eq.) was dissolved in DCM (30 mL) and DIPEA (3.0 mL, 17.9 mmol, 3.0 eq.) was added. The resulting solution was added dropwise to the previous mixture with a nitrogen counterflow. After 24 h of stirring at r.t. the reaction mixture was diluted by the addition of a saturated solution of NaHCO₃ (7 mL). The resulting suspension was extracted with CHCl₃ (3 x 20 mL) and the organic layer was dried over Na₂SO₄. After evaporation of the solvent *in vacuo*, further purification proceeded via flash chromatography (Lichroprep®, RP18, ACN: H₂O, 8:1). **Yield:** 2.3 g (4.3 mmol, 79%), colorless oil. **Chemical formula:** C₂₉H₃₆N₄O₆. **ESI-HRMS** (MeOH) (*positive*) (*m/z*): 537.2710 ([M+H]⁺,

calc 537.2708), 559.2533 ($[M+Na]^+$, calc 559.2527). $^1\text{H-NMR}$ (400 MHz, CDCl_3 , 298 K): $\delta = 9.16$ (t, 1H, $^3J = 5.2$ Hz, NH), 8.83 (s, 2H, CH^{py}), 8.77 (ddd, 2H, $^3J = 4.7$ Hz, CH^{py}), 8.66 (dt, 2H, $^3J = 7.9$ Hz, CH^{py}), 8.04 (td, 2H, $^3J = 7.7$ Hz, CH^{py}), 7.54 (ddd, 2H, $^3J = 7.6$ Hz, CH^{py}), 3.62–3.44 (m, 14H, CH_2^{EG}), 2.36 (t, 2H, $^3J = 6.2$ Hz, $\alpha\text{-CH}_2$), 1.36 (s, 9H, $\text{CH}_3^{\text{tertBu}}$) ppm.

Compound 6.7

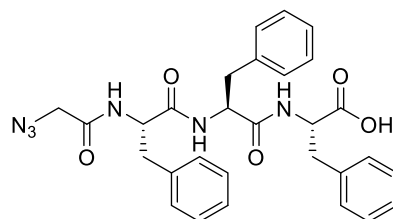
Compound **6.6** (2.3 g, 4.3 mmol, 1.0 eq.) was dissolved in 1,4-dioxane (65 mL). With stirring, a solution of HCl (4 M) in 1,4-dioxane (65 mL) was added dropwise and the solution was stirred for 3 h at r.t. The mixture was concentrated under reduced pressure and remaining solvent



was removed via freeze-drying. **Yield:** 1.94 g (4.0 mmol, 94%), colorless solid. **Chemical formula:** $\text{C}_{25}\text{H}_{28}\text{N}_4\text{O}_6$. **ESI-HRMS** (MeOH) (*positive*) (m/z): 519.2117 ($[M+K]^+$, calc. 519.1640). $^1\text{H-NMR}$ (300 MHz, $\text{DMSO-}d_6$, 298 K): $\delta = 9.28$ (t, 1H, $^3J = 5.3$ Hz, NH), 8.94 (s, 2H, CH^{py}), 8.88–8.81 (m, 4H, CH^{py}), 8.26 (td, 2H, $^3J = 8.6$ Hz, CH^{py}), 7.73 (ddd, 2H, $^3J = 7.9$ Hz, CH^{py}), 3.64–3.45 (m, 14H, CH_2^{EG}), 2.41 (t, 2H, $^3J = 6.3$ Hz, $\alpha\text{-CH}_2$) ppm.

Compound 6.8

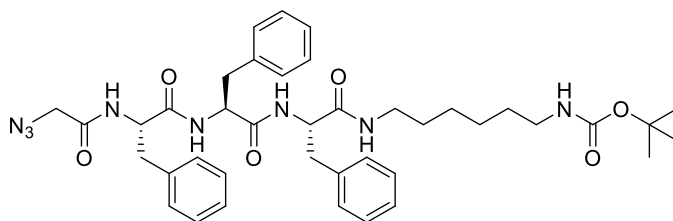
The peptide was synthesized by following SOP 1, using Fmoc-Phe-OH and N_3 -Gly-OH. **Yield:** 824 mg (1.52 mmol, 95%), colorless solid. **Chemical formula:** $\text{C}_{29}\text{H}_{30}\text{N}_6\text{O}_5$. **ESI-HRMS** (MeOH) (*positive*) (m/z): 543.2356 ($[M+H]^+$, calc. 543.2350), 565.2173 ($[M+Na]^+$, calc. 565.2170). $^1\text{H-NMR}$



(400 MHz, $\text{DMSO-}d_6$, 298 K): $\delta = 12.8$ (s, 1H, COOH), 8.32 (d, $^3J = 7.7$ Hz, 1H, NH), 8.26 (d, $^3J = 8.4$ Hz, 1H, NH), 8.19 (d, $^3J = 8.6$ Hz, 1H, NH), 7.30–7.12 (m, 15H, CH^{Phe}), 4.59–4.44 (m, 3H, $\alpha\text{-CH}^{\text{Phe}}$), 3.69 (dd, $^2J = 15.6$ Hz, 2H, CH_2^{Gly}), 3.13–2.60 (m, 6H, CH_2^{Phe}) ppm.

Compound 6.10

Compound **6.8** (300 mg, 0.55 mmol, 1.0 eq.), compound **6.9** (168 mg, 0.66 mmol, 1.2 eq.), PyBOP (374 mg, 0.72 mmol, 1.3 eq.) and HOBt (97 mg, 0.72 mmol, 1.3 eq.) were

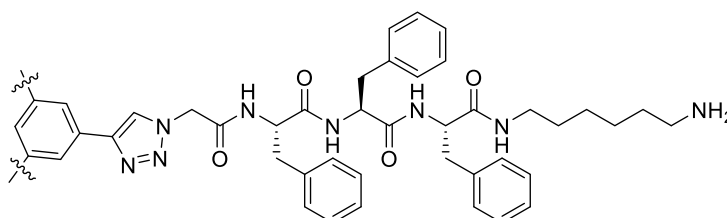


dissolved in a 2:1 mixture of DCM and DMF (15 mL) and the solution was cooled to 0 °C. DIPEA (122 μL , 0.72 mmol, 1.3 eq.) was added dropwise and the solution was stirred for 4 h at r.t.. The solvent was removed under reduced pressure and the residue was purified via SEC (LH-20, CHCl_3 : MeOH, 2:1). **Yield:** 188 mg (0.25 mmol, 46%), yellow oil. **Chemical formula:**

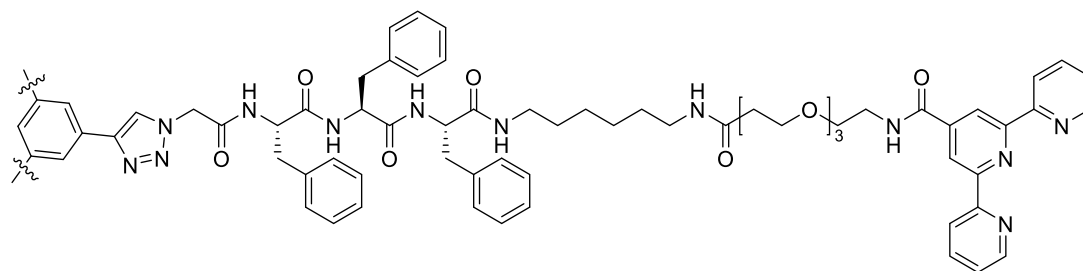
$C_{40}H_{52}N_8O_6$. **ESI-HRMS** (MeOH) (*positive*) (m/z): 741.4079 ($[M+H]^+$, calc. 741.4088), 763.3904 ($[M+Na]^+$, calc. 763.3905). **1H -NMR** (400 MHz, DMSO- d_6 , 298 K): δ = 8.24 (t, 2H, 3J = 8.4 Hz, NH), 8.14 (d, 2H, 3J = 8.1 Hz, NH), 7.79 (t, 1H, 3J = 5.6 Hz, NH^{Ahx}), 7.27–7.13 (m, 15H, CH^{Ar}), 6.77 (t, 1H, 3J = 5.5 Hz, NH^{Ahx}), 4.59–4.43 (m, 3H, α - CH^{Phe}), 3.71 (dd, 2H, 3J = 7.4 Hz, CH_2^{Gly}), 3.08–2.62 (m, 10H, CH^{Phe} , $NHCH_2$), 1.37 (s, 9H, CH_3^{tert} Bu), 1.35–1.10 (m, 8H, CH_2^{Ahx}) ppm.

Compound 6.11

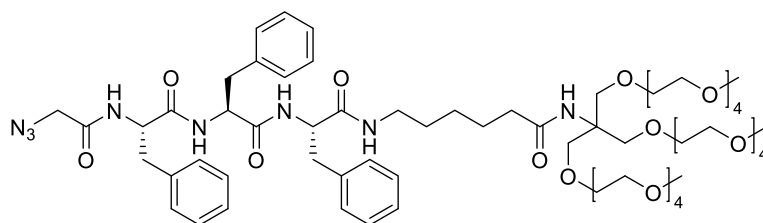
Compound **6.10** (150 mg, 0.20 mmol, 3.5 eq.), TBTA (22 mg, 0.04 mmol, 0.7 eq.) and $CuSO_4 \cdot 5 H_2O$ (9 mg, 0.06 mmol, 1.0 eq.) were dissolved in DMSO



(5 mL) and 1,3,5-triethynylbenzene (9 mg, 0.06 mmol, 1.0 eq.) was added with an argon counterflow. After three freeze-pump-thaw cycles, sodium ascorbate (26 mg, 0.13 mmol, 2.3 eq.) was added with an argon counterflow and the mixture was stirred overnight at r.t. under an argon atmosphere. The solvent was removed via freeze-drying and the residue was suspended in DCM (5 mL) and cooled to 0 °C. TFA (5 mL) was added dropwise to give a clear solution. The reaction mixture was stirred for 2 h at r.t. and the solvent was removed under reduced pressure. The crude product was purified via SEC (LH-20, DMF). **Yield:** 41 mg (0.02 mmol, 31%), colorless solid. **Chemical formula:** $C_{117}H_{138}N_{24}O_{12}$. **MALDI-MS** (CHCA) (*positive*) (m/z): 2094.4380 ($[M+Na]^+$, calc. 2094.0822). **1H -NMR** (400 MHz, DMSO- d_6 , 298 K): δ = 8.62 (d, 3H, 3J = 8.3 Hz, NH^{Phe}), 8.47 (s, 3H, CH^{Ph}), 8.35 (d, 3H, 3J = 8.0 Hz, NH^{Phe}), 8.27 (s, 3H, $CH^{Triazol}$), 8.14 (d, 3H, 3J = 8.0 Hz, NH^{Phe}), 7.82 (t, 3H, 3J = 5.6 Hz, NH^{Ahx}), 7.28–7.10 (m, 45H, CH^{Ar}), 5.11 (dd, 6H, 2J = 16.5 Hz, CH_2^{Gly}), 4.64–4.42 (m, 9H, α - CH^{Phe}), 3.09–2.62 (m, 30H, $NHCH_2$, CH_2^{Phe}), 1.51–1.10 (m, 24H, CH_2^{Ahx}) ppm.

Compound 6.12

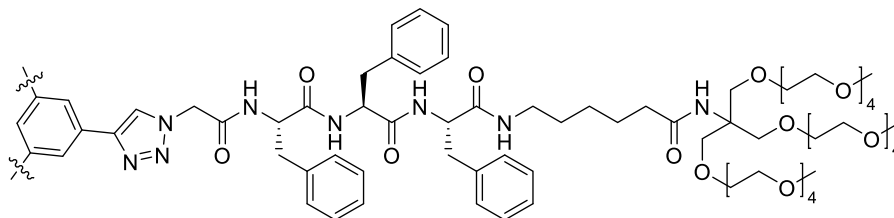
Compound **6.11** (25 mg, 0.01 mmol, 1.0 eq.), **6.14** (18 mg, 0.04 mmol, 3.5 eq.), PyBOP (22 mg, 0.04 mmol, 3.5 eq.) and HOBt (6 mg, 0.04 mmol, 3.5 eq.) were dissolved in DMSO (3.0 mL) and the solution was cooled to 0 °C. DIPEA (7.8 μ L, 0.06 mmol, 5.0 eq.) was added dropwise and the solution was stirred overnight at r.t. The solvent was removed under reduced pressure and the crude product was purified via SEC (LH-20, DMF: DMSO, 2:1). **Yield:** 21 mg (0.01 mmol, 50%), colorless solid. **Chemical formula:** C₁₉₂H₂₁₆N₃₆O₂₇. **MALDI-MS** (CHCA) (*positive*) (*m/z*): 3458.5550 ([M+H]⁺, calc. 3458.6713), 3480.4231 ([M+Na]⁺, calc. 3480.6532). **¹H-NMR** (400 MHz, DMSO-*d*₆, 298 K): δ = 9.17 (t, ³*J* = 5.6 Hz, 3H, NH^{TriEG}), 8.83 (s, 6H, CH^{py}), 8.76 (ddd, ³*J* = 4.6 Hz, 6H, CH^{py}), 8.65 (dt, ³*J* = 7.9 Hz, 6H, CH^{py}), 8.60 (d, 3H, ³*J* = 8.2 Hz, CH^{py}), 8.46 (s, 3H, CH^{Ph}), 8.35 (d, ³*J* = 8.0 Hz, 3H, NH^{Phe}), 8.27 (s, 3H, CH^{Triazol}), 8.14 (d, 3H, ³*J* = 8.0 Hz, NH^{Phe}), 8.03 (td, 6H, ³*J* = 7.9 Hz, CH^{py}), 7.80–7.73 (m, 6H, NH^{Ahx}), 7.53 (ddd, 6H, ³*J* = 4.7 Hz, CH^{py}), 7.26–7.11 (m, 45H, CH^{Phe}), 5.10 (dd, 6H, ²*J* = 16.8 Hz, CH₂^{Gly}), 4.65–4.44 (m, 9H, α -CH^{Phe}), 3.61–3.46 (m, 36H, CH₂^{TriEG}), 3.45–3.42 (m, 6H, NHCH₂^{TriEG}), 3.05–2.62 (m, 30H, CH₂^{Phe}, NHCH₂^{Ahx}), 2.25 (t, 6H, ³*J* = 6.4 Hz, COCH₂^{TriEG}), 1.35–1.06 (m, 24H, CH₂^{Ahx}) ppm.

Compound 6.14

Compound **6.13** (125 mg, 0.16 mmol, 1.0 eq.), compound **6.8** (110 mg, 0.20 mmol, 1.3 eq.), PyBOP (105 mg, 0.20 mmol, 1.3 eq.) and HOBt (27 mg, 0.20 mmol, 1.3 eq.) were dissolved in a 4:1 mixture of DCM and DMF (5 mL) and the solution was cooled to 0 °C. DIPEA (34.3 μ L, 0.36 mmol, 2.3 eq.) was added dropwise and the solution was stirred for 4 h at r.t.. The solvent was removed under reduced pressure and the residue was purified via SEC (LH-20, CHCl₃: MeOH, 2:1) and MPLC (CHROMABOND[®] RP-C₁₈, ACN 10% → ACN 100% 25 min). **Yield:** 94 mg (0.07 mmol, 46%), colorless amorphous solid. **Chemical formula:** C₆₆H₁₀₄N₈O₂₀. **ESI-HRMS** (MeOH) (*positive*) (*m/z*): 1329.7449 ([M+H]⁺, calc. 1329.7440), 1351.7265 ([M+Na]⁺, calc. 1351.7259). **¹H-NMR** (400 MHz, DMSO-*d*₆, 298 K): δ = 8.27–8.21 (m, 2H, NH^{Phe}), 8.13 (d, 1H, ³*J* = 8.3 Hz, NH^{Phe}), 7.81 (t, 1H, ³*J* = 5.2 Hz, NH^{Ahx}), 7.29–7.13 (m, 15H,

CH^{Phe}), 7.00 (s, 1H, NH^{Tris}), 4.58–4.43 (m, 3H, $\alpha-CH^{Phe}$), 3.70 (dd, 2H, $^2J = 15.8$ Hz, CH_2^{Gly}), 3.59 (s, 6H, CH_2^{Tris}), 3.53–3.47 (m, 42H, CH_2^{TEG}), 3.44–3.39 (m, 6H, CH_2^{TEG}), 3.23 (s, 9H, CH_3^{TEG}), 3.04–2.89 (m, 6H, CH_2^{Phe}), 2.77–2.67 (m, 2H, $\varepsilon-CH_2^{Ahx}$), 2.03 (t, 2H, $^3J = 7.4$ Hz, $\alpha-CH_2^{Ahx}$), 1.45–1.37 (m, 2H, $\beta-CH_2^{Ahx}$), 1.31–1.24 (m, 2H, $\delta-CH_2^{Ahx}$), 1.18–1.10 (m, 2H, $\gamma-CH_2^{Ahx}$) ppm.

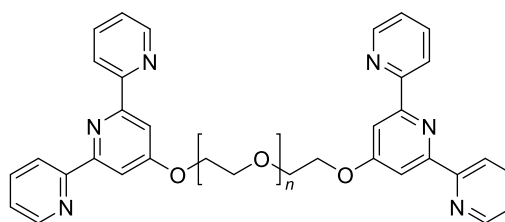
Compound 6.15



Compound **6.14** (77.5 mg, 0.06 mmol, 3.5 eq.), TBTA (6.2 mg, 0.01 mmol, 0.7 eq.) and $CuSO_4$ (2.7 mg, 0.02 mmol, 1.0 eq.) were dissolved in DMSO (3 mL) and 1,3,5-triethynylbenzene (2.5 mg, 0.02 mmol, 1.0 eq.) was added with an argon counterflow. After three freeze-pump-thaw cycles, sodium ascorbate (8.6 mg, 0.04 mmol, 2.3 eq.) was added with an argon counterflow and the mixture was stirred overnight at 40 °C under an argon atmosphere. The solvent was removed *via* freeze drying and the residue was purified first *via* flash chromatography (SiO_2 , $CHCl_3$: MeOH, 9:1), followed by further separation *via* MPLC (CHROMABOND® RP-C₁₈, ACN 10% → ACN 100% 50 min). **Yield:** 27.7 mg (0.01 mmol, 40%), colorless amorphous solid. **Chemical formula:** $C_{210}H_{318}N_{24}O_{60}$. **MALDI-MS** (CHCA) (*positive*) (m/z): 4139.1595 ($[M+H]^+$, calc. 4139.2710), 4161.9500 ($[M+Na]^+$, calc. 4161.2529). **1H -NMR** (400 MHz, DMSO- d_6 , 298 K): $\delta\delta = 8.61$ (d, 3H, $^3J = 7.8$ Hz, NH^{Phe}), 8.47 (s, 3H, CH^{Ph}), 8.36 (d, 3H, $^3J = 8.2$ Hz, NH^{Phe}), 8.28 (s, 3H, $CH^{Triazol}$), 8.15 (d, 3H, $^3J = 7.8$ Hz, NH^{Phe}), 7.81 (t, 3H, $^3J = 4.9$ Hz, NH^{Ahx}), 7.29–7.11 (m, 45H, CH^{Phe}), 7.01 (s, 3H, NH^{Tris}), 5.11 (dd, 6H, $^2J = 16.8$ Hz, CH_2^{Gly}), 4.66–4.45 (m, 9H, $\alpha-CH^{Phe}$), 3.60 (s, 18H, CH_2^{Tris}), 3.53–3.47 (m, 126H, CH_2^{TEG}), 3.44–3.39 (m, 18H, CH_2^{TEG}), 3.23 (s, 27H, CH_3^{TEG}), 3.07–2.84 (m, 18H, CH_2^{Phe}), 2.77–2.67 (m, 6H, $\varepsilon-CH_2^{Ahx}$), 2.04 (t, 6H, $^3J = 6.6$ Hz, $\alpha-CH_2^{Ahx}$), 1.47–1.36 (m, 6H, $\beta-CH_2^{Ahx}$), 1.33–1.24 (m, 6H, $\delta-CH_2^{Ahx}$), 1.19–1.09 (m, 6H, $\gamma-CH_2^{Ahx}$) ppm.

Compound 6.18

Finely crushed potassium hydroxide (dried under vacuum for 24 h, 49.4 mg, 0.83 mmol, 10.0 eq.) was suspended in anhydrous DMSO (3 mL) under nitrogen atmosphere in a 50 mL Schlenk-flask equipped with a reflux condenser and heated to 70



°C. A solution of freshly dried polyethylene glycol **6.16** ($M_n = 6.27 \cdot 10^3 \text{ g mol}^{-1}$, 0.5 g, 0.08 mmol, 1.0 eq.) and [2.2.2]Cryptand (15.2 mg, 0.04 mmol, 0.5 eq.) in anhydrous DMSO (3 mL) was added to the suspension and then stirred for 1 h at 70 °C. Afterwards, 4'-chloro-2,2':6',2''-terpyridine **6.17** (138 mg, 0.5 mmol, 6.0 eq.) was added under nitrogen counterflow and the yellow solution was stirred for 72 h at 70 °C. After cooling to r.t., the brown solution was poured into ice-cold water (30 mL). The precipitate was removed by filtration and the aqueous phase was extracted with dichloromethane (4 x 100 mL), dried over MgSO_4 and concentrated under vacuum. Activated carbon was added to the concentrated solution (6 mL) and after refluxing for 20 min the mixture was filtered through a syringe filter (PTFE, 450 μm) into ice-cold Et_2O (1 L). The product was isolated by filtration and dried under vacuum for 24 h. **Yield:** 360 mg (67%), colorless amorphous solid. **Chemical formula:** $\text{C}_{312}\text{H}_{584}\text{N}_6\text{O}_{142}$. **UV-Vis** (CHCl_3 , $\epsilon_{\text{tpy}} = 21.1 \cdot 10^3 \text{ L mol}^{-1} \text{ cm}^{-1}$): tpy-functionalization: 103%. **MALDI-MS** (DHB) (*positive*) (m/z): 6686.2400 ($[\text{M}+\text{H}]^+$, calc. 6692.0040 ($n = 140$)). **$^1\text{H-NMR}$** (400 MHz, $\text{DMSO-}d_6$, 298 K): $\delta = 8.72$ (ddd, $^3J = 4.7 \text{ Hz}$, $^4J = 1.8 \text{ Hz}$, $^5J = 0.9 \text{ Hz}$, 4H, tpy: $\text{C}_{6'/6''}\text{-H}$), 8.62 (dt, $^3J = 7.9$, $^4J = 1.1$, 4H, tpy: $\text{C}_{3'/3''}\text{-H}$), 8.01 (atd, $^3J = 7.9 \text{ Hz}$, $^4J = 1.8 \text{ Hz}$, 4H, tpy: $\text{C}_{4'/4''}\text{-H}$), 7.99 (s, 4H, tpy: $\text{C}_{3/5}\text{-H}$), 7.50 (ddd, $^3J = 4.7 \text{ Hz}$, $^4J = 1.8 \text{ Hz}$, $^5J = 0.9 \text{ Hz}$, 4H, tpy: $\text{C}_{5'/5''}\text{-H}$), 4.38 (m, 4H, tpy- $\text{OCH}_2\text{CH}_2\text{O}$), 3.84 (m, 4H, tpy- $\text{OCH}_2\text{CH}_2\text{O}$), 3.50 (m, 540H, $(\text{CH}_2\text{CH}_2\text{O})_n$) ppm.

CD spectroscopy

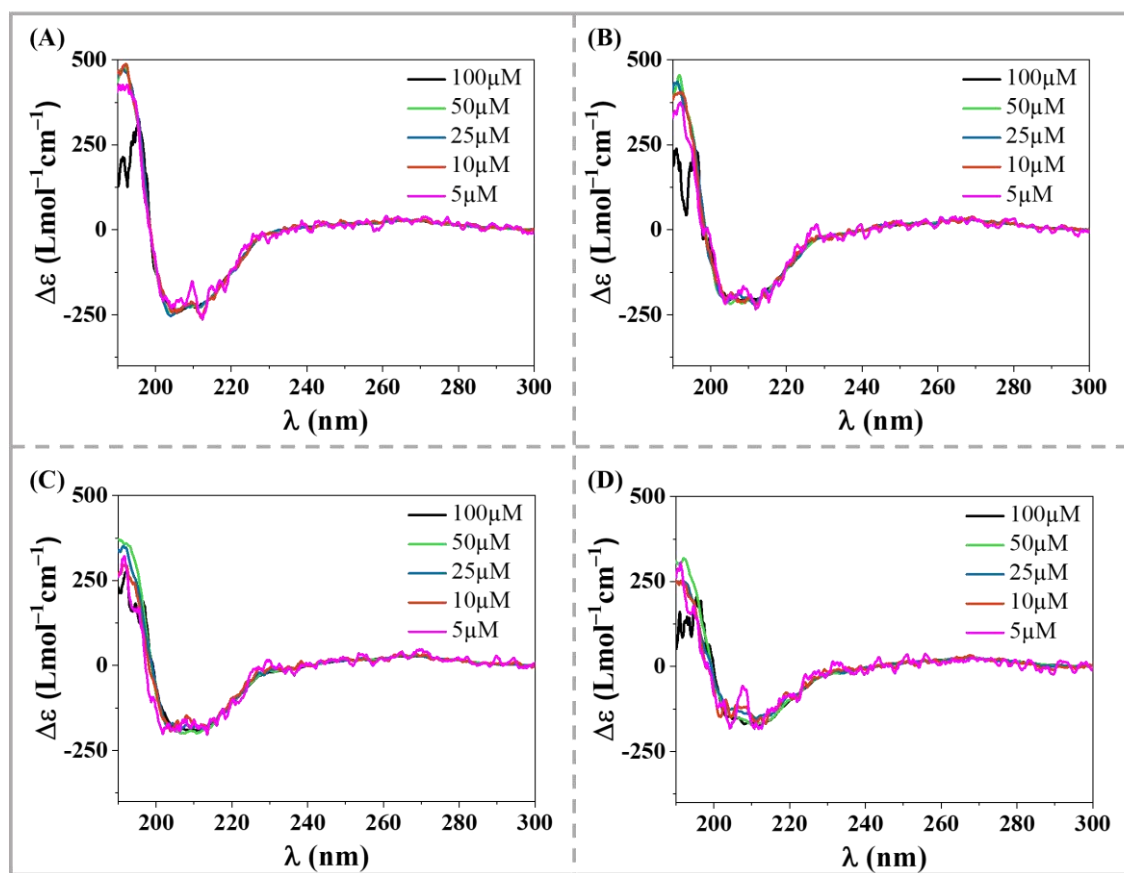


Figure 6.6. (A) CD spectra of pure C_3^{EG} in water at varying concentrations (B) CD spectra of $\text{C}_3^{\text{EG}}:\text{C}_3^{\text{tpy}}$ (100:1) in water at varying concentrations. (C) CD Spectra of $\text{C}_3^{\text{EG}}:\text{C}_3^{\text{tpy}}$ (50:1) in water at varying concentrations. (D) CD Spectra of $\text{C}_3^{\text{EG}}:\text{C}_3^{\text{tpy}}$ (10:1) in water at varying concentrations.

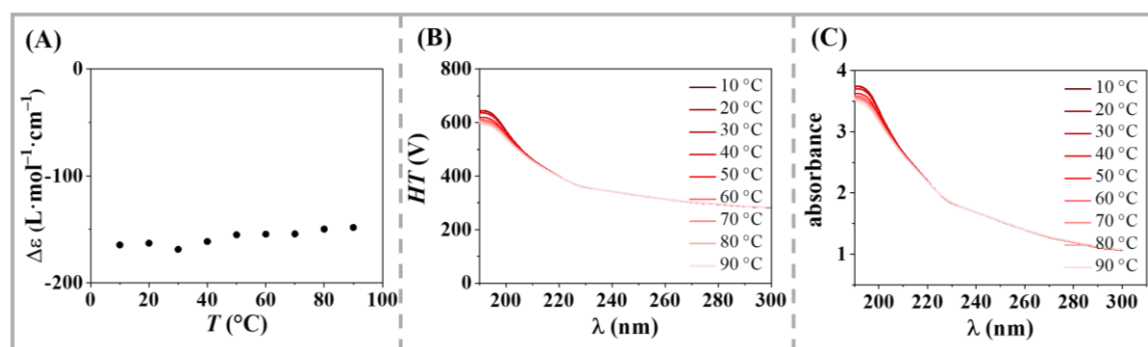


Figure 6.7. (A) CD signal of the copolymeric aqueous solution of $\text{C}_3^{\text{EG}}:\text{C}_3^{\text{tpy}}$ (10:1) at $\lambda = 210 \text{ nm}$ plotted against the temperature ($c = 50 \mu\text{M}$). (B) HT- and (C) absorbance signal of the copolymeric aqueous solution of $\text{C}_3^{\text{EG}}:\text{C}_3^{\text{tpy}}$ (10:1) at varying temperatures ($c = 50 \mu\text{M}$).

6.5 References

- (1) [REDACTED] Breul, K.; [REDACTED] Bridging Rigidity and Flexibility: Modulation of Supramolecular Hydrogels by Metal Complexation. *Macromol. Rapid Commun.* **2021**, *2100473*, 1–7.
- (2) Kirschner, M.; Mitchison, T. Beyond Self-Assembly: From Microtubules to Morphogenesis. *Cell* **1986**, *45* (3), 329–342.
- (3) Fletcher, D. A.; Mullins, R. D. Cell Mechanics and the Cytoskeleton. *Nature* **2010**, *463* (7280), 485–492.
- (4) Merindol, R. R.; Walther, A. Materials Learning from Life: Concepts for Active, Adaptive and Autonomous Molecular Systems. *Chem. Soc. Rev.* **2017**, *46* (18), 5588–5619.
- (5) Xia, F.; Jiang, L. Bio-Inspired, Smart, Multiscale Interfacial Materials. *Adv. Mater.* **2008**, *20* (15), 2842–2858.
- (6) Wegst, U. G. K.; Bai, H.; Saiz, E.; Tomsia, A. P.; Ritchie, R. O. Bioinspired Structural Materials. *Nat. Mater.* **2015**, *14* (1), 23–36.
- (7) Lehn, J.-M. Toward Self-Organization and Complex Matter. *Science* **2002**, *295* (5564), 2400–2403.
- (8) Whitesides, G. M.; Grzybowski, B. Self-Assembly at All Scales. *Science* **2002**, *295* (5564), 2418–2421.
- (9) Mattia, E.; Otto, S. Supramolecular Systems Chemistry. *Nat. Nanotechnol.* **2015**, *10* (2), 111–119.
- (10) Grzybowski, B. A. A.; Huck, W. T. S. T. S. The Nanotechnology of Life-Inspired Systems. *Nat. Nanotechnol.* **2016**, *11* (7), 585–592.
- (11) Ghislaine, V.; E.W, M. The Construction of Supramolecular Systems. *Science* **2019**, *363* (6434), 1396–1398.
- (12) Brunsveld, L.; Folmer, B. J. B.; Meijer, E. W.; Sijbesma, R. P. Supramolecular Polymers. *Chem. Rev.* **2001**, *101* (12), 4071–4097.
- (13) Aida, T.; Meijer, E. W.; Stupp, S. I. Functional Supramolecular Polymers. *Science* **2012**, *335* (6070), 813–817.
- (14) Besenius, P. Controlling Supramolecular Polymerization through Multicomponent Self-Assembly. *J. Polym. Sci. Part A Polym. Chem.* **2017**, *55* (1), 34–78.
- (15) Sijbesma, R. P.; Beijer, F. H.; Brunsveld, L.; Folmer, B. J. B.; Hirschberg, J. H. K. K.; Lange, R. F. M.; Lowe, J. K. L.; Meijer, E. W. Reversible Polymers Formed from Self-Complementary Monomers Using Quadruple Hydrogen Bonding. *Science* **1997**, *278* (5343), 1601–1604.
- (16) Folmer, B. J. B.; Sijbesma, R. P.; Versteegen, R. M.; Van Der Rijt, J. A. J.; Meijer, E. W. Supramolecular Polymer Materials: Chain Extension of Telechelic Polymers Using a Reactive

- Hydrogen-Bonding Synthons. *Adv. Mater.* **2000**, *12* (12), 874–878.
- (17) Cordier, P.; Tournilhac, F.; Soulié-Ziakovic, C.; Leibler, L. Self-Healing and Thermoreversible Rubber from Supramolecular Assembly. *Nature* **2008**, *451* (7181), 977–980.
- (18) Jorgensen, W. L.; Pranata, J. Importance of Secondary Interactions in Triply Hydrogen Bonded Complexes: Guanine-Cytosine vs Uracil-2,6-Diaminopyridine. *J. Am. Chem. Soc.* **1990**, *112* (5), 2008–2010.
- (19) Pranata, J.; Wierschke, S. G.; Jorgensen, W. L. OPLS Potential Functions for Nucleotide Bases. Relative Association Constants of Hydrogen-Bonded Base Pairs in Chloroform. *J. Am. Chem. Soc.* **1991**, *113* (8), 2810–2819.
- (20) Wang, L.; Gong, C.; Yuan, X.; Wei, G. Controlling the Self-Assembly of Biomolecules into Functional Nanomaterials through Internal Interactions and External Stimulations: A Review. *Nanomaterials* **2019**, *9* (2), 285.
- (21) Hagan, M. F. Modeling Viral Capsid Assembly. *Adv. Chem. Phys.* **2013**, *155*, 1–68.
- (22) Kegel, W. K.; Van Der Schoot, P. Physical Regulation of the Self-Assembly of Tobacco Mosaic Virus Coat Protein. *Biophys. J.* **2006**, *91* (4), 1501–1512.
- (23) Li, G.; McGown, L. B. Molecular Nanotube Aggregates of β - and γ -Cyclodextrins Linked by Diphenylhexatrienes. *Science* **1994**, *264* (5156), 249–251.
- (24) Serreli, V.; Lee, C. F.; Kay, E. R.; Leigh, D. A. A Molecular Information Ratchet. *Nature* **2007**, *445* (7127), 523–527.
- (25) Whittell, G. R.; Hager, M. D.; Schubert, U. S.; Manners, I. Functional Soft Materials from Metallopolymers and Metallosupramolecular Polymers. *Nat. Mater.* **2011**, *10* (3), 176–188.
- (26) Rossow, T.; Bayer, S.; Albrecht, R.; Tzschucke, C. C.; Seiffert, S. Supramolecular Hydrogel Capsules Based on pEG: A Step toward Degradable Biomaterials with Rational Design. *Macromol. Rapid Commun.* **2013**, *34* (17), 1401–1407.
- (27) Rossow, T.; Seiffert, S. Supramolecular Polymer Gels with Potential Model-Network Structure. *Polym. Chem.* **2014**, *5* (8), 3018–3029.
- (28) Cuccia, L. A.; Lehn, J. M.; Homo, J. C.; Schmutz, M. Encoded Helical Self-Organization and Self-Assembly into Helical Fibers of an Oligoheterocyclic Pyridine-Pyridazine Molecular Strand. *Angew. Chem. Int. Ed.* **2000**, *39* (1), 233–237.
- (29) Hartlieb, M.; Mansfield, E. D. H.; Perrier, S. A Guide to Supramolecular Polymerizations. *Polym. Chem.* **2020**, *11* (6), 1083–1110.
- (30) Hoeben, F. J. M.; Jonkheijm, P.; Meijer, E. W.; Schenning, A. P. H. J. About Supramolecular Assemblies of π -Conjugated Systems. *Chem. Rev.* **2005**, *105* (4), 1491–1546.
- (31) Martinez, C. R.; Iverson, B. L. Rethinking the Term “Pi-Stacking.” *Chem. Sci.* **2012**, *3* (7), 2191–2201.
- (32) Chen, Z.; Lohr, A.; Saha-Möller, C. R.; Würthner, F. Self-Assembled π -Stacks of Functional Dyes in Solution: Structural and Thermodynamic Features. *Chem. Soc. Rev.* **2009**, *38* (2), 564–

584.

(33) Xian, S.; Webber, M. J. Temperature-Responsive Supramolecular Hydrogels. *J. Mater. Chem. B* **2020**, *8* (40), 9197–9211.

(34) Cui, H.; Webber, M. J.; Stupp, S. I. Self-Assembly of Peptide Amphiphiles: From Molecules to Nanostructures to Biomaterials. *Biopolymers* **2010**, *94* (1), 1–18.

(35) Sato, K.; Hendricks, M. P.; Palmer, L. C.; Stupp, S. I. Peptide Supramolecular Materials for Therapeutics. *Chem. Soc. Rev.* **2018**, *47* (20), 7539–7551. <https://doi.org/10.1039/C7CS00735C>.

(36) Boekhoven, J.; Stupp, S. I. 25th Anniversary Article: Supramolecular Materials for Regenerative Medicine. *Adv. Mater.* **2014**, *26* (11), 1642–1659.

(37) Stupp, S. I. On Supramolecular Self-Assembly: Interview with Samuel Stupp. *Adv. Mater.* **2020**, *32* (20), 1906741.

(38) Appel, R.; Fuchs, J.; Tyrrell, S. M.; Korevaar, P. A.; Stuart, M. C. A.; Voets, I. K.; Schönhoff, M.; Besenius, P. Steric Constraints Induced Frustrated Growth of Supramolecular Nanorods in Water. *Chem. Eur. J.* **2015**, *21* (52), 19257–19264.

(39) Ahlers, P.; Frisch, H.; Besenius, P. Tuneable PH-Regulated Supramolecular Copolymerisation by Mixing Mismatched Dendritic Peptide Comonomers. *Polym. Chem.* **2015**, *6* (41), 7245–7250.

(40) Ahlers, P.; Frisch, H.; Spitzer, D.; Vobecka, Z.; Vilela, F.; Besenius, P. The Synthesis of Dendritic EDOT-Peptide Conjugates and Their Multistimuli-Responsive Self-Assembly into Supramolecular Nanorods and Fibers in Water. *Chem. Asian J.* **2014**, *9* (8), 2052–2057.

(41) Frisch, H.; Nie, Y.; Raunser, S.; Besenius, P. PH-Regulated Selectivity in Supramolecular Polymerizations: Switching between Co- And Homopolymers. *Chem. Eur. J.* **2015**, *21* (8), 3304–3309.

(42) Van Buel, R.; Spitzer, D.; Berac, C. M.; Van Der Schoot, P.; Besenius, P.; Jabbari-Farouji, S. Supramolecular Copolymers Predominated by Alternating Order: Theory and Application. *J. Chem. Phys.* **2019**, *151* (1).

(43) Berac, C. M.; Zengerling, L.; Straßburger, D.; Otter, R.; Urschbach, M.; Besenius, P. Evaluation of Charge-Regulated Supramolecular Copolymerization to Tune the Time Scale for Oxidative Disassembly of B-Sheet Comonomers. *Macromol. Rapid Commun.* **2020**, *41* (1), 1900476.

(44) Otter, R.; Berac, C. M.; Seiffert, S.; Besenius, P. Tuning the Life-Time of Supramolecular Hydrogels Using ROS-Responsive Telechelic Peptide-Polymer Conjugates. *Eur. Polym. J.* **2019**, *110* (November 2018), 90–96.

(45) Spitzer, D.; Rodrigues, L. L.; Straßburger, D.; Mezger, M.; Besenius, P. Tuneable Transient Thermogels Mediated by a PH- and Redox-Regulated Supramolecular Polymerization. *Angew. Chem. Int. Ed.* **2017**, *56* (48), 15461–15465.

- (46) Andres, P. R.; Schubert, U. S. New Functional Polymers and Materials Based on 2,2':6', 2''-Terpyridine Metal Complexes. *Adv. Mater.* **2004**, *16* (13), 1043–1068.
- (47) Schmolke, W.; Ahmadi, M.; Seiffert, S. Enhancement of Metallo-Supramolecular Dissociation Kinetics in Telechelic Terpyridine-Capped Poly(Ethylene Glycol) Assemblies in the Semi-Dilute Regime. *Phys. Chem. Chem. Phys.* **2019**, *21* (35), 19623–19638.
- (48) Koziol, M. F.; Fischer, K.; Seiffert, S. Structural and Gelation Characteristics of Metallo-Supramolecular Polymer Model-Network Hydrogels Probed by Static and Dynamic Light Scattering. *Macromolecules* **2021**, *54* (9), 4375–4386.
- (49) Breul, K.; Seiffert, S. Amphiphilic Poly(Ether Urethanes) Carrying Associative Terpyridine Side Groups with Controlled Spacing. *Polym. Chem.* **2021**, *12* (15), 2305–2316.
- (50) Vereroudakis, E.; Bantawa, M.; Lafleur, R. P. M.; Parisi, D.; Matsumoto, N. M.; Peeters, J. W.; Del Gado, E.; Meijer, E. W.; Vlassopoulos, D. Competitive Supramolecular Associations Mediate the Viscoelasticity of Binary Hydrogels. *ACS Cent. Sci.* **2020**, *6* (8), 1401–1411.
- (51) Glassman, M. J.; Chan, J.; Olsen, B. D. Reinforcement of Shear Thinning Protein Hydrogels by Responsive Block Copolymer Self-Assembly. *Adv. Funct. Mater.* **2013**, *23* (9), 1182–1193.
- (52) Noteborn, W. E. M.; Zwagerman, D. N. H.; Talens, V. S.; Maity, C.; van der Mee, L.; Poolman, J. M.; Mytnyk, S.; van Esch, J. H.; Kros, A.; Eelkema, R.; Kieltyka, R. E. Crosslinker-Induced Effects on the Gelation Pathway of a Low Molecular Weight Hydrogel. *Adv. Mater.* **2017**, *29* (12), 1603769.
- (53) Kieltyka, R. E.; Pape, A. C. H.; Albertazzi, L.; Nakano, Y.; Bastings, M. M. C.; Voets, I. K.; Dankers, P. Y. W.; Meijer, E. W. Mesoscale Modulation of Supramolecular Ureidopyrimidinone-Based Poly(Ethylene Glycol) Transient Networks in Water. *J. Am. Chem. Soc.* **2013**, *135* (30), 11159–11164.
- (54) Koenigs, M. M. E.; Pal, A.; Mortazavi, H.; Pawar, G. M.; Storm, C.; Sijbesma, R. P. Tuning Cross-Link Density in a Physical Hydrogel by Supramolecular Self-Sorting. *Macromolecules* **2014**, *47* (8), 2712–2717.
- (55) Zhukhovitskiy, A. V.; Zhong, M.; Keeler, E. G.; Michaelis, V. K.; Sun, J. E. P.; Hore, M. J. A.; Pochan, D. J.; Griffin, R. G.; Willard, A. P.; Johnson, J. A. Highly Branched and Loop-Rich Gels via Formation of Metal-Organic Cages Linked by Polymers. *Nat. Chem.* **2016**, *8* (1), 33–41.
- (56) Eelkema, R.; Pich, A. Pros and Cons: Supramolecular or Macromolecular: What Is Best for Functional Hydrogels with Advanced Properties? *Adv. Mater.* **2020**, *32* (20), 1906012.
- (57) Straßburger, D.; Stergiou, N.; Urschbach, M.; Yurugi, H.; Spitzer, D.; Schollmeyer, D.; Schmitt, E.; Besenius, P. Mannose-Decorated Multicomponent Supramolecular Polymers Trigger Effective Uptake into Antigen-Presenting Cells. *ChemBioChem* **2018**, *19* (9), 912–916.
- (58) Holyer, R. H.; Hubbard, C. D.; Kettle, S. F. A.; Wilkins, R. G. The Kinetics of Replacement Reactions of Complexes of the Transition Metals with 2,2',2''-Terpyridine. *Inorg. Chem.* **1966**, *5* (4), 622–625.

(59) Dobrawa, R.; Ballester, P.; Saha-Möller, C. R.; Würthner, F. *Metal-Containing and Metallo-Supramolecular Polymers and Materials (ACS Symposium Series, No. 928)*, 1st ed.; American Chemical Society, **2006**.

(60) Ahmadi, M.; Seiffert, S. Dynamic Model Metallo-Supramolecular Dual-Network Hydrogels with Independently Tunable Network Cross-links. *J. Polym. Sci.* **2020**, *58* (2), 330–342.

(61) Mahmud Rasid, I.; Ramirez, J.; Olsen, B. D.; Holten-Andersen, N. Understanding the Molecular Origin of Shear Thinning in Associative Polymers through Quantification of Bond Dissociation under Shear. *Phys. Rev. Mater.* **2020**, *4* (5), 55602.

CHAPTER 7: THERMORESPONSIVE POLYURETHANE GELS FOR BIOLOGICAL APPLICATIONS

Publication:

Cell Adhesion on UV Cross-Linked Polyurethane Gels with Adjustable Mechanical Strength and Thermoresponsiveness

K. Breul*, [REDACTED]
[REDACTED] *Macromolecular rapid communications* 2021, e2100505
(<https://doi.org/10.1002/marc.202100505>).

*The authors contributed equally.

The results presented in the following chapter (p. 193–225) were first published on September 25, 2021 and are adapted with permission.¹

Further supporting information can be found in appendix, **Chapter A.7**.

Copyright © 2021 The Authors. *Macromolecular Rapid Communications* published by Wiley-VCH GmbH.

Summary

The responsivity of soft materials does not exclusively originate from reversible, supramolecular associations. An adjustment of the material properties to external stimuli can also result from the macromolecular backbone itself. In this regard, the temperature-induced solubility gaps of certain polymer–solvent mixtures represent a prominent example. Resulting from the temperature-dependent balance of entropic and enthalpic forces, aqueous polymer solutions can exhibit a lower critical solution temperature (LCST) above which the polymer coils contract and precipitate from the solution. If the thermosensitive polymer is covalently cross-linked and forms a percolated network, the coil contraction leads to a macroscopic deswelling of the corresponding gel. This temperature-sensitive, often reversible change of the swelling degree and thus the stiffness of polymer gels, is a promising tool for tissue engineering and biomedical applications.

In this context, thermoresponsive polyurethane (PU) hydrogels received increasing interest over the last years. Their often-superior mechanical strength and intrinsically hydrolysable backbone composition offer attractive assets and complement established LCST systems. For biological or biomedical applications, the non-toxicity of the polymer is a fundamental prerequisite, which is generally fulfilled by many PUs.

Besides this basic compatibility, it is however very advantageous for the design of cell-contacting materials, if the bio-adhesive properties of the applied polymer matrix can be adjusted to the application-specific demands. To contribute a material basis which meets these criteria, the amphiphilic nature of the PUs presented in **Chapter 3** is further explored to create thermoresponsive, covalent polymer gels. For this purpose, the terpyridine ligand is replaced with a dimethylmaleimide (DMMI) unit, which undergoes a UV-light induced dimerization reaction in the presence of a suitable photosensitizer. The cloud point temperatures of the linear precursor PUs in water can be adjusted by the molar ratio between hydrophobic diisocyanate and DMMI groups and hydrophilic ethylene glycol units. From the viscous precursor solutions, stable hydrogels are obtained by UV cross-linking. Rheological experiments demonstrate the dependence of the gelation time on photosensitizer concentration and light intensity. The plateau moduli of the finally obtained gels are determined by the polymer concentration and the average spacing of the DMMI groups ($G_N = 0.200\text{--}4$ kPa). Regarding the thermosensitivity of the hydrogels, the swelling ratios Q show significant changes between 5 °C and 40 °C, which increase with the hydrophobicity of the precursor polymer ($Q_{5^\circ\text{C}}/Q_{40^\circ\text{C}} = 180\text{--}350\%$). Finally, it is shown that a low amount of a covalently attached catechol bio-linker strongly improves the cell-adhesiveness of the gels without significantly affecting their mechanical properties.

Author Contributions:

Katharina Breul:	Concept development, PU and bio-linker synthesis, turbidity, swelling and rheological measurements, manuscript preparation.
██████████	Concept development, cell experiments, confocal laser scanning microscopy, graphical design, manuscript preparation.
██████████	Peptide synthesis, assistance with RP-HPLC purification.
██████████	Magic-angle solid state NMR measurements.
██████████████████	PU synthesis, bio-linker synthesis, turbidity measurements.
██████████	Implementation of the DMMI diol synthesis.
██████████████████	Optimization of the PU synthesis.
██████████	Manuscript correction.
██████████████████	Scientific supervision, manuscript correction.

Acknowledgments:

Parts of the results of this study were acquired with a Confocal Laser Scanning Microscope funded in part by the Major Research Instrumentation Program of the German Research Foundation under grant No. INST 247/878-1 FUGG. The authors wish to thank ██████████ (JGU Mainz, Institute for Pathology) for providing osteoblasts expressing GFP (MG-63-GFP). Open access funding enabled and organized by Projekt DEAL.

7.1 Introduction

Thermoresponsive hydrogels are one of the most promising material platforms for modern biomedical applications with a scope ranging from nanomedical drug carriers to 3D *in vitro* models and tissue engineering applications.^{2,3} Especially in the latter cases, it is crucial to provide soft materials which resemble the biological extracellular matrix (ECM). To ensure an efficient nutrient and waste transport as well as tissue-like mechanics, this requires hydrogels with swelling ratios between 50–85 wt%.^{4,5} Depending on the respective application, the adaptive hydrogels should further be cell adhesive, biodegradable, and exhibit robust and distinct thermoresponsive properties.

While natural hydrogels such as protein gels usually fulfill the bio-related requirements, their weak mechanical properties as well as the batch-to-batch variations resulting from their animal-based origins limit the application scope.^{6,7} By contrast, the chemical and mechanical properties of synthetic hydrogels can be easily adjusted to the application specific demands. However, synthetic materials are usually bioinert, and cell-adhesion must be enabled through additional bio-linkers or coatings that allow interactions with cell surface receptors.^{8–11} Due to these complementary properties, the development of hydrogel platforms, that combine the advantages of natural and synthetic materials, is an ongoing challenge for materials scientists.

Regarding the thermal adaptivity of responsive hydrogels, poly(*N*-isopropylacrylamide) (pNiPAm) is still the most popular polymer backbone due its sharp volume phase transition (VPT) in aqueous media close to the physiological temperature range. Nevertheless, it has drawbacks. Although much progress was achieved with respect to the often-insufficient mechanical performance of pNiPAm-based hydrogels,¹² fundamental issues such as the non-degradability of the vinyl backbone remain.¹³ To provide versatile alternatives, thermoresponsive polyurethane (PU) hydrogels received increasing interest. The general biocompatibility of PU materials is widely established and enabled various medical applications, ranging from controlled drug delivery carriers,^{14–16} to promising or already commercialized materials for blood contacting devices like prosthetic heart valves.¹⁷ In these materials, the urethane groups in the polymer backbone are not only responsible for the often-superior mechanical strength of PU networks but are also intrinsically hydrolysable.^{15,18–20}

To obtain thermoresponsive PUs, the combination of a hydrophilic, oligomeric diol (soft segment) and a hydrophobic diisocyanate (hard segment) has been established as versatile design approach. Due to its commercial availability, pronounced hydrophilicity and nontoxicity, poly(ethylene glycol) (pEG) became the most applied soft segment. As shown by Fu *et al.*, the variation of the polyether molar mass and thus the molar ratio of hydrophilic and hydrophobic segments allows for an easy variation of the lower critical solution temperature (LCST) of such amphiphilic PUs in aqueous solutions.¹⁹ Nevertheless, it should be noted that their turbidity measurements showed a

rather broad (≈ 10 °C) and partially incomplete LCST transition in comparison to pNiPAm. This has been strongly improved through the introduction of charged comonomers, which further allowed an even more flexible variation of the LCST, as demonstrated by Sardon *et al.*^{14,21}

To transfer the obtained insights from linear chains to 3D cross-linked networks, PU hydrogels have either been obtained in a cross-linking polymerization in the presence of a trifunctional comonomer^{18,22,23} or through the consecutive cross-linking of linear precursor polymers with reactive side-groups.^{21,24} As shown in the studies of Frydrych *et al.* and Li *et al.*, the absolute swelling ratio of the PU gels can be varied through the molar mass of the polyether soft segment in both cases. The comparison of the equilibrium swelling ratios Q (in wt%) at 4 °C and 40 °C demonstrates a $Q_{4^\circ\text{C}}/Q_{40^\circ\text{C}}$ switching around 100% in a purely pEG-based system¹⁸ while up to 600% can be achieved through the implementation of oligo(ethylene glycol) side chains as demonstrated by Aoki and Ajiro.²³

Despite the numerous improvements achieved with respect to the processability, mechanical performance, and thermal adaptivity of pEG-based PU hydrogels, strategies to achieve cell adhesion have been rarely implemented. To overcome this limitation, in the present work, we apply the modular design principles established for thermoresponsive PUs to create hydrogels with adjustable mechanical strength and thermoresponsiveness that can additionally be bio-activated through the covalent attachment of cell-adhesive groups. As a consecutive cross-linking strategy provides a greater flexibility with respect to the material's processability, we focus on the synthesis of linear PUs based on pEG and isophorone diisocyanate (IPDI). To avoid unspecific cross-linking, toxic catalysts, or a strong pH dependency, an uncharged dimethylmaleimide (DMMI) comonomer is incorporated as reactive side-group, which undergoes a dimerization reaction in the presence of a photosensitizer and UV light.²⁵ To improve the cell adhesion on these gels, we further attach arginine-glycine-aspartate- (RGD) amino acid sequences and catechol groups to the network through the identical DMMI dimerization reaction.

7.2 Results & Discussion

Thermoresponsive, UV-Cross-Linkable Polyurethanes

Linear PUs are synthesized in a pre-polymer procedure starting from pEG diols with differing molar masses ($M_n \approx 1.0$ (**7.1a**), 1.5 (**7.1b**), 2.0 (**7.1c**) and 4.0 (**7.1d**) $\text{kg}\cdot\text{mol}^{-1}$) that are added to the asymmetric isophorone diisocyanate (IPDI) **7.2** and converted into the corresponding macrodiisocyanates (pEG/IPDI) **7.3a–d** by reaction with the cycloaliphatic, secondary isocyanate group under organo-tin catalysis (**Figure 7.1 A**).^{26–28} To incorporate dimerizable DMMI-groups, 2,3-dimethyl maleic anhydride **7.10** is attached to the hydrophilic triethylene glycol linker **7.9**, which is then coupled with the acetone protected 2,2-bis(hydroxymethyl)propionic acid **7.14** as shown in **Scheme 7.1** in **Chapter 7.4**.

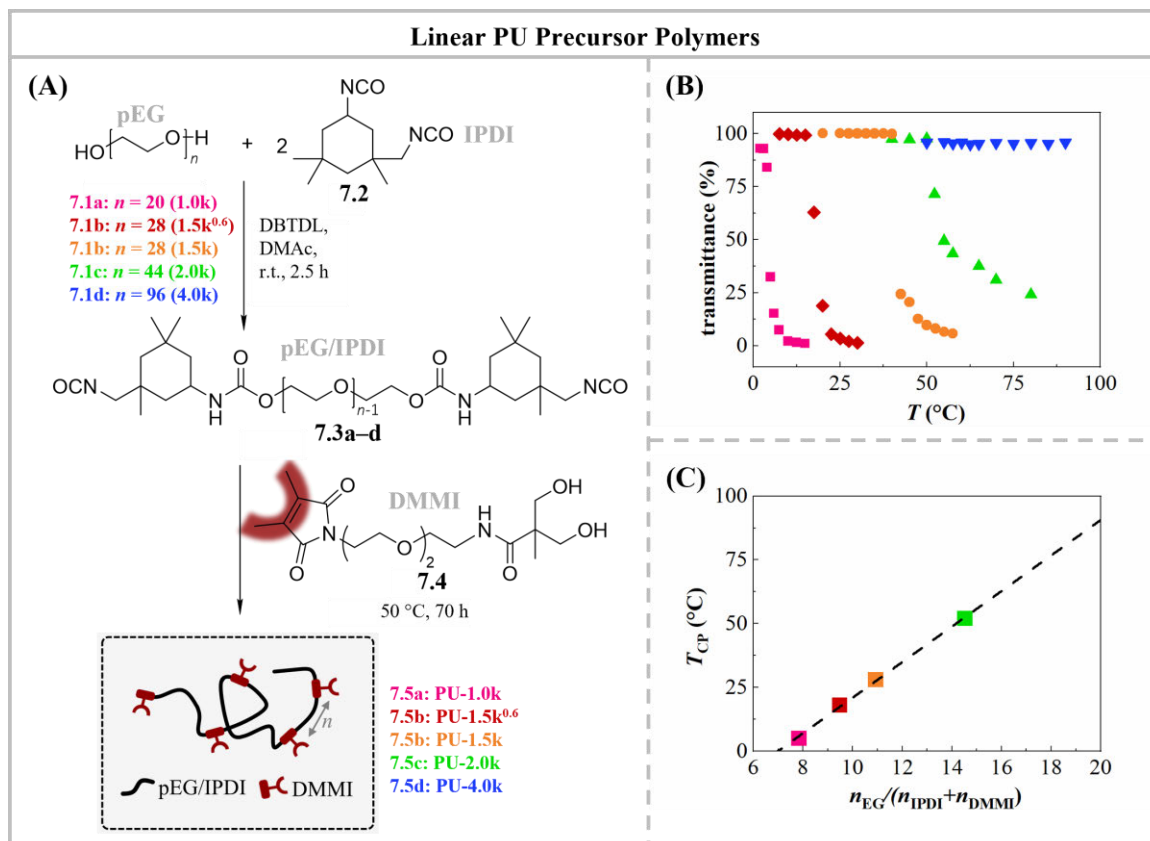


Figure 7.1. (A) Synthesis of linear pEG/IPDI-based PUs with DMMI pendant groups (**7.5a–e**). (B) Turbidity measurements of PU-1.0k **7.5a** (■), PU-1.5k^{0.6} **7.5b** (◆), PU-1.5k **7.5c** (●), PU-2.0k **7.5d** (▲) and PU-4.0k **7.5e** (▼) in water (5 g·L⁻¹). (C) Cloud point temperatures as a function of the molar ratio between EG, IPDI and DMMI with linear regression (dashed line).

The deblocked DMMI-diol **7.4** is then applied as chain extender for the pEG diisocyanates **7.3a–d**. Gel permeation chromatography (GPC) measurements of the pEG diols **7.3a–d** and the obtained linear PUs **5a–e** demonstrate moderate, but sufficient chain elongation efficiencies as summarized in **Table 7.1** and **Figure 7.6**.

The molar ratios between the hydrophilic ethylene glycol (EG) units of the pEG backbone and the hydrophobic IPDI-DMMI blocks are investigated by ¹H-NMR spectroscopy. Comparing the characteristic signals of the DMMI methyl groups (1.89 ppm), the IPDI cycloaliphatic methylene- and methyl-groups (1.19–0.06 ppm) and the pEG backbone (3.76–3.40 ppm) reveals the intended increase of the molar content of hydrophilic EG groups with the molar mass of the polyether diol (**Table 7.1**, **Figure S7.16–7.20**). To enable an even finer variation of the hydrophilic-to-hydrophobic balance than accessible through the commercially available pEG diols, the molar feed ratio between pEG and DMMI is additionally varied from 1:1 to 1:2.3 for pEG-1.5k (PU-1.5k^{0.6} **7.5b**). The ¹H-NMR analysis verifies that this approach is another facile option to alter the PU composition. All experimental details and full characterizations can be found in **Chapter 7.4**.

To investigate how the variation of the amphiphilic balance influences the thermoresponsivity, the cloud point temperatures T_{cp} are determined through UV-Vis transmittance measurements in dilute aqueous solutions ($c_{PU} = 5 \text{ g}\cdot\text{L}^{-1}$, **Figure 7.1 B**). As shown in **Figure 7.1 C**, the cloud point temperatures depend linearly on the molar ratio between hydrophilic EG and hydrophobic IPDI and DMMI groups and can be varied from 5° to over 90°C . In accordance with the observations reported by Li *et al.* and Ronco *et al.*, the turbidity curves depicted in **Figure 7.2 B** also reveal a sharper and more pronounced LCST transition for the more hydrophobic PU compositions.^{21,24}

Table 7.1. pEG diols applied in the polymerization. Characterization of the synthesized PUs.

sample	M_n (pEG diol) ^{a)} ($\text{kg}\cdot\text{mol}^{-1}$)	M_w (PU) ^{a)} ($\text{kg}\cdot\text{mol}^{-1}$)	\bar{D} (PU) ^{a)}	$n_{EG}/n_{IPDI}/n_{DMMI}$ ^{b)}	T_{cp} ($^\circ\text{C}$)
7.5a - PU-1.0k	0.88	6.3	1.5	29:2.7:1	5
7.5b - PU-1.5k ^{0.6}	1.24	12.0	1.9	36:2.8:1	18
7.5c - PU-1.5k	1.24	12.4	1.8	47:3.3:1	28
7.5d - PU-2.0k	1.95	14.6	1.6	61:3.2:1	52
7.5e - PU-4.0k	4.22	30.3	1.5	140:4.5:1	> 90

^{a)} GPC (DMF, pEG calibration); ^{b)} $^1\text{H-NMR}$ analysis (EG: 3.76–3.40 ppm, 4H; IPDI: 1.19–0.06 ppm, 15H; DMMI: 1.89 ppm, 6H).

Gelation and Mechanical Properties

Further on, the UV-induced cross-linking of the linear precursor polymer solutions in the presence of the photosensitizer thioxanthone disulfonate (TXS) is investigated by linear shear rheological experiments. Applying PU-4.0k **7.5e** ($c_{PU} = 100 \text{ g}\cdot\text{L}^{-1}$) as a representative example, the gelation time in terms of the G' – G'' crossover is determined as $t_{gel} = 8 \text{ min}$ at a TXS concentration of 1 mM and an irradiation aperture of 1% and is shown to be temperature independent between 5 – 20°C (**Figure 7.7**). When the TXS concentration is reduced to 0.1 mM while the irradiation intensity is kept constant at 1%, the gelation time increases to 68 min while the obtained gel strength remains constant. The gelation time at the lower TXS concentration (0.1 mM) can however be reduced to 7 min if the irradiation aperture is increased to 10%. This qualitative parameter screening demonstrates how the gelation time of the DMMI cross-linked hydrogels can be readily adjusted by these two external parameters.

Next, we investigate how the gel strength in terms of the plateau modulus depends on the precursor polymer concentration of PU-4.0k **7.5e** ($T = 5^\circ\text{C}$). As indicated in **Figure 7.2 A**, no stable gel is obtained below a concentration of $c_{PU} = 100 \text{ g}\cdot\text{L}^{-1}$. Above this gelation threshold, the plateau moduli increase approximately linearly from 200 to 3900 Pa with the polymer concentration (**Figure 7.2 B**), as expected for affine and phantom networks. It should be noted though that the precursor solutions become increasingly viscous (**Figure 7.2 A**), which leads to inhomogeneities and handling difficulties.

Further on, we compare the mechanical properties of hydrogels obtained from the different precursor polymers ($c_{\text{PU}} = 100 \text{ g}\cdot\text{L}^{-1}$). PU-1.0k **7.5a** is excluded from all further experiments due to its incomplete dissolution in water at higher polymer contents. As shown in **Figure 7.2 C**, the plateau moduli clearly demonstrate the dependency of the gel strength on the average sticker spacing, which is mainly determined by the pEG molar mass (**Figure 7.2 D**). As expected, the PU-1.5k^{0.6} **7.5b** hydrogel shows the highest plateau modulus (1200 Pa), which decreases with the pEG content and molar mass to 990 Pa (PU-1.5k **7.5c**), 370 Pa (PU-2.0k **7.5d**), and finally 200 Pa (PU-4.0k **7.5e**). In summary, the concentration and precursor polymer dependent mechanical properties are qualitatively consistent with the expected structure–property relations and allow an easy adjustment of the gel strength between 200–4000 Pa though the precursor polymer concentration and average sticker density.

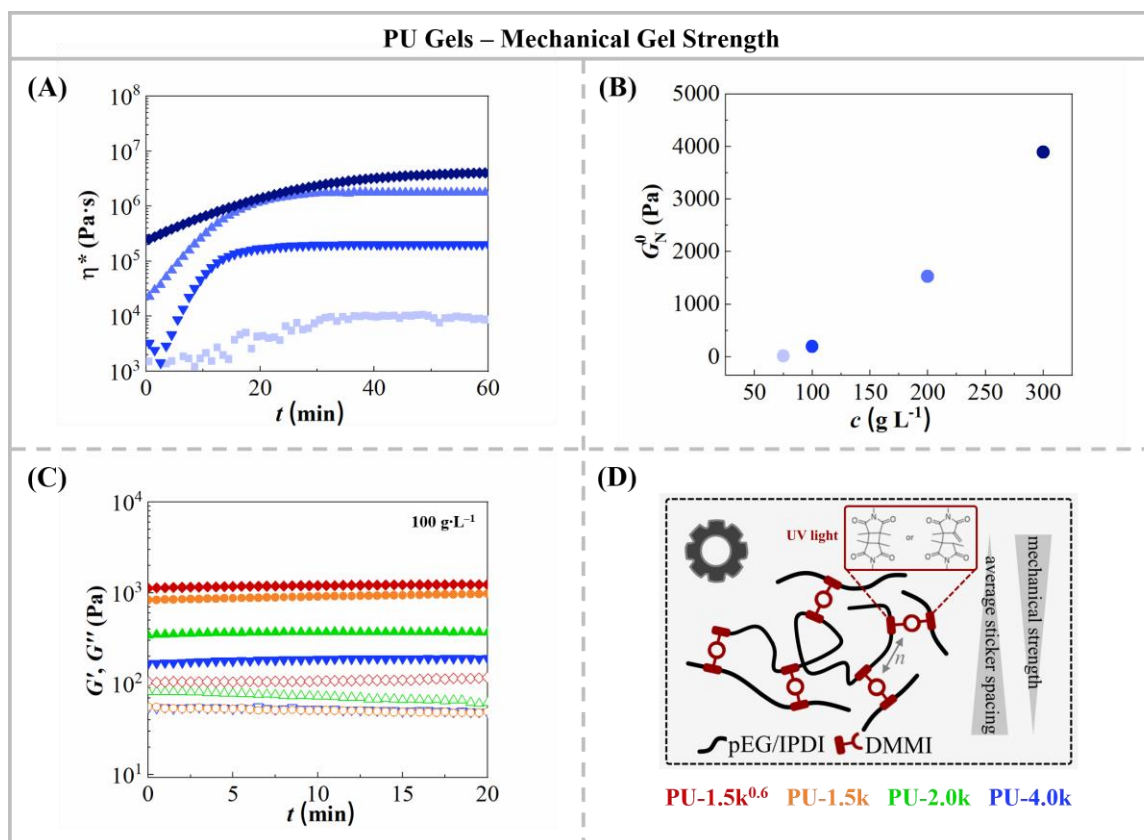


Figure 7.2. (A) Time-dependent complex viscosity of PU-4.0k **7.5e** solutions under UV irradiation at a concentration of 75 (■), 100 (▼), 200 (▲), and 300 g·L⁻¹ (◆). Gelation occurs at a TXS concentration of 1 mM, an irradiation aperture of 1% (320–500 nm), and at a temperature of 5 °C. (B) Plateau moduli as a function of the PU-4k concentration. (C) Time-dependent storage G' (closed symbols) and loss G'' moduli (open symbols) of PU-1.5k^{0.6} **7.5b** (◆), PU-1.5k **7.5c** (●), PU-2.0k **7.5d** (▲) and PU-4.0k **7.5e** (▼) hydrogels at a concentration of 100 g·L⁻¹ ($T = 5$ °C). (D) Schematic representation of the DMMI cross-linked PU networks.

Swelling Properties of PU Hydrogels

To investigate the temperature-dependent hydration behavior (**Figure 7.3 A**), the swelling degrees of PU gels cross-linked at $c_{PU} = 100 \text{ g}\cdot\text{L}^{-1}$ are measured at 5, 20, and 40 °C after equilibration for 12 h at each temperature. Note that the synthesized hydrogels are thoroughly dialyzed beforehand to avoid interferences with a potentially occurring sol fraction. It can first be observed that the swelling degrees of the fully hydrated networks at 5 °C show the same cross-linking-density dependency as the gel strength and increase from 2700% (PU-1.5k^{0.6}), to 4100% (PU-1.5k), 5000% (PU-2.0k) and finally 7800% (PU-4.0k) with increasing soft segment length (**Figure 7.3 B**). This tendency is in accordance with the findings reported by Li *et al.* and Frydrych *et al.*, who also varied the pEG molar mass in chemically cross-linked PU hydrogels and investigated the temperature-dependent equilibrium swelling.^{18,24}

The thermal responsiveness of the hydrogels is further evaluated by comparing the equilibrium swelling degrees at 5 °C and 40 °C. As depicted in **Figure 7.3 C**, the temperature induced volume switch decreases around a factor two from $(350 \pm 12)\%$ to $(180 \pm 4)\%$ from the most hydrophobic (PU-1.5k^{0.6} **7.5b**) to the most hydrophilic (PU-4.0k **7.5e**) PU.

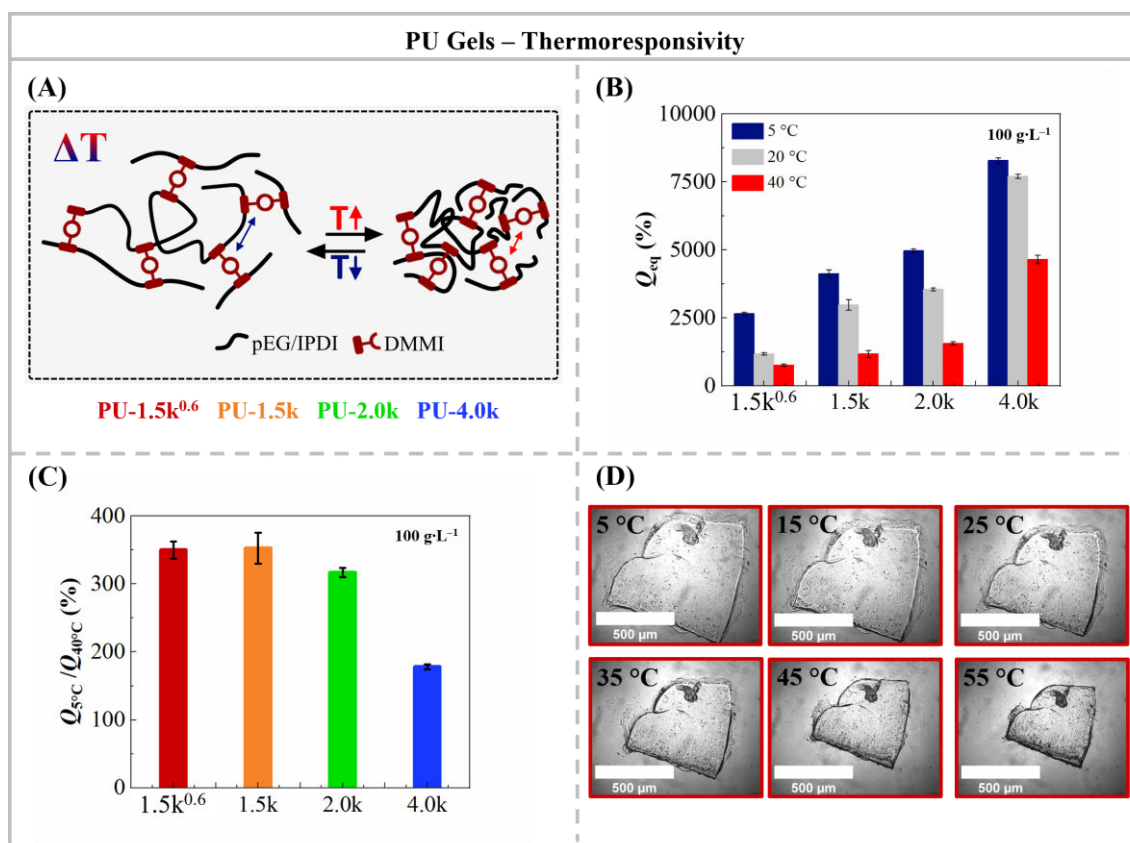


Figure 7.3. (A) Schematic representation of the temperature-induced hydrogel deswelling. (B) Equilibrium swelling degrees and (C) swelling degree switches between 5 °C and 40 °C of PU-1.5k^{0.6} **7.5b** (—), PU-1.5k **7.5c** (—), PU-2.0k **7.5d** (—) and PU-4.0k **7.5e** (—) hydrogels cross-linked at a concentration of $100 \text{ g}\cdot\text{L}^{-1}$ and equilibrated for 12 h at 5 °C, 20 °C and 40 °C. (D) Microscope images of PU-1.5k^{0.6} gels at increasing temperatures.

This trend qualitatively reflects the LCST behavior of the dilute precursor polymer solutions, which was shown to depend linearly on the balance between hydrophilic EG and hydrophobic DMMI- and IPDI-monomers (**Figure 7.1 C**). However, within the cross-linked gels, this dependency is not as clearly pronounced and the volume switches of the PU-1.5k⁰⁶ and PU-1.5k gels even coincide within the margin of error. Note, that the considerable weighing error and small sample number (performed in triplicate) limit the accuracy of the swelling degree determinations in contrast to the turbidity measurements. Nonetheless, in comparison to the formerly mentioned studies on similar PU hydrogels, it can be observed that the volume switches between 5 °C and 40 °C of the pEG-2.0k (320%) and pEG-1.5k (350%) based hydrogels significantly exceed those reported by Li *et al.* (pEG-2.0k, $\approx 100\%$)²⁴ and Frydrych *et al.* (pEG-1.5k, $\approx 200\%$).¹⁸ This is likely caused by the additionally incorporation of the hydrophobic DMMI-groups and generally depends on the overall amphiphilic balance. As exemplarily shown for PU-1.5k⁰⁶, the temperature-induced deswelling is also accompanied by a significant size reduction corresponding to 83% (25 °C), 69% (45 °C) and finally 63% (55 °C) of the initial diameter at 5 °C (**Figure 7.3 D**).

Bio-Linker Attachment and Cell Adhesion

To generate bio-adhesive hydrogel surfaces, we further investigated the possibility to incorporate integrin-binding ligands such as catechol groups or RGD sequences into the PU networks, since both groups are known to promote the cell adhesion. To keep the polymer design simple, the initially incorporated DMMI side-groups are also used for the attachment of these bio-linkers. For this purpose, 3,4-(dihydroxyphenyl)propionic acid **7.16** is coupled with a DMMI-functionalized triethylene glycol linker **7.12** in an HATU mediated amidation to obtain the DMMI-functionalized catechol **7.6** (**Figure 7.4 A, Scheme 7.2**). Analogously, the RGD-alkyne derivate **7.23**, synthesized by solid phase peptide synthesis, is coupled with a triethylene glycol-DMMI azide linker **7.22** in a copper catalyzed azide-alkyne cycloaddition (**Figure 7.4 A, Scheme 7.3**). The triethylene glycol linker ensures the water solubility of both bio-linkers. The schematic incorporation of RGD-DMMI units into the PU gel is shown in **Scheme 7.5**. To further ensure the mechanical integrity of the hydrogels and ensure a good material handling, we changed the polymer concentration from 100 to 200 g·L⁻¹.

Analytical evidence for the bio-linker incorporation into the PU gels is provided by ¹H-magic angle spinning (MAS) NMR spectroscopy (**Figure 7.4 B**). The ¹H-MAS-NMR spectra of thoroughly dialyzed PU-2.0k (200 g·L⁻¹) gels with 0 mol% RGD (i) and 25 mol% RGD (ii) (compared to the PU-DMMI groups) are analyzed and compared to the one of pure RGD-DMMI **7.7** (iii). As shown in **Figure 7.4 B** (ii) the ¹H-NMR spectrum is dominated by the PU backbone resonances, but the additionally occurring signals at 7.87 ppm (triazole-CH), 4.58 ppm (triazoleN-CH₂), 3.22 ppm (arginine NHCH), 3.06 ppm (triazoleC-CH₂CH₂), and 2.73 ppm (triazoleC-

CH_2CH_2) can be assigned to the RGD-DMMI and indicate the successful incorporation into the network. An especially clearly visible example is the resonance of the triazole proton at $\delta = 7.82$ ppm. The weak, low field-shoulder observed in the reference spectrum in aqueous solution is presumably caused by a second triazole tautomer.^{29,30} Nonetheless, it can be noted that the signal of the RGD-DMMI linker is shifted to $\delta = 7.87$ ppm inside the gel and significantly broadened as shown by the increased full width at half height (solution: fwhh = 2.42 Hz; gel: fwhh = 9.05 Hz). A similar broadening is observed for all related signals and can be explained by the confinement in the gel pores resulting in reduced chain dynamics. An analogous measurement with 5 mol% RGD shows the same characteristic signals (**Figure 7.8**).

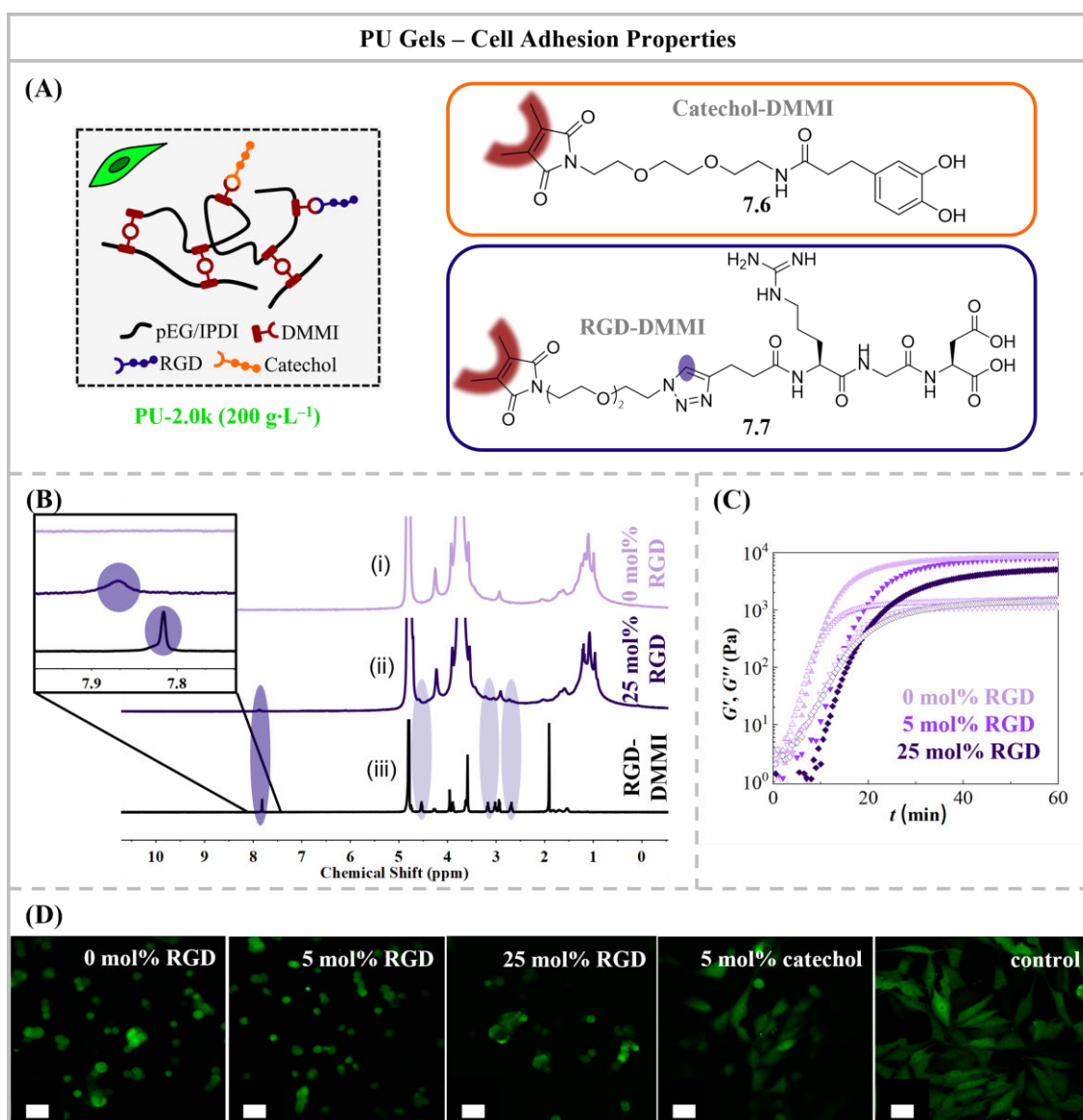


Figure 7.4. (A) Incorporation of RGD-DMMI (purple) or catechol-DMMI (orange) groups into the PU networks to increase their cell adhesive properties. (B) ¹H-MAS-NMR spectra of PU-2.0k gels (200 g·L⁻¹) containing 0 mol% (i) and 25 mol% RGD-DMMI (ii) and of the free DMMI-RGD (iii) in D₂O. (C) Mechanical strength of PU-2.0k gels (200 g·L⁻¹) with 0, 5, and 25 mol% RGD-DMMI bio-linker. (D) CLSM imaging of green-fluorescent cells (MG-63-GFP) after 24 h incubation on PU-2.0k gels (200 g·L⁻¹) with 0, 5, and 25 mol% RGD, and 5 mol% catechol. Left: Control experiment with cells growing on polystyrene-based petri dishes with cell adhesive properties is also shown. The scale bars refer to 50 μm.

Since the DMMI groups that react with a linker molecule cannot contribute to the 3D cross-linking reaction, it is further investigated how the attachment of RGD sequences influences the gelation of the PU-2.0k gels ($200 \text{ g}\cdot\text{L}^{-1}$). As shown in **Figure 7.4 C**, the addition of 5 mol% RGD to the precursor solution does not significantly affect the plateau modulus. If the concentration is however increased to 25 mol%, a 40% lower plateau modulus results. In addition to this investigation during the gelation process, it is also probed, how the incorporation of the catechol linker influences the mechanical properties of the purified gels under equilibrium swelling conditions (**Figure 7.9**). The results coincide with the gelations experiments and demonstrate that the applicable concentration range of the bio-linkers is limited by the accessible number of DMMI groups in the PU chains.

To analyze the cell adhesive properties of the PU gels with RGD or catechol bio-linkers, cell experiments are performed (**Figure 7.4 D**). For this purpose, green-fluorescent osteoblasts (MG-63-GFP) are cultured on PU-2k gels ($200 \text{ g}\cdot\text{L}^{-1}$) with 0 and 5 mol% RGD and catechol. After 24 h, the gels are analyzed by Confocal Laser Scanning Microscopy (CLSM). The cells on the 0 and 5 mol% RGD gels show a spherical morphology, indicating a low cell adhesion capacity. By contrast, the cells on the 5 mol% catechol gels show an elongated morphology comparable to the control experiment, indicating a pronounced cell adhesion. Consequently, the question arises as to why the cells adhere to the catechol-based but not to the RGD-based PU-2k hydrogels. This is likely due to the insufficient amount of integrins in the RGD-based polymer, as the cells require a certain concentration of integrins to adhere.³¹³² Although the same concentration of RGD and catechol units was used, the total integrin density in catechol is higher because serum proteins from the culture medium adhere to the catechol units, which have a higher number of integrin binding sites than single amino acid sequences such as RGD.³³³⁴ To probe whether an analogous behavior can be achieved at a higher RGD concentration, the experiment is repeated with a 25 mol% RGD containing gel. However, as can be seen in **Figure 7.4 D**, this increase in concentration is still insufficient, which can be explained by the decreasing mechanical gel strength. The more RGD sequences are incorporated into the network, the fewer network junctions can be formed which increases the swelling degree of the corresponding hydrogels. Due to this counteracting behavior, an increase of the RGD concentration does not efficiently increase the RGD density in the network and thus prevents an improvement of the cell attachment. Beyond that, sufficiently stable gels are not obtained with more than 25 mol% RGD. Hence, it is not practicable to improve the cell adhesion by a further increase of the RGD concentration. Based on this comparison, the catechol linkers are found to be the most suitable way to increase the biocompatibility of the PU hydrogels.

7.3 Conclusions

In this study, thermoresponsive, pEG–IPDI-based PUs with dimerizable DMMI side groups are synthesized. The cloud point temperatures of the dilute, aqueous PU solutions depend linearly on the molar ratio between hydrophilic EG and hydrophobic IPDI and DMMI groups and can be varied from 5 °C to over 90 °C. Soft hydrogels are obtained through the UV-light induced cross-linking of the precursor polymers in the presence of a photosensitizer. The equilibrium swelling ratio ($Q_{5^{\circ}\text{C}} = 2700\text{--}7800\%$) and gel strength in terms of the plateau modulus ($G' = 200\text{--}4000$ Pa) are both determined by the precursor polymer concentration and the average DMMI density. The swelling ratio switches of the hydrogels ($Q_{5^{\circ}\text{C}}/Q_{40^{\circ}\text{C}}$) reflect the cloud point temperature dependency on the amphiphilic balance, and increase from 180% to 350% for the more hydrophobic PU compositions. Furthermore, the cell adhesive properties of these nontoxic PU gels can be significantly improved by incorporating low concentrations of a catechol bio-linker through DMMI side groups without significantly affecting the mechanical properties.

7.4 Experimental Section

Materials

O-(7-Aza-1*H*-benzotriazol-1-yl)-*N,N,N',N'*-tetramethyluronium hexafluorophosphate (HATU, Alfa Aesar, 99%), 2,2-bis(hydroxymethyl)propionic acid (Aldrich, 98%), copper(II)sulfate (Sigma, 98%), *N,N*-diisopropylethylamine (DIPEA, Aldrich, 99.5%), 3,4-dihydroxyhydrocinnamic acid (Aldrich, 98%), 2,2-dimethoxypropane (DMP, Merck, 98%), 2,3-dimethylmaleic anhydride (Alfa Aesar, 97%), di-*n*-butyltin dilaurate (DBTDL, 98%, Alfa Aesar), di-*tert*-butyl dicarbonate (Merck Millipore, 98%), hydrogen chloride solution (4.0 M in dioxane, TCI), *p*-toluenesulfonic acid monohydrate (PTSA, TCI, 98%), (+)-Sodium L-ascorbate (Acros Organics, 99%), sodium azide (Alfa Aesar, 99%), triphenylphosphine (Alfa Aesar, 99%), tris[(1-benzyl-1*H*-1,2,3-triazol-4-yl)methyl]amine (TBTA, TCI, 97%) and trifluoroacetic acid (TFA, Alfa Aesar, 99%) are purchased from commercial resources and used without further purification. DOWEX X50W-X8 and Chelex 100 resin are thoroughly washed with MeOH prior to use. Isophorone diisocyanate (IPDI, mixture of *cis/trans* isomers (72:28), 98%, Acros Organics) and 1,2-bis(2-chloroethoxy)ethane (Aldrich, 97%) are freshly distilled prior to use. The poly(ethylene glycol)s (Sigma Aldrich) are first purified by precipitation into diethyl ether, freeze dried from benzene and further dried in high vacuum prior to polymerization. Cyclohexan (^cHex), ethylacetate (EA), dichloromethane (DCM), 1,4-dioxane, and methanol (MeOH) are used as received. Anhydrous toluene, acetone, dimethyl sulfoxide (DMSO), *N,N*-dimethylformamid (DMF), and *N,N*-dimethylacetamide (DMAc) are purchased from Acros Organics and used as received. For cell experiments: Phosphate buffer (DPBS)-D8537 (Sigma-Aldrich), Dulbecco's Modified Eagle Medium (DMEM) high glucose-D5796 (Sigma-Aldrich), fetal bovine serum (FBS)-F7524 (Sigma-Aldrich), GlutaMAX (Gl.) (Thermo Fisher Scientific), Penicillin-Streptomycin (P/S)-P4333 (Sigma-Aldrich), trypsin EDTA solution (Sigma-Aldrich), Osteoblasts (MG-63-GFP obtained from R. E. Unger – Johannes Gutenberg University Mainz, Institute of Pathology).

Chromatography

Thin-layer chromatography is performed on F₂₅₄ silica gel 60 (Merck) or silica gel 60 RP-18 (Merck) coated plates. Spots are detected with UV-light ($\lambda = 254$ nm), iodine or ninhydrin (0.2 g in 100 mL EtOH) solution. Flash chromatography is performed on silica gel 60 (40–63 μm , Merck Millipore) and LiChroprep[®] RP-18 (40–63 μm , Merck Millipore). Size exclusion chromatography (SEC) measurements are performed at 60 °C in DMF (+ 1 g L⁻¹ LiCl) using a 1260 Infinity GPC/SEC-system from Agilent (PSS SECcurity pump, VWR Elite Chrom RI detector) equipped with a PSS GRAM guard column, two PSS GRAM 1000Å and one PSS GRAM 100 Å columns at a flow rate of 1 mL min⁻¹. All data are analyzed with the software PSS WinSEC provided by PSS. The number- and weight average molecular weight (M_n , M_w) and

dispersity (\mathcal{D}) are calculated with a pEG calibration (calibration standards provided by PSS). Samples (2 g L^{-1}) are filtered through a Chromafil PET-45/15 MS syringe filter prior to injection. Analytical and semipreparative HPLC were performed on a JASCO (Tokyo, Japan) LC-4000 system equipped with a binary pump system, an in-line degasser, dynamic mixer and a UV/VIS-detector. Signals were detected in a range from 400–200 nm. The system was operated by the software ChromNAV by JASCO in its version 2.00.02. For analytical purpose, a reverse phase Luna C18(2) ($250 \times 4.6 \text{ mm}$), 100 \AA pore size, $10 \text{ }\mu\text{m}$ particle size, by Phenomenex (Torrance, USA) was used as stationary phase, operated at $20 \text{ }^\circ\text{C}$ with a flow rate of 1.5 mL/min . Semipreparative HPLC was performed on a reverse phase Macherey-Nagel Nucleodur C18 Pyramid ($250 \times 21 \text{ mm}$), 100 \AA pore size, $5 \text{ }\mu\text{m}$ particle size with a flow rate of 18.9 mL/min . The fractions were collected automatically by a CHF122SC fraction collector (*Advantec MFC Inc.*, Dublin, USA). Acetonitrile (B) and ultrapure water (A), each with 0.1% TFA, were used as eluents. Analytical gradient: 5% B (1 min) \rightarrow 30% B (in 15 min) \rightarrow 30% B (3 min) \rightarrow 50% B (in 5 min); Semi-preparative gradient: 15% B (1 min) \rightarrow 50% B (in 24 min) \rightarrow 100% B (3 min).

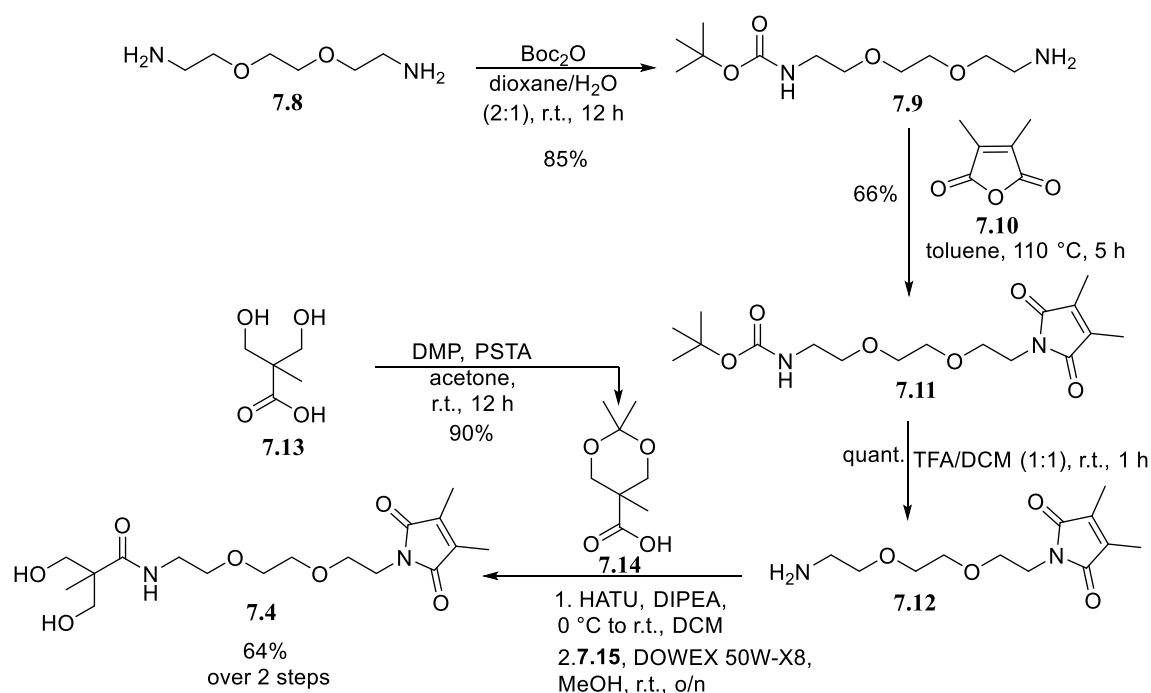
Instrumentation

NMR spectra are recorded on a Bruker Avance-II HD 400 instrument at $20 \text{ }^\circ\text{C}$. The chemical shift δ is given in ppm by using tetramethylsilane as internal standard ($\delta = 0 \text{ ppm}$) and deuterated solvents (CDCl_3 , $\text{DMSO-}d_6$) as internal reference. The reported signal splittings are abbreviated as follows: s = singlet, d = doublet, t = triplet. Coupling constants J are reported in Hz. High resolution electron spray mass spectra (HR-ESI MS) are measured with an Agilent 6545 QTOF-instrument. Turbidity measurements are performed on a Jasco UV-Vis V-760 Spectrophotometer equipped with a mechanical stirrer and external thermostat using 1 cm quartz class cuvettes. Optical swelling measurements are performed using a Zeiss Primovert inverted microscope with a 4x objective. Images are recorded using a ABS UK155m microscope camera. The samples immersed in water are sealed between two microscope cover slides divided by a silicone isolator before they are placed in an Instec TSA12Gi thermal stage controlled by a mK2000 temperature controller equipped with an external industrial chiller (C500WU) (all components by Instec). UV-irradiations are performed with the UV lamp OmniCure, Series 1500 (Model No. S1500A, 200 Watt Mercury Arc, 320–500 nm) from Lumen Dynamics Group Inc equipped with a fiber optic light guide. Linear shear rheology is performed on a stress-controlled modular compact rheometer of the type MCR 302 (Anton Paar, Graz, Austria) equipped with UV-transparent lower glass plate, a stainless-steel cone–plate geometry and a solvent trap. The temperature is controlled by a Peltier plate. Motor adjustment and inertial calibration are performed before each measurement. ^1H -MAS-NMR spectroscopy measurements are performed on a Bruker Avance DSX 400 NMR spectrometer operating at 399.87 MHz ^1H frequency using 4 mm rotors and inserts specially developed to investigate gels and soft matter. The ^1H single pulse excitation

NMR spectra are recorded using a commercial three channel Bruker 4 mm probe head at 4 kHz Magic Angle Spinning (MAS), averaging 512 scans with a 5 s recycle delay. Confocal Laser Scanning Microscopy (CLSM) is performed using a Leica TCS-SP8 AOBS SMD microscope with an HCPL APO CS2 10×/0.40 DRY objective. GFP expressing cells are excited with 488 nm (argon laser), while their green fluorescence is detected between 500 nm and 600 nm (PMT2 detector).

Synthesis

DMMI-^TEG diol 7.4

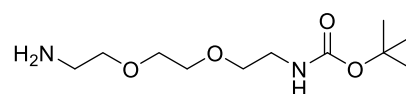


Scheme 7.1. Synthesis of DMMI-^TEG diol 7.4.

tert-Butyl-(2-(2-(2-aminoethoxy)ethoxy)ethyl)carbamate 7.9

According to a literature procedure, 1,8-Diamino-3,6-dioxoctan **7.8** (30.0 g, 202 mmol, 1 eq.) is dissolved in a 1,4-dioxane/water mixture ($v/v = 2:1$, 300 mL) in a 500 mL

Schlenk flask under Argon atmosphere and cooled in a water-ice-bath (2–5 °C).³⁵ A solution of di-*tert*-butyl dicarbonate (14.5 g, 66.4 mmol, 0.33 eq.) in 1,4-dioxane (100 mL) is added dropwise over 5 h. Afterwards, the ice-bath is removed and the reaction mixture is stirred for 17 h at r.t. before the turbid solution is concentrated under reduced pressure. After dilution with brine (200 mL), the pH is adjusted to 3 with an aqueous citric acid solution (3%) under ice-cooling (1.2 L). The aqueous phase is washed with DCM (3 x 200 mL) and the pH is adjusted to 10 with sodium carbonate (190 g). Finally, the basic aqueous phase is extracted with DCM (5 x 300 mL) before the organic layer is dried over Na_2SO_4 and the solvent is removed under reduced pressure.

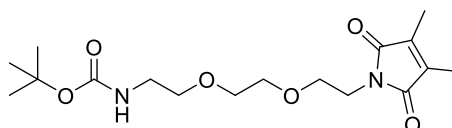


Amine **7.9** is obtained as colorless liquid (14.1 g, 56.9 mmol, 85%). **Molecular formula:** C₁₁H₂₄N₂O₄. **TLC:** $R_f = 0.33$ (DCM:MeOH = 10:3, SiO₂). **ESI-HRMS** (m/z): Calculated for [M+H]⁺: 249.181, found: 249.181 **¹H-NMR, COSY** (300 MHz, DMSO-*d*₆) $\delta = 6.78$ (t, 1H, C(=O)NH), 3.47 (m, 4H, OCH₂CH₂O), 3.40–3.28 (m, 6H, H₂NCH₂CH₂O, OCH₂CH₂NHC(=O)), 3.05 (q, 2H, CH₂NHC(=O)), 2.63 (t, 2H, NH₂), 1.37 (s, 9H, CH₃) ppm. **¹³C-NMR, HMBC, HSQC** (75 MHz, DMSO-*d*₆) $\delta = 155.6$ (OC(=O)NH), 77.6 (C(CH₃)₃), 73.1 (CH₂O), 69.6 (CH₂O), 69.5 (CH₂O), 69.1 (CH₂O), 41.4 (CH₂NH₂), 39.7 (CH₂NHC(=O)), 28.3 (CH₃) ppm.

DMMI-TEG ^{tert}butyl amine **7.11**

^{tert}Butyl-(2-(2-(2-aminoethoxy)ethoxy)ethyl)carbamate

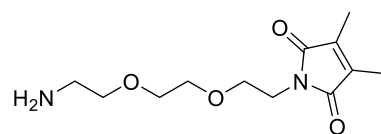
7.9 and 2,3-dimethyl maleic anhydride **7.10** are dissolved in toluene (95 mL each) and added to a 250 mL two-



neck flask equipped with a Dean-Stark apparatus. The colorless solution is heated under reflux for 11 h before the solvent is removed under reduced pressure and the crude product is obtained as orange liquid. After chromatographical purification (^CHex/EA = 3:2, SiO₂), DMMI-TEG BOC-protected amine **7.11** is obtained as slightly yellow, viscous liquid (13.5 g, 37.8 mmol, 66%). **Molecular formula:** C₁₇H₂₈N₂O₆. **TLC:** $R_f = 0.25$ (^CHex/EA = 3:2, SiO₂). **ESI-HRMS** (m/z): Calculated for [M+H]⁺: 357.2025, [M+Na]⁺: 379.1840, found: [M+H]⁺: 357.2018, [M+Na]⁺: 379.1836 **¹H-NMR, COSY** (300 MHz, CDCl₃) $\delta = 5.05$ (s, 1H, C(=O)NH), 3.72–3.66 (m, 2H, NCH₂), 3.6–3.50 (m, 8H, CH₂O), 3.28 (q, ³J = 5.1 Hz, 2H, CH₂NH(C=O)), 1.95 (s, 6H, (C=C)CH₃), 1.44 (s, 9H, OCCH₃) ppm. **¹³C-NMR, HMBC, HSQC** (75 MHz, CDCl₃) $\delta = 172.2$ (C(=O)N), 156.2 (OC(=O)NH), 137.4 (CH₃C=CCH₃), 77.3 (C(CH₃)₃), 70.4 (CH₂O), 69.9 (CH₂O), 68.3 (CH₂O), 40.5 (CH₂NH(C=O)), 37.1 (NCH₂), 28.6 (C(CH₃)₃), 8.9 (C=C)CH₃) ppm.

DMMI-¹EG amine **7.12**

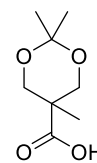
The Boc protected amine **7.11** (13.1 g, 36.8 mmol, 1.0 eq.) is dissolved in DCM (18.5 mL) under inert atmosphere before trifluoro acetic acid (18.4 mL, 239 mmol, 6.5 eq.) and



triethylsilane (0.37 mL, 1 vol%) are added. After stirring at r.t. for 60 min, TFA and solvent are removed under reduced pressure. The yellow residue is repeatedly re-dissolved in toluene which is then removed under reduced pressure (6 x) before the highly viscous TFA salt is finally dried under high vacuum for 48 h. **Molecular formula:** C₁₂H₂₀N₂O₄. **TLC:** $R_f = 0.44$ (DCM/MeOH = 10:3, SiO₂). **ESI-HRMS** (m/z): Calculated for [M+H]⁺: 257.1501, found: [M+H]⁺: 257.1500 **¹H-NMR, COSY** (300 MHz, CDCl₃): $\delta = 7.26$ (*s_{br}*, 3H, NH₃), 3.76–3.57 (m, 10H, CH₂O), 3.22 (m, 2H, CH₂NH⁺), 1.94 (s, 6H, CH₃) ppm. **¹³C-NMR, HMBC, HSQC** (75 MHz, CDCl₃): $\delta = 172.6$ (C(=O)N), 137.6 (CH₃C=CCH₃), 70.2 (CH₂O), 68.8 (CH₂O), 66.6 (CH₂O), 40.0 (CH₂NH₃⁺), 37.5 (NCH₂), 8.8 (CH₃) ppm.

2,2,5-trimethyl-1,3-dioxane-5-carboxylic acid 7.14

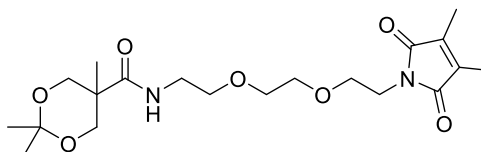
According to a literature procedure, 2,2-bis(hydroxymethyl)propionic acid **7.13** (10 g, 74.5 mmol, 1.0 eq.), 2,2-dimethoxypropan (13.8 mL, 113 mmol, 1.5 eq.) and *p*-toluene sulfonic acid monohydrate (0.78 g, 4.1 mmol, 0.05 eq.) are dissolved in anhydrous acetone and stirred at r.t. for 16 h under inert atmosphere.²¹ Afterwards, a



1:1 mixture of EtOH and 37% ammonia solution (1 mL) is added and the solvent is removed under reduced pressure. The residue is dissolved in DCM (150 mL) and washed with water (3 x 30 mL) before the organic phase is dried over Na₂SO₄. Removal of the solvent yields 2,2,5-trimethyl-1,3-dioxane-5-carboxylic acid **7.14** as colorless solid (11.6 g, 67.0 mmol, 90%). **Molecular formula:** C₈H₁₄O₄. **TLC:** R_f = 0.70 (EA, SiO₂). **ESI-HRMS** (*m/z*): Calculated for [M]⁻: 173.0814, found: 173.0820. **¹H-NMR, COSY** (300 MHz, DMSO-*d*₆): δ = 4.00 (d, 2H, ²J = 11.6 Hz, CH₂''), 3.55 (d, 2H, ²J = 11.6 Hz, CH₂''), 3.35 (s, 1H, C(=O)OH), 1.34 (s, 3H, CH₃), 1.26 (s, 3H, CH₃), 1.07 (s, 3H, CH₃) ppm. **¹³C-NMR, HMBC, HSQC** (75 MHz, DMSO-*d*₆): δ = 175.6 (C(=O)OH), 97.3 (OC_qO), 65.2 (CH₂), 40.7 (C_q(CH₂)₂), 24.7 (CH₃), 22.7 (CH₃), 18.4 (CH₃) ppm.

DMMI-¹EG diol acetonide 7.15

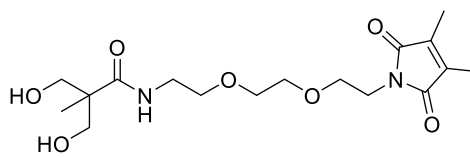
DMMI-TEG amine **7.12***TFA (1.00 g, 2.7 mmol, 1.0 eq.) is dissolved in anhydrous DMF (15 mL) in a 100 mL Schlenk flask under inert atmosphere before 2,2,5-trimethyl-1,3-dioxane-5-carboxylic acid **7.14**



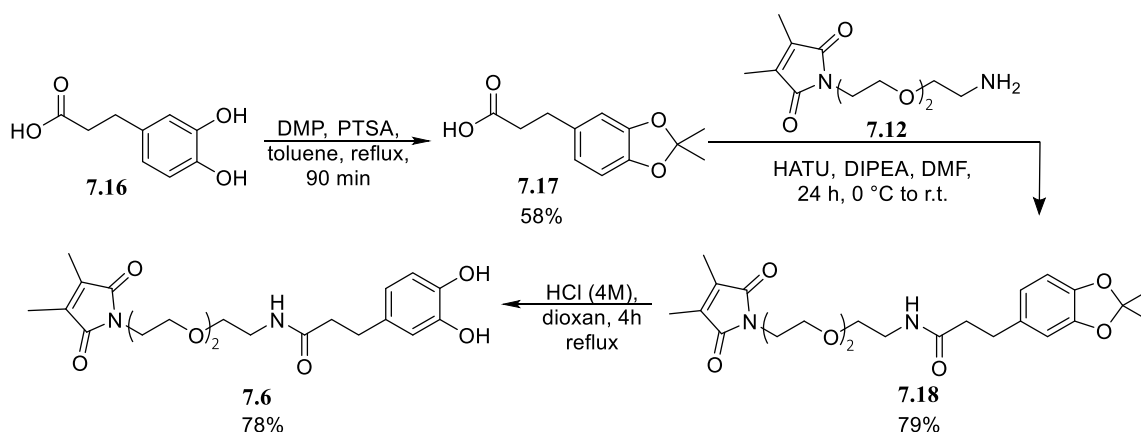
(0.57 g, 3.24 mmol, 1.2 eq.) is added. The solution is cooled in an ice-bath and a solution of HATU (1.23 g, 3.24 mmol, 1.2 eq.) in DMF (12 mL) and DIPEA (1.85 mL, 10.5 mmol, 3.9 eq.) are slowly added. After stirring for 3 h at r.t., the solvent is distilled off under high vacuum (40 °C oil bath) and the residue is dissolved in DCM (150 mL). After washing the organic phase with a saturated NaHCO₃ (3 x 50 mL) and water (1 x 50 mL) and drying over Na₂SO₄, the solvent is removed under reduced pressure. The crude product is chromatographically purified (ACN/H₂O = 1:1, RP₁₈ silica gel) and compound **7.15** is obtained as colorless, highly viscous oil (749 mg, 1.82 mmol, 67%) after lyophilization. **Molecular formula:** C₂₀H₃₂N₂O₇. **TLC:** R_f = 0.47 (ACN/H₂O = 1:1, RP₁₈ silica gel). **ESI-HRMS** (*m/z*): Calculated for [M+H]⁺: 413.2288, [M+Na]⁺: 435.2107; found: [M+H]⁺: 413.2293, [M+Na]⁺: 435.2105. **¹H-NMR, COSY** (400 MHz, DMSO-*d*₆): δ = 7.57 (t, ³J = 5.5 Hz, NHC(=O)), 3.90 (d, 2H, ²J = 11.8 Hz, OCH₂'C_q), 3.61 (d, 2H, ²J = 11.8 Hz, OCH₂'C_q), 3.53–3.44 (m, 8H, CH₂O), 3.38 (t, ³J = 5.8 Hz, 2H, CH₂N), 3.21 (m, 2H, CH₂NH(C=O)), 1.89 (s, 6H, (C=C)CH₃), 1.35 (s, 3H, CH₃), 1.28 (s, 3H, CH₃), 1.00 (s, 3H, CH₃) ppm.

DMMI-^TEG diol 7.4

Compound **7.15** (1.11 g, 2.69 mmol) is dissolved in MeOH (220 mL) before DOWEX X50W-X8 (5.28 g, 4.8 wt%) is added and the colorless suspension is stirred for 19 h at r.t. The solvent is removed under



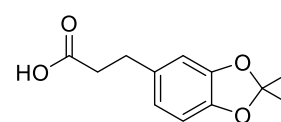
reduced pressure and the diol is obtained as slightly yellow, highly viscous oil (0.969 g, 2.58 mmol, 96%). **Molecular formula:** C₁₇H₂₈N₂O₇. **TLC:** R_f = 0.44 (ACN/H₂O = 1:1, RP₁₈ silica gel). **ESI-HRMS** (*m/z*): Calculated for [M+Na]⁺: 395.1794; found: [M+Na]⁺: 395.1793. **¹H-NMR, COSY** (300 MHz, CDCl₃): δ = 7.49 (*s_{br}*, 1H, C(=O)NH), 3.63–3.49 (m, 14H, CH₂CH₂O, CH₂OH), 3.44 (m, 2H, CH₂NH(C=O)), 3.23 (*s_{br}*, 2H, OH), 1.94 (s, 6H, CH₃), 1.11 (s, 3H, CH₃) ppm. **¹³C-NMR, HMBC, HSQC** (75 MHz, CDCl₃): δ = 177.0 (C(=O)NH), 172.4 (C(=O)N), 137.5 (CH₃C=CCH₃), 70.3 (CH₂O), 70.1 (CH₂O), 69.6 (CH₂OH), 68.3 (CH₂O), 67.9 (CH₂O), 47.8 (CH₂NHC(=O)), 39.1 (C_q(CH₂)₂), 37.3 (NCH₂), 18.14 (CH₃), 8.8 ((C=C)CH₃) ppm.

DMMI-^TEG-Catechol 7.6

Scheme 7.2. Synthesis of DMMI-^TEG-Catechol **7.6**.

2,2-Dimethyl-1,3-benzodioxole-5-propanoic acid 7.17

2,2-Dimethyl-1,3-benzodioxole-5-propanoic acid **7.17** is synthesized according to a modified procedure by Liu *et al.*³⁶ 3,4-(Dihydroxyphenyl)propionic acid **7.16** (1.05 g, 5.76 mmol, 1.0 eq) is



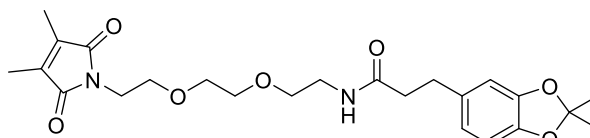
dissolved in anhydrous toluene (100 mL) in a flame-dried 250 mL two neck-flask equipped with reflux condenser and septum. 2,2-dimethoxypropan (2.2 mL, 22 mmol, 3.8 eq.) and *p*-toluene sulfonic acid monohydrate (50 mg, 0.26 mmol, 0.05 eq.) are added and the reaction mixture is refluxed for 90 min under nitrogen atmosphere. After cooling to r.t., the organic phase is washed with water (3 x 25 mL), dried over Na₂SO₄ before the solvent is removed under reduced pressure. The yellow residue is recrystallized from ^cHex (15 mL) to yield **7.17** as colorless crystalline solid (708 mg, 58%). **Molecular formula:** C₁₂H₁₄O₄. **TLC:** R_f = 0.27 (ACN:H₂O = 2:1, RP₁₈ silica gel). **ESI-HRMS** (*m/z*): Calculated for [M+H]⁺: 223.097, found: 223.090 **¹H-NMR, COSY**

(400 MHz, DMSO- d_6): δ = 12.09 (s, 1H, C(=O)OH), 6.70 (m, 2H, Catechol: C₃H/C₆H), 6.60 (m, 1H, Catechol: C₅H), 2.71 (t, 2H, 3J = 7.6 Hz, CH₂-Ar), 2.47 (t, 2H, 3J = 7.6 Hz, CH₂C(=O)OH), 1.66 (s, 6H, CH₃) ppm. **¹³C-NMR, HMBC, HSQC** (101 MHz, DMSO- d_6): δ = 173.8 (C(=O)OH), 146.8 (Catechol: C₁), 145.1 (Catechol: C₂), 134.1 (Catechol: C₄), 120.5 (Catechol: C₅H), 117.5 (OC_qO), 108.5 (Catechol: C₃H), 107.8 (Catechol: C₆H), 35.6 (CH₂C(=O)OH), 30.2 (CH₂-Ar), 25.6 (CH₃) ppm.

DMMI-¹EG-Catechol Acetonide 7.18

DMMI-triEG amine*TFA 7.12 (600 mg,

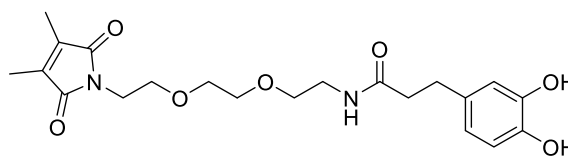
1.62 mmol, 1.2 eq.) is dried under high vacuum at r.t. in a 25 mL Schlenk flask for 4 h and afterwards dissolved in anhydrous



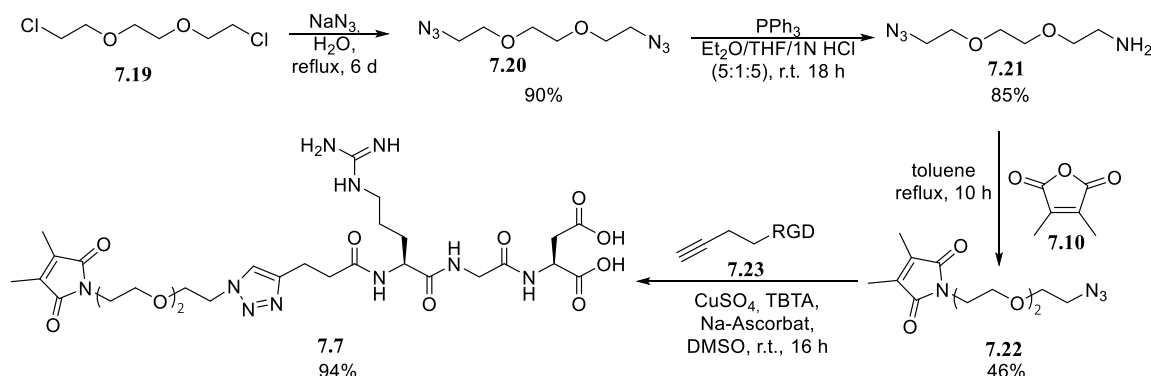
DMF (2 mL) under nitrogen atmosphere before 2,2-dimethyl-1,3-benzodioxole-5-propanoic acid 7.17 (301.6 mg, 1.35 mmol, 1.0 eq) is added. Under ice cooling, a solution of HATU (770 mg, 2.0 mmol, 1.5 eq.) in DMF (2 mL) and finally DIPEA (0.92 mL, 5.40 mmol, 4.0 eq) are added dropwise and the reaction mixture is stirred for 1 h at 0 °C and another 23 h at r.t. Afterwards, the solvent is removed under reduced pressure and the residue is dissolved in DCM (80 mL). The organic phase is washed with saturated Na₂CO₃ solution (2 x 50 mL) and Brine (2 x 50 mL) before it is dried over Na₂SO₄, and the solvent is removed under reduced pressure. The residue is purified by column chromatography (ACN/H₂O = 1:1, RP₁₈ silica gel) and the product is isolated as colorless oil after lyophilization (490 mg, 79%). **Molecular formula:** C₂₄H₃₂N₂O₇. **TLC:** R_f = 0.25 (ACN:H₂O = 1:1, RP₁₈ silica gel). **ESI-HRMS** (m/z): Calculated for [M+H]⁺: 461.2288, found: 461.227. **¹H-NMR, COSY** (400 MHz, CDCl₃): δ = 6.61 (m, 3H, Catechol: C₃H, C₅H, C₆H), 6.20 (s, 1H, (C=O)NH), 3.57 (m, 12H, (CH₂CH₂O)₂CH₂CH₂), 2.86 (m, 2H, CH₂-Ar), 2.49 (m, 2H, NHC(=O)CH₂), 1.94 (s, 6H, (C=C)CH₃), 1.65 (s, 6H, OC_qCH₃) ppm. **¹³C-NMR, HMBC, HSQC** (101 MHz, CDCl₃): δ = 172.7 (C(=O)NH), 172.6 (C(=O)N), 147.9 (Catechol: C₁), 145.8 (Catechol: C₂), 137.4 (CH₃C=CCH₃), 134.3 (Catechol: C₄), 120.7 (Catechol: C₅), 117.7 (OC_qO), 108.8 (Catechol: C₃), 108.1 (Catechol: C₆), 70.4 (CH₂O), 70.1 (CH₂O), 69.9 (NCH₂CH₂O), 68.3 1 (CH₂O), 39.6 (CH₂NH(C=O)), 39.1 (CH₂O), 37.6 (NH(C=O)CH₂), 32.0 (CH₂-Ar), 26.3 (OCCH₃), 9.2 (CH₃) ppm.

DMMI-Catechol 7.6

Compound **7.18** (473 g, 1.03 mmol, 1.0 eq.) is dissolved in HCl in dioxane (4M, 10 mL) and heated under reflux in a nitrogen atmosphere for 10 h. After lyophilization of the reaction



mixture, the product is purified by column chromatography (ACN/H₂O = 2:1, RP₁₈ silica gel) and isolated as highly viscous, yellow oil (327 mg, 78%). **Molecular formula:** C₂₁H₂₈N₂O₇. **TLC:** R_f = 0.55 (ACN:H₂O = 2:1, RP₁₈ silica gel). **ESI-HRMS** (*m/z*): Calculated for [M+H]⁺: 421.19 found: 421.197. **¹H-NMR, COSY** (400 MHz, DMSO-*d*₆): δ = 8.69 (s, 1H, -OH), 8.59 (s, 1H, OH), 7.81 (t, ³J = 5.7 Hz, 1H, (C=O)NH), 6.59 (d, ³J = 7.9 Hz, 1H, Catechol: C₆H), 6.55 (d, ⁴J = 2.1 Hz, 1H, Catechol: C₃H), 6.41 (dd, ³J = 7.9 Hz, ⁴J = 2.1 Hz, 1H, Catechol: C₅H), 3.47 (m, 8H, CH₂OCH₂CH₂OCH₂), 3.31 (m, 2H, NCH₂), 3.14 (m, 2H, CH₂NH(C=O)), 2.60 (m, 2H, CH₂-Ar), 2.26 (m, 2H, NHC(=O)CH₂), 1.89 (s, 6H, CH₃) ppm. **¹³C-NMR, HMBC, HSQC** (101 MHz, DMSO-*d*₆): δ = 171.62 (C(=O)NH), 171.5 (C(=O)N), 144.9 (Catechol: C₁), 143.3 (Catechol: C₂), 136.7 (CH₃C=CCH₃), 132.2 (Catechol: C₄), 118.7 (Catechol: C₅), 115.6 (Catechol: C₃), 115.4 (Catechol: C₆), 69.5 (CH₂O), 69.3 (CH₂O), 69.2 (NCH₂CH₂O), 67.1 (CH₂O), 38.46 (CH₂NH(C=O)), 37.9 (NH(C=O)CH₂), 37.4 (CH₂O), 30.6 (CH₂-Ar), 1, 8.4 (CH₃) ppm.

DMMI-^TEG-RGD 7.7

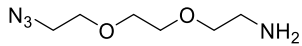
Scheme 7.3. Synthesis of DMMI-^TEG RGD **7.7**.

1,2-Bis(2-azidoethoxy)ethane 7.20

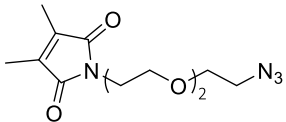
According to a literature procedure, freshly distilled 1,2-bis(2-chloroethoxy)ethane **7.19** (6.00 mL, 38.4 mmol, 1 eq.) is dissolved in water (100 mL) before sodium azide (13.8 g, 212 mmol, 5.5 eq.) is added and the colorless emulsion is heated under reflux for 6 days. After cooling to r.t., the aqueous phase is extracted with DCM (3 x 100 mL) and the combined organic phases are dried over Na₂SO₄. 1,2-Bis(2-azidoethoxy)ethane **7.20** (6.90 g, 34.5 mmol, 90%) is obtained as colorless liquid after removal of the solvent under reduced pressure. **Molecular formula:** C₆H₁₂N₆O₂. **TLC:** R_f = 0.19 (ACN/H₂O = 1:1, RP₁₈ silica gel). **ESI-HRMS** (*m/z*): Calculated for [M+Na]⁺: 223.0919, found:

223.0914 ¹H-NMR, COSY (300 MHz, CDCl₃): δ = 3.74–3.65 (m, 8H, CH₂O), 3.40 (t, ³J = 5.0 Hz, 4H, CH₂N₃) ppm. ¹³C-NMR, HMBC, HSQC (75 MHz, CDCl₃): δ = 70.9 (OCH₂CH₂O), 70.3 (CH₂CH₂N₃), 50.8 (CH₂N₃) ppm.

2-[2-(2-Azidoethoxy)ethoxy]ethan-1-amine **7.21**

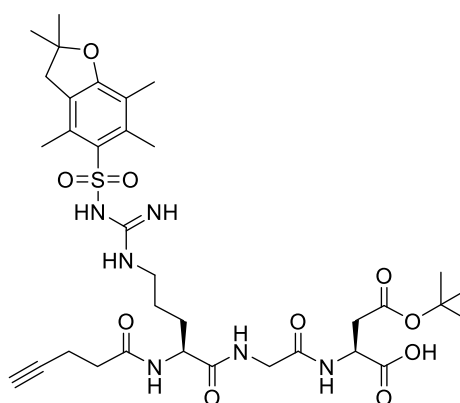
According to a literature procedure, 1,2-bis(2-azidoethoxy)ethane **7.20** (4.15 g, 20.7 mmol, 1.0 eq.) is dissolved in a mixture of Et₂O, THF  and 1N HCl_{aq} (5:1:5, 57.5 mL) in a 100 mL two-neck flask equipped under inert atmosphere.³⁷ Triphenylphosphine (5.42 g, 20.7 mmol, 1.0 eq.) is dissolved in Et₂O (30 mL) and added over 3 h under vigorous stirring over a dripping funnel before the reaction mixture is stirred for 18 h at r.t.. Afterwards, the organic phase is separated and extracted with 4N HCl_{aq} (100 mL). Both aqueous phases are combined and washed with Et₂O (4 x 100 mL) and toluene (2 x 100 mL) before the pH is adjusted to 14 by addition of sodium hydroxide. Finally, the basic aqueous phase is extracted with DCM (2 x 100 mL) and the organic phase is dried over Na₂SO₄ before the solvent is removed under reduced pressure. 2-[2-(2-Azidoethoxy)ethoxy]ethan-1-amine **7.21** is obtained as colorless liquid (3.06 g, 17.5 mmol, 85%). **Molecular formula:** C₆H₁₄N₄O₂. **TLC:** R_f = 0.63 (ACN/H₂O = 10:1, RP₁₈ silica gel). **ESI-HRMS (m/z):** Calculated for [M+H]⁺: 175.1195, found: 175.1189. Calculated for [M+Na]⁺: 197.1014, found: 197.1004. ¹H-NMR, COSY (300 MHz, CDCl₃): δ = 3.82–3.59 (m, 6H, CH₂O), 3.53 (t, ³J = 5.2 Hz, 2H, CH₂CH₂NH₂), 3.40 (t, ³J = 5.0 Hz, 2H, CH₂N₃), 2.88 (t, ³J = 5.2 Hz, 2H, CH₂NH₂), 1.74 (s, 2H, NH₂) ppm. ¹³C-NMR, HMBC, HSQC (75 MHz, CDCl₃): δ = 73.44 (CH₂CH₂NH₂), 70.81 (CH₂O), 70.45 (CH₂O), 70.21 (CH₂O), 50.81 (CH₂N₃), 41.85 (CH₂NH₂) ppm.

DMMI-¹EG-azide **7.22**

2-[2-(2-Azidoethoxy)ethoxy]ethan-1-amine **7.21** (1.59g, 9.1 mmol, 1.0 eq.) and 2,3-dimethyl maleic anhydride **7.10** (1.15 mg, 9.1 mmol, 1.0 eq.) are dissolved in toluene (50 mL) and a 100 mL two-neck flask equipped with a Dean-Stark apparatus. The colorless solution is heated under reflux for 10 h under inert atmosphere. After removal of the solvent under reduced pressure, the obtained orange oil is purified by column chromatography (^CHex/EA = 3:2, SiO₂). DMMI-TEG-azide **7.22** (1.18 g, 4.2 mmol, 46%) is obtained as colorless viscous liquid. **Molecular formula:** C₁₂H₁₈N₄O₄. **TLC:** R_f = 0.39 (^CHex/EA = 3:2, SiO₂). **ESI-HRMS (m/z):** Calculated for [M+Na]⁺: 305.1226, found: 305.1222 ¹H-NMR, COSY (300 MHz, CDCl₃): δ = 3.71–3.60 (m, 10H, CH₂O), 3.36 (m, 2H, CH₂N₃), 1.95 (s, 6H, CH₃) ppm. ¹³C-NMR, HMBC, HSQC (75 MHz, CDCl₃): δ = 172.2 (C(=O)N), 137.3 (CH₃C=CCH₃), 70.79 (CH₂O), 70.20 (CH₂O), 70.16 (CH₂O), 68.33 (CH₂O), 50.80 (CH₂N₃), 37.21 (CH₂N), 8.83 (CH₃) ppm. 

Protected-RGD-alkyne 7.23a

The peptide is synthesized on solid support. *Loading of the resin:* 2-Chloro-tritylchloride polystyrene resin (loading = 1.60 mmol/g 2-chloro-tritylchloride, 1.00 g, 1.60 mmol) is placed in a Merrifield-reactor. A solution of Fmoc-L-Asp(O^{tert}Bu)-OH (1.32 g, 3.20 mmol, 2.0 eq.) in DCM (10 mL) with a small amount of DMF is added to the resin. After the addition of DIPEA (0.56 ml, 3.20 mmol, 2.0 eq.), the mixture is shaken for 5 min. DIPEA (0.84 mL, 4.80 mmol, 3.0 eq.) is added

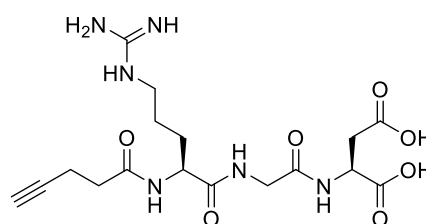


and the mixture agitated for 1 h. MeOH (1 mL) is added, the mixture shaken for 15 min before draining the reactor. The resin is washed consecutively with DCM (3 × 10 mL), DMF (3 × 10 mL), DCM (3 × 10 mL) and MeOH (3 × 10 mL). The resin is transferred in an automated peptide synthesizer and swollen by shaking it in DCM/DMF (1:1) for 15 min. The *N*-terminal *Fmoc*-group is removed by the treatment of the resin with piperidine in DMF (20v% in DMF) for 5 min and subsequently for 20 min. The liquid is removed by suction and the resin washed with DMF (2×), DCM (2×) and DMF (2×). The *coupling of the following amino acid* is performed by treating the growing peptide with a solution of the Fmoc-Amino acid (4.0 eq.), HBTU (4.0 eq.), HOBT (4.4 eq.) and DIPEA (6.0 eq.) in DMF. After 1 h of shaking, the reactor is drained, and the resin washed with DMF twice. The procedure is repeated for the third amino acid. After the final removal of Fmoc, the peptide was capped by shaking the resin in a solution of 4-pentynoic acid (314 mg, 3.2 mmol, 2.0 eq.), HATU (791 mg, 3.2 mmol, 2.0 eq.), HOAt (436 mg, 3.2 mmol, 2.0 eq.) and DIPEA (1.11 mL, 6.4 mmol, 4.0 eq.) for 2 h. The *peptide is cleaved* from the resin by shaking it in TFE in DCM (20 vol%, 3×20 mL) for 2 h. The cleavage cocktail is concentrated under reduced pressure and precipitated into cold water (45 mL). The residue is washed with water twice and subjected to lyophilization. The crude is purified by flash chromatography (EA/MeOH (+0.1% AcOH) = 5:1→1:1, SiO₂) and the product isolated as colorless solid after lyophilization (988 mg, 1.34 mmol, 84% relative to resin loading capacity). **Molecular formula:** C₅₄H₅₀N₆O₁₀S. **TLC:** R_f = 0.43 (EA/MeOH (+0.1% AcOH) = 3:1, SiO₂). **ESI-HRMS** (*m/z*): Calculated for [M+H]⁺: 735.3387, [M+Na]⁺: 757.3207, found: [M+H]⁺: 735.3366, [M+Na]⁺: 757.3188. **¹H-NMR, COSY** (400 MHz, DMSO-*d*₆): δ = 12.82 (*s*_{br}, 1H, **D**: C(=O)OH), 8.25 (m, 1H, **G**: NH), 8.12 (d, ³*J* = 7.5 Hz, 1H, **R**: C(=O)NH), 8.03 (m, 1H, **D**: C(=O)NH), 7.19–6.21 (2× *s*_{br}, 3H, **R**: NH), 4.50 (m, 1H, **D**: CH), 4.20 (m, 1H, **R**: CH), 3.69 (m, 2H, **G**: CH₂), 3.02 (m, 2H, **R**: NHCH₂), 2.96 (s, 2H, CH₂(Pbf)), 2.74 (s, 1H, C≡CH), 2.64 (dd, ¹*J* = 16.0 Hz, ³*J* = 6.1 Hz, 1H, **D**: CH₂'), 2.53 (dd, ¹*J* = 16.0 Hz, ³*J* = 7.1 Hz, 1H, **D**: CH₂''), 2.47 (s, 3H, **R**: CH₃(Pbf)), 2.42 (s, 3H, **R**: CH₃(Pbf)), 2.34 (m, 4H, HC≡CCH₂CH₂), 2.01 (s, 3H, **R**: CH₃(Pbf)), 1.65 (m, 1H, **R**:

NHCH₂CH₂CH₂'), 1.52–1.38 (m, 9H, **R**: NHCH₂CH₂CH₂'', NHCH₂CH₂, OC(CH₃)₂(Pbf)), 1.37 (s, 9H, **D**: OC(CH₃)₃). ¹³C-NMR, HMBC, HSQC (101 MHz, DMSO-*d*₆): δ = 172.2 (**D**: C(=O)OH), 171.8 (**R**: C(=O)NH), 170.6 (CH₂CH₂C(=O)NH), 169.2 (**D**: C(=O)O(CH₃)₃), 168.4 (**G**: C(=O)NH), 157.4 (C-7a(Pbf)), 156.1 (**R**: NHC(=NH)), 137.3 (C-6(Pbf)), 134.2 (C-5(Pbf)), 131.4, (C-4(Pbf)), 124.3 (C-3a(Pbf)), 116.3 (C-7(Pbf)), 86.3 (C-2(Pbf)), 83.7 (C≡CH), 80.3 (C(CH₃)₃), 71.3 (C≡CH), 52.5 (**R**: CH), 49.0 (**D**: CH), 42.5 (C-3(Pbf)), 41.7 (**G**: CH₂), 40.1 (**R**: NHCH₂), 37.3 (**D**: CH₂), 33.9 (HC≡CCH₂CH₂), 29.4 (**R**: NHCH₂CH₂CH₂), 28.3 (C-2-(CH₃)₂(Pbf)), 27.7 (C(CH₃)₃), 25.5 (**R**: NHCH₂CH₂), 19.0 (C-4-CH₃ (Pbf)), 17.6 (C-6-CH₃ (Pbf)), 14.1 (HC≡CCH₂CH₂), 12.30 (C-7-CH₃ (Pbf)) ppm.

RGD-alkyne 7.23

Protected RGD-alkyne **7.23a** (988 mg, 1.34 mmol) is dissolved in a mixture of TFA (9.0 mL), TIPS (0.5 mL) and H₂O (0.5 mL) and agitated for 1.5 h at r.t. The mixture is concentrated under reduced pressure and subsequently precipitated into cold Et₂O (45 mL). The precipitate is

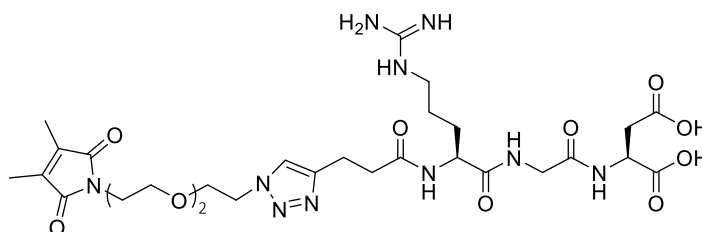


washed with Et₂O (45 mL) twice, dried under reduced pressure, taken up in water and subjected to lyophilization to yield the product as colorless solid (TFA salt, 720 mg, 1.33 mmol, 99%).

Molecular formula: C₁₇H₂₆N₆O₇. **TLC:** *R*_f = 0.08 (⁶Hex/EA = 1:1, SiO₂). **ESI-HRMS** (*m/z*): Calculated for [M+H]⁺: 427.1941, found: 427.1934. **¹H-NMR, COSY** (400 MHz, DMSO-*d*₆): δ = 8.27 (t, ³*J* = 5.8 Hz, **G**: C(=O)NH), 8.17 (d, ³*J* = 8.2 Hz, 1H, **R**: C(=O)NH), 8.09 (d, ³*J* = 8.1 Hz, 1H, **D**: C(=O)NH), 7.87 (m, 1H, **R**: NH), 7.16 (*s_{br}*, 4H, **R**: NH/NH₂), 4.46 (m, 1H, **D**: CH), 4.25 (m, 1H, **R**: CH), 3.71 (m, 2H, **G**: CH₂), 3.08 (m, 2H, **R**: NHCH₂), 2.74 (s, 1H, C≡CH), 2.59 (m, 2H, **D**: CH₂), 2.35 (m, 4H, HC≡CCH₂CH₂), 1.72 (m, 1H, **R**: NHCH₂CH₂CH₂''), 1.50 (m, 3H, **R**: NHCH₂CH₂'CH₂') ppm. **¹³C-NMR, HMBC, HSQC** (101 MHz, DMSO-*d*₆): δ = 172.6 (**D**: CHC(=O)OH), 172.1 (**D**: CH₂C(=O)OH), 171.8 (**R**: C(=O)NH), 170.7 (CH₂CH₂C(=O)NH), 168.5 (**G**: C(=O)NH), 156.80 (**R**: NH₂C(=NH)), 83.8 (C≡CH), 71.4 (C≡CH), 52.3 (**R**: CH), 48.7 (**D**: CH), 41.7 (**G**: CH₂), 40.46 (**R**: NHCH₂), 36.69 (**D**: CH₂), 34.0 (HC≡CCH₂CH₂), 29.2 (**R**: NHCH₂CH₂CH₂), 24.96 (**R**: NHCH₂CH₂), 14.2 (HC≡CCH₂CH₂) ppm.

DMMI-¹EG-RGD 7.7

RGD-azide **7.23** (100 mg, 0.23 mmol, 1.0 eq.) and DMMI-TEG-azide **7.22** (99.3 mg, 0.35 mmol, 1.5 eq.) are dissolved in DMSO (3 mL) and oxygen is



removed by three consecutive freeze-pump thaw cycles. A solution of tris[(1-benzyl-1H-1,2,3-triazol-4-yl)methyl]amine (TBTA, 37.9 mg, 0.07 mmol, 0.3 eq.) and CuSO₄·5H₂O (11.2 mg,

0.07 mmol, 0.3 eq.) in DMSO (1 mL) is inserted before sodium ascorbate (35.8 mg, 0.18 mmol, 0.8 eq.) is added in a argon counter flow one minute later which changes the color from blue to colorless. The solution is stirred for 16 h at r.t. before the solvent is distilled off under high vacuum and the residue is dissolved in water (50 mL). After washing with Et₂O (2 x 100 mL) and EA (2 x 50 mL), Chelex 100 resin is added to the blue solution, stirred at r.t. for 12 h and filtered off. After two additional Chelex treatments, DMMI-TEG-RGD **7.7** (156 mg) is obtained as colorless solid by lyophilization. Further purification is performed by semi-preparative HPLC (acetonitrile (B) and ultrapure water (A), each with 0.1% TFA, gradient: 15% B (1 min) → 50% B (in 24 min) → 100% B (3 min)). **Molecular formula:** C₂₉H₄₄N₁₀O₁₁. **TLC:** *R*_f = 0.60 (ACN, RP₁₈ silica gel). **MALDI-MS** (CHCA, *m/z*): Calculated for [M+H]⁺: 709.327, found: 709.742; Calculated for [M+Na]⁺: 731.309, found: 731.738. **¹H-NMR, COSY** (400 MHz, D₂O): δ = 7.81 (s, 1H, triazole: CH), 4.75 (m, 1H, **D**: CH), 4.53 (t, ³*J* = 5.0 Hz, 2H, triazoleN-CH₂), 4.26 (m, 1H, **R**: CH), 3.95 (s, 2H, **G**: CH₂), 3.88 (t, ³*J* = 5.0 Hz, 2H, triazoleN-CH₂CH₂), 3.64–3.56 (m, 8H, CH₂O, CH₂NC(=O)), 3.16 (m, 2H, **R**: NHCH), 3.01 (m, triazoleC-CH₂CH₂), 2.92 (m, 2H, **D**: CH₂), 2.68 (m, 2H, triazoleC-CH₂CH₂), 1.90 (s, 6H, CH₃), 1.80 (m, 1H, **R**: NHCH₂CH₂''), 1.67 (m, 1H, **R**: NHCH₂CH₂CH₂''), 1.52 (m, 2H, **R**: NHCH₂CH₂'CH₂') ppm. **¹³C-NMR, HMBC, HSQC** (101 MHz, DMSO-*d*₆/D₂O): δ = 175.3 (**R**: C(=O)NH), 174.3 (DMMI: C=O), 174.2 (**D**: CHC(=O)OH), 174.1 (**D**: C(=O)OH), 170.8 (**G**: C(=O)NH), 156.7 (**R**: NH₂C(=NH)), 146.2 (triazole: C=CCH₂), 137.7 (DMMI: C=C), 123.7 (triazole: C=CCH₂), 69.6 (CH₂O), 69.2 (CH₂O), 68.7 (triazoleN-CH₂CH₂), 67.7 (CH₂O), 53.6 (**R**: CH), 50.7 (triazoleN-CH₂), 49.2 (**D**: CH), 42.2 (**G**: CH₂), 40.4 (**R**: NHCH₂), 37.0 (DMMI-CH₂), 35.6 (**D**: CH₂), 34.6 (triazoleC-CH₂CH₂), 27.9 (**R**: NHCH₂CH₂CH₂), 24.2 (**R**: NHCH₂CH₂CH₂), 20.7 (triazoleC-CH₂), 7.8 (CH₃) ppm.

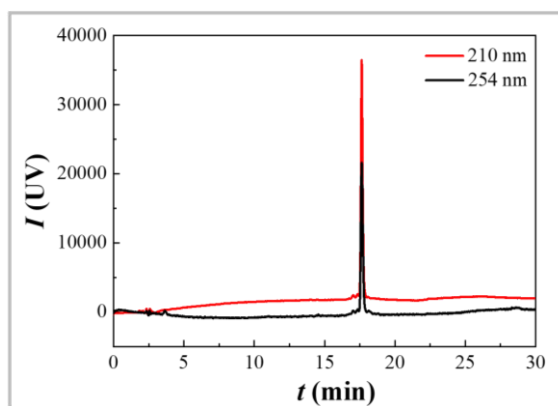
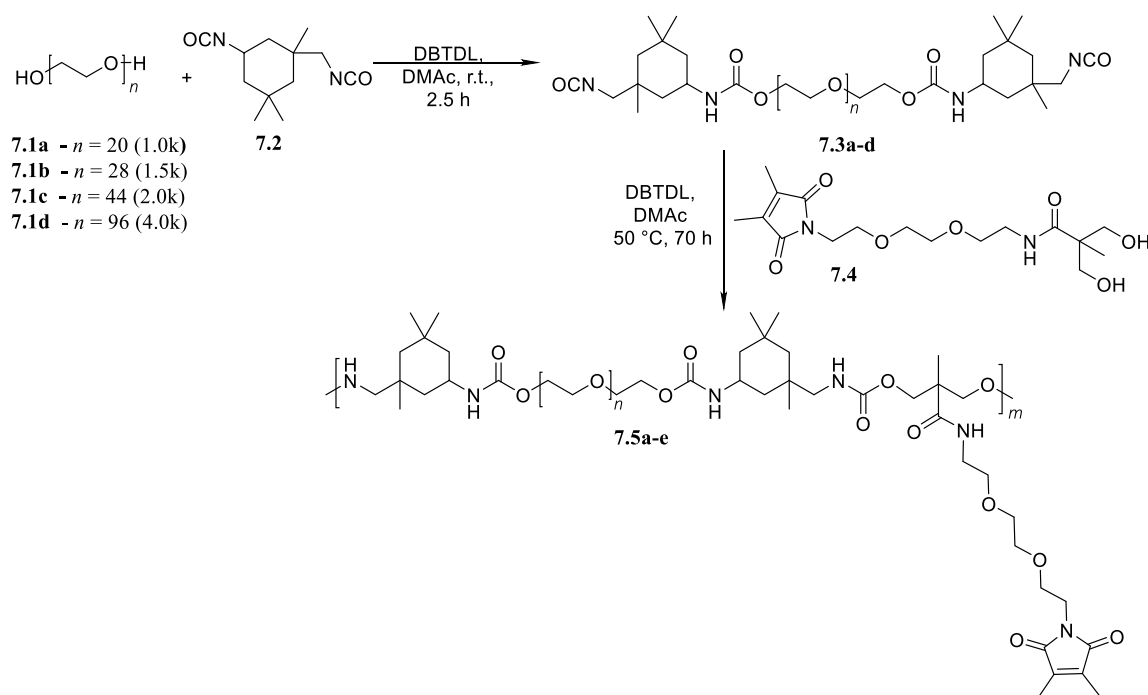


Figure 7.5. Chromatogram of Compound **7.7** (acetonitrile (B) and ultrapure water (A), each with 0.1% TFA; gradient: 5% B (1 min) → 30% B (in 15 min) → 30% B (3 min) → 50% B (in 5 min)).

Linear pEG-IPDI-DMMI Polyurethanes



Scheme 7.4. Synthesis of linear pEG/IPDI PUs with pendant DMMI groups.

SOP

All reaction steps are carried out under argon atmosphere in flame dried glassware. An IPDI **7.2** stock solution in DMA (2.0 eq., 0.95 M) is added to a 100 mL three-neck flask with dripping funnel, valve, and septum. Poly(ethylene glycol) **7.1a–d** (500 mg, 1.0 eq) of the appropriate molar mass is freshly freeze-dried from benzene and dissolved in DMA (3 mL) and transferred to the dripping funnel with a syringe. After addition of one drop DBTDL to the IPDI, the pEG solution is added over 15–30 min and the reaction mixture is stirred for another 2 h. Afterwards, the DMMI diol **7.4** (1.0 eq, 0.45 M) is added as a stock solution in DMA and the reaction mixture is heated to 50 °C. After 48 h, an additional portion of IPDI (0.1 eq.) is added and the solution is stirred for another 24 h. Next, the reaction is quenched with MeOH (2 mL) and cooled to r.t. The polymer solution is precipitated into ice-cold Et₂O (160 mL) and reprecipitated one time from DCM. Finally, the PU is isolated by lyophilization from ACN/H₂O. All polymerizations are carried out according to this SOP.

PU-1.0k **7.5a**

The polymerization is carried out with pEG-1.0k ($M_n = 0.88 \text{ kg mol}^{-1}$, 401 mg, 1.0 eq.), and IPDI (stock solution: 0.94 M, 0.85 mL, 2.0 eq.) and DMMI (stock solution: 0.45 M, 0.89 mL, 1.0 eq.). **Yield:** 0.528 mg (71%). **GPC:** $M_n = 4.15 \text{ kg mol}^{-1}$, $M_w = 6.28 \text{ kg mol}^{-1}$, $D = 1.5$ **¹H-NMR** (400 MHz, DMSO-*d*₆): $\delta = 7.55$ (m, 1.1H, C(=O)NH), 7.12 (m, 2H, OC(=O)NH), 5.69 (m, 2H, OC(=O)NH), 4.87 (m, 1H, CH), 4.03 (m, 6H, NH(C=O)O-CH₂), 3.50 (m, 90H, CH₂O), 2.73 (m, 4H, O(C=O)NH-CH₂), 1.89 (s, 4.5H, (C=C)CH₃), 1.60–0.72 (m, 36H, CH₃/CH₂) ppm. **¹³C-**

NMR (101 MHz, DMSO- d_6): $\delta = 173.7$ (C(=O)NH), 171.6 (DMMI: C(=O)N), 158.5 (OC(=O)NH), 156.5 (OC(=O)NH), 155.4 (OC(=O)NH), 136.8 (CH₃C=CCH₃), 69.5 (CH₂O), 69.3 (CH₂O), 68.9 (CH₂O), 62.9 (CH₂O), 54.4 (IPDI), 47.2 (CH₂NHC(=O)), 45.5 (IPDI), 43.9 (IPDI), 41.6 (IPDI), 38.6 (IPDI), 36.9 (IPDI), 36.0 (IPDI), 35.0 (IPDI), 31.4 (IPDI), 27.5 (IPDI: CH₃), 23.2 (IPDI: CH₃), 17.4 (CH₃), 8.5 (DMMI: CH₃) ppm.

Peak assignment according to literature reports and comparison with educt spectra.³⁸

PU-1.5k^{0.6} 7.5b

The polymerization is carried out with pEG-1.5k ($M_n = 1.24$ kg mol⁻¹, 301 mg, 0.6 eq.), and IPDI (2.0 eq., stock solution: 0.43 M, 1.13 mL) and DMMI (stock solution: 0.21 M, 1.35 mL, 1.4 eq.). **Yield:** 0.417 mg (89%). **GPC:** $M_n = 6.55$ kg mol⁻¹, $M_w = 12.0$ kg mol⁻¹, $D = 1.9$. **¹H-NMR** (400 MHz, DMSO- d_6): $\delta = 7.60$ (m, 1.1H, C(=O)NH), 7.13 (m, 2.2H, OC(=O)NH), 5.84 (m, 1.8H, OC(=O)NH), 4.89 (m, 1H, CH), 4.02 (m, 6.1H, NH(C=O)O-CH₂), 3.34 (m, 113H, CH₂O), 2.72 (m, 3.6H, O(C=O)NH-CH₂), 1.89 (s, 4.8H, (C=C)CH₃), 1.55–0.81 (m, 38.5H, CH₃/CH₂) ppm. **¹³C-NMR** (101 MHz, DMSO- d_6): $\delta = 173.8$ (C(=O)NH), 171.7 (DMMI: C(=O)N), 158.5 (OC(=O)NH), 157.0 (OC(=O)NH), 156.9 (OC(=O)NH), 155.4 (OC(=O)NH), 136.8 (CH₃C=CCH₃), 69.6 (CH₂O), 68.9 (CH₂O), 67.1 (CH₂O), 62.9 (CH₂O), 53.4 (IPDI), 46.7 (CH₂NHC(=O)), 45.5 (IPDI), 43.9 (IPDI), 41.6 (IPDI), 38.6 (IPDI), 36.9 (IPDI), 36.0 (IPDI), 35.0 (IPDI), 31.5 (IPDI), 27.5 (IPDI: CH₃), 23.2 (IPDI: CH₃), 17.5 (CH₃), 8.5 (DMMI: CH₃) ppm.

PU-1.5k 7.5c

The polymerization is carried out with pEG-1.5k ($M_n = 1.24$ kg mol⁻¹, 500 mg, 1.0 eq.), IPDI (stock solution: 0.94 M, 0.71 mL, 2.0 eq.) and DMMI (stock solution: 0.45 M, 0.74 mL, 1.0 eq.). **Yield:** 0.566 mg (73%). **GPC:** $M_n = 7.02$ kg mol⁻¹, $M_w = 12.4$ kg mol⁻¹, $D = 1.8$. **¹H-NMR** (400 MHz, DMSO- d_6): $\delta = 7.56$ (m, 1H, C(=O)NH), 7.12 (m, 2H, OC(=O)NH), 5.74 (m, 2.6H, OC(=O)NH), 4.87 (m, 1H, CH), 4.03 (m, 6H, NH(C=O)O-CH₂), 3.51 (m, 113H, CH₂O), 2.72 (m, 4.1H, O(C=O)NH-CH₂), 1.89 (s, 3.6H, (C=C)CH₃), 1.61–0.73 (m, 34H, CH₃/CH₂) ppm. **¹³C-NMR** (101 MHz, DMSO- d_6): $\delta = 173.7$ (C(=O)NH), 171.61 (DMMI: C(=O)N), 156.8 (OC(=O)NH), 155.4 (OC(=O)NH), 136.8 (CH₃C=CCH₃), 69.7 (CH₂O), 69.5 (CH₂O), 69.3 (CH₂O), 68.9 (CH₂O), 67.1 (CH₂O), 66.2 (CH₂O), 63.1 (CH₂O), 62.9 (CH₂O), 60.2 (CH₂O), 47.0 (CH₂NHC(=O)), 46.6 (IPDI), 45.5 (IPDI), 43.9 (IPDI), 38.6 (IPDI), 36.9 (IPDI), 36.3 (IPDI), 36.0 (IPDI), 35.0 (IPDI), 31.4 (IPDI), 27.5 (IPDI: CH₃), 23.2 (IPDI: CH₃), 17.5 (CH₃), 8.5 (DMMI: CH₃) ppm.

PU-2.0k 7.5d

The polymerization is carried out with pEG-2k ($M_n = 1.95$ kg mol⁻¹, 502 mg, 1.0 eq.), IPDI (stock solution: 0.95 M, 0.53 mL, 2.0 eq.) and DMMI (stock solution: 0.46 M, 0.55 mL, 1.0 eq.). **Yield:** 0.522 mg (74%). **GPC:** $M_n = 8.93$ kg mol⁻¹, $M_w = 14.62$ kg mol⁻¹, $D = 1.6$. **¹H-NMR**

(400 MHz, DMSO- d_6): δ = 7.55 (m, 0.8H, C(=O)NH), 7.14 (m, 2H, OC(=O)NH), 5.69 (m, 2H, OC(=O)NH), 4.86 (m, 0.6H, CH), 4.03 (m, 5.2H, NH(C=O)O-CH₂), 3.51 (m, 175H, CH₂O), 2.73 (m, 4.3H, O(C=O)NH-CH₂), 1.89 (s, 4.3H, (C=C)CH₃), 1.61–0.72 (m, 41.3H, CH₃/CH₂) ppm. ¹³C-NMR (101 MHz, DMSO- d_6): δ = 173.7 (C(=O)NH), 171.61 (DMMI: C(=O)N), 158.5 (OC(=O)NH), 158.4 (OC(=O)NH), 156.8 (OC(=O)NH), 155.4 (OC(=O)NH), 136.8 (CH₃C=CCH₃), 70.0 (CH₂O), 69.3 (CH₂O), 68.9 (CH₂O), 67.9 (CH₂O), 63.1 (CH₂O), 62.9 (CH₂O), 54.4 (IPDI: CH₂NHC(=O)O), 53.4 (IPDI), 46.6 (IPDI), 45.5 (IPDI), 43.9 (IPDI), 38.6 (IPDI), 36.9 (IPDI), 36.0 (IPDI), 35.0 (IPDI), 31.4 (IPDI), 30.0 (IPDI), 27.5 (IPDI: CH₃), 23.0 (IPDI: CH₃), 17.5 (CH₃), 8.5 (DMMI: CH₃) ppm.

PU-4.0k 7.5e

The polymerization is carried out with pEG-4k ($M_n = 4.22 \text{ kg mol}^{-1}$, 485 mg, 1.0 eq.) IPDI (stock solution: 0.95 M, 0.25 mL, 2.0 eq.) and DMMI (stock solution: 0.46 M, 0.26 mL, 1.0 eq.).

Yield: 0.436 mg (72%). **GPC:** $M_n = 20.03 \text{ kg mol}^{-1}$, $M_w = 30.27 \text{ kg mol}^{-1}$, $D = 1.5$. ¹H-NMR (400 MHz, DMSO- d_6): δ = 7.55 (m, 0.8H, C(=O)NH), 7.14 (m, 2H, OC(=O)NH), 5.69 (m, 2H, OC(=O)NH), 4.88 (m, 0.3H, CH), 4.03 (m, 4.8H, NH(C=O)O-CH₂), 3.51 (m, 381H, CH₂O), 2.92–2.60 (m, 4H, O(C=O)NH-CH₂), 1.89 (s, 4.1H, (C=C)CH₃), 1.78–0.63 (m, 53H, CH₃/CH₂) ppm. ¹³C-NMR (101 MHz, DMSO- d_6): δ = 176.8 (C(=O)NH), 171.6 (DMMI: C(=O)N), 158.5 (OC(=O)NH), 157.6 (OC(=O)NH), 156.8 (OC(=O)NH), 155.4 (OC(=O)NH), 136.8 (CH₃C=CCH₃), 69.8 (CH₂O), 68.9 (CH₂O), 67.1 (CH₂O), 63.1 (CH₂O), 62.9 (CH₂O), 47.0 (IPDI), 45.6 (IPDI), 43.9 (IPDI), 38.6 (IPDI), 36.9 (IPDI), 36.1 (IPDI), 35.0 (IPDI), 31.4 (IPDI), 31.3 (IPDI), 27.5 (IPDI: CH₃), 23.0 (IPDI: CH₃), 8.4 (DMMI: CH₃) ppm.

Molar Mass Distributions

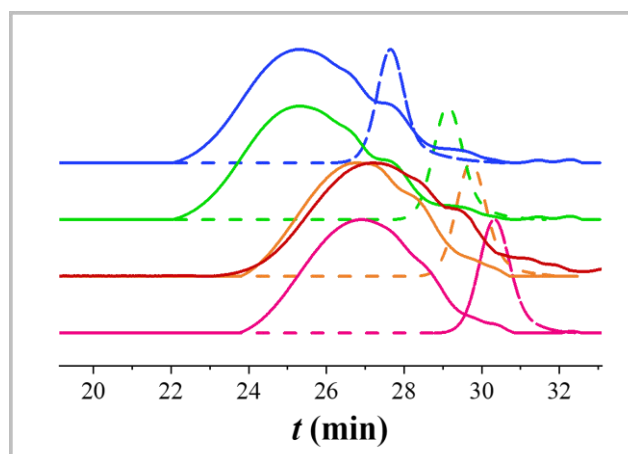


Figure 7.6. GPC elograms of pEG-diols **7.1a–d** (dashed) and the corresponding pEG/IPDI/DMMI PUs (PU-1.0k **5a** (—), 1.5k^{0.6} **7.5b** (—), PU-1.5k **7.5c** (—), PU-2.0k **7.5d** (—) and PU-4.0k **7.5e** (—) (measured in DMF + LiCl 1 g·L⁻¹).

Turbidity Measurements

The PUs are dissolved in MilliQ water (3 mL) to a concentration of $c_{\text{PU}} = 5 \text{ g}\cdot\text{L}^{-1}$. Afterwards, the solutions are transferred to a quartz glass cuvette equipped with a stirring bar. For the turbidity measurements, a wavelength of 550 nm is chosen, and a dark measurement is performed, before a baseline measurement is conducted with pure water. Then the PU-cuvette is placed in the spectrometer and equilibrated for 10 min at each temperature under vigorous stirring before the measurement is started. After another 10 min at the same temperature, a further measurement is performed and if both values coincide the temperature is increased (5 °C or 2.5 °C steps). Otherwise, the equilibration is continued at the same temperature. The cloud point temperatures are determined from the inflection points of the recorded curves shown in **Figure 7.1 B**.

Rheological Measurements

The PUs are dissolved to the appropriate concentration in an aqueous thioxanthone disulfonate (TXS) solution (0.1 or 1 mM). For gelation experiments, 80 μL of this solution are placed on the rheometer (plate-plate geometry, diameter: 25 mm) and the sample is equilibrated for 5 min at 5 °C at a constant shear amplitude and frequency ($\gamma = 0.1\%$; $\omega = 1 \text{ rad}\cdot\text{s}^{-1}$). Afterwards, the UV irradiation (1 or 10% aperture) is started through the transparent lower glass plate and a time dependent measurement is started ($\gamma = 0.1\%$; $\omega = 1 \text{ rad}\cdot\text{s}^{-1}$) at 5 °C.

Gelation Time Measurements

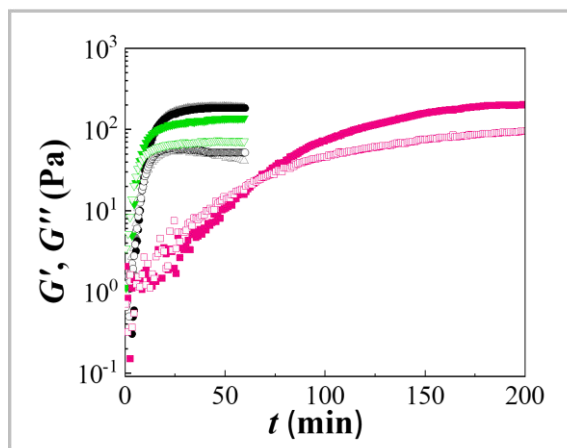


Figure 7.7. Time-dependent storage G' (closed symbols) and loss G'' (open symbols) moduli of PU-4k ($100 \text{ g}\cdot\text{L}^{-1}$) in an aqueous thioxanthone disulfonate (TXS) solution under UV irradiation at a TXS concentration of 1 mM and a light aperture of 1% at 20 °C (\bullet) and 5 °C (\blacktriangle) as well as at a TXS concentration of 0.1 mM and a light aperture of 1% (\blacksquare) and 10% (\blacktriangledown) at 5 °C.

Equilibrium Swelling Experiments

Around 10 mg precursor polymer are dissolved to a concentration of $100 \text{ g}\cdot\text{L}^{-1}$ in aqueous thioxanthone disulfonate solution (1 mM) and irradiated with UV light for 60 min. The obtained gels are dialyzed against MeOH (2 x) and water (4 x) to remove a potential sol fraction. The gels are then immersed in water (5 mL) and kept in a 5, 20 or 40 °C water bath for 12 h before the gel

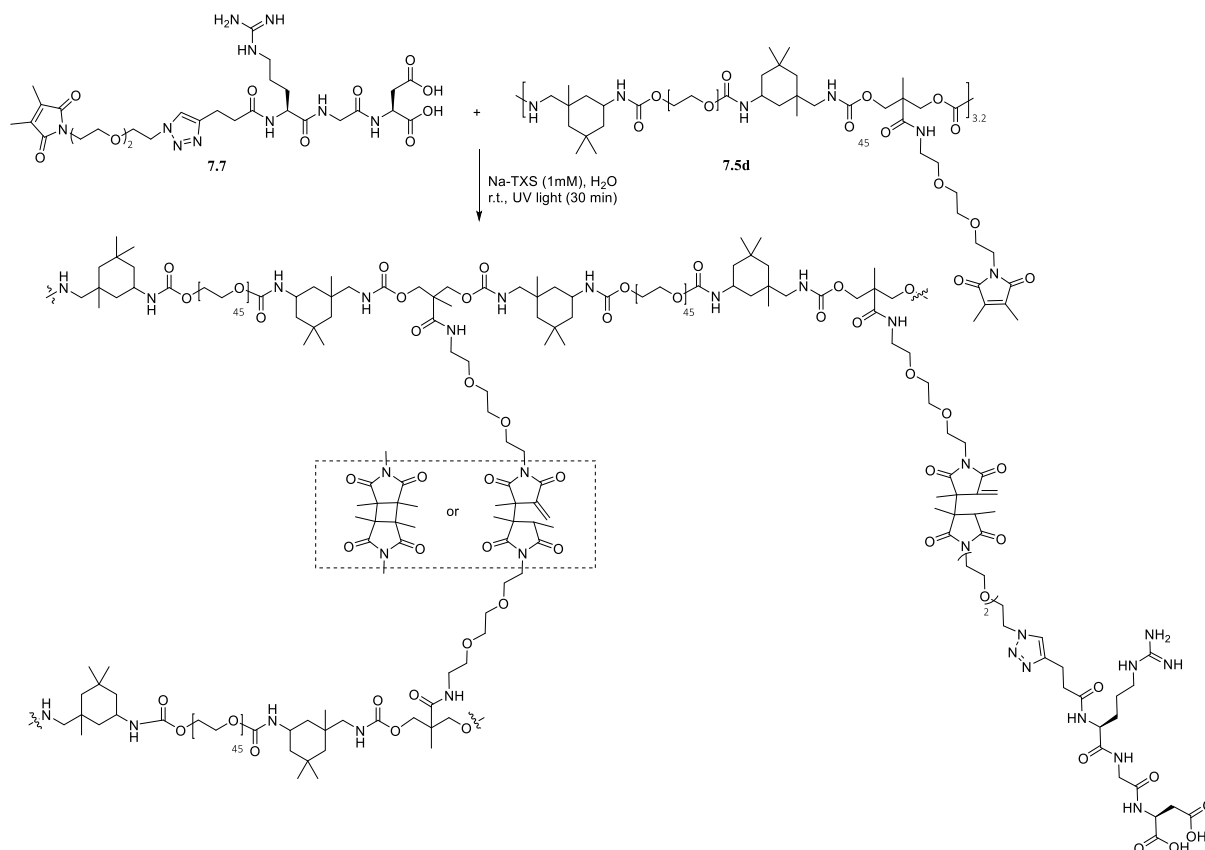
is removed from the water and weighed (m_T). Finally, the gels are freeze dried and the dry mass (m_{dry}) is determined by difference weighing. The swelling degree Q_T is calculated as $Q_T = 100\% \cdot (m_T - m_{\text{dry}}) / m_{\text{dry}}$. Each measurement is performed at least in duplicate.

Temperature Induced Volume Change

A PU-1.5k⁰⁶ gel piece of ≈ 2 mm size is cut from the macroscopic gel, immersed in water and sealed between two microscopy slides. After placing the sample on an Instec Thermostage under an optical microscope (4x objective), a temperature ramp from 5 to 61 °C is started. During this, the temperature is increased in 2 °C steps and the samples are equilibrated for 10 min at each temperature. The diameter of the gel piece is measured at three different positions at each temperature using the software ImageJ. The measured distances are normalized to the one measured at 5 °C and an average of the normalized values from the three different positions is calculated.

Gel Preparation for ¹H MAS-NMR and Cell Experiments

The schematic gelation reaction is shown in **Scheme 7.5**. Stock solutions of the Catechol- **7.6** or RGD- **7.7** DMMI (50 mM) are prepared in MilliQ water. Afterwards, a volume portion containing 0, 5 or 25 mol% of the respective bio-linker in comparison to the DMMI groups in the PU ($n_{\text{DMMI}} = f_{\text{DMMI}} \cdot N_x \cdot n_{\text{PU}}$ with the DMMI functionalization degree $f_{\text{DMMI}} = 0.78$ derived from the ¹H-NMR analysis ($f_{\text{DMMI}} = \text{integral}(1.89 \text{ ppm}^{\text{exp}}) / \text{integral}(1.89 \text{ ppm})^{\text{theo}}$), the average number of repeating units per chain $N_x = M_n(\text{PU}) / M_n(\text{repeating unit}) = 8.9 \text{ kg} \cdot \text{mol}^{-1} / 2.8 \text{ kg} \cdot \text{mol}^{-1} = 3.2$, and the molar amount of the PU $n_{\text{PU}} = m_{\text{PU}} / M_n(\text{PU})$) are added to in a previously weighed amount of PU-2k **7.5d** (10–20 mg). An aqueous thioxanthone disulfonate solution (1 mM) is added to obtain a polymer concentration of 200 g·L⁻¹. After dissolution overnight, the solution is irradiated with UV light for 30 min. Afterwards, the obtained gel is dialyzed against DMSO (2 x 12 h), MeOH (2 x 12 h) and water (4 x 12 h) to remove any excess of bio-linker and photosensitizer. For ¹H-MAS-NMR measurements, the gels are then freeze-dried and immersed in D₂O for at least 12 h prior to measurement. For cell tests, the gels are transferred into phosphate buffer and purified over 3 days, while changing the buffer every day.



Scheme 7.5. Schematic incorporation of RGD-DMMI units into the PU gel.

¹H-MAS-NMR Spectroscopy

PU-2k **7.5d** gels with 0 mol% RGD (i), 5 mol% RGD (ii), and 25 mol% RGD (iii) are analyzed by ¹H-MAS-NMR spectroscopy (**Figure 7.9**). Subsequent peak assignments are made according to literature reports and comparison with educt spectra.³⁸

0 mol% RGD (i): ¹H-MAS-NMR (400 MHz, D₂O) $\delta = 4.25$ (PU: NH(C=O)O-CH₂), 3.75 (PU: CH₂O), 2.93 (PU: O(C=O)NH-CH₂), 2.17–0.72 (PU: (C=C)CH₃, CH₃/CH₂) ppm.

5 mol% RGD (ii) and 25 mol% RGD (iii): ¹H MAS NMR (400 MHz, D₂O) $\delta = 7.87$ (s, RGD: triazole-CH), 4.58 (RGD: triazoleN-CH₂), 4.23 (PU: NH(C=O)O-CH₂), 3.73 (PU: CH₂O), 3.22 (RGD: **R**: NHCH), 3.06 (RGD: triazoleC-CH₂CH₂), 2.98 (PU: O(C=O)NH-CH₂), 2.73 (RGD: triazoleC-CH₂CH₂), 2.17–0.72 (PU: (C=C)CH₃, CH₃/CH₂) ppm.

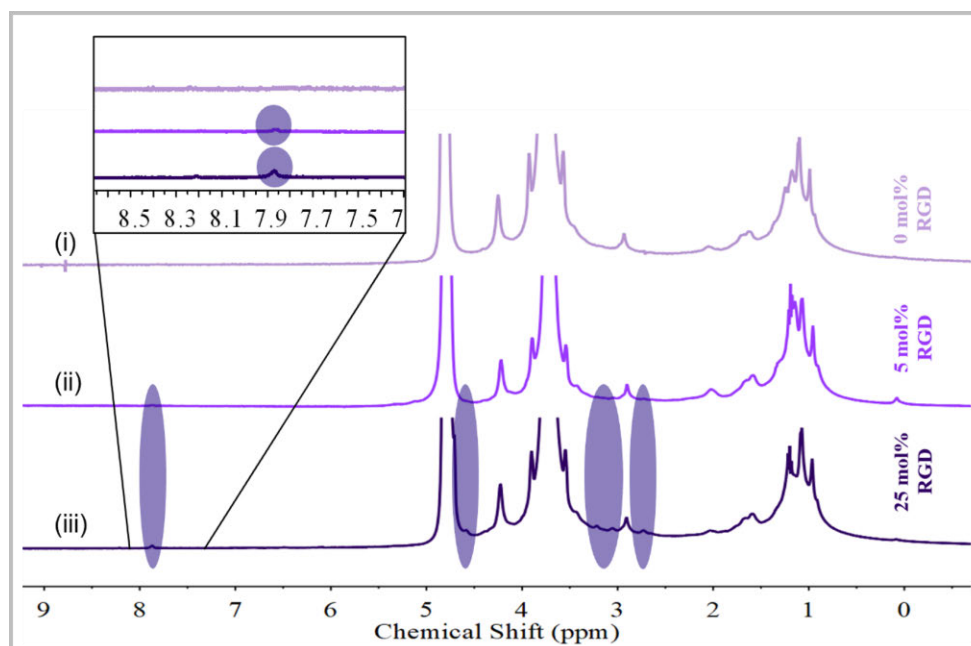


Figure 7.8. ^1H -MAS-NMR spectroscopy measurements in D_2O of PU-2.0k gels ($200\text{ g}\cdot\text{L}^{-1}$) containing 0 mol% (i), 5 mol% (ii), and 25 mol% RGD-DMMI (iii). Respective RGD-DMMI signals in (i) and (ii) are highlighted in purple.

Mechanical Properties

Correspondingly synthesized and purified PU-2k **7.5** hydrogels with 0, 5 and 25 mol% incorporated catechol-linker are immersed in water at $5\text{ }^\circ\text{C}$ for 24 h and probed by linear shear rheology (plate-plate geometry, diameter: 7 mm). Consistent with our previous findings on 5 and 25 mol% RGD hydrogels, the plateau moduli of the 0 and 5 mol% catechol-containing gels are in agreement, while the incorporation of 25 mol% results in a 35% lower plateau modulus.

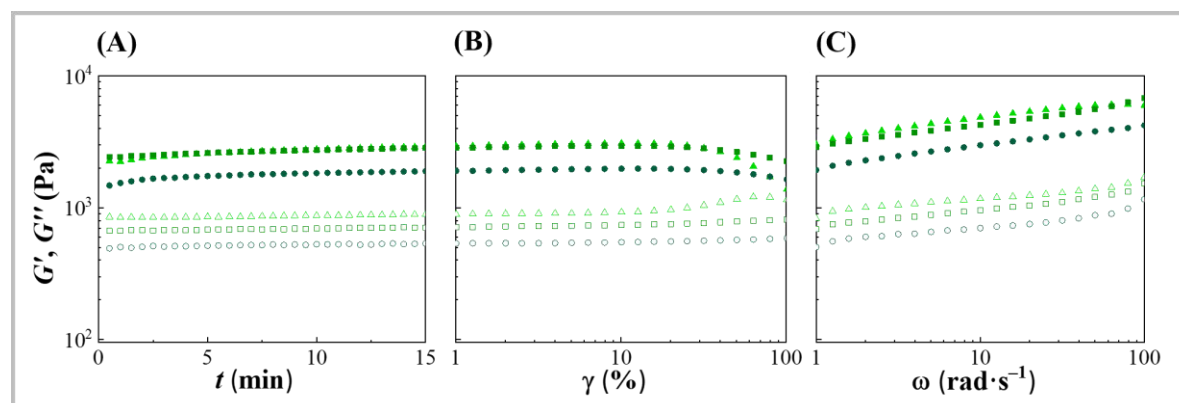


Figure 7.9. Time-, amplitude- and frequency sweeps of dialyzed and fully hydrated PU-2k hydrogels ($200\text{ g}\cdot\text{L}^{-1}$) cross-linked in the presence of 0 mol% (\blacktriangle), 5 mol% (\blacksquare) and 25 mol% (\bullet) catechol-DMMI ($\gamma = 1\%$, $\omega = 1\text{ rad}\cdot\text{s}^{-1}$, G' : closed symbols, G'' : open symbols, $T = 20\text{ }^\circ\text{C}$).

Cell Experiments

Osteoblasts (MG-63-GFP) are cultured on polystyrene (11.9 cm²) in DMEM (10% FBS, 1% Gl., 1% P/S) at 37 °C and 5% CO₂ using standard cell culture methods. For the cell experiments cells are detached from plastic by trypsinization with trypsin EDTA solution. After centrifugation (1000 rpm, 5 min), the resulting cell pellet is resuspended in DMEM (10% FBS, 1% Gl., 1% P/S) and adjusted to 1.5×10^5 cells·mL⁻¹ (cell counting by Neubauer counting chamber). PU-2k gels with 0, 5, and 25 mol% RGD, as well as 5 mol% catechol, are transferred into 8well plates from ibidi and covered with 300 μL of cell suspension. After 24 h cell-coated hydrogels are analyzed by CLSM.

7.5 References

- (1) Breul, K.; [REDACTED] Cell Adhesion on UV-Crosslinked Polyurethane Gels with Adjustable Mechanical Strength and Thermoresponsiveness. *Macromolecular rapid communications* **2021**, e2100505.
- (2) Doberenz, F.; Zeng, K.; Willems, C.; Zhang, K.; Groth, T. Thermoresponsive polymers and their biomedical application in tissue engineering - a review. *J. Mater. Chem. B* **2020**, *8*, 607–628.
- (3) Klouda, L.; Mikos, A. G. Thermoresponsive hydrogels in biomedical applications. *European journal of pharmaceuticals and biopharmaceutics : official journal of Arbeitsgemeinschaft für Pharmazeutische Verfahrenstechnik e.V* **2008**, *68*, 34–45.
- (4) Fan, H.; Gong, J. P. Fabrication of Bioinspired Hydrogels: Challenges and Opportunities. *Macromolecules* **2020**, *53*, 2769–2782.
- (5) DeForest, C. A.; Anseth, K. S. Advances in bioactive hydrogels to probe and direct cell fate. *Annual review of chemical and biomolecular engineering* **2012**, *3*, 421–444.
- (6) Rice, J. J.; Martino, M. M.; Laporte, L. de; Tortelli, F.; Briquez, P. S.; Hubbell, J. A. Engineering the regenerative microenvironment with biomaterials. *Advanced healthcare materials* **2013**, *2*, 57–71.
- (7) Dippold, D.; Cai, A.; Hardt, M.; Boccaccini, A. R.; Horch, R. E.; Beier, J. P.; Schubert, D. W. Investigation of the batch-to-batch inconsistencies of Collagen in PCL-Collagen nanofibers. *Materials science & engineering. C, Materials for biological applications* **2019**, *95*, 217–225.
- (8) Zhang, Y.; Hu, J.; Zhao, X.; Xie, R.; Qin, T.; Ji, F. Mechanically Robust Shape Memory Polyurethane Nanocomposites for Minimally Invasive Bone Repair. *ACS Appl. Bio Mater.* **2019**, *2*, 1056–1065.
- (9) Wei, K.; Chen, X.; Zhao, P.; Feng, Q.; Yang, B.; Li, R.; Zhang, Z.-Y.; Bian, L. Stretchable and Bioadhesive Supramolecular Hydrogels Activated by a One-Stone-Two-Bird Postgelation Functionalization Method. *ACS applied materials & interfaces* **2019**, *11*, 16328–16335.
- (10) Dennes, T. J.; Schwartz, J. Controlling cell adhesion on polyurethanes. *Soft Matter* **2008**, *4*, 86–89.
- (11) Stengelin, E.; Nzigou Mombo, B.; Mondeshki, M.; Beltramo, G. L.; Lange, M. A.; Schmidt, P.; Frerichs, H.; Wegner, S. V.; Seiffert, S. Rational Design of Thermoresponsive Microgel Templates with Polydopamine Surface Coating for Microtissue Applications. *Macromol. Biosci.* **2021**, e2100209.
- (12) Bin Imran, A.; Esaki, K.; Gotoh, H.; Seki, T.; Ito, K.; Sakai, Y.; Takeoka, Y. Extremely stretchable thermosensitive hydrogels by introducing slide-ring polyrotaxane cross-linkers and ionic groups into the polymer network. *Nature communications* **2014**, *5*, 5124.

- (13) Pertici, V.; Pin-Barre, C.; Rivera, C.; Pellegrino, C.; Laurin, J.; Gignes, D.; Trimaille, T. Degradable and Injectable Hydrogel for Drug Delivery in Soft Tissues. *Biomacromolecules* **2019**, *20*, 149–163.
- (14) Sardon, H.; Tan, J. P. K.; Chan, J. M. W.; Mantione, D.; Mecerreyes, D.; Hedrick, J. L.; Yang, Y. Y. Thermoresponsive Random Poly(ether urethanes) with Tailorable LCSTs for Anticancer Drug Delivery. *Macromolecular rapid communications* **2015**, *36*, 1761–1767.
- (15) Polo Fonseca, L.; Trinca, R. B.; Felisberti, M. I. Amphiphilic polyurethane hydrogels as smart carriers for acidic hydrophobic drugs. *International journal of pharmaceutics* **2018**, *546*, 106–114.
- (16) Ding, M.; Song, N.; He, X.; Li, J.; Zhou, L.; Tan, H.; Fu, Q.; Gu, Q. Toward the next-generation nanomedicines: design of multifunctional multiblock polyurethanes for effective cancer treatment. *ACS nano* **2013**, *7*, 1918–1928.
- (17) Oveissi, F.; Naficy, S.; Lee, A.; Winlaw, D. S.; Dehghani, F. Materials and manufacturing perspectives in engineering heart valves: a review. *Materials today. Bio* **2020**, *5*, 100038.
- (18) Frydrych, M.; Román, S.; Green, N. H.; MacNeil, S.; Chen, B. Thermoresponsive, stretchable, biodegradable and biocompatible poly(glycerol sebacate)-based polyurethane hydrogels. *Polym. Chem.* **2015**, *6*, 7974–7987.
- (19) Fu, H.; Gao, H.; Wu, G.; Wang, Y.; Fan, Y.; Ma, J. Preparation and tunable temperature sensitivity of biodegradable polyurethane nanoassemblies from diisocyanate and poly(ethylene glycol). *Soft Matter* **2011**, *7*, 3546.
- (20) Santerre, J. P.; Woodhouse, K.; Laroche, G.; Labow, R. S. Understanding the biodegradation of polyurethanes: from classical implants to tissue engineering materials. *Biomaterials* **2005**, *26*, 7457–7470.
- (21) Ronco, L. I.; Basterretxea, A.; Mantione, D.; Aguirresarobe, R. H.; Minari, R. J.; Gugliotta, L. M.; Mecerreyes, D.; Sardon, H. Temperature responsive PEG-based polyurethanes “à la carte”. *Polymer* **2017**, *122*, 117–124.
- (22) Aoki, D.; Ajiro, H. Thermoresponsive Polyurethane Bearing Oligo(Ethylene Glycol) as Side Chain Without Polyol at Polymer Backbone Achieved Excellent Hydrophilic and Hydrophobic Switching. *Macromolecular rapid communications* **2018**, *39*, e1800239.
- (23) Aoki, D.; Ajiro, H. One-Shot Preparation of Thermoresponsive Comb Polyurethane Hydrogel for Both Excellent Toughness and Large Volume Switching. *Macromolecular rapid communications* **2021**, e2100128.
- (24) Li, K.; Zhou, C.; Liu, S.; Yao, F.; Fu, G.; Xu, L. Preparation of mechanically-tough and thermo-responsive polyurethane-poly(ethylene glycol) hydrogels. *Reactive and Functional Polymers* **2017**, *117*, 81–88.
- (25) Seiffert, S.; Oppermann, W.; Saalwächter, K. Hydrogel formation by photocrosslinking of dimethylmaleimide functionalized polyacrylamide. *Polymer* **2007**, *48*, 5599–5611.

- (26) Karpov, S. V.; Lodygina, V. P.; Komratova, V. V.; Dzhalumukhanova, A. S.; Malkov, G. V.; Badamshina, E. R. Kinetics of urethane formation from isophorone diisocyanate: The catalyst and solvent effects. *Kinet Catal* **2016**, *57*, 422–428.
- (27) Ono, H.-K.; Jones, F. N.; Pappas, S. P. Relative reactivity of isocyanate groups of isophorone diisocyanate. Unexpected high reactivity of the secondary isocyanate group. *J. Polym. Sci. B Polym. Lett. Ed.* **1985**, *23*, 509–515.
- (28) Breul, K.; Seiffert, S. Amphiphilic poly(ether urethanes) carrying associative terpyridine side groups with controlled spacing. *Polym. Chem.* **2021**, *12*, 2305–2316.
- (29) Lunazzi, L.; Parisi, F.; Macciantelli, D. Conformational studies by dynamic nuclear magnetic resonance spectroscopy. Part 27. Kinetics and mechanism of annular tautomerism in isomeric triazoles. *J. Chem. Soc., Perkin Trans. 2* **1984**, *0*, 1025.
- (30) Cox, J. R.; Woodcock, S.; Hillier, I. H.; Vincent, M. A. Tautomerism of 1,2,3- and 1,2,4-triazole in the gas phase and in aqueous solution: a combined ab initio quantum mechanics and free energy perturbation study. *J. Phys. Chem.* **1990**, *94*, 5499–5501.
- (31) Rowley, J. A.; Mooney, D. J. Alginate type and RGD density control myoblast phenotype. *J. Biomed. Mater. Res.* **2002**, *60*, 217–223.
- (32) Burdick, J. A.; Anseth, K. S. Photoencapsulation of osteoblasts in injectable RGD-modified PEG hydrogels for bone tissue engineering. *Biomaterials* **2002**, *23*, 4315–4323.
- (33) Spaans, S.; Fransen, P. P. K. H.; Ippel, B. D.; Bont, D. F. A. de; Keizer, H. M.; Bax, N. A. M.; Bouten, C. V. C.; Dankers, P. Y. W. Supramolecular surface functionalization via catechols for the improvement of cell-material interactions. *Biomaterials science* **2017**, *5*, 1541–1548.
- (34) Tsai, W.-B.; Chen, W.-T.; Chien, H.-W.; Kuo, W.-H.; Wang, M.-J. Poly(dopamine) coating of scaffolds for articular cartilage tissue engineering. *Acta biomaterialia* **2011**, *7*, 4187–4194.
- (35) Wendeln, C.; Rinnen, S.; Schulz, C.; Kaufmann, T.; Arlinghaus, H. F.; Ravoo, B. J. Rapid preparation of multifunctional surfaces for orthogonal ligation by microcontact chemistry. *Chemistry (Weinheim an der Bergstrasse, Germany)* **2012**, *18*, 5880–5888.
- (36) Liu, Z.; Hu, B.-H.; Messersmith, P. B. Acetonide Protection of Dopamine for the Synthesis of Highly Pure N-docosahexaenoyldopamine. *Tetrahedron Letters* **2010**, *51*, 2403–2405.
- (37) Klein, E.; DeBonis, S.; Thiede, B.; Skoufias, D. A.; Kozielski, F.; Lebeau, L. New chemical tools for investigating human mitotic kinesin Eg5. *Bioorganic & medicinal chemistry* **2007**, *15*, 6474–6488.
- (38) Prabhakar, A.; Chattopadhyay, D. K.; Jagadeesh, B.; Raju, K. V. S. N. Structural investigations of polypropylene glycol (PPG) and isophorone diisocyanate (IPDI)-based polyurethane pre-polymer by 1D and 2D NMR spectroscopy. *J. Polym. Sci. Part A: Polym. Chem.* **2005**, *43*, 1196–1209.

CHAPTER 8: CONCLUSIONS & OUTLOOK

In this thesis, different structure–property relationships of supramolecular polymer gels (**Chapter 3–5**), supramolecular gels (**Chapter 4**), and covalent polymer gels (**Chapter 7**) are investigated with newly designed model systems.

A first study focuses on the synthesis of supramolecular associating, linear chains with multiple side-stickers, in which the spacing of these stickers can be altered from uniform to irregular. This is realized through polyurethanes (PUs) with alternating or random sequences of terpyridine (tpy) side-stickers and poly(ethylene) glycol (pEG) spacers. The analysis of the precursor polymer properties in bulk and solution indicates that the random polymers contain multiplets of neighboring tpy–stickers. This presumed structure explains the increased association tendency of the random chains and the enforcement of the corresponding, Mn^{2+} cross-linked gels. Regarding the terminal flow regime in the viscoelastic spectra, it is further observed that the random sticker distribution leads to an exacerbated shallowing of the power-law scaling.

For future investigations, the presented synthesis platform could be used to create not only random but multimodal sticker distributions. This could be achieved by mixing pEG diols with different molar masses and applying the pre-polymer procedure that yields strictly alternating sequences. Alternatively, the pre-polymerization could be used to purposely create tpy–multiplets, which can then be chain-elongated with pEG diols. The derived polymers would allow to study the influence of sticker multiplets in more detail and with higher consistency.

In a second project, the iterative, solid phase synthesis of supramolecular associating side-sticker polymers is investigated, which allows to control the primary sequence with higher precision. The consecutive coupling of tpy– and pEG–amino acid analogues by established amide coupling protocols yields sequence-controlled pEG–tpy conjugates. The flexibility of this modular approach is highlighted using different tpy–amino acids and pEG fragments. It is further shown that defined tpy multiplets with up to three adjacent stickers can be created. The solid phase synthesis of amide-bond containing multiblocks from these pEG–tpy conjugates is finally proven for one representative example.

The inherently limited scalability and high financial and time expenditures of this approach restrict its applicability for material science studies, which usually require product amounts on a gram scale. It appears however reasonable to use the high level of control provided by the iterative coupling strategy for the synthesis of polymer–sticker conjugates with complicated sequences. These heterobifunctional blocks could then be used as repeating units with built-in sequences for a consecutive step-growth polymerization.

Further on, the third project further focuses on the influence of sticker duplets on the macroscopic properties of metallo-supramolecular polymer gels. For this purpose, two complimentary model systems, either based on a telechelic four-arm pEG or a linear pEG-based PU with equally spaced side-stickers (project 1) are chosen. Both polymer types are equipped with isolated, monotopic tpy-stickers or pairs of directly neighboring tpy ligands (ditopic stickers). At identical tpy concentrations, the network strength increases through the introduction of the ditopic stickers, which indicates the formation of network junctions with higher branch functionalities ($f > 4$). Besides this enforcing effect, the ditopic stickers also prolong the terminal relaxation times, which can be explained by an increased rebinding rate of the supramolecular cross-links.

For future investigations, it would be beneficial to firstly investigate the network homogeneity of the applied model gels by an appropriate scattering technique. The uncertainty about the formation and extent of sticker clusters in the investigated PU gels impedes a clear interpretation of the experimental results. Secondly, it would be interesting to further increase the number of neighboring tpy ligands (three- and tetratopic sticker). A non-linear increase of network strength and/or relaxation dynamics could then prove a truly cooperative enhancement.

The macroscopic rheological investigations could further be complemented with a microscopic perspective e.g., by measuring the diffusivity of fluorescently labeled tracer chains inside the networks by fluorescence recovery after photobleaching. Such a study could show to which extent the mobility of the polymer chains is reduced by the multivalent interchain sticking.

Finally, it would be interesting to compare the experimental observations with the modelling predictions from modern network theories, which could improve the molecular understanding of the retarded relaxation mechanisms.

In a fourth, collaborative project, a multi-stimuli responsive, supramolecular hydrogelator is designed and characterized. Tpy-decorated, supramolecular nanorods are obtained through the β -sheet driven self-assembly of a structural and a tpy-functionalized C_3 -symmetric peptide amphiphile in dilute, aqueous solutions. In the presence of a flexible, telechelic pEG linker, these one-dimensional structures can be cross-linked through the formation of *bis*(tpy)-metal complexes (Zn^{2+} , Fe^{2+}) to yield very soft, fully reversible hydrogels. The thermoresponsive properties of the ethylene glycol Newkome-type dendron in the hydrophilic corona of the nanorods, lead to an increase of the gel strength by one order of magnitude if the temperature is increased from 20 °C to 50 °C.

For a follow-up study, it could be interesting to investigate whether and to what extent the length and architecture of the telechelic linkers affects the gel properties. Besides that, the temporal structural evolution of the nanostructural assemblies should be investigated in further detail by transmission electron microscopy.

Finally, it could be examined whether the use of a non-symmetric, three-functional monomer, in which two arms contain the hydrophilic ethylene glycol dendron, while the third arm is equipped with a tpy group, could improve the hydrogel properties.

The last chapter of this theses deals with the design of a thermoresponsive, covalently cross-linked hydrogel platform with tunable mechanical and cell-adhesive properties. It is demonstrated that the lower critical solution temperature (LCST) of pEG-based PU precursors (project 1) in water depends linearly on the amphiphilic balance of the applied comonomers. Dimethylmaleimide side groups further enable the UV-light induced cross-linking of the linear PU precursors. The strength of the obtained hydrogels depends on the polymer concentration and the density of the cross-linkable groups while the temperature-induced deswelling of the gels qualitatively reflects the LCST behavior of the precursors. Finally, it could be shown that the covalent attachment of a low amount of catechol groups significantly improves the cell-adhesiveness of the gel surface.

To specifically target (micro)tissue engineering applications, it would further be beneficial to investigate the processing and shaping of the hydrogels by microfluidics or 3D printing, which is generally enabled by the UV-light induced gelation switch. Regarding the lacking reversibility of the PU gels, it could also be interesting to replace the covalent cross-links with a biocompatible, supramolecular associating groups that forms stable interactions in aqueous environments such as a catechol– or DOPA–ligand. Due to the modularity of the PU synthesis, such a replacement could be easily implemented. To overcome the need for the functional diol, it would also be possible to use the biocompatible L-lysine ethyl ester diisocyanate which would offer the possibility to post-functionalize the obtained PU chains directly and reduce the influence of batch-to-batch variations.

In summary, the five presented studies explore the importance of a rational chemical design of reversible and/or responsive gels to facilitate the comprehensive understanding of fundamental structure–property relationships and enable the implementation of new material functions.

LIST OF ABBREVIATIONS

ACN	Acetonitrile	IEG	Iterative exponential growth
ACS	American Chemical Society	IPDI	Isophorone diisocyanate
AFM	Atomic force microscopy	ITC	Isothermal titration calorimetry
AIP	American Institute of Physics	IUPAC	International Union of Pure and Applied Chemistry
Ale	Alendronate	k	kg·mol ⁻¹
alt	alternating	LCST	Lower critical solution temperature
Arg (R)	Arginine	Lys	L-Lysine
Asp (D)	Asparagine	MALDI-Tof	Matrix assisted laser desorption-time of flight
ATR	Attenuated total reflection	MeOH	Methanol
Bn	Benzyl	MS	Mass spectrometry
BTA	Benzene-1,3,5-tricarboxamide	NMR	Nuclear magnetic resonance
^tBu	<i>tert</i> -Butyl	Pa	Pascal
Cat	Catechol	PDI	Polydispersity index
CD	Circular dichroism	pEG	Poly(ethylene glycol)
CLSM	Confocal laser scanning microscopy	Phe (F)	Phenylalanine
DCM	Dichloromethane	PmbS	<i>p</i> -methoxybenzyl
DLS	Dynamic light scattering	pNiPAm	Poly(<i>N</i> -isopropylacrylamide)
DMA	Dimethylacetamide	ppm	Parts per million
DMF	Dimethylformamide	prep	Preparative
DMMI	Dimethylmaleimide	PS	polystyrene
DMSO	Dimethyl sulfoxide	PU	Polyurethane
DSC	Differential scanning calorimetry	Py	Pyridine
DOPA	Dihydroxy phenylalanine	PyBOP	Benzotriazole-1-ylxytripyrrolidino phosphonium hexafluorophosphate
DSC	Differential scanning calorimetry	ran	random
EA	Ethyl acetate	RP	Reversed phase
ECM	Extracellular matrix	r.t.	Room temperature
EDTA	Ethylene diamine tetra acetic acid	SEC	Size exclusion chromatography
EG	Ethylene glycol	SLS	Static light scattering
eq.	Equivalents	SP(P)S	Solid phase (peptide) synthesis
ESI	Electron spray ionization	SOP	Standard operating procedure
Et₂O	Diethyl ether	Ts	Tosyl
EtOH	Ethanol	TEM	Transmission electron microscopy
Fmoc	Fluorenyl methoxycarbonyl	TFA	Trifluoro acetic acid
FT-IR	Fourier-transformed infrared	THF	Tetrahydrofuran
Gly (G)	Glycine	TIPS	Triisopropyl silance
GPC	Gel permeation chromatography	tpy	2,2':6',2''-Terpyridine
HATU	Hexafluorophosphate Azabenzotriazole Tetramethyl Uronium	TLC	Thin layer chromatography
^cHex	Cyclohexane	TXS	Thioxanthone disulfonate
His (H)	Histidine	UPy	2-Ureido-4-pyrimidinone
HPLC	High performance liquid chromatography	UV-Vis	Ultraviolet-visible
Hz	Hertz	VPT	Volume phase transition

LIST OF SYMBOLS

α	Functionalization degree	c	Concentration
β	Overall complexation constant/Sticker content	cac	Critical aggregation concentration
γ	Strain	c^*	Overlap concentration
δ	Chemical shift	\mathcal{D}	Dispersity
$\tan \delta$	Loss factor	D	Diffusion coefficient
ε	Molar extinction coefficient	E_A	Activation energy
η	Viscosity	f	Branch functionality of cross-links
θ	Scattering angle	f_{tpy}	Molar tpy content per gram polymer
σ	Stress	G^*	Complex modulus
φ	Polymer volume fraction	G'	Elastic part of the shear modulus
Π	Osmotic pressure	G''	Viscous part of the shear modulus
λ	Wavelength	$g^{(1)}(\tau)$	First-order autocorrelation function
ν	Number concentration of elastically active strands	ΔG_{mix}	Gibbs free energy of mixing
ρ	Network mass density	G_N	Plateau module
τ	Relaxation time/ lag time	M_n	Number average of the molecular weight
τ_a	Mean complex lifetime	M_w	Weight average of the molecular weight
χ	Flory-Huggins parameter	N	Polymerization degree
ω	Angular frequency	N_x	Number of non-associating monomers between two supramolecular stickers
		J	Number of returns/Coupling constant
		k_d	Dissociation rate constant
		k_B	Boltzmann constant
		K	Equilibrium binding constant
		M_x	Average molar mass of the networks strand between two cross-links
		n	Amount of substance
		N_A	Avogadro constant
		q	Scattering vector
		Q	Swelling degree
		R	Universal gas constant
		R_h	Hydrodynamic radius
		R_G	Gyration radius
		T	Temperature
		T_g	Glass transition temperature
		T_m	Melting temperature

APPENDIX

A.3 Supplementary Information Chapter 3

Compound 3.2

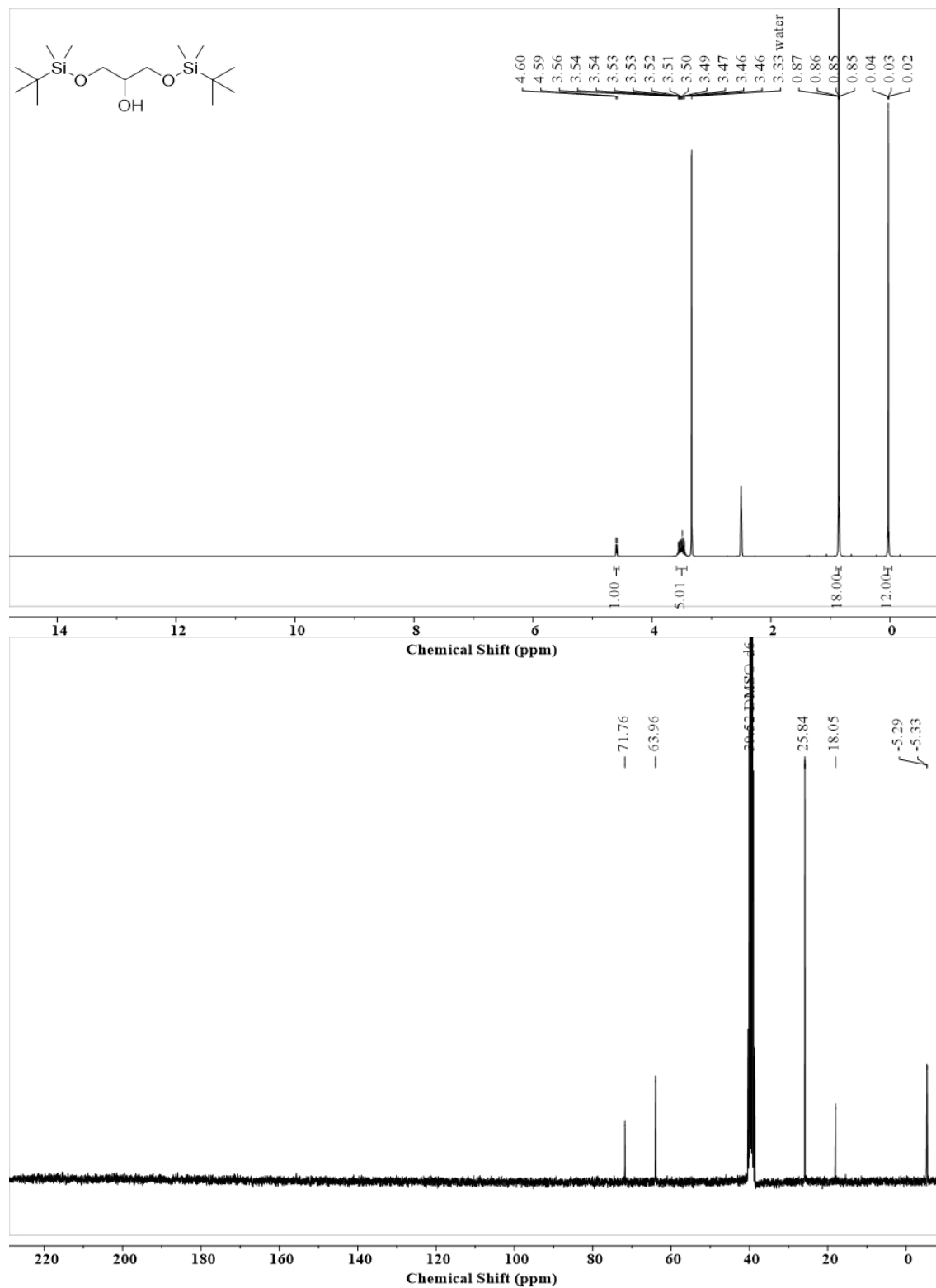
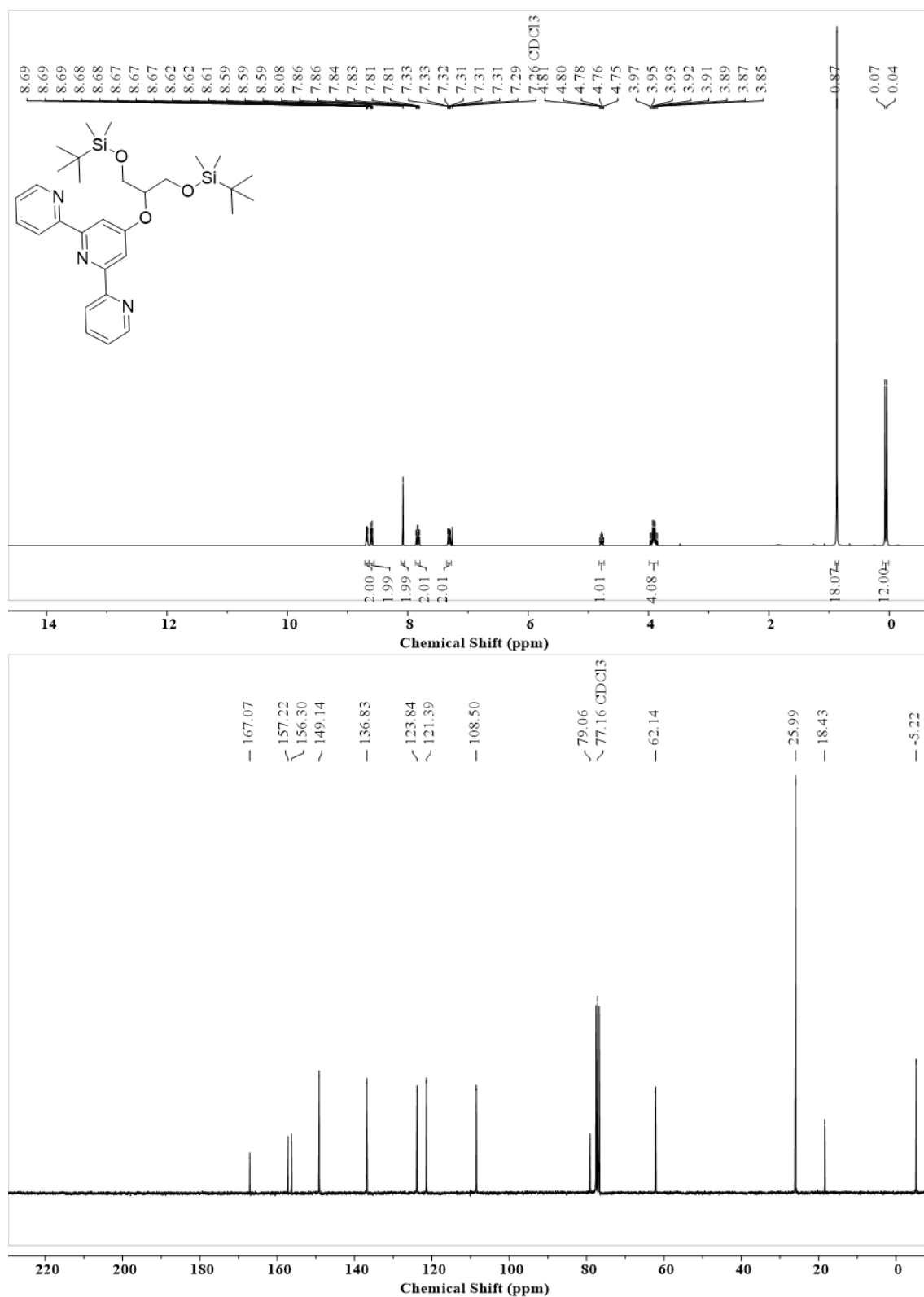
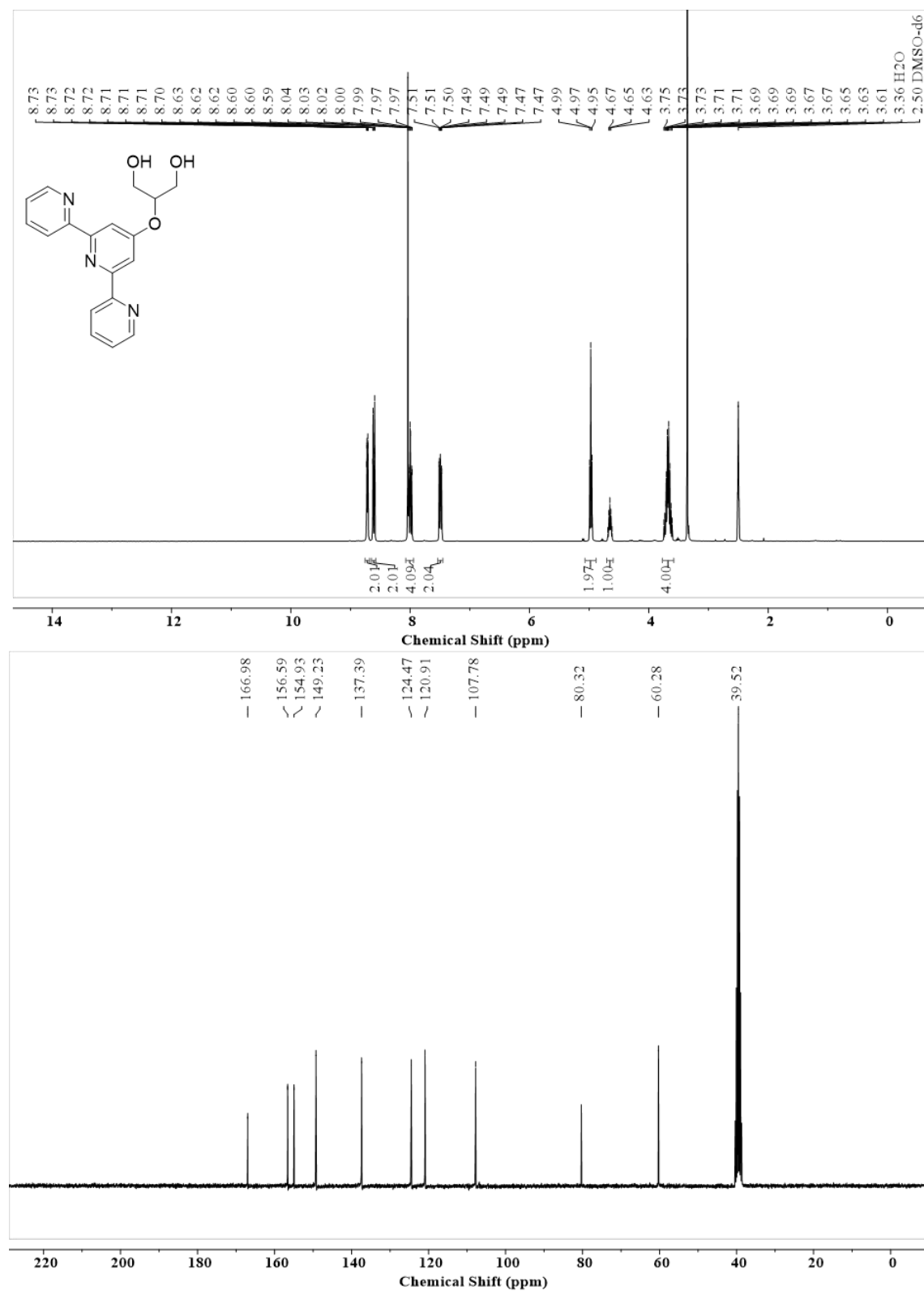


Figure S3.1. ¹H- and ¹³C-NMR of compound 3.2 (300 MHz, 75MHz, DMSO-*d*₆).

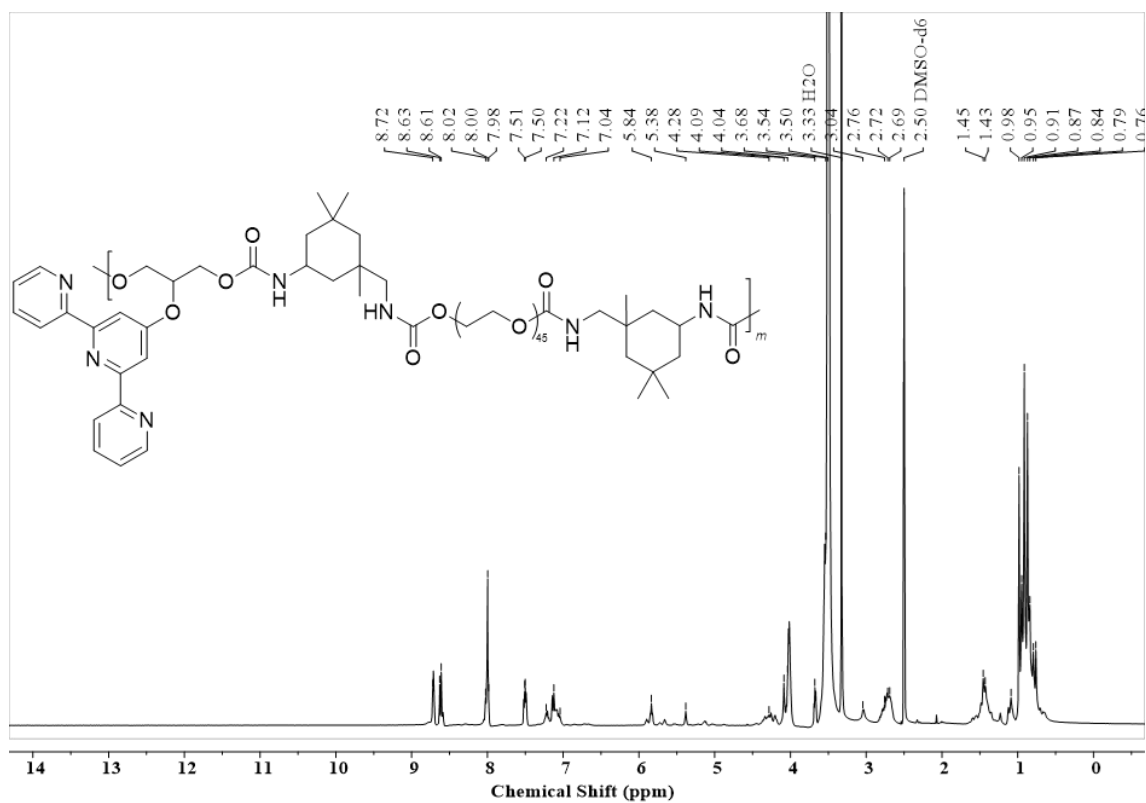
Compound 3.2a

Figure S3.2. ¹H- and ¹³C-NMR of compound 3.2a (300 MHz, 75 MHz, CDCl₃).

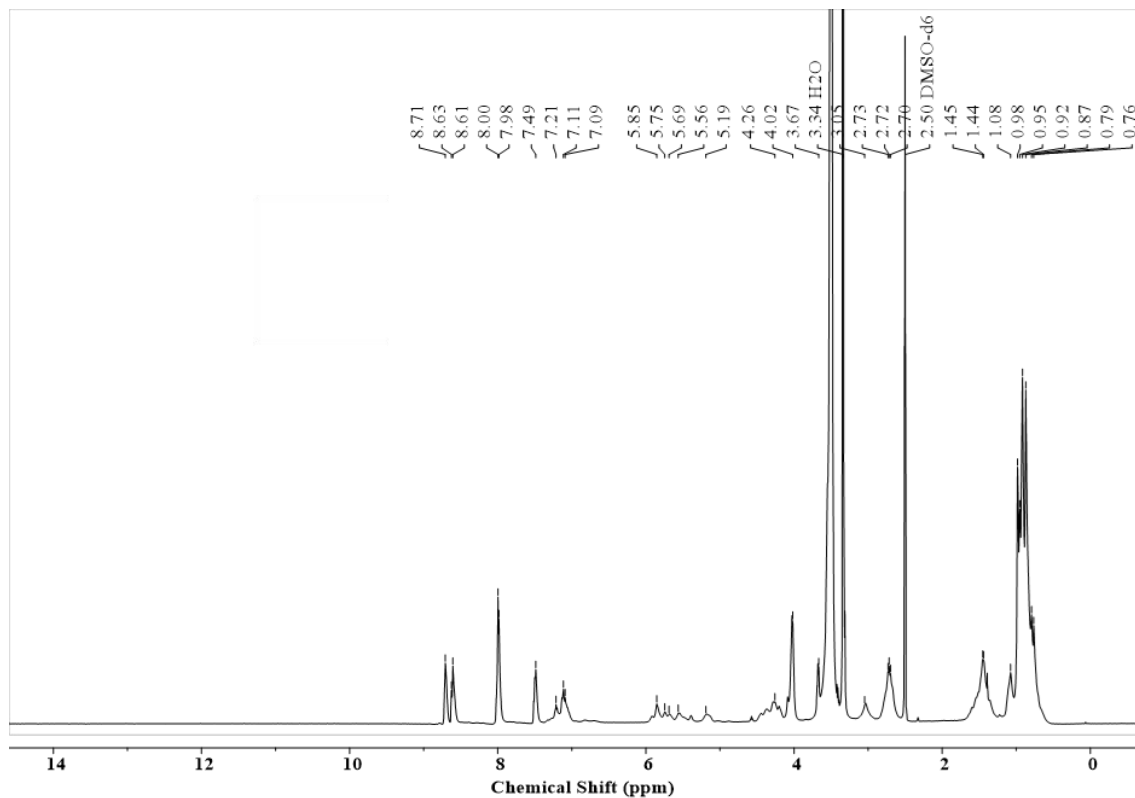
Compound 3.4

Figure S3.3. ^1H - and ^{13}C -NMR of compound 3.4 (300 MHz, 75 MHz, DMSO- d_6).

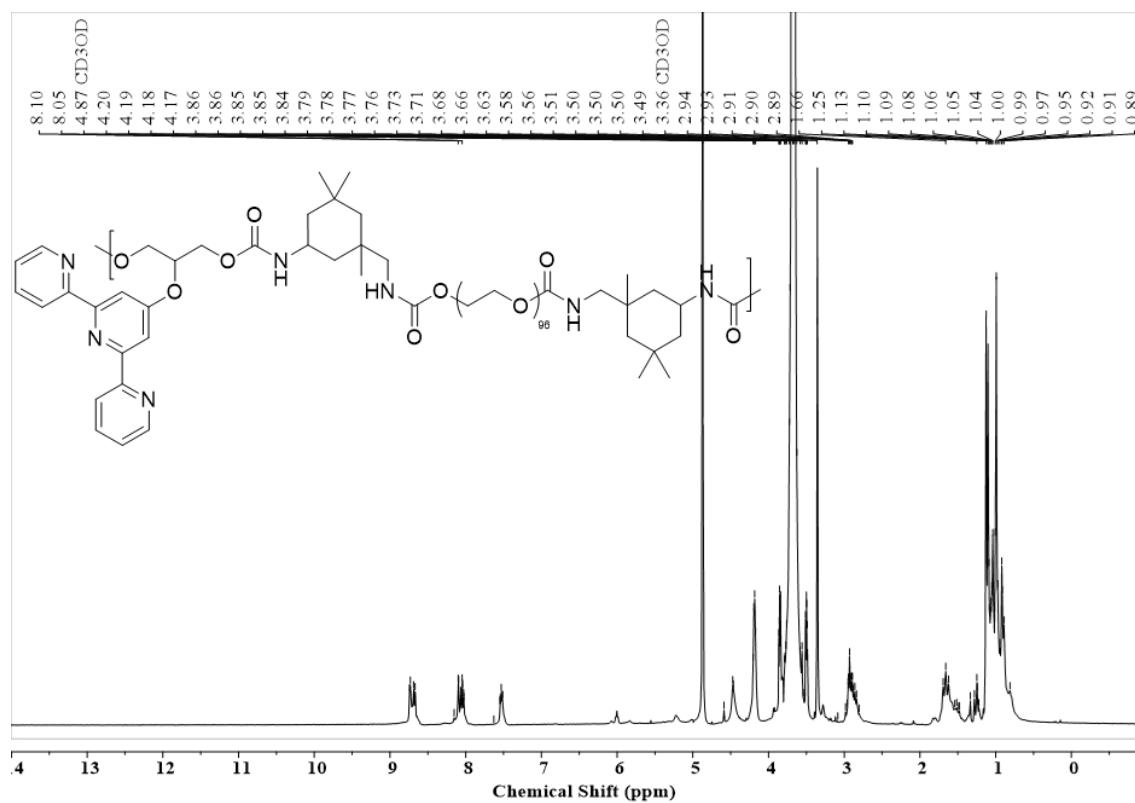
PU_2k-alt

Figure S3.4. ¹H-NMR of PU_2k-alt (400 MHz, DMSO-*d*₆).

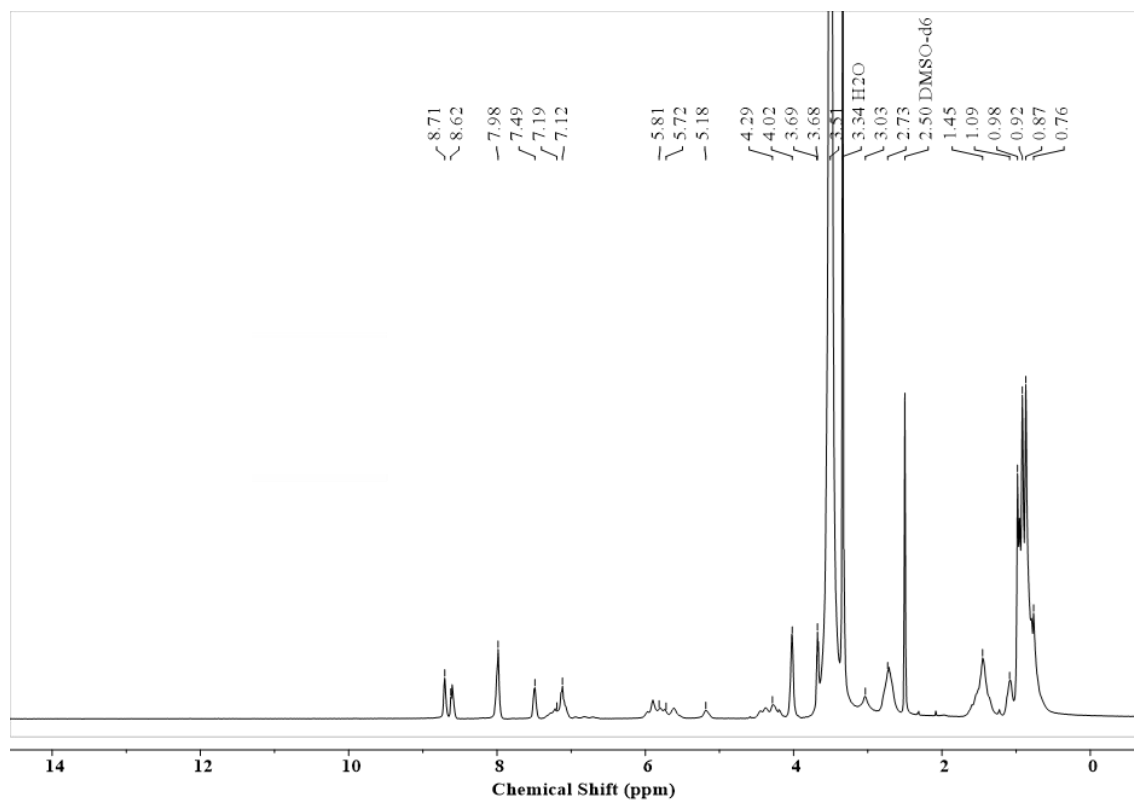
PU_2k-ran

Figure S3.5. ¹H-NMR of PU_2k-ran (400 MHz, DMSO-*d*₆).

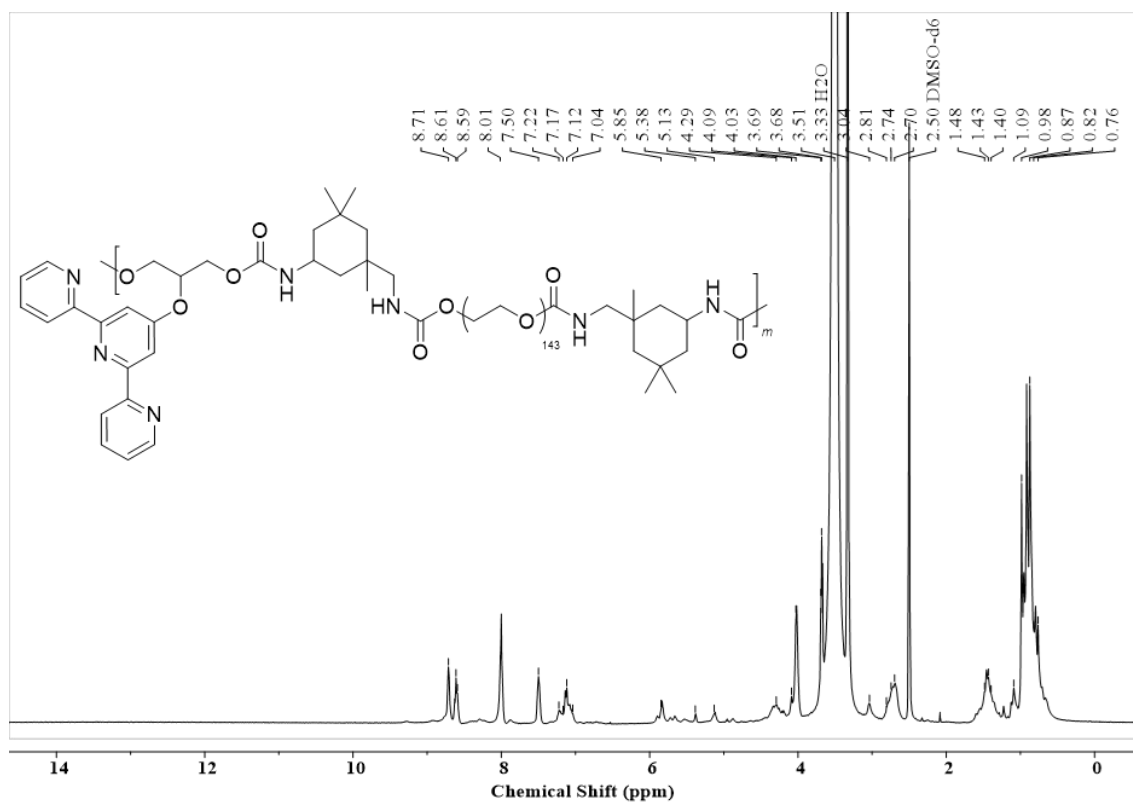
PU_4k-alt

Figure S3.6. $^1\text{H-NMR}$ of PU-alt (400 MHz, MeOD).

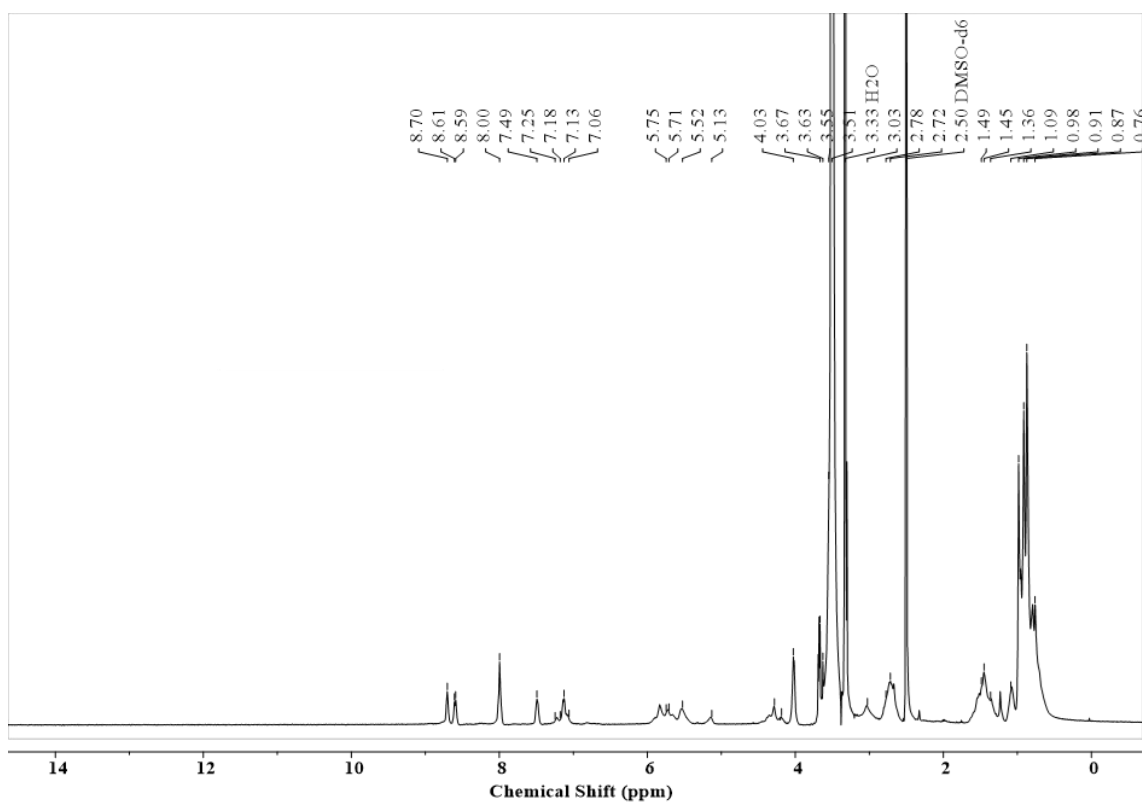
PU_4k-ran

Figure S3.7. $^1\text{H-NMR}$ of PU_4k-ran (400 MHz, DMSO- d_6).

PU_6k-alt

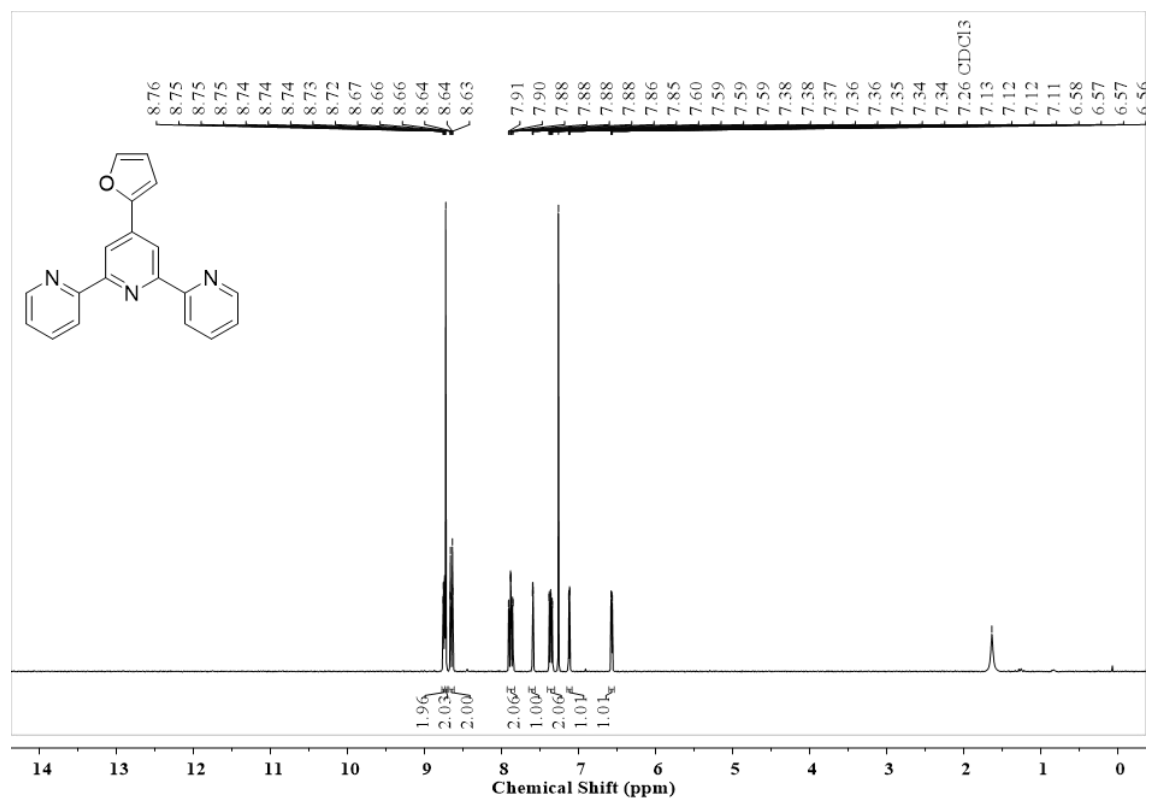
Figure S3.8. $^1\text{H-NMR}$ of PU_6k-alt (400 MHz, $\text{DMSO-}d_6$).

PU_6k-ran

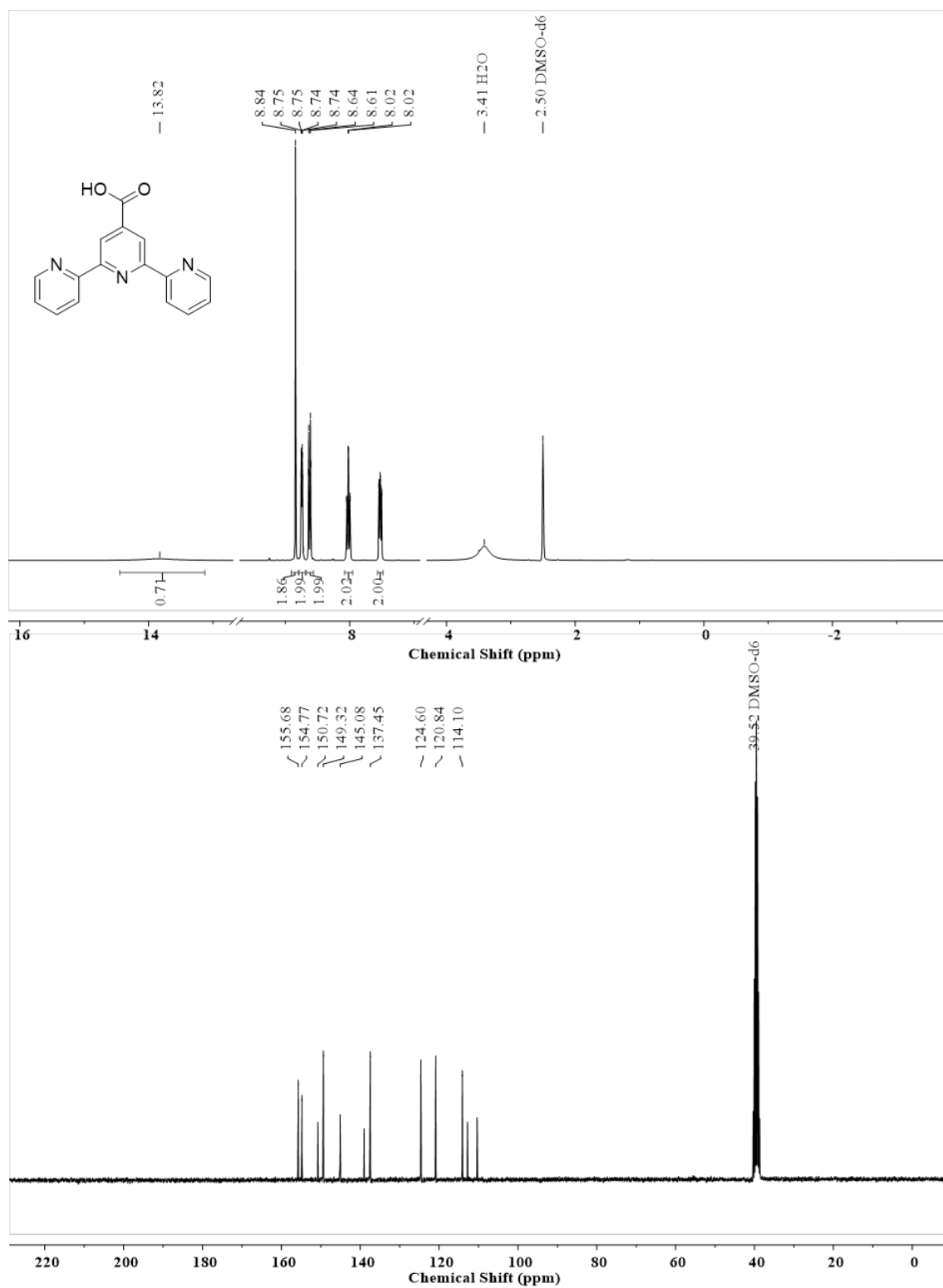
Figure S3.9. $^1\text{H-NMR}$ of PU_6k-ran (400 MHz, $\text{DMSO-}d_6$).

A.4 Supplementary Information Chapter 4

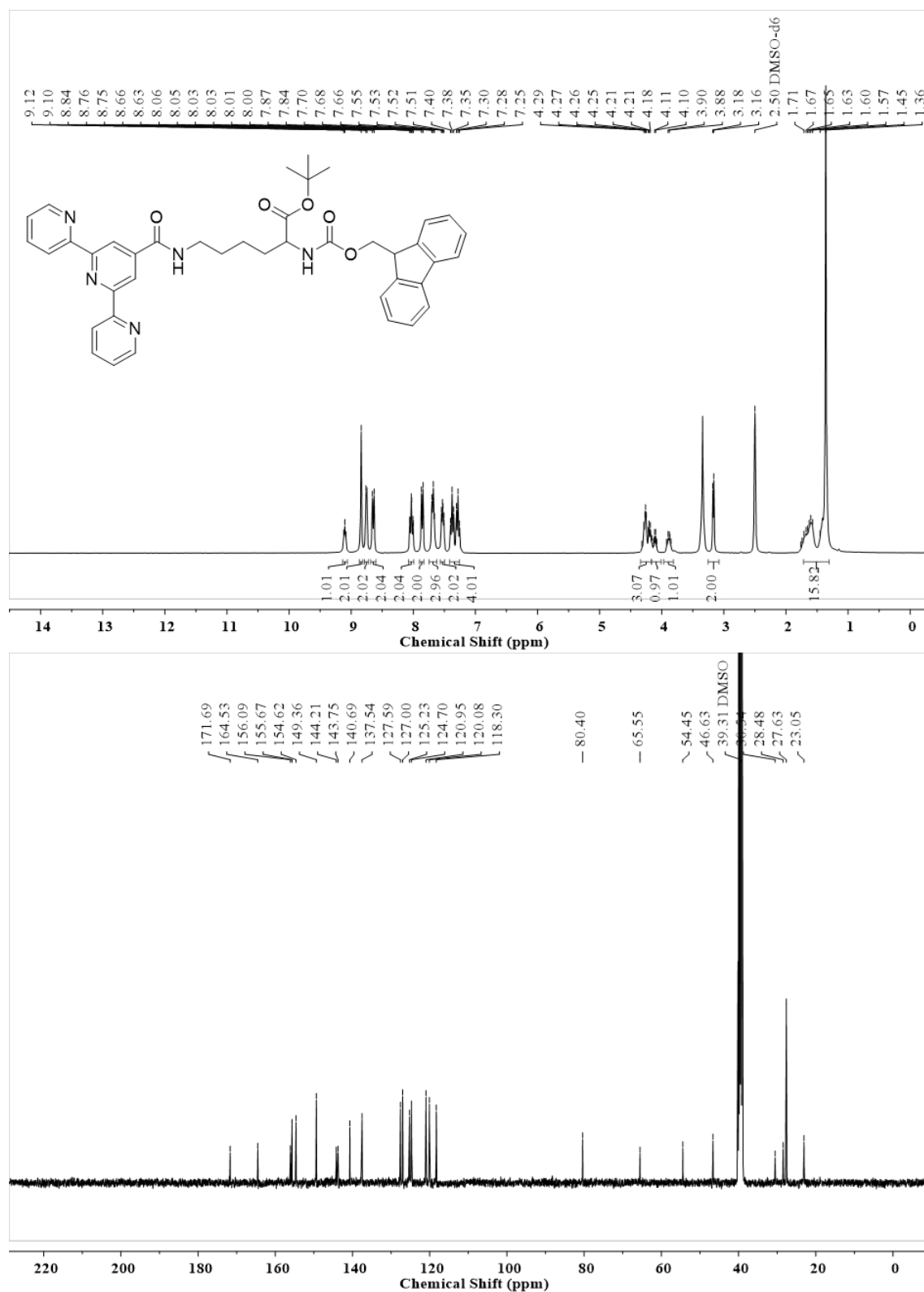
Compound 4.27

Figure S4.1. ¹H NMR of compound 4.27 (300 MHz, CDCl₃).

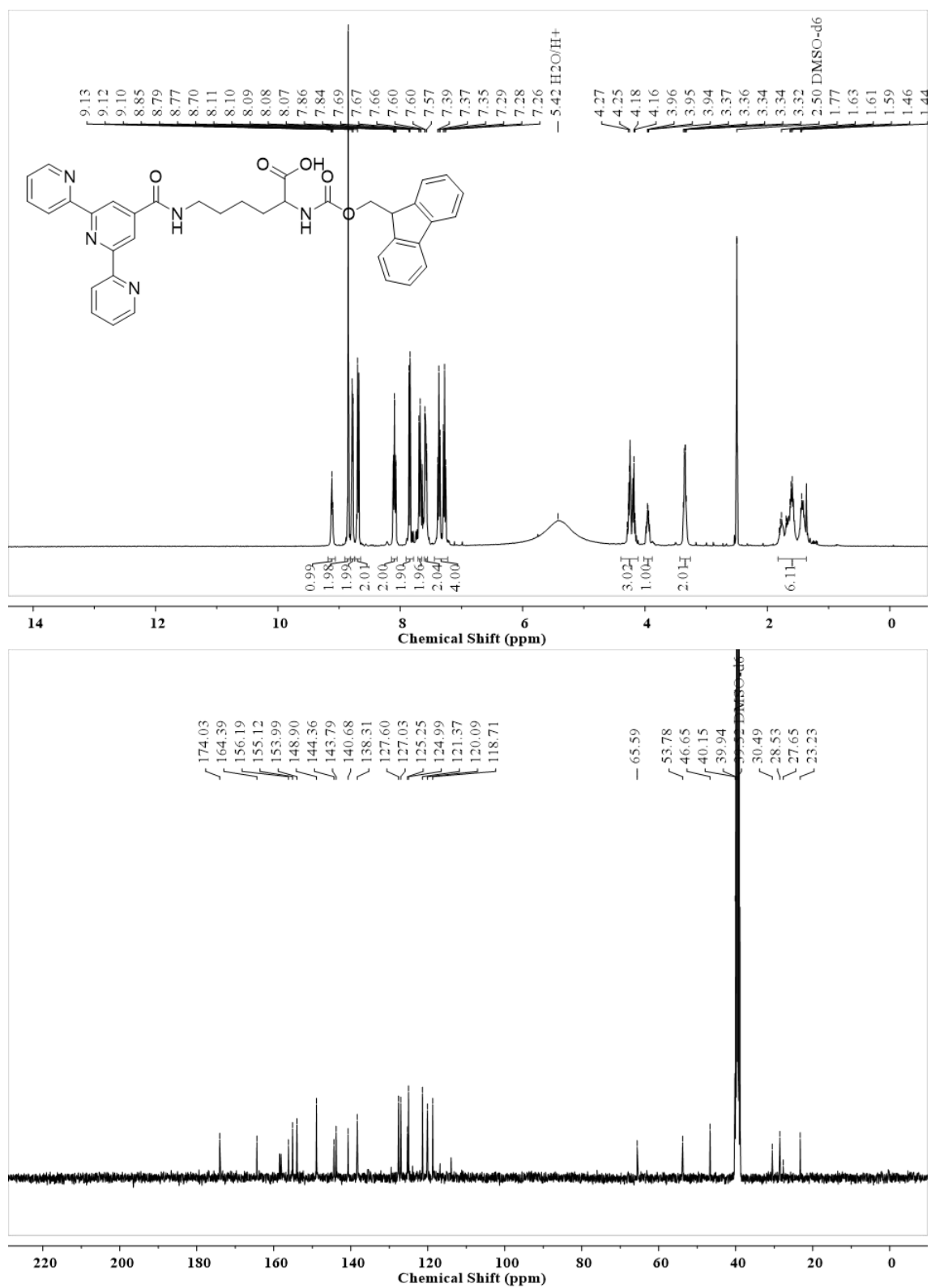
Compound 4.1

Figure S4.2. ¹H and ¹³C NMR of compound 4.1 (300 MHz, 75 MHz, DMSO-*d*₆).

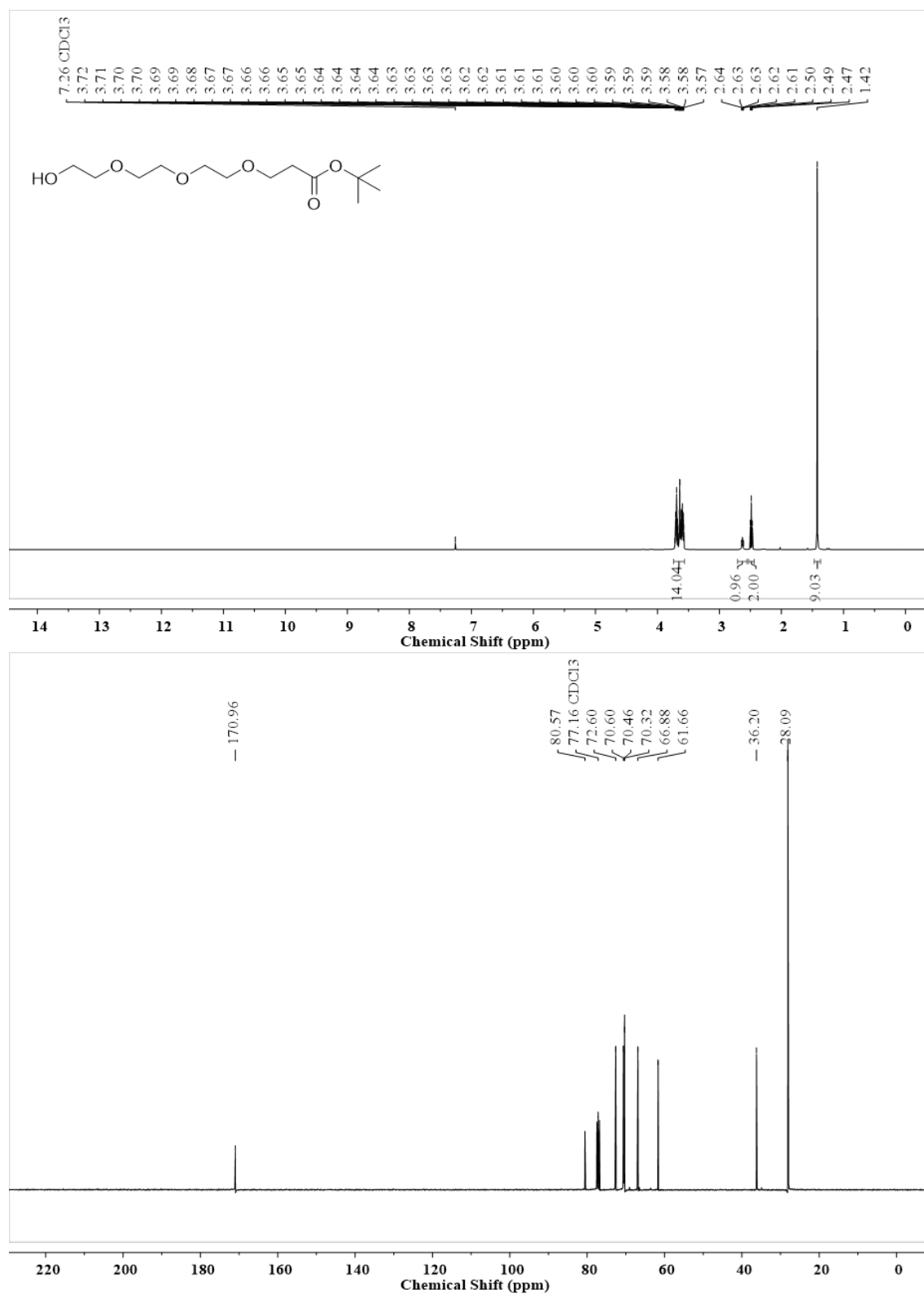
Compound 4.10

Figure S4.3. ^1H and ^{13}C NMR of compound 4.10 (400 MHz, 101 MHz, $\text{DMSO-}d_6$).

Compound 4.3

Figure S4.4. ^1H and ^{13}C NMR of compound 4.3 (400 MHz, 101 MHz, $\text{DMSO-}d_6$).

Compound 4.13

Figure S4.5. ¹H and ¹³C NMR of compound 4.13 (300 MHz, 75 MHz, DMSO-*d*₆).

Compound 4.14

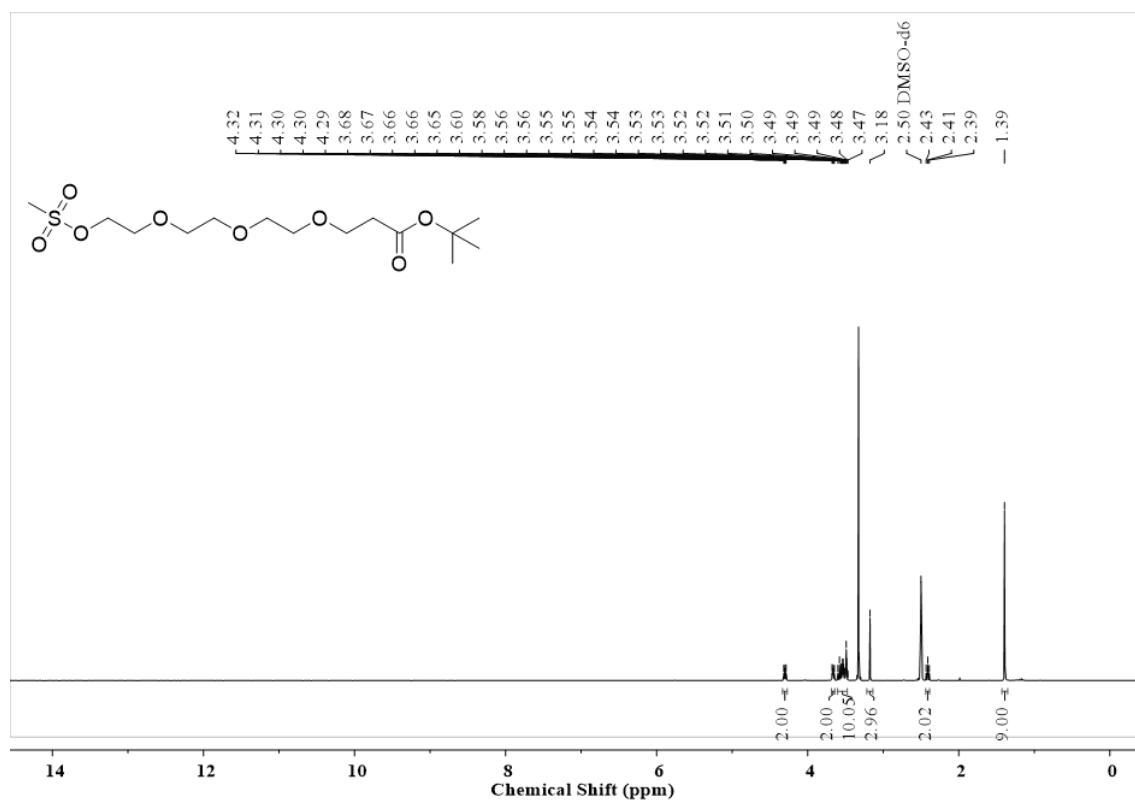
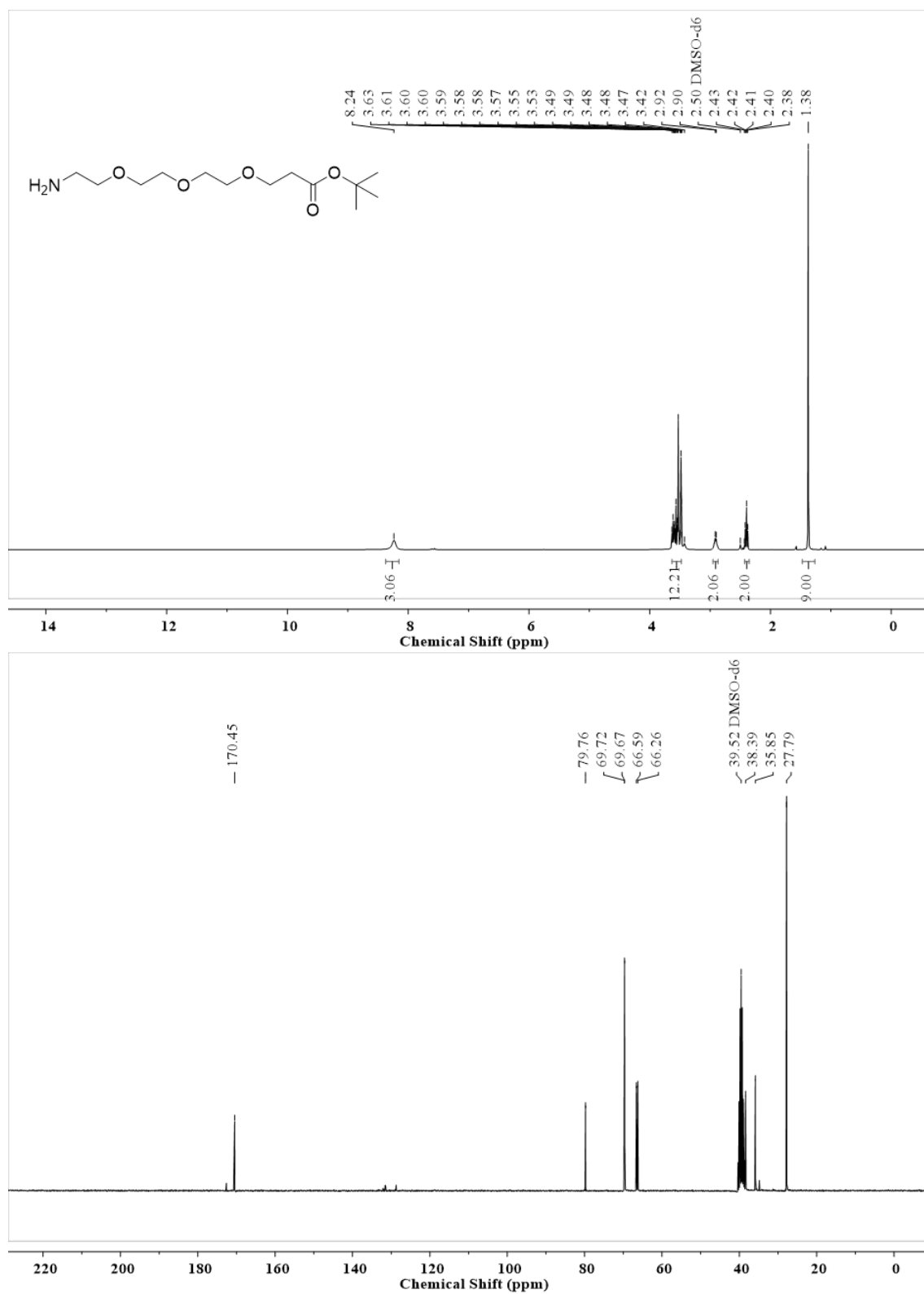
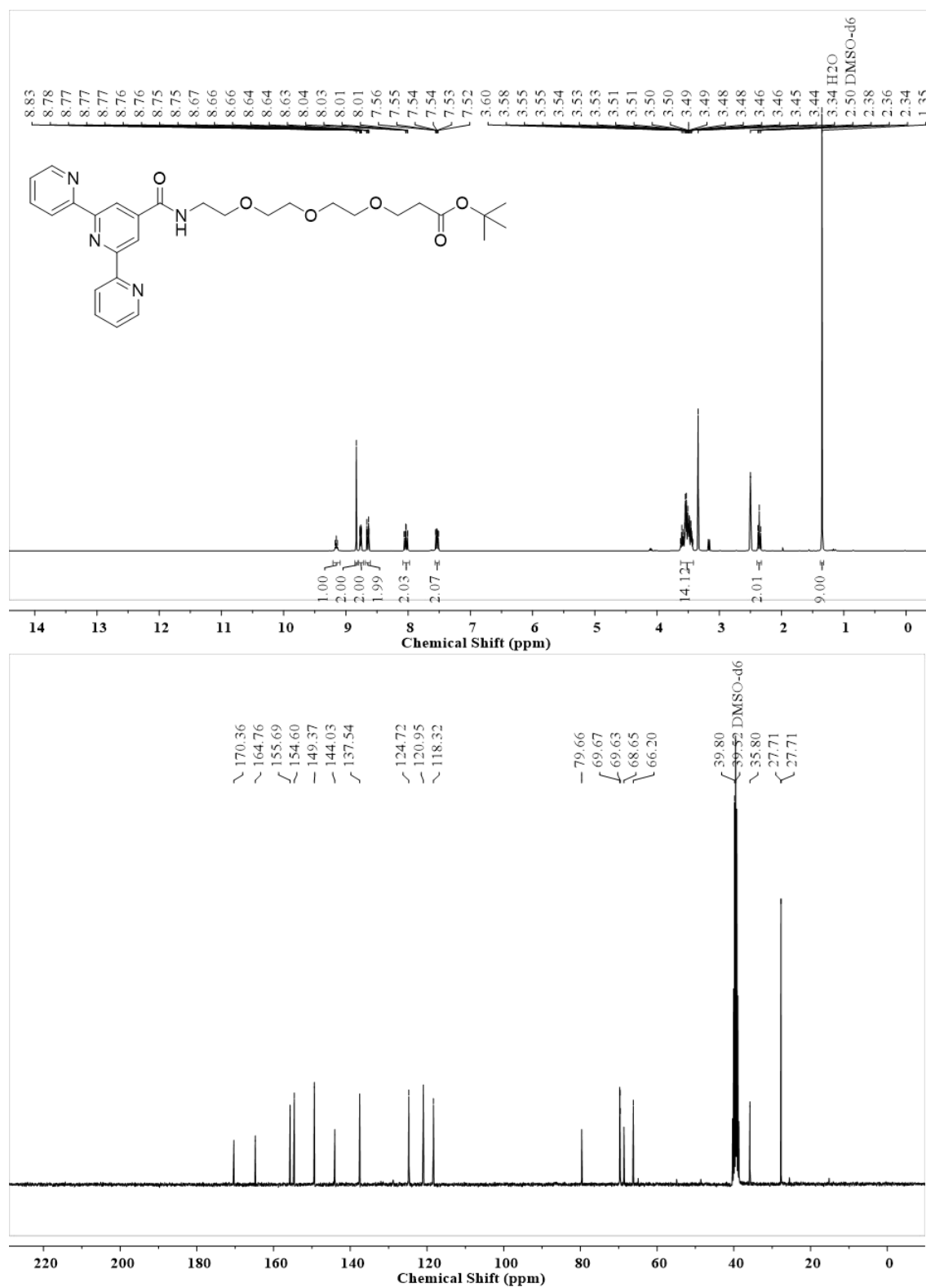


Figure S4.6. ¹H NMR of compound 4.14 (300 MHz, DMSO-*d*₆).

Compound 4.4

Figure S4.8. ¹H and ¹³C NMR of compound 4.4 (300 MHz, 75 MHz, DMSO-*d*₆).

Compound 4.16

Figure S4.9. ¹H and ¹³C NMR of compound 4.16 (300 MHz, 75 MHz, DMSO-d₆).

Compound 4.5

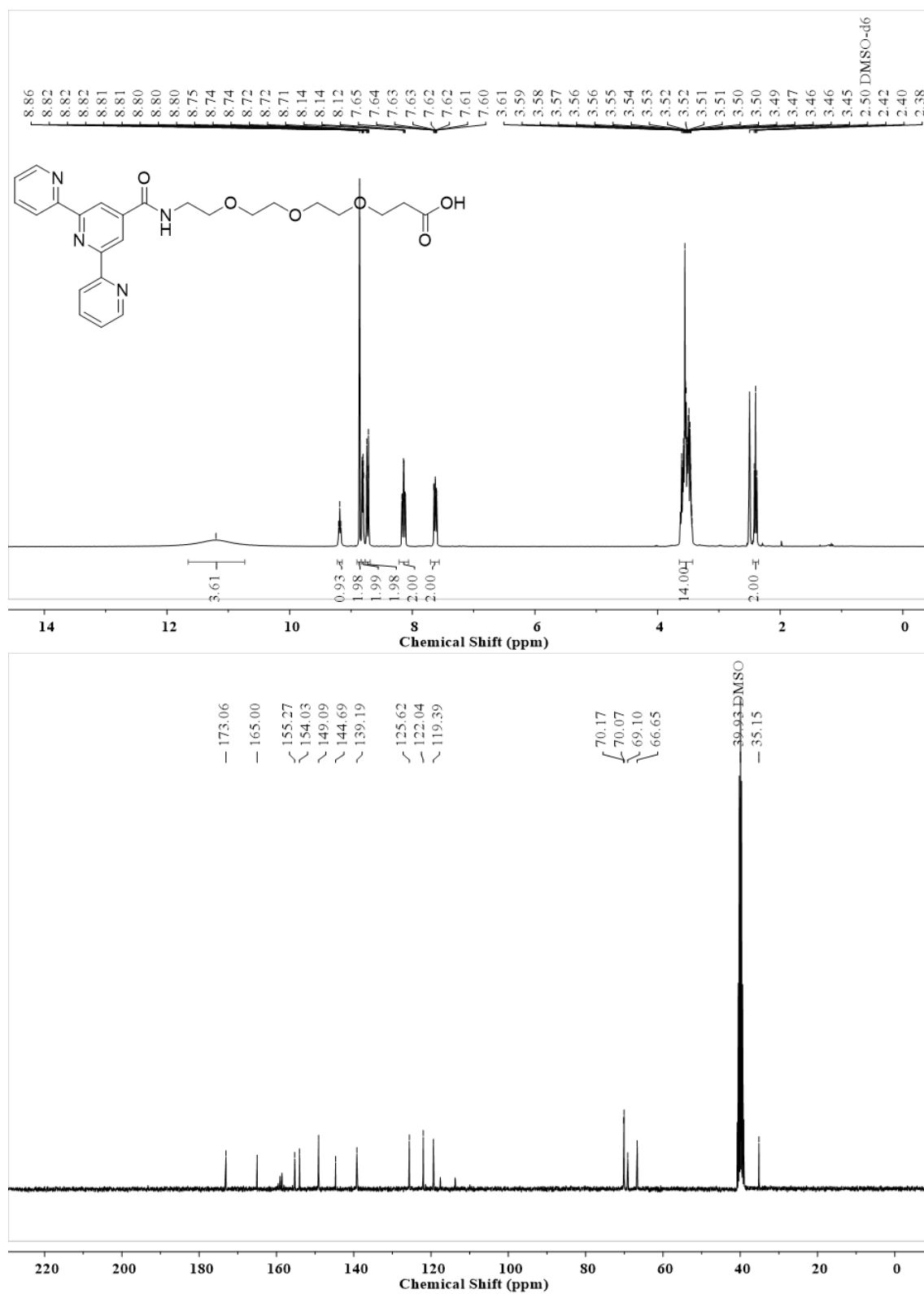
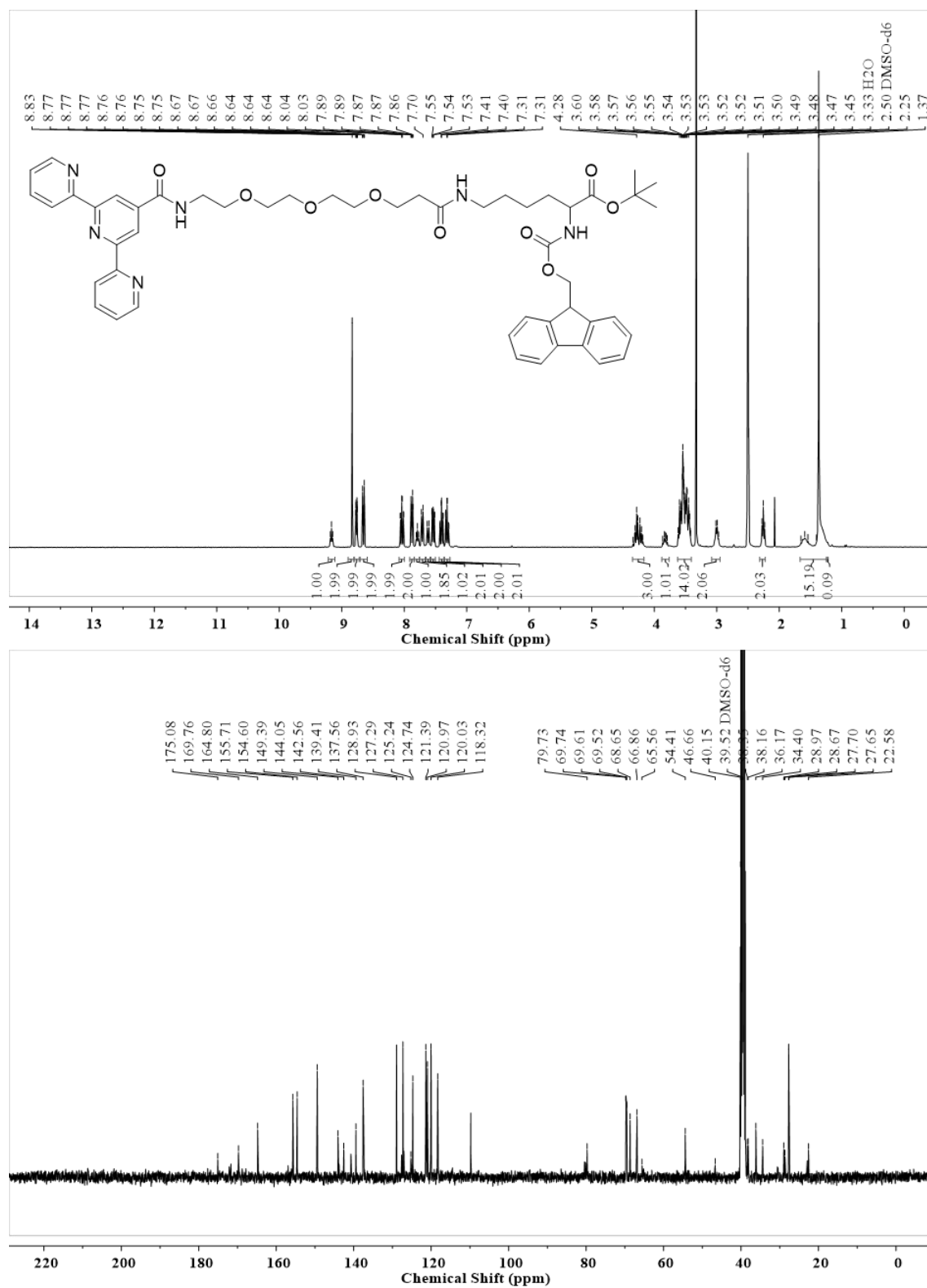
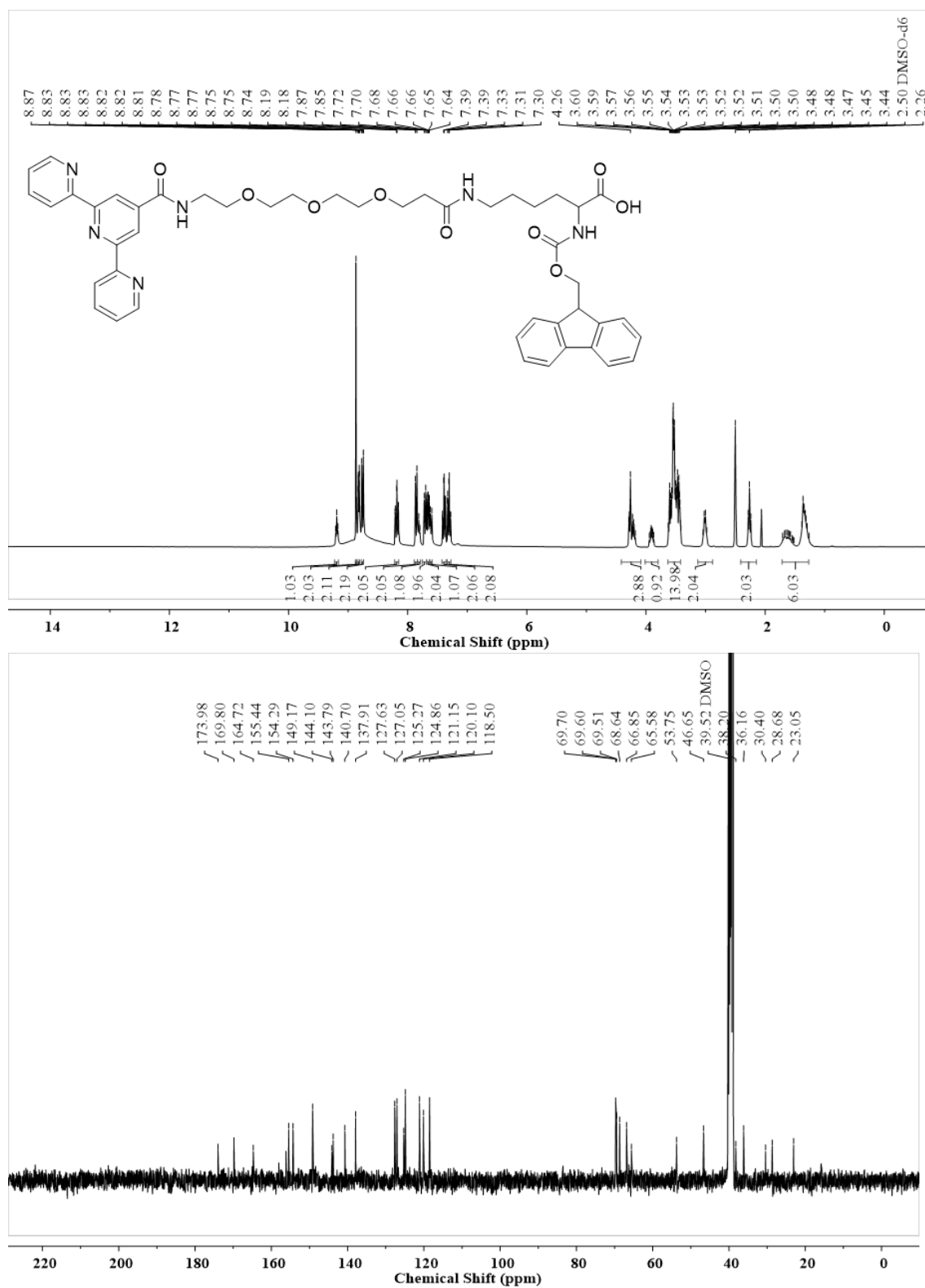


Figure S4.10. ^1H and ^{13}C NMR of compound 4.5 (300 MHz, 75 MHz, DMSO- d_6).

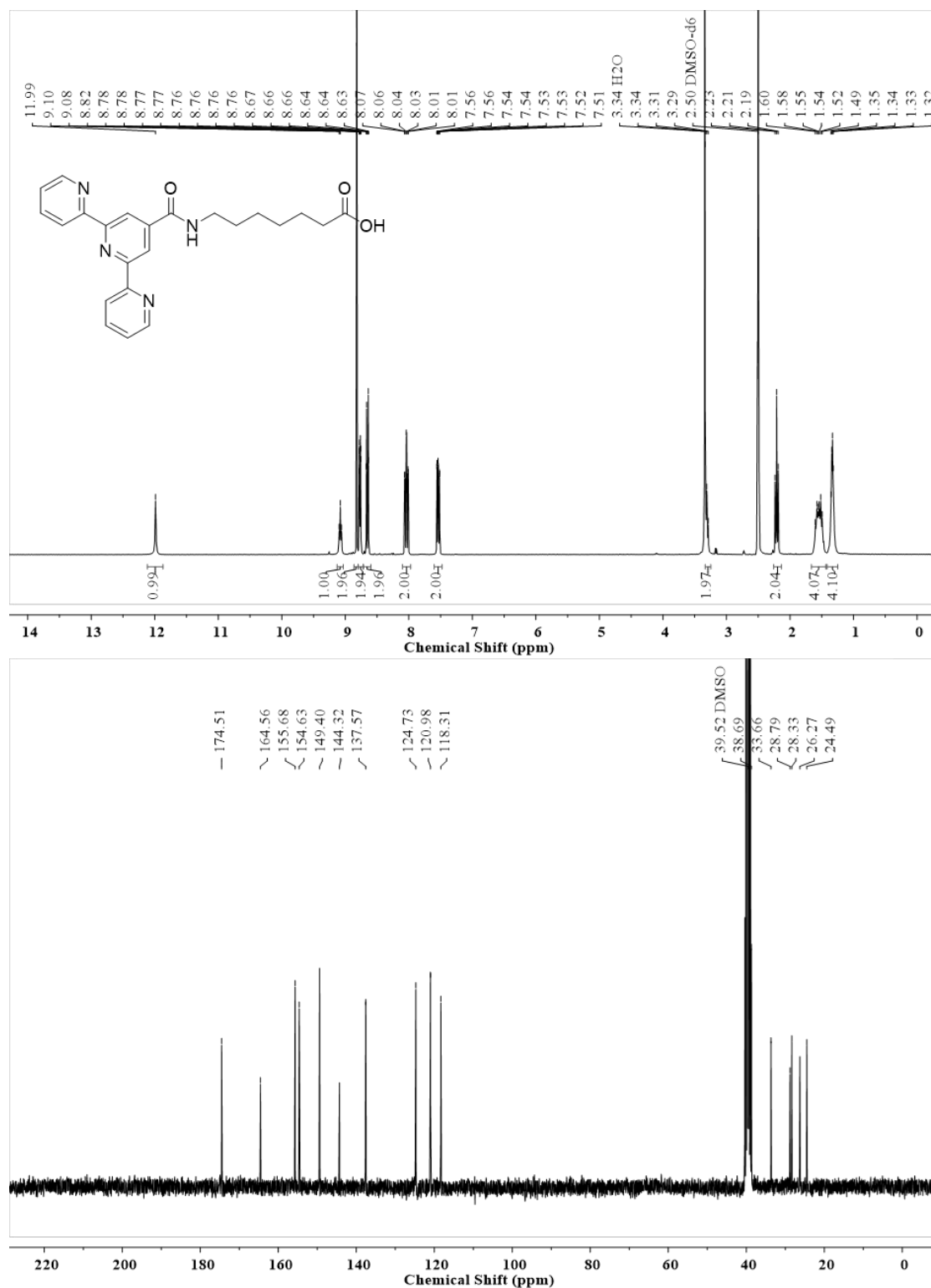
Compound 4.17

Figure S4.11. ^1H and ^{13}C NMR of compound 4.17 (300 MHz, 75 MHz, $\text{DMSO-}d_6$).

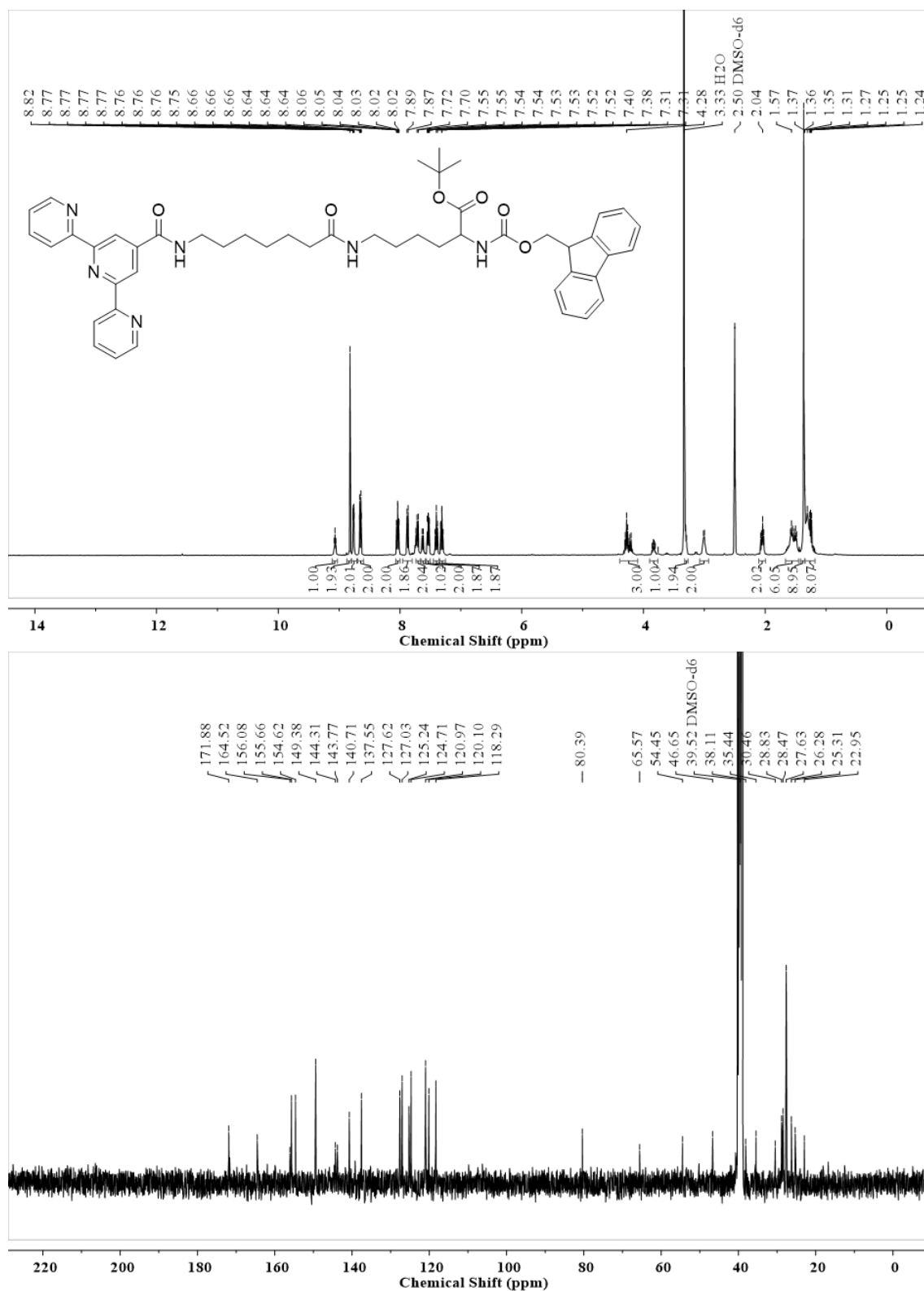
Compound 4.6

Figure S4.12. ^1H and ^{13}C NMR of compound 4.6 (400 MHz, 101 MHz, DMSO- d_6).

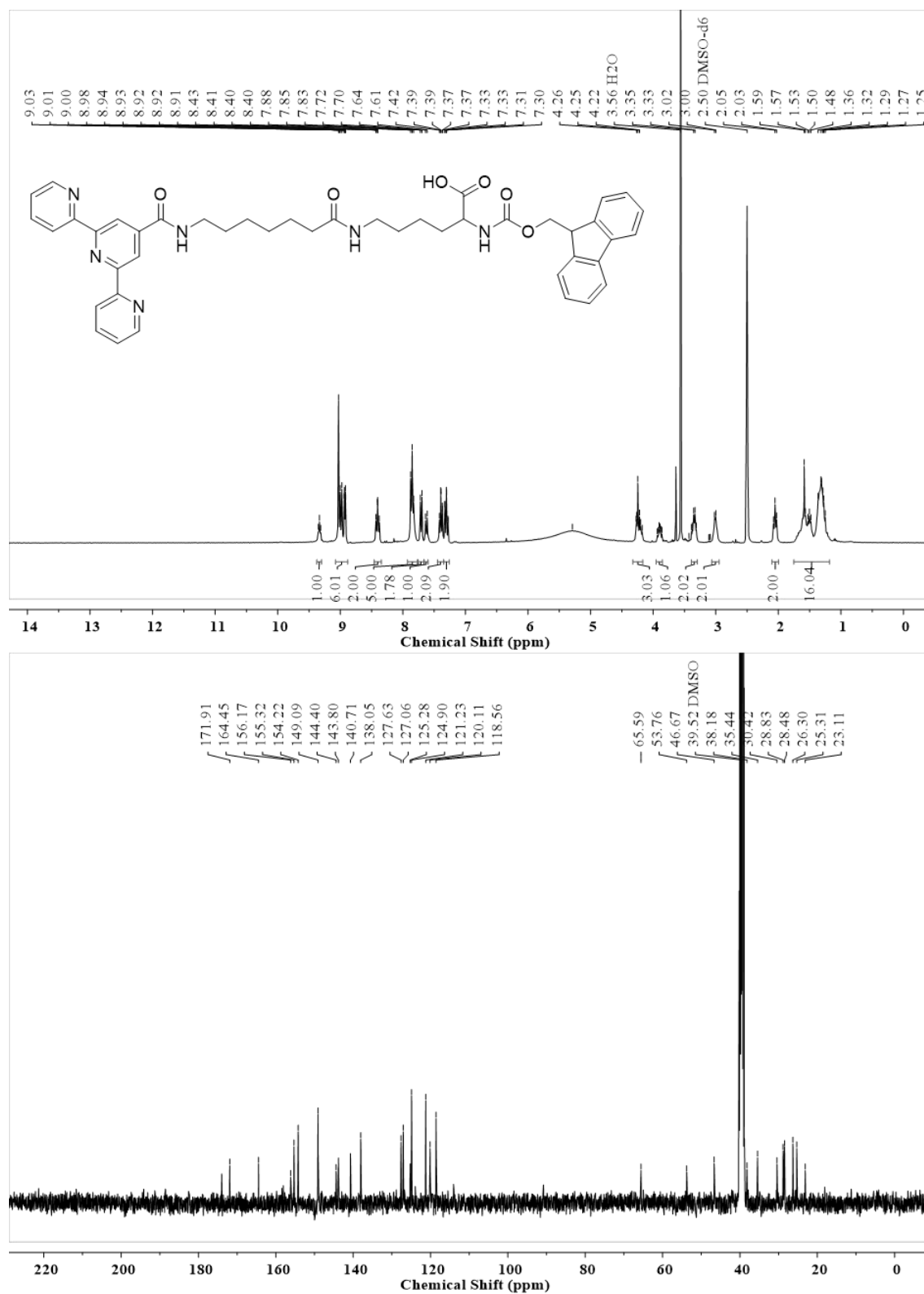
Compound 4.8

Figure S4.13. ¹H and ¹³C NMR of compound 4.8 (400 MHz, 101 MHz, DMSO-*d*₆).

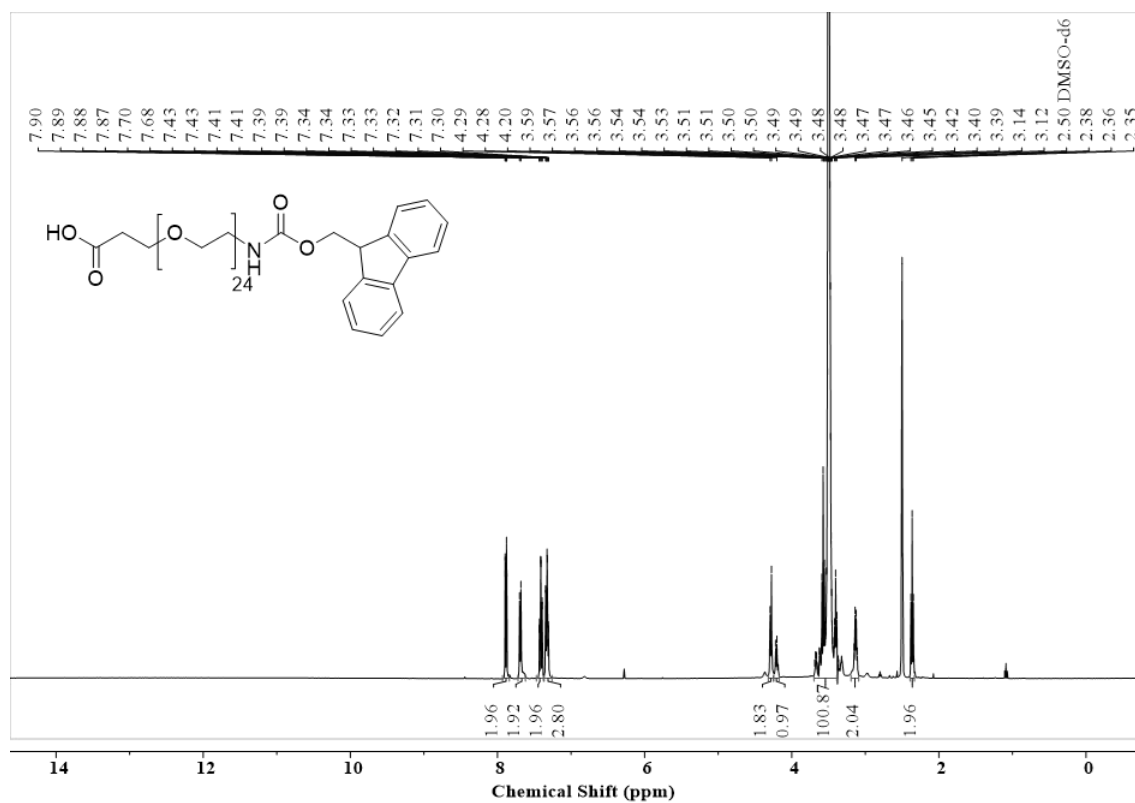
Compound 4.18

Figure S4.14. ^1H and ^{13}C NMR of compound 4.18 (400 MHz, 101 MHz, $\text{DMSO-}d_6$).

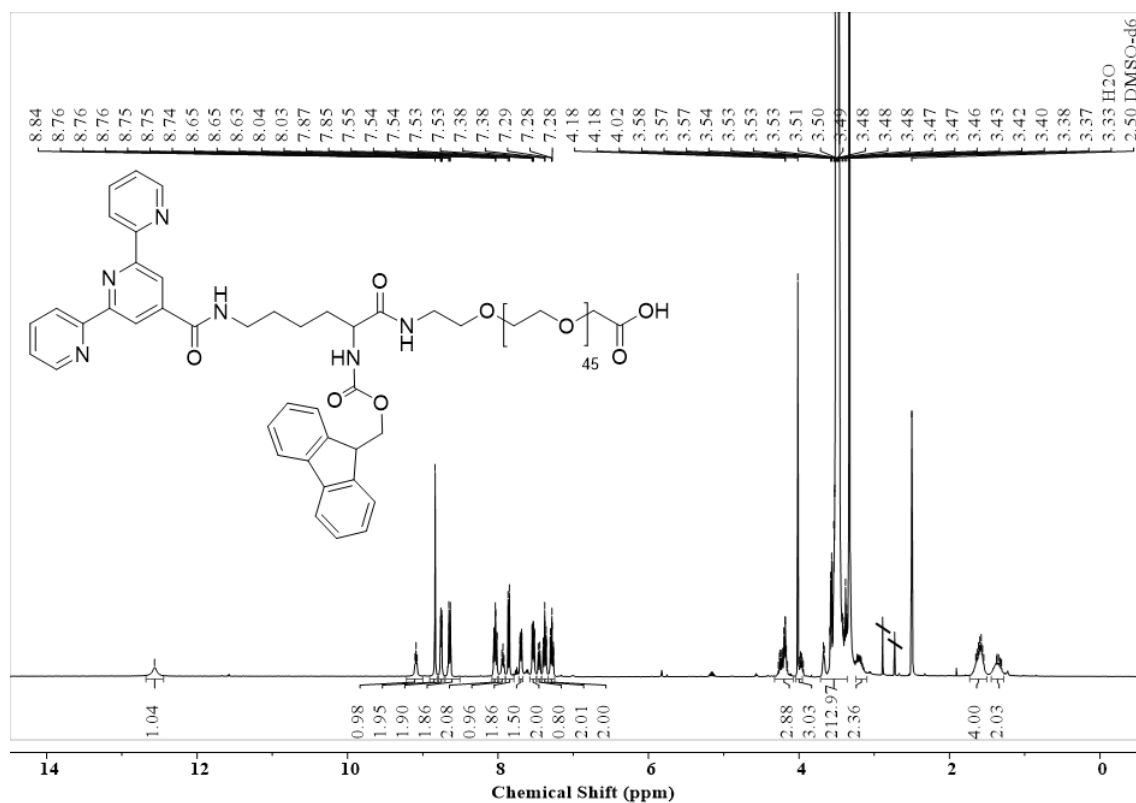
Compound 4.9

Figure S4.15. ^1H and ^{13}C NMR of compound 4.9 (400 MHz, 101 MHz, DMSO- d_6).

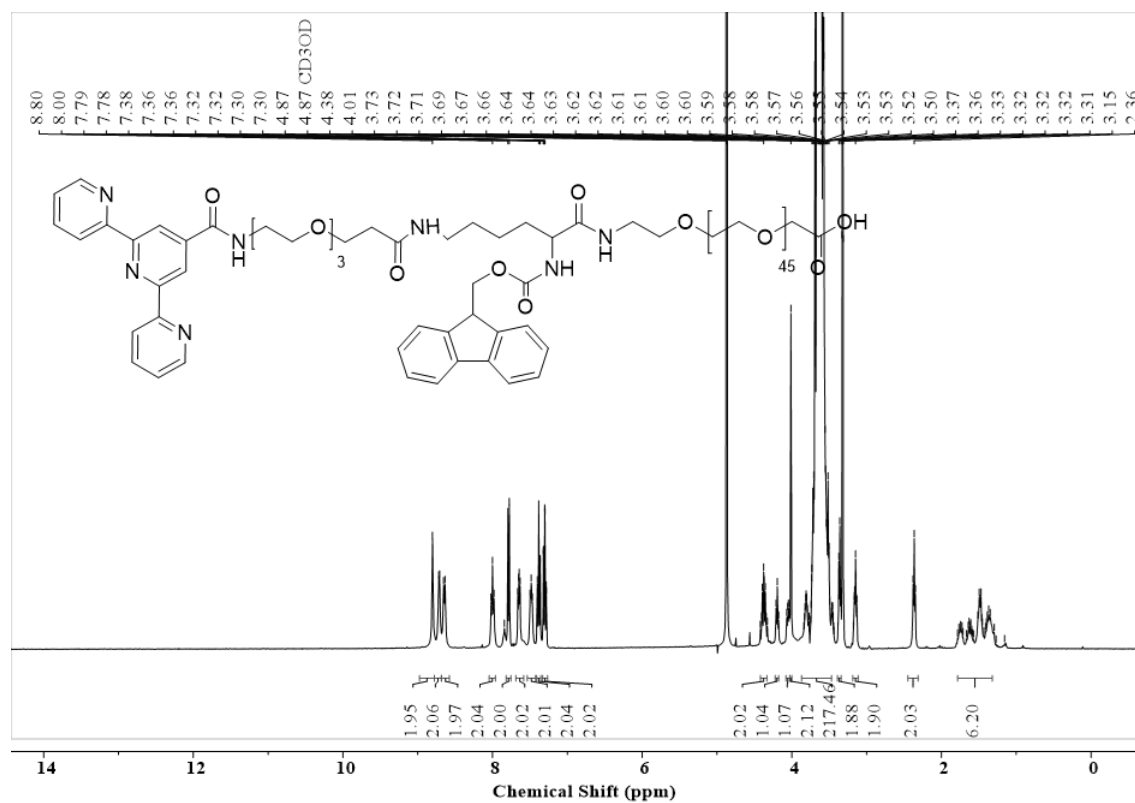
Compound 4.19



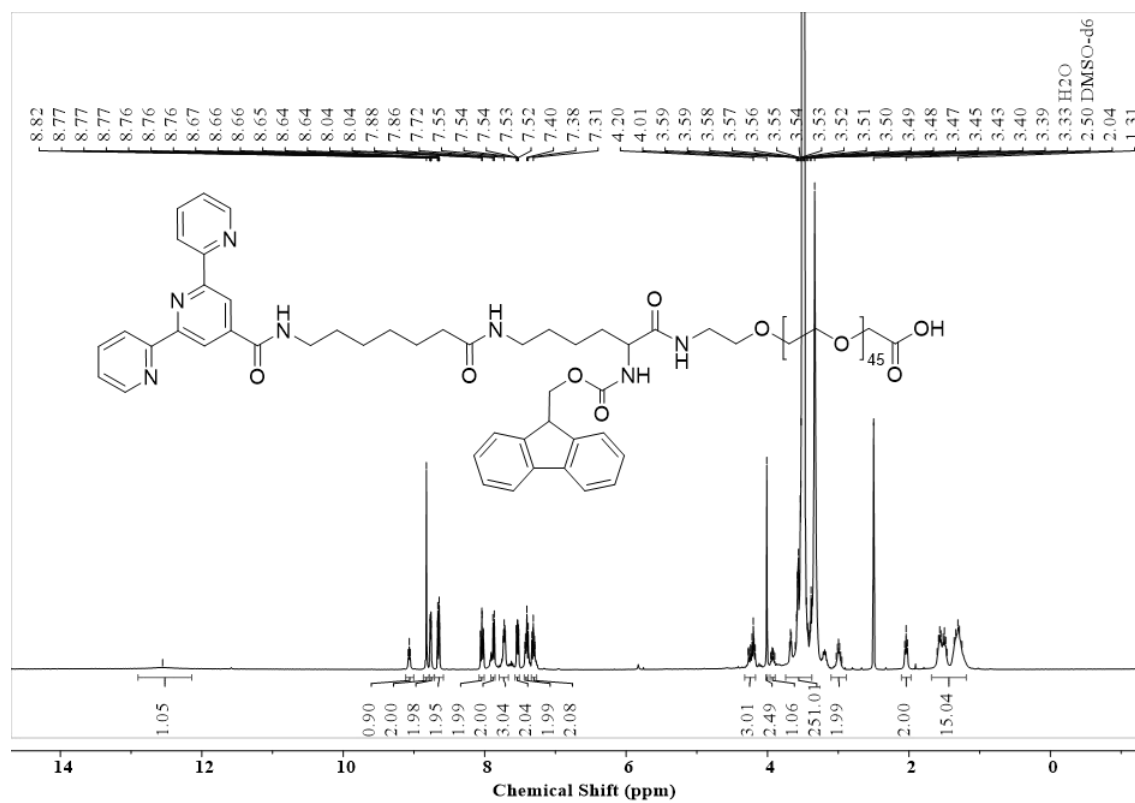
Compound 4.21



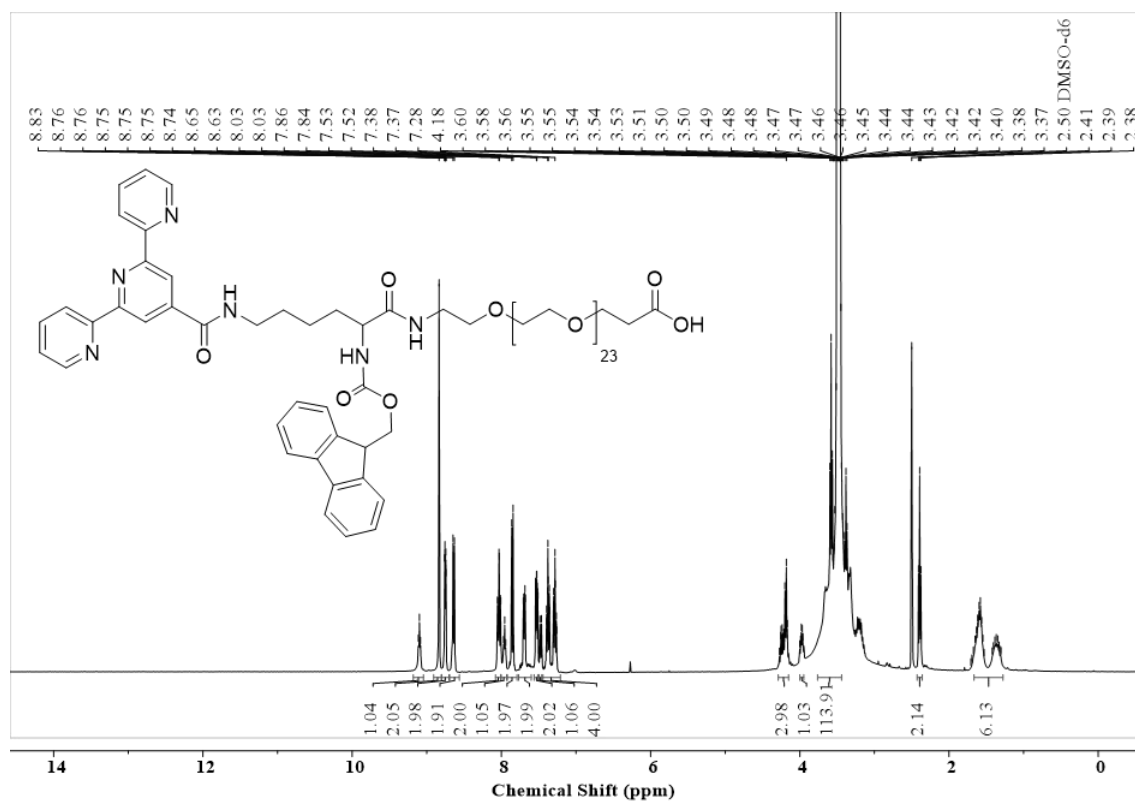
Compound 4.23

Figure S4.18. ^1H NMR of compound **4.23** (400 MHz, MeOD).

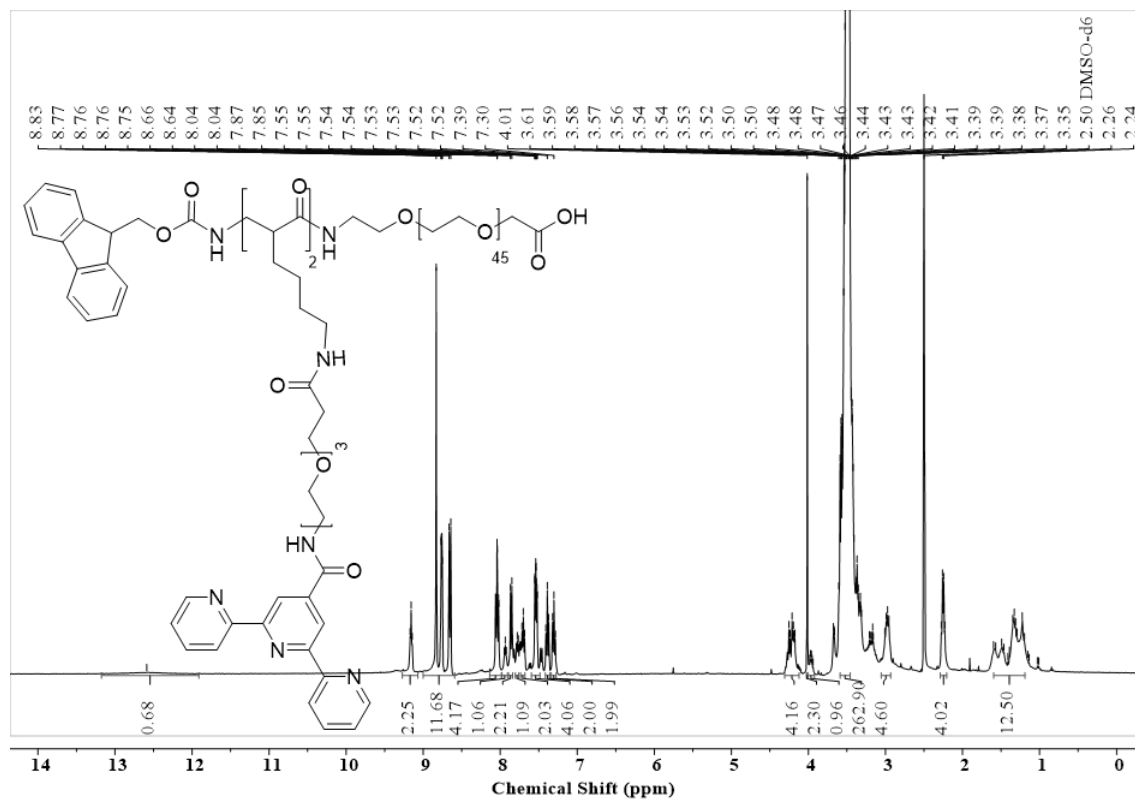
Compound 4.26

Figure S4.19. ^1H NMR of compound **4.26** (400 MHz, DMSO- d_6).

Compound 4.22

Figure S4.20. ^1H NMR of compound 4.22 (400 MHz, $\text{DMSO-}d_6$).

Compound 4.24

Figure S4.21. ^1H NMR of compound 4.24 (400 MHz, $\text{DMSO-}d_6$).

A.5 Supplementary Information Chapter 5

Mono terpyridine amine 5.3

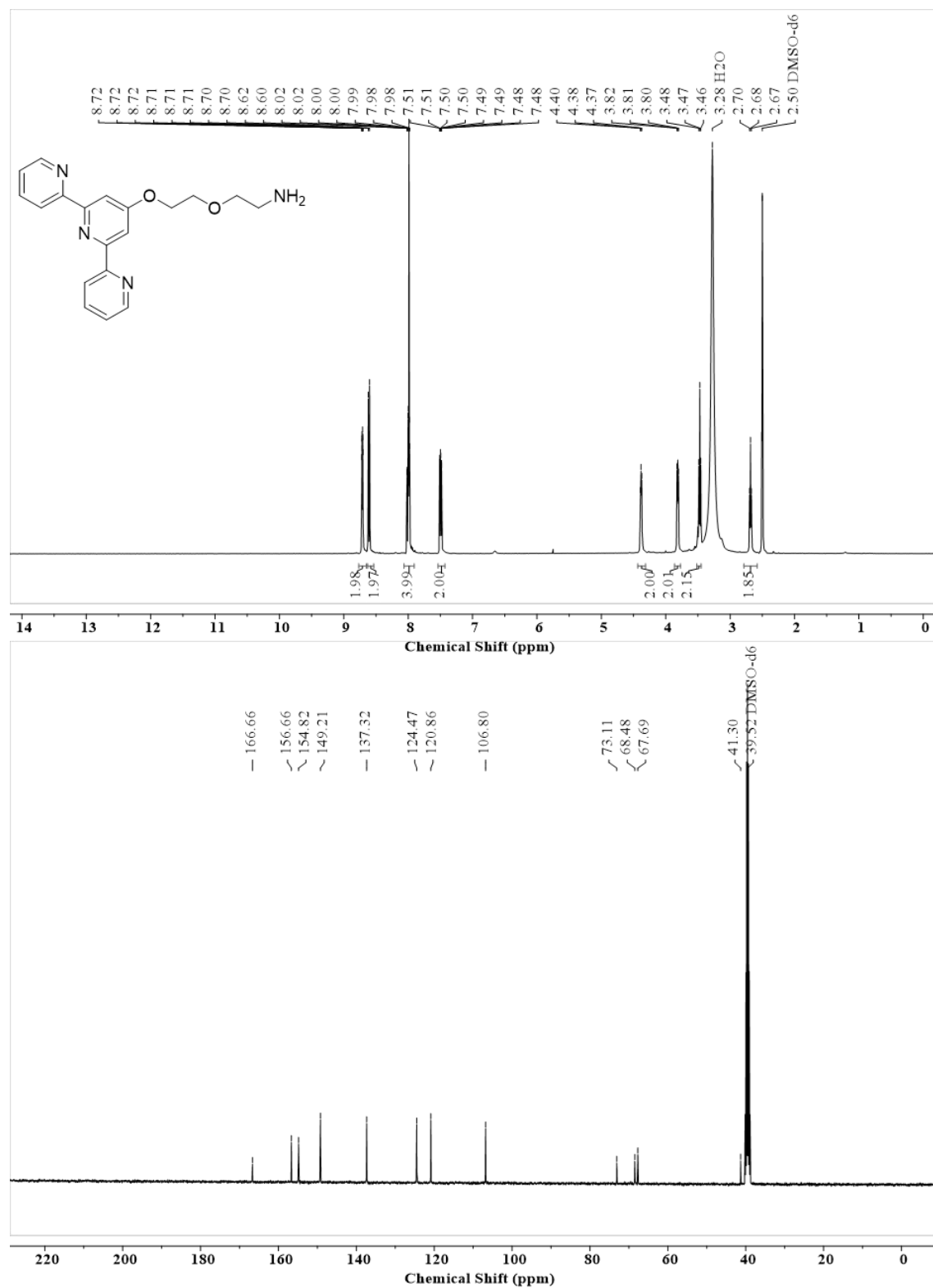


Figure S5.1. ¹H- and ¹³C-NMR of mono-terpyridine amine 5.3 (400 MHz, 100.1 MHz, DMSO-*d*₆).

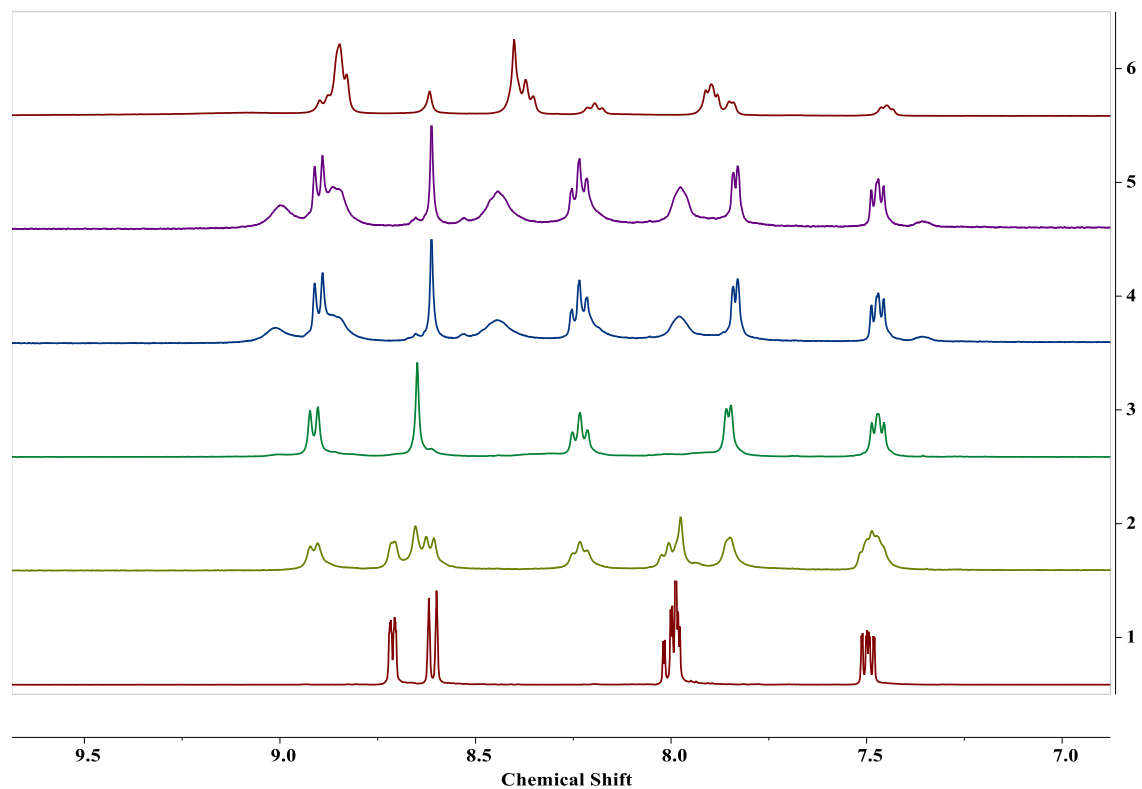


Figure S5.2. ¹H-NMR of mono-tpy amine **5.3** with 0 (#1), 0.25 (#2), 0.5 (#3), 1 (#4), 1.3 (#5) and 5.0 eq. (#6) ZnOTf₂ (bottom to top, 400 MHz, DMSO-*d*₆).

Ditopic terpyridine amine 5.5

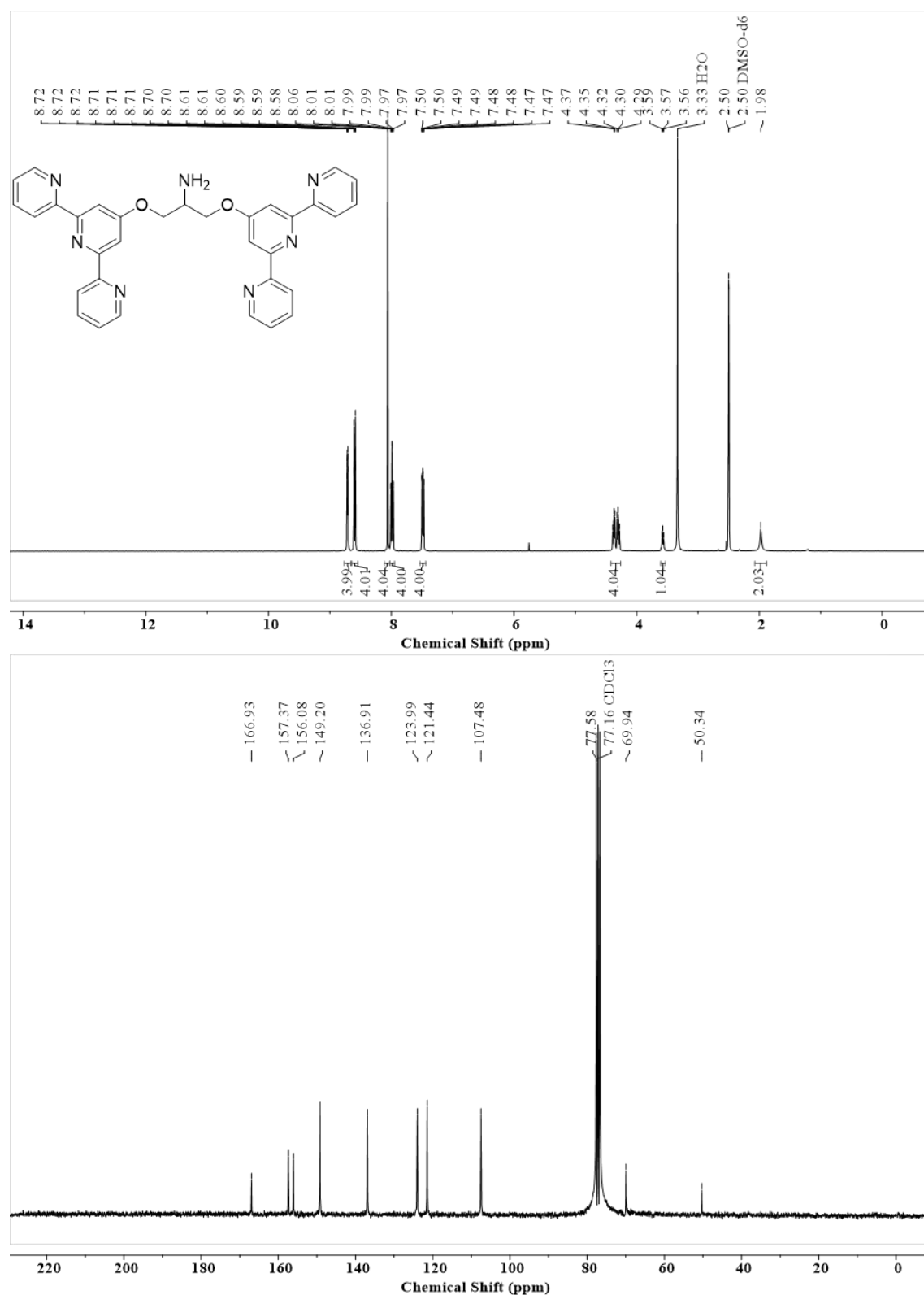
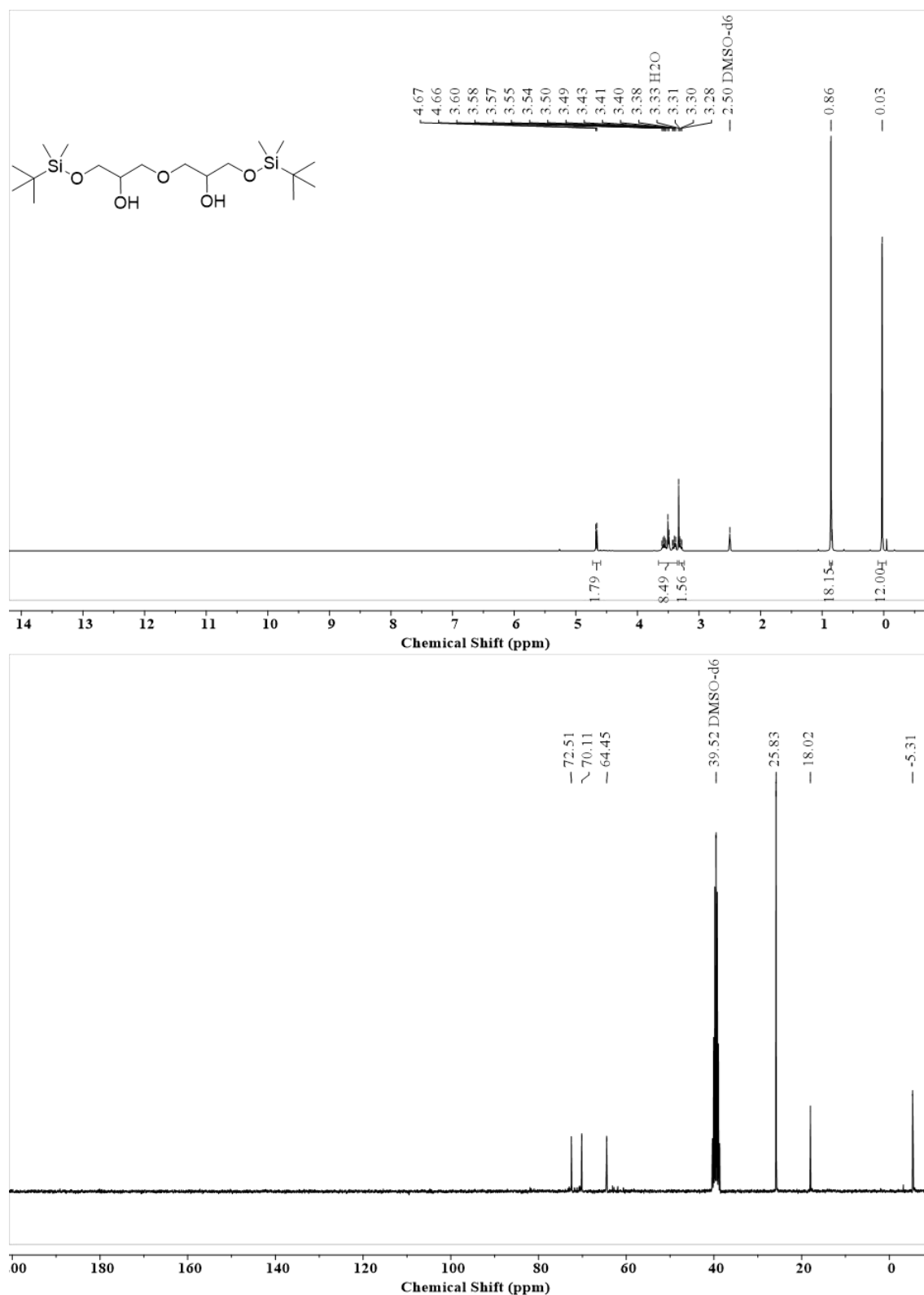
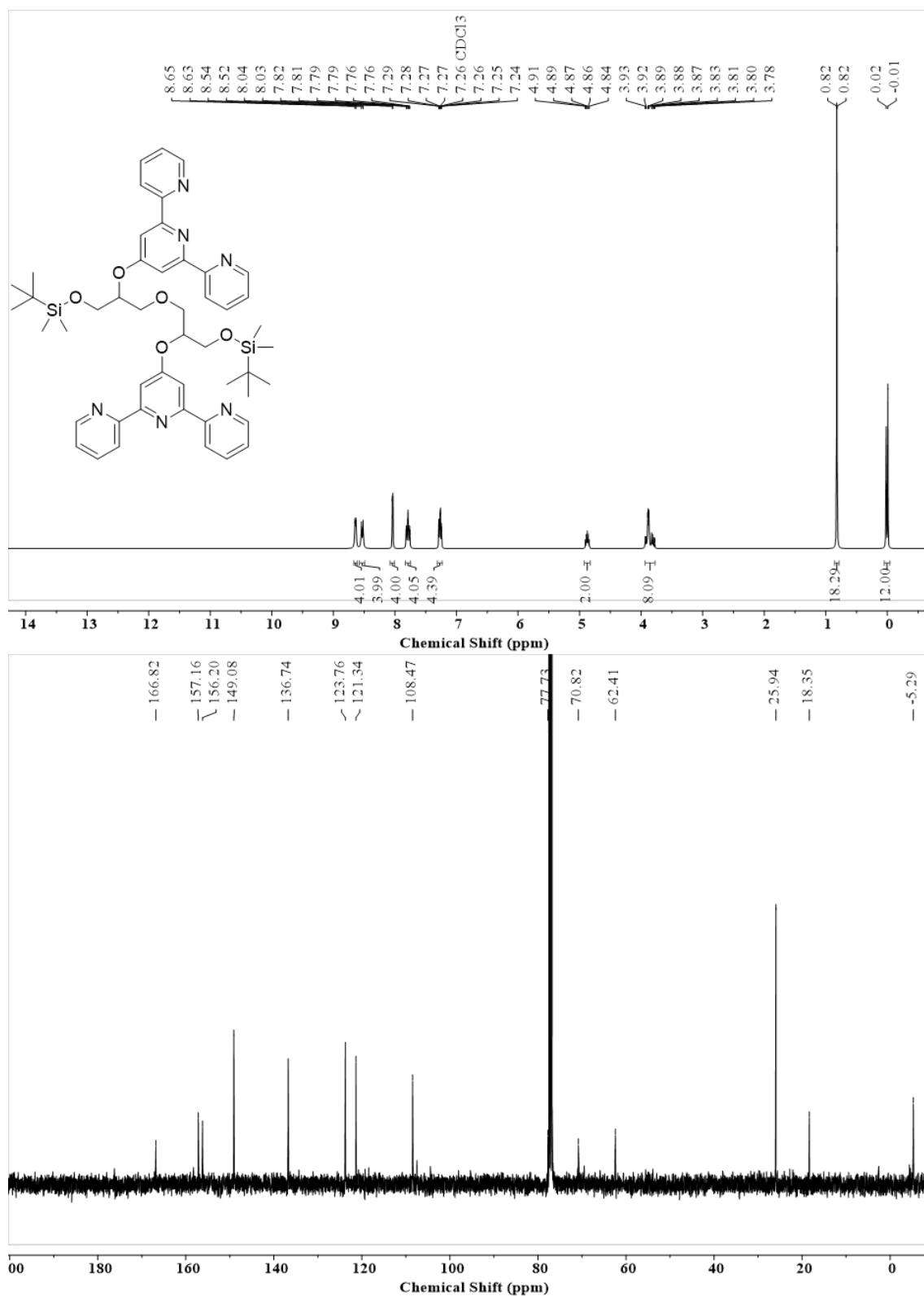


Figure S5.3. ^1H - and ^{13}C -NMR of ditopic terpyridine amine 5.5 (400 MHz, 100.1 MHz, $\text{DMSO-}d_6/\text{CDCl}_3$).

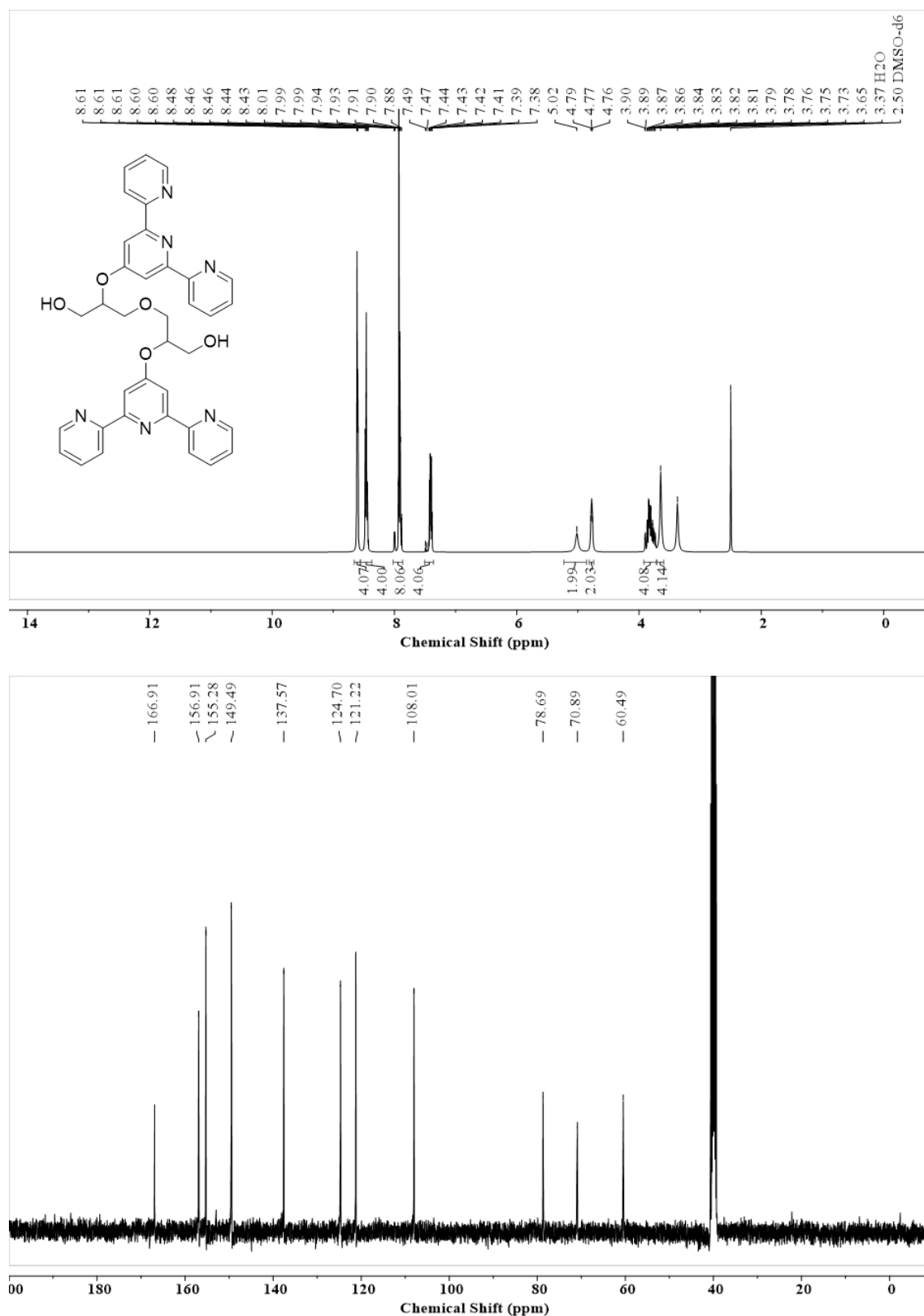
Compound 5.7b

Figure S5.4. ^1H - and ^{13}C -NMR of Compound 5.7b (400 MHz, 100.6 MHz, $\text{DMSO-}d_6$).

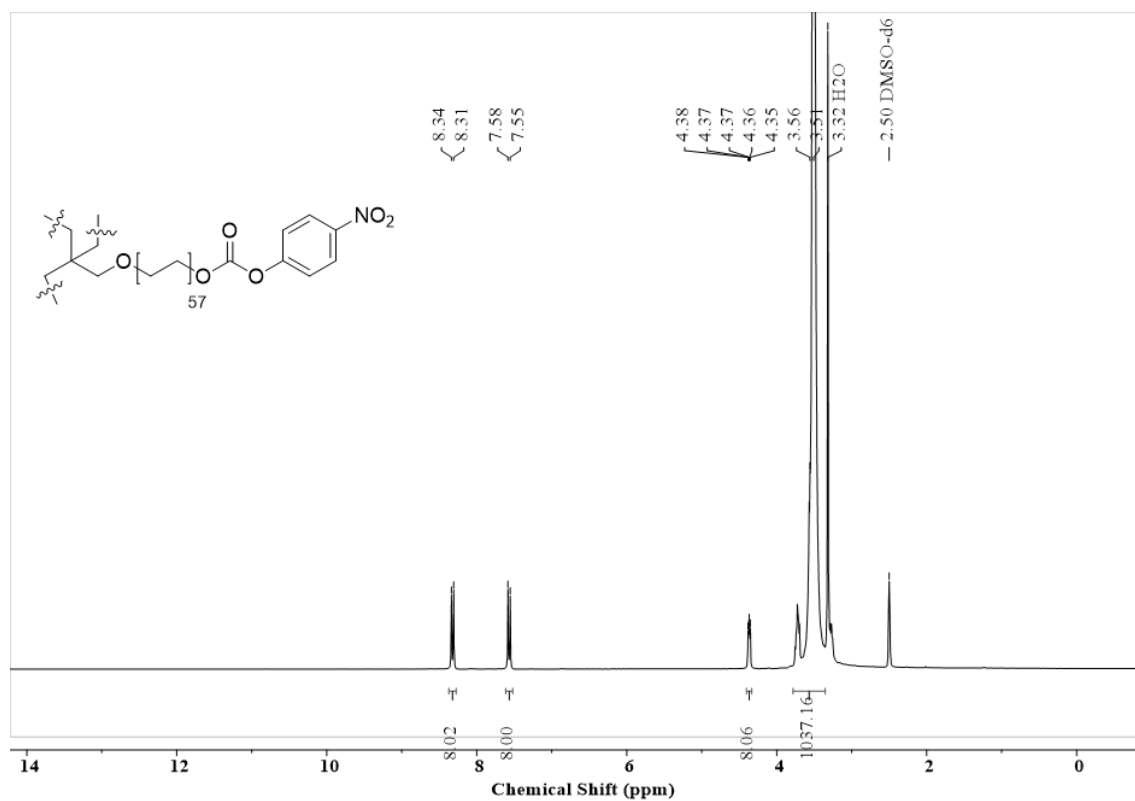
Compound 5.7.1b

Figure S5.5. ^1H - and ^{13}C -NMR of Compound 5.7.1b (300 MHz, 75 MHz, CDCl_3).

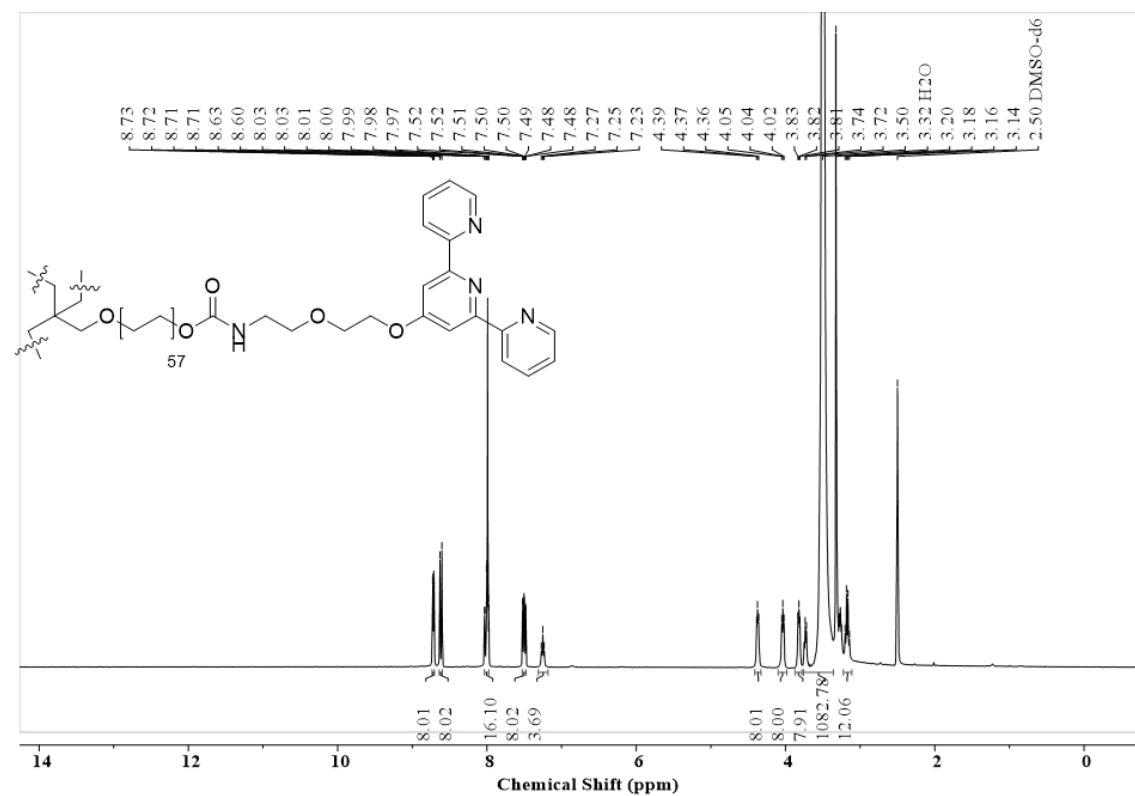
Compound 5.9b

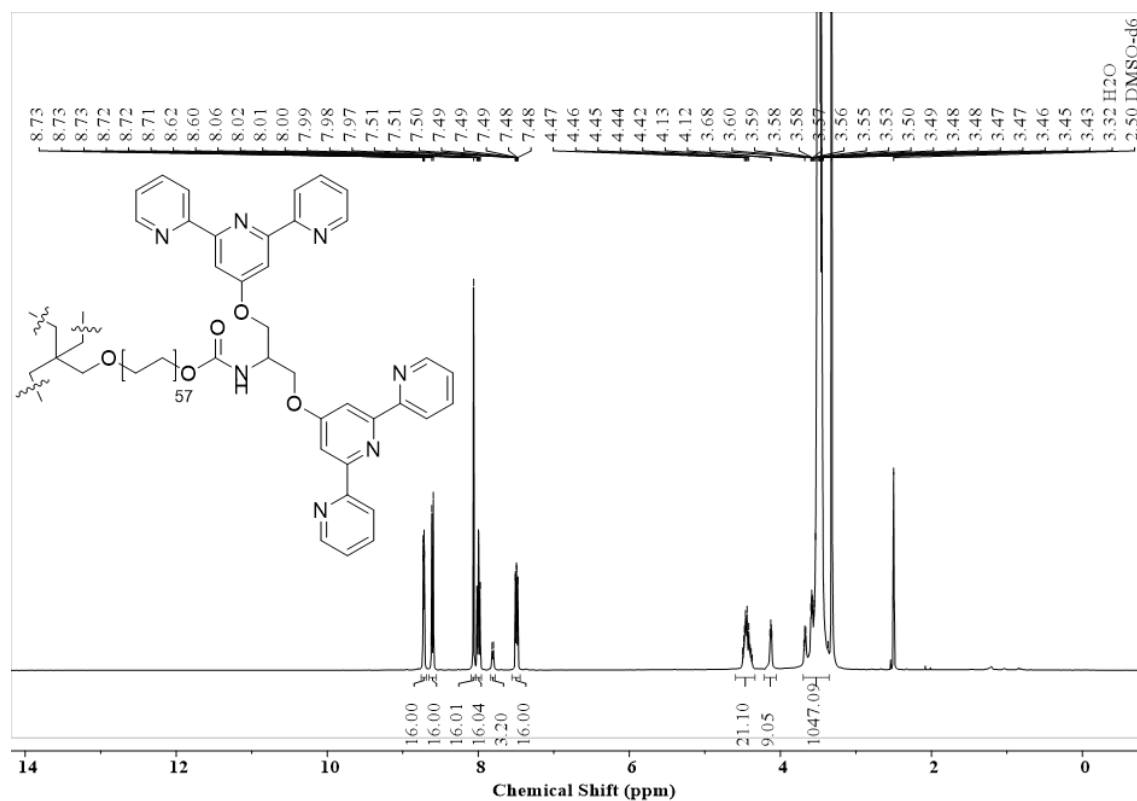
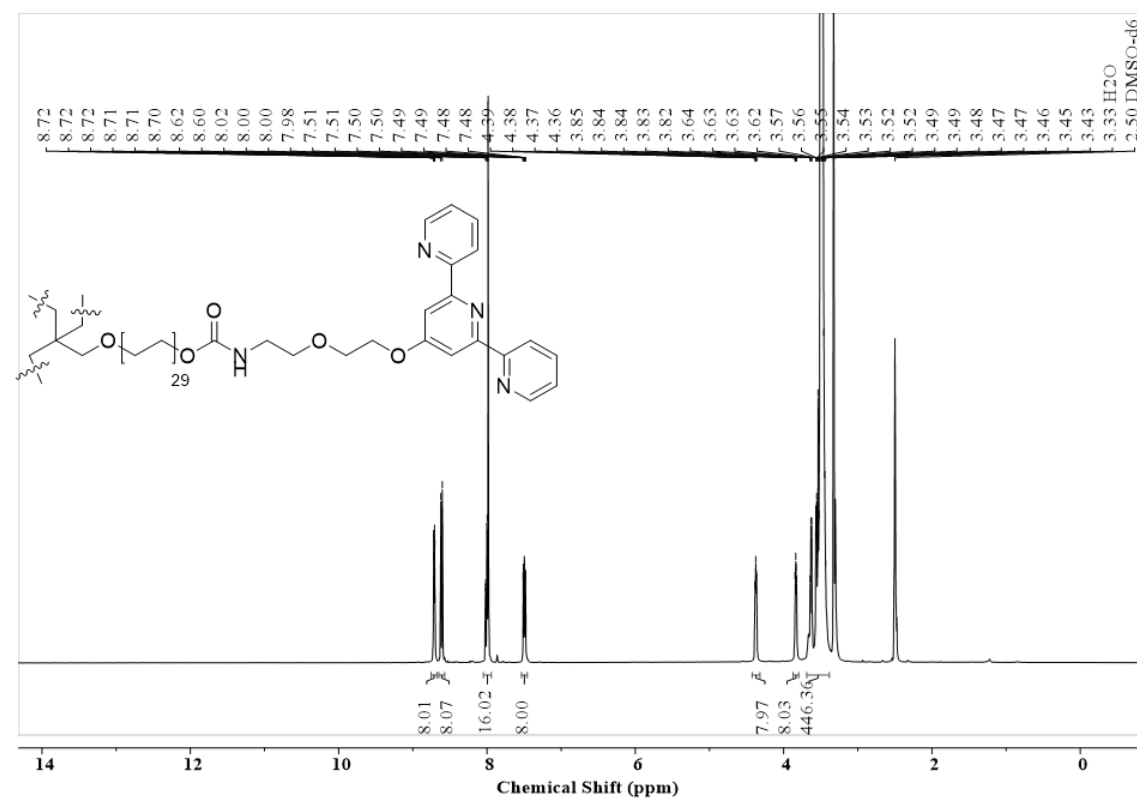
Figure S5.6. ^1H - and ^{13}C -NMR of ditopic terpyridine diol **5.9b** (400 MHz, 100.6 MHz, DMSO- d_6).

Compound 5.11

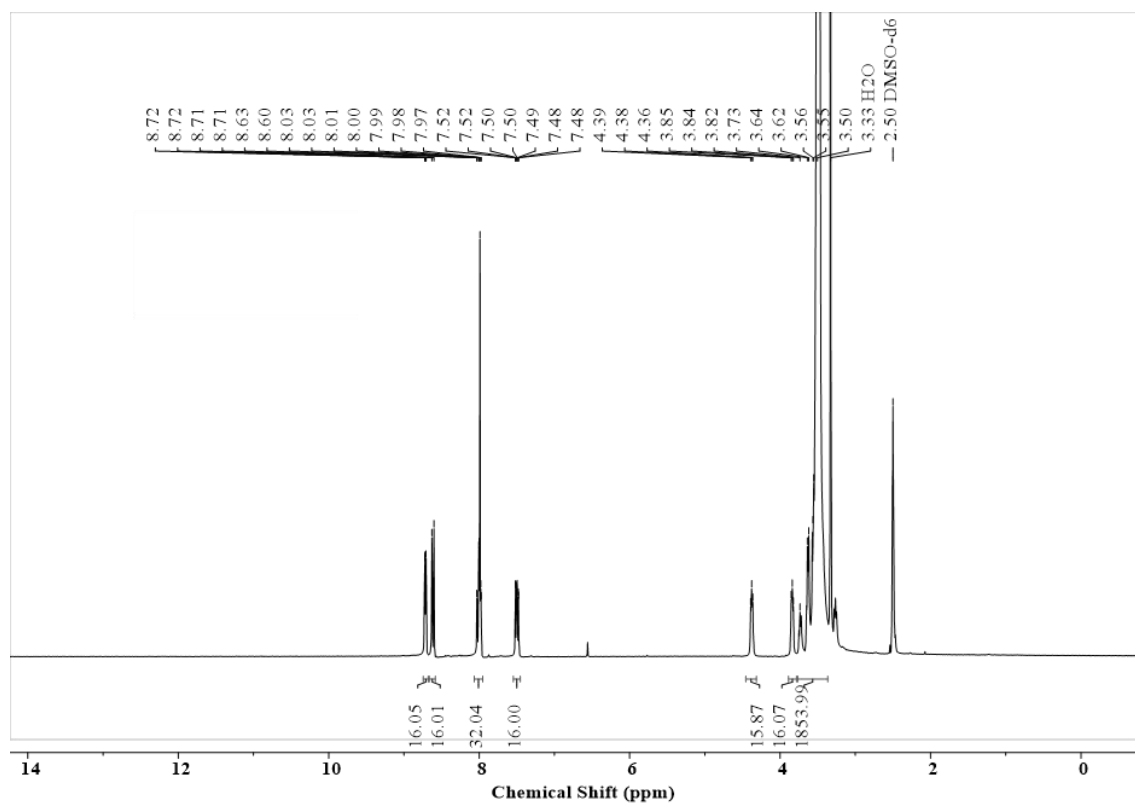
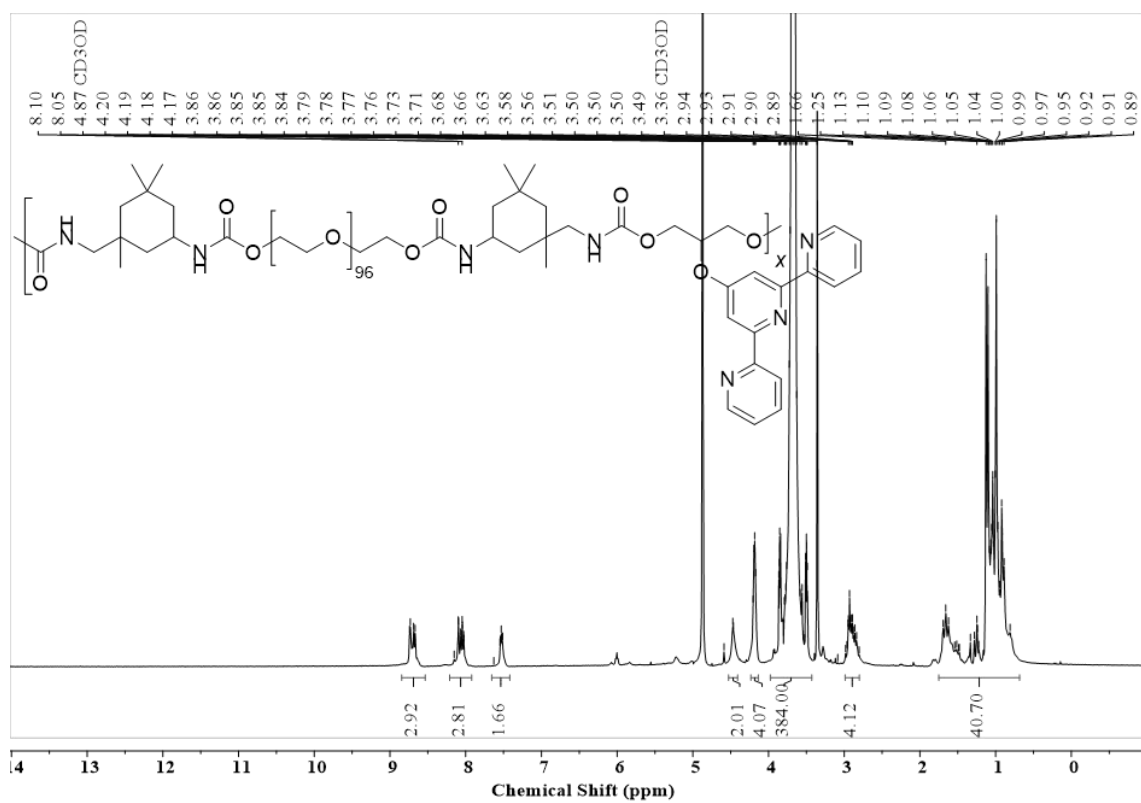
Figure S5.7. ¹H-NMR of Compound 5.11 (400 MHz, DMSO-*d*₆).

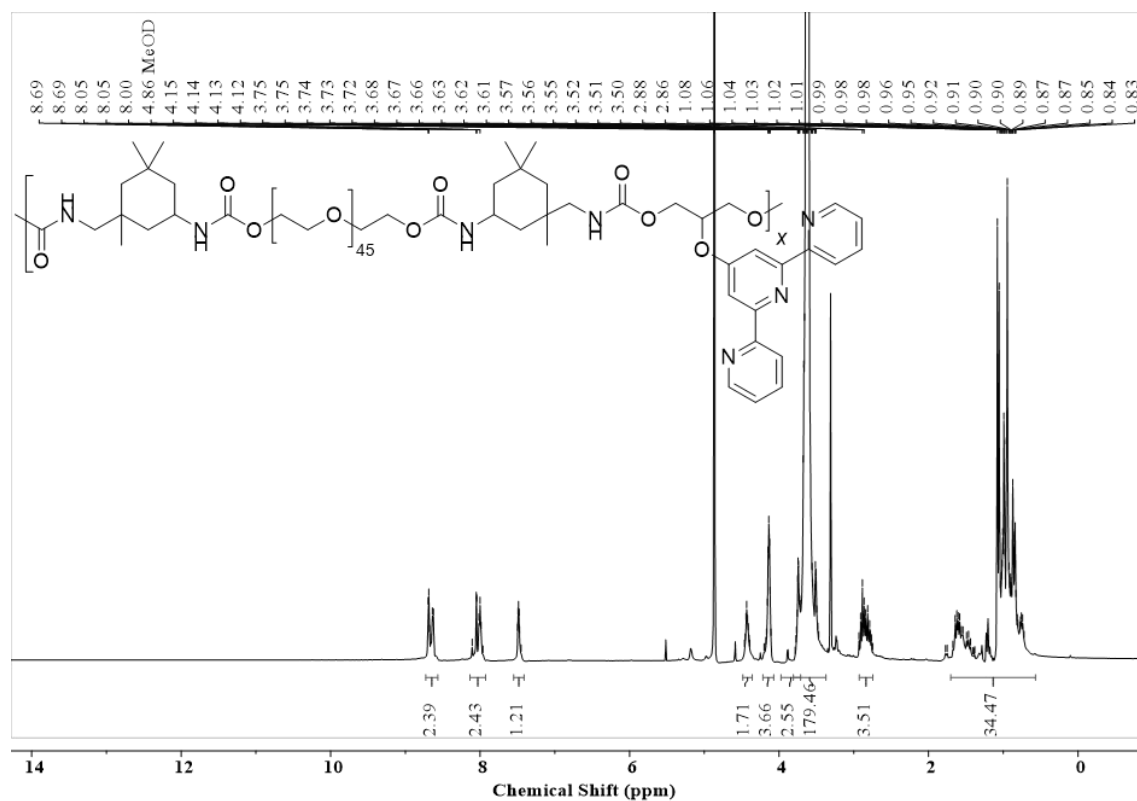
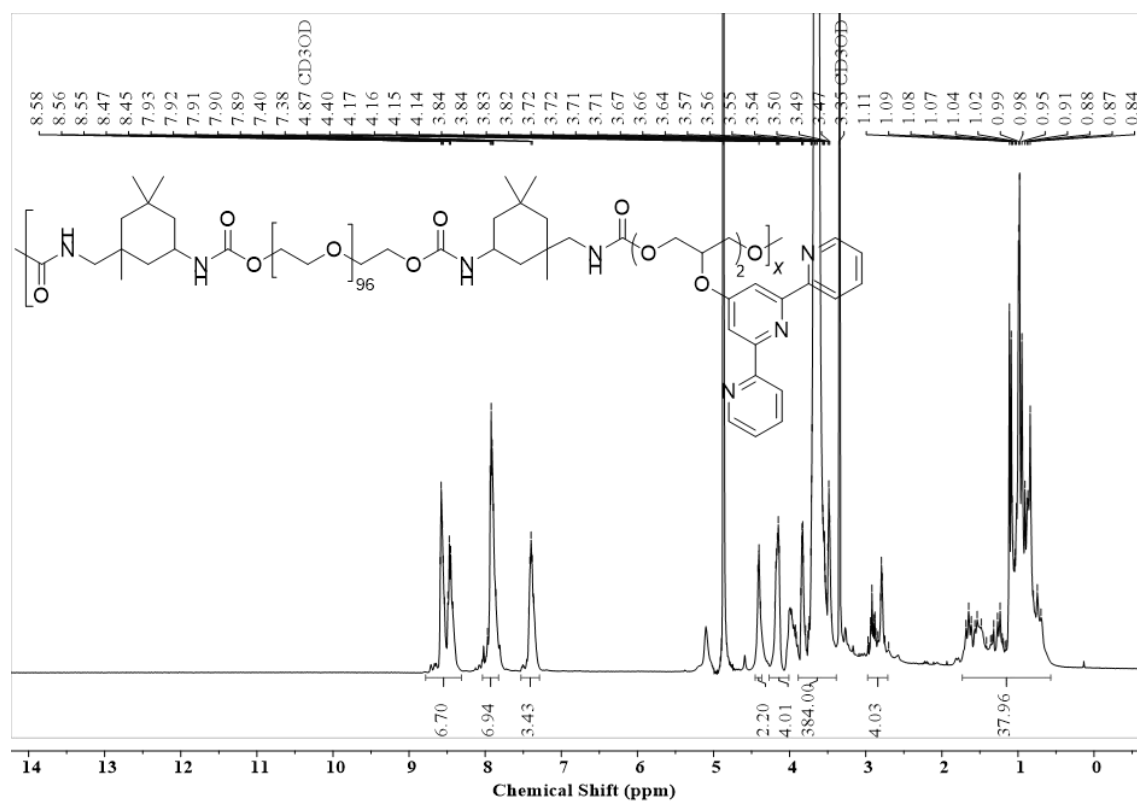
4-pEG-10k-1 5.12

Figure S5.8. ¹H-NMR of 4-pEG-10k-1 5.12 (400 MHz, DMSO-*d*₆).

4-pEG-10k-2 5.13**Figure S5.9.** $^1\text{H-NMR}$ of 4-pEG-10k-2 **5.13** (400 MHz, $\text{DMSO-}d_6$).**4-pEG-5k-1 5.20****Figure S5.10.** $^1\text{H-NMR}$ of 4-pEG-5k-1 **5.20** (400 MHz, $\text{DMSO-}d_6$).

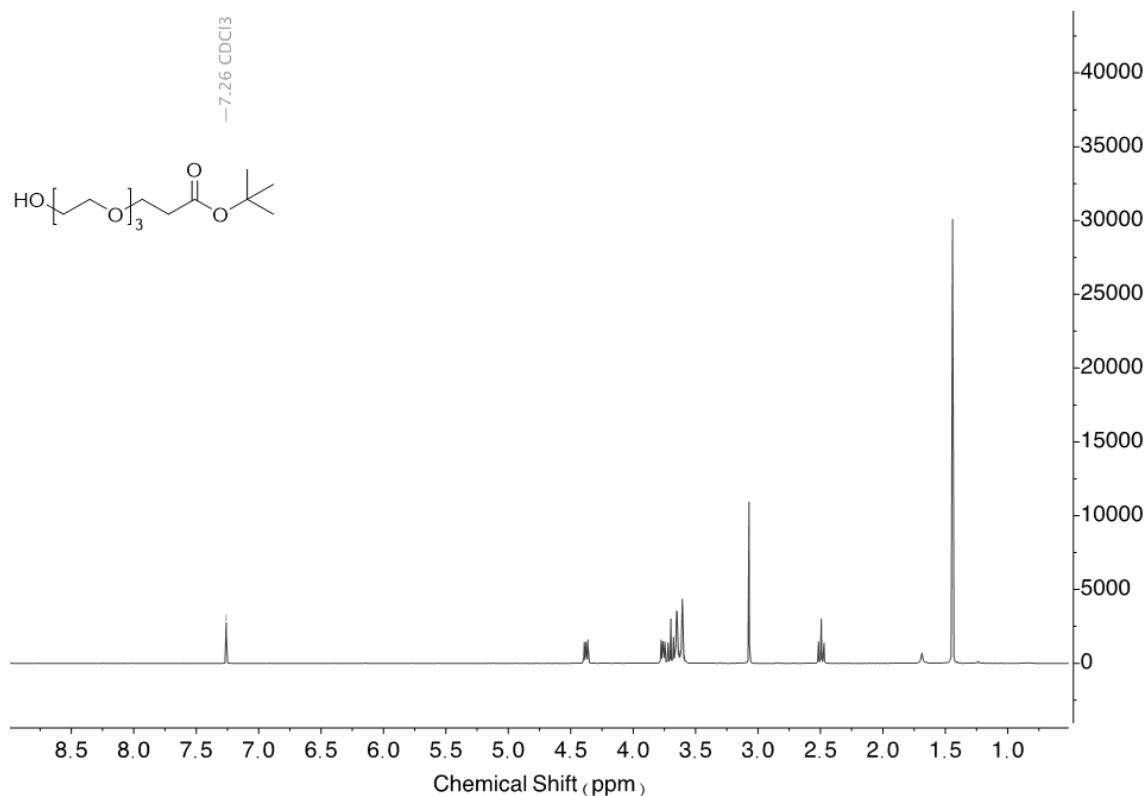
8-pEG-20k-1 5.21

Figure S5.11. ¹H-NMR of 4-pEG-20k-1 5.21 (400 MHz, DMSO-d₆).PU-1^{4k} 5.17Figure S5.12. ¹H-NMR of PU-1 5.17 (400 MHz, MeOD).

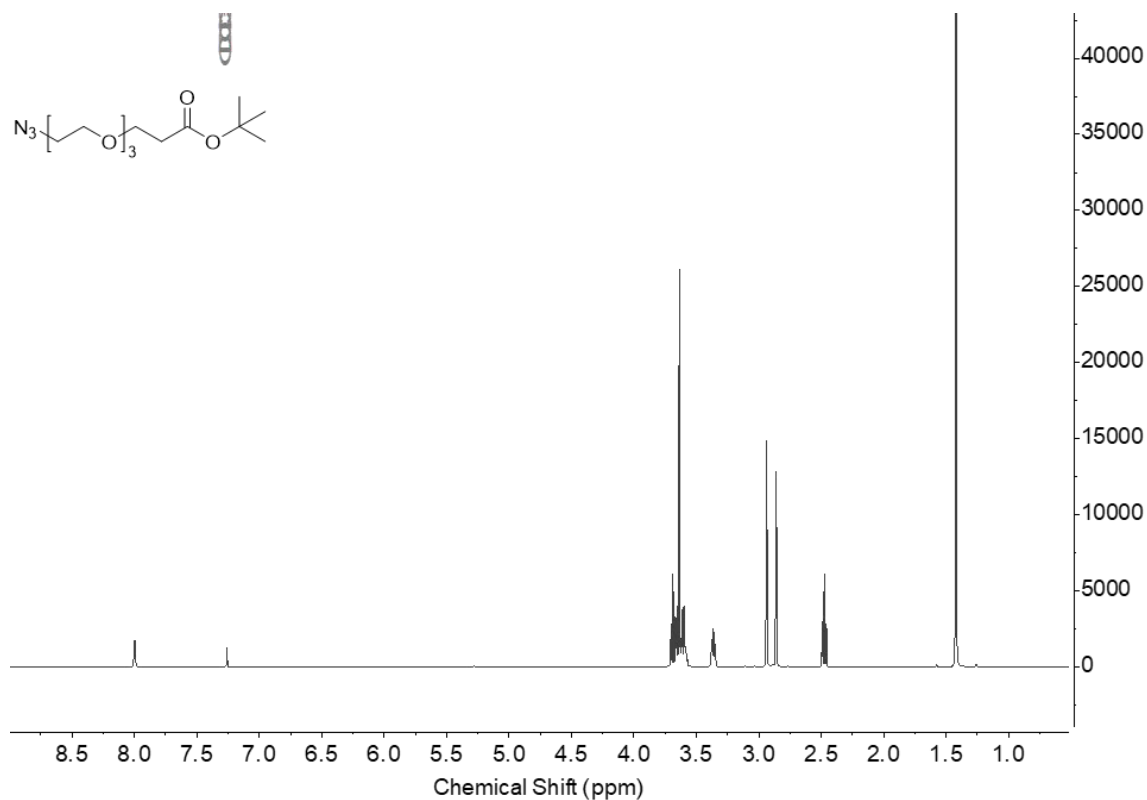
PU-1^{2k} 5.19Figure S5.13. ¹H-NMR of PU-1^{2k} 5.19 (400 MHz, MeOD).PU-2^{4k} 5.18Figure S5.14. ¹H-NMR of PU-2 5.18 (400 MHz, MeOD).

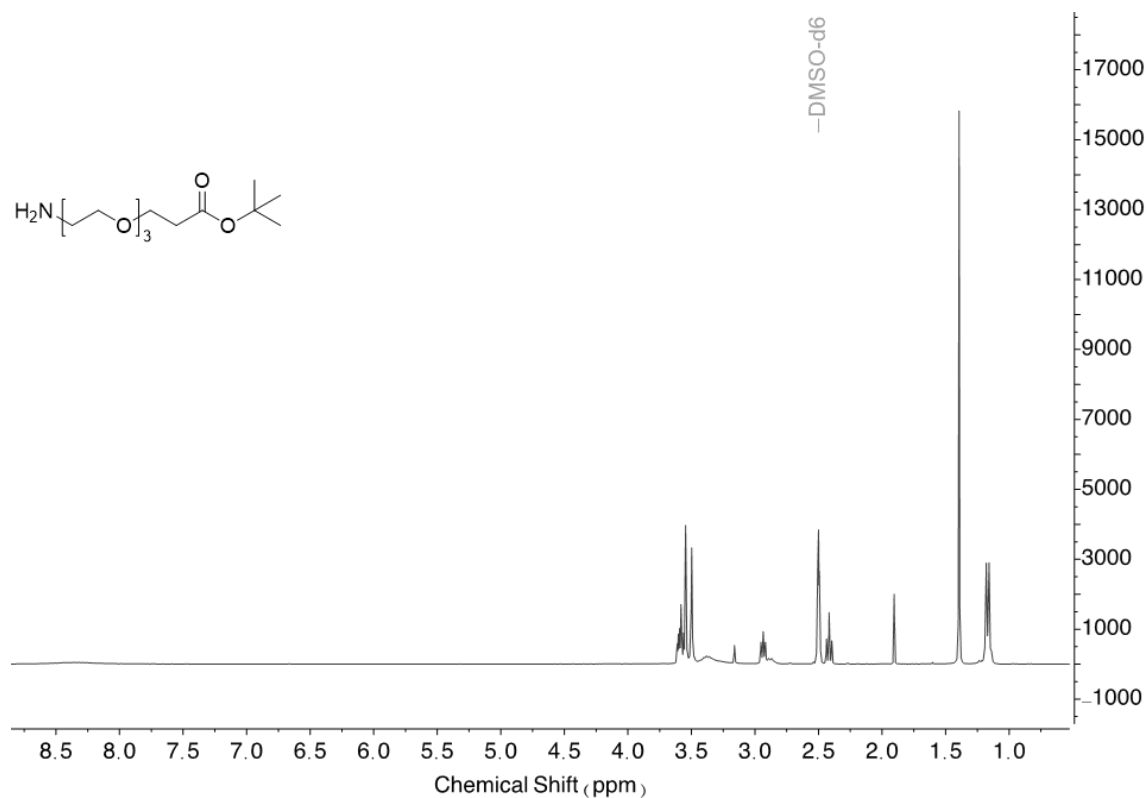
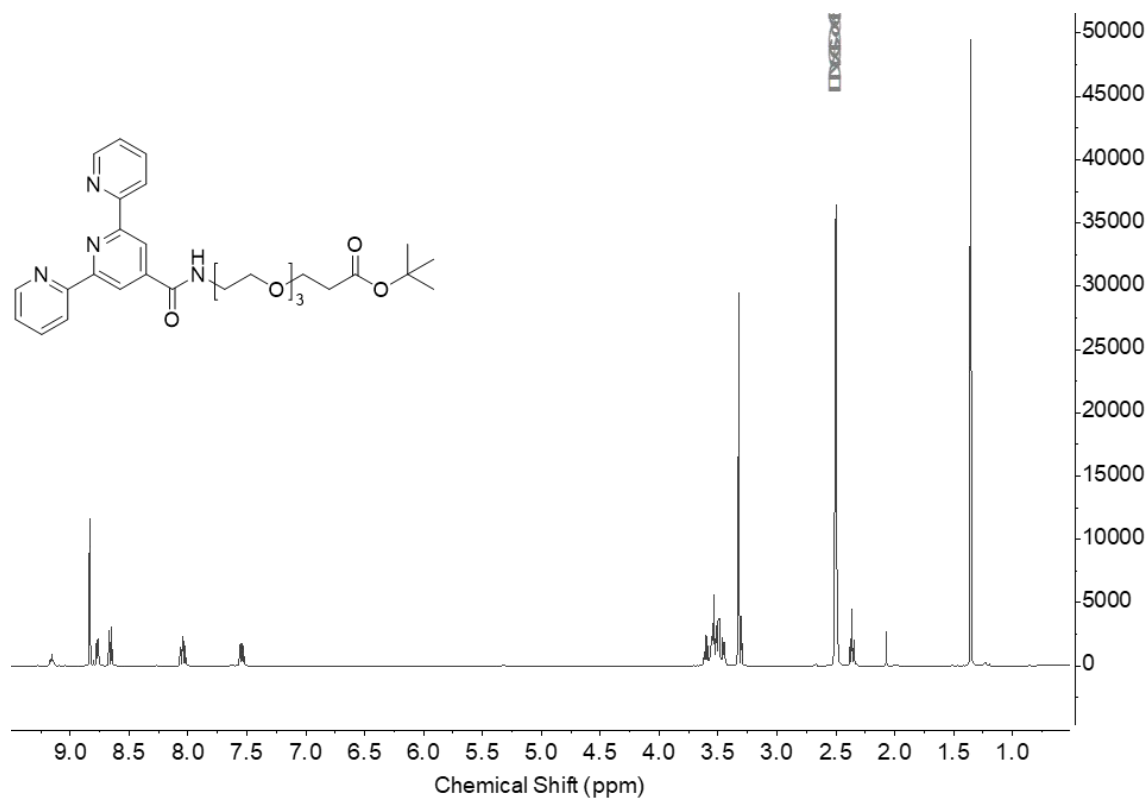
A.6 Supplementary Information Chapter 6

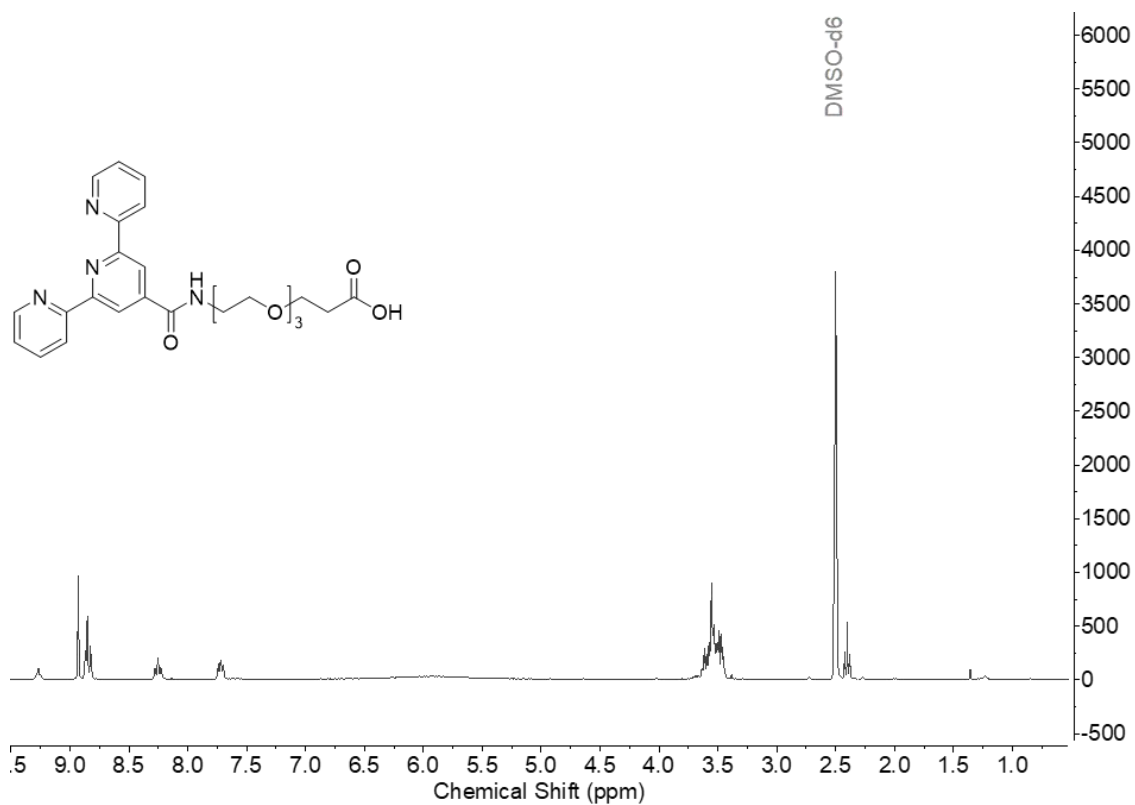
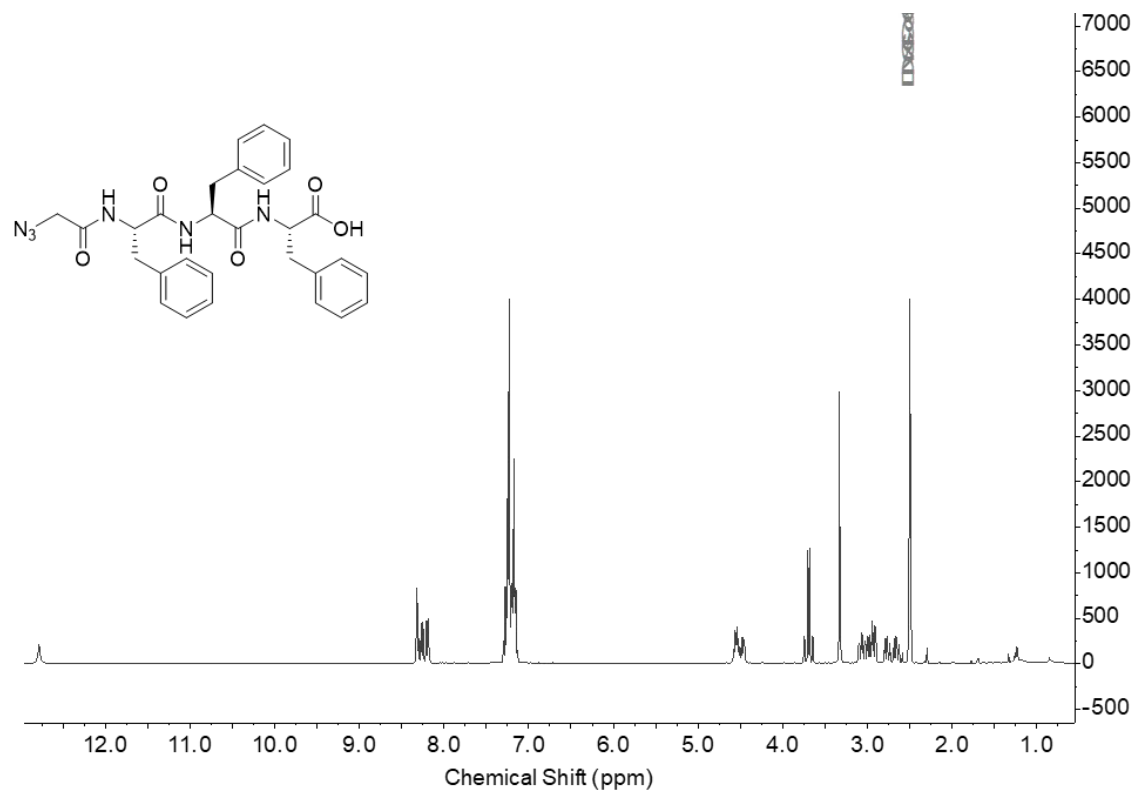
Compound 6.2

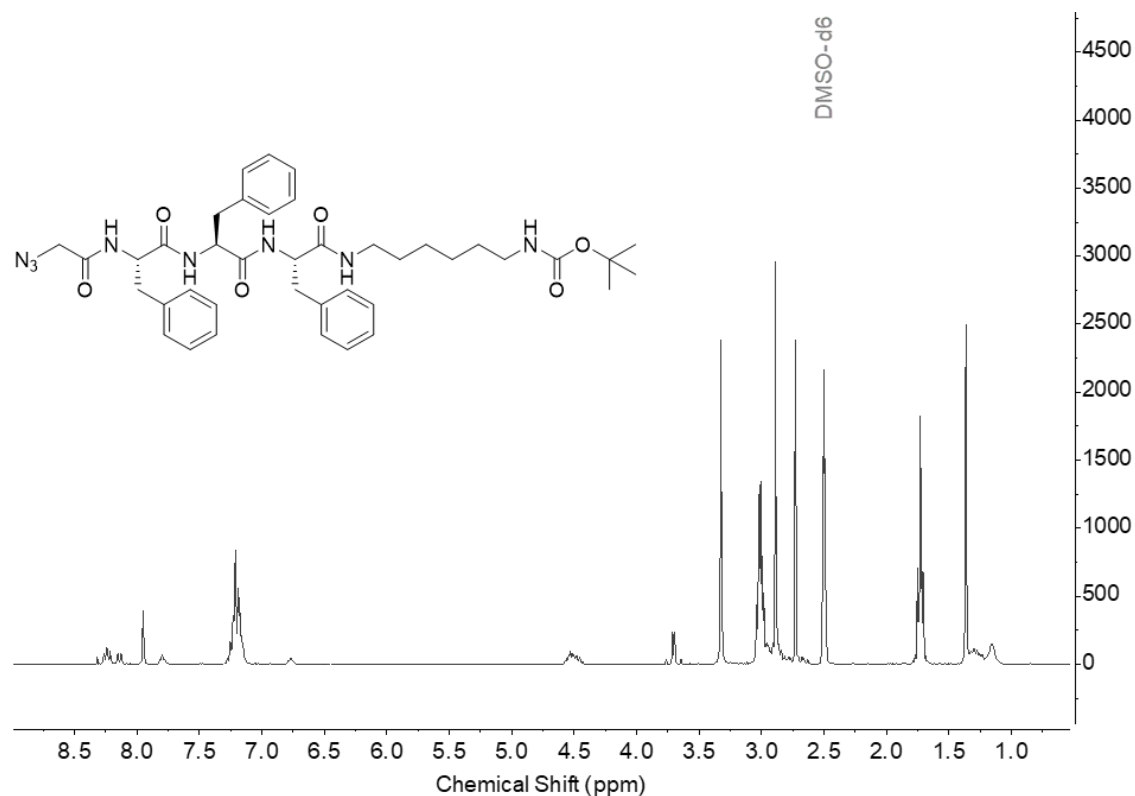
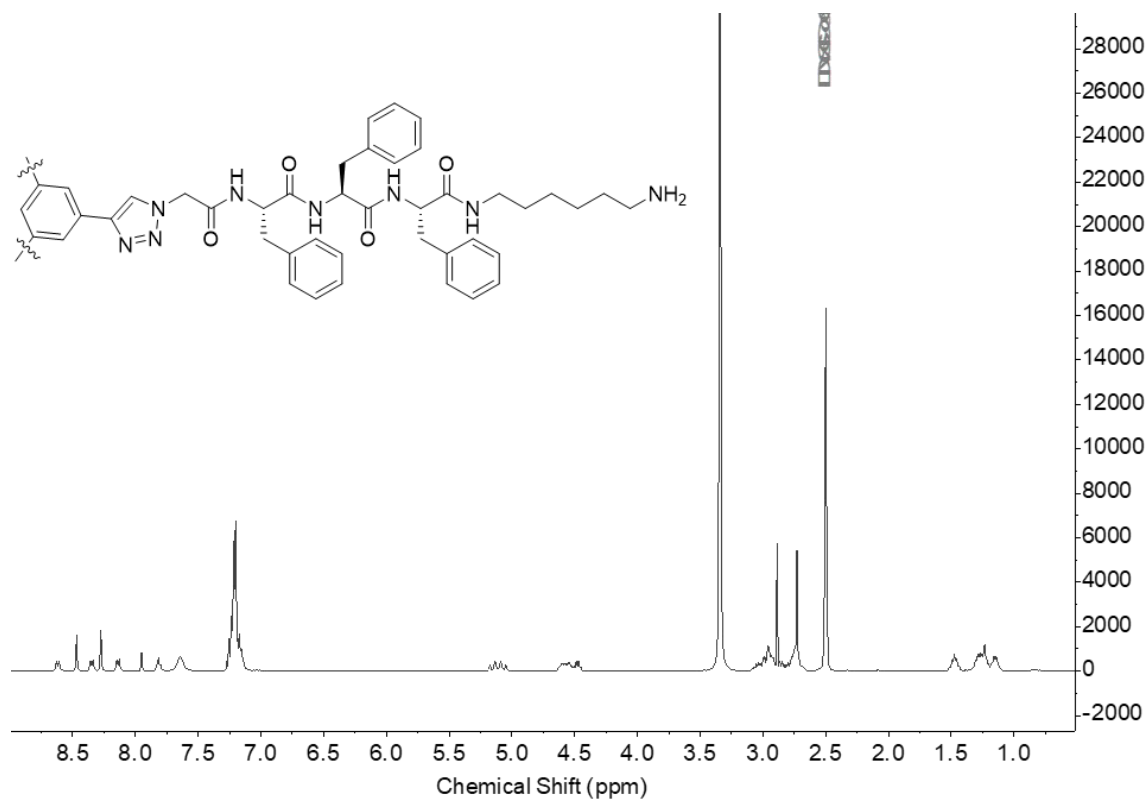
Figure S6.1. ¹H-NMR spectrum of compound 6.2 (300 MHz, CDCl₃, 298 K).

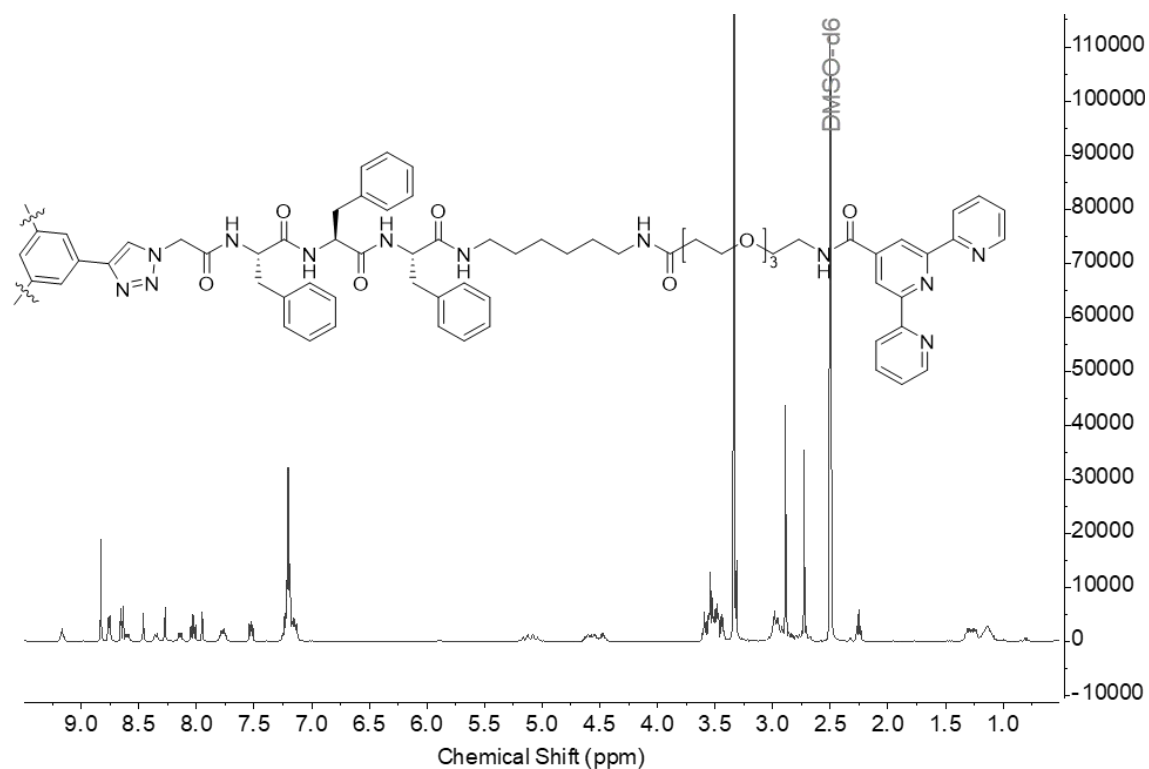
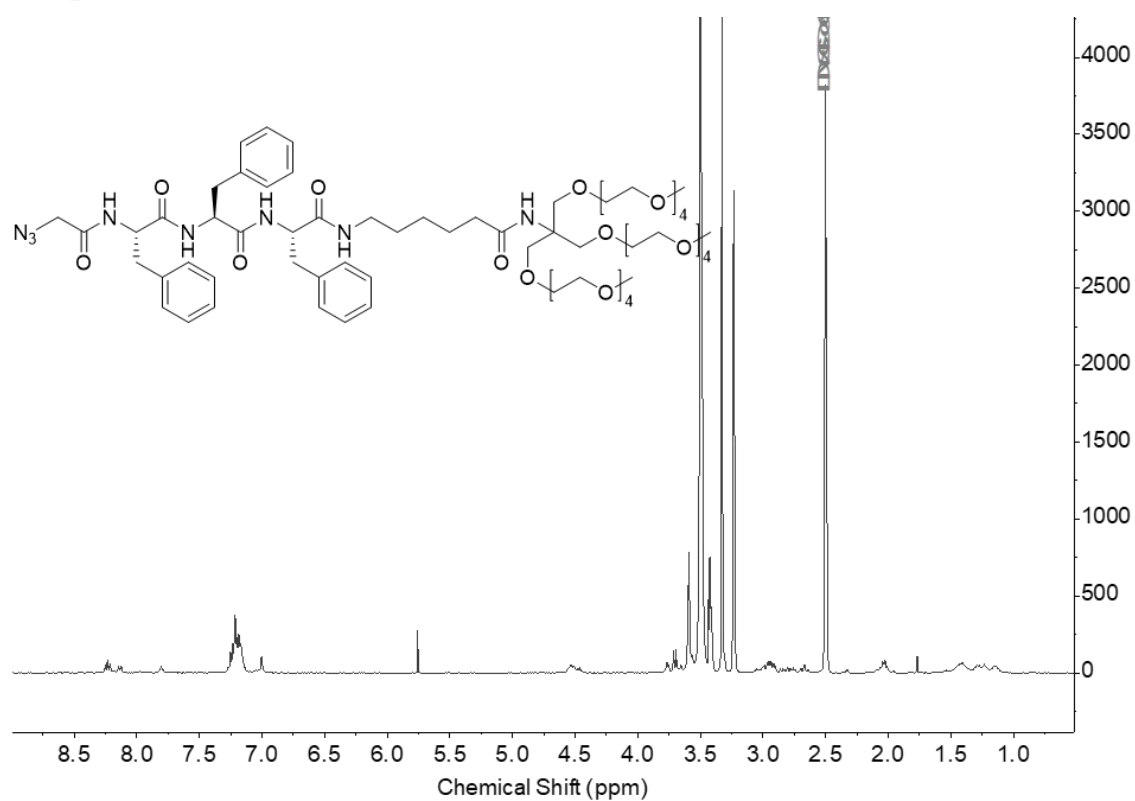
Compound 6.3

Figure S6.2. ¹H-NMR spectrum of compound 6.3 (300 MHz, CDCl₃, 298 K).

Compound 6.4**Figure S6.3.** $^1\text{H-NMR}$ spectrum of compound **6.4** (300 MHz, $\text{DMSO-}d_6$, 298 K).**Compound 6.6****Figure S6.4.** $^1\text{H-NMR}$ spectrum of compound **6.6** (400 MHz, $\text{DMSO-}d_6$, 298 K).

Compound 6.7**Figure S6.5.** ¹H-NMR spectrum of compound 6.7 (300 MHz, DMSO-*d*₆, 298 K).**Compound 6.8****Figure S6.6.** ¹H-NMR spectrum of compound 6.8 (400 MHz, DMSO-*d*₆, 298 K).

Compound 6.10**Figure S6.7** ¹H-NMR spectrum of compound **6.10** (400 MHz, DMSO-*d*₆, 298 K).**Compound 6.11****Figure S6.8.** ¹H-NMR spectrum of compound **6.11** (400 MHz, DMSO-*d*₆, 298 K).

Compound 6.12**Figure S6.9.** ¹H-NMR spectrum of compound 6.12 (400 MHz, DMSO-*d*₆, 298 K).**Compound 6.14****Figure S6.10.** ¹H-NMR spectrum of compound 6.14 (400 MHz, DMSO-*d*₆, 298 K).

Compound 6.15

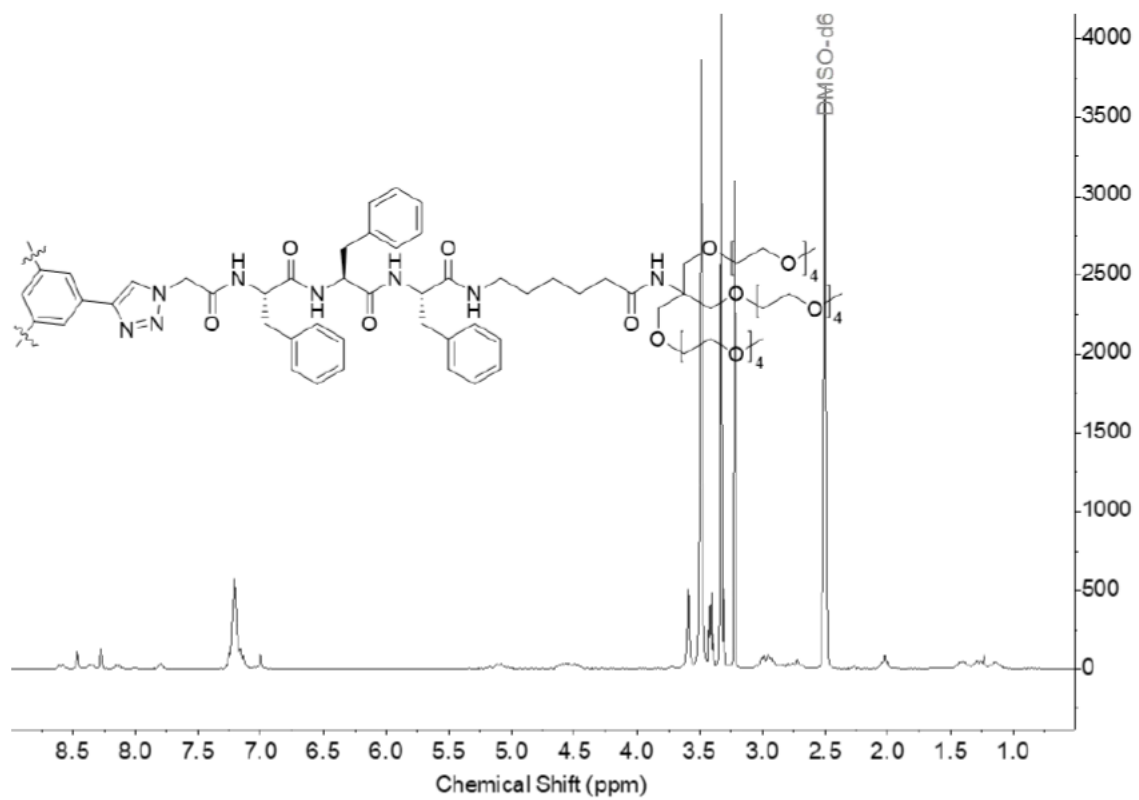
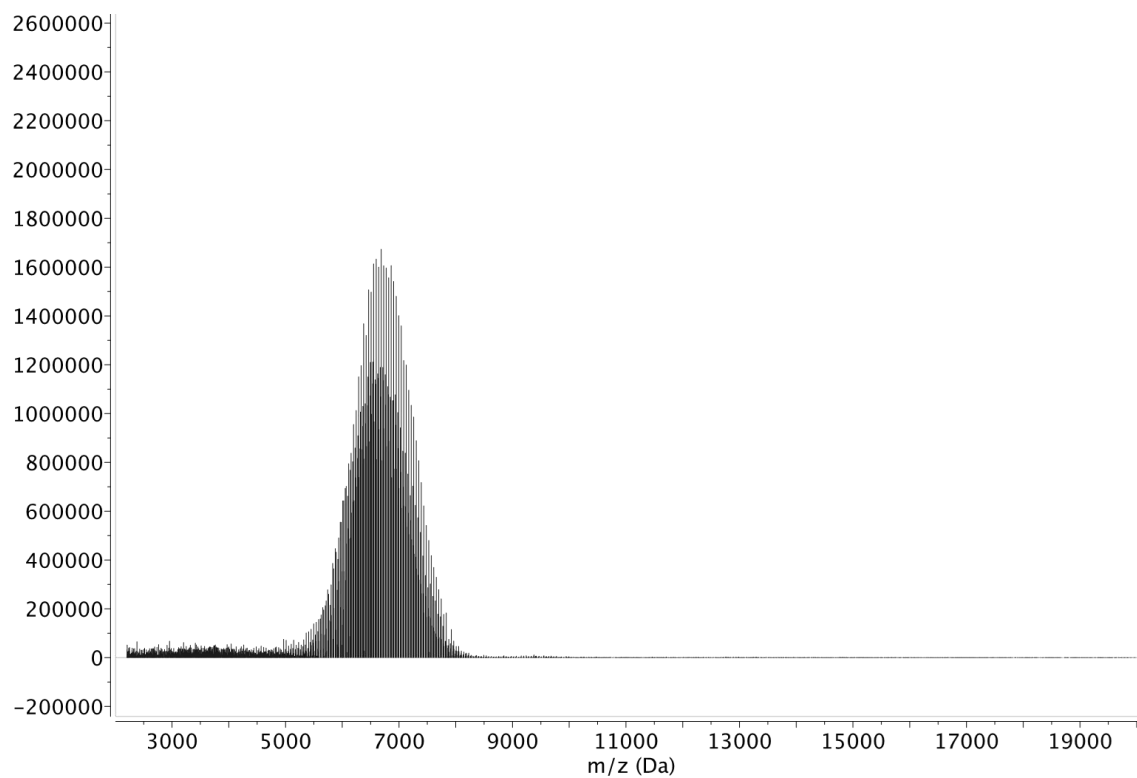
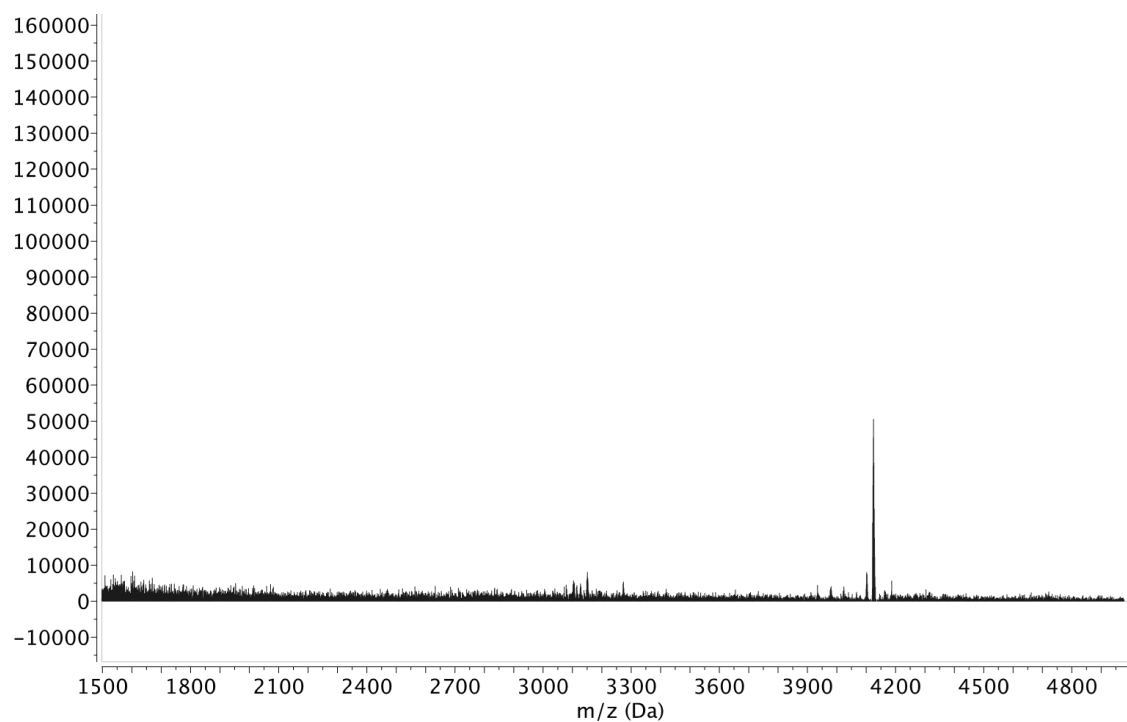


Figure S6.11. $^1\text{H-NMR}$ spectrum of compound 6.15 (400 MHz, $\text{DMSO-}d_6$, 298 K).

MALDI spectra**Figure S6.12.** MALDI spectrum of compound **6.18** (DHB, positive).**Figure S6.12.** MALDI spectrum of component **6.15** (CHCA, positive).

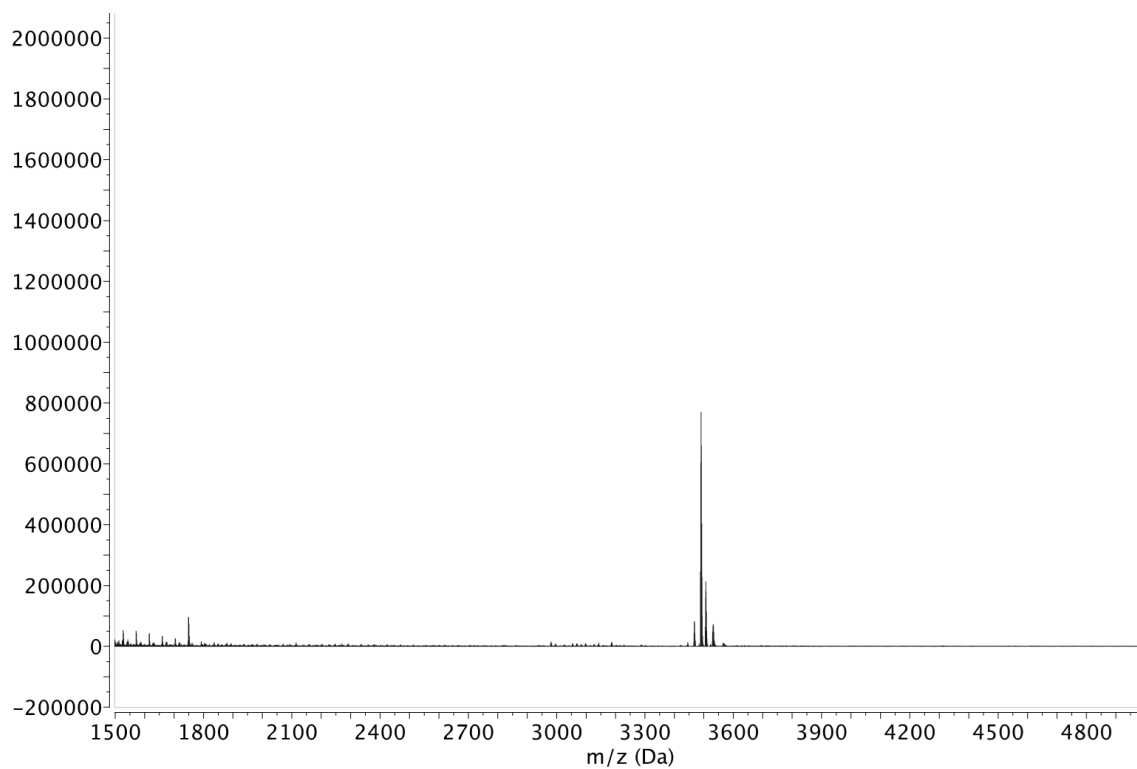
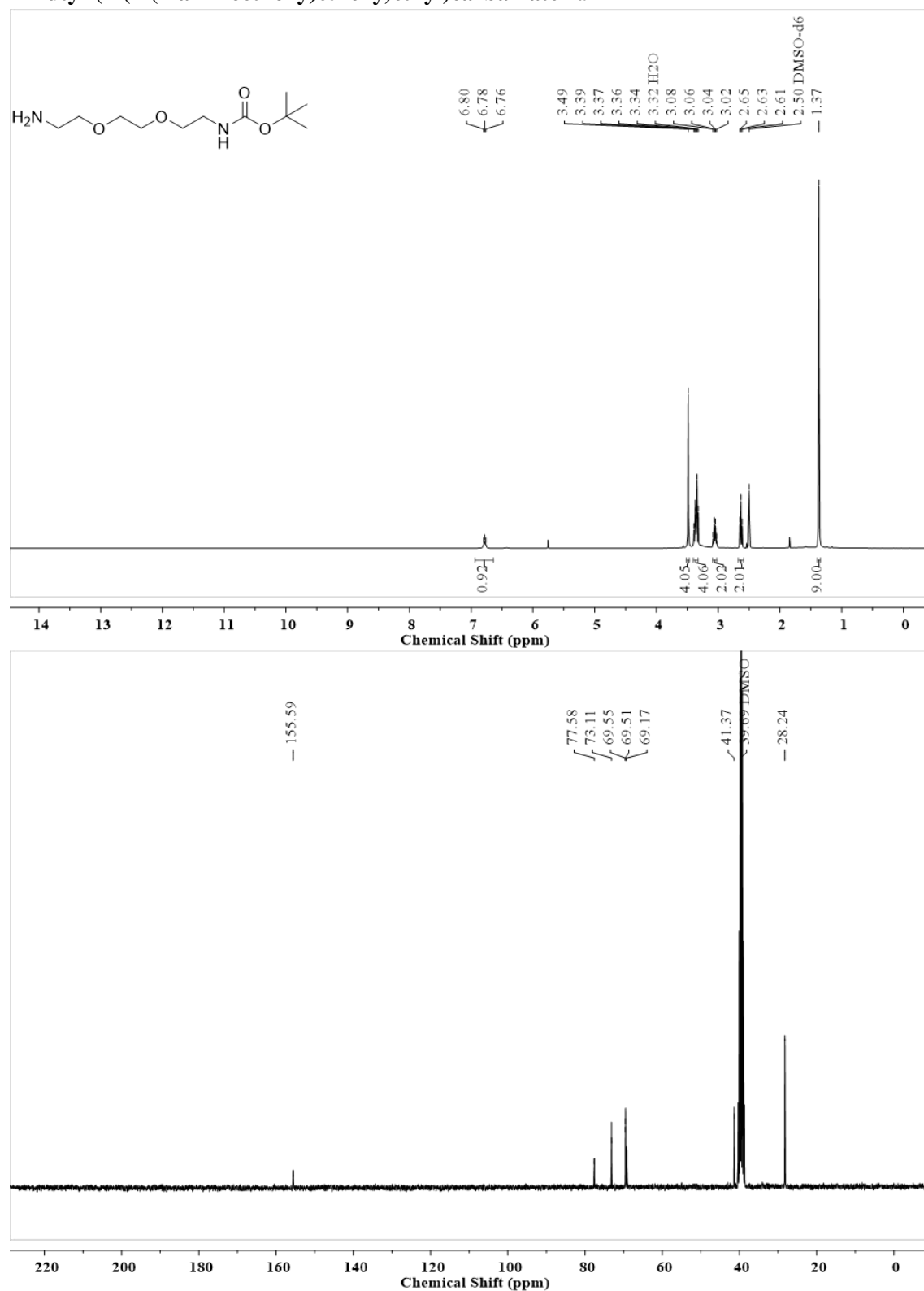
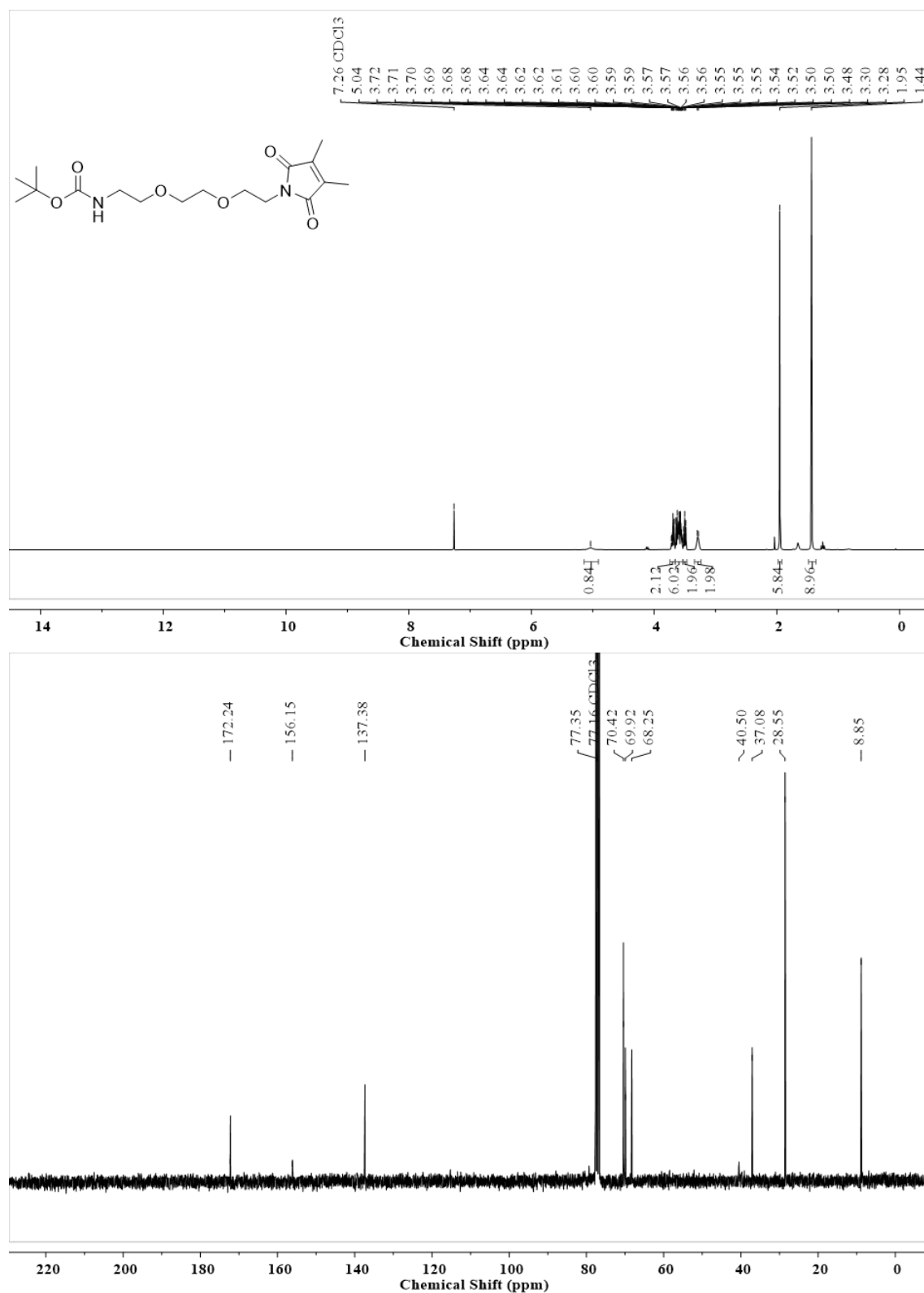
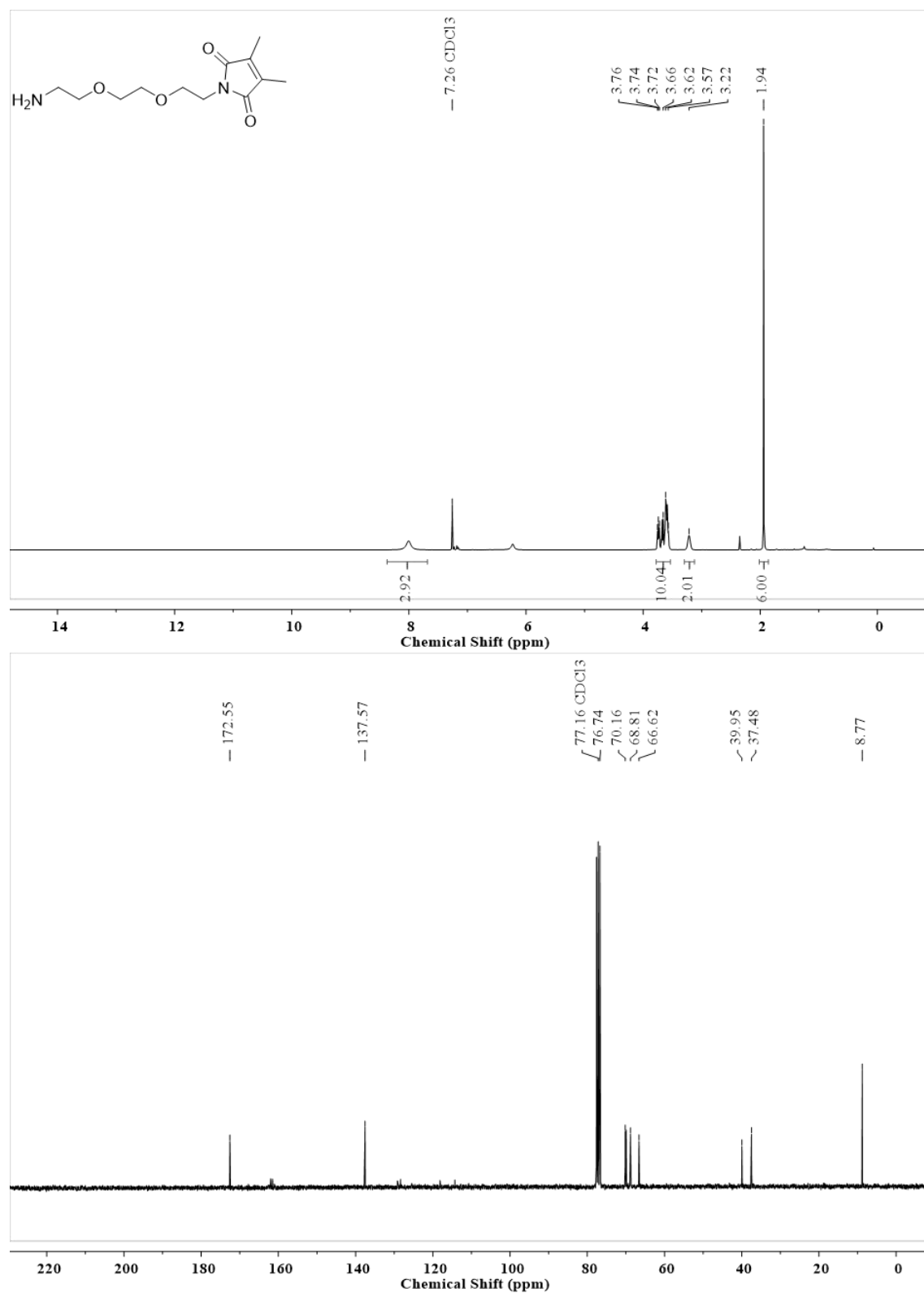


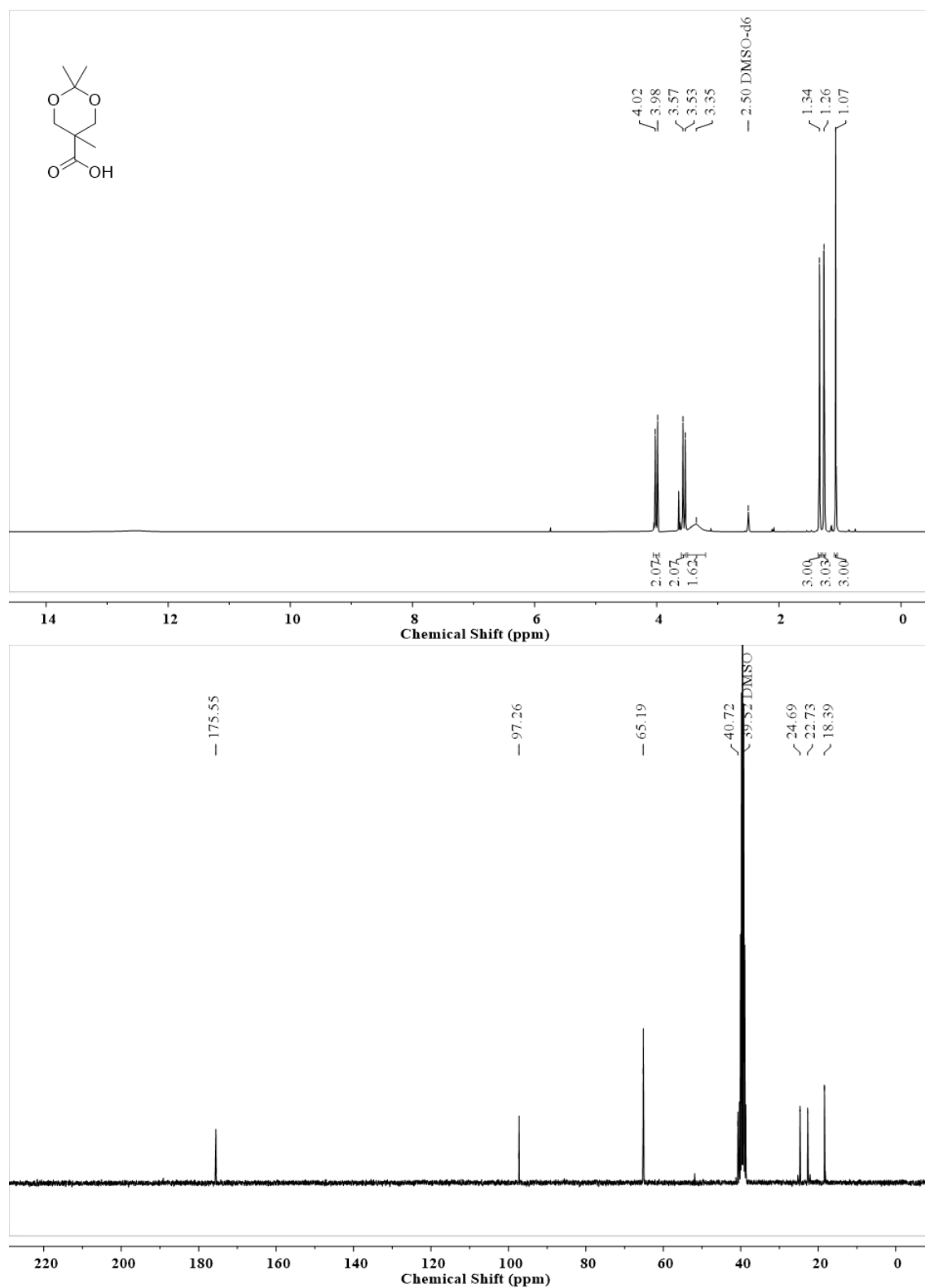
Figure S6.13. MALDI spectrum of component **6.12** (CHCA, positive).

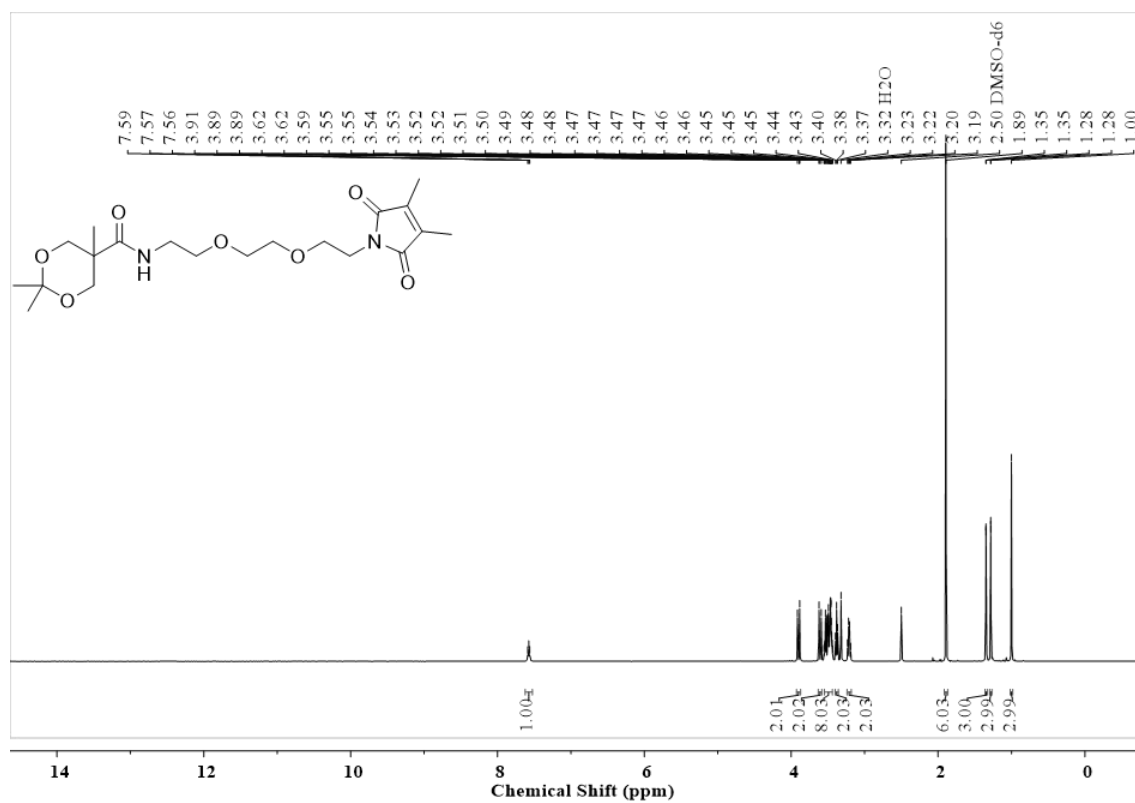
A.7 Supplementary Information Chapter 7

tert-Butyl-(2-(2-(2-aminoethoxy)ethoxy)ethyl)carbamate 7.9Figure S7.1. ¹H- and ¹³C-NMR of compound 7.9 (300 MHz, 75 MHz, DMSO-*d*₆).

DMMI-TEG *tert*-butyl amine 7.11Figure S7.2. ¹H- and ¹³C-NMR of compound 7.11 (300 MHz, 75 MHz, CDCl₃).

DMMI-¹EG amine 7.12Figure S7.3. ¹H- and ¹³C-NMR of compound 7.12 (300 MHz, 75 MHz, CDCl₃).

2,2,5-trimethyl-1,3-dioxane-5-carboxylic acid 7.14**Figure S7.4.** ¹H- and ¹³C-NMR of compound 7.14 (300 MHz, 75 MHz, DMSO-d₆).

DMMI-¹EG diol acetonide 7.15Figure S7.5 ¹H-NMR of compound 7.15 (400 MHz, DMSO-*d*₆).

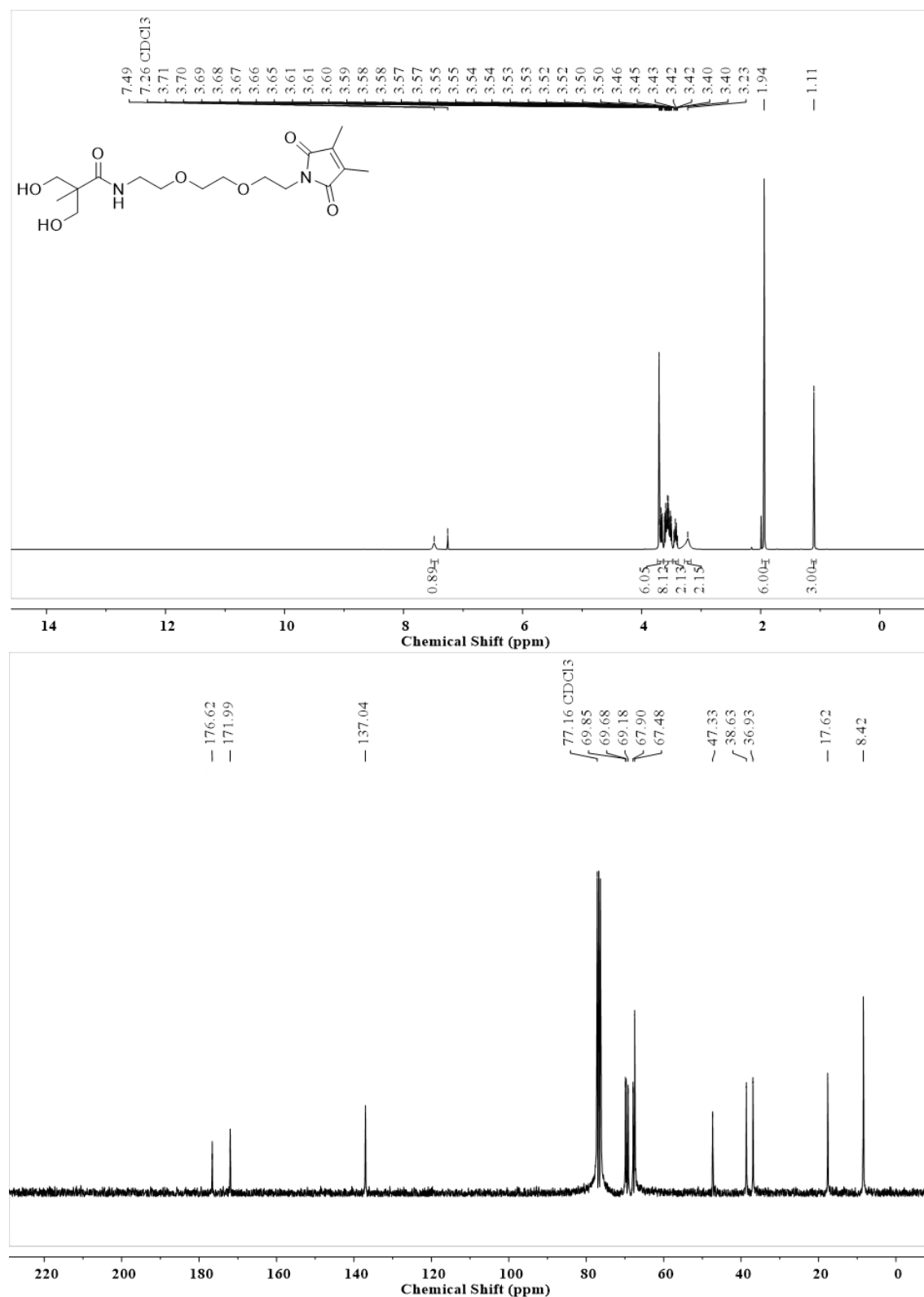
DMMI-¹EG diol 7.4

Figure S7.6. ¹H- and ¹³C-NMR of compound 7.4 (400 MHz, 101 MHz, CDCl₃).

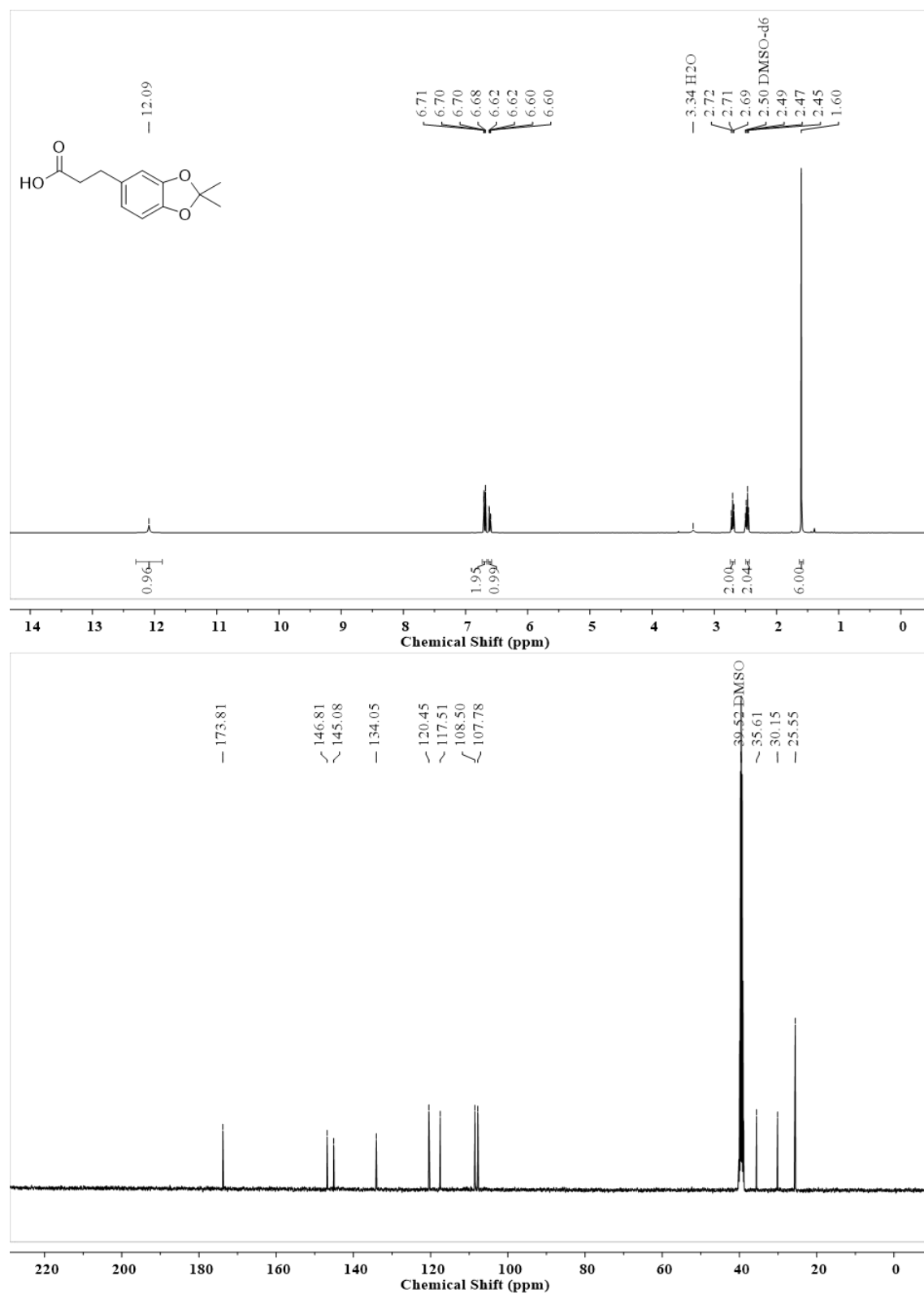
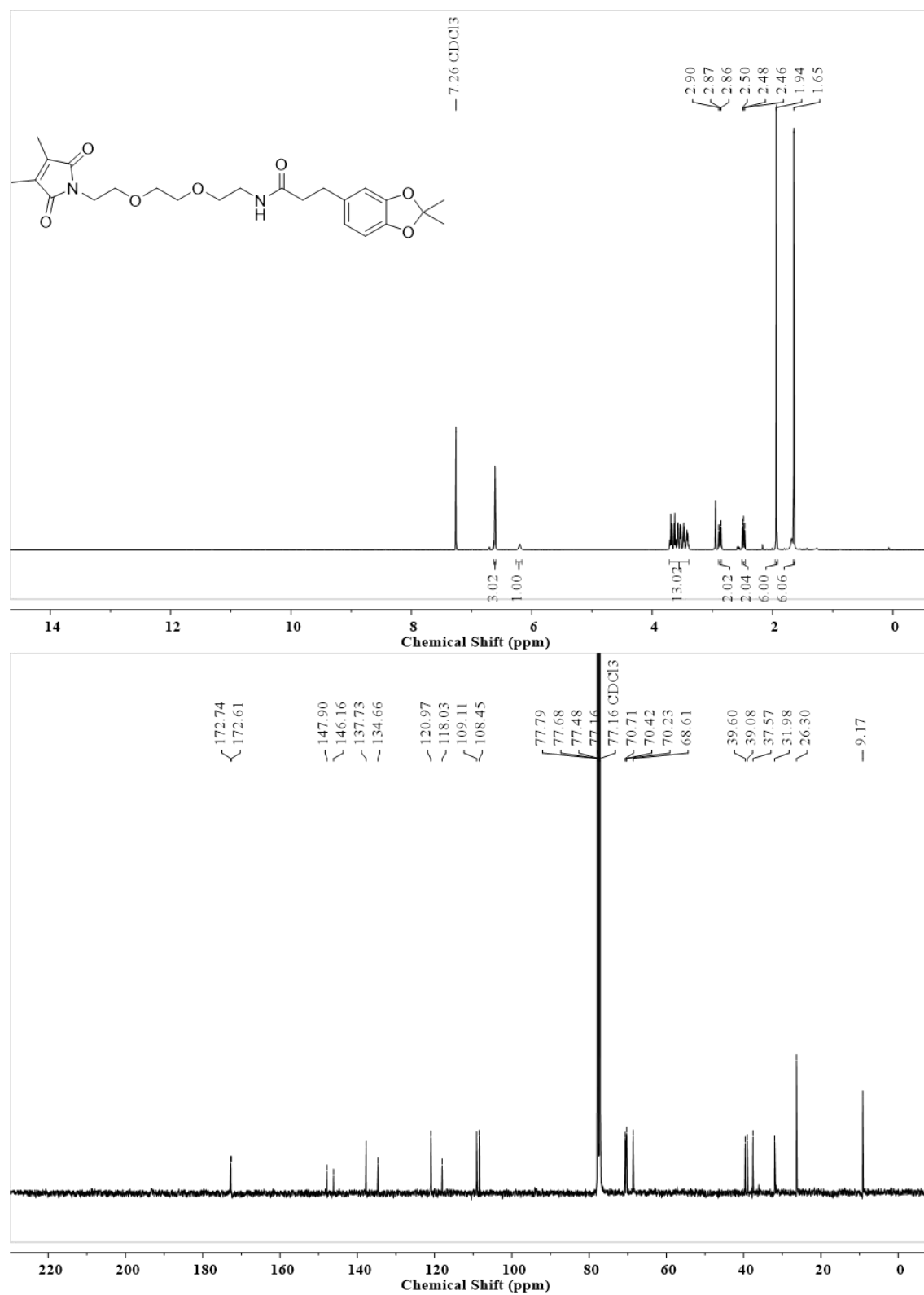
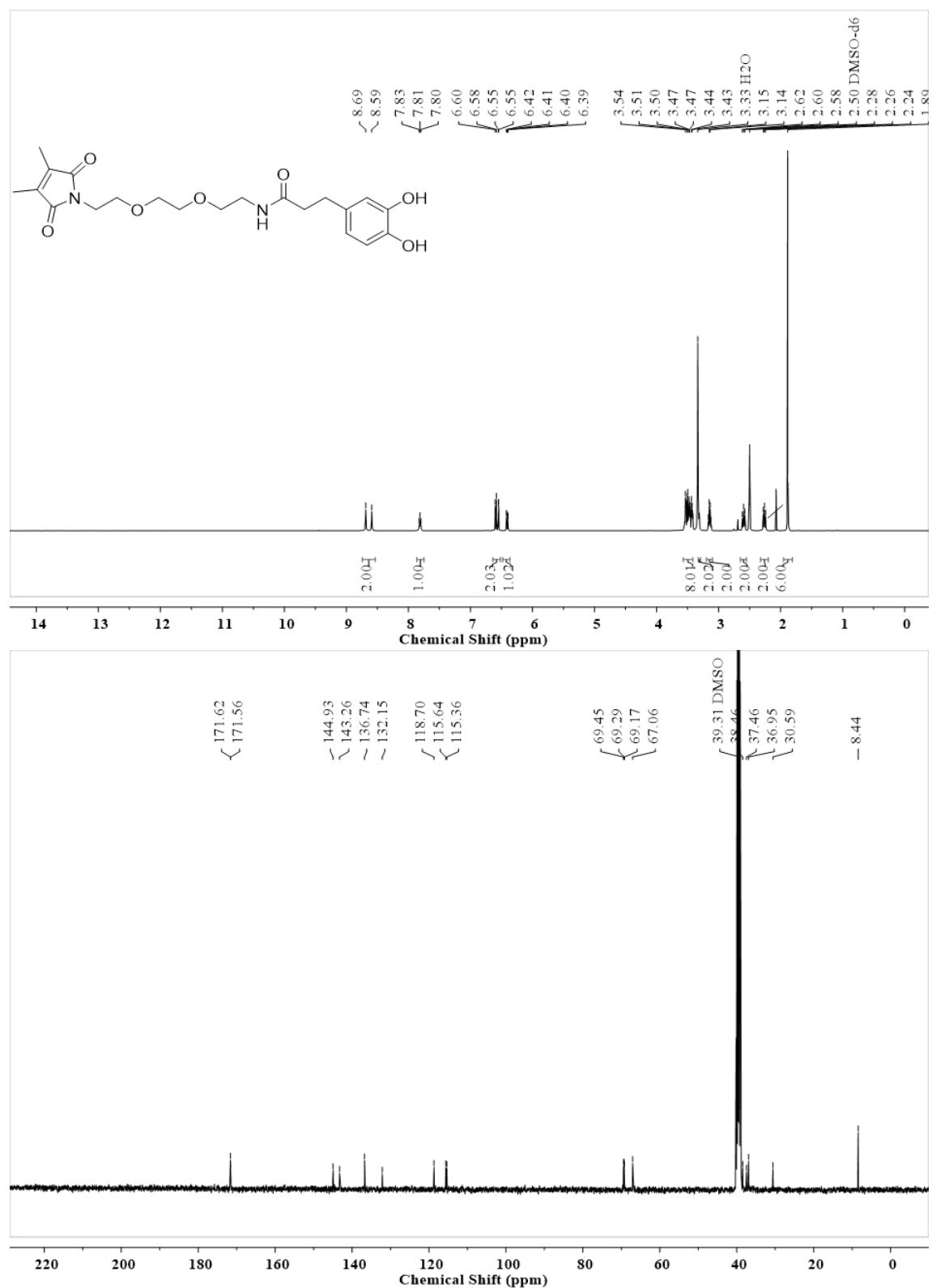
2,2-Dimethyl-1,3-benzodioxole-5-propanoic acid **7.17**

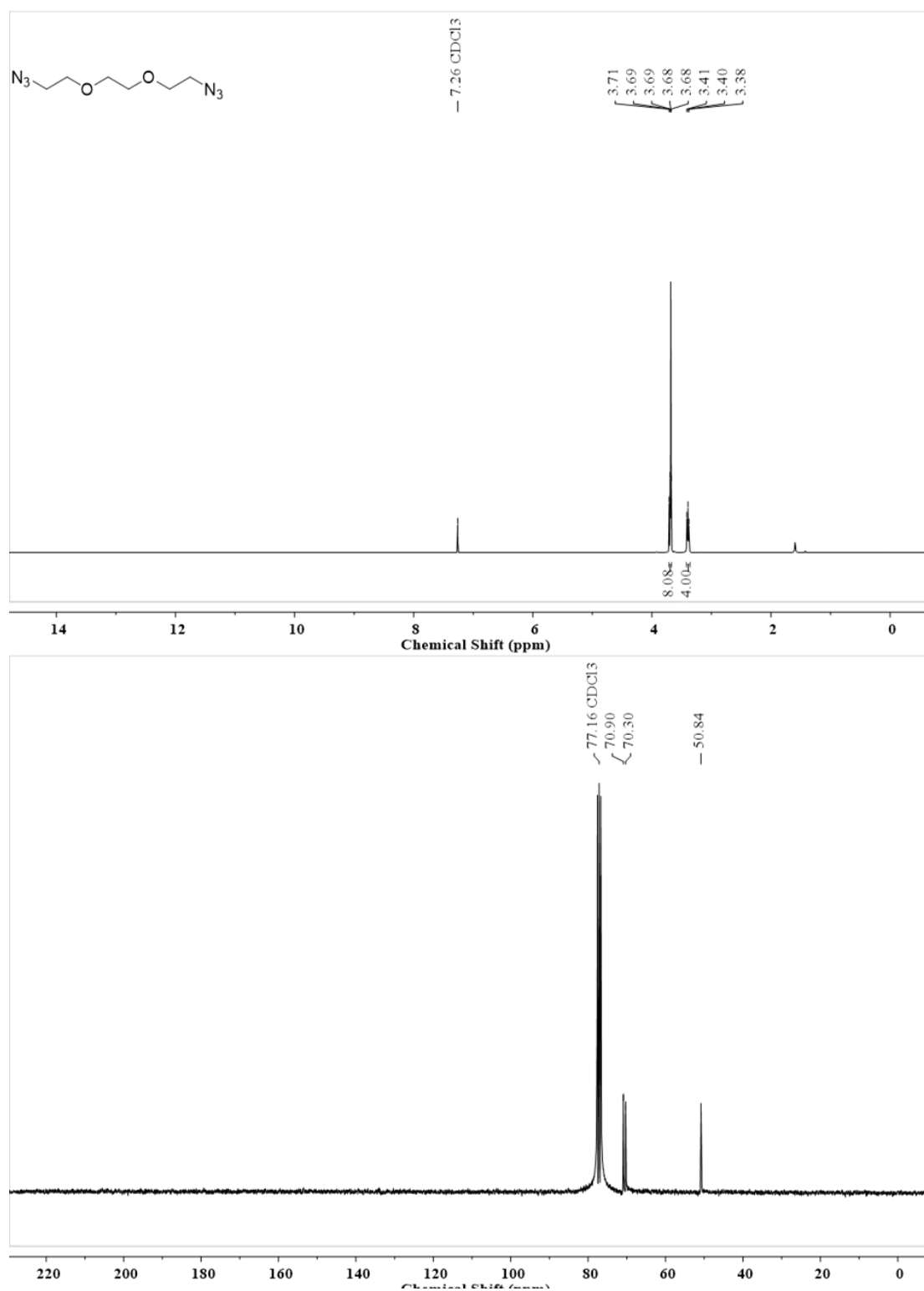
Figure S7.7. ^1H - and ^{13}C -NMR of compound **7.17** (400 MHz, 101 MHz, $\text{DMSO-}d_6$).

DMMI-Catechol-Acetonide 7.18

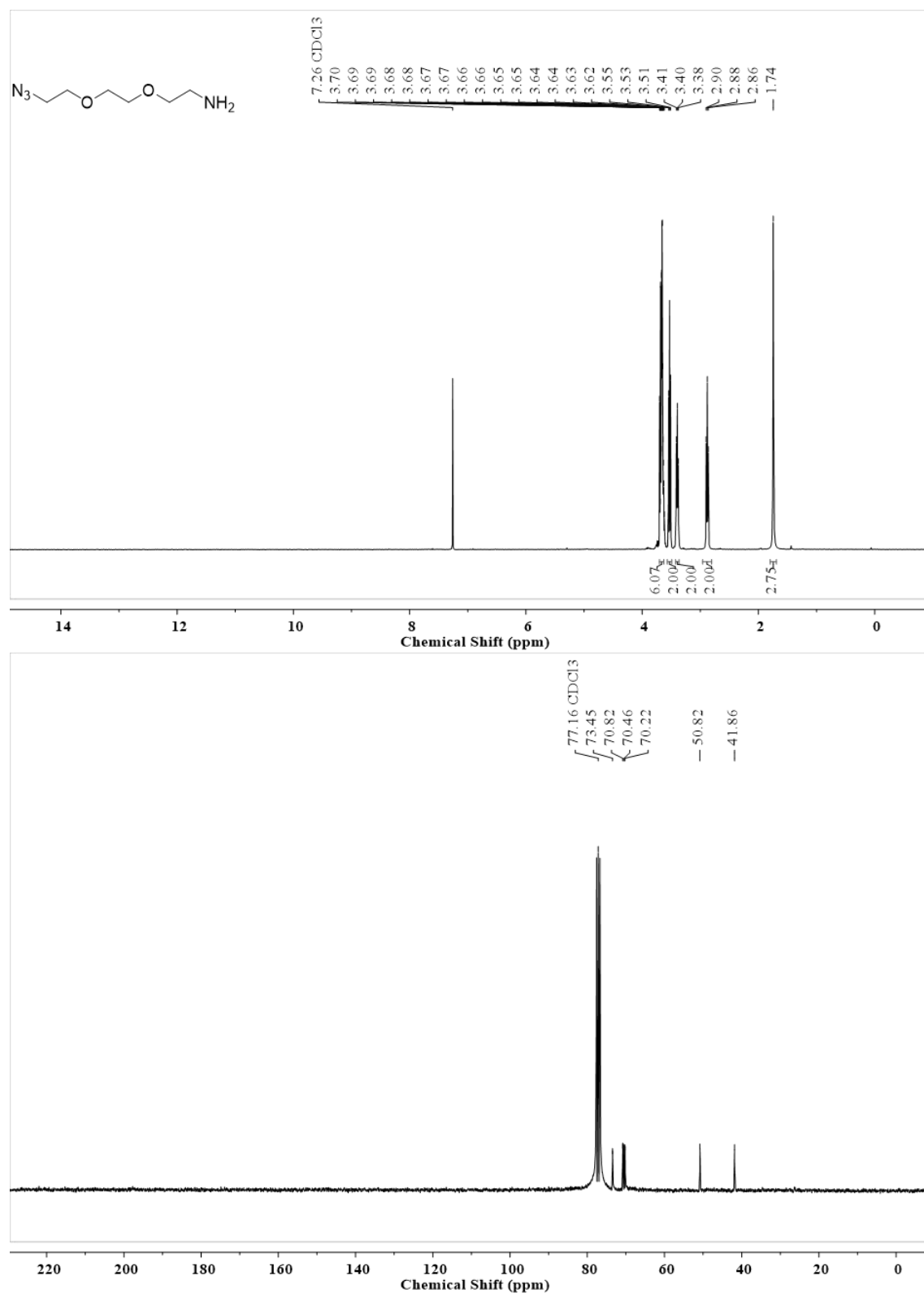
Figure S7.8 ^1H - and ^{13}C -NMR of Compound 7.18 (400 MHz, 101 MHz, CDCl_3).

DMMI-Catechol 7.6

Figure S7.9. ¹H- and ¹³C-NMR of Compound 7.6 (400 MHz, 101 MHz, DMSO-*d*₆).

1,2-Bis(2-azidoethoxy)ethane 7.20**Figure S7.10.** ¹H- and ¹³C-NMR of Compound 7.20 (300 MHz, 75 MHz, CDCl₃).

2-[2-(2-Azidoethoxy)ethoxy]ethan-1-amine 7.21

Figure S7.11 ¹H- and ¹³C-NMR of compound 7.21 (300 MHz, 75 MHz, CDCl₃).

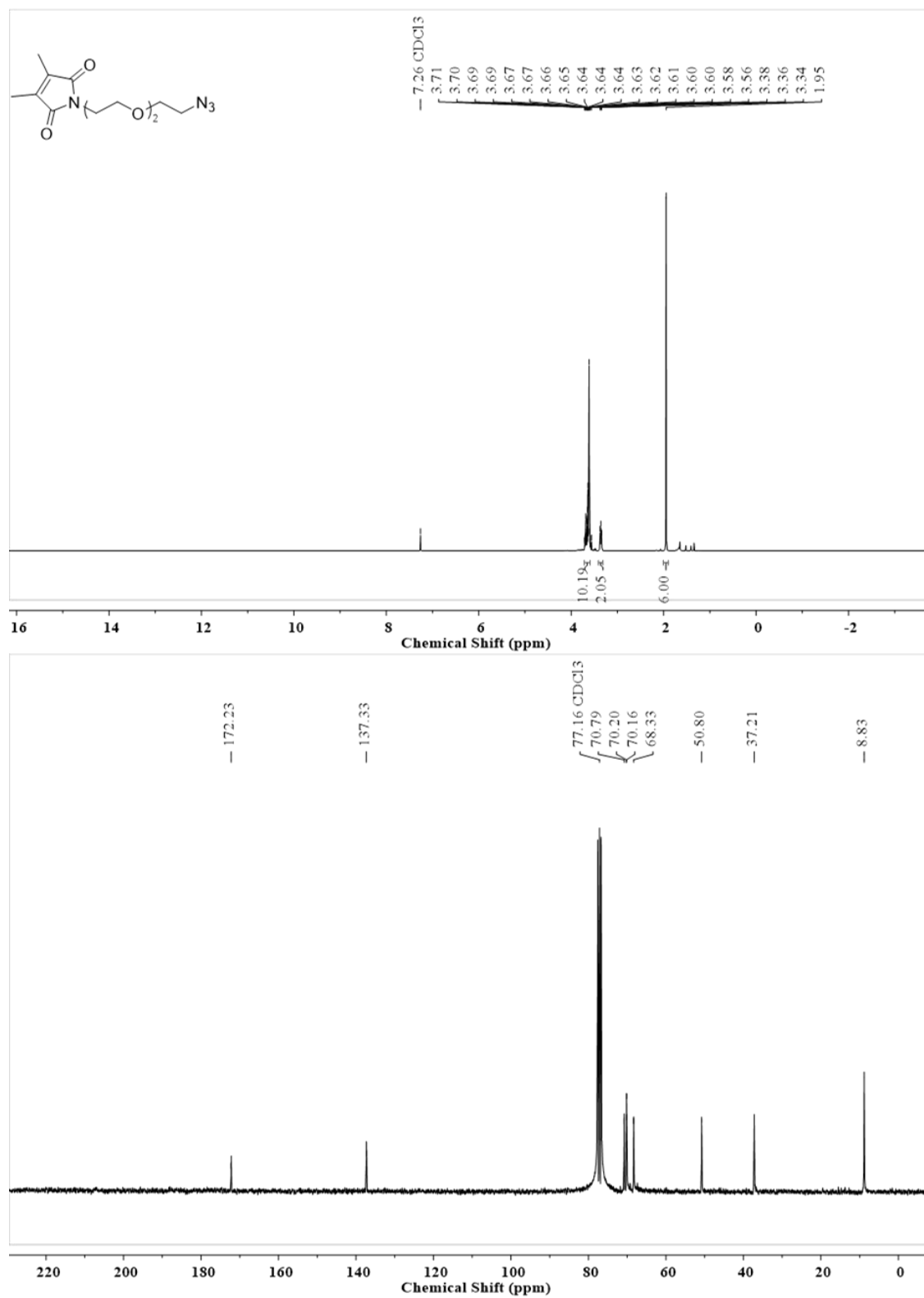
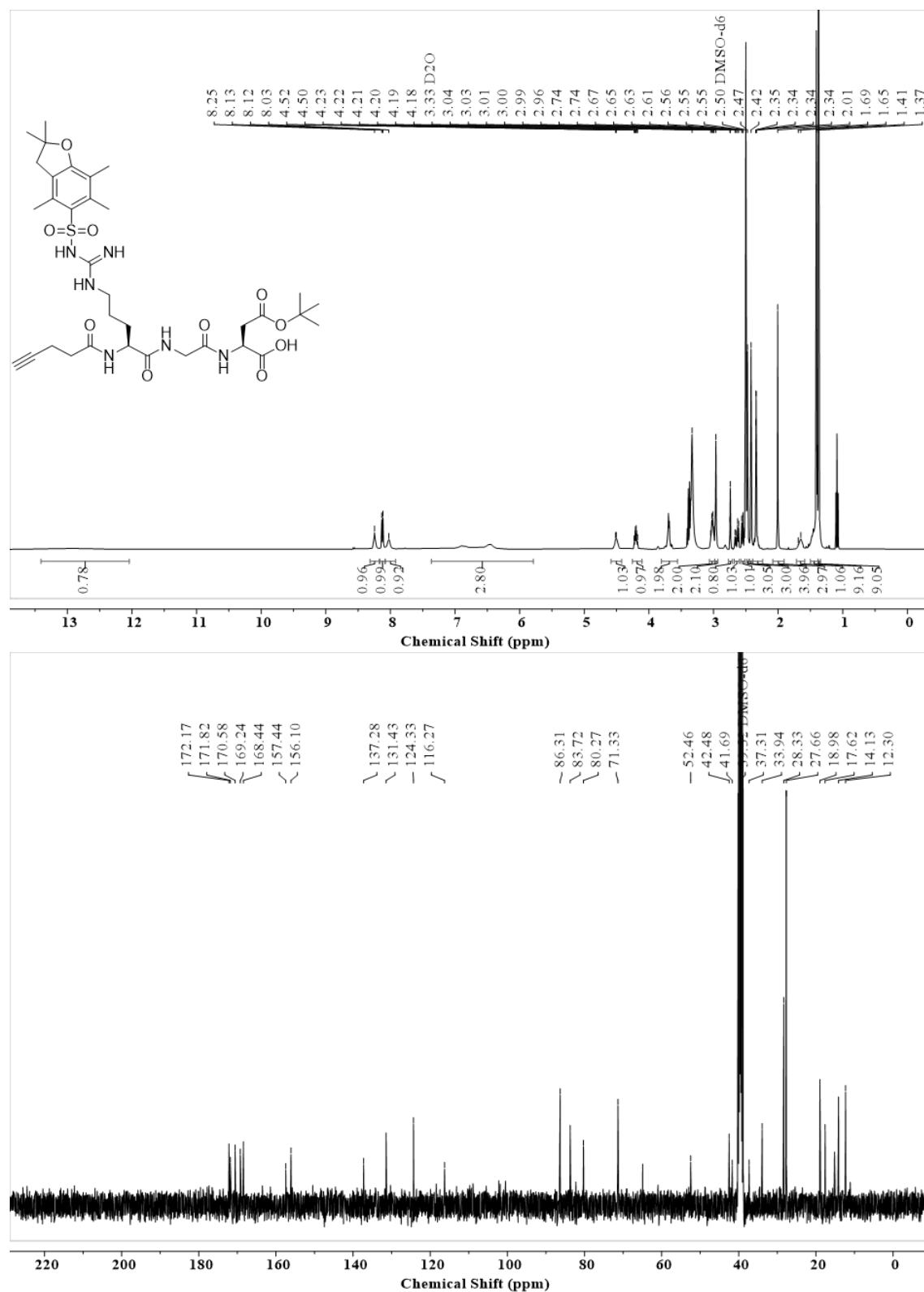
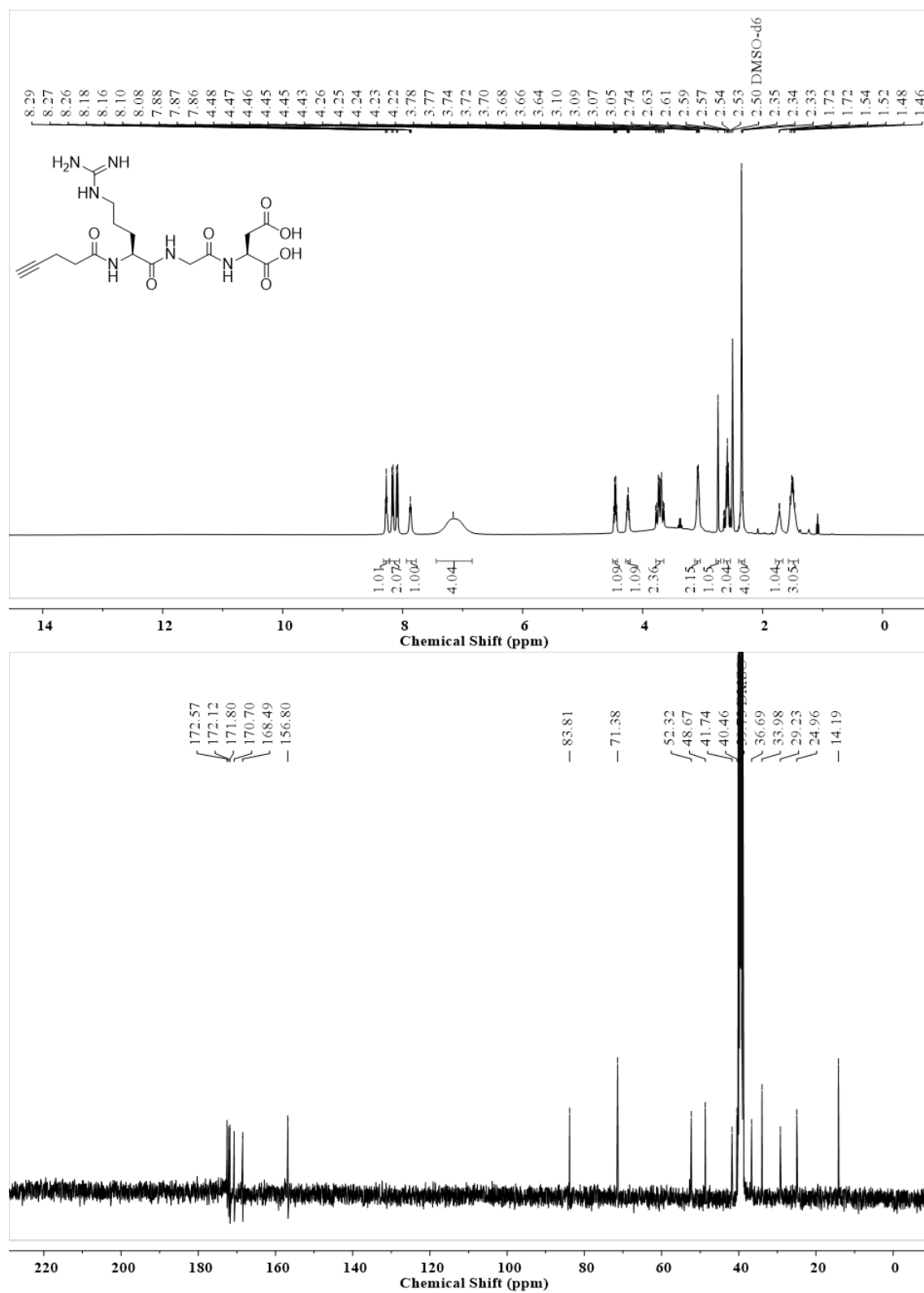
DMMI-¹EG-azide 7.22

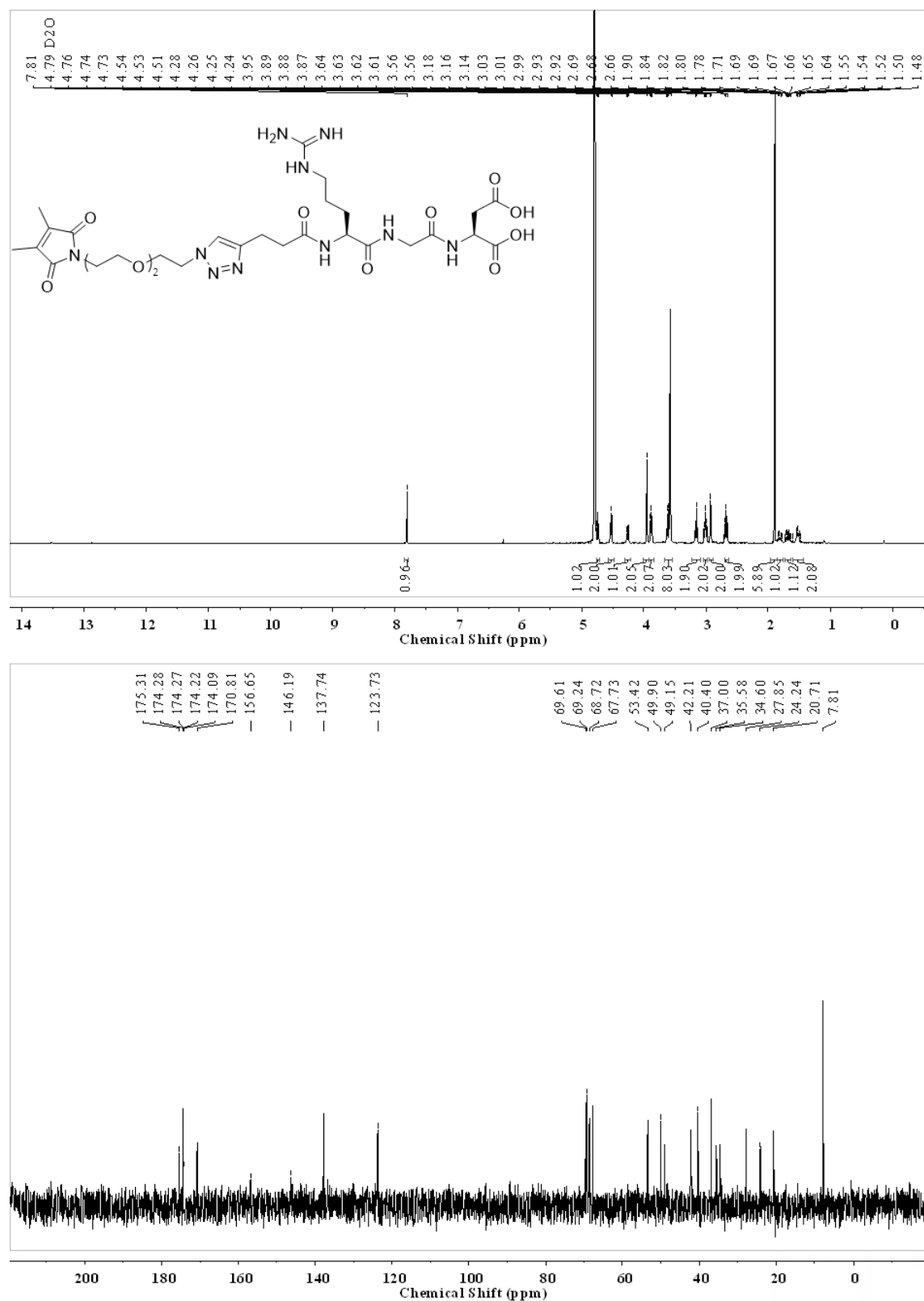
Figure S7.12. ¹H- and ¹³C-NMR of compound 7.22 (300 MHz, 75 MHz, CDCl₃).

Protected RGD-alkyne 7.23a

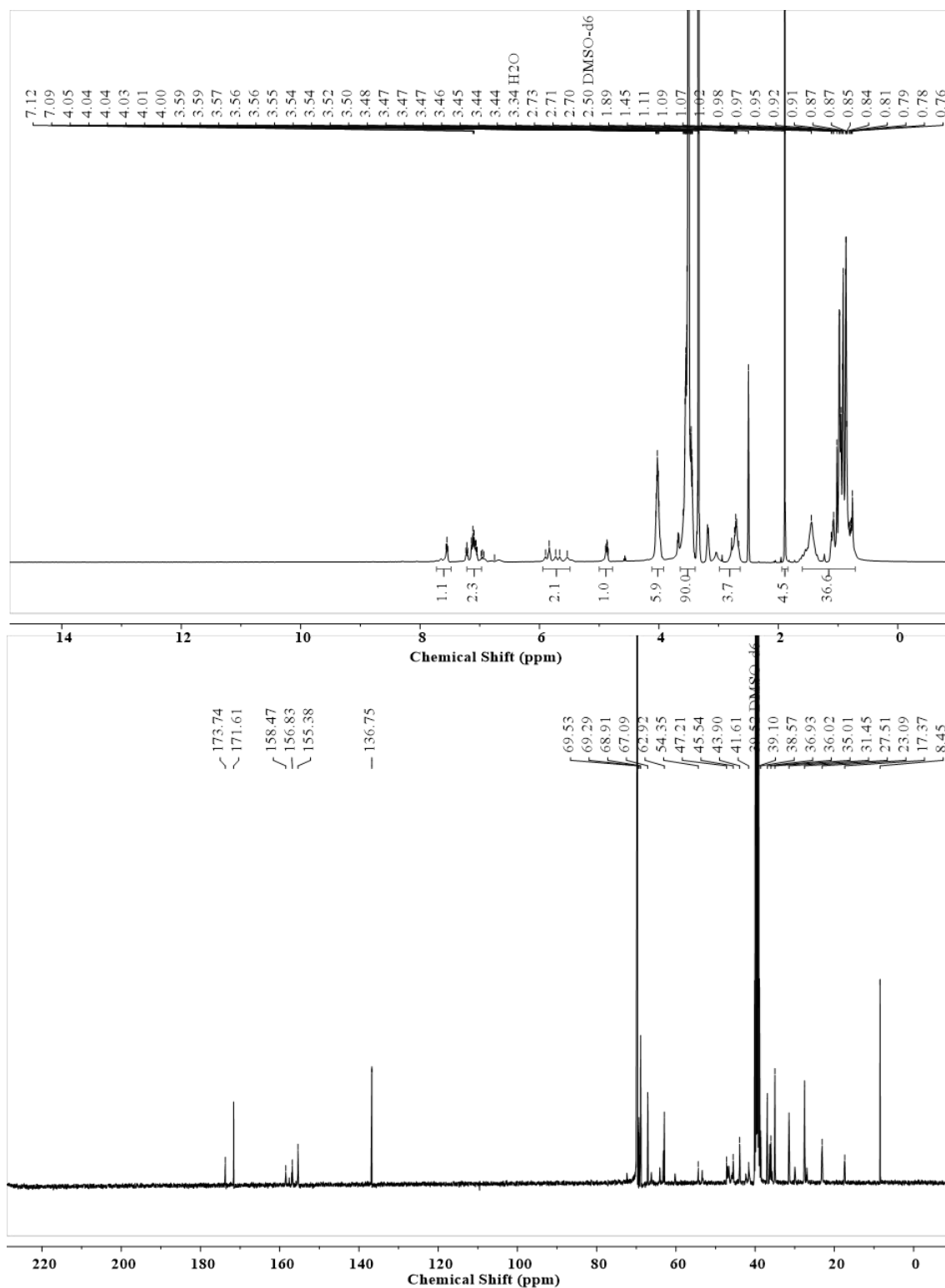
Figure S7.13. ¹H- and ¹³C-NMR of compound 7.23a (400 MHz, 101 MHz, DMSO-d₆).

RGD-alkyne 7.23

FigureS7.14. ^1H - and ^{13}C -NMR of compound 7.23 (400 MHz, 101 MHz, $\text{DMSO-}d_6$).

DMMI-¹EG-RGD 7.7Figure S7.15 ¹H- and ¹³C-NMR of Compound 7.7 (400 MHz, 101 MHz, D₂O).

PU-1.0k 7.5a

Figure S7.16. ^1H - and ^{13}C -NMR of compound 7.5a (400 MHz, 101 MHz, $\text{DMSO-}d_6$).

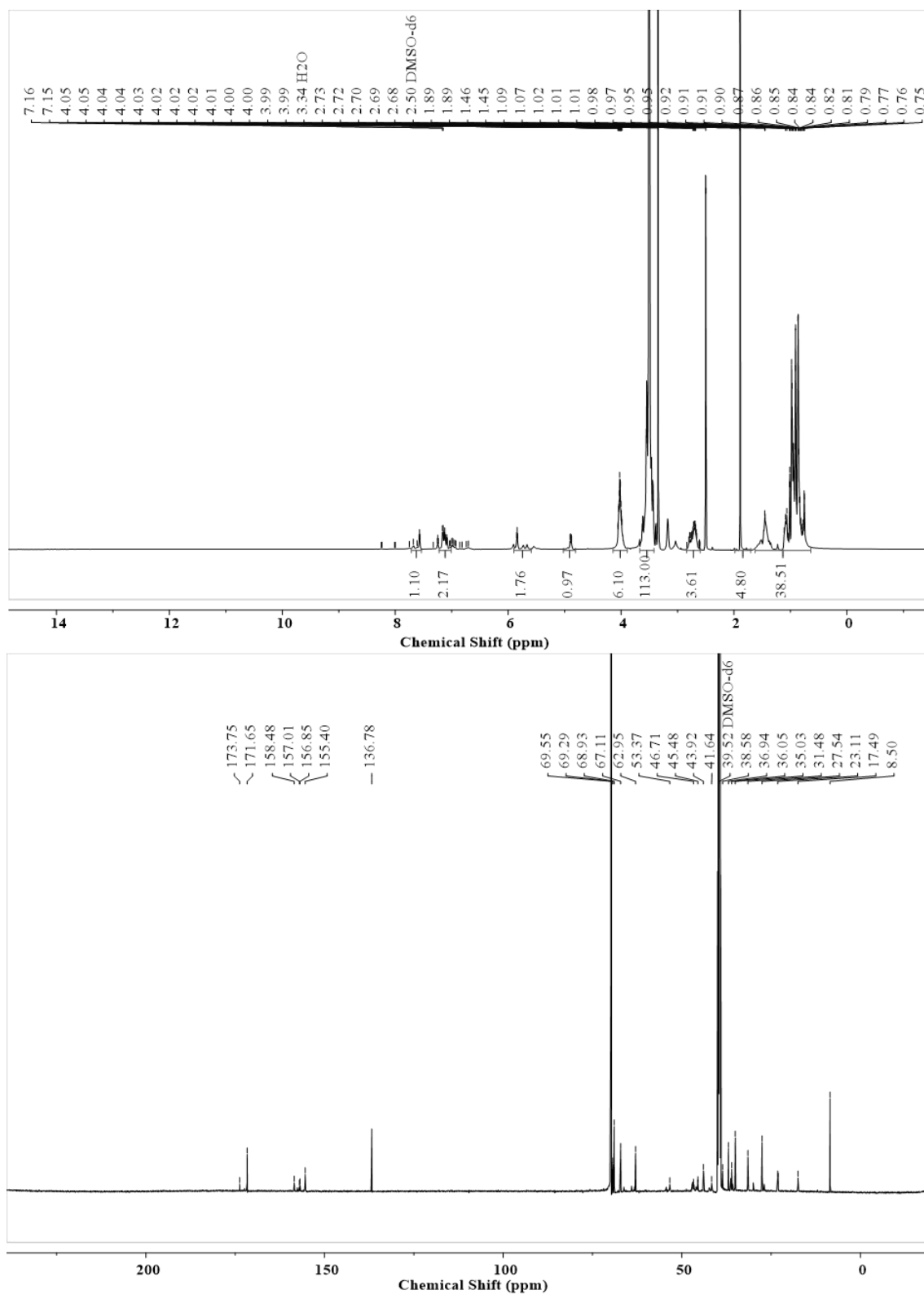
PU-1.5k^{0.6} 7.5b

Figure S7.17. ¹H- and ¹³C-NMR of compound 7.5b (400 MHz, 101 MHz, DMSO-*d*₆).

PU-1.5k 7.5c

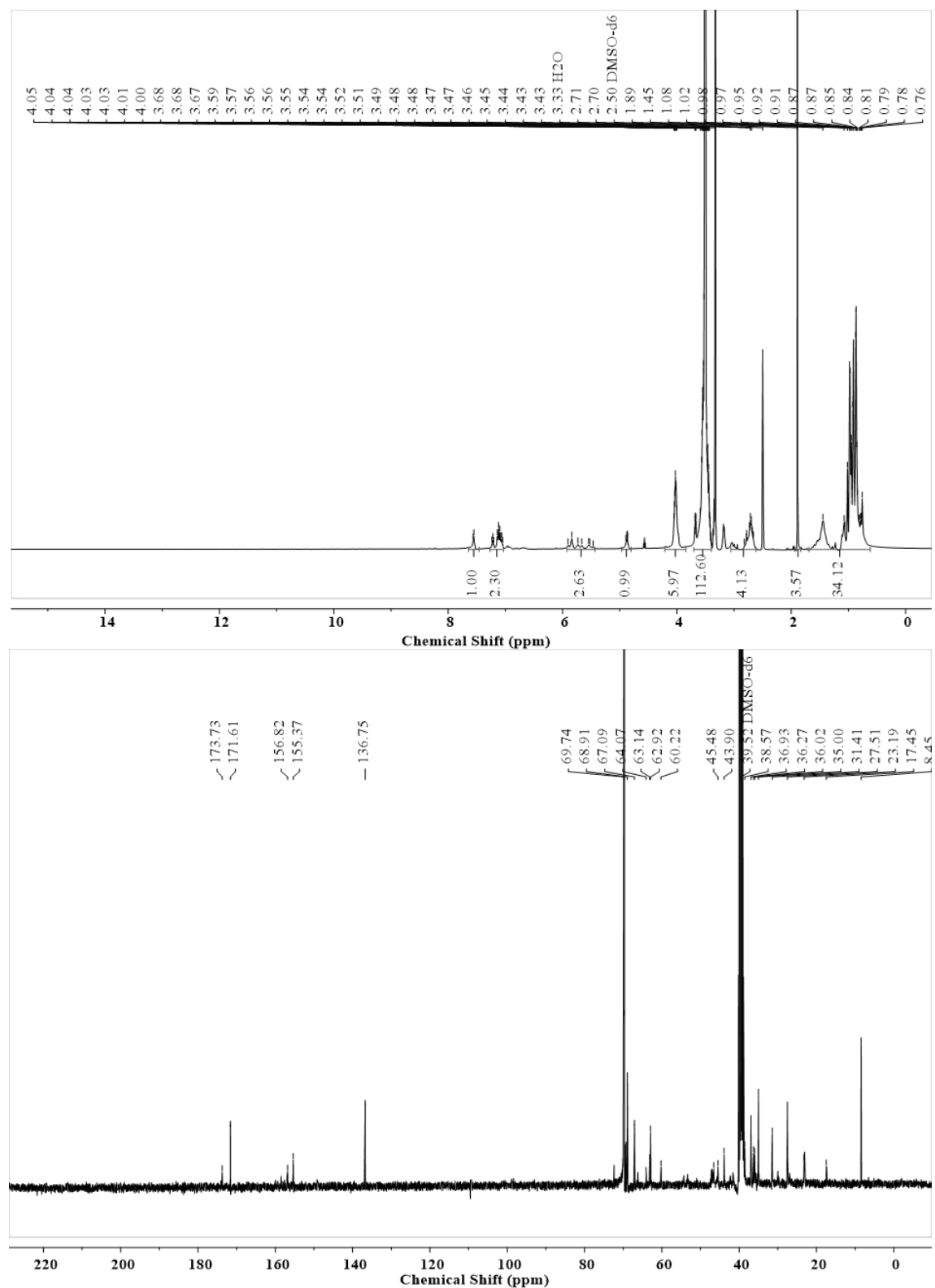
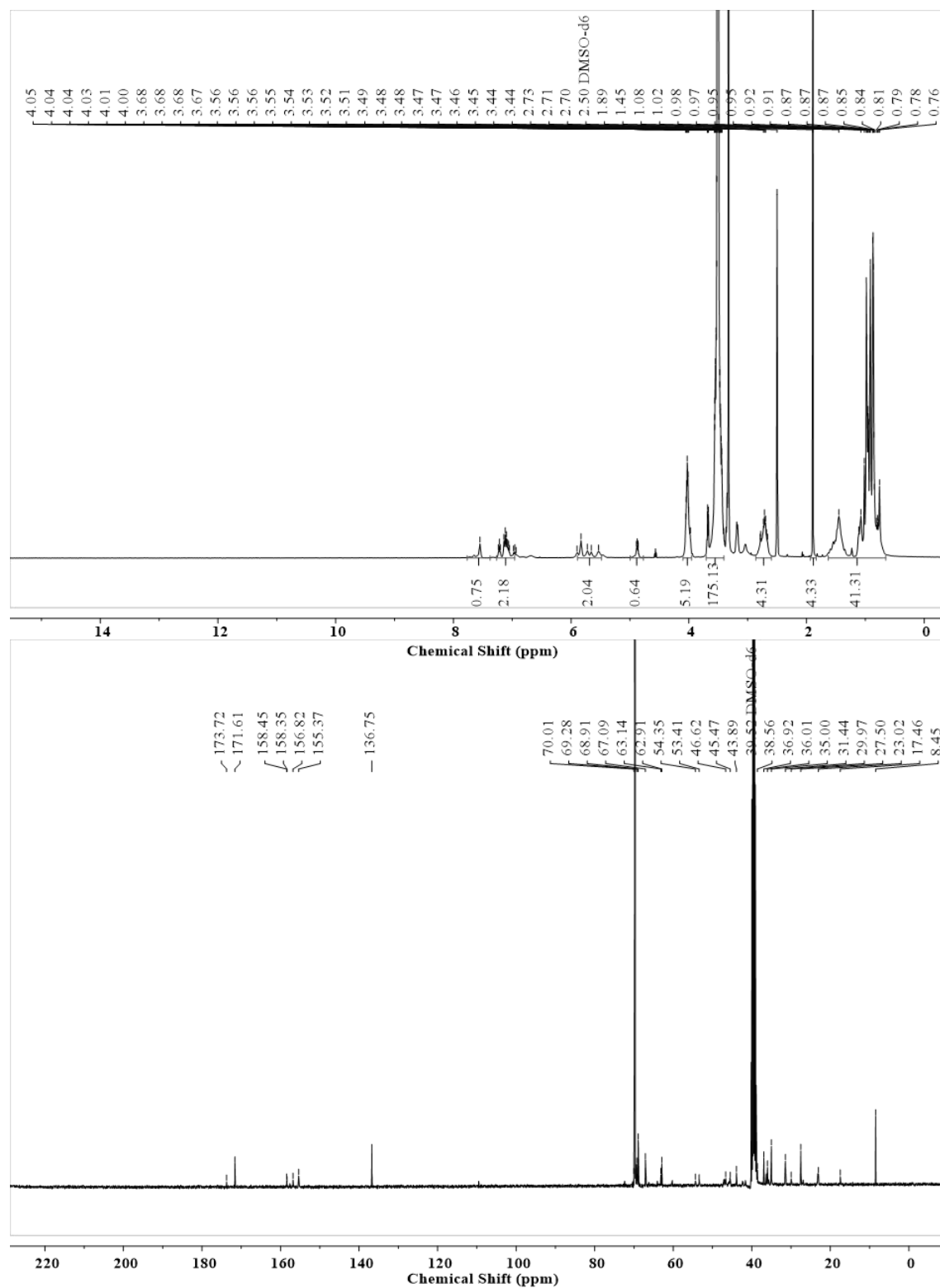
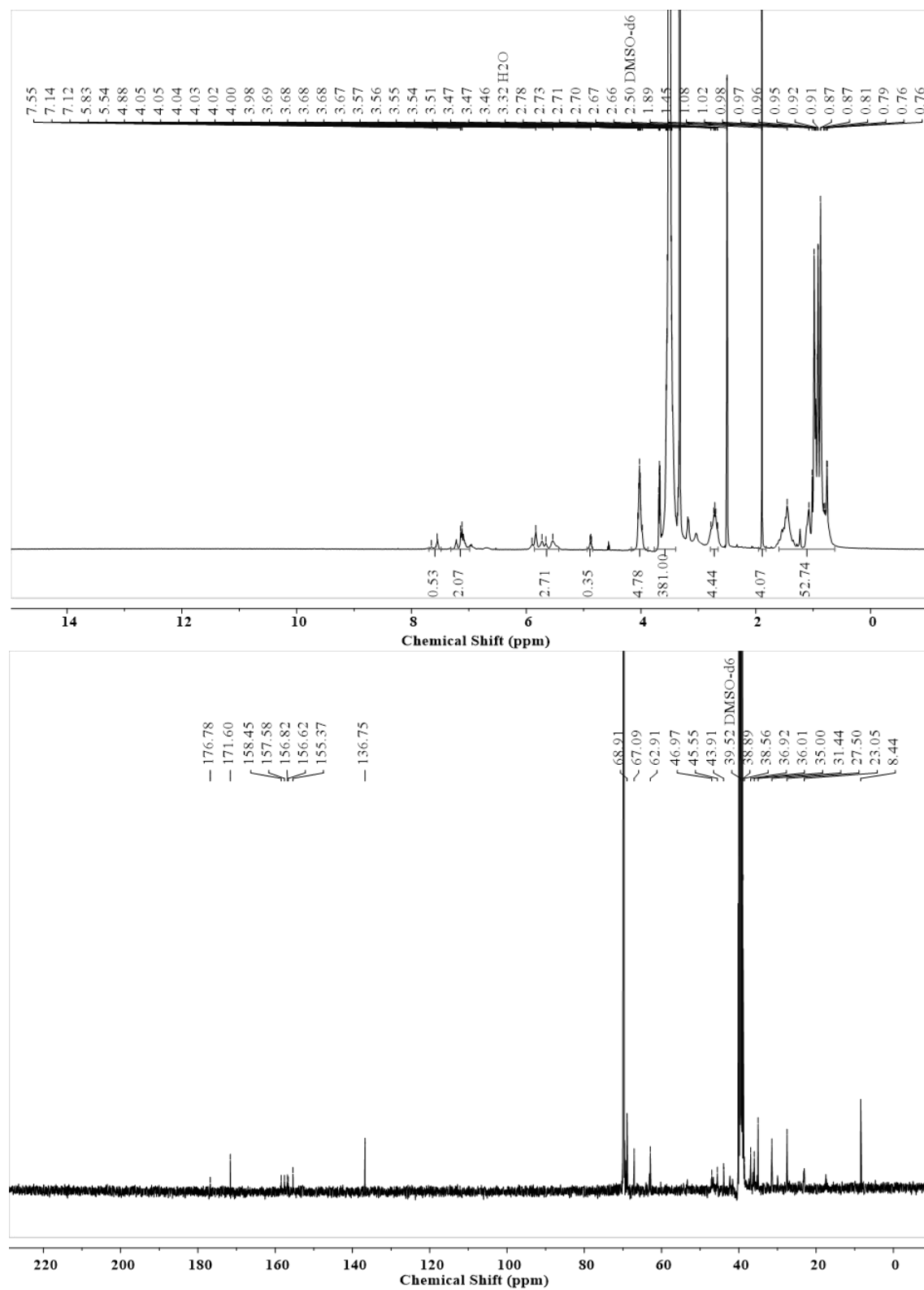


Figure S7.18. ^1H - and ^{13}C -NMR of compound 7.5c (400 MHz, 101 MHz, $\text{DMSO-}d_6$).

PU-2.0k 7.5d

Figure S7.19 ¹H- and ¹³C-NMR of PU-2k 7.5d (400 MHz, 101 MHz, DMSO-*d*₆).

PU-4.0k 7.5e

Figure S7.20 ¹H- and ¹³C-NMR of PU-4k 7.5e (400 MHz, 101 MHz, DMSO-d₆).

